Institute for Space and Nuclear Power Studies
School of Engineering
University of New Mexico
Albuquerque, NM 87131-0001

MULTI-PHYSICS DESIGN AND ANALYSES OF LONG LIFE REACTORS FOR LUNAR OUTPOSTS

TIMOTHY M. SCHRIENER and MOHAMED S. EL-GENK

FINAL REPORT No. UNM-ISNPS-1-2015

July, 2015

ACKNOWLEDGEMENTS

This research is partially funded by the University of New Mexico's Institute for Space and Nuclear Power Studies and is partially supported by a U.S. NRC Graduate Fellowship Grant # NRC-38-09-931 to the University of New Mexico.

MULTI-PHYSICS DESIGN AND ANALYSES OF LONG LIFE REACTORS FOR LUNAR OUTPOSTS

Timothy M. Schriener

B.S. Nuclear Engineering, Oregon State University, 2006

Ph.D. Engineering, University of New Mexico, 2015

Executive Summary

Future human exploration of the solar system is likely to include establishing permanent outposts on the surface of the Moon. These outposts will require reliable sources of electrical power in the range of 10's to 100's of kW_e to support exploration and resource utilization activities. This need is best met using nuclear reactor power systems which can operate steadily throughout the long ~27.3 day lunar rotational period, irrespective of location. Nuclear power systems can potentially open up the entire lunar surface for future exploration and development.

Desirable features of nuclear power systems for the lunar surface include passive operation, the avoidance of single point failures in reactor cooling and the integrated power system, moderate operating temperatures to enable the use of conventional materials with proven irradiation experience, utilization of the lunar regolith for radiation shielding and as a supplemental neutron reflector, and safe post-operation decay heat removal and storage for potential retrieval. In addition, it is desirable for the reactor to have a long operational life. Only a limited number of space nuclear reactor concepts have previously been developed for the lunar environment, and these designs possess only a few of these desirable design and operation features.

The objective of this research is therefore to perform design and analyses of long operational life lunar reactors and power systems which incorporate the desirable features listed above. A long reactor operational life could be achieved either by increasing the amount of highly enriched uranium (HEU) fuel in the core or by improving the neutron economy in the reactor through reducing neutron leakage and parasitic absorption. The amount of fuel in surface power reactors is constrained by the launch safety requirements. These include ensuring that the bare reactor core remains safely subcritical when

submerged in water or wet sand and flooded with seawater in the unlikely event of a launch abort accident. Increasing the amount of fuel in the reactor core, and hence its operational life, would be possible by launching the reactor unfueled and fueling it on the Moon. Such a reactor would, thus, not be subject to launch criticality safety requirements. However, loading the reactor with fuel on the Moon presents a challenge, requiring special designs of the core and the fuel elements, which lend themselves to fueling on the lunar surface.

This research investigates examples of both a solid core reactor that would be fueled at launch as well as an advanced concept which could be fueled on the Moon. Increasing the operational life of a reactor fueled at launch is exercised for the NaK-78 cooled Sectored Compact Reactor (SCoRe). A multi-physics design and analyses methodology is developed which iteratively couples together detailed Monte Carlo neutronics simulations with 3-D Computational Fluid Dynamics (CFD) and thermal-hydraulics analyses. Using this methodology the operational life of this compact, fast spectrum reactor is increased by reconfiguring the core geometry to reduce neutron leakage and parasitic absorption, for the same amount of HEU in the core, and meeting launch safety requirements. The multi-physics analyses determine the impacts of the various design changes on the reactor's neutronics and thermal-hydraulics performance.

The option of increasing the operational life of a reactor by loading it on the Moon is exercised for the Pellet Bed Reactor (PeBR). The PeBR uses spherical fuel pellets and is cooled by He-Xe gas, allowing the reactor core to be loaded with fuel pellets and charged with working fluid on the lunar surface. The performed neutronics analyses ensure the PeBR design achieves a long operational life, and develops safe launch canister designs to transport the spherical fuel pellets to the lunar surface. The research also investigates loading the PeBR core with fuel pellets on the Moon using a transient Discrete Element Method (DEM) analysis in lunar gravity. In addition, this research addresses the post-operation storage of the SCoRe and PeBR concepts, below the lunar surface, to determine the time required for the radioactivity in the used fuel to decrease to a low level to allow for its safe recovery.

The SCoRe and PeBR concepts are designed to operate at coolant temperatures ≤ 900 K and use conventional stainless steels and superalloys for the structure in the reactor core and power system. They are emplaced below grade on the Moon to take advantage of the regolith as a supplemental neutron reflector and as shielding of the lunar outpost from the reactors' neutron and gamma radiation. The SCoRe and PeBR concepts are designed with cores divided into six and three sectors, respectively. The sectors are thermally and neutronically coupled but hydraulically decoupled. Each sector is served by a separate cooling loop(s), with independent energy conversion and heat rejection radiator panels. This combination of a sectored core and power system integration with multiple loops avoids single point failures in reactor cooling, energy conversion, and heat rejection. These unique attributes would allow the reactor power system to continue operation, but at lower power, in the event one of the sectors experiences a Loss of Coolant (LOC) or a Loss of Cooling (LOCo). The power system could thus maintain a vital supply of electrical power to the lunar outpost for crew life support.

The performed multi-physics design and performance analyses of the SCoRe show that increasing the diameter of the UN fuel rods increases the core excess reactivity. The larger diameter rods, however, increase the NaK-78 coolant flow bypass near the walls of the core sectors. Scalloping the dividing walls of the core sectors produces a more even flow distribution. The use of ^{151}Eu spectral neutron poison additive to the UN fuel ensures subcriticality during a water submersion accident, for the compact SCoRe core, with the highest excess reactivity and lowest mass. The redesigned Solid-Core Sectored Compact Reactor (SC-SCoRe) with a monolithic solid core of Oxide Dispersion Strengthened Molybdenum (ODS-Mo) achieves a long operational life of 21 years at a nominal power of 1,000 kW_{th}. The high thermal conductivity ODS-Mo core structure allows the reactor to continue safe operation in the event that one of the core sectors experiences a LOC of LOCo. The ODS-Mo solid core readily conducts heat generated in that sector to the adjacent core sectors, to be removed by the flowing liquid metal coolant. The SCoRe power system with SiGe energy conversion is fully passive and load following. In addition, the decay heat is removed safely and passively following shutdown of the reactor at end of life.

Neutronics and analyses show that the PeBR can achieve a very operational life of 66 years at a nominal thermal power of 471 kW_{th} by fueling the reactor core on the Moon. This full power operational life is beyond what is possible with a reactor fueled at launch like the SC-SCoRe. Neutronics safety analysis of the fuel pellets transport canisters for the PeBR shows that they are made highly subcritical in a water submersion accident. This is achieved using a combination of favorable geometry and neutron absorbers. The DEM fuel loading simulation of the PeBR on the lunar surface demonstrates that the PeBR core sectors can be successfully fueled in lunar gravity.

Post-operation storage analyses of the SC-SCoRe and PeBR concepts show that the radioactivity in the fuel decays away to a sufficiently low level within 300 years. The radiation field around the post-operational reactor at that time is low enough to allow humans to safely handle and retrieve the cores, for potential recovery of the valuable quantities of ^{235}U remaining in the fuel.

TABLE OF CONTENTS

EXECUTIVE SUMMARY…… iii

LIST OF FIGURES……..…… x

LIST OF TABLES……..…… xxiv

NOMENCLATURE……...… xxvi

1. INTRODUCTION…… 1

1.1. Selected Reactor Concepts for Lunar Surface Power…….. 5

1.2. Research Objectives……. 7

2. BACKGROUND…….. 10

2.1. The Lunar Environment…….. 10

2.2. Future Lunar Outposts…… 14

2.3. Space Nuclear Power Systems for Lunar Outposts…… 16

2.4. Placement of Nuclear Reactor Power System on the Moon…….. 20

2.5. Proposed Surface Power Reactor Designs…….……. 26

3. MULTI-PHYSICS DESIGN AND ANALYSES OF SECTORED COMPACT REACTOR (SCoRe) FOR LUNAR OUTPOSTS…… 34

3.1. Multi-Physics Analyses Methodology…… 35

3.2. SCoRe Reactor Design Evolution ……..… 39

3.2.1. Placement of SCoRe Integrated Power System on the Lunar Surface …… 43

3.2.2. SCoRe-N_{18}……. 47

3.2.3. SCoRe-N_5……..…… 50

3.2.3. SC-SCoRe……..…… 50

3.3. Multi-Physics Design and Analyses…….……. 54

3.3.1. Neutronics Analyses…….. 56

3.3.2. Thermal-Hydraulics Analyses Component…… 59

3.3.3. Integrated System Analyses…….. 62

3.4. Parametric Analyses of the SCoRe-N_{18}……..…… 63

3.4.1. Geometrical Considerations…….. 66

3.4.2 Effect of Fuel Rod Diameter…….. 69

3.4.2.1. Effect of ^{157}GdN concentration…….. 69

3.4.3. Redundancy in Reactor Control…… 71

3.5. Neutronics and Thermal-Hydraulics Analyses of SCoRe-N_5…….**....** 79

3.5.1. Analyses Methodology …… 80

3.5.2. Effects of the Scalloped Core Sectors Walls…… 81

3.5.3. Effect of Spectral Shift Absorber Isotopes…… 83

3.6. Thermal-Hydraulic Analyses of SCoRe-N_5 …… 90

3.7. Hot-Clean Reactivity of the Reference SCoRe-N_5 …… 98

3.8. Thermal-Hydraulics and Safety Analysis of SCoRe-N_5…….**....** 99

3.8.1. Analyses Methodology……. 100

3.8.2. Thermal-Hydraulics Analyses at Nominal Operation…… 103

3.8.3. Thermal Analyses of Core Sector Experiencing a LOC…… 105

3.8.4. Modified Core Structure to Enhance Thermal Conductance… 109

3.9. Thermal-Hydraulics and Safety Analyses of the SC-SCoRe……. 113

3.9.2. Nominal Operation Result…… 117

3.9.3. Analyses Results of a SC-SCoRe with a Sector Experiencing a LOC or a LOCo…….. 119

3.9.4. Calculated Temperature and Flow Fields in the Upper Plenum and Exit Duct of SC-SCoRe…….. 131

3.10. Neutronics Analyses and Reactor Operation Life Estimate of SC-SCoRe …… 137

3.10.1. SC-SCoRe Neutronics Results…… 138

3.10.2. Estimate of Reactor Operation Life…… 139

3.11. Highlights and Concluding Remarks…….. 140

4. DESIGN AND FUEL LOADING ANALYSES OF THE PELLET BED REACTOR (PeBR) FOR LUNAR SURFACE POWER…….. 142

4.1. Analyses Methodology…….. 142

4.2. PeBR Design and Lunar Surface Power System…… 146

4.2.1. Placement of PeBR on the Lunar Surface……. 148

4.2.2. PeBR Power System for Lunar Surface Power…… 150

4.2.3. Fuel Pellet Design……. 152

4.2.4. Selection of Structural Materials…….. 154

4.3. Neutronics Analysis Methodology for the PeBR…… 158

4.3.1. Fuel Depletion Analysis Methodology …… 159

4.3.2. Design and Analyses of the PeBR for Lunar Surface Power… 159

4.4. Analyses Results and Discussion…… 160

4.4.1. Neutron Energy Spectra and Power Profiles in the PeBR Core 165

4.4.2. PeBR Operational Life Estimate…… 169

4.4.3. Analysis of Fuel Pellets Launch Canisters…… 171

4.5. Fuel Loading on the Lunar Surface…… 175

4.5.1. Simulation Methodology…….. 175

4.5.2. Results and Discussion …… 181

4.5.3. Spatial Porosity Distributions…… 183

4.6. Highlights and Concluding Remark…… 187

5. POST-OPERATION STORAGE OF REACTORS FOR LUNAR SURFACE POWER…….. 188

5.1 Post-Operation Storage of Nuclear Reactors on the Moon…….. 188

5.2. Radioactivity Source Term in the SC-SCoRe……. 190

5.3. SC-SCoRe Post-Operation Storage…… 192

5.3.1. Radiation Field around the Post-Operational SC-SCoRe……. 194

5.4. Post-Operational Storage of PeBR Fuel Pellets……. 198

5.5. Decay Heat Removal Following Shutdown at End-of-Life…… 200

5.6. Highlights and Concluding Remarks ……. 204

6. SUMMARY AND CONCLUSIONS…… 206

6.1. Recommendations for Further Research…… 211

APPENDICES…… 212

APPENDIX A: Methods for Determining Operation Life for Space Reactors with Fast Energy Spectra…….. 212

A.1. Methods and Validation…….. 213

A.2. Simplified Method for Burnup Analysis…….…… 213

A.3. Comparison of Code Packages…….…. 215

A.4. Application to Space Reactors……..…….. 220

A.4.1. Operation Life Estimates…… 221

A.5. Application of the Simplified Method to PWRs……..… 225

APPENDIX B: Effect of Reactivity Control Options on Space Nuclear Reactors …… 229

B.1. S^4 Reactor Core Design……..... 229

B.2. Control Options for the S^4 Reactor…… 231

B.3. Reactivity Requirements…….…… 233

B.4. Methods and Analysis…….…..... 234

B.5. Rotating Control Drums……..…… 236

B.5.1. Effect of B_4C Segment Thickness on Reactivity……... 236

B.5.2. Effect of B_4C Segments on Operation Life…….……... 237

B.6. Performance Comparisons of Rotating Drums and Sliding Reflector Segments Control…… 239

B.6.1. Reactor Reactivity Control……. 239

B.6.2. Neutron Flux Distributions……. 241

B.6.3. Fission Power Profiles……..….. 242

B.6.4. Reactor Operational Life……..….. 247

APPENDIX C: Transient DynMo-TE Simulation of the SCoRe Power System …… 249

C.1. Description of the SCoRe-NaK-TE Power System……..…… 249
C.2. DynMo-TE Simulation Model……..… 252
C.3. Transient Simulation Results and Analyses……. 254
C.3.1. Power System Startup……....……. 254
C.3.2. Reactor Nominal Operation…….……. 257
C.3.2.1. Reactivity Depletion during Nominal Operation……. 258
C.3.2.2. Effect of the Interval of External Reactivity Insertion.... 259
C.3.3. Power System Shutdown at End-of-Life.....….... 262
APPENDIX D: Comparative Analyses of CFD and Thermal-Hydraulics Methodology for the SC-SCoRe……. 266
D.1. Methodology…….…….. 267
D.1.1. Turbulence Models…….…… 269
D.1.2. Numerical Meshing……..….. 271
D.2. Results and Discussion……..……. 275
D.2.1. Fuel Stacks and Solid Core Temperatures……. 275
D.2.2. Temperature and Velocity Profiles in Flow Channels…… 278
D.2.3. Velocity Profiles in Coolant Channels……... 282
D.2.4. Pressure Losses……..… 285
D.2.5. Mixing in Upper Plenum and Exit Duct…… 290
D.3. Computational Requirements…….……. 295
D.4. Comparison with the Detached Eddy Simulation Model……..... 296
REFERENCES…….. 301

LIST OF FIGURES

Fig. 1.1. - Artist's conceptions of space nuclear power system concepts emplaced on the lunar surface [NASA]…….…. 2

Fig. 1.2. - SCoRe reactor emplaced in a trench below grade on the Moon and surrounded by backfilled regolith……. 6

Fig. 2.1. - Lunar surface temperatures versus the Moon's rotational period [Dallas, Diaguila, and Saltsman 1971]…….…….. 14

Fig. 2.2. - Schematic of generic space nuclear power system for lunar surface power …….…... 17

Fig. 2.3. - Placement options for lunar power reactors…….…….. 21

Fig. 2.4. - Prometheus FSPS elements deployed on the surface before construction of regolith sandbag shield [Elliott et al. 2005]…….…. 27

Fig. 2.5. - Radial cross section views of SCoRe-S concepts; (a) with 16 cm thick BeO radial reflector, (b) with radial reflector thickness sized to have equal excess reactivity using supplemental regolith reflector [Hatton and El-Genk 2009; El-Genk et al. 2005]…….…….…. 29

Fig. 2.6. - Schematic of SCoRe-S_{11} power system [El-Genk and Tournier 2006a] ……. 30

Fig. 2.7. - Artist's conception of AFSPS power system emplaced on the Moon with the reactor core buried in the lunar regolith. [Mason, Poston, and Qualls 2008]……. 31

Fig. 3.1. - Iterative coupling scheme for neutronics and thermal-hydraulics in the developed multi-physics methodology……. 34

Fig. 3.2. - Schematic of the SCoRe integrated power system with thermoelectric (TE) energy conversion, showing a pair of primary and the secondary loops with EM pumps coupled to a core sector and heat rejection radiator panels [Schriener and El-Genk 2014b]……... 36

Fig. 3.3. - An outline of multi-physics design and safety analyses for SCoRe concepts for a lunar outpost…… 37

Fig. 3.4. - Sodium-potassium binary phase diagram [Foust 1972]…….…… 41

Fig. 3.5. - Below grade SCoRe power system with heat pipes radiator panels erected on the lunar surface [Schriener and El-Genk 2014b]……...….. 44

Fig. 3.6. - Cross-sectional views of the initial SCoRe-N_{18} [Schriener and El-Genk 2011] …..……..… 46

Fig. 3.7. - Heat flow path for a core sector experiencing a LOC or LOCo [Schriener and El-Genk 2011]…… 47

Fig. 3.8. - Partial cross-sectional view of a UN fuel rod [Schriener and El-Genk 2011] …… 48

Fig. 3.9. - Cross-section views of the SCoRe-N_5 core: (a) elevation view and (b) plan view [Schriener and El-Genk 2012a]…… 49

Fig. 3.10. - SCoRe-N_5 core sector arrangements …… 51

Fig. 3.11. - Cross-section views of the SC-SCoRe core: (a) elevation view and (b) plan view [Schriener and El-Genk 2014b]……. 52

Fig. 3.12. - Section views of SC-SCoRe MCNPX and STAR-CCM+ models 55

Fig. 3.13. - Emplacement of SCoRe reactor below grade on the lunar surface and surrounded with backfilled regolith…….. 57

Fig. 3.14. - Arrangement of rows of UN fuel rods in SCoRe-N_{18} core sector [Schriener and El-Genk 2011]…… 64

Fig. 3.15. - Reference flow areas for constant unit cell porosity and constant sector porosity [Schriener and El-Genk 2011]…… 65

Fig. 3.16. - Radial cross section views of selected SCoRe-N_x design concepts [Schriener and El-Genk 2011]……. 66

Fig. 3.17. - Effects of porosity on UN fuel rod diameter and p/d [Schriener and El-Genk 2011]……. 67

Fig. 3.18. - Effects of R_f on the total reactor mass and the active core H/D [Schriener and El-Genk 2011]…… 68

Fig. 3.19. - Changes in the concentration of ^{157}GdN spectral shift absorber in the UN fuel pellets with the number of rows of fuel rods per sector, R_f [Schriener and El-Genk 2011]…… 70

Fig. 3.20. - Neutron absorption in (a) ^{157}GdN fuel additive, and (b) $^{157}Gd_2O_3$ vessel coating in bare reactors submerged in wet sand and flooded with sea water, following a launch abort accident [Schriener and El-Genk 2011]….. 72

Fig. 3.21. - SCoRe-N_5-S with 12, 9, and 6 control drums in the shutdown position [Schriener and El-Genk 2011]……. 73

Fig. 3.22. - Reactivity effects for varying B_4C segment thickness and shutdown requirement for SCoRe-N_5-S [Schriener and El-Genk 2011]…… 74

Fig. 3.23. - Design surface of SCoRe-N_x-U concepts with constant unit cell porosity of the UN fuel rods. [Schriener and El-Genk 2011]…….. 75

Fig. 3.24. - Design surface of SCoRe-N_x-S concepts with constant sector porosity [Schriener and El-Genk 2011]…… 76

Fig. 3.25. - Comparison of design surfaces of SCoRe-N-U and SCoRe-N-S concepts [Schriener and El-Genk 2011]…….. 77

Fig. 3.26. - Calculated temperatures in SCoRe-N_5 core sector at 200 kW_{th} with (a) smooth sector walls and (b) scalloped sector walls at the axial location of the peak fuel temperature……. 82

Fig. 3.27. - Reactivity levels for SCoRe-N_5 concepts with candidate SSA additives [Schriener and El-Genk 2012a]…… 84

Fig. 3.28. - Effect of the SSA additive isotopes on the active height of the SCoRe-N_5 reactor core [Schriener and El-Genk 2012a]……. 86

Fig. 3.29. - SSAs' neutron cross sections and energy spectrum in reactor core submerged in wet sand and flooded with seawater [Schriener and El-Genk 2012a] …… 87

Fig. 3.30. - Calculated average axial and radial fission power profiles in the selected SCoRe-N_5 reference reactor design [Schriener and El-Genk 2012a] 89

Fig. 3.31. - Calculated temperatures in a hydraulic sector of the SCoRe-N_5 reference design at 200 kW_{th} [Schriener and El-Genk 2012a]…….. 92

Fig. 3.32. - Calculated temperatures in a hydraulic sector of the SCoRe-N_5 reference design at 500 kW_{th} [Schriener and El-Genk 2012a]……. 93

Fig. 3.33. - Calculated temperatures in a hydraulic sector of the SCoRe-N_5 reference design at 1,000 kW_{th} [Schriener and El-Genk 2012a]…….. 94

Fig. 3.34. - Calculated radial temperature profiles in reference SCoRe-N_5 reactor at location of peak fuel temperature. [Schriener and El-Genk 2012a] 96

Fig. 3.35. - Calculated axial temperature profiles in reference SCoRe-N_5 reactor along the fuel rod centerline. [Schriener and El-Genk 2012a]……. 97

Fig. 3.36. - Reactivity for reference SCoRe-N_5 design with ^{151}EuN SSA at nominal powers of 200, 500, and 1,000 kW_{th}. [Schriener and El-Genk 2012a] 99

Fig. 3.37. - Computational mesh grid for the thermal-hydraulics analysis of a core sector [Schriener and El-Genk 2012b]…….…… 101

Fig. 3.38. - Integrated power system performance results: coolant temperatures and load electrical power [Schriener and El-Genk 2012b]……..… 102

Fig. 3.39. - Calculated temperatures at in a SCoRe-N_5 sector with wire wrapped fuel rods at a nominal power of 1,000 kW_{th} [Schriener and El-Genk 2012b] 104

Fig. 3.40. - Calculated temperatures at core mid-plane in the sector experiencing a LOC at a reactor power of 166.67 kW_{th} [Schriener and El-Genk 2012b] 106

Fig. 3.41. - Perspective view of the core sector experiencing a LOC, with wire wrapped UN fuel rods a reactor power of 166.67 kW_{th} [Schriener and El-Genk 2012b]…….. 107

Fig. 3.42. - Calculated temperatures at core mid-plane in the sector experiencing a LOC without wire-wrap at 166.67 kW_{th} [Schriener and El-Genk 2012b] 108

Fig. 3.43. - A fuel rod unit cell with 316L SS 'cusps'. [Schriener and El-Genk 2012b] …… 109

Fig. 3.44. - Calculated temperatures at mid-plane of the core sector experiencing a LOC at 166.67 kW_{th} for: (a) 10° cusped fuel rods, (b) 15° cusped fuel rods, and (c) 20° cusped fuel rods (thermal radiation disabled) [Schriener and El-Genk 2012b]…… 111

Fig. 3.45. - Calculated temperatures at the core sector experiencing a LOC with 20° cusped fuel rods at 166.6 kW_{th} (with thermal radiation)…..…… 112

Fig. 3.46. - Calculated axial and radial power profiles for the SC-SCoRe sector during nominal operation using MCNPX [Schriener and El-Genk 2014b] 114

Fig. 3.47. - Thermal-hydraulics analysis of SC-SCoRe meshing grid [Schriener and El-Genk 2014b]…….. 116

Fig. 3.48. - Calculated temperatures in a SC-SCoRe core sector during nominal operation: (a) 316L solid core and (b) ODS-Mo solid core [Schriener and El-Genk 2014b]……..…… 118

Fig. 3.49. - Heat transfer from a SC-SCoRe sector experiencing a LOC to adjacent sectors [Schriener and El-Genk 2014b]…… 120

Fig. 3.50. - SC-SCoRe power system operating conditions at reduced power levels during nominal operation and following a sector LOC [Schriener and El-Genk 2014b]…… 121

Fig 3.51. - Calculated temperatures in an SC-SCoRe core sector experiencing a LOC: (a) 316L solid core, and (b) ODS-Mo solid core [Schriener and El-Genk 2014b] ……. 124

Fig. 3.52. - Centerline temperatures in select UN fuel stacks in an SC-SCoRe core sector experiencing a LOC and adjacent sector when reactor thermal power is 167.67 kW_{th}: (a) 316L solid core, and (b) ODS-Mo solid core [Schriener and El-Genk 2014b]…… 125

Fig 3.53. - Calculated temperatures in a SC-SCoRe with ODS-Mo solid core at 323.0 kW_{th} and a sector experiencing a LOC [Schriener and El-Genk 2014b] ……. 126

Fig. 3.54. - Flow velocities of liquid NaK-56 in the coolant channels at the core mid-plane of (a) a sector experiencing a LOCo and (b) adjacent functioning sector [Schriener and El-Genk 2014b]…… 127

Fig. 3.55. - Calculated temperatures in SC-SCoRe with ODS-Mo solid core at 323.0 kW_{th} and a sector experiencing a LOCo [Schriener and El-Genk 2014b] 130

Fig. 3.56. - Calculated centerline temperatures of selected UN fuel stacks in SC-SCoRe operating at 323.0 kW_{th} with a core sector experiencing: (a) a LOCo and (b) a LOC [Schriener and El-Genk 2014b]…….. 131

Fig. 3.57. - Calculated velocity field of liquid NaK-56 demonstrating flow mixing in coolant channels, upper plenum and exit duct of SC-SCoRe core operating at nominal conditions [Schriener and El-Genk 2014b]…..…… 132

Fig. 3.58. - Calculated temperature fields of liquid NaK-56 in upper plenum 1 mm above the core block (a) and the calculated temperature field and tangential velocity vectors at select location in the exit duct (b, c, and d) at nominal reactor operation [Schriener and El-Genk 2014b]…… 133

Fig. 3.59. - Calculated coolant temperature distribution in upper plenum, 1.0 mm above core block) of adjacent to that experiencing: (a) a LOC and (b) a LOCo [Schriener and El-Genk 2014b]…… 134

Fig. 3.60. - Calculated coolant temperature distribution and tangential velocity vectors at select locations in the exit ducts of a functioning core sector adjacent to that experiencing a LOC or a LOCo [Schriener and El-Genk 2014b] 132

Fig. 3.61. - Reactivity depletion in SC-SCoRe during nominal operation at 1,000 kW_{th} …… 140

Fig. 4.1. – The design and fuel pellets loading analyses of long operation life PeBR concept for a lunar outpost ……. 143

Fig. 4.2. - Schematic of one CBC loop in the PeBR power system for lunar surface power [El-Genk and Schriener 2011]…….. 145

Fig. 4.3. - A radial cross-sectional view of the PeBR with three core sectors loaded with spherical fuel pellets [El-Genk and Schriener 2011]…… 146

Fig. 4.4. - Schematics of PeBR core showing the cold and hot frits and the He-Xe gas radial flow in a core sector [El-Genk and Schriener 2011]…… 148

Fig. 4.5. - PeBR emplaced below grade on the lunar surface. [El-Genk and Schriener 2011]……. 149

Fig. 4.6. - Loading PeBR sectors with fuel pellets on the lunar surface (not to scale) [El-Genk and Schriener 2011]…… 151

Fig. 4.7. - PeBR fuel pellets and ZrC coated UC particles (not to scale) [El-Genk and Schriener 2011]……. 153

Fig. 4.8. - Design envelopes for the iron-based structural materials: (a) AISI 316 SS [Booker et al. 1981; Akiyama 1991; Margolin et al. 2010], (b) modified 9Cr-1Mo steel [Booker et al. 1981], and (c) 12Cr-1Mo-WV steel [Booker et al. 1981; Akiyama 1991]……l……. 156

Fig. 4.9. - Design envelopes of the nickel-based structural materials: (a) Hastelloy X [Heynes International 1997], (b) Inconel 617 [McCoy and King 1985; Davis 2000], and (c) Inconel X750 [Special Metals Corporation 2004] 157

Fig. 4.10. - A design surface for the long life PeBR for lunar outposts, -$1 shutdown at BOL using 12 control drums [El-Genk and Schriener 2011]…… 162

Fig. 4.11. - A design surface for the long life PeBR with 25% ASM at BOL [El-Genk and Schriener 2011]……. 163

Fig. 4.12 - Reactivity worth estimates of the lunar regolith as a PeBR supplemental reflector [El-Genk and Schriener 2011]…… 165

Fig. 4.13 - Neutron energy spectra at different radial locations within the reference long life PeBR core at BOL [El-Genk and Schriener 2011]..…….. 166

Fig. 4.14. - Normalized radial neutron flux and fission power density profiles for the long life PeBR at BOL [El-Genk and Schriener 2011]…….…… 167

Fig. 4.15. - Normalized axial neutron flux and fission power density profiles for the long life PeBR at BOL [El-Genk and Schriener 2011].…… 168

Fig. 4.16. - Estimates of the full-power operation life of and the ^{235}U inventory in the reference PeBR for lunar surface power [El-Genk and Schriener 2011] …… 170

Fig. 4.17. - A schematic of launch canisters of fresh fuel pellets to the lunar surface [El-Genk and Schriener 2011]…… 172

Fig. 4.18 - Criticality estimates of the canisters loaded fresh fuel pellets in the unlikely event of a launch abort accident [El-Genk and Schriener 2011]… 174

Fig. 4.19. - A PeBR core sector while being loaded with fuel, containing ~2,000 fuel pellets [Schriener and El-Genk 2012c]…….…… 177

Fig. 4.20. - A PeBR core sector while being loaded with fuel, containing ~10,000 fuel pellets [Schriener and El-Genk 2012c]…….…… 178

Fig. 4.21. - A PeBR core sector while being loaded with fuel, containing ~22,000 fuel pellets [Schriener and El-Genk 2012c]……..… 179

Fig. 4.22. - A PeBR core sector while being loaded with fuel, containing ~28,000 fuel pellets [Schriener and El-Genk 2012c]…….…… 180

Fig. 4.23. - Section views of the top of partially loaded sector with fuel pellets (pellets to scale) [Schriener and El-Genk 2012c]……..……. 182

Fig. 4.24. - Calculated axial distribution of the volume porosity of loaded pellets in a PeBR core sector [Schriener and El-Genk 2012c]…… 183

Fig. 4.25. - Radial distributions of the volume porosity of loaded pellets at different axial locations [Schriener and El-Genk 2012c]…….. 184

Fig. 4.26. - Plane-view images of the loaded fuel pellets at selected axial locations in the PeBR core sector (see Fig. 4.24) (pellets not to scale) [Schriener and El-Genk 2012c]……... 186

Fig. 5.1. - Placement of SC-SCoRe and PeBR during post-operation storage below the lunar surface…….. 189

Fig. 5.2. - Radioactivity source term in SC-SCoRe during full power operation [Schriener and El-Genk 2013]…… 191

Fig. 5.3. - Radioactivity source term in post-operation SC-SCoRe in storage for up to 1,000 years [Schriener and El-Genk 2013]…… 193

Fig. 5.4. - Emitted neutron and gamma photon spectra of the post-operation SC-SCoRe with time after reactor shutdown. ……..... 195

Fig. 5.5. - Radiation dose around excavated post-operation SC-SCoRe, with regolith shielding removed, following 300 years of storage. [Schriener and El-Genk 2013]…….. 196

Fig. 5.6. - Estimates of radioactivity source term in post-operation PeBR while in long term storage on the lunar surface [El-Genk and Schriener 2011]... 199

Fig. 5.7. - Power system integrations of (a) SC-SCoRe and (b) PeBR designs for lunar surface power [Schriener and El-Genk 2013; El-Genk and Schriener 2011]…….…… 201

Fig. 5.8. - DynMo-TE simulation of earlier version of SCoRe power system showing passive decay heat removal following shutdown (see Appendix C) [El-Genk and Schriener 2010]…….. 203

Fig. A.1. - Layout of Calvert Cliffs assembly D047 [Schriener and El-Genk 2009a] .....……. 216

Fig. A.2. - Measured and calculated nuclide mass concentrations in fuel pellet of rod MKP109 [Schriener and El-Genk 2009a]……. 217

Fig. A.3. - Comparison of calculated to measured mass concentrations of nuclides [Schriener and El-Genk 2009a]…… 218

Fig. A.4. - Relative error in calculated mass concentrations of nuclides [Schriener and El-Genk 2009a]……..…… 219

Fig. A.5. - Effect of timestep size on k_{eff} of the system [Schriener and El-Genk 2009a] ……. 220

Fig. A.6. - Operational lifetime estimates of SCoRe-S_{11} [Schriener and El-Genk 2009a] ……..…….. 222

Fig. A.7. - Operational lifetime estimates of S^4 reactor [Schriener and El-Genk 2009a] …… 223

Fig. A.8. - Calculated neutron energy spectra of the analyzed space reactors [Schriener and El-Genk 2009a]…….. 226

Fig. B.1. - Radial section view of S^4 reactor [King and El-Genk 2007]….. 230

Fig. B.2. - Radial reflector panel with sliding segment [Schriener and El-Genk 2009b] …… 231

Fig. B.3. - Isometric views of S^4 reactor with different control configurations [Schriener and El-Genk 2009b]…….. 232

Fig. B.4. - Effect of B_4C absorber thickness on S^4 reactivities [Schriener and El-Genk 2009b]……...…… 237

Fig. B.5. - Operational life estimates for S^4 reactor with rotating drums control [Schriener and El-Genk 2009b]…… 238

Fig. B.6. - Reactivity change over the full range of control element movement [Schriener and El-Genk 2009b]…….. 240

Fig. B.7. - Normalized neutron flux contours in S^4 reactor with rotating drums and sliding reflector segments control [Schriener and El-Genk 2009b] 243

Fig. B.8. - Normalized neutron flux contours in S^4 reactor with rotating drums control [Schriener and El-Genk 2009b]…… 244

Fig. B.9. - Normalized neutron flux contours in S^4 reactor with sliding reflector segments control [Schriener and El-Genk 2009b]……..... 245

Fig. B.10. - Normalized core power distributions in S^4 reactor [Schriener and El-Genk 2009b]……..……. 246

Fig. B.11 - Operational life estimates for S^4 reactor with rotating drums and sliding reflector segments control [Schriener and El-Genk 2009b]……. 248

Fig. C.1. - A line diagram of a pair of primary and secondary loops in the SCoRe-NaK-TE space power system with nominal operation parameters [El-Genk and Tournier 2006a; El-Genk and Schriener 2010]…….. 250

Fig. C.2. - Startup procedures and operation parameters of the SCoRe-NaK-TE power system [El-Genk and Schriener 2010]…….. 253

Fig. C.3. - Coolant flow rates and EM pump current during system startup [El-Genk and Schriener 2010]…….. 256

Fig. C.4. - The SCoRe-NaK-TE system parameters for periodic adjustment of reactivity [El-Genk and Schriener 2010]…….. 260

Fig. C.5. - Effect of the reactivity adjustment period on the operation margins for the power system [El-Genk and Schriener 2010]……..…. 261

Fig. C.6. - Operation parameters of the power system after reactor shutdown [El-Genk and Schriener 2010]…….……. 263

Fig. C.7. - Decay heat generation in the reactor core after shutdown [El-Genk and Schriener 2010]…….. 265

Fig. D.1. - Cross-section views of SC-SCoRe: (a) elevation view and (b) plane view [Schriener and El-Genk 2014a]……..…….. 266

Fig. D.2. - Normalized radial fission power profile at active core mid-plane (z/L = 0) and axial power profile for innermost fuel stack in the core sectors (r./R = 0.227), Fig, D.1b [Schriener and El-Genk 2014a]……..….. 268

Fig. D.3. - Cross-sectional views of triangular element using different numerical mesh refinements (Table D.1) [Schriener and El-Genk 2014a]……. 273

Fig. D.4. - Arrangements of fuel stacks and tri-lobe channels in a single core sector (yellow areas are the flat potassium heat pipes dividers) [Schriener and El-Genk 2014a]…….……. 274

Fig. D.5. - Effect of mesh refinement on peak temperatures: (a) UN fuel and solid structure in core sector, and (b) select UN fuel stacks [Schriener and El-Genk 2014a]…… 277

Fig. D.6. - Effect of numerical mesh refinement and the choice of turbulence model on the calculated temperature profiles in coolant channels: (a,c) channel A1, and (b,d) channel A4 (Fig. D.4) [Schriener and El-Genk 2014a]…… 279

Fig. D.7. - Effect of numerical mesh grid refinement and the choice of turbulence model on the velocity profiles: (a,c) coolant channel A1, and (b,d) channel A4 [Schriener and El-Genk 2014a]……..…….. 281

Fig. D.8. - Comparisons of the calculated temperature and velocity fields in selected liquid NaK-56 flow channels at core mid-plane using the k-ε and k-ω turbulence models with the finest numerical mesh 'a' (Table D.1) [Schriener and El-Genk 2014a]……..…… 283

Fig. D.9. - Comparison of liquid NaK-56 mass flow rates in tri-lobe coolant channels using the k-ε and k-ω turbulence models with the finest numerical mesh 'a' [Schriener and El-Genk 2014a]……. 285

Fig. D.10. - Locations along the flow path in a core sector for reporting calculated pressure losses in the core sector using the k-ω turbulence model with the finest numerical mesh grid 'a' (Table D.1) [Schriener and El-Genk 2014a] …….. 287

Fig. D.11. - Effects of mesh refinement and choice of turbulence model on calculated: (a) pressure losses and (b) total pressure in core sector [Schriener and El-Genk 2014a]…….…….. 288

Fig. D.12. - Effects of mesh refinement and choice of turbulence model on the temperature differences in upper plenum and exit duct [Schriener and El-Genk 2014a]…….…… 290

Fig. D.13. - Location of flow field images of the liquid NaK-56 flow in the upper plenum and exit duct [Schriener and El-Genk 2014a]……..…….. 291

Fig. D.14. - Calculated temperature fields, tangential velocity vectors and liquid turbulence eddies in the upper plenum using the k-ω and k-ε turbulence models with the finest mesh gird 'a' in Table D.1: (a-b) at section A-A in Fig. D.13, and (c-d) at the sector symmetry plane (Fig. D.4) [Schriener and El-Genk 2014a]……..…… 292

Fig. D.15. - Calculated temperature fields, tangential velocity vectors, and mixing eddies in the exit duct using the k-ω and k-ε turbulence models with the finest numerical mesh gird 'a' in Table D.1: (a-b) at Section B-B, (c-d) at section C-C, and (d-e) at section D-D in Fig. D.13 [Schriener and El-Genk 2014a] …… 293

Fig. D.16. - Effects of the numerical mesh refinement and the choice of turbulence model on the CPU time to complete the analyses [Schriener and El-Genk 2014a] …… 296

Fig. D.17. - Comparison of the calculated performance parameters for a triangular element with a single, tri-lobe flow channel using the DES turbulence model and both k-ω and k-ε linear turbulence models versus the relative CPU running time [Schriener and El-Genk 2014a]…… 298

Fig. D.18. - Comparison of the calculated fully developed Nu values in a circular, uniformly heat tube with reported correlations [Schriener and El-Genk 2014a] ……. 299

LIST OF TABLES

Table 2.1. - Best estimates of bulk density for lunar regolith [Mitchell et al. 1974] …… 11

Table 2.2. - Chemical composition of average regolith samples at lunar landing sites [Heiken, Vaniman, and French 1991]……... 12

Table 2.3. - Electrical power needs for a crewed lunar outpost……..... 15

Table 2.4. - Reactor concepts for lunar surface power……... 24

Table 2.5. - Power system concepts for lunar surface power…….……. 25

Table 3.1. - Properties NaK-78 and NaK-56 liquids at 0.10 MPa & 875 K [Foust 1972] ……..... 42

Table 3.2. - Corrosion results of molybdenum in sodium, potassium, and NaK-78 …….. 53

Table 3.3. - Composition of JSC-1 lunar soil simulant [McKay et al. 1994]. 58

Table 3.4. - Design parameters of selected SCoRe-N_x concepts…….…… 78

Table 3.5. - SCoRe-N_5 dimensions and BOL excess reactivity estimates…. 85

Table 3.6. - BOL reactivity values of the SC-SCoRe with ODS-Mo solid core ……..…… 138

Table 4.1. - Discrete Elements Method (DEM) simulation phase parameters 176

Table 5.1. - Radiation dose rate estimates for the lunar surface [Schriener and El-Genk 2013]…… 198

Table A.1 - Operation history of assembly D047 [Hermann et al. 1995]….. 216

Table A.2. - Temperatures used in neutronics analysis for SCoRe-S_{11} and S^4 space reactors [Schriener and El-Genk 2009a]…… 224

Table A.3. - Fuel composition for S^4 at 1,376 MWd [Schriener and El-Genk 2009a] ……..…….. 227

Table A.4. - Fuel composition for Calvert Cliffs benchmark at the end of Cycle 1 [Schriener and El-Genk 2009a]……..…….. 228

Table B.1. - S^4 reactor dimensions and operation temperatures [Schriener and El-Genk 2009b]…….…….. 233

Table B.2. - Excess and shutdown reactivity for S^4 with rotating drums and sliding reflector segments control [Schriener and El-Genk 2009b]……. 235

Table D.1. - Numerical mesh cells for various levels of mesh refinement [Schriener and El-Genk 2014a]……. 272

NOMENCLATURE

A_{lv}	surface area of heat-pipe liquid-vapor interface, m^2
A_{wick}	surface area of heat-pipe wick, m^2
AC	alternating current
AFSPS	affordable fission surface power system
ALIP	annular linear induction pump
AMTEC	alkali metal thermal-to-electric conversion
ASM	additional shutdown margin
BOL	beginning of life
C_p	specific heat, J/kg.K
CBC	closed Brayton cycle
CCNPP	Calvert Cliffs Nuclear Power Plant
CF	capture factor, captures/cm^3-SP
CF_i	capture factor for nuclide i , captures/cm^3-SP
CF_{in}	gain of nuclide due to capture from other nuclides, captures/cm^3-SP
CF_{out}	loss of nuclide due to capture to other nuclides, captures/cm^3-SP
CFD	computational fluid dynamics
d	fuel rod diameter, m
D	core diameter or flat-to-flat dimension, m
D_e	equivalent hydraulic diameter, m
D_{in}	gain of nuclide from decay of other nuclides, decays/cm^3-s
D_{out}	loss of nuclide from decay to other nuclides, decays/cm^3-s
DBTT	ductile-to-brittle transition temperature
DC	direct current

DEM	discrete element method
DES	detached eddy simulation
DNS	direct numerical simulation
DynMo	Dynamic Simulation Model
EM	electromagnetic
EOL	end of life
FF	fission factor, fissions/cm^3-SP
FF_i	fission factor for nuclide i , fissions/cm^3-SP
FPSE	free piston Stirling engine
FPY	full power years
FSPS	fission surface power system
GCR	galactic cosmic rays
h_{gap}	heat transfer coefficient of the fuel pellet-cladding gap, W/m^2-K
H	active core height, m
H/D	active core height/flat-to-flat ratio
HOMER	heat-pipe operated moon exploration reactor
HPCMR	heat-pipe cooled modular reactor
HX	heat exchanger
JIMO	Jupiter icy moons orbiter
k	turbulent kinetic energy, m^2/s^2
k_{eff}	effective neutron multiplication factor
L	total length of reactor core
L_{hv}	length of heat-pipe vapor core
LANL	Los Alamos National Laboratory
LES	large eddy simulation

LOC	Loss of Coolant
LOCo	Loss of Cooling
N_i	atom fraction for nuclide, i atoms/barn-cm
N_{EOT}	atom density at end of timestep, atoms/cm^3
N_{BOT}	atom density at beginning of timestep, atoms/cm^3
NaK	sodium-potassium alloy
NASA	National Aerospace Agency
Nu	Nusselt number, h Cp/λ
ODS-Mo	oxide dispersion strengthened molybdenum
p	fuel rod pitch
p/d	fuel rod pitch-to-diameter ratio
P_{int}	heat-pipe internal pressure, Pa
P_v	vapor pressure, Pa
PCA	power conversion assembly
Pe	Peclet number, D_e v/α
PeBR	Pellet Bed Reactor
PF	packing fraction
PMA	permanent magnet alternator
Pr	Prandtl Number, ν/α
Pr_t	turbulent Prandtl number
PV	photovoltaic
PWR	Pressurized Water Reactor
Q_i	recoverable energy from fission for nuclide i, MeV/fission
Q_{remove}	heat removed, W
Q_{th}	reactor thermal power, kW_{th}
r	radial coordinate, m

r_{cd}	control drum radius, m
r_{gap}	average radius of fuel pellet-cladding gap, m
r_{lv}	radius of heat-pipe liquid-vapor interface, m
R	core radius, m
R*	normalized radial distance, r/R
R_f	rows of fuel rods per SCoRe sector
R_{gap}	thermal resistance of fuel pellet-cladding gap, K/W
R_{lv}	thermal resistance of heat-pipe liquid-vapor interface, K/W
R_s	specific gas constant, J/kg.K
R_v	thermal resistance of heat-pipe vapor core, K/W
R_{wick}	thermal resistance of heat-pipe wick, K/W
R_x	reactor
RANS	Reynolds averaged Navier-Stokes
Re	Reynolds number, D_e v/ν
RPS	radioisotope power system
RTG	radioisotope thermoelectric generator
$\dot{S}$	source strength (SP/s)
SCoRe	sectored compact reactor
SC-SCoRe	solid core sectored compact reactor
SEP	solar energetic particles
SNAP	systems for nuclear auxiliary power
SP	MCNP source particle
SS	stainless steel
SSA	spectral shift absorber
SST	shear stress transport

t	time, s
T	temperature, K
T_{ave}	average temperature, K
T_{ex}	reactor exit temperature, K
T_{fo}	fuel pellet outer surface temperature, K
T_s	length of timestep, s
T-H	thermal-hydraulics
TCA	thermoelectric conversion assembly
TD	theoretical density
TE	thermoelectric
TI	thermionic
TPV	thermos-photovoltaic
v	flow velocity, m/s
V_{fuel}	volume of fuel, cm^3
W	width of tri-lobe flow channel, m
XS	neutron cross section
y_i	fission yield of actinide i for selected nuclide (atoms/fission)
y^+	dimensionless distance from wall
z	axial coordinate
Z*	normalized axial distance, z/L
α	thermal diffusivity, m^2/s
β_{eff}	effective delayed neutron fraction
δ	thickness of B_4C segment in control drum, m
δ_{gap}	width of fuel pellet-cladding gap, m

δ_{wick}	thickness of heat-pipe wick, m
ΔP_{Losses}	pressure losses, Pa
ε	porosity
ε_c	emissivity of cladding
ε_f	emissivity of fuel
η_{th}	thermal efficiency, %
λ	thermal conductivity, W/m.K
λ_l	thermal conductivity of liquid in heat-pipe wick, W/m.K
λ_s	thermal conductivity of solid in heat-pipe wick, W/m.K
λ_{wick}	effective thermal conductivity of liquid filled wick, W/m.K
μ	dynamic viscosity, Pa.s
ρ	density, kg/m^3
ρ_{ex}	excess reactivity, $
ρ_{sd}	shutdown reactivity, $
ρ_{sd9}	shutdown with 9 control drums operational reactivity, $
ρ_{sd12}	shutdown with all 12 control drums operational reactivity, $
ρ_{wsa}	water flooding and submersion in wet sand reactivity, $
σ_a	microscopic neutron absorption cross section, barn
ν	kinematic viscosity, m^2/s
ω	turbulence kinetic energy specific dissipation rate, s^{-1}

1. INTRODUCTION

The exploration of space has expanded our understanding of our own planet as well as the larger universe. Investment in and development of space technologies has revolutionized numerous fields, including global communications, weather forecasting and climate planning, environmental monitoring, imaging and land-use planning among others [Abbey and Lay 2005]. With the establishment of the International Space Station in 1998, there has been a continuous human presence in Earth orbit for over 15 years. In the past decade there has been renewed interest in expanding human space exploration out of Earth orbit, returning humans to the Moon and sending the first people to Mars. The Moon has long been considered a destination for future human exploration and colonization. Astronomers and philosophers have considered the possibility of humans traveling to the lunar surface, since at least the 17th century [Wilkins 1638]. The Moon is the only planetary body, beyond Earth, on which humans have set foot; the six Apollo landings delivering a total of twelve US astronauts to the Moon between 1969 and 1972. In the years since, many nations, including the United States, China, India, Russia, Japan, as well as the European Union, have expressed interest in sending crewed missions to the Moon with the eventual goal of building permanent outposts on the lunar surface, both as a source of national pride as well as for access to the Moon's valuable natural resources.

Future lunar outposts could engage in a wide variety of activities, including scientific exploration, resources mining and processing, manufacturing, and even tourism. The unique geology of the Moon makes it an attractive destination for future scientific study. The lunar farside presents an unparalleled environment for deploying radio telescopes for peering into the far corners of the universe [Lowman 1985]. In addition, the Moon's lower gravity means that it takes less energy to send material into Earth orbit from the lunar surface than from Earth, making the Moon a useful source for space resources. Water ice deposits in permanently shadowed craters could be a source of oxygen and hydrogen for manufacturing rocket propellants and drinking water for life support [Duke, Mendell, and Roberts 1985]. The relatively high concentrations of titanium and aluminum in the lunar regolith could be mined to support construction of large space stations and solar power satellites capable of beaming power back to Earth's surface

[O'Neill 2000]. The near vacuum environment on the lunar surface could also assist in the manufacturing of highly pure materials for use in space or back on Earth [Heiken, Vaniman, and French 1991]. The Moon is also considered a source for the valuable aneutronic fusion fuel ^{3}He, accumulated in the regolith from exposure to the solar wind [Heiken, Vaniman, and French 1991]. The Moon's close proximity to the Earth also makes it a possible destination for future space tourists as lunar outposts mature.

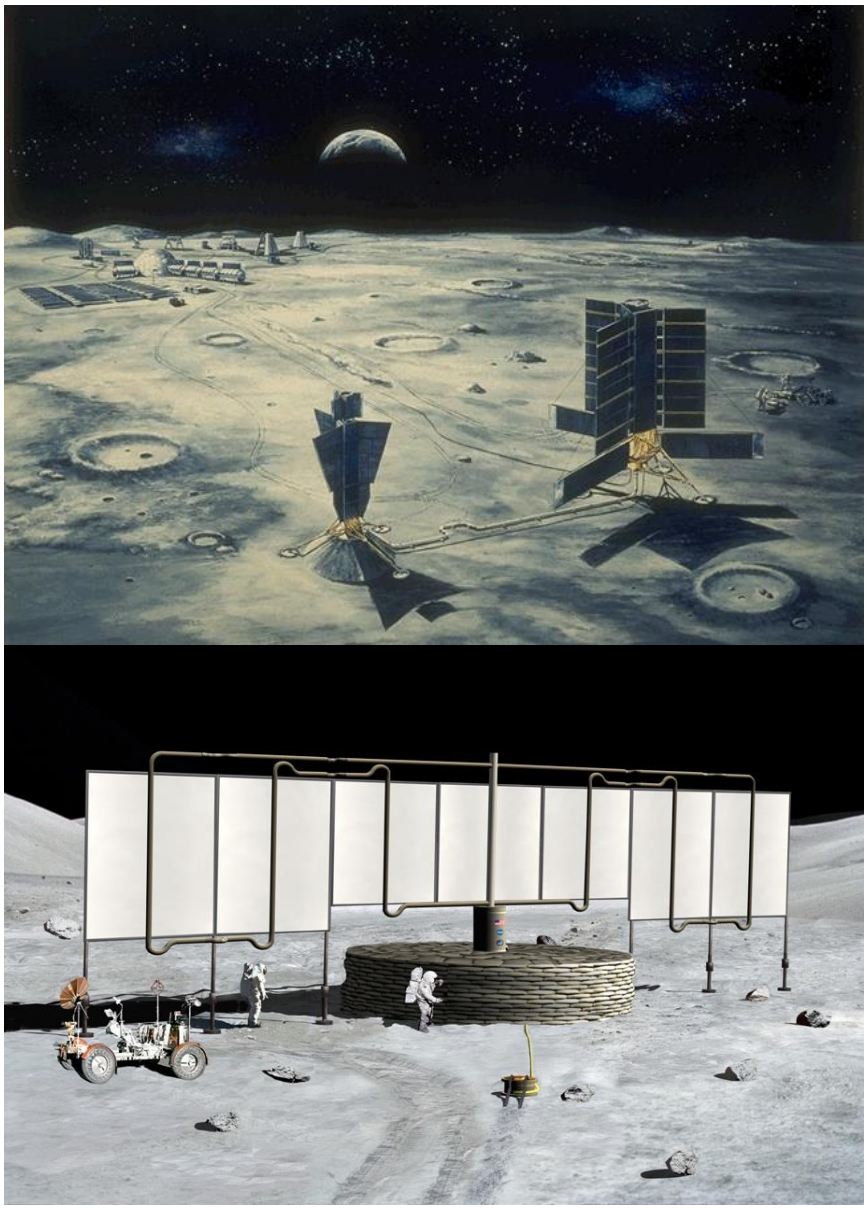

Fig. 1.1. - Artist's conceptions of space nuclear power system concepts emplaced on the lunar surface [NASA].

Future lunar outposts will require reliable sources of electrical power for life support and surface operations. This electrical power could be supplied using a number of technologies including solar Photovoltaic (PV), radioisotope and nuclear fission reactor power systems, or combinations of all three. Solar PV power systems with nighttime energy storage and Radioisotope Power Systems (RPS) could provide electrical power on the lunar surface for relatively low requirements of up to a few kW_e. As the electrical power demands of the lunar outpost increase, however, these options run into limitations. Solar PV power systems with nighttime energy storage, such as rechargeable batteries or regenerative fuel cells, scale poorly with increasing power level due to the mass of the energy storage system, increasing launch costs [Freeh 2009]. In addition, exposure to space radiation could result in relatively short lifetimes. Multi-kW_e RPSs using dynamic energy conversion such as Free Piston Stirling Engines (FPSE) or Closed Brayton Cycle (CBC) would require large quantities of isotopes, such as ^{238}Pu, to generate the required thermal power. The future supply of ^{238}Pu, which has powered prior space Radioisotope Thermoelectric Generators (RTGs), is extremely limited [Witze 2014]. This, as well as the low specific power of radioisotope heat sources, makes large scale RPS systems impractical as principle power sources for a lunar outpost.

Nuclear fission reactors represent the best choice for lunar outposts with electrical power needs in the 10's-100's of kW_e. These power systems are more compact and much lighter compared to the other two options [Littman 1992; Mason, Poston, and Qualls 2008, Freeh 2009]. They can steadily supply electrical power throughout the long ~27.3 day lunar day/night rotational period, irrespective of the latitude of the outpost on the lunar surface. Reactor power systems could potentially open up the entire lunar surface for human exploration and development activities, rather than limiting outposts to sites at the poles where solar energy is more plentiful [Elliott et al. 2005]. Nuclear reactor power systems could also operate in the bottom of permanently shadowed craters to support water ice mining and rocket propellant production on the Moon. In addition, these power systems scale up favorably with increasing power output, are cost effective, and would support the growing power needs as outposts expand and develop [Elliott et al. 2005; Schriener and El-Genk 2012a].

Compact nuclear reactors for lunar surface power and exploration use Highly Enriched Uranium (HEU) fuel and are typically designed to operate continuously for 3-10 years without refueling. They are designed to meet stringent launch safety requirements. These include requiring that the bare reactor core remain sufficiently subcritical when submerged in wet sand and flooded with seawater in the unlikely event of a launch abort accident. Desirable design features include a negative temperature reactivity feedback, utilizing static components, when possible, avoiding single point failures in reactor cooling and the power system integration, utilizing the lunar regolith as a supplemental shielding and neutron reflector material, ensuring, by design, a safe removal of post-operation decay heat, and a safe post operation storage of the reactor core, for eventual retrieval [El-Genk 2008]. To enhance the reliability of long life lunar power reactors, they could be designed to operate at moderate temperatures and use conventional structural materials with extensive space and terrestrial reactor experience and well developed fabrication methods [Poston and Marcille 2006]. An additional desirable feature is having a long operational life, which among other benefits would reduce the number of reactors required over the lifetime of a lunar outpost. This could result in a large savings in the total launch costs for the outpost.

The use of nuclear fission surface power systems have been considered in every major planned NASA human lunar exploration program, since the Apollo program in the 1960's and 70's thorough the Space Exploration Initiative (SEI) of the late 1980's to early 1990's, to the most recent Constellation program and beyond [Bennett 2008a]. The limited number of reactor concepts developed specifically for the lunar environment, however, possess only a few of the desirable design features described above, and have relatively short operational lives $\leq$ 10 years [Dieckamp 1967; Elliott et al. 2005; Amiri et al. 2006; Mason, Poston, and Qualls 2008; Hatton and El-Genk 2009].

The research described in this dissertation investigates the development of long operational life lunar surface power reactors, which incorporate the desirable design features described above. Achieving a long operational life requires that the reactor possess sufficient Beginning-Of-Life (BOL) excess reactivity to account for the fissile depletion during operation and the accumulation of fission products. Increasing the BOL

excess reactivity could be accomplished either by increasing the amount of HEU fuel in the reactor core, or by improving the neutron economy of the reactor through reducing neutron leakage and parasitic absorption. However, for solid core reactors to be launched from Earth, the amount of fuel in the core is limited by the stringent launch safety requirements. An option for increasing the fuel mass, and hence the reactor operation life, is to launch the reactor unfueled and subsequently load it with fuel elements on the Moon. Since such reactors would not be subject to the launch criticality safety requirements, they could be designed with a higher fuel mass, potentially providing for a longer operational life. This concept, however, requires unique reactor and fuel element designs that lend themselves to fueling the core on the Moon.

1.1. Selected Reactor Concepts for Lunar Surface Power

This research investigates long life concepts of both a solid core reactor fueled at launch as well as an advanced concept which is fueled on the lunar surface. The considered solid core reactor that is fueled at launch is the fast-neutron spectrum, NaK-78 cooled Sectored Compact Reactor (SCoRe) [El-Genk et al. 2005; Hatton and El-Genk 2009; Schriener and El-Genk 2011]. The operational life of this compact reactor is increased by reconfiguring the reactor core to reduce neutron leakage and parasitic absorption, while keeping the total fissile loading constant and satisfying launch criticality safety requirements. A multi-physics design and analyses methodology is developed to capture the interrelated effects of the different design changes on the reactor core neutronics and thermal-hydraulics. This methodology iteratively couples the Monte Carlo neutronics using MCNPX [Pelowitz et al. 2011] with 3-D Computational Fluid Dynamics (CFD) and thermal-hydraulics analyses using the finite volume CFD code STAR-CCM+ [CD-adapco 2012]. The methodology also incorporates integrated system analyses of the SCoRe power system using the dynamic system modeling tool DynMo-TE [El-Genk and Tournier 2006a].

Increasing the operational life through fueling the reactor on the lunar surface is exercised for the Pellet Bed Reactor (PeBR) concept [El-Genk et al. 1990, 1994a,b; Morley and El-Genk 1994; El-Genk and Morley 1993]. The PeBR core is loaded with randomly packed spherical fuel pellets and cooled by circulating He-Xe gas. The multi-

physics design and analyses for the PeBR concept focus on its ability to achieve a long operation life, as well as investigating launching the fuel pellets to the Moon and loading them into the reactor core.

The SCoRe and PeBR operate at coolant exit temperatures ≤ 900 K and use conventional stainless steel and nickel-based super alloys for the reactor core and power system structure. These reactors would be emplaced below grade on the lunar surface, placed in an excavated hole or trench which is then backfilled with lunar regolith (Fig. 1.2). The SCoRe and PeBR concepts for lunar power would utilize the regolith as a supplemental neutron reflector and radiation shielding material to protect the nearby lunar outpost from the reactors' neutron and gamma radiation. This placement also allows for the safe storage of the post-operation reactors for the time required for the radioactivity in the core to decay to a sufficiently low level, near background, for the safe recovery to retrieve the valuable ^{235}U remaining in the fuel.

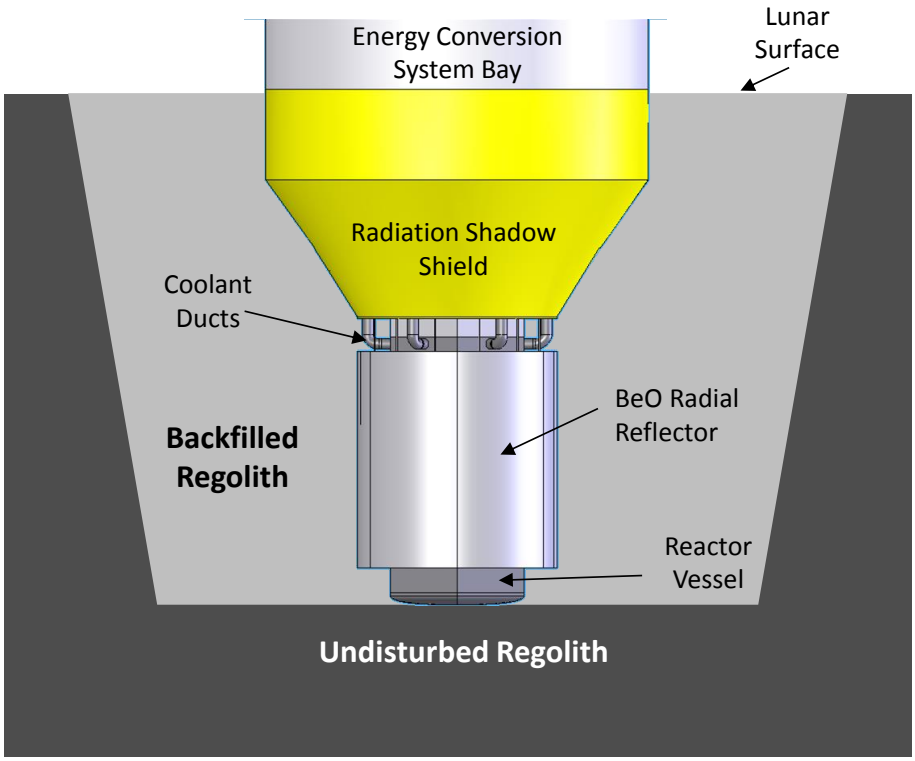

Fig. 1.2. - SCoRe reactor emplaced in a trench below grade on the Moon and surrounded by backfilled regolith.

The cores of the SCoRe and PeBR are divided into sectors (6 for the SCoRe, and 3 for the PeBR). These sectors are thermally and neutronically coupled, but hydraulically decoupled. Each sector is served by separate coolant loops, energy conversion modules, and heat rejection radiator panels. This combination of sectored core and power system integration with multiple loops avoids single point failures in reactor cooling, energy conversion, and heat rejection [El-Genk 2008]. In the unlikely event that a sector experiences a Loss of Coolant (LOC) in a primary coolant loop or Loss of Cooling (LOCo) in a secondary cooling loop, the reactor power is reduced and the fission heat generated in the affected sector would transfer to the adjacent core sectors, where it would be removed by the circulating coolant therein [El-Genk et al. 2005; El-Genk 2008; Schriener and El-Genk 2012b, 2014]. This would allow the reactor power system to continue operating to supply some electrical power to the outpost. The decreased reactor thermal power prevents overheating the fuel and structural materials in the affected sector.

1.2. Research Objectives

The specific objectives of the performed research discussed in this dissertation are as follows:

1. Develop a multi-physics design and analyses methodology which couples Monte-Carlo neutronics, CFD and thermal-hydraulics, and dynamic modeling of the integrated power system to investigate different design options for the SCoRe to increase excess reactivity and operational life, while keeping the amount of uranium fuel constant. These include changing the diameter of the fuel rods, the external reactivity control elements, and the choice of spectral shift absorber isotope while satisfying launch and operation safety requirements.
2. Perform CFD and thermal-hydraulic analyses of the SCoRe reactor during nominal operation to determine the core temperatures, pressure losses, and flow mixing, as well as make necessary design changes to ensure that the peak cladding and fuel temperatures are within acceptable levels.
3. Investigate the dynamic system performance of the SCoRe power system with thermoelectric energy conversion using DynMo-TE to calculate the reactor inlet

and outlet temperatures and coolant flow rates at different thermal power levels for use in the thermal-hydraulic and safety analyses.

4. Perform thermal-hydraulic and safety analyses investigating the SCoRe with a sector experiencing a LOC and a LOCo to determine the thermal power level at which the reactor could safely continue operation, without overheating the fuel and core structural materials in the affected sector.
5. Perform parametric neutronics analyses of the PeBR to estimate the effect of varying the fuel mass and radial neutron reflector thickness on the total reactor mass and BOL excess reactivity and determine the operational life, while the reactor is emplaced below grade on the lunar surface.
6. Design launch canisters for the spherical fuel pellets to transport them to the Moon that meet launch criticality safety requirements
7. Simulate fueling the PeBR on the Moon using Discrete Element Method (DEM) analysis of loading one of the three reactor core sectors with spherical pellets on the lunar surface.
8. Investigate storage of the post operation SCoRe and PeBR reactors to determine the time required for the radioactivity in the cores to decay down to a low enough level, near background, to allow for the safe recovery and retrieval of the reactors.

The next chapter provides a background on the lunar environment, the electrical supply needs for future lunar outposts, and reviews proposed lunar surface reactors and their integrated power systems. Chapter 3 presents the multi-physics design and safety analyses methodology used for the SCoRe reactor and power system for lunar surface power and discusses the results of the coupled neutronics, CFD and thermal-hydraulics, and integrated system analyses. Chapter 4 describes the design of the PeBR and power system for lunar surface power and the results of the parametric neutronic analyses. This chapter also presents results of the design of the fuel pellets transport canisters and the transient fuel loading simulation of the spherical fuel pellets on the Moon. Chapter 5 presents analyses of post-operation storage of the SCoRe and PeBR concepts to investigate the time required to allow for the safe recovery of the reactors. Chapter 6 summarizes the results from the previous chapters as well as providing suggestions for future work.

The appendices provide supplemental information on the design and analysis of long life space nuclear reactors. Appendix A compares the performance of commonly used fuel depletion codes for determining the operational life of fast neutron spectrum space reactors. Appendix B investigates the effect of different reactivity control options on the core neutronics and operational life. Appendix C presents results of a transient system simulation of an earlier version of the SCoRe power system. Appendix D presents the results of a comparative CFD analysis to determine the effect of the choice of turbulence model and mesh refinement on the CFD and thermal-hydraulic results for the final SCoRe design.

2. BACKGROUND

The potential of lunar surface nuclear power systems has been investigated since the Apollo program in the 1960's and as recently as part of NASA's Constellation program. The compactness and ability of nuclear reactor power systems to operate independent of the Sun makes them uniquely suited for powering future lunar outposts. This chapter reviews the lunar environment and the electrical power needs for lunar outposts, describes the building blocks of a space nuclear power system, and discusses possible placements of nuclear reactor power systems on the lunar surface. This chapter also briefly reviews proposed nuclear reactor concepts developed for lunar surface power systems.

2.1. The Lunar Environment

The Moon is a rocky body, 27.3% the size, and 1.2% the Mass of the Earth [Heiken, Vaniman, and French 1991]. The native atmosphere is practically nonexistent, and the Moon's surface gravity is ~1/6 that of Earth. The Moon's surface is divided into two major classes of geologic regions that are visible from the Earth as light and dark colored areas. The lighter-colored regions are referred to as the highlands and consist of the ferroan anorthosites which make up the Moon's original crustal material [Heiken, Vaniman, and French 1991]. The dark-colored regions are called mare and consist mostly of basalt and other volcanic rocks. The mare regions formed from volcanic lava floods erupting out from the interior and spreading iron-rich basalts across the low-laying regions. The lunar surface is extensively cratered from meteor impacts during the formative bombardment phase of the solar system. These craters offer areas that are almost permanently shadowed, preserving possible sources of water ice for future human outposts [Colaprete et al. 2010].

The surface of the Moon is covered by a mixture of larger rocks and a layer of fine soil called regolith. The lunar regolith is a key resource for future lunar exploration and development. It is the primary mineral source of extractable metals, oxygen for life support, and light volatiles such as the fusion fuel ^{3}He [Heiken, Vaniman, and French 1991]. Regolith can also be collected and piled on top of habitats to shield crew from

space radiation [Pham and El-Genk 2009], or be formed into a concrete for use as a sturdy building material [Kaden 1991; Matsumoto et al. 1992]. Lunar nuclear reactor power systems can utilize the regolith both for radiation shielding and as a supplemental neutron reflector for enhancing the operational life of the reactor and reducing the total mass of the launched system from Earth [Kang, Lipinski, and McAlpine 2006; Hatton and El-Genk 2009].

The regolith is formed of rock particles broken up by meteor impacts and lofted up before falling back down to the surface. The bulk of the surface regolith material consists or particles < 1 cm in size [Heiken, Vaniman, and French 1991]. The regolith layer has built up from impact events over billions of years, covering the solid lunar bedrock to a depth of ~4-5 m in the volcanic mare regions and may be as thick as 10-15 m in the older lunar highlands [Heiken, Vaniman, and French 1991]. The regolith is loosely packed near the surface, with a bulk density between 1.1 – 1.2 g/cm^3 [Heiken, Vaniman, and French 1991]. The density increases as the regolith particles compact with depth (Table 2.1). This higher density improves the regolith's effectiveness as a radiation shielding material and supplemental reflector for nuclear power systems emplaced below grade.

Table 2.1. – Best estimates of bulk density for lunar regolith [Mitchell et al. 1974].

Depth Range (cm)	Average Bulk Density (g/cm^3)
0-15	1.50 ± 0.05
0-30	1.58 ± 0.05
30-60	1.74 ± 0.05
0-60	1.66 ± 0.05

Samples of the lunar regolith were collected and returned to Earth for further analysis during each of the six successful US manned landings (Apollo 11, 12, 14, 15, 16, and 17) as well as by three of the Soviet robotic Luna landers (Luna 16, 20, and 24). Table 2.2 lists the average measured compositions of the lunar regolith at these nine landing sites. Apollo 11 and 12 landed in lunar mare regions, Apollo 14 landed on an impact ridge near a large crater basin, Apollo 15 and 17 landed near the boundary between mare and

highlands regions, while Apollo 16 landed in a highlands region. The Luna 16 and 24 landers collected samples from Mare regions, while Luna 20 collected samples from the lunar highlands.

Table 2.2. - Chemical composition of average regolith samples at lunar landing sites [Heiken, Vaniman, and French 1991].

Chemical	**Apollo Samples (wt%)**						**Luna Samples (wt%)**		
Composition	11	12	14	15	16	17	L16	L20	L24
SiO_2	42.2	46.3	48.1	46.8	45	43.2	41.7	45.1	43.9
TiO_2	7.8	3	1.7	1.4	0.54	4.2	3.4	0.55	1.3
Al_2O_3	13.6	12.9	17.4	14.6	27.3	17.1	15.3	22.3	12.5
Cr_2O_3	0.3	0.34	0.23	0.36	0.33	0.33	0.28	-	0.32
FeO	15.3	15.1	10.4	14.3	5.1	12.2	16.7	7	19.8
MnO	0.2	0.22	0.14	0.19	0.3	0.17	0.23	0.13	0.25
MgO	7.8	9.3	9.4	11.5	5.7	10.4	8.8	9.8	9.4
CaO	11.9	10.7	10.7	10.8	15.7	11.8	12.5	15.1	12.3
Na_2O	0.47	0.54	0.7	0.39	0.46	0.4	0.34	0.5	0.31
K_2O	0.16	0.31	0.55	0.21	0.17	0.13	0.1	0.1	0.04
P_2O_3	0.05	0.4	0.51	0.18	0.11	0.12	0.12	0.16	0.11
S	0.12	-	-	0.06	0.07	0.09	0.21	0.08	0.14
Total	99.9	99.1	99.8	100.8	100.8	100.1	99.7	100.8	100.4
Element	**Apollo Samples (ppm)**						**Luna Samples (ppm)**		
Sc	60	38	23	25.3	8.7	37	37	16	34
U	0.5	1.7	1.5	0.73	0.53	0.41	0.25	0.29	0.26
Th	1.9	6.4	6.7	2.3	2	1.9	0.8	0.85	1.1
La	16	39	70	26.3	10.7	8.5	13	5	5

The lunar regolith consists of >40 wt% silica and significant concentrations of oxides of iron, aluminum, titanium, magnesium, and calcium (Table 2.2). The composition of the regolith varies considerably between the mare and highlands regions. The impact

origin of the regolith layer, however, has resulted in a mixture of rock particles originating from both regions at any given location [Heiken, Vaniman, and French 1991]. The regolith samples collected in the mare regions are richer in iron and titanium, while the highland samples typically contain higher concentrations of calcium and aluminum. Volatile materials, such as hydrogen and helium deposited in the regolith by the solar wind, exist in only trace concentrations [Heiken, Vaniman, and French 1991].

Although the composition of the lunar regolith varies at different locations, previous research has shown that the variances in the composition from sites sampled have little impact on its performance for radiation shielding and as a supplemental neutron reflector [Kang, Lipinski, and McAlpine 2006; Hatton and El-Genk 2009; Pham and El-Genk 2009]. The regolith composition has little effect on its effectiveness in protecting lunar habitats from high energy space radiation [Pham and El-Genk 2009]. Thus, the results of calculations performed with a general regolith composition should be representative for the different lunar regions.

The Moon is tidally locked by the Earth's gravity with the same hemisphere, the lunar nearside, always facing Earth. The Moon rotates slowly as it travels along its orbit, resulting in a rotational period of 27.32 d. Thus operations on the lunar surface must deal with a much longer cycle of light and darkness than is typical on the surface of Earth or Mars. This makes it unattractive to use large scale solar PV power systems in the range of 10's to 100's of kW_e as the mass of the energy storage system becomes prohibitive for powering the outpost during the nearly 14 d long lunar nighttime [Littman 1992; Mason, Poston, and Qualls 2008, Freeh 2009].

The long rotational period and lack of an atmosphere result in significant temperature swings on the lunar surface. During the nearly 14 d long lunar daytime the surface temperature can reach as high as 396 K at the equator [Dallas, Diaguila, and Saltsman 1971; Heiken, Vaniman, and French 1991]. Through the cold lunar nighttime, surface temperature may reach as low as 40 K, with an average of 120 K over all latitudes during the dark period. The variation in the surface temperature over a typical lunar rotational period is shown in Fig. 2.1. These swings in surface temperature can impact the performance of heat rejection radiators as they change the radiator's effective heat sink

temperature, and thus the heat rejection efficiency [Dallas, Diaguila, and Saltsman 1971]. Temperature changes during the lunar rotational period could also impact crew operations at future lunar outposts. The next section describes the possible design and purposes of early lunar outposts and their estimated electrical power requirements.

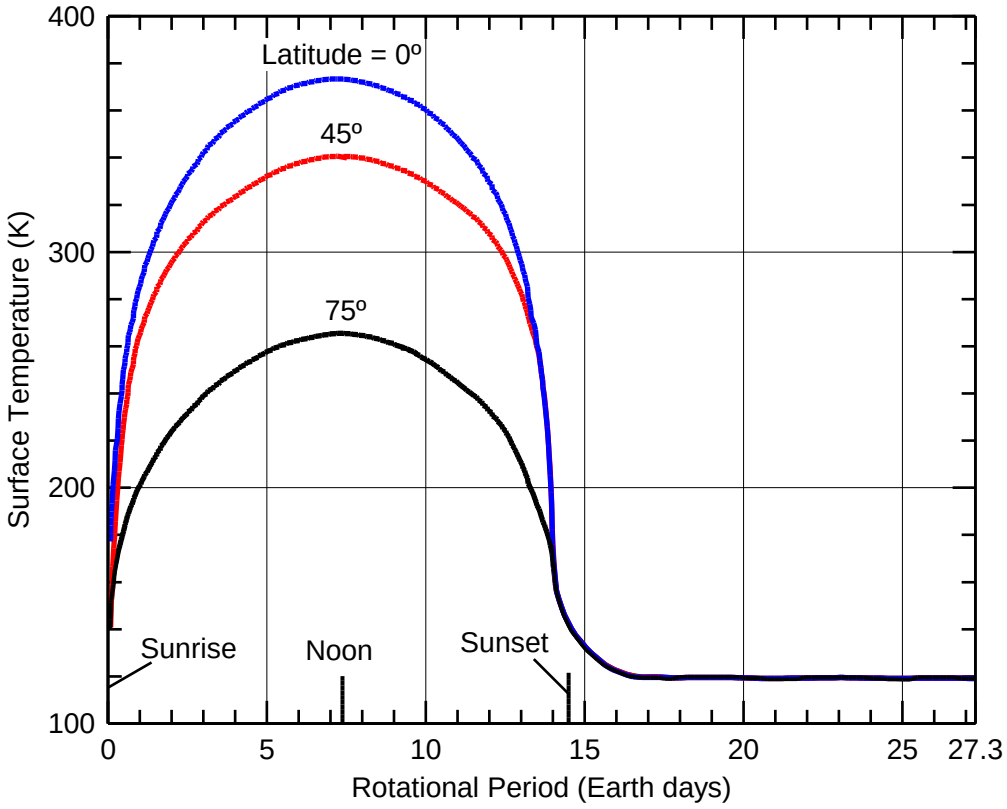

Fig. 2.1. - Lunar surface temperatures versus the Moon's rotational period [Dallas, Diaguila, and Saltsman 1971].

2.2. Future Lunar Outposts

The first lunar outposts are likely to take the form of scientific research stations similar in nature to the present International Space Station (ISS) and Antarctic research bases [Lowman 1985]. These early outposts might house small crews of 4-12 astronauts [Gylfe et al. 1967; Cataldo and Bozek 1993; Kerslake 2005]. Like the ISS the outpost could be built up from a series of interconnected modules, allowing the outpost to be built up over time as more modules are delivered to the lunar surface [Duke, Mendel, and Roberts 1985]. Lunar regolith could be piled on top of these modules to protect the crew

from damaging space radiation [Lowman 1985; Pham and El-Genk 2009]. Initial outposts would likely focus on performing geological exploration of the Moon while developing and testing technologies for extracting lunar resources, such as oxygen and water for life support and for the manufacturing of rocket propellants [Lowman 1985]. A permanent outpost would operate throughout the rotational period; however, darkness and low surface temperatures (Fig. 2.1) during the lunar nighttime may limit some crew activities on the surface [Littman 1992].

Table 2.3. - Electrical power needs for a crewed lunar outpost.

Study	Outpost Type	Power Requirements	Reference
NASA Apollo era	Initial outpost	20-35 kW_e	Gylfe et al. (1967)
NASA	Initial outpost	25-100 kW_e	Mason et al. (1989)
Pacific Northwest Laboratory Study	Initial outpost	100 kW_e	Bamberger and Gaustad (1992)
NASA Space Exploration Initiative Emplacement	Initial outpost	25 kW_e day, 12.5 kW_e night	Littman (1992)
NASA Space Exploration Initiative Consolidation	Developed outpost	100 kW_e	Littman (1992)
NASA Space Exploration Initiative Operations	Advanced developed outpost	550 kW_e	Littman (1992)
NASA First Lunar Outpost	Initial outpost	12 kW_e day, 11 kW_e night	Cataldo and Bozek (1993)
Lunar Research Institute	Advanced commercial outpost	25-75 kW_e per person	Lenard and Binder (1999)
Exploration Systems Architecture Study	Initial outpost	20-100 kW_e, 50 kW_e nominal	Kerslake (2005)
NASA Lunar Architecture Team	Initial outpost	5 kW_e day, 2 kW_e night per surface module	Freeh (2009)

Future lunar outposts will require reliable sources of electrical power for essential life support, crew surface activities, resource extraction, and fuel and propellant production.

Table 2.3 compares the estimated electrical power requirements for a number of lunar outpost architectures proposed in the literature. The power requirements for an early lunar outpost have been estimated to range from 12-100 kW_e [Gylfe et al. 1967; Littman 1992; Cataldo and Bozek 1993; Kerslake 2005; Mason, Poston, and Qualls 2008; Bennett 2008a]. These power requirements could eventually increase to 100's-1000's of kW_e as the lunar outpost expands in size and in the scope of its activities [Littman 1992; Lenard and Binder 1999]. Resource processing, such as the extracting oxygen or volatiles like hydrogen or ^3He from the lunar regolith, could require significant increases in electrical power [Littman 1992]. The effect of the Moon's rotational period on crew activities and life support can result in very different power requirements between the daytime and nighttime (Table 2.3).

Many studies of early lunar outposts suggest that power needs could be met with a single reactor power system generating ~30-50 kW_e, with a limited solar PV system as a backup power system. Expanded power generation at the outpost could be supplied by landing additional reactor power systems, possibly with upgraded energy conversion technology to increase their electrical power output [Harty and Mason 1993]. The next section describes the building blocks which make up a space nuclear reactor power system.

2.3. Space Nuclear Power Systems for Lunar Outposts

The layout of a generic reactor power system for lunar surface power is shown in Figure 2.2. The reactor power system is divided into three major subsystems coupled with heat transport processes: these are (1) the fission reactor, (2) the energy conversion subsystem, and (3) the heat rejection radiator. Nuclear fission in the reactor generates heat which is transported by the primary working fluid to the energy conversion subsystem. This subsystem converts a portion of the thermal power to electricity which is supplied to the outpost using the power management and distribution subsystem. Waste heat from the energy conversion subsystem is transported by the secondary working fluid or medium to be rejected into space using the heat rejection radiator panels. Radiation shielding is required to protect sensitive electrical components from the reactor's neutron and gamma radiation. Details on these subsystems are discussed next.

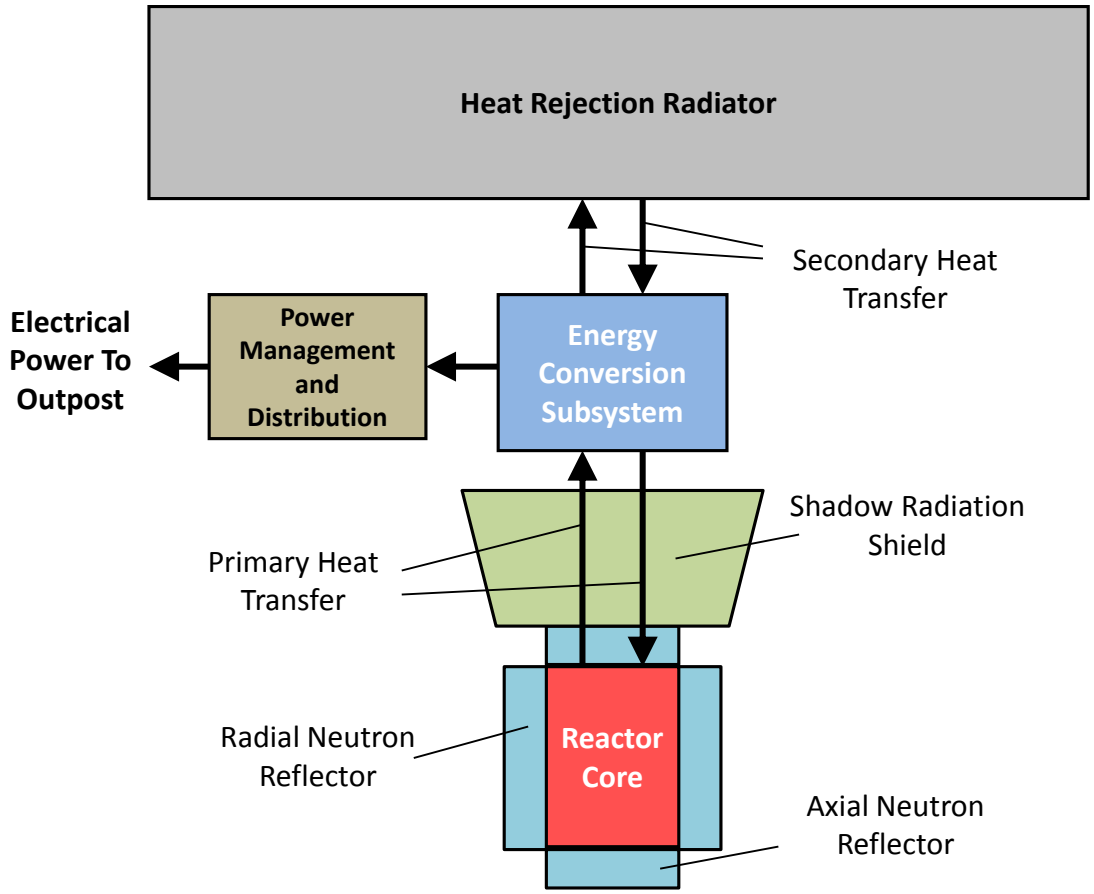

Fig. 2.2. – Schematic of generic space nuclear power system for lunar surface power.

The nuclear reactor core provides the thermal heat source in the integrated power system. Reactors developed for space exploration are typically fueled with Highly Enriched Uranium (HEU) (> 90 wt% ^{235}U) in order to minimize the size and mass of the reactor core and the power system. Fuels containing enriched uranium have very little initial radioactivity due to the long half-lives of the natural uranium isotopes ($T_{1/2}$ = $7.04x10^{8}$ years for ^{235}U, $4.47x10^{9}$ years for ^{238}U, and $2.46x10^{5}$ years for ^{234}U). Therefore, the reactor core poses very little radiological concern until the reactor starts up on the lunar surface.

The reactor core can be designed with either a fast-neutron or a moderated neutron energy spectrum. Fission neutrons originate with fast energies, and can be moderated by scattering off of light elements, such as hydrogen and carbon, losing energy with each collision. Moderated reactors require less fissile material in the core to be critical, as the

neutron fission cross sections are larger at lower energies. However, moderating neutrons in a compact reactor requires the core to contain hydrogen-bearing materials, which have the smallest moderation lengths, increasing the size and mass of the reactor and the integrated radiation shield [Dieckamp 1967; Poston 2005]. In addition, many moderating materials, such as metal hydrides, cannot operate at very high temperatures, limiting the reactor operating temperature and the power system conversion efficiency [Dieckamp 1967; Poston 2005].

Compact space reactors experience high neutron leakage rates which could be reduced using neutron reflectors (Fig. 2.2), increasing the core excess reactivity and operational life. Neutron reflectors are typically made from beryllium metal or beryllium oxide (BeO), due to their low mass, suitability at high temperatures, and the large ^{9}Be (n, 2n) neutron cross section, which increases the flux of neutrons returning to the core. Owing to the high neutron leakage rate from space reactors, these reactors use ex-core control elements within the radial neutron reflector. Details on the neutronics effects of several different options for reactivity control of space nuclear reactors are discussed in Appendix B. The lunar regolith can serve as a supplemental neutron reflector for the reactor core [Bess 2008; Hatton and El-Genk 2009]. The surrounding regolith reflects back a portion of the neutrons which escape through the integrated Be or BeO reflectors surrounding the core. Using the lunar regolith as a supplemental reflector allows the thickness of the integrated neutron reflectors to be reduced, while maintaining the same excess reactivity, reducing the reactor mass by hundreds of kilograms [Hatton and El-Genk 2009].

The fission heat generated inside the reactor is removed either by a circulating fluid or passively using heat-pipes. Space reactors typically operate at higher temperatures than terrestrial power reactors. This is to achieve a high energy conversion efficiency while maintaining a high heat rejection temperature, to limit the size and mass of the radiator panels. High temperature operation is compatible with the use of inert gas coolants (He or binary mixtures of noble gases such as He-Xe) and liquid metals (such as sodium, sodium-potassium alloys (NaK), or lithium). Alternatively the reactor can be cooled by multiple alkali-metal heat-pipes integrated into a solid core structure. The evaporator

sections of the heat-pipes are located inside the reactor core and the condenser sections are thermally coupled to the energy conversion subsystem. These heat-pipes can be designed to operate well below their prevailing limits during nominal operation, so that in the event a heat-pipe fails, the adjacent heat-pipes would safely and reliably carry the added heat load [El-Genk and Tournier 2004; Poston, Kapernick, and Guffee 2002].

The energy conversion subsystem converts a portion of the thermal energy generated in the reactor into electrical power for the crewed outpost. This could be accomplished using static technology generating direct current (DC) power, such as Thermoelectric (TE), Thermionic (TI), Thermo-Photovoltaic (TPV), or Alkali-Metal Thermal to Electric Conversion (AMTEC). Alternatively dynamic technology generating alternating current (AC) power should be used, such as Rankine Cycle (organic, or alkali metal), Closed Brayton Cycle (CBC), or Free Piston Stirling Engine (FPSE). Static energy conversion has the advantage of having no moving parts, and in many cases can enable passive load following responses to changes in electricity demand from the outpost [El-Genk 2009; El-Genk and Tournier 2006a]. Dynamic energy conversion technologies, in comparison, often have higher conversion efficiencies than static technologies. Some static technologies like AMTEC can achieve comparable thermal efficiencies to dynamic technologies like FPSE and CBC [El-Genk and Tournier 2004]. The power management and distribution subsystem conditions the generated electricity to the various currents and voltage levels required by the load (Fig. 2.2).

The selection of an energy conversion technology is typically closely tied to the choice of reactor coolant. Gas cooled reactors have excellent compatibility with CBC conversion [Wolman and Zika 2006; Gallo and El-Genk 2009; El-Genk and Gallo 2010]. To reduce mass, these systems use a direct CBC loop with the primary coolant serving as the working fluid [Wollman and Zika 2006]. Highly conductive liquid metal coolants are well suited for energy conversion with high heat flux requirements such as TE, AMTEC, or FPSE [El-Genk 2009; Mason and Schreiber 2007]. Heat-pipe cooled reactors have similar compatibilities as those cooled by liquid metals, but physically integrating the numerous heat-pipes with the energy conversion system can be challenging [El-Genk and Tournier 2004]. FPSEs require the heat to be effectively transferred to the relatively small

heater heads of the Stirling generators. This could require that a heat-pipe cooled system incorporate an intermediate heat-pipe-to-liquid metal heat exchanger so that the liquid metal can transfer the heat to the heater heads of the FPSEs [Poston et al. 2002]. Reactor power systems operating at lower temperatures could potentially use Rankine power systems with organic working fluids, but the low condenser temperature would require a very large and massive radiator [Mason, Poston, and Qualls 2008].

The residual heat from the energy conversion cycle is rejected into space using heat rejection radiator panels. As radiative heat transfer scales proportional to T^4, the size and mass of the radiator is strongly dependent on the heat rejection temperature. The radiator panels for a lunar power reactor would be erected on the surface above the shielded reactor core (Fig. 2.2). Some space reactor designs have used pumped loop radiator panels where the secondary coolant flows through tubes integrated with panels [Glyfe et al. 1967; Nikitin et al. 2000]. To reduce the pressure losses in the secondary loop and achieve a more uniform heat rejection temperature for the radiator panels, the panels could use passive heat-pipes to efficiently spread the heat across the width of the panel. For heat rejection temperatures < 500 K the working fluid in these heat pipes can be water. Operating at higher temperatures alkali metals, such as rubidium, potassium, or sodium, could be used [Tournier and El-Genk 2006].

2.4. Placement of Nuclear Reactor Power System on the Moon

The siting of a reactor power system for lunar surface power is driven mostly by the need to protect the crew at the nearby outpost from the neutron and gamma radiation emitted from the reactor and safe post-operation storage. During operation, the radiation emitted from the reactor core will require likely require an exclusion zone around the reactor to limit the exposure to the crew operating on the lunar surface [Elliott et al. 2005]. Following a reactor shutdown, the emitted radiation level significantly decreases as the accumulated radionuclides in the nuclear fuel during operation decay away, reducing the size of the exclusion zone [Elliott et al. 2005]. The dose level to the outpost's crew is affected by the reactor operating power, the distance between the

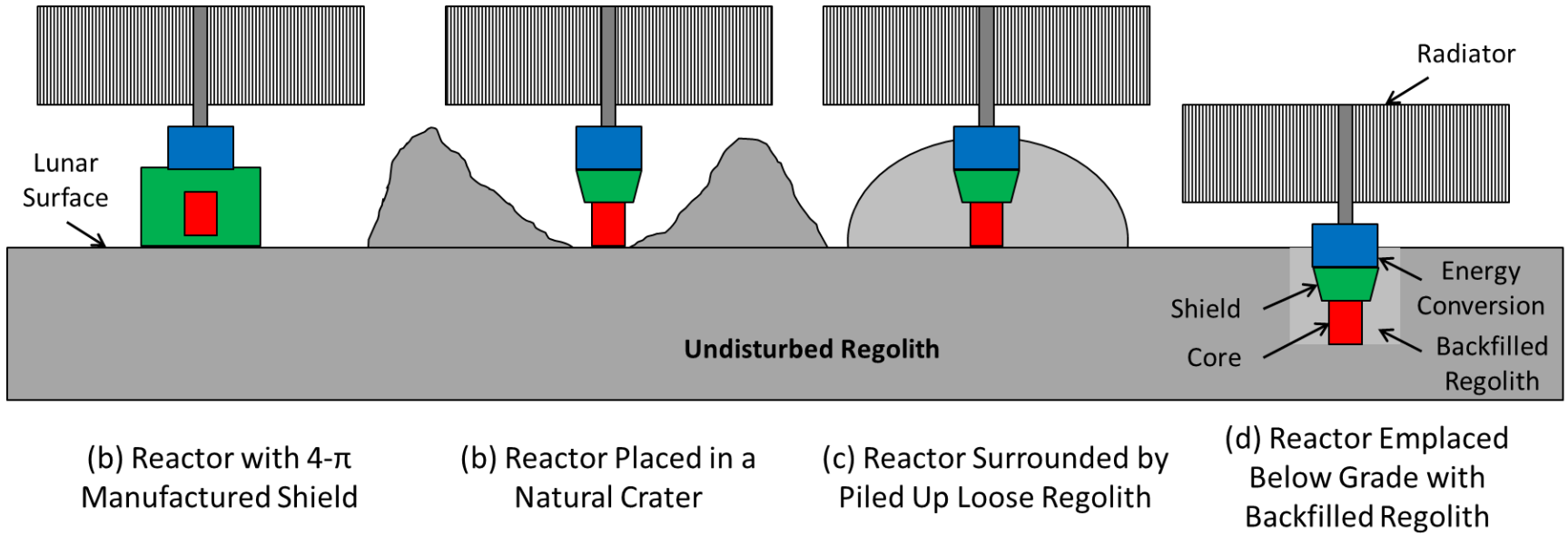

Fig. 2.3. - Placement options for lunar power reactors.

reactor and the outpost, and by the amount of radiation shielding surrounding the reactor. Locating the reactor far from the outpost (2-5 km) reduces the amount of shielding required, but results in a large radiation exclusion zone and increases the length, mass, and complexity of the electrical transmission cables [Elliott et al. 2005]. Increasing the amount of radiation shielding helps minimize the size of the exclusion zone and allows emplacing the reactor much closer to the outpost (200-500 m). This simplifies deployment of the power system and electrical distribution grid. Sensitive electronic components could be located a short distance (10's of m) away from the reactor to reduce their radiation exposure and allow for regular maintenance and repairs by the outpost's crew [Glyfe, et al 1967; Elliott et al. 2005].

Exploration nuclear reactor systems utilize directional shadow shields to protect the spacecraft and payload contained within a narrow solid cone angle, a distance (10-25 m) away from the reactor. Operating on the surface of Moon, power reactors need 4-π shielding in all directions to protect both radiation sensitive components in the power system and nearby crew on the surface. The lunar regolith can be used for radiation shielding to reduce the mass of manufactured shielding which must be brought from Earth. The lunar regolith is, however, a much less effective shielding material on a per-volume basis than manufactured shielding materials [Kang et al. 2006]. Thus reactor power systems for the Moon are typically designed to use the lunar regolith as radiation shielding [Glyfe et al. 1967; Elliott et al. 2005; Amari et al. 2006; Mason, Poston, and Qualls 2008; Schriener and El-Genk 2011; El-Genk and Schriener 2011]. A manufactured shield may also be required to protect the energy conversion equipment, power electronics, and reactor controller and instrumentation [Elliott et al. 2005].

In addition to serving as radiation shielding, lunar regolith can also serve as a supplemental neutron reflector for the reactor core. The regolith reflects back a portion of the neutrons which escape through the integrated Be or BeO reflectors surrounding the core. The composition of the lunar regolith (Table 2.2) makes it a poor neutron reflector on a per volume basis. However, the thickness required for shielding is sufficient to provide an infinite reflector of regolith. Using the lunar regolith as a supplemental reflector allows the thickness of the integrated neutron reflectors to be reduced, while

maintaining the same excess reactivity, and thus reactor operational life [Hatton and El-Genk 2009]. The reduced reflector thickness can reduce the reactor mass at launch by hundreds of kilograms [Hatton and El-Genk 2009].

In addition to the neutron and gamma radiation emitted by the reactor, space radiation in the form of high energy charged Solar Energetic Particles (SEPs) and Galactic Cosmic Rays (GCR) will also contribute to the dose to crew and the electronic components of the power system [Pham and El-Genk 2010]. The exposure to both high energy charged space radiation and the radiation emitted directly by the reactor will require significant shielding. Radiation sensitive components may need to be buried underneath a sufficient depth of lunar regolith to protect them from the steady exposure to GCR and brief, but intense bursts of SEPs [Pham and El-Genk 2010]. For SEP with energies < 100 MeV a thickness of ~12 cm of regolith is sufficient to reduce the dose to electronics due directly to the solar protons by almost eight orders of magnitude [Pham and El-Genk 2010]. Shielding these high energy charged particles is challenging due to the generation of high energy secondary neutrons within the shield by spallation reactions. Protecting against these secondary neutrons requires adding additional shielding reduce the dose to sensitive electronic systems [Pham and El-Genk 2010].

Fig. 2.3 presents potential placement options of a nuclear reactor power system on the lunar surface. Fig. 2.3a shows a power system mounted on a lunar lander with manufactured 4-π radiation shield. This approach results in both the highest system mass as well as the largest separation distance between the reactor and the lunar outpost. Figs. 2.3b-d show different regolith shielding arrangements; a reactor placed above grade within a natural feature like a small crater using the raised lip as shielding (Fig. 2.3b), a reactor emplaced above grade and surrounded by piled regolith (Fig. 2.3c), and a reactor emplaced below grade in a hole or trench, backfilled with regolith (Fig. 2.3d). Placing the reactor within a natural obstacle (Fig. 2.3b) requires locating the outpost near a suitable crater or a hill. It also provides no protection to landing spacecraft, while flying over the reactor's position. The most effective arrangement is emplacing the reactor below grade (Fig. 2.3d) due to the increased density of the undisturbed regolith with depth (Table 2.1). This also maximizes the regolith effectiveness as a supplemental neutron reflector and

Table 2.4. - Reactor concepts for lunar surface power

Reactor	Neutron Energy Spectrum	Fuel		Reactor Coolant	T_{ex} (K)	Core Materials		Thermal Power (kW_{th})	Operation Life	
		Form	Enrichment			Fuel Cladding	Vessel/ Structure		FPY	MWd
SNAP-8 [Gylfe et al. 1967]	Epithermal	$U/ZrH_{1.79}$	93%	NaK-78	977	Hastelloy N	316 SS	541	4	740
Prometheus FSPS [Elliot et al. 2005]	Fast	UO_2	93%	He-Xe	1,150	Ni-1%Zr	Alloy 625	222	10	811
SCoRe-S_{11} [Hatton and El-Genk 2009]	Fast	UN	95%	Li	1,150	Mo-14%Re	Mo-14%Re	2600	3.26	3100
HOMER-25 [Amiri et al. 2006]	Fast	UO_2	93%	K Heat-Pipes	880	316 SS	316 SS	95	5	173
AFSPS [Mason, Poston, and Qualls 2008]	Fast	UO_2	93%	NaK-78	890	316L SS	316L SS	175	8	511
HPCMR [Gu et al. 2013]	Fast	UN	42%	Li Heat-Pipes	1,525	Mo-14%Re	Mo-14%Re	1600	10	5844

Table 2.5. - Power system concepts for lunar surface power

Reactor	Power System Energy Conversion		Electrical Power (kW_e)	Total System Mass (kg)	Reactor Mass (kg)	Shielding Mass (kg)	Shielding Implementation
	Type	Efficiency, η_{th}					
SNAP-8 [Gylfe et al. 1967]	PbTe TE	3.7%	20	17,345	499	1,2074	4-π Manufactured Shield
Prometheus FSPS [Elliot et al. 2005]	CBC	24.3%	50	6,481	700	2,402	Manufactured + Regolith
SCoRe-S_{11} [Hatton and El-Genk 2009]	SiGe TE	4.4%	113.1	-	351	-	Manufactured + Regolith
HOMER-25 [Amiri et al. 2006]	FPSE	26.3%	25	2,133	462	569	Manufactured + Regolith
AFSPS [Mason, Poston, and Qualls 2008]	FPSE	22.8%	40	4,928	439	1,676	Manufactured + Regolith
HPCMR [Gu et al. 2013]	SiGe TE	7%	112	3,181 w/o Shielding	1,198	-	Manufactured + Regolith

shielding. A surface shield of piled regolith (Fig. 2.3b) is less effective than the below grade emplacement due to the lower mean density of the loosely packed regolith (Section 2.1). Designing a nuclear reactor power system for use on the Moon requires accounting for the siting and emplacement of the reactor and power system on its performance. Proposed designs of lunar nuclear power reactors and integrated power systems are the subject of the next section.

2.5. Proposed Surface Power Reactor Designs

This section provides a historical review of proposed space nuclear power systems designed for lunar surface power. While many reactors and power system concepts have been proposed for powering early lunar outposts, only a few are actually designed taking the lunar environment into account. Design details for the reactors and integrated surface power systems are summarized in Tables 2.4 and 2.5, respectively.

The US Systems for Nuclear Auxiliary Power (SNAP) program had developed several moderated space reactors, which used uranium/zirconium hydride (U/ZrH) fuel. These include the SNAP-10A system, the only US reactor power system flown in space [Dieckamp 1967]. For a post-Apollo lunar outpost, a lunar surface power system concept was studied using the SNAP-8 reactor, then undergoing nuclear ground testing [Gylfe et al. 1967]. This lunar power system concept used a fully passive power system with PbTe TE energy conversion to provide 20 kW_e to a lunar outpost for only up to 4 FPY. The study focused on the design of the integrated power system without modifying the reactor for the Moon. The favored implementation had the reactor integrated on a lander with a massive 4-π manufactured radiation shield. The study also considered emplacing the reactor below grade and utilize the regolith along with a shadow shield, but there were concerns over how difficult it would be to excavate the regolith [Gylfe et al. 1967]. To increase mission reliability over the operational life the reactor, the power system electronics were designed to be able to be serviced by crew members on the lunar surface if necessary [Gylfe et al. 1967].

The space reactor design group at Los Alamos National Laboratory (LANL) has developed the Heat-pipe Operated Mars/Moon Exploration Reactor (HOMER) family for

surface power applications on the lunar and Martian surface [Poston et al. 2002; Amiri et al. 2006]. The HOMER reactor concepts integrate alkali-metal heat-pipes into a solid core structure containing the fuel pellets and B_4C rods as a Spectral Shift Absorber (SSA). The HOMER-25 was developed for use in a lunar power system with six opposed pairs of FPSEs to generate 25 kW_e to a lunar outpost for up to 5 FPY [Amiri et al. 2006]. A challenge for heat-pipe cooled reactors is thermally coupling the reactor heat-pipes to the energy conversion system. In the HOMER-25, the condensers of the reactor heat-pipes penetrate into a common liquid potassium pool boiler, and the generated potassium vapor carries the reactor thermal power to the heater heads of the of FPSEs (Fig. 2.6) [Amiri et al. 2006]. The use of a common heat exchanger in the power system results in a single- point failure in reactor cooling, despite the apparent redundancy provided by the multitude of reactor heat pipes. The reactor would be emplaced below grade on the Moon and use a liquid borated water radiation shield in addition to the surrounding regolith. Analysis of the HOMER-25 focused on the reactor neutronics and did not include detailed analysis of the reactor thermal or power system.

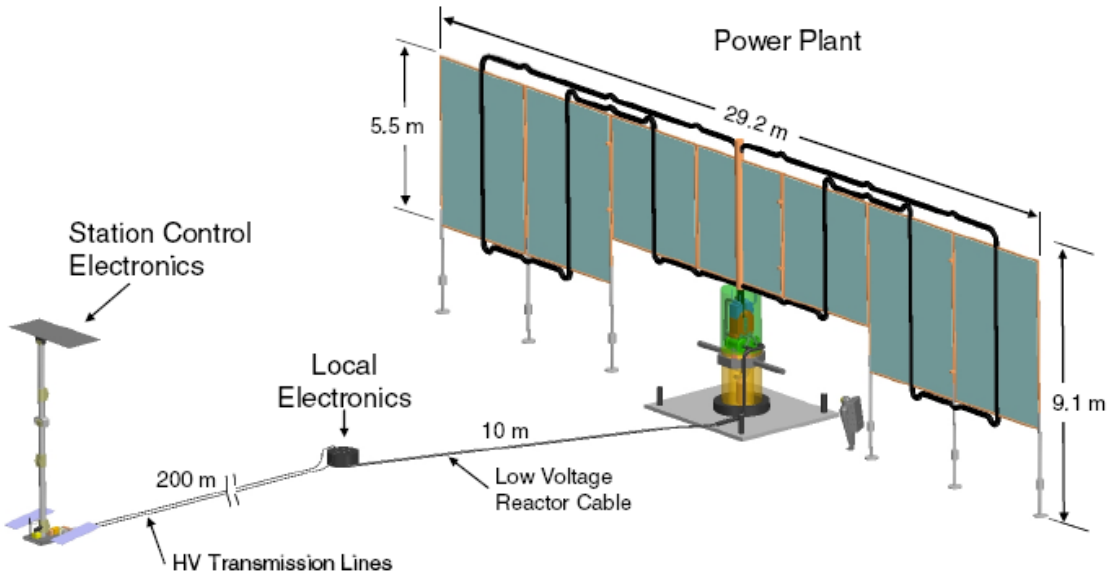

Fig. 2.4. - Prometheus FSPS elements deployed on the surface before construction of regolith sandbag shield [Elliott et al. 2005].

NASA's Project Prometheus selected a He-Xe cooled gas cooled reactor with CBC energy conversion as the preliminary reactor power system design for the Jupiter Icy

Moons Orbiter (JIMO) spacecraft [Wollman and Zika 2006]. Following the cancellation of the JIMO mission, the Prometheus project studied adapting the gas cooled reactor technology to powering a lunar outpost [Elliott et al. 2005]. The design effort focused on developing an integrated power system design with regolith shielding and its deployment on the lunar surface (Fig. 2.4) [Elliott et al. 2005]. The Prometheus Fission Surface Power System (FSPS) was sized to supply 50 kW_e to a nearby lunar outpost for up to 10 FPY [Elliott et al. 2005]. The reactor core is cooled by a He-20%Xe binary gas mixture that also serves as the working fluid for the two CBC units; one operating and one spare in case of a failure [Elliott et al. 2006]. The residual heat is rejected through vertically-oriented water heat-pipes radiator panels (Fig. 2.4). The Prometheus FSPS would be placed on the surface and surrounded by a 3.5-4 m thick regolith sandbag radiation shield (Fig. 1.1 lower image). Sensitive electronics components of the power system, including the reactor controllers and power electronics, were designed to be placed ~10 m away from the reactor outside the thick regolith shield. This placement reduces their exposure to the reactor's radiation and possibly allows for crew access in case repairs are needed (Fig. 2.4).

The Sectored Compact Reactor for Small power (SCoRe-S) design concepts have been developed at The University of New Mexico's Institute for Space and Nuclear Power Studies covering a wide range of thermal power levels [El-Genk et al. 2005]. These liquid metal cooled, fast-neutron spectrum reactors are designed for the avoidance of single point failures in reactor cooling and energy conversion. The hexagonal core is divided into six identical sectors separated by metal dividers. The sectors are thermally and neutronically coupled, but hydraulically decoupled. In the unlikely event a sector would experience a Loss of Coolant (LOC) or Loss of Cooling (LOCo) the heat generated in the affected sector transfers to the adjacent sectors aided by flat heat-pipes located within the sector dividing walls [El-Genk et al. 2005]. The SCoRe-S concepts are identified by the number of rows of the wire-wrapped UN fuel rods in the triangular core sectors, from the smallest SCoRe-S_7 with seven rows to the largest SCORe-S_{11} with eleven (Fig. 2.5) [El-Genk et al. 2005; Hatton and El-Genk 2009].

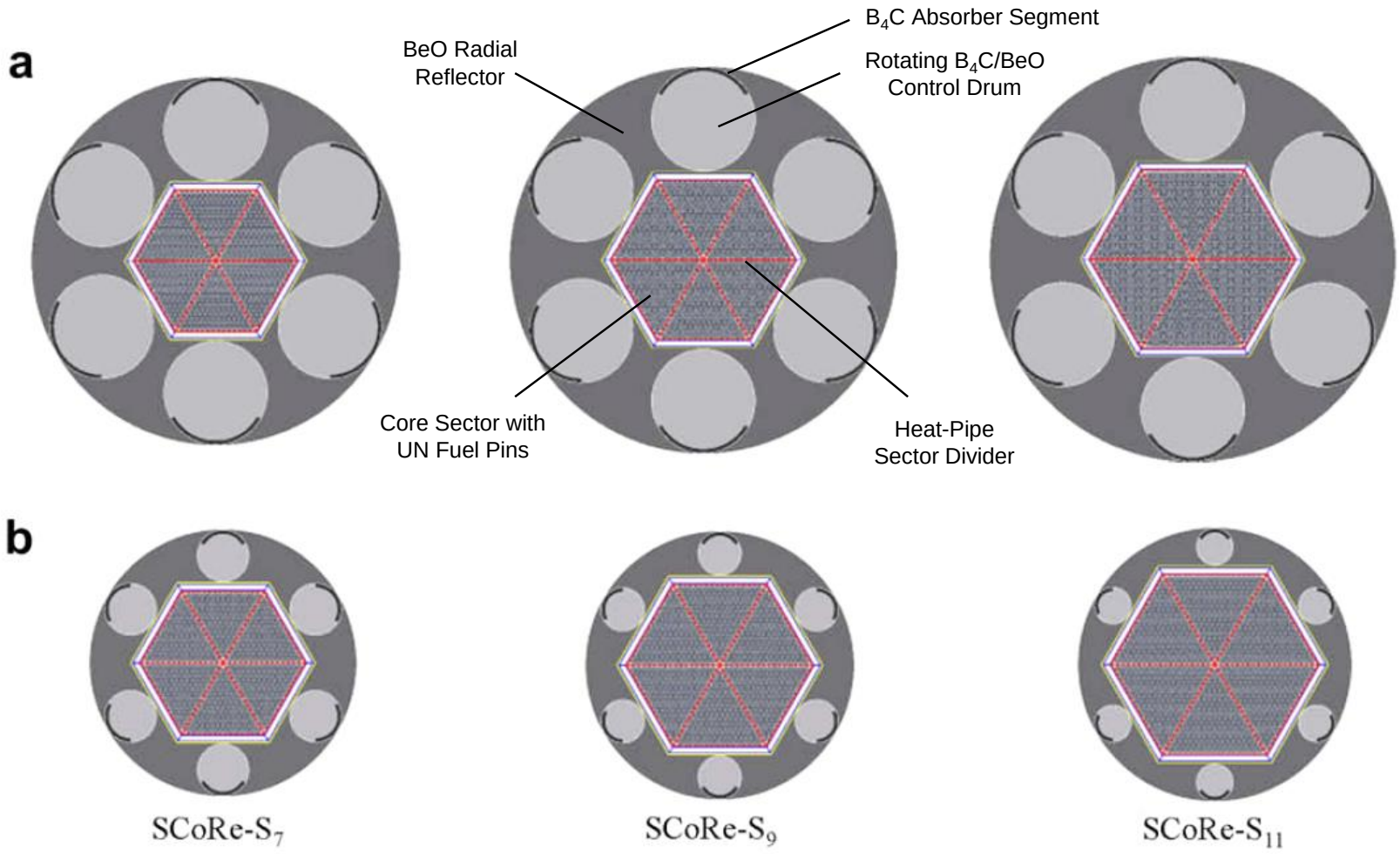

Fig. 2.5. - Radial cross section views of SCoRe-S concepts; (a) with 16 cm thick BeO radial reflector, (b) with radial reflector thickness sized to have equal excess reactivity using supplemental regolith reflector [Hatton and El-Genk 2009; El-Genk et al. 2005].

The SCoRe-S has been studied for lunar surface power, being designed to utilize the lunar regolith as a supplemental neutron reflector [Hatton and El-Genk 2009]. On the lunar surface, the reactor core would be placed in a trench or borehole to be the backfilled with regolith. The supplemental regolith reflector made it possible to reduce the thickness of the BeO radial neutron reflector while maintaining the same core excess reactivity (Fig. 2.5). Reducing the thickness of the heavy BeO reflector decreased the mass of the reactor by 150-200 kg [Hatton and El-Genk 2009]. The baseline SCoRe-S power system (Fig. 2.6) utilizes a lithium cooled SCoRe-S_{11} fission heat source with SiGe TE energy conversion subsystem, TE powered DC EM pumps, and rubidium heat-pipe radiator panels. Each of the six core sectors is served by a pair of primary and secondary loops with separate energy conversion and radiator panels. The SCoRe-S_{11} power system is designed to be able to supply up to 114 kWe at a thermal power of 2.89 MWth for at least 7 years (Fig. 2.6) [El-Genk and Tournier 2006a].

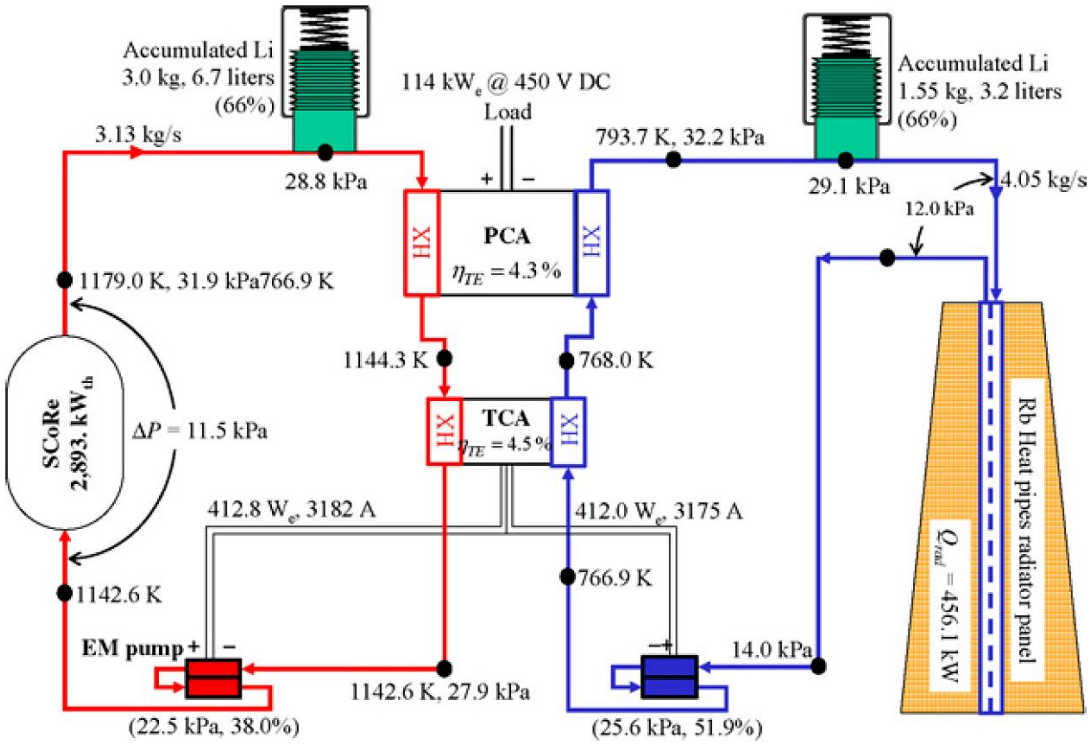

Fig. 2.6. - Schematic of SCoRe-S_{11} power system [El-Genk and Tournier 2006a].

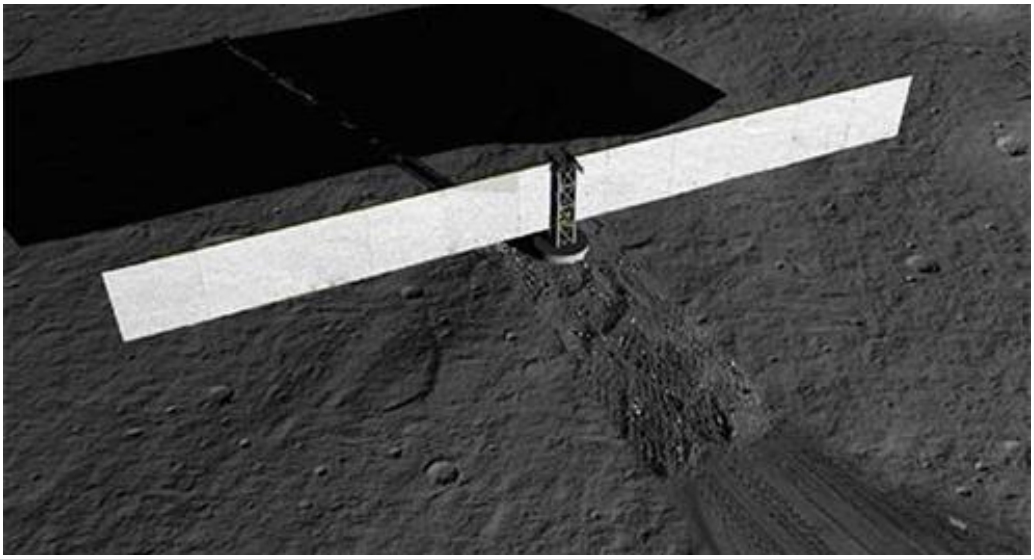

Fig. 2.7. - Artist's conception of AFSPS power system emplaced on the Moon with the reactor core buried in the lunar regolith [Mason, Poston, and Qualls 2008].

In 2006, a NASA and DOE initiated study of the Affordable Fission Surface Power System (AFSPS) aimed to develop a low cost, near term reactor power system concept for use on the Moon and Mars [Mason, Poston, and Qualls 2008]. The performed trade studies investigated concepts, with a variety of reactor fuel, coolant, and energy conversion combinations. The trade studies compared both fast and moderated neutron spectrum reactors with power system using PbTe TE, FPSE, CBC, and organic Rankine cycle energy conversion. All of the reactor power system concepts were designed to generate 40 kW_e for 8 FPY at fuel temperatures < 900 K to maximize the use of conventional reactor materials [Mason, Poston, and Qualls 2008]. These studies resulted in selecting a reference system concept for detailed costing analysis. The selected AFSPS reference concept features a fast neutron spectrum liquid NaK-78 cooled reactor coupled to six opposed pairs of FPSE for energy conversion. The NaK-78 coolant has an exit temperature of 890 K and uses 316 stainless steel for the reactor vessel and coolant loop ducting [Mason, Poston, and Qualls 2008]. The reference design uses conventional UO_2 fuel pellets and 316L stainless steel for the fuel rods cladding. On the Moon, the AFSPS reactor would be emplaced below grade and utilize the lunar regolith to supplement the integrated B_4C radiation shielding (Fig. 2.7). The initial AFSPS study focused on the reactor neutronics, although subsequent analyses have been performed of the reactor

thermal-hydraulics and integrated power system of the NaK-78 cooled reference concept [Fission Surface Power Team 2010].

The Heat Pipe Cooled Modular fast Reactor (HPCMR) concept developed at the China Institute of Atomic Energy is a high temperature, lithium heat pipe cooled surface power system concept [Gu et al. 2013]. The performed analysis focused on the neutronics of the reactor core on the Moon. The solid reactor core uses high temperature Mo-14Re refractory metal alloy, and is cooled with a multitude of lithium heat pipes. The spaces between the fuel clad and core heat-pipes are filled with Mo-14%Re random fiber matrices with 35% porosity to accommodate core thermal expansion while maintaining good thermal contact. To meet launch criticality safety requirements, without using SSAs, the core of the HPCMR is split into three separate modules each consisting of a 1/3 section of the active core, the BeO radial reflector, with independent SiGe TE conversion units and potassium heat-pipe heat radiator panels [Gu et al. 2013]. Launched separately the three modules would be combined on the lunar surface into a single critical assembly, capable of generating up to 112 kW_e for up to 10 FPY.

The few proposed reactor concepts designed for use on the Moon have been designed with relatively short operational lives < 10 FPY. In addition, the level of design analysis performed for many of these concepts has been limited to either the reactor neutronics or simplified state point analyses of the integrated power system. None of these studies coupled together the neutronics and thermal-hydraulics analyses to develop the reactor design. Much more comprehensive design and safety analyses would be needed to develop long life nuclear power reactors for the Moon.

The research presented in Chapters 3-5 performs detailed design and analyses of the long operational life SCoRe and PeBR concepts and power systems for lunar surface power. The next chapter describes multi-physics design and safety analyses methodology for the SCoRe concept and power system for lunar outposts. Presented are the results of the coupled neutronics, CFD and thermal-hydraulics analyses to investigate the effect of the fuel rods diameter and choice of spectral neutron absorber on the BOL excess reactivity and operational life, and the thermal-hydraulic performance during nominal operation. Chapter 3 also presents CFD and thermal-hydraulic safety analyses of the

SCoRe operating at reduced power levels with a core sector experiencing a LOC or LOCo. Chapter 4 describes the PeBR concept and power system for lunar surface power and presents the results of the parametric neutronics analyses for achieving a long operation life and the design of the fuel pellets transport canisters. Also presented are the results of the fuel loading analysis of the PeBR on the Moon and the spatial porosity distributions in the loaded core sector. Chapter 5 examines the post operation storage of the SCoRe and PeBR concepts to investigate the time required for the radioactivity inside the core to decay to allow for the recovery and retrieval of the reactors. Also investigated is the decay heat removal from the reactors following shutdown at end-of-life.

3. MULTI-PHYSICS DESIGN AND ANALYSES OF SECTORED COMPACT REACTOR (SCoRe) FOR A LUNAR OUTPOST

This chapter presents the multi-physics design and analyses methodology developed in this research and applies it to the Sectored Compact Reactor (SCoRe) to develop a long operational life reactor which is fueled at launch. This methodology iteratively couples together the results of Monte Carlo neutronics simulations with CFD and thermal-hydraulic analyses of the reactor to investigate the effects of the different design changes on the reactor's safety and performance. The Monte Carlo code MCNPX [Pelowitz et al. 2011] performs the reactor neutronics while the commercial CFD package STAR-CCM+ [CD-adapco 2012] models the reactor thermal-hydraulics. The manual coupling scheme passes the fuel rod power profiles calculated using MCNPX to the STAR-CCM+ code to define the thermal heat sources inside the fuel pellets to model the reactor's thermal-hydraulic performance (Fig. 3.1). The core temperatures calculated using the STAR-CCM+ code are then incorporated into the MCNPX simulations to account for the effects of thermal expansion of the core materials and Doppler broadening of the neutron cross sections on the core reactivity and operation life (Fig. 3.1). This allows for accurate modeling of the reactor's neutronic and thermal-hydraulics performance during nominal operation.

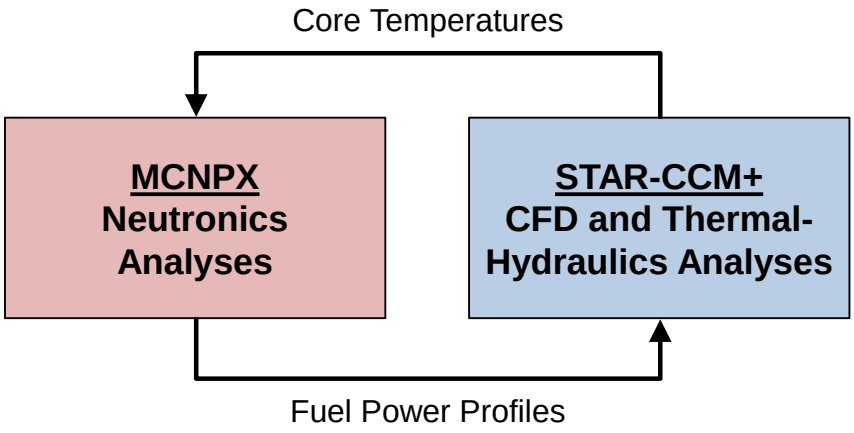

Fig. 3.1. - Iterative coupling scheme for neutronics and thermal-hydraulics in the developed multi-physics methodology.

Thermal-hydraulic safety analyses of the SCoRe reactor and power system additionally requires modeling the behavior of the integrated power system (Fig. 3.2). This system couples together the liquid metal cooled SCoRe with passive thermoelectric energy conversion, DC electromagnetic pumps, and rubidium heat-pipes radiator panels. The dynamic system simulation tool DynMo-TE [El-Genk and Tournier 2006; El-Genk and Schriener 2010] is used to model the performance of the SCoRe power system. The DynMo-TE simulations determine the reactor inlet and outlet temperatures and the coolant flow rates for the core sectors of the reactor during nominal operation, and when operating at a lower power with a sector experiencing a loss of coolant (LOC) or a Loss of Cooling (LOCo).

This research develops the fast energy spectrum SCoRe concept and power system for lunar surface power. The reactor operates at moderate temperatures of 850-900 K, uses conventional 316L SS for the reactor and power system structure, and is cooled with circulating liquid sodium-potassium alloy (NaK).The multi-physics design and analyses mythology presented in this chapter investigates increasing the operational life of the SCoRe concept. This is accomplished by reconfiguring the core geometry to reduce neutron leakage and parasitic absorption while maintaining the same amount of uranium fuel in the reactor core and satisfying launch and operational safety requirements. The next section describes the flow of the design and analyses methodology used to develop the SCoRe concepts investigated in the course of this research.

3.1. Multi-Physics Analyses Methodology

The SCoRe design is developed using the multi-physics analyses methodology outlined in Fig. 3.3. This outline shows the flow path of the coupled analyses. The design of the SCoRe for lunar surface power underwent three major design upgrades in the course of this research, from the initial SCoRe-N_{18} [Schriener and El-Genk 2011] to the SCoRe-N_5 [Schriener and El-Genk 2012a] and finally to the Solid Core-Sectored Compact Reactor (SC-SCoRe) [Schriener and El-Genk 2013, 2014a] (Fig. 3.3). Details of the design of these reactors (Fig. 3.2) and their placement on the Moon are described in Section 3.2. Section 3.3 provides details on the computational methodology used in performing the multi-physics design and analyses in this chapter.

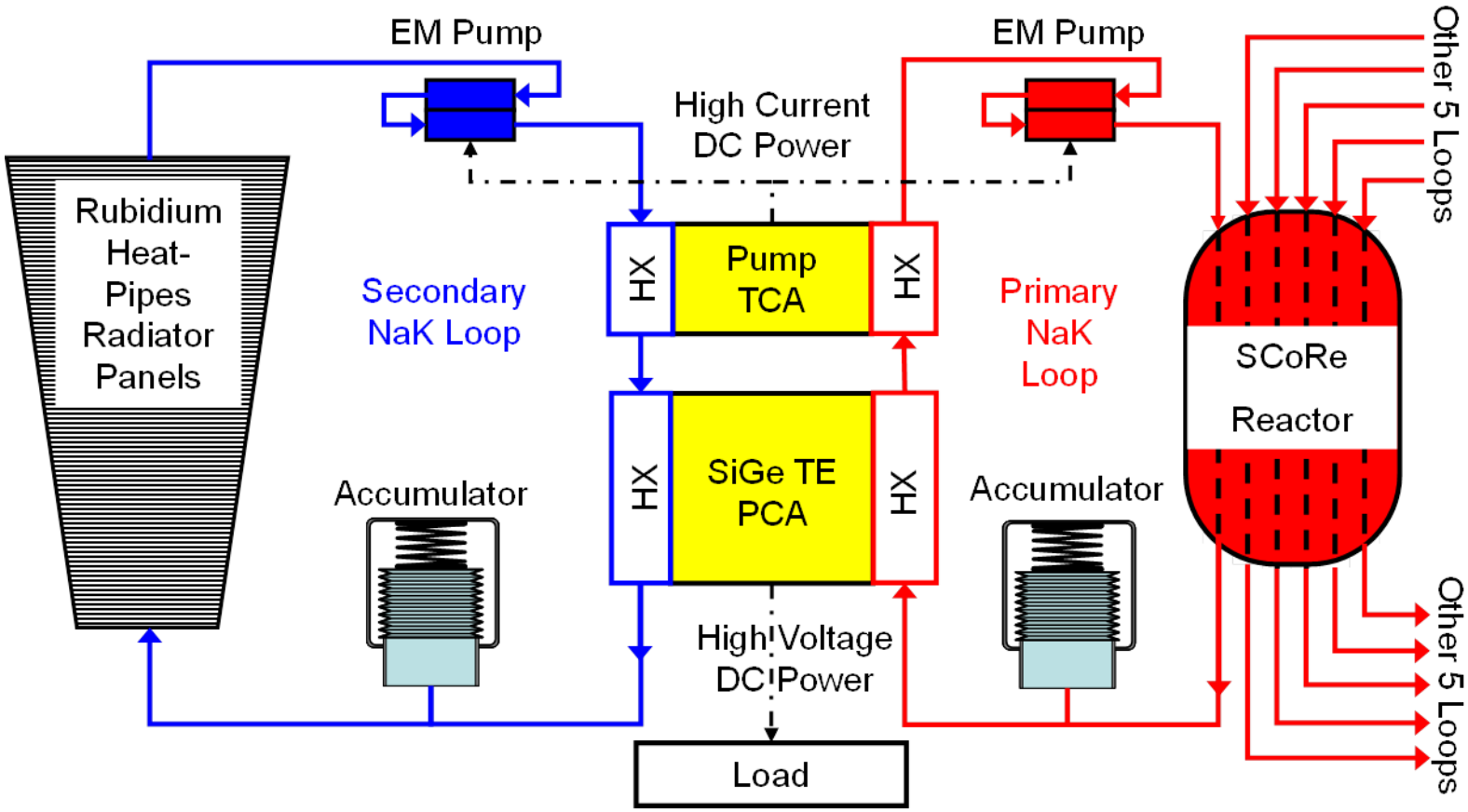

Fig. 3.2. - Schematic of the SCoRe integrated power system with thermoelectric (TE) energy conversion, showing a pair of primary and the secondary loops with EM pumps coupled to a core sector and heat rejection radiator panels [Schriener and El-Genk 2014b].

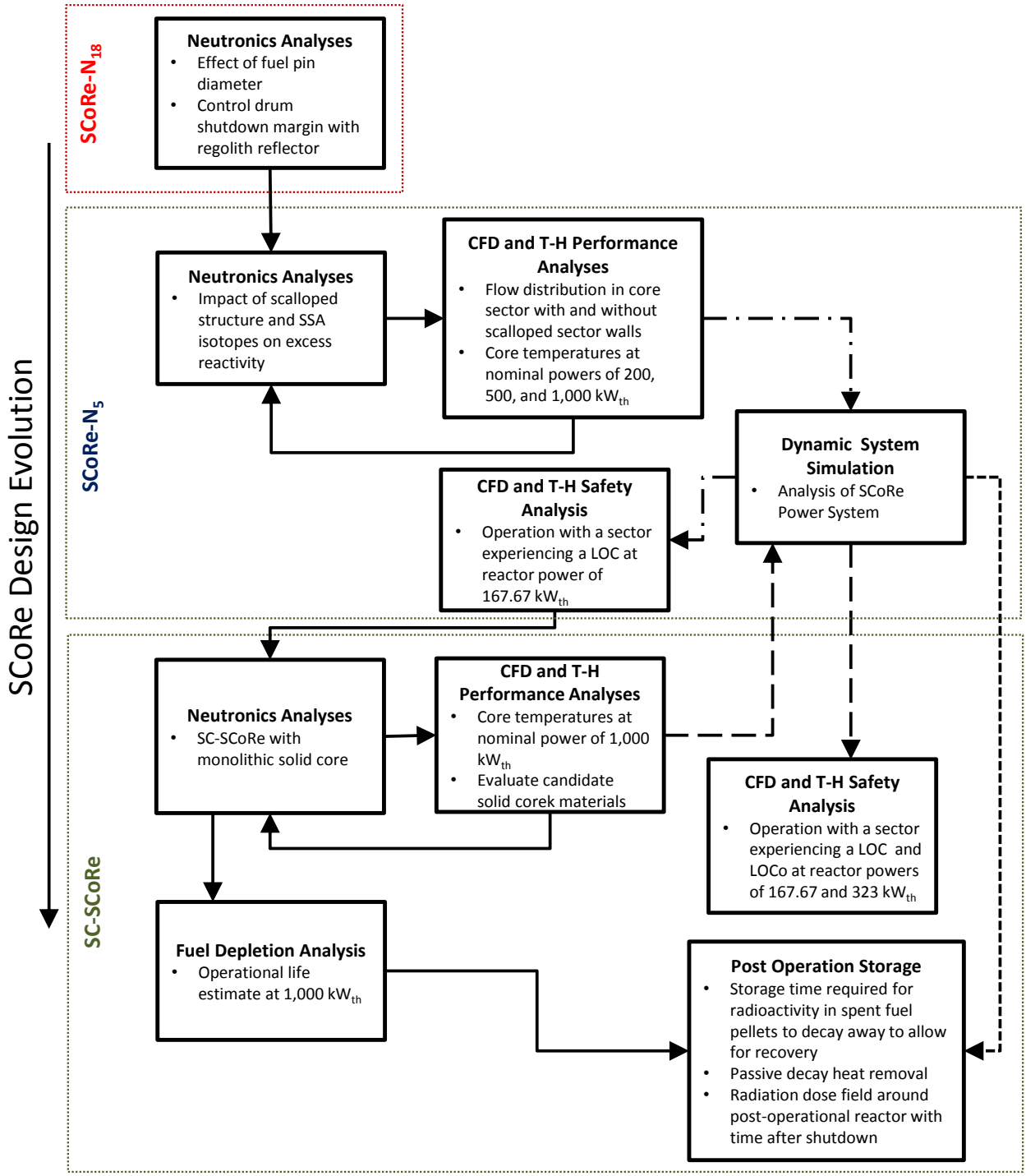

Fig. 3.3. - An outline of multi-physics design and safety analyses for SCoRe concepts for a lunar outpost.

The design and analyses methodology starts with the neutronics analysis of the SCoRe reactor core. This analysis is performed to ensure that the various reactor designs satisfy the launch safety requirement of ensuring that the bare reactor core remains at least -$1.0 subcritical, when submerged in wet sand (30 vol% seawater and 70 vol% sand) and flooded with seawater. Other neutronics design requirements include having a control shutdown margin of at least -$1, and providing enough excess reactivity for a long operational life of at least 20 years. The design process for the SCoRe outlined in Fig. 3.3 begins with the neutronics analyses of the initial SCoRe-N_{18} concept. These analyses investigated the effect of increasing the fuel rod diameter as well as the control drum shutdown margin on the BOL excess reactivity and the reactor total mass.

Results of the neutronics analyses of the SCoRe-N_{18} led to the development of the SCoRe-N_5. The analyses of the SCoRe-N_5 (Section 3.5) investigated first the flow distribution in the core sectors, and the effects of adding scalloped sector walls on the thermal-hydraulic performance. The coupled neutronics and thermal-hydraulics analyses that follow investigated the effects of the scalloped sector core structure and choice of Spectral Shift Absorber (SSA) additive isotope on the Beginning-of-Life (BOL) excess reactivity, total reactor mass, and thermal-hydraulic performance at nominal reactor powers of 200 kW_{th}, 500 kW_{th}, and 1,000 kW_{th} (Section 3.6) (Fig. 3.3). The coupled analyses in Section 3.7 determine the temperature reactivity effect in the reactor at the different power levels. Dynamic simulations of the power system (Fig. 3.2) are performed using DynMo-TE (Fig. 3.3) to determine the reactor inlet and exit temperatures and coolant flow rates at different power levels. These values are used in the thermal-hydraulics and safety analyses investigating the continued operation of the SCoRe-N_5 with a sector experiencing a LOC at a reduced reactor power of 167.67 kW_{th}. (Section 3.8). The analyses calculate the peak temperatures of the fuel and fuel rods cladding in the affected sector to determine if they remain well below their melting points.

The evolution of the SCoRe for lunar surface power culminated in the SC-SCoRe. The analyses of the SC-SCoRe in Sections 3.9-10 investigate the effects of the reactor's monolithic solid core structure on the BOL excess reactivity and the thermal-hydraulic

performance at a nominal power of 1,000 kW_{th} for two core block materials, 316L stainless steel and Oxide Dispersion Strengthened Molybdenum (ODS-Mo) (Fig. 3.3). Safety analyses are performed of continued operation of the SC-SCoRe with a core sector experiencing a LOC or a LOCo. The operating conditions for the adjacent reactor sectors at the reduced power levels are determined from the DynMo-TE integrated system analyses of the power system. Investigated are the peak fuel and 316L or ODS-Mo core structure temperatures at reduced reactor powers of 167.67 kW_{th} and 323 kW_{th}.

Fuel depletion analysis of the SC-SCoRe, presented in Section 3.10, uses the internal BURN feature in MCNPX [Pelowitz et al. 2011] to estimate the operational life of the reactor at a nominal power of 1,000 kW_{th} (Fig. 3.3). The calculated radionuclide inventory in the post-operational reactor is used to determine the storage time required for the radioactivity to decay down to a low enough level for crewmembers to recover the reactor, which is the subject of Chapter 5. In addition, the post-operation analyses calculate the radiation field around the stored SC-SCoRe reactor core. The next section describes the design of the SCoRe-N_{18}, and SCoRe-N_5, and SC-SCoRe concepts developed and analyzed in this chapter.

3.2. SCoRe Reactor Design Evolution

The design of the initial SCoRe-N_{18} concept [Schriener and El-Genk 2011] is adapted from that of the SCoRe-S_{11} (Fig. 2.5) [El-Genk et al. 2005; Hatton and El-Genk 2009]. The SCoRe-S_{11}, developed for operation in deep space as well as on the lunar surface [Hatton and El-Genk 2009], uses Mo-14%Re refractory metal alloy for the fuel rods cladding and reactor vessel and is cooled by liquid lithium at a reactor outlet temperature of 1,150-1,250 K [El-Genk et al. 2005]. This chapter develops the SCoRe for a long operation life on the lunar surface by nominally operating at low inlet and exit temperatures of 850 K and 900 K, and utilizing conventional structural materials.

The SCoRe-N_{18} and SCoRe-N_5 are cooled with liquid NaK-78 (22 wt% Na, 78 wt% K) [Schriener and El-Genk 2011, 2012] while SC-SCoRe is cooled with liquid NaK-56 (44 wt% Na, 56 wt% K) [Schriener and El-Genk 2014b; 2015a]. The SCoRe-N_{18}, SCoRe-N_5, and SC-SCoRe employ austenitic 316L stainless steel for the reactor vessel

and coolant ducts [IAEA 2006; Poston and Marcille 2006; Staub 1967; El-Genk 2009], and use UN fuel. The high uranium density in UN (13.5 gU/cm^3) reduces the mass and size of the reactor core, and its high thermal conductivity decreases the fuel operating temperatures and hence, fission gas release, consistent with a long operation life [Ross et al., 1988]. Keeping the UN operating temperature low also reduces swelling and minimizes fuel restructuring [Ross et al. 1988, 1990].

The choices of operating the reactors at a relatively low exit temperature and using 316L stainless steel core structure support the design objective of a long operating life of > 20 years. 316L stainless steel has an extensive irradiation database in fast neutron spectrums, is easy to work and fabricate, and is compatible with the liquid NaK-78 and -56 coolants [Angelo and Buden 1985; El-Genk and Tournier 2005; Poston and Marcille 2006; Staub 1967; Zhang et al., 2010]. The UN fuel is also chemically compatible with the stainless steel cladding [Rogozkin, Stepennova, and Proshkin 2003].

The SCoRe-N_{18}, SCoRe-N_5, and SC-SCoRe are designed to be emplaced below grade on the lunar surface, and surrounded with backfilled regolith. These reactors use the surrounding lunar regolith as supplemental radiation shielding to protect the nearby lunar outpost from their neutron and gamma radiation [Kang et al. 2006]. The lunar regolith also serves as a supplemental neutron reflector in order to reduce the reactor mass at launch and hence, the mission and launch cost [Hatton and El-Genk 2009].

The SCoRe reactor cores are divided into six equal sectors separated using flat, potassium heat pipe dividers [El-Genk et al. 2005; Hatton and El-Genk 2009; El-Genk and Schriener 2010; Schriener and El-Genk 2011, 2012a, 2013; 2015a]. Each SCoRe-N_{18} triangular core sector is loaded with 171 fuel rods arranged in a triangular lattice, for a total of 1026 fuel rods in the core. The fuel rods are loaded with highly enriched (95 wt% ^{235}U) UN pellets and have 316L stainless steel cladding with wires wrapped spirally on the cladding outside surface to maintain uniform flow area and provide structural support to the rods during operation. At Beginning-of-Life (BOL) the SCoRe-N_{18} core contains a total of 119.5 kg of ^{235}U. The SCoRe-N_5 sectors are each loaded instead with 15 316L SS clad UN fuel rods, for a total of 90 rods in the core. The SC-SCoRe solid core structure contains 90 stacks of UN fuel pellets, 15 per core sector.

Following the unlikely event of a launch abort accident, the bare reactor, when submerged in wet sand and flooded with seawater remains at least -$1 subcritical. To satisfy safety requirements a 0.15 mm coating of Spectral Shift Absorber (SSA) thermal neutron poison is applied to the outer surface of the reactor vessel and as an additive mixed with the UN fuel pellets [Hawley 1967; Amiri and Poston 2005; King and El-Genk 2006; El-Genk 2008]. SSA isotopes readily absorb moderated neutrons in the water flooded reactor core, but have a small absorption cross section for the fast neutrons to affect the operating reactor, thus minimally affecting the excess reactivity in the core [King and El-Genk 2006].

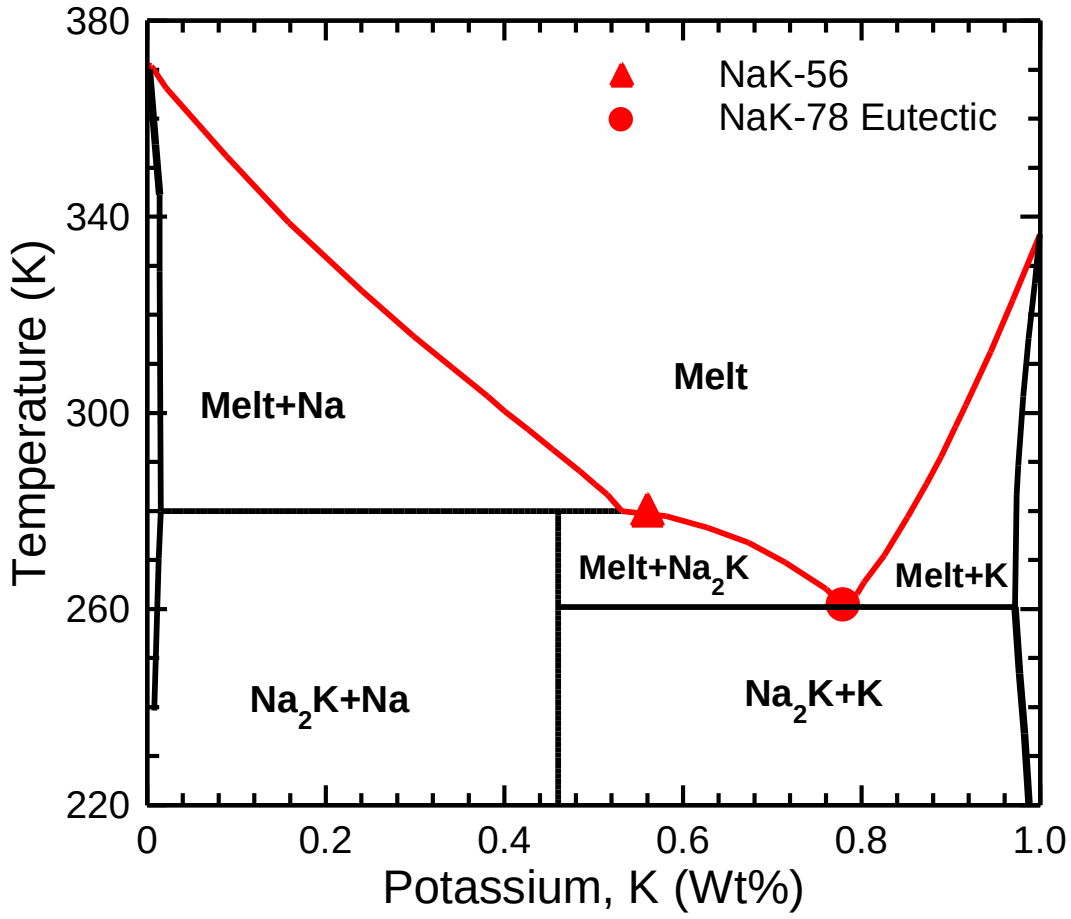

Fig. 3.4. - Sodium-potassium binary phase diagram [Foust 1972].

The SCoRe-N_{18}, SCoRe-N_5 and SC-SCoRe are cooled by liquid NaK-78 and NaK-56 alloys. Fig. 3.4 presents the binary phase diagram for the sodium-potassium alloys. The lowest melting temperature (-12.3^o C or 261 K) is that of the eutectic NaK-78 used by the SCoRe-N_{18} and SCoRe-N_5, indicated by the solid circle symbol in Fig. 3.4. The solid triangle symbol in this figure indicates the melting temperature of the liquid NaK-56 coolant used by the SC-SCoRe, which has a slightly higher melting temperature (6.25^o C or 279.4 K). Liquid NaK-78 has been used in the USA SNAP-10A space nuclear reactor and power system launched in 1965 and the former Soviet Union's RORSAT and TOPAZ reactor power systems, primarily for its low melting point [Angelo and Buden 1985; El-Genk 2009; El-Genk and Schriener 2010; Mason et al. 2008; Staub 1967]. This low melting point could simplify reactor startup procedures by avoiding having to thaw the liquid metal coolant from a frozen state.

Table 3.1. - Properties NaK-78 and NaK-56 liquids at 0.10 MPa & 875 K [Foust 1972].

Property	**Value**	
	NaK-78	**NaK-56**
Boiling Point (K)	1,057.2	1,084.5
Melting Point (K)	260.7	279.4
Density, ρ (kg/m^3)	739.0	757.2
Th. Conductivity, λ (W/m K)	25.6	26.5
Dynamic Viscosity, μ (Pa.s)	1.54×10^{-4}	1.67×10^{-4}
Specific Heat, C_p (J/kg-K)	875.2	982.1
Thermal Diffusivity, α (m^2/s)	3.95×10^{-5}	3.56×10^{-5}
$\mu^{0.2}/(\rho^2 C_p^{2.8})$	1.00	0.701

Table 3.1 compares the properties of liquid eutectic NaK-78 and liquid NaK-56 at the average operating temperature in the SCoRe cores during nominal operation (875 K) [Foust 1972]. Liquid NaK-56 has a higher density, specific heat capacity, and thermal

conductivity than NaK-78. The specific pumping power (pumping power per unit reactor thermal power removed), for forced convection and same temperature rise in the reactor core is proportional to $\mu^{0.2}/(\rho^2 C_p^{2.8})$. The specific pumping power of NaK-56 is ~ 30% lower than that with liquid NaK-78 (Table 3.1). The higher melting point, however, raises the temperature at which the coolant would freeze in the power system loops during launch and post operation storage. The next section describes the integrated SC-SCoRe power system with liquid NaK-56 coolant and its placement on the lunar surface.

3.2.1. Placement of SCoRe Integrated Power System on the Lunar Surface

The SCoRe power system integration avoids single point failures in reactor cooling and electrical power generation (Fig. 3.2). The six sectors of the core are each served by a separate pair of primary and secondary loops with circulating liquid NaK, EM pumps, one in each loop, powered by Thermoelectric Conversion Assemblies (TCAs), a SiGe thermoelectric Power Conversion Assembly (PCA) that supplies electric power to the load at 400 VDC, and a series of three rubidium heat pipes radiator panels (Fig. 3.2). The radiator panels erected on the lunar surface reject the excess heat from the secondary loop into space (Fig. 3.5).

The thermoelectric elements in the six TCAs and the six PCAs of the power system are thermally coupled to the circulating liquid NaK-56 in the primary and secondary loops. The liquid NaK-56 in the primary loops removes the heat generated in the reactor core sectors and transports it to the hot side of the TE elements in the PCAs and TCAs where it is partially converted to DC electrical power. The circulating liquid NaK-56 in the secondary loops removes the heat rejected at the cold side of the TE elements in the PCAs and TCAs and transports it to the heat pipes radiator panels erected on the lunar surface (Fig. 3.5). The fully passive operation of the power system, with no moving parts, ensures operation reliability, and together with the negative reactivity feedback in the reactor core, allows the power system to respond to changes in the load demand without an active control. During nominal reactor operation at a thermal power of 1,000 kW_{th}, liquid NaK-56 enters the core sectors at 850 K and exits at 900 K. During nominal operation, the power system has a net thermal efficiency of 3.8%, continuously supplying 38 kW_e (or 6.33 kW_e from each PCA) to the lunar outpost.

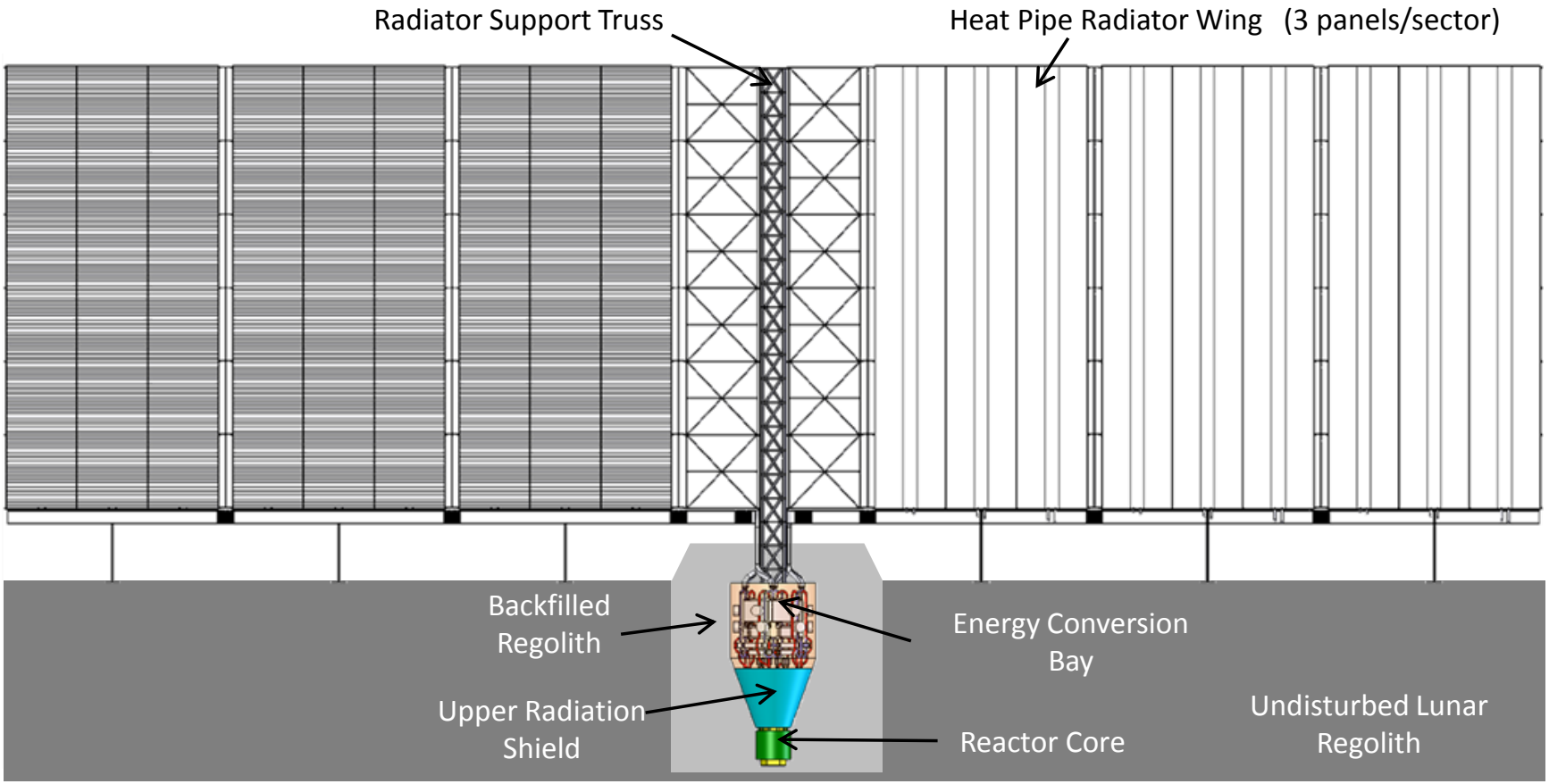

Fig. 3.5. - Below grade SCoRe power system with heat pipes radiator panels erected on the lunar surface [Schriener and El-Genk 2014b].

The SiGe TE elements in the PCAs and the TCAs of the SCoRe power system have had successful history of operating reliably on board numerous NASA space exploration missions deployed during the past 50 years [Angelo and Buden 1985; El-Genk 2008a, 2009; Staub 1967]. The TE elements in the PCAs are connected in series in a number of parallel strings to enhance operation reliability and eliminate single point failures. The PCAs provide electrical power to the load for the lunar outpost at 400 VDC. The TCAs supply the EM pumps in the primary and secondary loops with very high current (> 1,500 A) and low voltage (~ 0.1 VDC) electrical power. Each TCA has at least two parallel strings of series connected TE elements for operation reliability and avoidance of a single point failure [El-Genk and Tournier 2006a].

The rubidium heat pipes of the radiator panels erected vertically on the lunar surface (Fig. 3.5). The radiator heat-pipes nominally operate at $\leq$ 50% of prevailing operation limits, and thus could accommodate multiple heat pipe failures without affecting the power system operation [Tournier and El-Genk 2006b]. In the event one or more heat pipes fail, the adjacent heat pipes in the panels would carry the additional thermal load without exceeding design operation limits. Carbon-carbon composite armor is applied to the exposed surfaces of the panels (Fig. 3.5) to protect the heat pipes from meteorites' impact and limits potential failures.

The SCoRe reactor core would be placed below the lunar surface in a ~ 2.5 m deep trench backfilled with regolith (Fig. 3.5). The regolith, piled ~ 1 m high on top of the reactor, protects radiation sensitive equipment and nearby crew from exposure to emanating neutrons and gamma photons from operating reactor (Fig. 3.5) [Hatton and El-Genk 2009; Kang et al. 2006]. The lunar regolith also serves as a supplemental neutron reflector that helps prolong the reactor's operation life by increasing the core excess reactivity. This eliminates the need to use a thick BeO radial reflector for the reactor launched from Earth [Hatton and El-Genk 2009]. Reducing the thickness of the radial BeO reflector decreases the reactor's total mass at launch from Earth saving millions of dollars in launch cost. The SCoRe starts up only after emplaced safely below the lunar surface (Fig. 3.5). Such a placement also provides for safe storage of post-operation

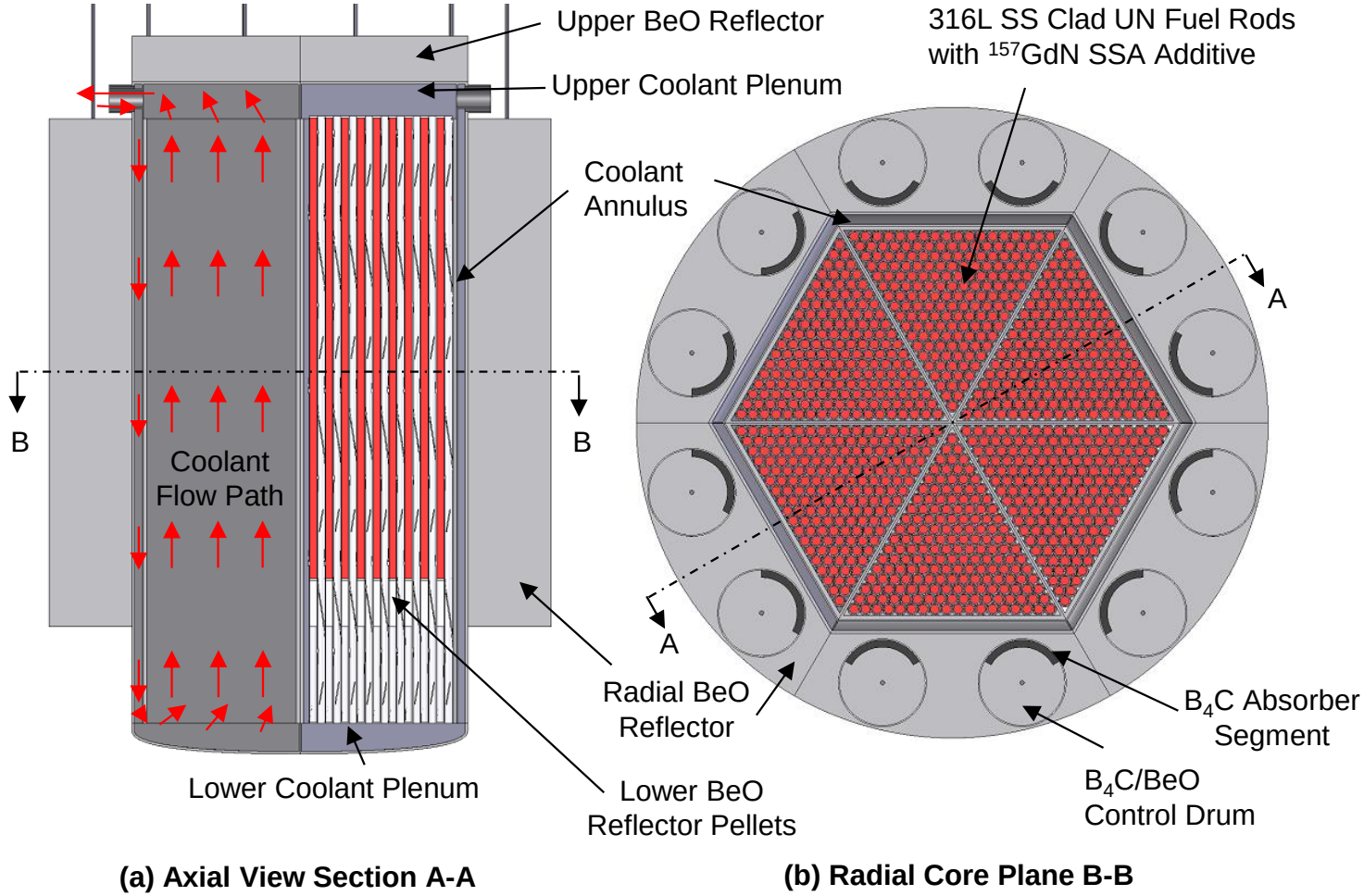

Fig. 3.6. - Cross-sectional views of the initial SCoRe-N_{18} [Schriener and El-Genk 2011].

reactor for hundreds of years. The following section describes the design of the initial SCoRe-N_{18} concept which ultimately led to the SC-SCoRe design

3.2.2. SCoRe-N_{18}

The design of the NaK-78 cooled SCoRe-N_{18} is adapted from the earlier SCoRe-S_{11}, maintaining the same fuel rods diameter and core vessel cross section dimensions. Axial and radial cross sectional views of the SCoRe-N_{18} reactor are shown in Fig 3.6. Fig. 3.6a shows the flow path for the liquid NaK-78 coolant through the SCoRe-N_{18} core sectors. During nominal operation, the circulating liquid NaK-78 enters the reactor through separate annular ducts at 850 K (Fig. 3.6a), and flows down through the annulus on the inside of the reactor vessel, before entering the lower coolant plenums. From there, the liquid NaK-78 passes through the orifices in the lower support plate, flowing up through the core sectors to cool the fuel rods. The liquid NaK-78 exiting the reactor core sector mixes in the upper coolant plenums then flows through the inner passage of the concentric coolant ducts at an average temperature of 900 K (Fig. 3.6).

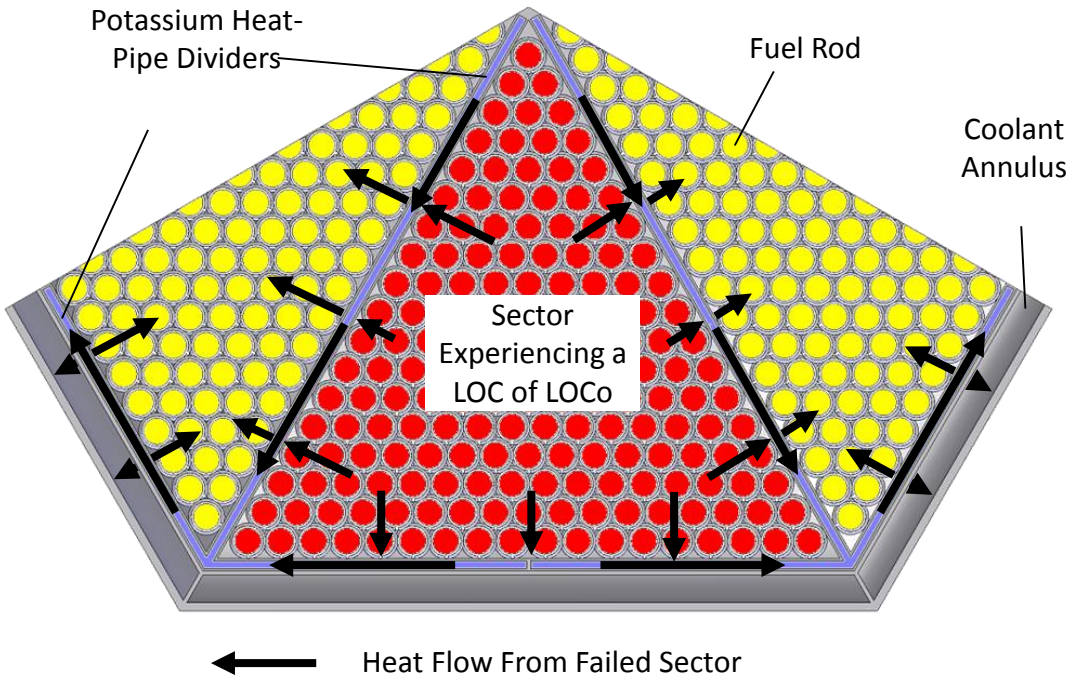

Fig. 3.7. - Heat flow path for a core sector experiencing a LOC or LOCo [Schriener and El-Genk 2011].

In the unlikely event that a sector experiences a LOC or a LOCo, the fission heat generated in the affected sector transports, aided by the flat potassium heat-pipes dividers, to the two adjacent sectors cooled by circulating liquid NaK-78 (Figs. 3.7). The circulating liquid NaK-78 in the adjacent core sectors convectively removes both the heat generated in that sector and the heat transferred from the sector experiencing a LOC or LOCo. The heat-pipes dividers help spread the heat removed from the affected sector to the colder zones near the inlet annuli of the adjacent functioning sectors. Thus, a pipe break in the primary or the secondary loop for a reactor core sector will not fully compromise the operation of the power system. In this case, the reactor power system may continue operating, but at a reduced thermal power level to prevent overheating the fuel rods in the core sector experiencing a LOC or a LOCo.

The hexagonal core of the SCoRe-N_{18} is surrounded by six, 7 cm thick BeO radial reflector panels, one per core sector. (Fig. 3.6b). These panels, clad in thin 316L SS and held together by retention metal bands, are designed to disassemble upon impact onto a solid or water surface, in the unlikely event of a postulated launch abort accident [Staub 1967; King and El-Genk 2006]. The 4 cm thick BeO axial reflector slab, outside the reactor vessel is also clad in thin 316L SS. The 4 cm thick, BeO axial reflector at the opposite end of the reactor core consists of stacks of pellets inside the fuel rods (Fig. 3.8). The stack of the BeO reflector pellets is separated from the UN fuel pellets in the rods by a thin rhenium disk to avoid reactions between the nitride fuel and oxide reflector pellets (Fig. 3.8).

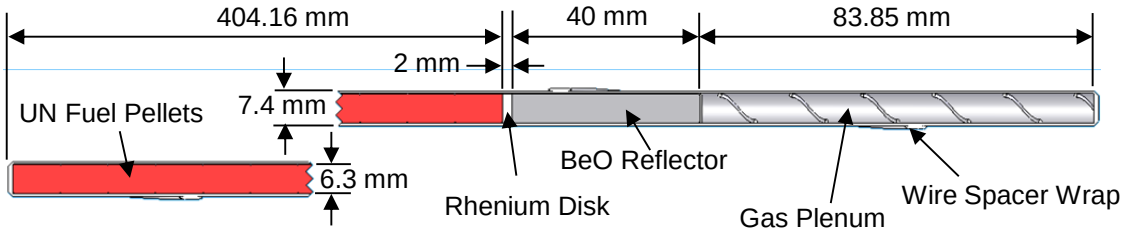

Fig. 3.8. - Partial cross-sectional view of a UN fuel rod [Schriener and El-Genk 2011].

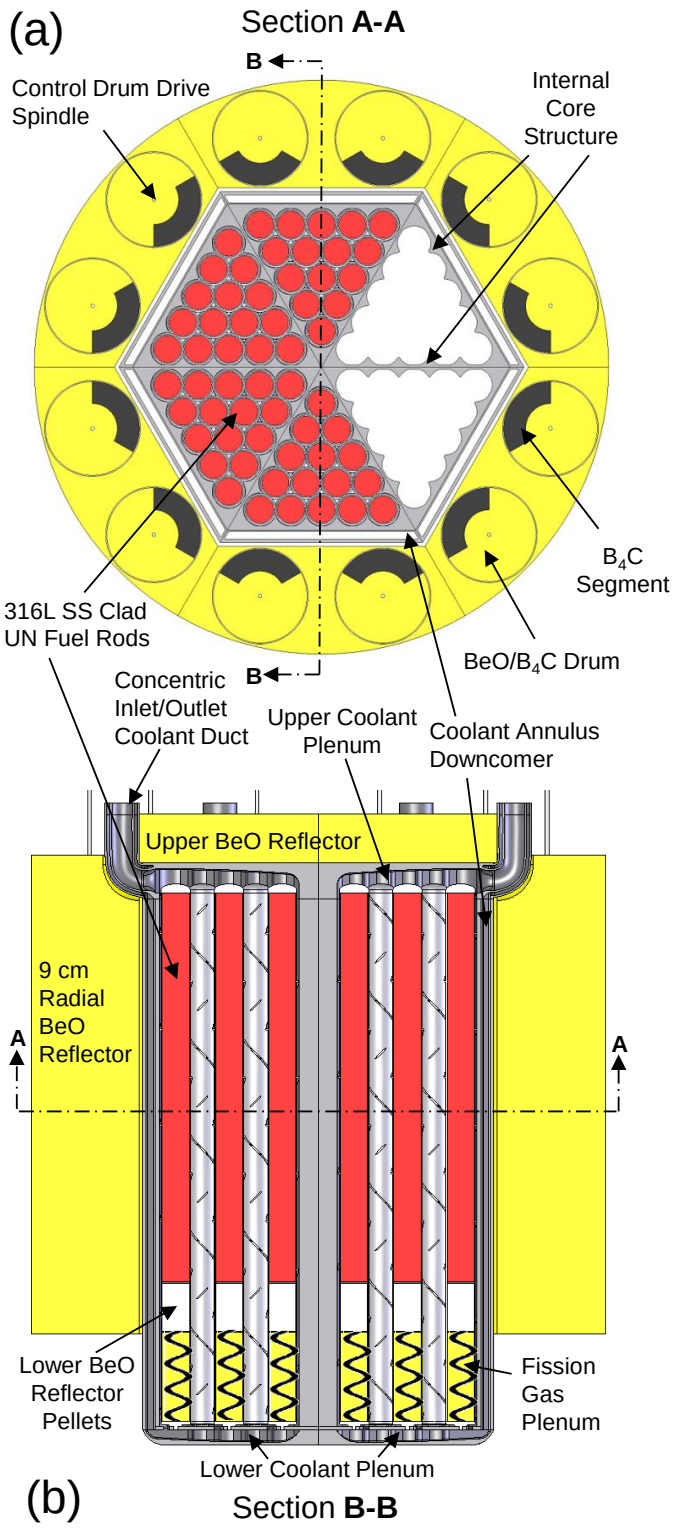

Fig. 3.9. - Cross-section views of the SCoRe-N_5 core: (a) elevation view and (b) plan view [Schriener and El-Genk 2012a].

Each radial BeO reflector panel contains two B_4C/BeO rotating control drums (Fig. 3.6) to keep the reactor sufficiently subcritical during launch. These drums also control the reactivity in the reactor core during startup and nominal operation and shutdown the reactor at EOL or in case of an emergency. The boron in the B_4C segments (120° arc) in the 12 control drums is fully enriched in ^{10}B. The segments in the drums face the reactor core in the shutdown configuration (Fig. 3.6b) and face 180° away from the core at EOL.

Results of the parametric neutronics analyses discussed in Section 3.4 led to the development of the evolved design of the SCoRe-N_5.

3.2.3. SCoRe-N_5

The evolved SCoRe-N_5 design is presented in Fig. 3.9. This figure shows radial and longitudinal cross-section views for the SCoRe-N_5 reactor with the arrangement of the UN fuel rods in the core sectors, the coolant inlet and exit ducts, and flow path into and out of the reactor core sectors. The SCoRe-N_5 reactor with six sectors has the same core cross sectional dimensions as the SCoRe-N_{18}, except that each core sector is loaded with five rows of larger diameter (2.43 cm) UN fuel rods. The large (2.43 cm) diameter fuel rods increase the coolant flow area along the edges and corners of the core sectors (Fig. 3.10a). To compensate for this, the 316L SS sector walls are scalloped to produce a more uniform flow distribution and cooling of the fuel rods (Fig. 3.10b). The scalloped walls even out the flow area for the fuel rods and reduce flow bypass in the core sectors. The SCoRe-N_5 hexagonal core is surrounded by six, 9 cm thick BeO radial reflector panels clad in thin 316L stainless steel (Fig. 3.9). A thicker radial reflector is required to increase the reactivity worth of the 12 rotating B_4C/BeO control drums to handle the higher BOL cold-clean excess reactivity in the SCoRe-N_5 core.

3.2.3. SC-SCoRe

Unlike the earlier reactor designs (SCoRe-N_{18} and SCoRe-N_5), the SC-SCoRe has a monolithic solid core structure. This enhances the heat transfer by conduction from a core sector experiencing a LOC to the potassium heat-pipes dividers (Fig. 3.11). The monolithic structure also increases the structure strength of the core. The metallic solid core is contained within the 316L stainless steel reactor vessel. The performed CFD

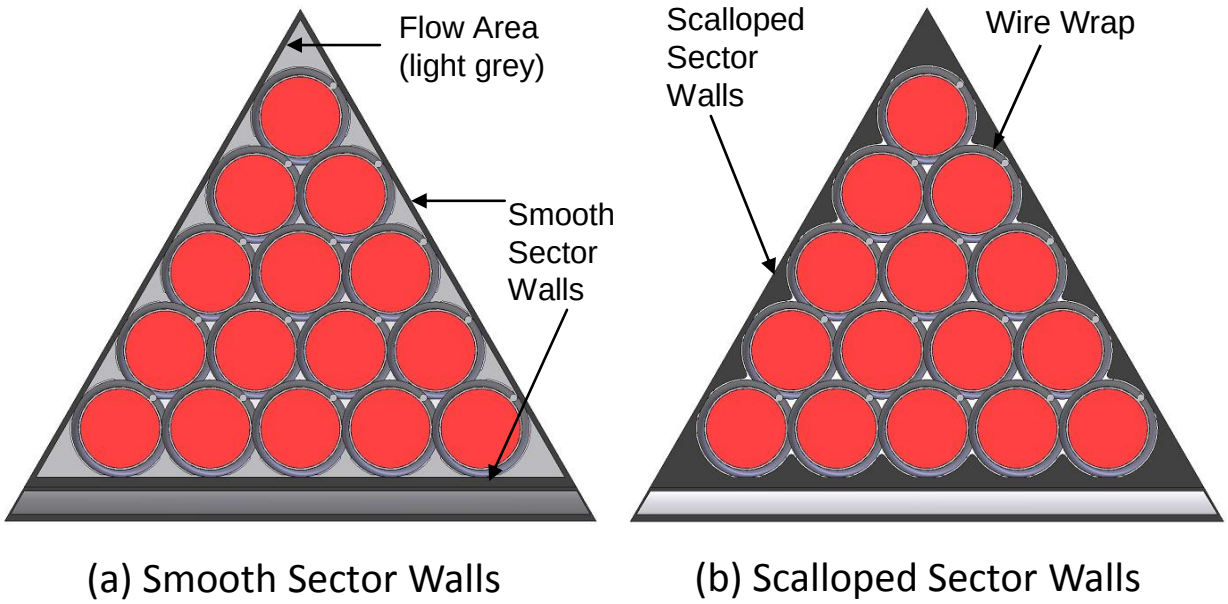

Fig. 3.10. - SCoRe-N_5 core sector arrangements.

and thermal-hydraulics analyses of the SCoRe-N_5 showed that the majority of the reactor pressure losses occurred in the inlet and exit ducts. Thus of the concentric inlet and exit ducts of the SC-SCoRe are redesigned to increase the flow area and reduce the pressure losses in the liquid NaK-56 coolant flow through the reactor.

Figures 3.11a and 3.11b present axial and radial cross-sectional views of the SC-SCoRe solid core with six sectors and flat potassium heat pipes dividers. Tri-lobe shaped coolant channels pierce the solid core to allow the circulating liquid NaK-56 to cool the core during nominal operation and after shutdown. In addition to the tri-lobe coolant channels, the monolithic SC-SCoRe core encompasses cylindrical axial cavities, 15 per sector, loaded with highly enriched (92.7 wt% ^{235}U) UN fuel pellet. The materials investigated for the solid reactor core block (Section 3.9) are 316L stainless steel and an Oxide Dispersion Strengthened Molybdenum (ODS-Mo) alloy [Bianco and Buckman 1997; Cockeram et al. 2005; Mueller 2000].

The ODS-Mo alloy with < 0.1 vol% La_2O_3 nanoparticles has high temperature strength, high melting point (~ 2880 K) and high thermal conductivity. The La_2O_3

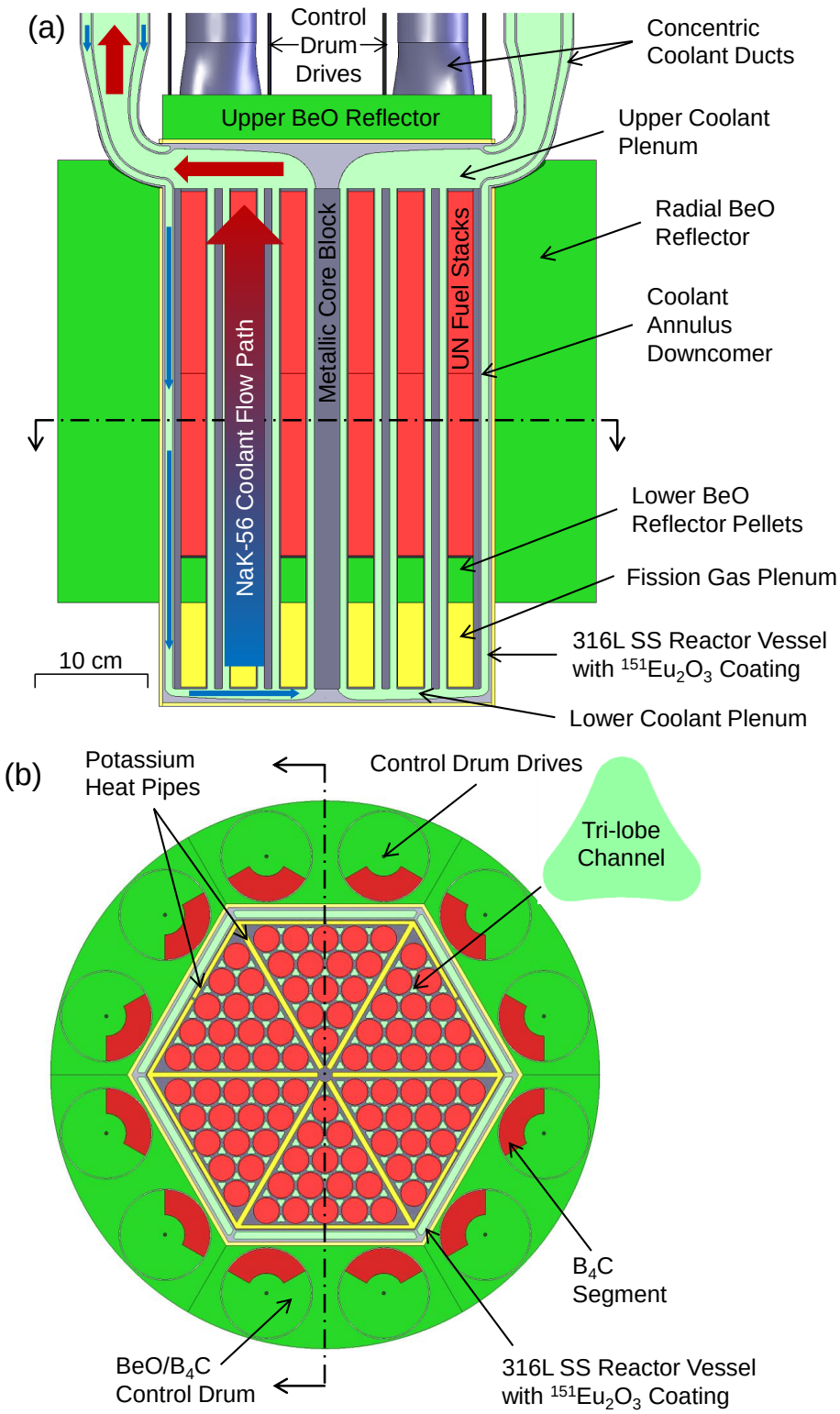

Fig. 3.11. - Cross-section views of the SC-SCoRe core: (a) elevation view and (b) plan view [Schriener and El-Genk 2014b].

nanoparticles precipitate within the grains and at the grain boundaries and increase the alloy's high temperature strength, decrease its embrittlement after exposure to fast-neutron during reactor operation, and maintain the Ductile-to-Brittle Transition Temperature (DBTT) close to room temperature [Bianco and Buckman 1997; Mueller 2000]. Although this ODS-Mo alloy has not undergone extensive lifetime testing in alkali metals, molybdenum has shown good compatibility with liquid sodium, potassium, and NaK at high temperatures [Devan et al. 1966; DiSteffano and Hoffman 1963; Jackson et al. 1955; Lundberg 1981].

Table 3.2. - Corrosion results of molybdenum in sodium, potassium, and NaK-78.

Test Conditions	T (K)	Time (hrs)	Remark	Reference
Flowing NaK-78 (<20 ppm O_2)	1,033	3,000	no attack	Perlow (1961)
Pool Boiling Potassium	1,533	Not given	good corrosion resistance	Devan et al. (1966)
Liquid Sodium (10 ppm O_2)	863	,,	no corrosion	Carter et al. (1958)
Liquid Sodium (oxygen free)	863	,,	no corrosion	Carter et al. (1958)
Liquid Sodium (<0.01 wt% O_2)	978	,,	no attack	Jackson et al. (1955)
Liquid Sodium (0.5 wt% O_2)	978	,,	surface roughening	Jackson et al. (1955)
Flowing Sodium (110 ppm O_2)	1,173	,,	excellent resistance	Weeks, et. al. (1966)
Pool Boiling Sodium	1,483	5,009	no corrosion	Winsche (1965)
Sodium Vapor	1,773	100	<0.025 mm loss	DiSteffano and Hoffman (1963)
Sodium liquid/vapor in a heat pipe	1,391	45,039	no reaction	Lundberg (1981)

Table 3.2 lists the results of corrosion experiments reported in the literature of molybdenum in alkali metals. Results showed that the corrosion rate of molybdenum alloys is strongly influenced by oxygen impurity levels in the alkali liquid metal [DiSteffano and Hoffman 1963; Jackson et al. 1955]. In high purity liquid sodium, potassium, or NaK, with low oxygen concentrations, virtually no attack is seen below 1,470 K (Devan et al. 1966). The 316L stainless steel has known properties, fabrication techniques, and high strength at the reactor nominal operating temperatures and is compatible with both UN fuel and liquid NaK-56 [Rogozkin, Stepennova, and Proshkin 2003; Angelo and Buden 1985; El-Genk and Tournier 2005; Staub 1967].

The design evolution of the SC-SCoRe is the result of the multi-physics design and analyses methodology developed in this research. The next section describes who this analyses methodology was implemented for the SCoRe reactors.

3.3. Multi-Physics Design and Analyses

The performed design and analyses for the three SCoRe reactor concepts (Fig. 3.3) couple the reactor core neutronics and thermal-hydraulics (Fig. 3.1). The neutronics analyses use the Monte Carlo code MCNPX 2.7E [Pelowitz et al. 2011] and the 3-D CFD and thermal-hydraulics analyses use the finite-volume CFD package STAR-CCM+ [CD-adapco 2012]. In addition the dynamic power system simulation tool DynMo-TE [El-Genk and Tournier 2006] is used to calculate the operation parameters of the integrated power system for use in the CFD and thermal-hydraulics safety analyses (Fig. 3.3).

In the present multi-physics methodology, MCNPX calculates the spatial axial and radial profiles of the fission power generation for use in the CFD and Thermal-hydraulics analyses. The UN fuel in each of the fuel rods/stacks in the MCNPX model geometry is divided into 10 axial segments (Fig. 3.12a). MCNPX F6 energy deposition tallies in these axial segments in the MCNPX model are used to calculate the axial power profile for each of the 90 fuel rods in the SCoRe-N_5 and the 90 fuel stacks in the SC-SCoRe (Figs. 3.9 and 3.11). Preliminary thermal-hydraulics analysis of the initial SCoRe-N_{18} instead used a uniform power profile. The fraction of the total fission heat deposited by the neutrons in the cladding and internal BeO reflector pellets is small, and thus neglected

(Fig. 3.8). The calculated fission power profiles are incorporated in the input to the STAR-CCM+ code as axially dependent volumetric heat sources inside the fuel regions of the STAR-CCM+ model geometry (Fig. 3.12b).

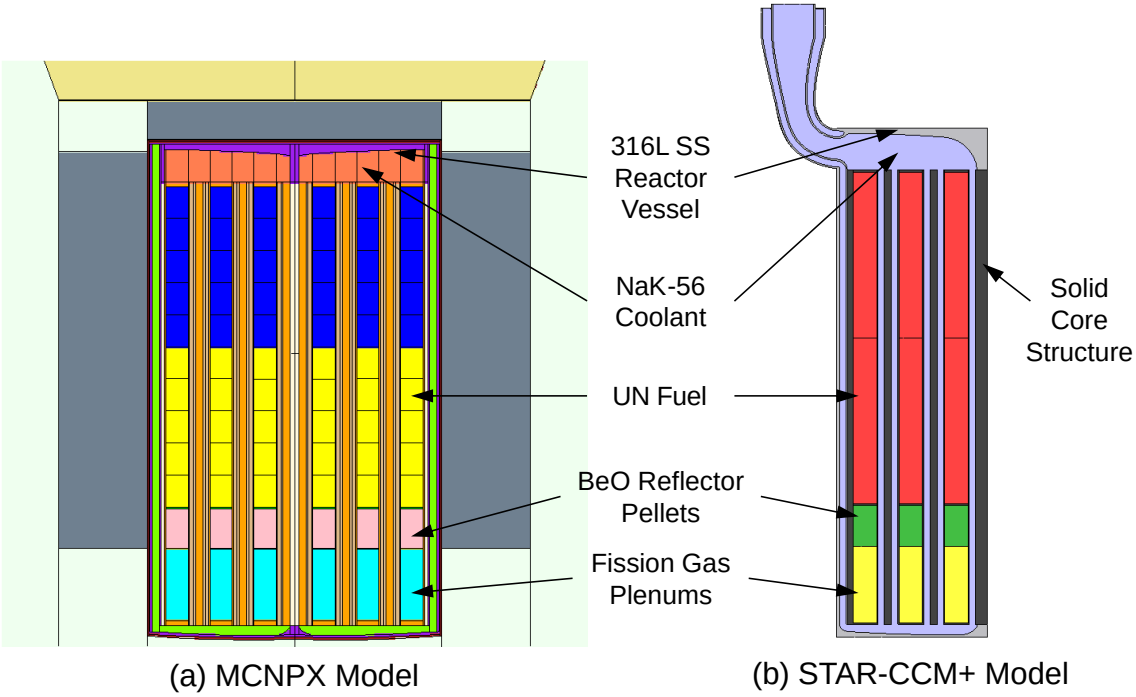

Fig. 3.12. - Section views of SC-SCoRe MCNPX and STAR-CCM+ models.

The CFD and thermal-hydraulics analyses calculate the temperatures in the reactor core during nominal operation, at inlet and exit temperatures of 850 and 900 K. These simulations determine the volume average temperatures in different regions of the STAR-CCM+ reactor model. The temperatures calculated in these regions are incorporated into the corresponding geometry cells in the MCNPX model. This allows the neutronics analyses to determine the effects of temperature on the excess reactivity and perform the fuel depletion analysis of the reactor during nominal operation for estimating its operational life.

In the developed multi-physics design methodology (Fig. 3.3), the DynMo-TE integrated system model [El-Genk and Tournier 2006a] calculates the coolant flow rates and inlet and exit temperatures in the core sectors at different reactor power levels. These operation parameters are used in performing the thermal-hydraulics safety analyses of the

reactor operating at a reduced power level with a core sector experiencing a LOC or LOCo. The inlet flow conditions in the functioning adjacent sectors in the STAR-CCM+ model are set to those determined by the DynMo-TE simulations at the reduced power level.

The outcomes of this iterative design and analyses methodology are estimates of the cold-clean and hot-clean excess reactivities and the thermal-hydraulic performance parameters of the reactor at different power levels. These parameters include the temperatures of the fuel and the cladding (SCoRe-N_5) or solid core (SC-SCoRe), and reactor vessel, the core pressure losses, the core sectors' coolant flow distribution and mixing in the upper coolant plenums. The operational life is estimated using MCNPX's internal fuel depletion capability, simulating the reactor continuously operating at temperature conditions for nominal operation. The following subsections provide details on the computational methodology used for the neutronics, thermal-hydraulics, and DynMo-TE system modeling components of the coupled multi-physics analyses.

3.3.1. Neutronics Analyses

The neutronics and fuel depletion analyses are performed using the Monte-Carlo radiation transport code MCNPX 2.7E [Pelowitz et al. 2011]. The MCNPX calculations of the cold-clean and hot-clean reactivities used 20,000 source particles per cycle and 100 skipped and 1,000 active cycles, for a relative error of 0.00014 or ~2¢ of reactivity. The term cold-clean refers to the reactor at BOL with fresh UN fuel pellets, and reactor core structure and BeO reflector at an isothermal temperature of 300 K. The term hot-clean indicates the same BOL conditions, except with the UN fuel and reactor structure are at their nominal operating temperatures for the prescribed reactor thermal power and the BeO reflector at 600 K. The fuel and core structure temperatures for the reactor during operation are obtained from the CFD and thermal-hydraulic analyses.

The neutronics design of the reactor ensures that it satisfies the operation and launch safety requirements. These requirements are: (a) the bare reactor core must remain at least -$1.0 subcritical when submerged in wet sand and flooded with seawater, following the unlikely event of a launch abort accident (The worst-case submersion is when the wet

sand consists of 30 vol.% seawater and 70 vol.% sand [Hatton and El-Genk 2009]); and (b) that the reactor is at least -$1 subcritical shutdown at BOL with only 75% of the rotating B_4C/BeO control drums (9 drums) in radial reflector operational and in the shutdown position, and with the remaining 25% (3 drums) stuck in the EOL position. This shutdown reactivity requirement provides redundancy in the reactor control, in the event one and up to three of the 12 rotating B_4C/BeO control drums fail during the reactor's long operation life.

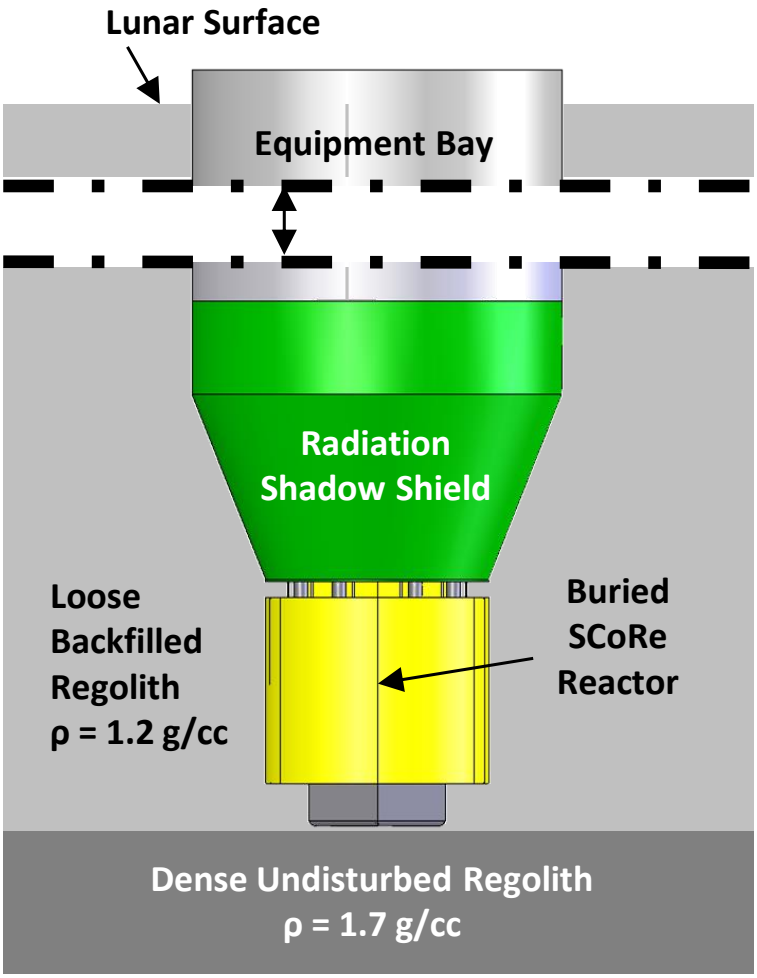

Fig. 3.13. - Emplacement of SCoRe reactor below grade on the lunar surface and surrounded with backfilled regolith.

In order to satisfy the launch safety requirement (a) above, an SSA isotope is mixed with the UN fuel pellets in the SCoRe reactor core and is applied as a thin film (0.15 mm

thick) of the SSA oxide coating onto the outer surface of the reactor vessel. While keeping the total uranium mass in the reactor constant, the concentration of the SSA additive in the UN fuel pellets is adjusted until the BOL cold-clean reactivity of the submerged and flooded bare reactor is subcritical by at least -$1.0. Once this launch safety requirement is satisfied, the next step in the neutronics analyses is to satisfy the shutdown safety requirement (b) above. In this phase of the analyses, the thickness of the B_4C absorber segments is varied in the rotating control drums in the radial BeO reflector (Figs. 3.6, 3.9, 3.11). The selected thickness of the B_4C segments in the drums is that to ensure a shutdown subcritical reactivity of at least -$1.0, with the segments in 9 of the 12 drums are facing the reactor core and those of the remaining 3 drums are facing 180° outward.

Table 3.3. - Composition of JSC-1 lunar soil simulant [McKay et al. 1994].

Element	Concentration (wt%)	Element	Concentration (wt%)
Al	7.95	Mn	0.14
Ca	7.45	Na	2.00
Cr	0.03	O	43.21
Fe	8.13	Si	22.30
K	0.68	Ti	0.95
Mg	5.43		

The cold-clean excess reactivity values are subsequently calculated for the SCoRe-N_{18}, SCoRe-N_5, and SC-SCoRe concepts that satisfy both the launch subcriticality and redundancy in reactor control requirements. The excess reactivity values are for the reactor emplaced on the lunar surface. The reactor is modeled on top of a layer of dense, undisturbed regolith (1.7 g/cc) and surrounded by 2.5 m of loose packed backfilled lunar regolith (1.2 g/cc) to a height of 80 cm on top of the reactor (Fig. 3.13) [Elliott et al. 2005; Heiken et al. 1991; Hatton and El-Genk 2009]. In these calculations, the JSC-1 lunar soil simulant [McKay et al. 1994] is selected as representative of the lunar regolith composition (Table 3.3). Previous investigations of the lunar regolith as a supplemental

neutron reflector compared the results of using several different samples recovered during the Apollo missions and the JSC-1 simulant, and determined that BOL reactivity estimates with the various regolith compositions varied by < \$0.08 [Hatton and El-Genk 2009].

The effects of temperature in the neutronics analyses are accommodated for in the MCNPX model in three ways: (a) changes in material densities, (b) physical thermal expansion of the reactor geometry, and (c) the Doppler broadening of the neutron transport cross sections. The reactor geometry is thermally expanded assuming isotopic expansion of the core materials to match their temperature dependent density values. The utility code DOPPLER [Mosteller et al. 2003] is used to broaden the MCNP neutron cross section data files to that of the average geometry cell temperatures.

The fuel depletion analysis utilizes the internal BURN feature in the MCNPX code [Pelowitz et al. 2011]. The fuel depletion calculations used 20,000 source particles per cycle and 100 skipped and 1,000 active cycles. The Doppler broadened neutron cross sections are generated for 42 actinides and 243 fission products and the SSA activation products to account for the UN fuel burnup and the depletion of SSA additive in the fuel pellets. The default MCNPX fission Q-values are used in the fuel depletion calculations to convert the reactor thermal power to a neutron flux for determining the neutron reaction rates in the tracked nuclides [Pelowitz et al. 2011]. The MCNPX depletion calculations use a time step of 2 years. The linear reactivity depletion rate seen in fast-spectrum space reactors allows the use of such large timesteps without significantly affecting the results (see Appendix A for more details).

3.3.2. Thermal-Hydraulics Analyses Component

Steady-state 3-D thermal-hydraulics analyses of the SCoRe are performed for the reactor at nominal operation of 1,000 kW_{th} with inlet and exit temperature of 850 K and 900 K, respectively. The thermal-hydraulics analyses calculate the temperatures in the fuel, cladding, and core structure, the pressure losses in the core sectors, as well as the flow mixing and coolant temperature distribution in the active core region, the upper plenum and the exit duct

A conduction resistance model is implemented in the thermal–hydraulics analyses for the heat transfer across the narrow helium-filled gap between the UN pellets and the stainless steel cladding of the SCoRe-N_5 or solid core cavities of the SC-SCoRe. The gap resistance is calculated using Equation 3.1 with the emissivity properties of the fuel and clad calculated at a temperature of 1000 K:

$$R_{gap} = \frac{1}{2\pi r_{gap} h_{gap}} \tag{3.1}$$

$$h_{gap} = \frac{\lambda_g}{\delta_{gap}} + \frac{\sigma T_{fo}^3}{\epsilon_f^{-1} + \epsilon_c^{-1} - 1} \tag{3.2}$$

Convection of the helium in the gas plenums of the rods is neglected but its properties are determined at the temperature and pressure at BOL in the thermal-hydraulics analyses.

The heat transport in the potassium heat-pipes dividers is modeled using an effective thermal conductance, whose value depends on the heat flow direction in the heat pipes. The thermal resistance across the heat-pipe is calculated by taking into account the heat conduction resistance across the sintered metal wicks on the evaporator and the condenser, the evaporation of the liquid potassium from the evaporator side, the condensation of the potassium vapor on the condenser side, and the flow of the vapor through the core region of the heat-pipe [Chi 1976]. The thermal resistance through the sintered metal wick is determined as:

$$R_{wick} = \frac{\delta_{wick}}{\lambda_{wick} A_{wick}} \tag{3.3}$$

With the wick effective thermal conductivity calculated as:

$$\lambda_{wick} = \frac{\lambda_l\left(2\lambda_s + \lambda_l - 2(1-0.69)(\lambda_s - \lambda_l)\right)}{(2\lambda_s + \lambda_l) + (1-0.69)(\lambda_l - \lambda_s)} \tag{3.4}$$

The thermal resistance of the liquid-vapor interface is calculated as:

$$R_{lv} = \frac{R_s T_{ave}^2 (2\pi r_{lv} T_{ave})^{0.5}}{L_{hv}^2 P_{int} A_{lv}} \tag{3.5}$$

with the resistance to heat transfer in the vapor core region calculated as:

$$R_v = \frac{R_S T_{ave}^2 \Delta P_v}{Q_{remove} L_{hv} P_v} \quad (3.6)$$

The sum of the resistances for the different regions is used to determine an effective thermal conductance of the heat-pipe for use in the STAR-CCM+ simulations. The outer surface of the thermally insulated reactor vessel is modeled with adiabatic boundaries.

The thermal-hydraulics and safety analyses performed using STAR-CCM+ for the SCoRe-N_{15} and SC-SCoRe employed the Shear Stress Transport (SST) k-ω turbulence model for the liquid NaK coolant in the core sectors [CD-Adapco 2012]. These simulations are for incompressible flow with non-slip condition at the wall, and are performed for standard lunar gravity of 1.63 m/s^2. The analyses with the SST k-ω model use the steady state solver, and options of the second order convection and the Durbin Scale limiter realizability, as well as the All y^+ wall treatment model. The SST k-ω model assumes that the eddy viscosity and the eddy heat diffusivity are related through a turbulent Prandtl number, Pr_t. In the STARCCM+ code, the default value for Pr_t is a constant 0.9, which is not suitable for modeling low Pr fluids like alkali liquid metals [Cheng and Tak 2006; Grötzbach 2013; Reynolds 1975]. To account for the high thermal diffusivity of the liquid NaK, the Pr_t equation developed by Reynolds [Reynolds 1975] is used instead, producing values of Pr_t close to ~2.0 for the modeled conditions inside the reactor core.

Some of the early CFD analyses of the SCoRe-N_{15} were performed instead using the COSMOS FloWorks (SolidWorks 2006) commercial CFD software package. The calculations used the k-e turbulent model and were performed for steady state conditions. The code's default turbulence parameters were used in the simulations. Owing to the limitation on the memory use in our version of the FloWorks CFD package to ~3 million volume elements, limiting the level of mesh refinement possible. These simulations were set up in a similar manner to those performed using STAR-CCM+, although the value of Pr_t couldn't be changed from the fixed value of 0.9.

3.3.3. Integrated System Analyses

The DynMo-TE simulation model developed by the University of New Mexico's Institute for Space and Nuclear Power Studies [El-Genk and Tournier 2006a] is used to simulate the dynamic performance of the SCoRe power system (Fig. 3.2). These simulations calculate the operation parameters of the SCoRe power system. In the developed multi-physics methodology, DynMo-TE determines the reactor inlet and exit temperatures as a function of the reactor thermal power level. The analyses using DynMo-TE also calculate the coolant temperatures and flow rates and in the primary and secondary loops, and the electrical power supplied by the SiGe PCAs for the lunar outpost (Fig. 3.2).

DynMo-TE is built using the SIMULINK platform, a symbolic modeling environment using MATLAB [Simulink 2004]. The dynamic system model of the reactor power system is comprised of a multitude of integrated physical models of the various system components (Fig. 3.2) [El-Genk and Tournier 2006a]. These include: (a) a coupled reactor thermal-hydraulics and six-point kinetics model; (b) thermal-hydraulics models of the primary and secondary loops; (c) models of EM pumps in the primary and the secondary loops; (d) models of the bellows-type accumulators in the primary and secondary loops; (e) models of the PCAs and the pumps' TCAs; and (f) a comprehensive model of the radiator that couples a thermal-hydraulics model of the radiator panels to a transient model of the rubidium heat pipes. A detailed example of DynMo-TE simulation capabilities modeling an earlier version of the SCoRe integrated power system is presented in Appendix C.

The DynMo-TE reactor model couples a six-group point reactor kinetic model with a thermal-hydraulic model of the core [El-Genk and Tournier 2006]. The point kinetic model incorporates reactivity feedback effects due to the temperature of the UN fuel and liquid NaK coolant, Doppler broadening reactivity feedback with temperature, reactivity depletion due to the cumulative burnup of the fuel, as well as external reactivity control using the rotating control drums [El-Genk and Tournier 2006a; El-Genk and Schriener 2010]. The flow rate and inlet and exit temperatures for the reactor are determined from

the overall momentum and energy balance in the pair of primary and secondary coolant loops.

DynMo-TE has detailed transient models of the components of the integrated power system that account for their designs and dimensions [El-Genk and Tournier 2006a]. The models of the DC EM pumps calculate the pressure head supplied to the coolant in the primary and secondary loops due to the current supplied by the pump TCAs. Models for the thermoelectric elements in the pump TCAs and PCAs use detailed models of the SiGe TE unicouples [El-Genk et al. 1987] to calculate the supplied voltage and current to the EM pumps and for the load, respectively. The accumulator model determines the system pressure in the primary and secondary loops, accounting for the thermal expansion of the liquid NaK alloy against the compression spring in the bellows-style accumulator [Tournier and El-Genk 2006]. The radiator model calculates the heat transfer from the secondary loop to the radiator heat-pipes, which is then spread across the panels to be rejected into space. The heat-pipes are simulated using a transient model that also calculates their operating limits [Tournier and El-Genk 2005].

The multi-physics methodology described above is used to investigate the effect of design changes on increasing the BOL excess reactivity and the operational life. This methodology is first implemented to the initial SCoRe-N_{18} design.

3.4. Parametric Analyses of SCoRe-N_{18}

This section presents the results of parametric neutronics analyses of the SCoRe-N_{18} investigating the effects of increasing the fuel rod diameter, for the same UN fuel mass, on the core geometry, number of rods, and BOL cold-clean excess reactivity. The concepts with different numbers of fuel rods are collectively referred to in this section as SCoRe-N_x, where the numeric index "x" indicates the number of rows of the UN fuel rods in each of the core sectors, e.g., x = 18 for the SCoRe-N_{18}. Fig. 3.14 shows the arrangement of the rows of fuel rods in one of the six triangular SCoRe-N_{18} core sectors.

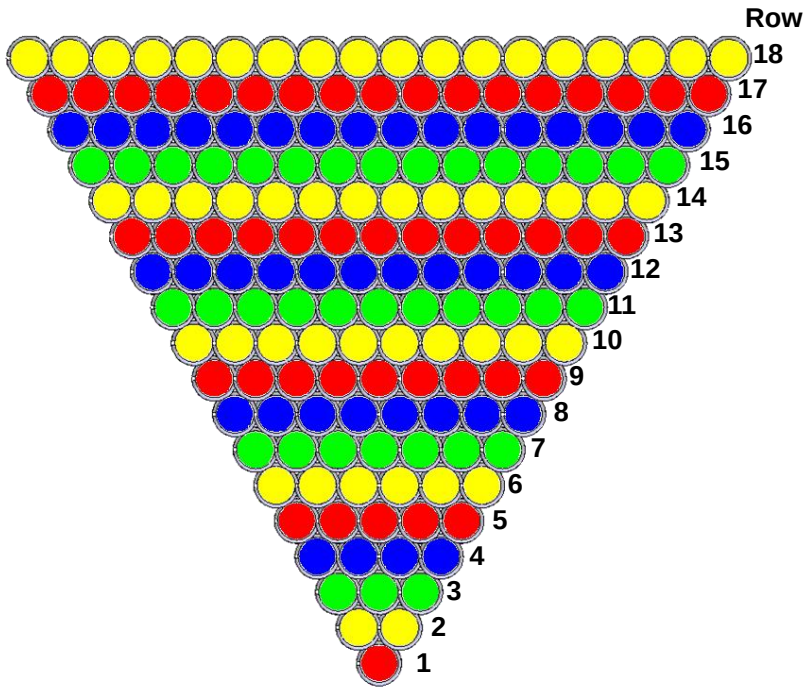

Fig. 3.14. - Arrangement of rows of UN fuel rods in SCoRe-N_{18} core sector [Schriener and El-Genk 2011].

The SCoRe-N_x concepts examined all have the same core cross-sectional dimensions and the total mass of uranium in the core as the SCoRe-N_{18}. Also, the cladding thickness, the outside diameter of the 7 cm thick BeO radial reflector (43.75 cm) and both the diameter (5.954 cm) and the number (12) of the control drums in the reflector are kept constant (Fig. 3.6). Thus, the number of rows of fuel rods in a core sectors decrease commensurate with increasing the diameter of the UN pellets.

The neutronics analysis of the SCoRe-N_x concepts is performed for two arrangements of the UN fuel rods in the core; namely: (a) constant flow area for the triangular unit cell of the UN fuel rods (Fig. 3.15a) and (b) constant total flow area or porosity of the core sector (Fig. 3.15b). For both arrangements, the number of rows of the fuel rods in the core sector, x, varied from 18 in the SCoRe-N_{18} concept with the smallest diameter rods to 5 in the SCoRe-N_5 concepts with the largest diameter fuel rods.

Investigated are the effects of changing the diameter (or number) of the UN fuel rods and the porosities of either the pins' unit cell (U) (Fig. 3.15a) or the core sector (S) (Fig.

3.15b) on the total mass of the reactor and the BOL excess reactivity. Also investigated are the effects of these parameters on the sub-criticality of the bare reactors in the case of submersion in wet sand and flooding with seawater, following the unlikely event of a launch abort accident.

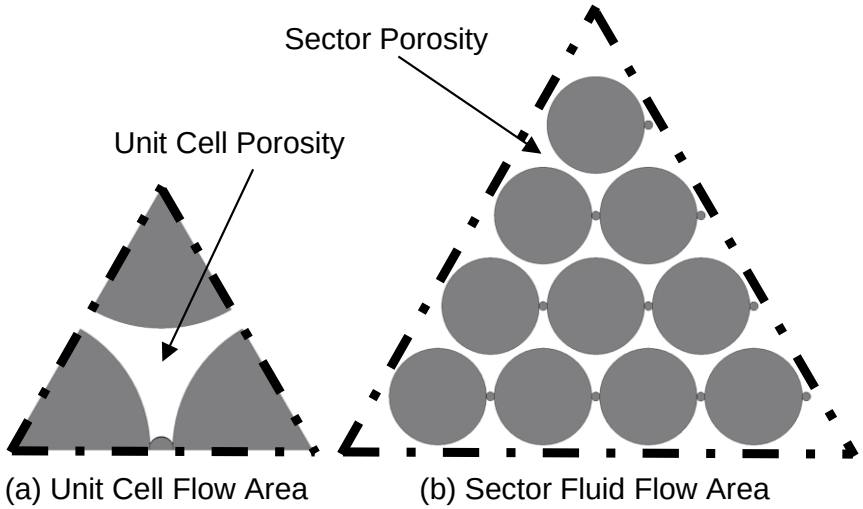

Fig. 3.15. - Reference flow areas for constant unit cell porosity and constant sector porosity [Schriener and El-Genk 2011].

The BOL cold-clean excess reactivities of the SCoRe-N_x concepts are determined for three shutdown requirements of the control drums in the radial BeO reflector (Fig. 3.6): (a) all twelve $^{10}B_4C$/BeO control drums are needed to shut down the reactor to at least -\$1 subcritical at BOL (no shutdown redundancy), (b) with three control drums assumed stuck in the outward-facing position, the remaining nine control drums would shut down the reactor to at least -\$1 subcritical at BOL (25% Additional Shutdown Margin (ASM)), and (c) with six control drums assumed stuck in the outward-facing position, the remaining six control drums would shut down the reactor to at least -\$1 subcritical at BOL (50% ASM). Varying the number of rows of fuel rods, while keeping the core cross-sectional dimensions the same, affects the reactor core geometry. The next section describes the geometric effects of the two fuel rod arrangements on the sector flow area and core dimensions.

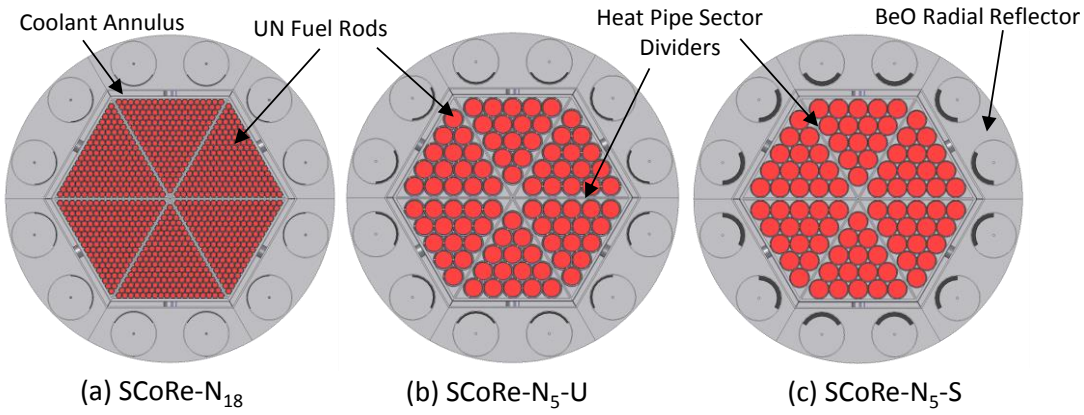

Fig. 3.16. - Radial cross section views of selected SCoRe-N_x design concepts [Schriener and El-Genk 2011].

3.4.1. Geometrical Considerations

As the number of rows of fuel rods per sector, R_f, decreases, the diameter of the rods increases to fill the triangular core sectors. For example, in the SCoRe-N_{16} concepts with 16 rows of rods in the core sectors, the rod outer diameter is 0.828 cm and there are a total of 136 rods per sector. In comparison to The SCoRe-N_{18} with 18 rows of 0.74 cm diameter rods and a total of 171 rods per sector. Fig. 3.16 shows radial section views of the SCoRe-N_{18}, SCoRe-N_5-U, and SCoRe-N_5-S concepts showing the larger diameter fuel rods in the core sectors. The identifier 'U' and 'S' refer to a constant fuel rods unit cell porosity (Fig. 3.15a) and a constant core sector porosity (Fig. 3.15b) in the SCoRe-N_x-U and SCoRe-N_x-S concepts, respectively. The unit cell porosity 'U' is defined as the ratio of the fluid flow area of the triangular sub-channel divided by the total cross-sectional area of unit cell (Fig. 3.15a). The sector porosity, defined as the ratio of the total cross-sectional flow area of the sector divided by its total geometrical area, accounts for the flow area near the walls and corners of the triangular sector (Fig. 3.15b). For the same R_f, these two geometrical arrangements of the fuel rods in the core sectors translate into slightly different pitch-to-diameter (p/d) ratios.

Results in Fig. 3.17 show the effects of changing R_f on the rod pitch-to-diameter ratio, p/d and the fuel rod diameter, d. When the sector porosity is kept constant at 0.248 (solid square symbols), decreasing R_f decreases p/d and increases the fuel rod diameter.

When the unit cell porosity is kept constant (solid circle symbols) the p/d of the fuel rods is constant at 1.081, and the sector porosity and the fuel rod diameter increase as R_f decreases. The lower values of p/d for the SCoRe-N_x-S concepts result in slightly larger fuel rod diameters than those of the SCoRe-N_x-U concepts for the value of R_f (Fig. 3.17).

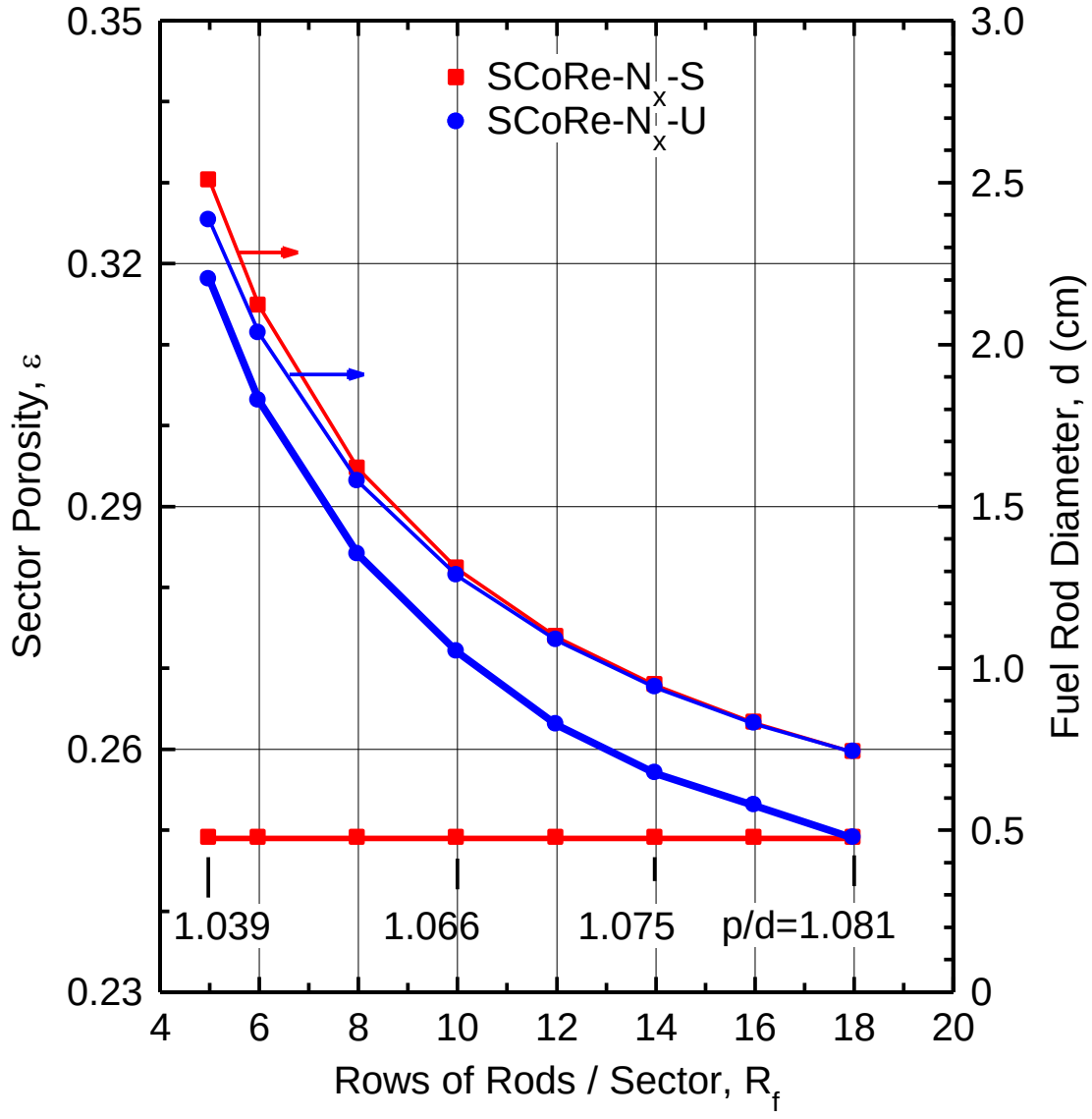

Fig. 3.17. - Effects of porosity on UN fuel rod diameter and p/d [Schriener and El-Genk 2011].

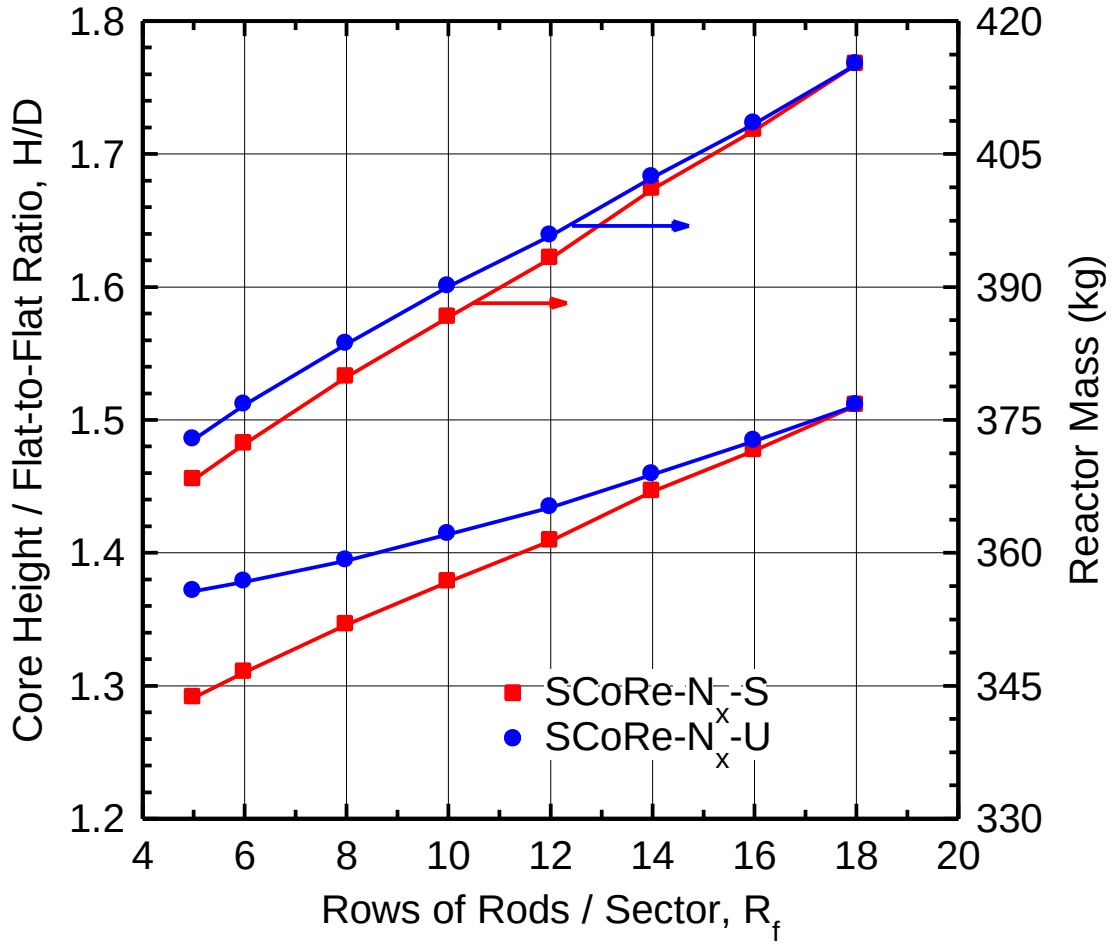

Fig. 3.18. - Effects of R_f on the total reactor mass and the active core H/D [Schriener and El-Genk 2011].

The results delineated in Fig. 3.18 show the effects of changing R_f on the active core height-to-flat-to-flat dimension ration, H/D, and the total reactor mass, including that of the BeO reflector. The larger diameter fuel rods result in a shorter, more compact reactor core. Since the total mass of the UN fuel in the SCoRe-N_x concepts and the flat-to-flat dimension of the hexagonal core, D, are kept constant (Fig. 3.6), decreasing R_f by increasing the fuel rod diameter decreases both the active core height, H, and H/D.

Since the height of the radial BeO reflector changes commensurate with the active core height, a lower H decreases the total reactor mass. For a given values of R_f, the reactor's total mass and H/D of the active core with constant unit cell porosity (U) are

higher than with when the sector porosity (S) in constant (Fig. 3.18). The estimated total reactor mass and the active core H/D decrease from 415.2 kg to 1.511 for the SCoRe-N_{18} to 372.8 kg and 1.371 for the SCoRe-N_5-U, and are 368.3 kg and 1.291 for the SCoRe-N_5-S. The decrease in the total reactor mass is mostly due to the decrease in the active core height, and hence the mass of the BeO radial reflector. Changes in the core geometry could have strong effects on the neutron leakage rate, and hence the core reactivity. The following section investigates the effects of the above design changes on the reactor neutronics of the SCoRe-N_x-S and SCoRe-N_x-U concepts.

3.4.2 Effect of Fuel Rod Diameter

This subsection presents results of changing the fuel rod diameter and of the additional control shutdown margin on the BOL cold-clean excess reactivity. In these calculations, all SCoRe-N_x concepts are at least -$1.0 subcritical during shutdown at BOL and when the bare core is submerged in wet sand and flooded with seawater, following the unlikely event of a launch abort accident. The MCNPX 2.7A Monte Carlo radiation transport code [Hendricks et al. 2008] is used to calculate the cold-clean reactivity for the SCoRe-N_x concepts. The quoted reactivity values in units of dollars ($) are based on an average effective delayed neutron fraction β_{eff} = 0.0064 [Stacey 2001; Hatton and El-Genk 2009].

In the SCoRe-N_{18} concept that satisfies these requirements, the ^{157}GdN neutron absorber additive in the UN fuel pellets is 23.3 at%. Since the total UN mass in the core is kept constant, for a given fuel rod diameter, the ^{157}GdN additive increases the total fuel volume and hence the active core's H and H/D. The increased H/D decreases both the BOL cold-clean and hot-clean excess reactivity and increases the total reactor mass. The results of sizing the SCoRe-N_x concepts to determine the amount of ^{157}GdN additive in the UN fuel pellets to satisfy the submersion and flooding sub-criticality requirement of at least -$1.0 are presented and discussed next.

3.4.2.1. Effect of ^{157}GdN concentration

The results in Fig. 3.19 show that when the unit cell porosity (or p/d = 1.081) is constant, the concentration of the ^{157}GdN in the UN fuel pellets increases initially with

decreasing R_f, from 23.3 at% for the SCoRe-N_{18} to 26.9 at% for the SCoRe-N_8-U. It then decreases with further decrease in R_f to 25.8 at% for the SCoRe-N_5-U. These results are indicated by the solid circle symbols in Fig. 3.16. When the sector porosity is a constant 0.248 (solid square symbols in Fig. 3.16), the concentration of ^{157}GdN needed in the fuel pellets is higher, and increases monotonically as R_f decreases. The SSA concentration increases from 23.3 at% for the SCoRe-N_{18} to as much as 29.1 at% for the SCoRe-N_5-S. The higher absorber concentration in the UN fuel pellets, as R_f decreases (or fuel rod diameter increases and the active core height deceases), is needed to compensate for the increase in the core reactivity. The increase in reactivity is partially due to the lower neutron leakage and parasitic neutron absorption in the 316L SS clad and the reduced effectiveness of the ^{157}GdN additives in the larger diameter fuel pellets because of self-shielding.

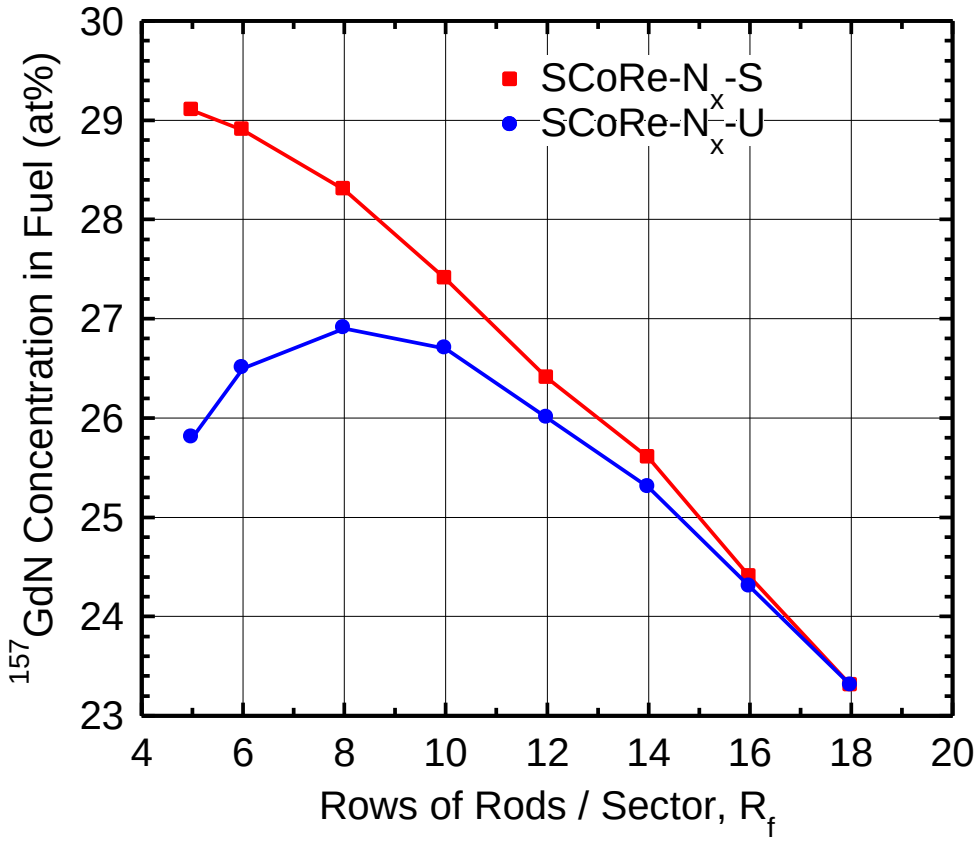

Fig. 3.19. - Changes in the concentration of ^{157}GdN spectral shift absorber in the UN fuel pellets with the number of rows of fuel rods per sector, R_f [Schriener and El-Genk 2011].

Fig. 3.20 compares the calculated total neutron absorption rate per MCNP source particle (SP) in the bare cores of the SCoRe-N_5-U and SCoRe-N_5-S concepts, when submerged in wet sand and flooded with seawater. Fig. 3.20a shows the absorption rate in the ^{157}GdN fuel additive, while Fig. 3.20b shows the absorption rate for the thin 0.15 mm $^{157}Gd_2O_3$ coating on the surface of the reactor vessel. The neutron absorption rate in the SCoRe-N_5-U is higher, particularly for neutrons with more moderated energies. The higher sector porosity of the SCoRe-N_5-U increases the moderator-to-fuel ratio, resulting in a slightly softer neutron spectrum that increases the effective absorption cross section of the ^{157}Gd isotope (Fig. 3.17b). Thus, the GdN additive in the UN fuel pellets is more effective in the SCoRe-N_5-U than in the SCoRe-N_5-S core. This helps explain why the needed concentrations of ^{157}GdN in the UN fuel pellets of the SCoRe-N_x-U concepts are lower than in the SCoRe-N_x-S concepts (Fig. 3.16).

The determined concentrations of the ^{157}GdN in the UN fuel pellets (Fig. 3.19) are used in the calculations of the BOL cold-clean excess reactivity as a function of R_f (or fuel rod diameter). In addition to the launch safety requirements, the SCoRe-N_x concepts must also possess sufficient redundancy in their reactivity control systems. The following section presents results of the BOL cold-clean excess reactivity of the SCoRe-N_x concepts for three control drum additional shutdown margins.

3.4.3. Redundancy in Reactor Control

The values of the BOL cold-clean excess reactivity for the SCoRe-N_x concepts are calculated for three conditions of the control drums in the radial BeO reflector: (a) the reference-case with no control redundancy (Fig. 3.21a) (b) 25% ASM (Fig. 3.21b), and (c) 50% ASM (Fig. 3.21c). In order to ensure that the shutdown reactor at BOL is at least -$1.0 subcritical, the thickness of the 120° B_4C absorber segments in the drums increases as the required ASM increases (cases (b) and (c) above). Increasing the thickness of the B_4C segments increases the reactivity worth of each control drum, allowing the shutdown reactor at BOL to meet the -$1.0 sub-criticality requirement with fewer control drums in the shutdown orientation (Fig. 3.21). However, increasing the thickness of the B_4C segments in the drums decreases the BOL cold-clean excess reactivity because of the increased neutron absorption in the thicker segments.

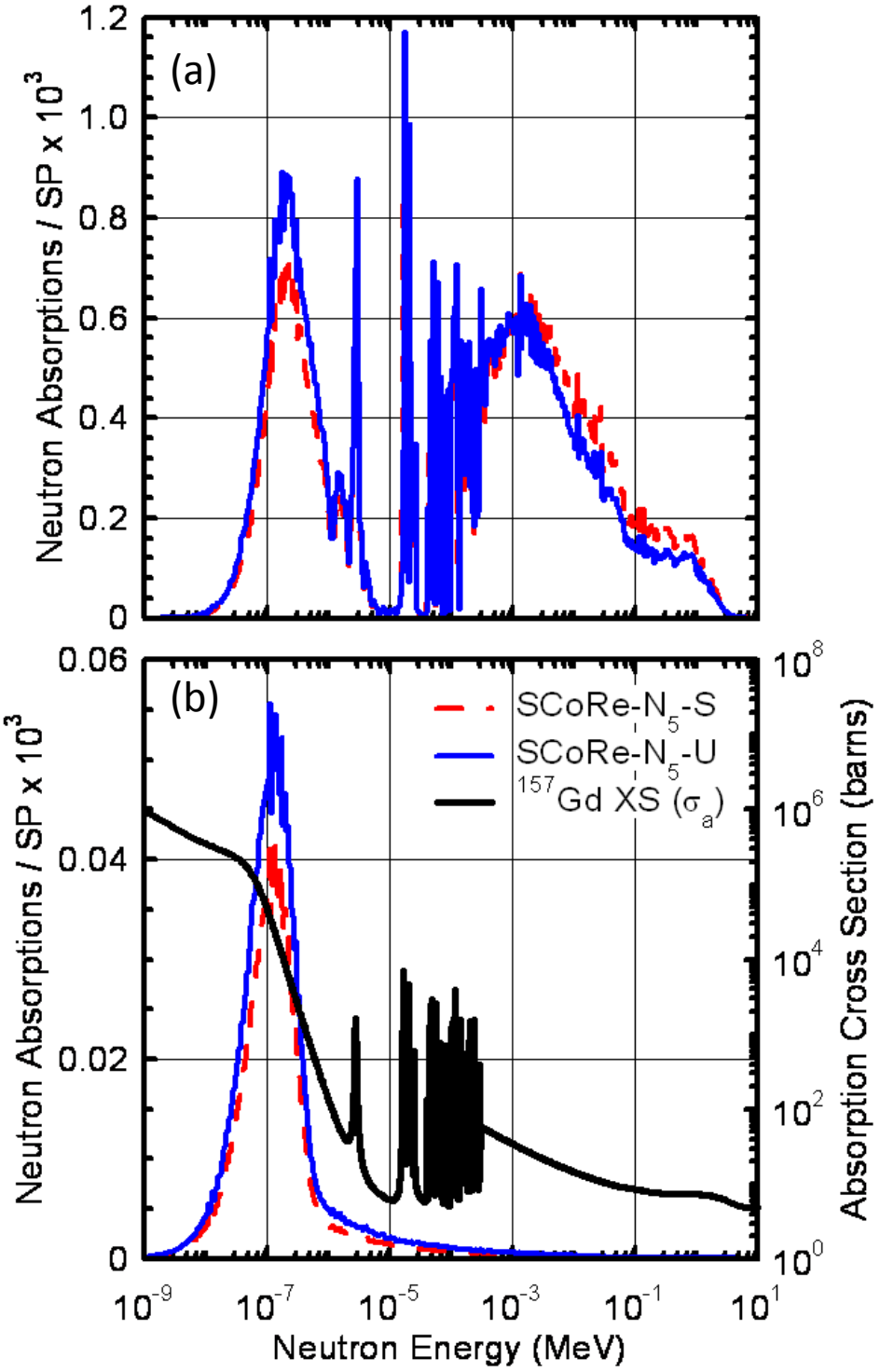

Fig. 3.20. - Neutron absorption in (a) ^{157}GdN fuel additive, and (b) $^{157}Gd_2O_3$ vessel coating in bare reactors submerged in wet sand and flooded with sea water, following a launch abort accident [Schriener and El-Genk 2011].

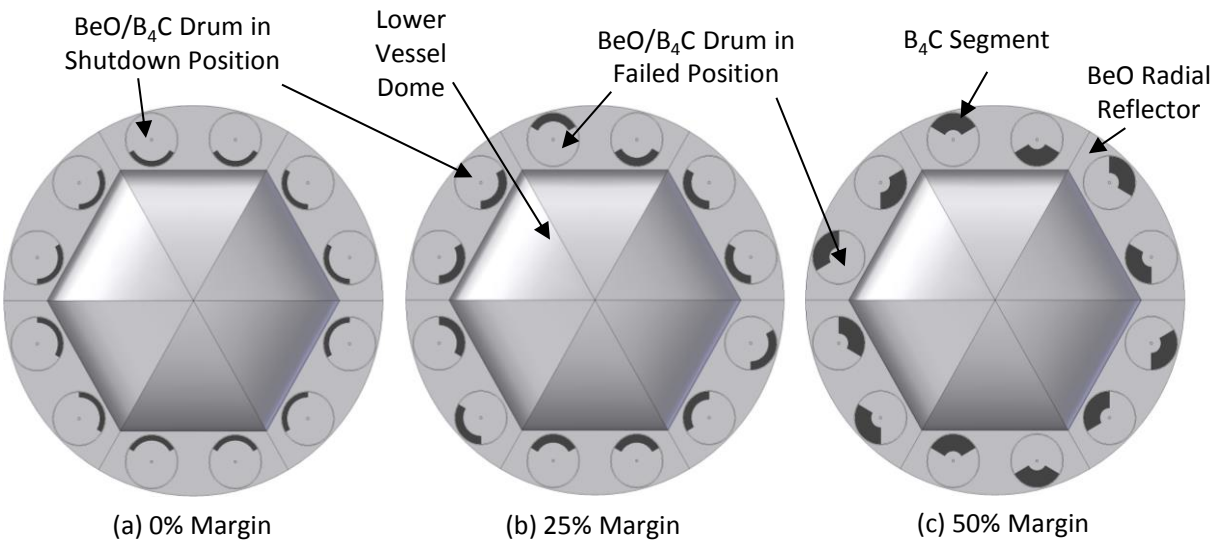

Fig. 3.21. - SCoRe-N_5-S with 12, 9, and 6 control drums in the shutdown position [Schriener and El-Genk 2011].

Fig. 3.22 compares the effects of increasing the thickness of the B_4C segment in the control drums on the BOL excess reactivity of the SCoRe-N_5-S concept and on the shutdown reactivity for the reference concept (Fig. 3.21a) and with 25% and 50% ASM (Fig. 3.21b and c). The solid circle symbols in Fig. 3.22 indicate the BOL excess reactivity for the reference SCoRe-N_5-S concept (Fig. 3.21a) and those with 25% and 50% ASM (Fig. 3.21b and c). The open circle symbols indicate the corresponding shutdown reactor reactivity level. The results in Fig. 3.22 indicate that increasing the thickness of the B_4C absorber segments in the control drums decreases the BOL design excess reactivity, but increases the total shutdown reactivity. The BOL excess reactivity decreases from \$6.30 for the reference design (Fig. 3.21a) to \$5.45 and \$3.97 with 25% and 50% ASM, respectively (Fig. 3.21b and c).

Figs. 3.23 and 3.24 present design surfaces of the calculated BOL cold-clean excess reactivity versus the thickness of the B_4C segments needed in the control drums to satisfy the reactor shutdown requirement of -\$1.0 subcritical at BOL. The results in Fig. 3.23 are for the SCoRe-N_x-U concepts with constant unit cell porosity, while those in Fig. 3.24 are for the SCoRe-N_x-S concepts with constant sector porosity. The design surfaces in these figures are grids comprised of curves representing the SCoRe-N_5 through SCoRe-N_{18}

concepts, and intersecting curves representing the reference concept and those with 25% and 50% ASM. The results in Figs. 3.23 and 3.24 show that the BOL cold-clean excess reactivity decreases as either the value of R_f or the design ASM increases. For the SCoRe-N_5-S (Fig. 3.23) with the highest BOL cold-clean excess reactivity, compared to the reference design the thickness of the B_4C segments in proportion to the drum diameter increases 60% (from 0.190 to 0.304) as ASM increases to 25%. The relative thickness of the B_4C segments increases an additional 107% (from 0.304 to 0.629) as the ASM increases from 25% to 50%.

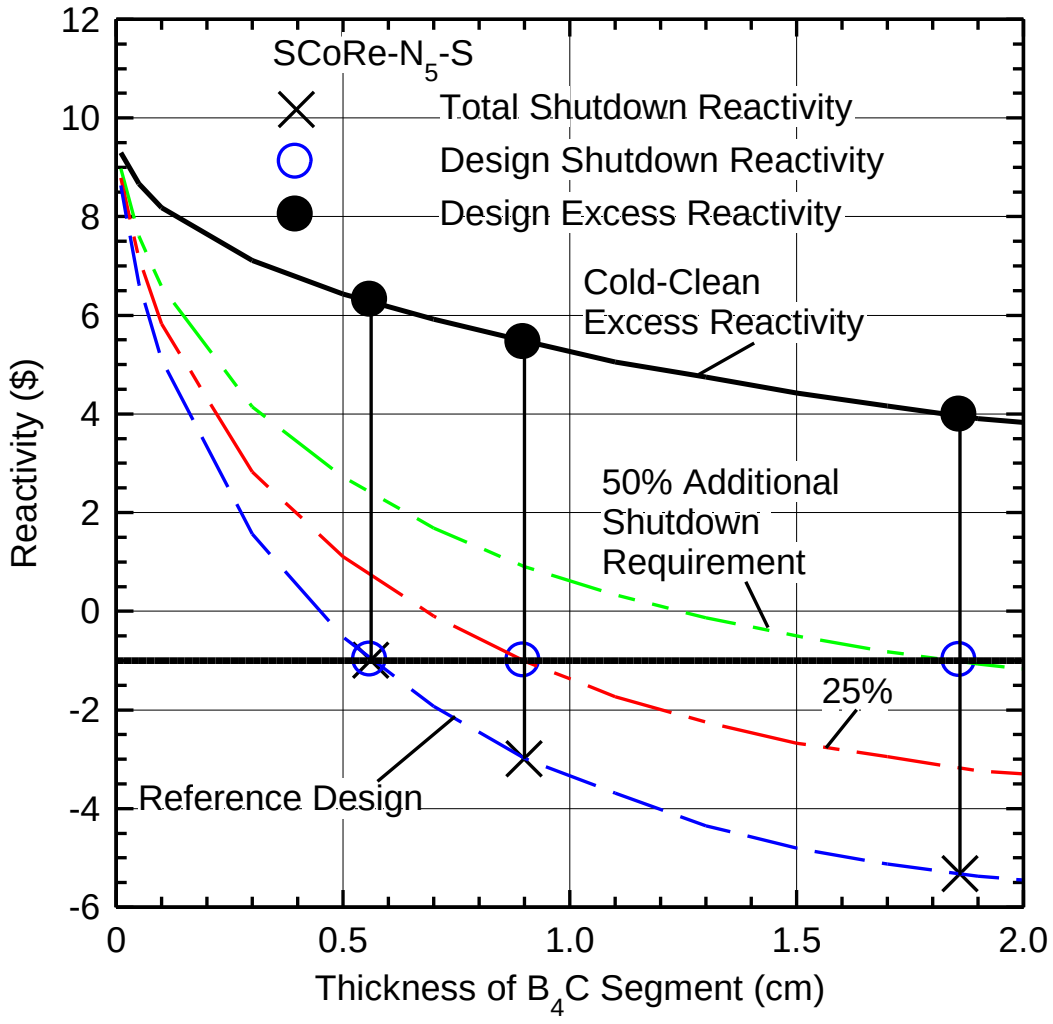

Fig. 3.22. - Reactivity effects for varying B_4C segment thickness and shutdown requirement for SCoRe-N_5-S [Schriener and El-Genk 2011].

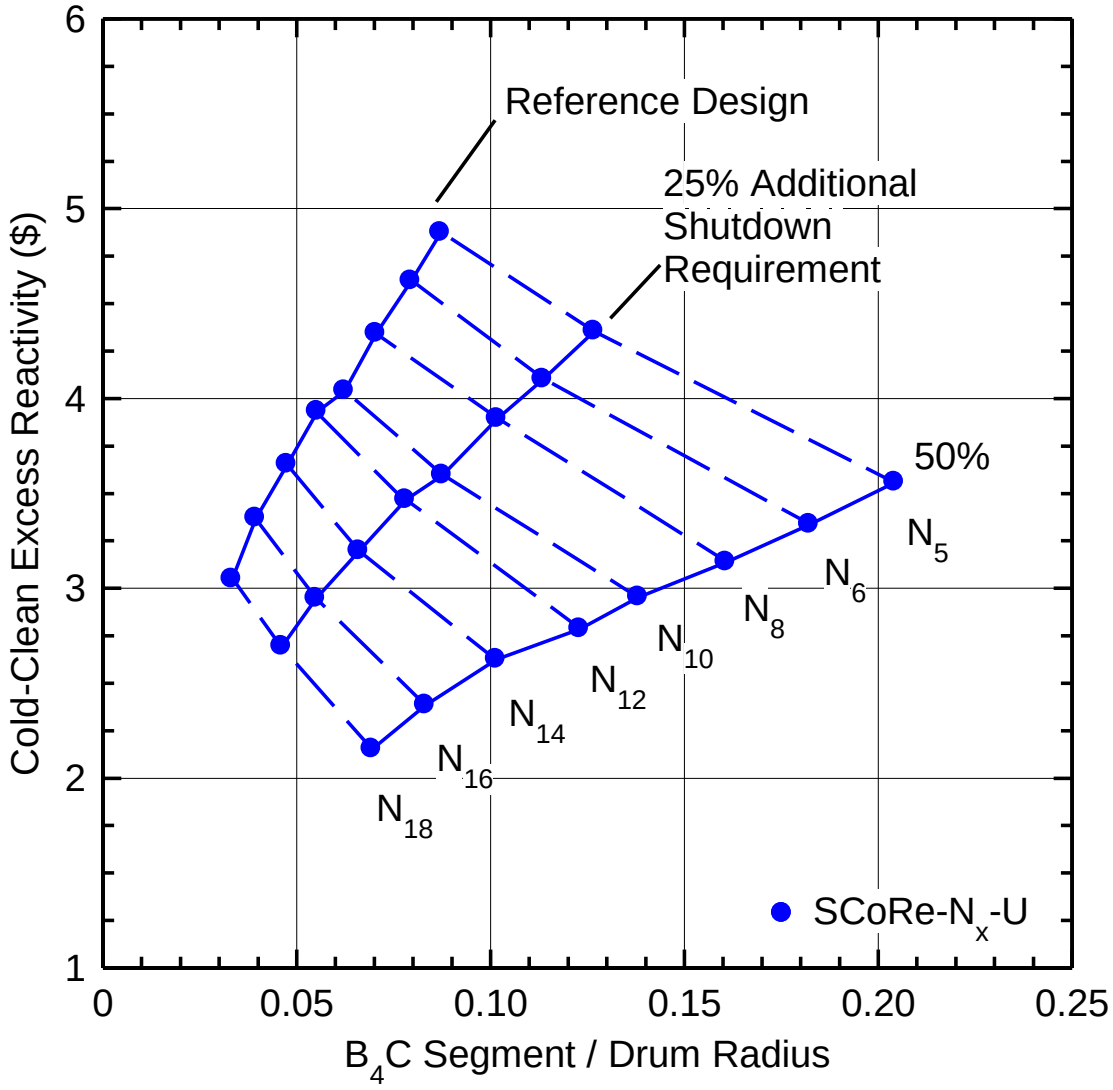

Fig. 3.23. - Design surface of SCoRe-N_x-U concepts with constant unit cell porosity of the UN fuel rods [Schriener and El-Genk 2011].

As the thickness of the 120° B_4C segments in the control drums increases, less poison is added per unit increase in thickness (Fig. 3.24). In addition, the increased self-shielding of the ^{10}B absorber in the B_4C segments with increased thickness further decreases the negative reactivity worth of the control drums. As a result, increasing the thickness of the B_4C segments in the control drums of the SCoRe-N_5-S decreases its BOL cold-clean excess reactivity from \$6.30 for the reference design to \$3.97 for that with a 50% ASM.

The corresponding reactivity values for the SCoRe-N_5-U (Fig. 3.23) are lower, \$4.89 and \$3.56, respectively.

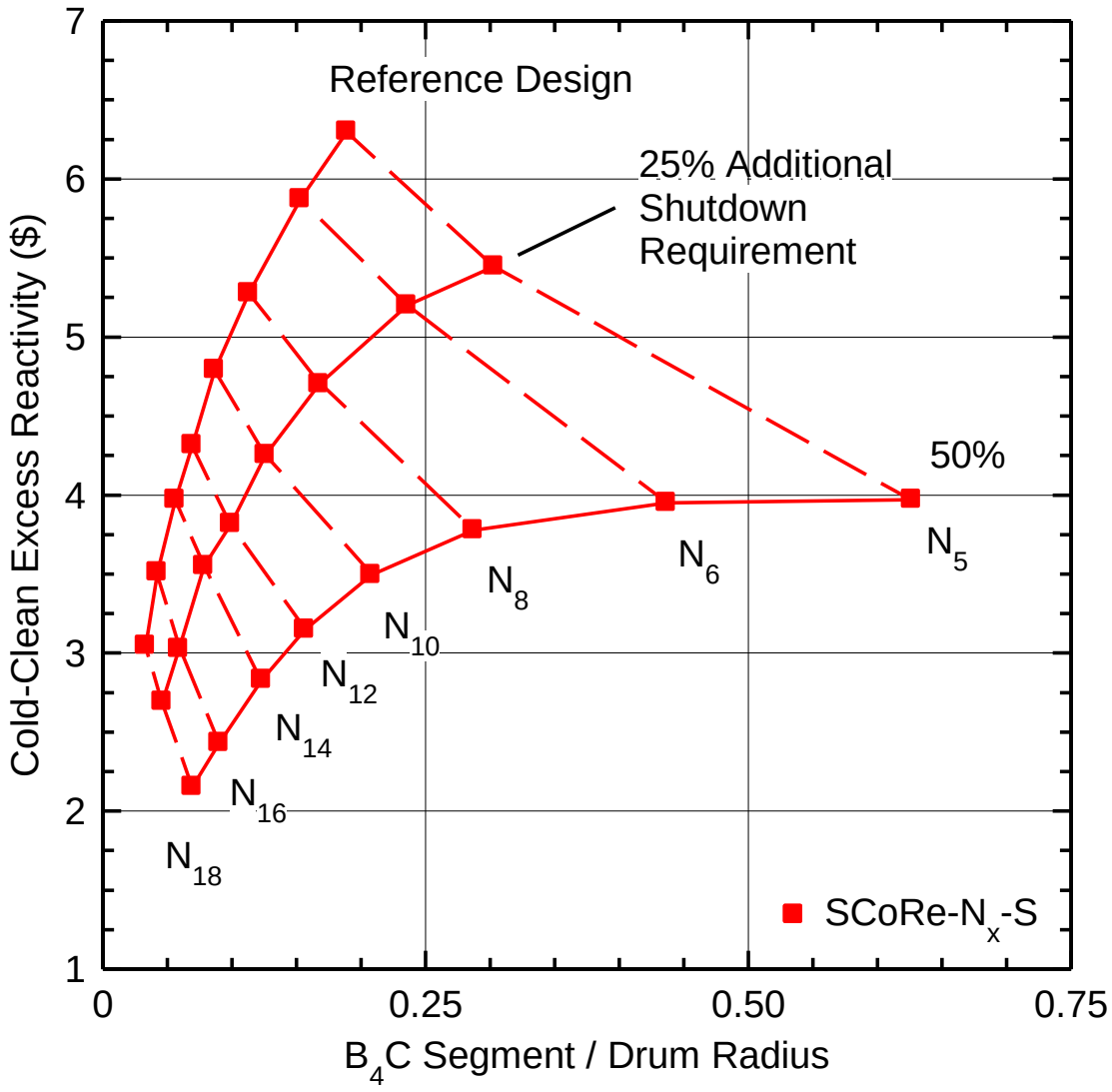

Fig. 3.24. - Design surface of SCoRe-N_x-S concepts with constant sector porosity [Schriener and El-Genk 2011].

For the same BOL cold-clean excess reactivity and design ASM, the thickness of the B_4C segments in the drums of the SCoRe-N_x-S concepts is approximately the same as for the SCoRe-N_x-U concepts (Fig. 3.25). For example, for the SCoRe-N_8-S with a BOL cold-clean excess reactivity of \$3.49 and 50% ASM, the needed thickness of the B_4C segments in the control drums is 6.17 mm (or 20.8% of the drum radius) compared to

6.06 mm (or 20.5% of the drum radius) for SCoRe-N_5-U with \$3.56 BOL cold-clean excess reactivity (Fig. 3.25).

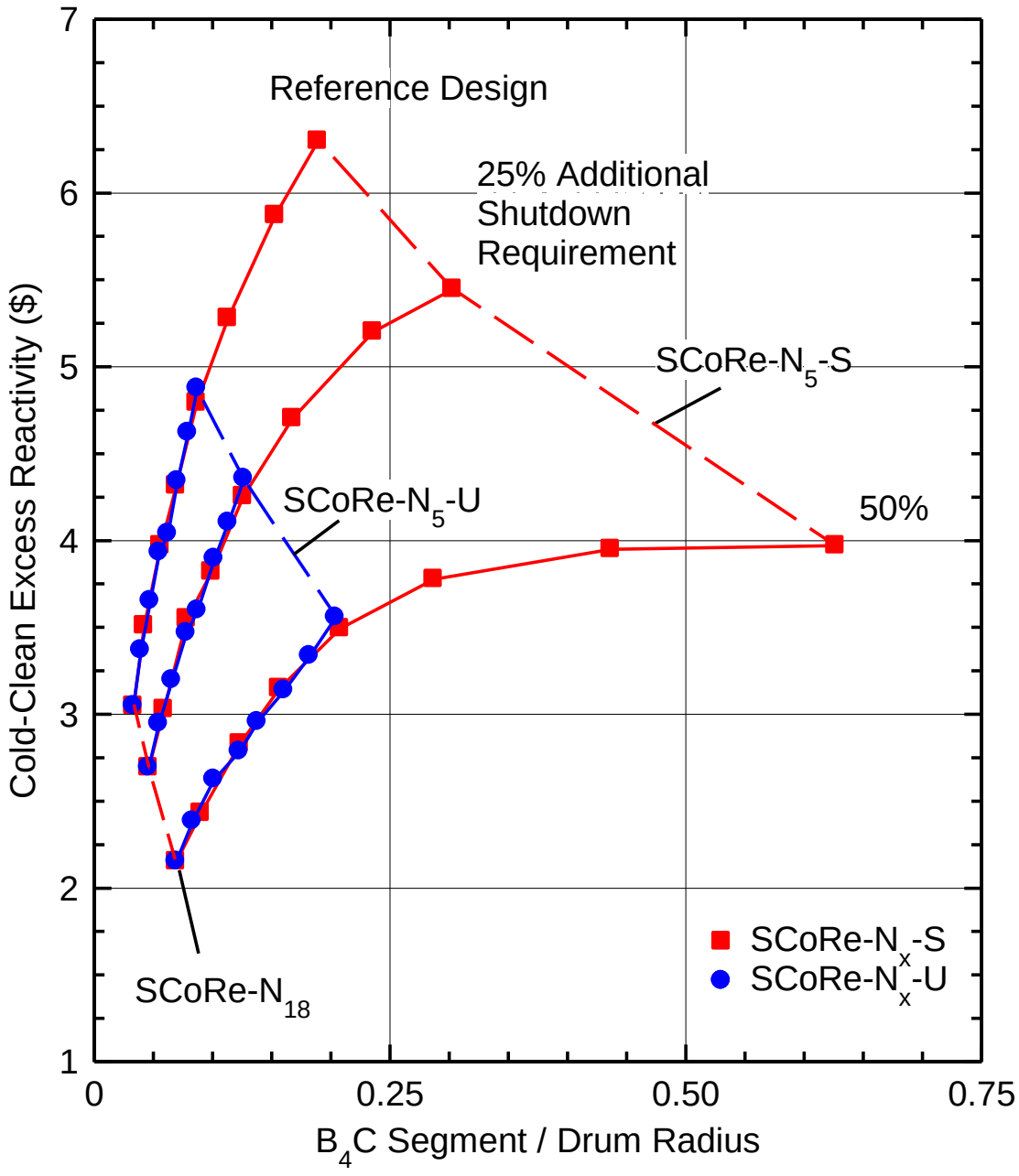

Fig. 3.25. - Comparison of design surfaces of SCoRe-N-U and SCoRe-N-S concepts [Schriener and El-Genk 2011].

The design surface for the SCoRe-N_x-U concepts in Fig. 3.25 is much smaller than that for the SCoRe-N_x-S concepts. The difference in the values of the BOL cold-clean excess reactivity for the SCoRe-N_x-U and SCoRe-N_x-S concepts, for the same R_f, decreases as the ASM increases. With all 12 control drums operational (Fig. 3.21a), the BOL cold-clean excess reactivity for the reference SCoRe-N_5-S concept is \$1.43 higher than for the reference SCoRe-N_5-U concept. This difference decreases to \$1.09 when assuming 25% ASM and to only \$0.41 with 50% ASM.

Table 3.4. - Design parameters of selected SCoRe-N_x concepts

Reactor Parameter	SCoRe-N_{18}	SCoRe-N_5-U	SCoRe-N_5-S
Rod p/d	1.081	1.081	1.039
Active Height (cm)	40.42	36.67	34.53
Core H/D Ratio	1.511	1.371	1.291
Total Reactor Mass (kg)	415.13	372.75	368.25
^{157}GdN Additive in Fuel (at%)	23.3	25.8	29.1
Cold-Clean Excess Reactivity (\$)	2.15	3.56	3.97
Cold-Clean Shutdown Reactivity (\$)	-1.00	-1.02	-1.01
Wet Sand Submersion and Water Flooding Accident Reactivity (\$)	-1.02	-1.01	-1.02
Cold-Clean Excess Reactivity without Supplemental Regolith Reflector (\$)	-5.70	-2.88	-0.77
Supplemental Regolith Reflector Reactivity Worth (\$)	7.84	6.43	4.74

Table 3.4 summarizes the design parameters for the initial SCoRe-N_{18} as well as the two cases with the highest BOL cold-clean excess reactivity, the SCoRe-N_5-U and SCoRe-N_5-S. Table 3.4 also shows the effect of the supplemental regolith reflector on the values of the cold-clean excess reactivity for the three SCoRe-N_x concepts (Table 3.4).

For these concepts the shutdown reactor is significantly subcritical, however, the reactivity worth of the regolith reflector is different. It equals the difference between the BOL cold-clean excess reactivity with and without the supplemental regolith reflector, and decreases from \$7.84 for the SCoRe-N_{18} to \$6.43 and \$4.74 for the SCoRe-N_5-U and SCoRe-N_5-S, respectively (Table 3.4). The BOL excess reactivity for the (SCoRe-N_5-S) concept increases the least with the addition of the supplemental regolith reflector on the lunar surface.

Results show that increasing the diameter of the fuel rods (or decreasing the number of the rods per sector, R_f), while keeping the total UN fuel mass in the reactor constant, increases the operational life of the reactor and simultaneously decreases its total mass. While the SCoRe-N_5-S has the highest BOL excess reactivity, compared to the SCoRe-N_5-U the design has a higher concentration of ^{157}Gd SSA in the fuel and a smaller fuel rod p/d ratio. The smaller fuel rod p/d would restrict the coolant flow through the core sector, increasing the core pressure losses. The SCoRe-N_5-U is therefore developed as the reference SCoRe-N_5 concept in this chapter. The larger diameter fuel rods of the SCoRe-N_5 increase the sector porosity, and hence the total cross sectional flow area. Coupled neutronics and thermal-hydraulics analyses are required to investigate the performance of the SCoRe-N_5 during nominal operation, which is the subject of the next section.

3.5. Neutronics and Thermal-Hydraulics Analyses of SCoRe-N_5

This section presents the results of a multi-physics design and performance analyses of the SCoRe-N_5 reactor design for lunar surface power (Fig. 3.9). The neutronics calculations and the 3-D thermal-hydraulics analyses of the reactor are iteratively coupled using the multi-physics methodology described in Section 3.3. These analyses ensure that the SCoRe-N_5 concept satisfies both the launch safety and reactor shutdown requirements, and provides adequate cooling of the fuel rods in the reactor core sectors. The multi-physics analyses are performed for nominal reactor thermal powers of 200 kW_{th}, 500 kW_{th} and 1,000 kW_{th} at different coolant flow rates, but same inlet and exit temperatures of 850 K and 900 K, respectively.

First, analyses are performed to investigate the flow distribution in the core sectors, both with smooth and scalloped sector walls (Fig. 3.10). Then the effectiveness of several

candidate SSA isotope additives is compared for attaining the highest excess reactivity and satisfying launch safety requirement. Next, 3-D CFD and thermal-hydraulic analyses are performed of the SCoRe-N_5 during nominal operation at 200 kW_{th}, 500 kW_{th}, and 1,000 kW_{th} to investigate the coolability of the fuel rods, the coolant flow distribution in the core sectors, and the coolant mixing in the exit plenums (Fig. 3.9b). Finally the core temperature distribution from the thermal-hydraulics calculation are coupled with the neutronics to determine the BOL hot-clean excess reactivity values for the reactor operating at the different power levels.

3.5.1. Analyses Methodology

Detailed and coupled multi-physics neutronics and 3-D thermal–hydraulic analyses of the SCoRe-N_5 reactor concept (Fig. 3.9) are performed to arrive at a design that satisfies the launch safety and both the performance and long operation life requirements. These analyses are for nominal thermal power levels of 200 kW_{th}, 500 $kW_{th,}$ and 1,000 kW_{th} at the same liquid NaK coolant inlet and exit temperatures of 850 and 900 K, but different flow rates. The neutronics analysis aims at maximizing the BOL reactivity, while satisfying the reactor control shutdown and launch safety requirements. The thermal-hydraulic analysis ensures that UN fuel rods in the reactor core are adequately cooled during nominal operation and that there is sufficient mixing of the liquid NaK-78 coolant exiting the reactor (Fig. 3.9).

The neutronics portion of the analyses is performed using the Monte-Carlo radiation transport code MCNPX 2.7C [Pelowitz et al. 2010]. The calculated excess reactivity values are for a 9 cm BeO radial reflector with a 25% ASM in the control drums and the reactor emplaced below grade on the Moon and surrounded with regolith (Fig. 3.12). The values of the cold-clean and hot-clean reactivities given in this paper in a unit of dollars, are based on an average delayed neutron fraction, $\beta_{eff} = 0.0069$. This fraction is estimated using MCNPX with the k-ratio method [Spriggs et al. 2001]. This method estimates the value of β_{eff} from the calculated values of k_{eff} with and without delayed neutron generation.

The COSMOS FloWorks [SolidWorks 2006] commercial software package is used to perform the 3-D CFD and thermal-hydraulic analyses of the SCoRe-N_5 reactor core. The analyses use a finite-volume laminar and k-ε turbulent flow solver that combines convective and conductive heat transfer. The code's default turbulence parameters were used in the simulations. The value of Pr_t in the code was fixed at 0.9 and couldn't be changed to a more appropriate value for the liquid NaK-78 coolant. The present analysis is performed for one of the six hydraulic sectors of the reactor (Fig. 3.9a), subject to adiabatic conditions along the outer boundary of the reactor vessel and symmetry plane through the sector dividing walls (Fig. 3.9). The hexahedral numerical mesh grid for the modeled geometry includes 5.40×10^5 solid mesh cells, 1.67×10^6 fluid cells, and 8.30×10^5 partial cells in the fluid-solid boundary regions, for a total of 3.04×10^6 mesh cells. The wire wrap was not modeled in the initial simulations to reduce the computational memory requirements. The axial and radial heat generation values of the volumetric heat sources in the fuel regions are obtained from the neutronics analysis for each of the 15 fuel rods in the core sector. The following section uses this methodology to investigate the flow distribution in the core sectors and the effects of scalloping the sector walls on the reactor's thermal-hydraulics and neutronics performance.

3.5.2. Effects of the Scalloped Core Sectors Walls

The large (2.43 cm) diameter fuel rods of the initial SCoRe-N_5 result in a larger cross sectional flow area along the edges and corners of the six hydraulic sectors of the core than that in the middle of the core sectors between the wire-wrapped fuel rods (Fig. 3.10a). The CFD results of the temperature distribution in one of the six identical core sectors of the reference SCoRe-N_5 with ^{151}EuN SSA at a nominal power of 200 kW_{th} are shown in Fig. 3.26. The large flow area near the sector walls results in maldistribution of the circulating liquid NaK-78 in the sector (Fig. 3.26a). The peak centerline fuel temperature in sector reaches 972 K, with the peak cladding temperature reaching 938 K. The large flow area along the edges and corners of the triangular sector allows cold liquid NaK-78 to bypass the fuel rods, resulting in a large temperature difference in the NaK-78 entering the upper coolant plenum. Insufficient mixing results in the temperature of the

NaK-78 exiting the inner concentric coolant duct varying from 882 to 915 K, a temperature difference of 33 K.

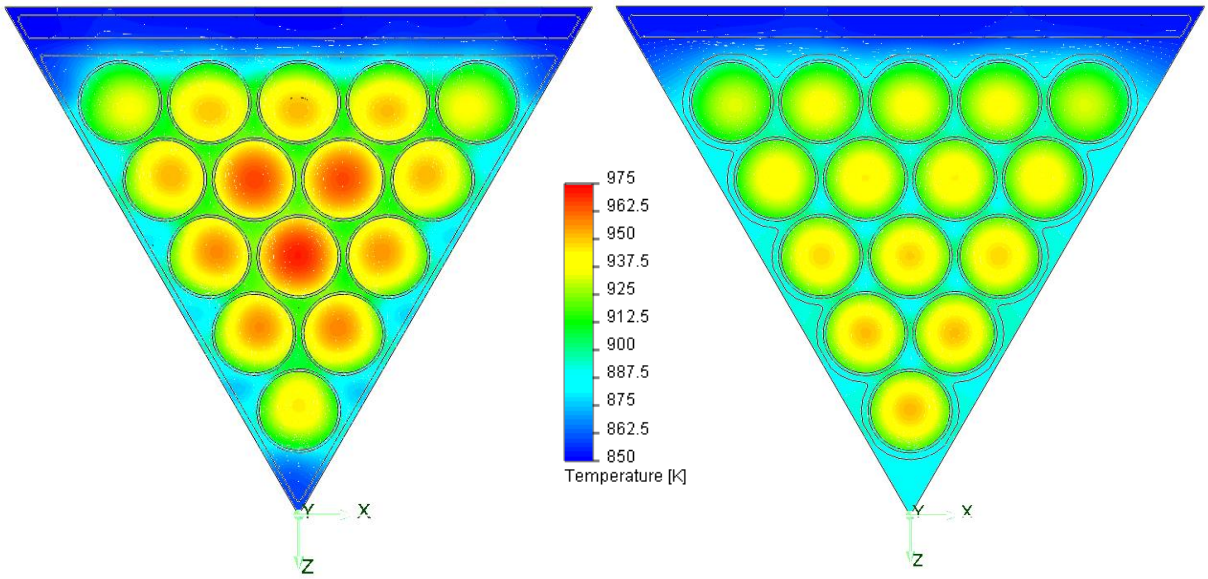

(a) Smooth Sector Walls (b) Scalloped Sector Walls

Fig. 3.26. - Calculated temperatures in SCoRe-N_5 core sector at 200 kW_{th} with (a) smooth sector walls and (b) scalloped sector walls at the axial location of the peak fuel temperature.

The 316L stainless steel sector dividing walls and internal structure is scalloped to minimize the flow bypass at the corners and edges of the sectors and achieve a more uniform flow distribution and cooling of the fuel rods (Fig. 3.10b). The temperature distribution for a SCoRe-N_5 sector with scalloped internal structure is shown in Fig. 3.26b. The scalloped internal structure restricts flow near the walls, increasing the coolant flow fraction passing through the middle of the sector, and reducing the peak fuel and cladding temperatures. The peak fuel temperature decreases by 20 K to 952 K, while the peak cladding temperature decreases by 19 K to 919 K (Fig. 3.26a and b). The scalloped internal structure does, however, slightly increase the core pressure losses for the core sector, due to the reduction in flow area and greater surface are in contact with the fluid flow.

The 316L SS scalloped walls of the core sectors also impact the neutronics of the SCoRe-N_5. The stainless steel scallops reduce neutron leakage from the reactor core sectors, increasing the excess reactivity. The BOL cold-clean reactivity for the SCoRe-N_5 with a 9 cm thick BeO radial reflector and a 25% ASM increases from \$5.43 up to \$5.83. The use of a thicker BeO radial reflector, compared to the 7 cm thickness for the SCoRe-N_{18}, was necessary due to the reduced neutron leakage from the core. The reduced leakage decreases the reactivity worth of the rotating control drums inside the BeO radial reflector. A thicker radial reflector allows for the use of larger diameter control drums with wider B_4C absorber segments. This increases the reactivity worth of the control drums, allowing the design to satisfy the design 25% ASM requirement. The reduced leakage also requires that the concentration of the ^{157}GdN SSA be increased from 25.8% to 29.2 at% to maintain the launch safety requirement of the bare reactor core being at least -\$1.0 subcritical submerged in wet sand and flooded with seawater, following the unlikely event of a launch abort accident.

The increase in the ^{157}Gd SSA additive concentration in the UN fuel pellets increases the active core height, and hence the total reactor mass. In order to reduce the concentration of the SSA additive in the UN fuel, the next section investigates several different SSA isotopes for ensuring the launch safety requirement.

3.5.3. Effect of Spectral Shift Absorber Isotopes

King and El-Genk [2006] have previously investigated a wide range of possible SSA materials for fast neutron spectrum space reactors for satisfying the launch safety subcritically requirement. They found that the ^{157}Gd isotope is a preferred choice because of the small reactivity penalty during reactor operation. The isotopes of ^{155}Gd, ^{151}Eu, and ^{149}Sm were also found as attractive options. The actual effectiveness of these isotopes in a given reactor design, however, depends on the neutron energy spectrum of the core and the performance requirements of the reactor. In the present neutronics analysis, the effectiveness of the SSA isotopes ^{157}Gd, ^{155}Gd, ^{151}Eu, and ^{149}Sm are investigated and compared for satisfying the launch safety and shutdown requirements of the ScoRe-N_5 reactor (Fig. 3.9).

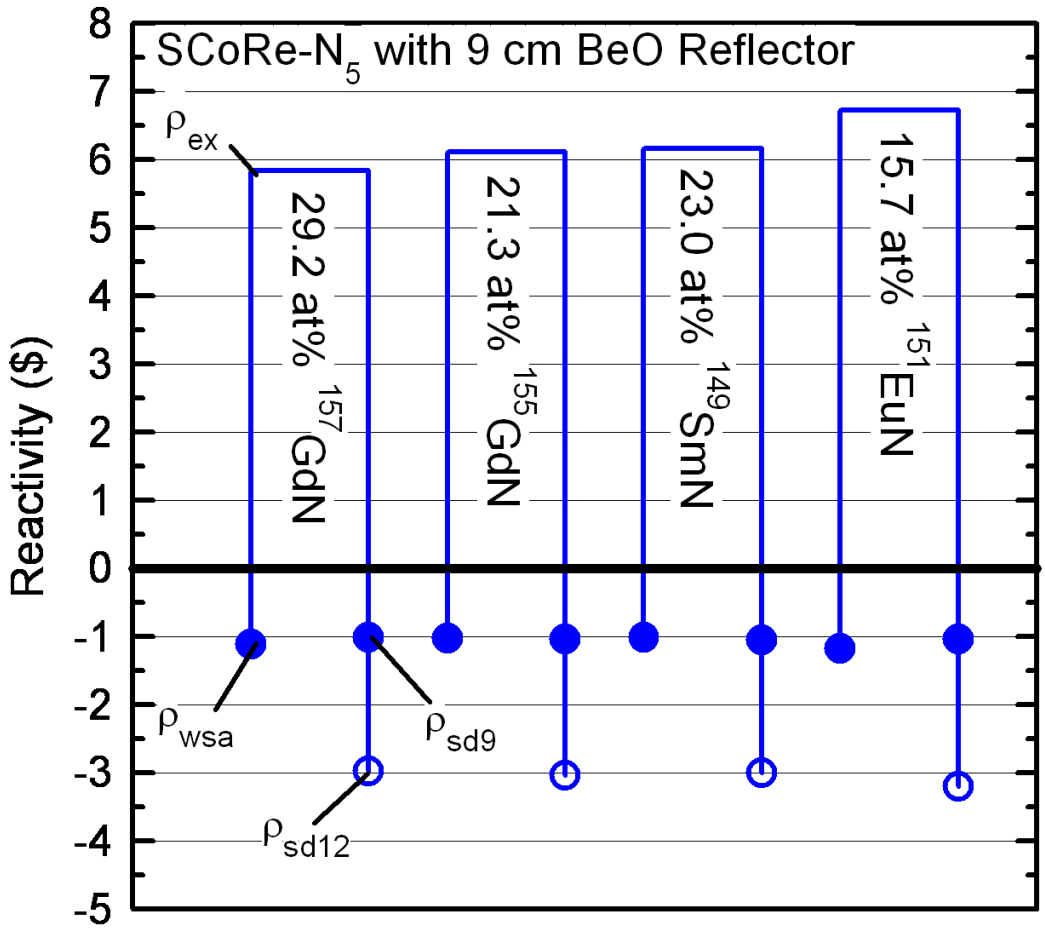

Fig. 3.27. - Reactivity levels for SCoRe-N_5 concepts with candidate SSA additives. [Schriener and El-Genk 2012a].

The calculated BOL reactivity values of the SCoRe-N_5 reactor with each of the four isotopes are presented and compared in Fig. 3.27. This figure shows that the cold-clean excess reactivity, ρ_{ex}, shutdown reactivity with 9 drums rotated towards the core, ρ_{sd9}, the shutdown reactivity with all 12 drums rotated towards the core, ρ_{sd12}, and the water submersion reactivity with the bare core submerged in saturated west sand and flooded with seawater, ρ_{wsa}. The investigated SSA isotopes are applied as a 0.15 mm-thick coating of Gd_2O_3, Eu_2O_3, or Sm_2O_3 on the outer surface of the reactor core vessel and mixed with the UN fuel pellets in nitride forms of GdN, EuN, or SmN. For the same fixed ^{235}U mass of 119.5 kg in the SCoRe-N_5 reactor core, the SSA concentration in the

UN fuel pellets is adjusted until the launch subcriticality requirement, ρ_{wsa} < -\$1.0, is satisfied.

With a constant total uranium mass in the reactor core, increasing the SSA concentration in the UN fuel pellets increases the active core height. Increasing the active core height also increases the height of the BeO radial neutron reflector and hence the total reactor mass (Table 3.5). The results in this table show the needed concentration of ^{157}Gd isotope in the UN fuel pellets is the highest. The needed concentration of ^{151}Eu in the UN fuel pellets is the smallest (15.7 at%). The results in Fig. 3.27 show that the needed concentrations of the different SSAs in the UN fuel pellets (Table 3.5), though they satisfy the same bare-reactor submersion and flooding subcriticality requirement (ρ_{wsa} < -\$1.0), result in different BOL excess reactively, ρ_{ex}.

Table 3.5. - SCoRe-N_5 dimensions and BOL excess reactivity estimates.

Parameter	**SSA Isotope**			
	^{157}Gd	^{155}Gd	^{149}Sm	^{151}Eu
SSA in UN Fuel Pellets (at%)	29.2	21.3	23.0	15.7
Active Core Height, H (cm)	38.45	34.46	35.51	32.54
Active Core H/D ratio	1.446	1.296	1.335	1.224
BOL Cold-Clean Excess Reactivity, ρ_{ex} (\$)	5.83	6.11	6.15	6.72
Total Reactor Mass (kg)	474.2	435.5	443.8	415.0
BOL Specific Reactivity (\$/kg)	0.0123	0.0140	0.0138	0.0162

^{151}Eu, with the lowest concentration in the UN fuel (15.7 at.%), results in the highest cold-clean excess reactivity, ρ_{ex} = \$6.72, the lowest reactor total mass of 415 kg, and the most compact reactor core (or smallest H or H/D, Fig. 3.28). The higher concentrations associated with additives of ^{149}SmN, ^{155}GdN, and ^{157}GdN to the UN fuel pellets increase the active core height and hence, the total reactor mass by 28.8, 20.6, and 59.2 kg,

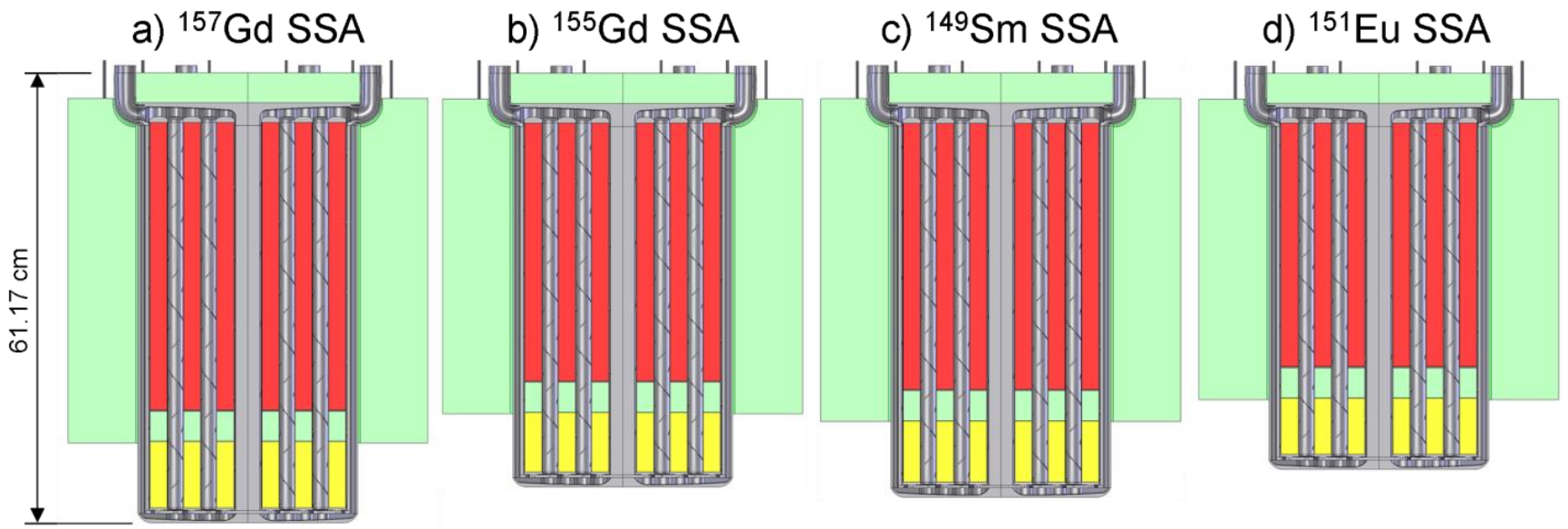

Fig. 3.28. - Effect of the SSA additive isotopes on the active height of the SCoRe-N_5 reactor core [Schriener and El-Genk 2012a].

respectively. These higher SSA concentrations also decrease the cold-clean ρ_{ex} by \$0.57, \$0.61, and \$0.89 to \$6.15, \$6.11, and \$5.83, respectively.

The higher the BOL excess reactivity, the greater thickness required for the B_4C absorber segments in the rotating control drums in the 9 cm-thick BeO radial reflector (Fig. 3.9) in order to meet the 25% ASM requirement. The SCoRe-N_5 reactor with ^{151}EuN SSA additive to the UN fuel requires having 1.83 cm-thick B_4C absorber segments in the control drums, compared to the 0.8 cm, 0.69 cm, and 0.42 cm-thick segments required with the ^{149}SmN, ^{155}GdN, and ^{157}GdN SSA additives, respectively. With all 12 drums operational and in the shutdown position during launch and BOL, ρ_{sd12}, these thicknesses result in the reactor being more than -\$3.0 subcritical (Fig. 3.27).

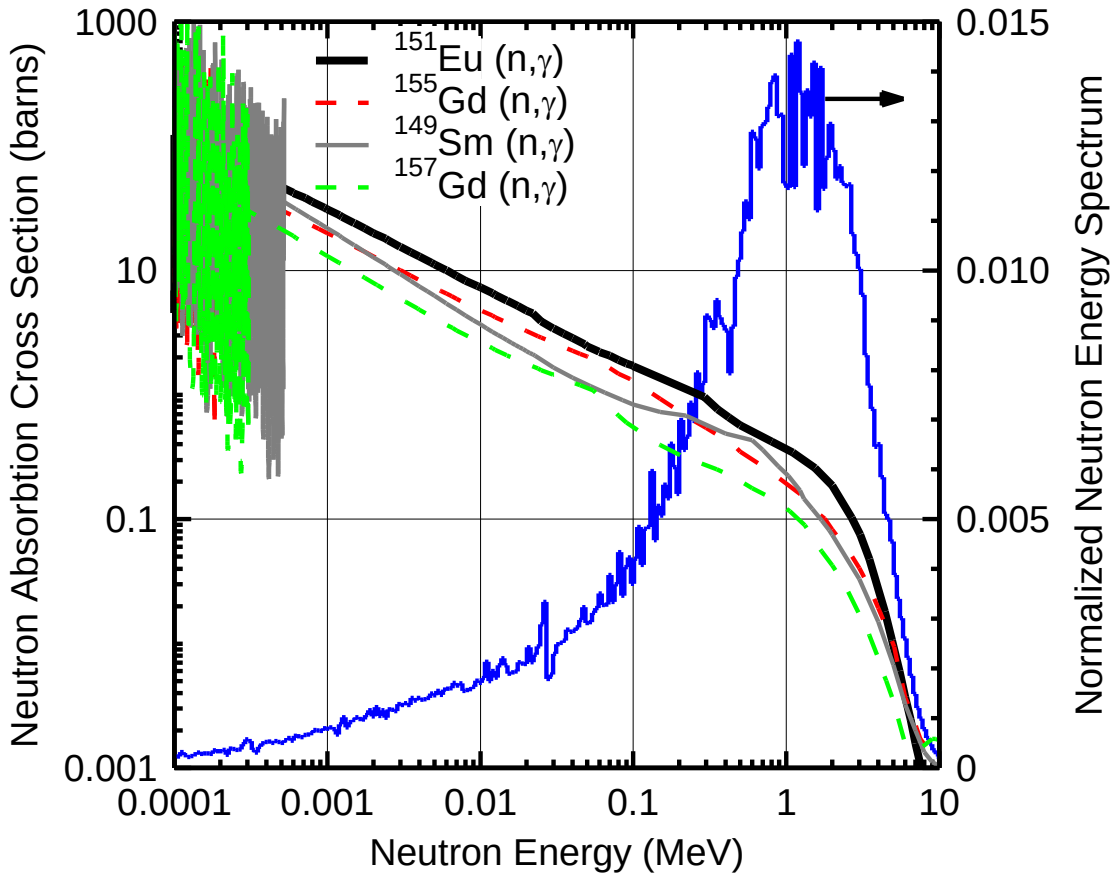

Fig. 3.29. - SSAs' neutron cross sections and energy spectrum in reactor core submerged in wet sand and flooded with seawater [Schriener and El-Genk 2012a].

Figure 3.29 compares the neutron absorption cross sections of the four SSA isotopes investigated (^{155}Gd, ^{157}Gd, ^{151}Eu, and ^{149}Sm). This figure also compares the corresponding neutron energy spectrum in the UN fuel of the submerged SCoRe-N_5 bare reactor in wet sand and flooded with seawater, following the unlikely event of a launch abort accident. Despite the moderating effect of the seawater in the submerged and flooded core, the results in Fig. 3.29 show that the neutron energy spectrum in the UN fuel remains hard. For the energy range of interest, the ^{151}EuN fuel additive has the largest neutron absorption cross section and hence is the most effective SSA, followed by ^{155}GdN and ^{149}SmN, and then ^{157}GdN. The larger the average neutron absorption cross-section, the lower is the subcritical reactivity of the submerged and flooded reactor. In other words, for the same subcriticality requirement of the submerged and flooded bar reactor, a smaller concentration of the most effective SSA (^{151}Eu) is required, decreasing the total volume of the fuel pellets and the active height of the core and that of the BeO radial reflector, and hence the reactor total mass. The shorter active core height also decreases neutron leakage during reactor operation, increasing the BOL excess reactivity, ρ_{ex}.

The increased excess reactivity due to the decreased neutron leakage outweighs the decrease in reactivity caused by the greater fast neutron absorption of ^{151}Eu (Fig. 3.29). This results in a net increase in the BOL excess reactivity, ρ_{ex}. This trend, however, does not hold true for all of the other SSAs investigated. For the ^{155}GdN and ^{149}SmN UN fuel additives, despite the larger ^{149}SmN concentration required (23.0 at% ^{149}SmN versus 21.3 at% ^{155}GdN), the lower neutron absorption cross section of ^{149}Sm results in a cold clean BOL excess reactivity that is statistically the same ($6.15 versus $6.11 with ^{155}GdN) (Fig. 3.27). The higher SSA concentration required for ^{157}GdN in the UN fuel pellets results in the lowest BOL cold clean excess reactivity of the SSAs evaluated (Fig. 3.27). Based on the results of the neutronics analysis discussed in this subsection, the SCoRe-N_5 reactor with ^{151}EuN additive in the UN fuel pellets and $^{151}Eu_2O_3$ reactor vessel coating is selected for further analysis. This reactor design has the highest BOL cold-clean excess reactivity, the smallest mass and active core height, and lowest SSA concentration in the UN fuel (Table 3.5).

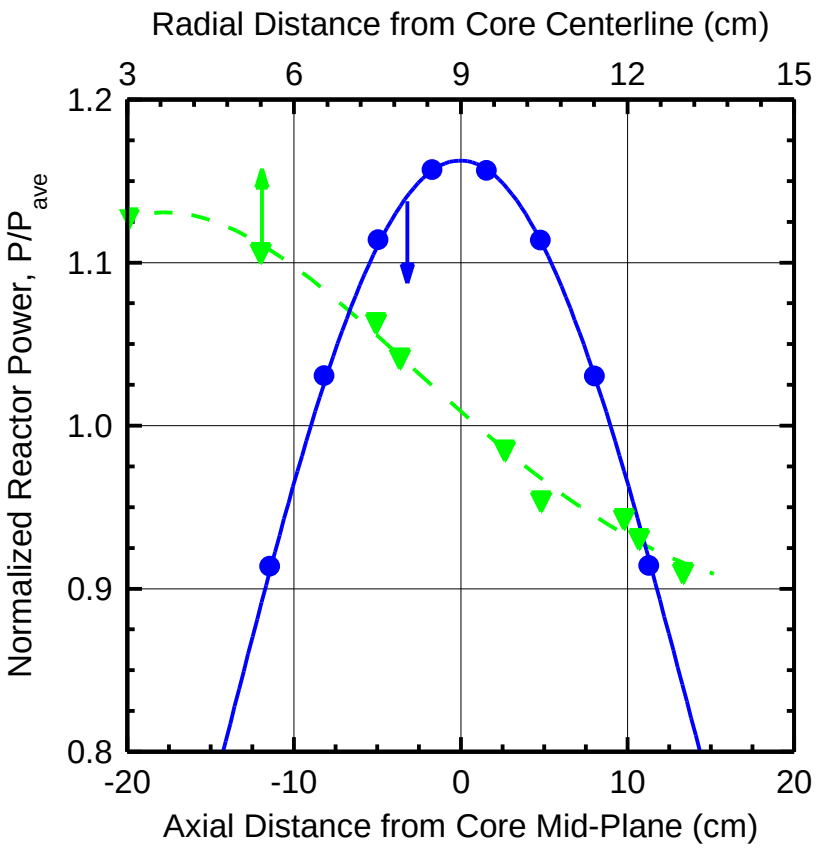

Fig. 3.30. - Calculated mean axial and radial fission power profiles in the selected SCoRe-N_5 reference reactor design [Schriener and El-Genk 2012a].

The spatial heat generation profiles in the UN fuel rods of the SCoRe-N_5 core are calculated using the F6 energy deposition tallies in the MCNPX code (Pelowitz et al. 2010). The axial power profiles (Fig. 3.30) are cosine-like and almost symmetric across the core mid-plane. The radial power profile is flatter due to the effects of the BeO radial reflector and the surrounding supplemental reflector of lunar regolith (Fig. 3.12). The lower energy neutrons returning from the radial BeO reflector into the reactor core, and the additional neutrons generated by (n,2n) and (γ,n) reactions in ^{9}Be, increase the fission rate in the outer rows of UN fuel rods in the core sectors, flattening the radial power profile. These fission power profiles are incorporated into the performed CFD and thermal-hydraulics performance analyses in the next section of the SCoRe-N_5 during nominal operation.

3.6. Thermal-Hydraulic Analyses of SCoRe-N_5

The calculated temperatures in a hydraulic sector of the SCoRe-N_5 design with ^{151}Eu SSA at nominal powers of 200 kW_{th}, 500 kW_{th}, and 1,000 kW_{th} (or 33.33, 83.33, and 166.67 kW_{th} per hydraulic sector) are shown in Figs. 3.31, 3.32, and 3.33. The corresponding NaK-78 flow rates to achieve the same inlet and exit temperatures in these sectors are 0.75 kg/s, 1.87 kg/s, and 3.74 kg/s, respectively. The images in Figs. 3.31-3.33 show the temperatures contours and the coolant flow distribution in the core sector and the upper plenum. A-A is a plane view of the hydraulic sector showing the temperatures of the UN fuel rods and the surrounding coolant flow at the axial location of the peak UN fuel centerline temperature in the reactor core. B-B presents an axial cross section view of the same core sector showing the axial and lateral changes of the temperatures in the fuel rods and the coolant sub-channels. The B-B axial cross section is taken along the center of the hydraulic sector.

At the reactor thermal powers of 200 kW_{th} and 500 kW_{th}, the coolant temperature entering the reactor core is 855 K, which is 5 K higher than that in the inlet duct (Fig. 3.9) of 850 K. At the lowest power of 200 kW_{th}, the peak centerline temperature of the UN fuel rods and cladding temperatures are 952 K and 919 K, while the average fuel and cladding temperatures in the core are 914 K and 878 K, respectively (Fig. 3.31a). At 500 kW_{th}, these peak temperatures are 1,041 K and 935 K, while the average temperatures in the core are 962 K and 885 K, respectively (Fig. 3.32).

Increasing the reactor thermal power to 1,000 kW_{th}, increases the UN fuel peak centerline and cladding temperatures and decreases the temperature of the coolant entering the reactor core (Fig. 3.33). The later decreases by 3 K, to 852 K before entering the reactor core sectors. The smaller temperature rise in the annulus on the inside of the reactor vessel is primarily due to the higher coolant flow rate (3.74 kg/s per reactor core sector). The results in Fig. 3.33 show that operating the reactor at 1,000 kW_{th} (or 166.67 kW_{th} per sector) increases the peak fuel centerline and cladding temperatures to 1,190 K and 964 K, and the average fuel and cladding temperatures in the reactor core to 1,065 K and 884 K, respectively (Fig. 3.33). The calculated UN fuel temperatures are relatively

low, thus expected to reduce fuel swelling and fission gas release over the operation life of the reactor, though further testing and validation would be needed.

The results in Figs. 3.31-3.33 also show that the increased flow rates of the liquid NaK-78 coolant entering the reactor at the higher nominal power levels improve mixing of the coolant exiting the reactor core. This improved mixing is due to the combined effects of turbulence at the higher flow rates along the fuel rods and lower coolant viscosity at the higher temperature. At the lowest reactor nominal power of 200 kW_{th} and coolant flow rate of 0.75 kg/s, the temperature of the liquid NaK-78 exiting the core into the exit plenum varies from 882 to 905 K, a temperature difference of 23 K (Fig. 3.31). At the reactor nominal power of 500 kW_{th} and coolant flow rate per hydraulic sector of 1.87 kg/s, the temperature of the exiting NaK-78 decreases, where its temperature varies from 889 to 903 K, a difference of 14 K (Fig. 3.32). Doubling the reactor power to 1,000 kW_{th} and the coolant mass flow rate to 3.74 kg/s per sector, enhances mixing and reduces the temperature difference in the exit plenum. The temperature of the liquid NaK-78 coolant in the exit plenum varies from 903 K to 894 K, a difference of only 9 K (Fig. 3.33).

Temperature profiles for representative UN fuel rods are plotted in Fig. 3.34 and 3.35. Fuel rods ‘‘A’’, ‘‘B’’, and ‘‘C’’ are centered along the middle of the core sector (Section B-B in Figs. 3.31-3.33) and thus demonstrate the effect of the radial power profile. The selected fuel rods also represent three different flow areas per fuel rod in the core sector; for the corner rod (pin ‘‘A’’) is 1.36 cm^2, the center rod (pin ‘‘B’’) is 1.08 cm^2 , and the edge rod (pin ‘‘C’’) is 1.22 cm^2. Fuel rods ‘‘D’’ are the furthest radially outward from the center of the sector, and while they are corner rods like rod ‘‘A’’ have a much lower power and enjoy additional cooling by convection to the cold NaK-78 flowing down the adjacent inlet coolant annulus (Fig. 3.34). Fig. 3.34 plots the radial power profile for the selected fuel rods in the core sector at the axial location of Section A-A in Figs. 3.31-3.33, while Fig. 3.35 plots the axial temperature profile along the centerline for these same fuel rods. The fuel temperature is highest in rod ‘‘A’’ where the power is highest and lower in the outer fuel rods due to their lower powers (Fig. 3.30). The lowest temperature and power are those for the outer corner rods ‘‘D’’.

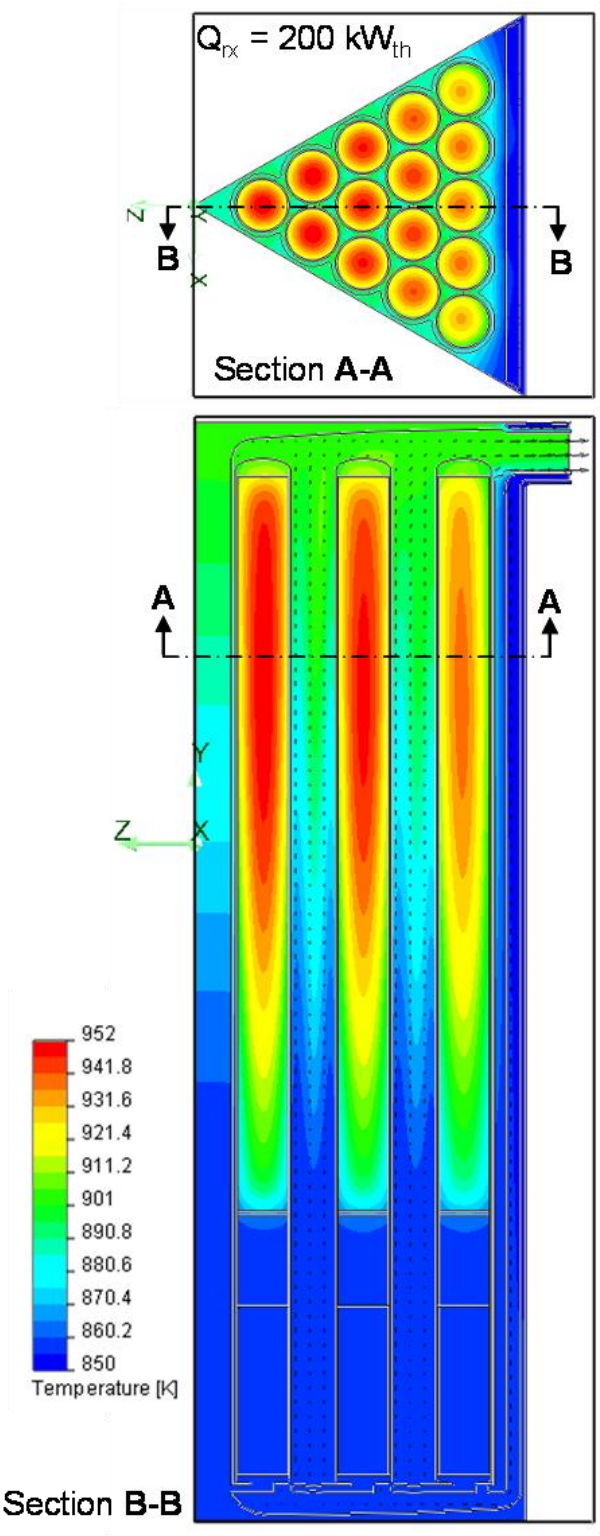

Fig. 3.31. - Calculated temperatures in a hydraulic sector of the SCoRe-N_5 reference design at 200 kW_{th} [Schriener and El-Genk 2012a].

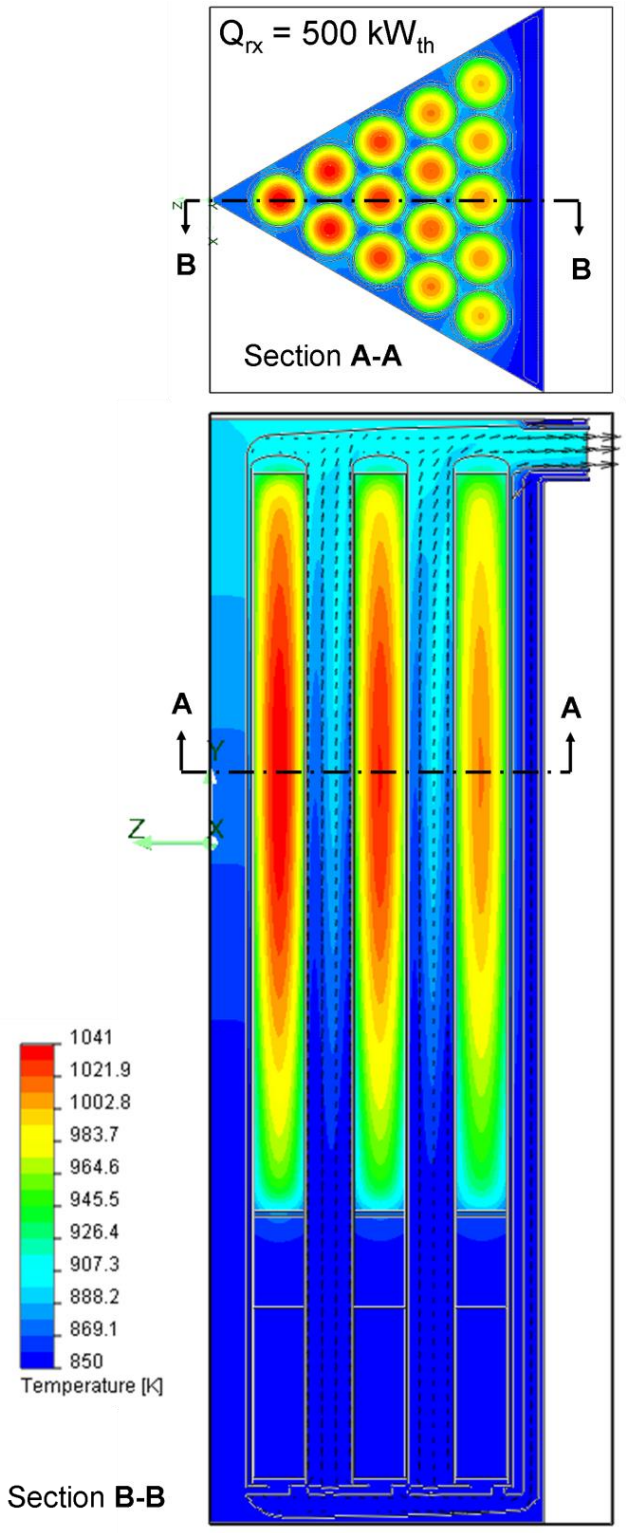

Fig. 3.32. - Calculated temperatures in a hydraulic sector of the SCoRe-N5 reference design at 500 kW_{th} [Schriener and El-Genk 2012a].

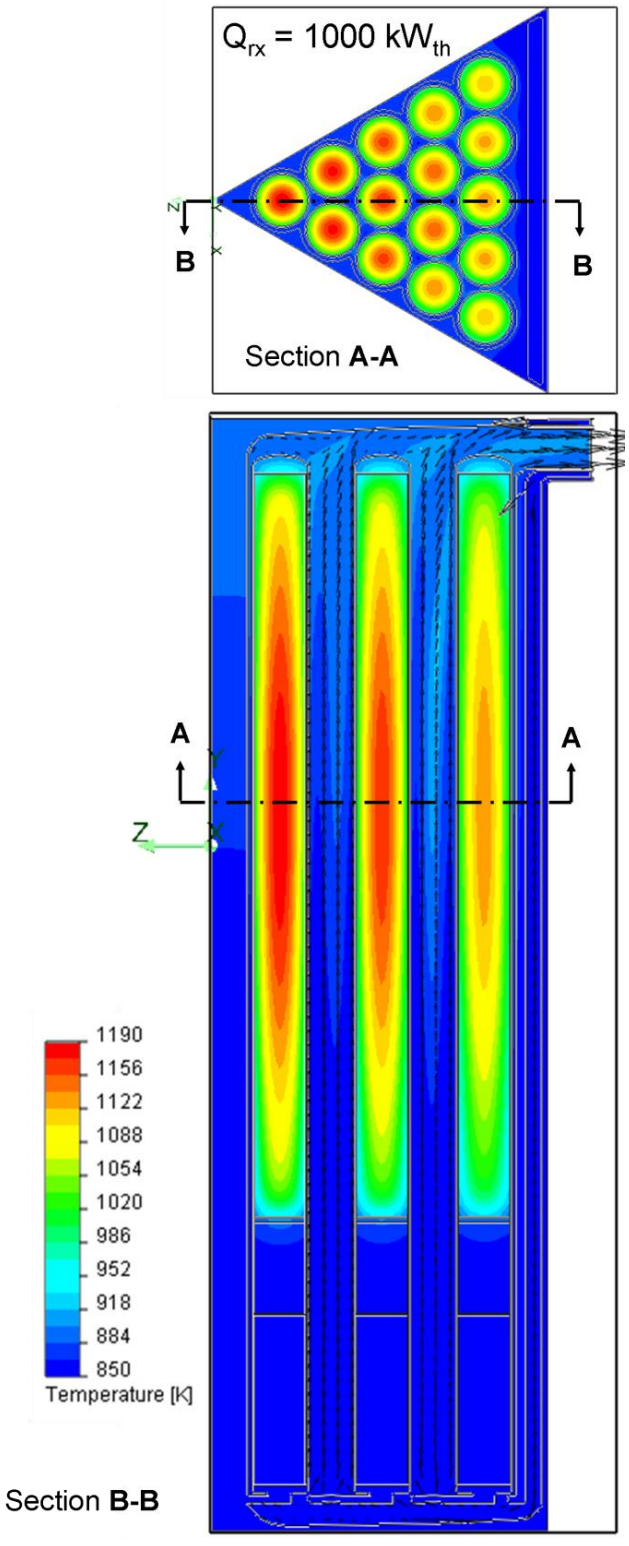

Fig. 3.33. - Calculated temperatures in a hydraulic sector of the SCoRe-N_5 reference design at 1,000 kW_{th} [Schriener and El-Genk 2012a].

Although the thermal power in the reactor core sector is highest in the innermost rows of the fuel rods (Figs. 3.31-3.33), the curved upper and lower coolant plenums (Fig. 3.9) help distribute the flow in sectors sub-channels. This helps to minimize the temperature increases in the inner most fuel rods and the radial variation in coolant temperature across the sector. As a result, the temperatures in the fuel rods are much closer to each other than their comparative fission power generation would suggest. For example, at the 500 kW_{th} power level for the reactor, the difference in the peak fuel temperature between rod ''A'' and rod ''D'' is only 5%, while the difference in the power density between these two fuel rods is almost 20%. For the higher 1,000 kW_{th} power level, the difference in the peak fuel temperature between rods ''A'' and ''D'' increases slightly to 6% for the same difference in the power density of almost 20%.

The radial temperature rise across the fuel rods in the core sectors (Fig. 3.34) is relatively small, despite the large 1.136 cm radius of the fuel pellets. The temperature rise across the fuel rods for the reactor at 200 kW_{th} is only 52 K, increasing at 500 kW_{th} to 153 K, and reaching 162 K at 1,000 kW_{th}. The larger fuel centerline temperatures at the higher power levels are also caused by the higher temperature drop across the fuel-clad gap. Despite the difference in the fuel temperatures at the two thermal power levels, the temperature of the 316L stainless steel cladding at the two axial locations (A-A in Figs. 3.31-3.33) is almost the same. The greater thermal expansion of the cladding compared to that of UN fuel and the low fuel swelling at the relatively low operating temperatures would reduce the stress in the cladding throughout the reactor's operation life.

The shape of the axial temperature profiles along the centerlines of the fuel rods (Fig. 3.35) in the SCoRe-N_5 sectors are different at the three thermal power levels is shown in. Increasing the reactor thermal power and the coolant flow rate not only increase the peak temperatures of the UN fuel and the cladding, but shift the locations of the peak values further down toward the core mid-plane. At 200 kW_{th} the peak axial fuel temperature occurs at a location shifted 7.5 cm above the core mid-plane. This is due to a combined effect of the high thermal conductivity of the UN fuel and the relatively low power density at the 200 kW_{th} power level. For the 500 kW_{th} power level, the peak axial fuel temperatures are shifted up 3 cm above the core mid-plane. At the 1,000 kW_{th} power

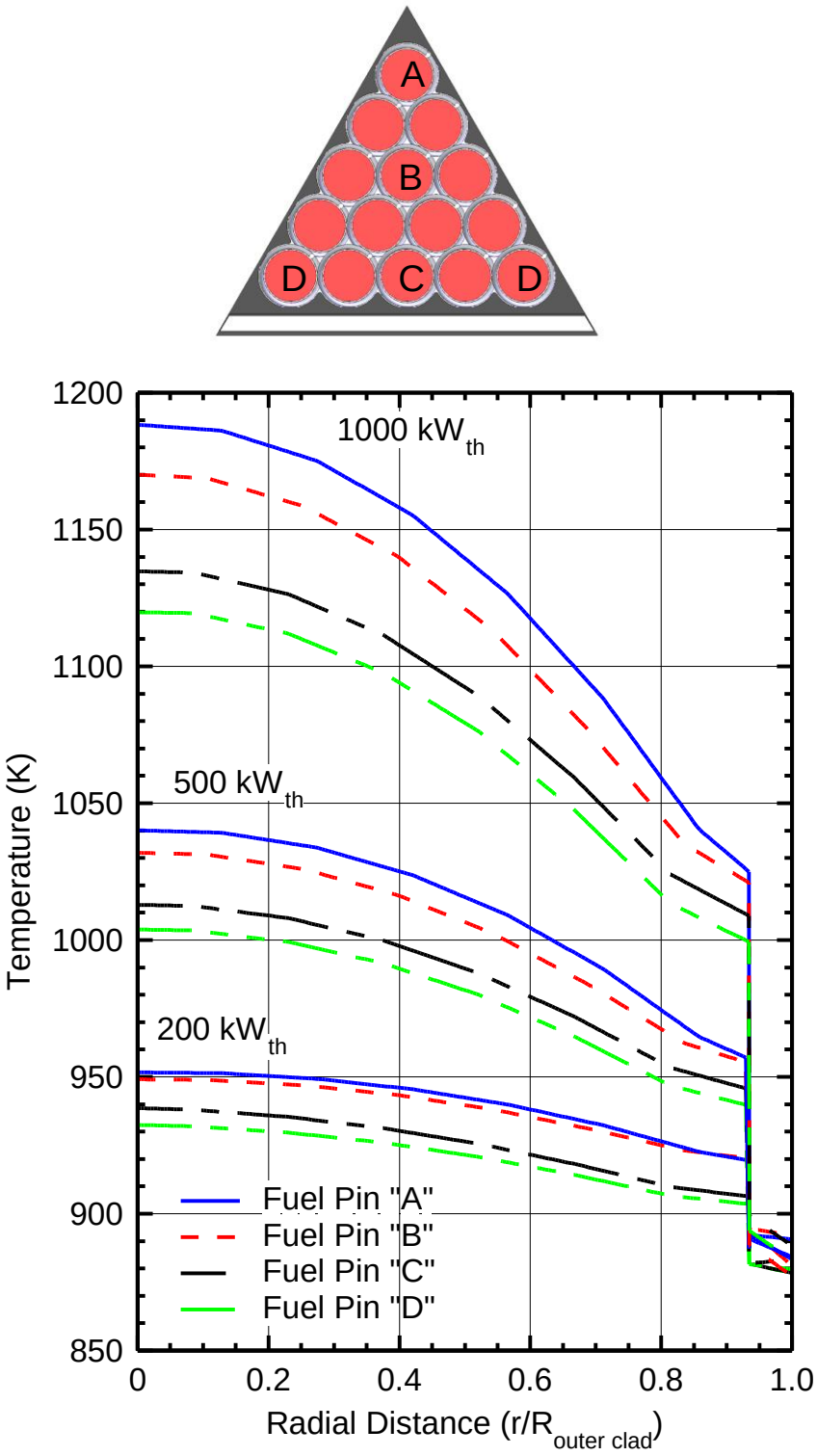

Fig. 3.34. - Calculated radial temperature profiles in reference SCoRe-N_5 reactor at location of peak fuel temperature [Schriener and El-Genk 2012a].

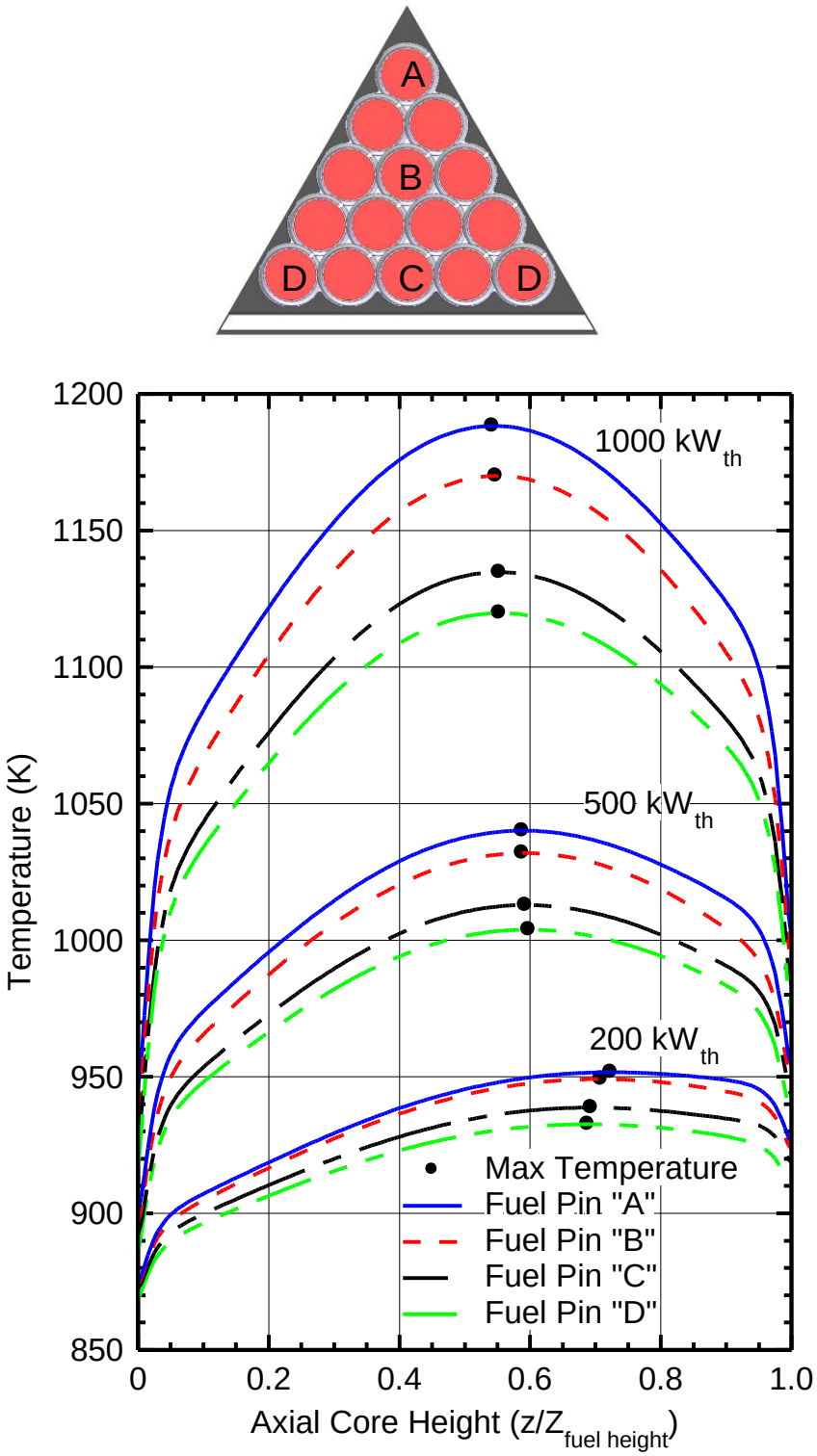

Fig. 3.35. - Calculated axial temperature profiles in reference SCoRe-N_5 reactor along the fuel rod centerline [Schriener and El-Genk 2012a].

level, the peak axial fuel temperature occurs only 1.6 cm above the core mid-plane. The increased power density at 500 kW_{th} and 1,000 kW_{th} shifts the location of the peak temperature towards the peak of the axial power profile (Fig. 3.30).

These CFD and thermal-hydraulics analyses are coupled back to the neutronics analyses b7y incorporating the calculated temperatures into the MCNPX neutronics model to determine the BOL hot-clean reactivity at the different power levels.

3.7. Hot-Clean Reactivity of the Reference SCoRe-N_5

The MCNPX model of the SCoRe-N_5 reactor accounts for the changes in the dimensions of the UN fuel and core structure and material densities with temperature. It assumes an isotropic expansion of all core materials. The gap between the fuel and clad remains as the coefficient for thermal expansion of stainless steel ($17.2x10^{-6}$ K^{-1}) is larger than that of the UN fuel ($9.2x10^{-6}$ K^{-1}). The temperature of the BeO radial reflector is taken equal to 600 K, and the changes in its radial and axial dimensions are accounted for in the MCNPX model. The temperature of the surrounding regolith is kept at 300 K.

Due to the thermal expansion of the UN fuel and core structure materials and the Doppler broadening of neutron cross sections, the values of BOL hot-clean reactivity, ρ_{ex}, for the reference SCoRe-N_5 reactor at the nominal operating powers of 200 kW_{th}, 500 kW_{th}, and 1,000 kW_{th} are lower than the BOL cold-clean values (Fig. 3.36). At the reactor thermal power of 200 kW_{th} the hot-clean ρ_{ex} of \$5.67 is \$1.05 lower than cold-clean value of \$6.72. For a reactor thermal power of 500 kW_{th} the hot-clean ρ_{ex} of \$5.64 is \$1.08 lower, and the hot-clean ρ_{ex} of \$5.60 is \$1.12 lower than the cold than the cold-clean value at the reactor thermal power to 1,000 kW_{th} (Fig. 3.36). The negative temperature reactivity feedback is mostly due to the thermal expansion of the core materials, particularly axial expansion of the UN fuel pellets against the compression springs in the gas plenums of the fuel rods (Fig. 3.9). The negative Doppler temperature reactivity feedback is small; only \$0.07 at 500 kW_{th} and \$0.08 at 1,000 kW_{th}, compared to the total negative temperature reactivity feedback of \$1.08 and \$1.12, respectively. This relatively large negative temperature reactivity feedback for the reference SCoRe-N_5 reactor design is desirable for operation safety and support load-following operation.

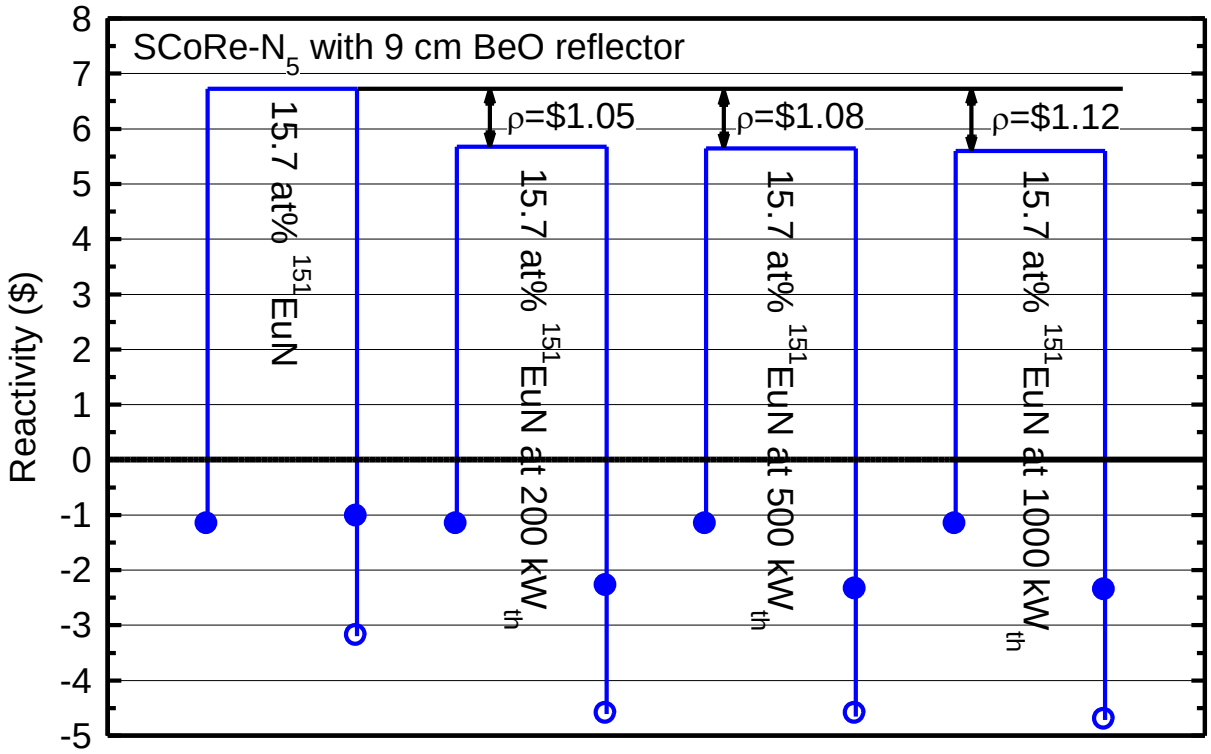

Fig. 3.36. - Reactivity for reference SCoRe-N_5 design with ^{151}EuN SSA at nominal powers of 200, 500, and 1,000 kW_{th} [Schriener and El-Genk 2012a].

Multi-physics performance analyses of the reference SCoRe-N_5 at nominal thermal power levels of 200, 500 and 1,000 kW_{th} confirm adequate cooling of the UN fuel rods and flow distribution of the liquid NaK-78 in the reactor core and mixing in the upper plenums and the exit ducts during nominal operation. In addition to the reactor thermal-hydraulics performance during nominal operation, the SCoRe-N_5 is also investigated for safe operation, at a lower power level, in the unlikely event one of the six core sectors experiences a LOC or a LOCo. The results of this safety analyses are discussed in the next section.

3.8. Thermal-Hydraulics and Safety Analysis of SCoRe-N_5

This section describes the performed 3-D thermal-hydraulic and safety analyses of the SCoRe-N_5 (Fig. 3.9), both during nominal operation at 1,000 kW_{th} and at a lower power level of 167.67 kW_{th} when a core sector experiences a Loss of Coolant (LOC). The

analyses are carried out using the commercial CFD package STAR-CCM+ version 6.02.9 [CD-adapco 2011]. The simulation of the SCoRe-N_5 during nominal operation is for reactor coolant inlet and exit temperature of 850 and 900 K, and a coolant flow rate per sector of 3.74 kg/s. The LOC analyses are performed with a total reactor power is 167.67 kW_{th}, which is equally removed by the coolant in the five operating sectors.

With a core sector experiencing a LOC, the operating temperatures and flow rates of the liquid NaK-78 in the other five sectors are determined as functions of the reactor thermal power using the integrated power system simulation code DynMo-TE [El-Genk and Tournier 2006a]. The operating parameter values are incorporated into the 3-D CFD and thermal hydraulics analyses of the reactor sectors. These safety analyses determine the thermal power level at which the reactor could continue to operate safely with one sector in the core experiencing a LOC. Details and results of these calculations are given next.

3.8.1. Analyses Methodology

The STAR-CCM+ commercial software package, version 6.02.9 is used to perform the 3-D thermal-hydraulics analyses. The simulations calculates the velocity field and flow distribution in reactor core and exit plenum of the SCoRe-N_5. In addition, the analyses calculate the temperature distributions in the UN fuel, cladding and the circulating liquid NaK-78. The analyses of the SCoRe-N_5 core with a sector experiencing a LOC calculate the temperature of the UN fuel and cladding in the affected sector and identify potential hot spots, and determine the operation margin, compared to the melting temperatures of UN fuel and 316L SS cladding.

To reduce the numerical meshing requirements and the computation time, the performed SCoRe-N_5 thermal-hydraulic analyses at nominal operation conditions (1,000 kW_{th} and coolant inlet and exit temperature of 850 and 900 K) is done for a single sector, with a similarity (or adiabatic) boundary condition at the dividing walls with adjacent sectors (Figs. 3.9). The forced convection flow of liquid NaK-78 is simulated using the Shear Stress Transport (SST) k-ω turbulence model in the STAR-CCM+ code. The analyses account for the changes in the material properties in the core with temperature,

and are performed with a turbulent Prandtl number, Pr_t, of ~2 to account for the high heat diffusivity of the liquid NaK-78 coolant.

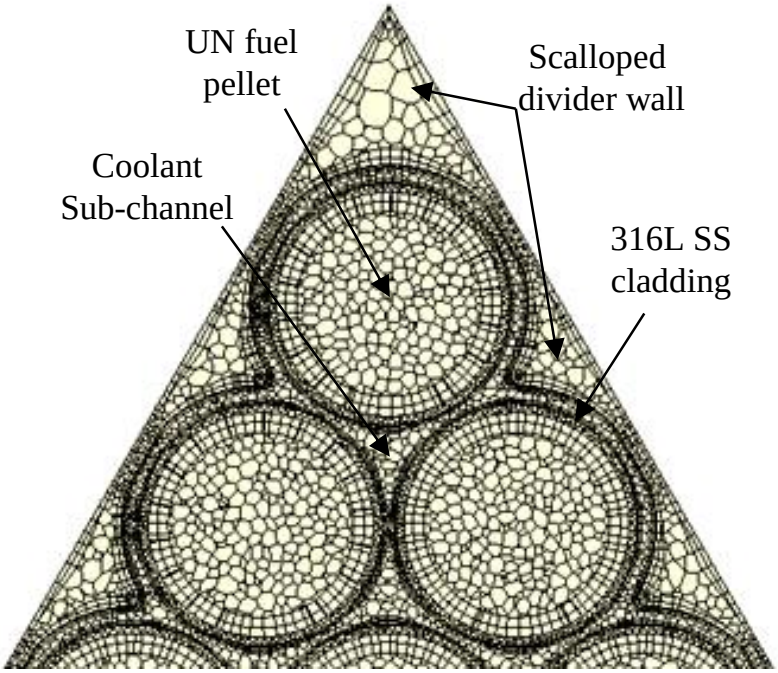

Fig. 3.37. - Computational mesh grid for the thermal-hydraulics analysis of a core sector [Schriener and El-Genk 2012b].

The implemented numerical mesh grid in the analyses is created using the polyhedral and prism layer meshing models. The grid includes $7.4x10^6$ solid mesh elements and ~$11.1x10^6$ fluid mesh elements (Fig. 3.37). The narrow gas gap between the SS cladding and fuel pellets in the rods is modeled as a thermal contact resistance. This approach effectively decreases the number of numerical mesh grid elements and the computational time and memory requirements. In the reactor thermal-hydraulics analyses at nominal operation conditions, the liquid NaK-78 enters the core sector through the inlet duct at 3.74 kg/s and 850 K. Its exits through the outlet duct at a constant pressure of 1 MPa and bulk exit temperature of 900 K. The calculated the axial and radial profiles for the heat generation rates in the UN pellets of the individual fuel rods are provided by the 3-D neutronics analysis of SCoRe-N_5.

The performed analyses of the SCoRe-N_5 with a core sector experiencing a LOC account for the heat transfer by conduction and thermal radiation amongst fuel rods in that sector voided of coolant, and between these rods and the heat-pipes dividing walls with the adjacent, convectively cooled sectors (Fig. 3.7). The voided volume by the drained liquid NaK-78 from the sector with a LOC is modeled as an enclosure with internal thermal radiation amongst the cladding surfaces of the fuel rods with the wire wrap and the dividing walls. The complexity of including thermal radiation taxes the analyses by increasing the computational time and the memory requirements. In order to reduce these requirements, the analysis within a core sector experiencing a LOC is performed for a half sector, with a symmetry boundary condition. This approach reduced the numerical mesh grid size to 5.1×10^6 elements. The analyses of the core sector experiencing a LOC uses the automatic ray-trace radiation view factors and the temperature dependent field function emissivity options in STAR-CCM+.

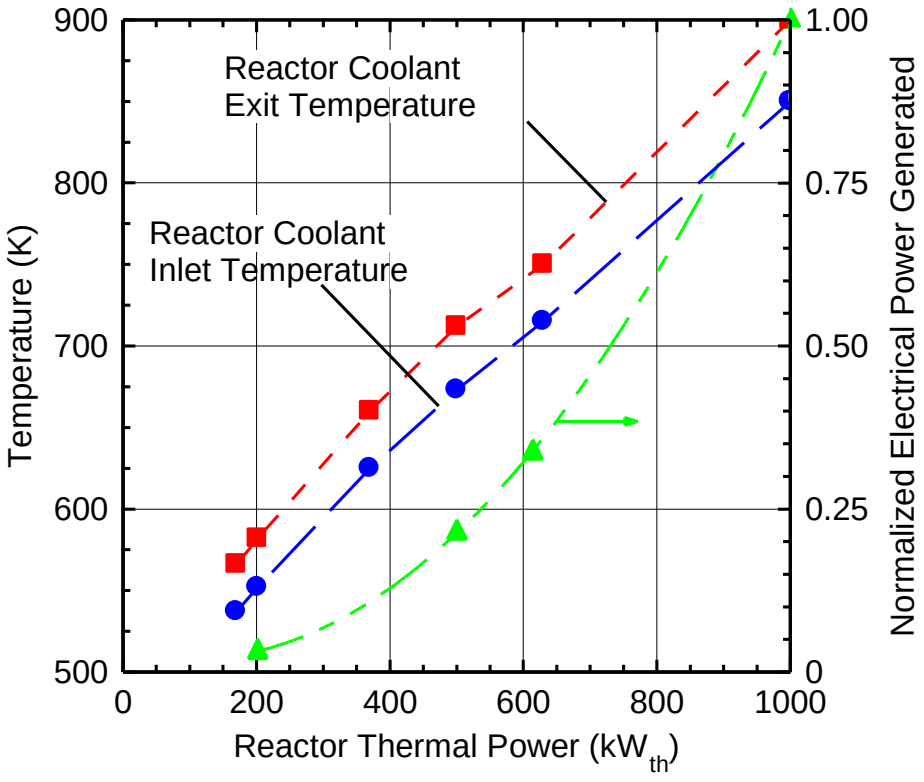

Fig. 3.38. - Integrated power system performance results: coolant temperatures and load electrical power [Schriener and El-Genk 2012b].

The potassium heat-pipes dividers are modeled as isothermal surfaces with the temperature equal to the mean value of the liquid metal coolant circulating in the adjacent, convectively cooled sectors (Fig. 3.38). These temperatures are calculated using the DynMo-TE model [El-Genk and Tournier 2006a] of the integrated SCoRe power system, with the results shown in Fig. 3.38. The temperature of the common wall of the core sector with the flow annulus on the inside of the reactor vessel is set equal to the coolant inlet temperature.

When one of the six core sectors experiences a LOC, the power system continues operation, but at a reduced power level. The fission heat generated in that sector transports to the two adjacent sectors. The NaK coolant flow rate and the inlet and exit temperatures in these sectors depend on the reactor thermal power. Fig. 3.38 presents the calculated coolant inlet and exit temperatures as functions of the reactor thermal power [El-Genk and Tournier 2006a; Schriener and El-Genk 2012a]. Also shown is the normalized electrical power of the power system to the nominal value of 38 kW_e, which corresponds to a nominal reactor thermal power of 1,000 kW_{th}. At a reduced reactor thermal power of 166.67 kW_{th}, the inlet and exit temperatures of the liquid NaK-78 coolant in the other five operating sectors in the reactor core are 530 and 560 K, and the power generation per sector is ~27.8 kW_{th}, including that experiencing a LOC. The corresponding electric power of the integrated power system for lunar surface power decreases to only 1.3 kW_e (Fig. 3.38). This corresponds to only ~3.4% of the nominal electrical power of 38 kW_e. The results of the 3-D thermal-hydraulic analyses of the SCoRe-N_5 at nominal operation conditions (1,000 kW_{th}, and 850 and 900 K coolant inlet and exit temperatures) are presented and discussed in next section.

3.8.2. Thermal-Hydraulics Analyses at Nominal Operation

Figure 3.39 presents an axial section view of the calculated temperature field at the symmetry plane in a core sector when the reactor operates at nominal conditions (coolant inlet and exit coolant temperatures of 850 K and 900 K and reactor thermal power of 1000 kW_{th} or 166.67 kW_{th} per sector). The highest UN fuel and cladding temperatures occur in the innermost fuel rods near the centerline of the core (Fig. 3.9), where the radial

fission power is the highest. The peak UN fuel and cladding temperatures of 1,191 K and 966 K are within the operation limits of the 316L SS cladding (< 1,000 K).

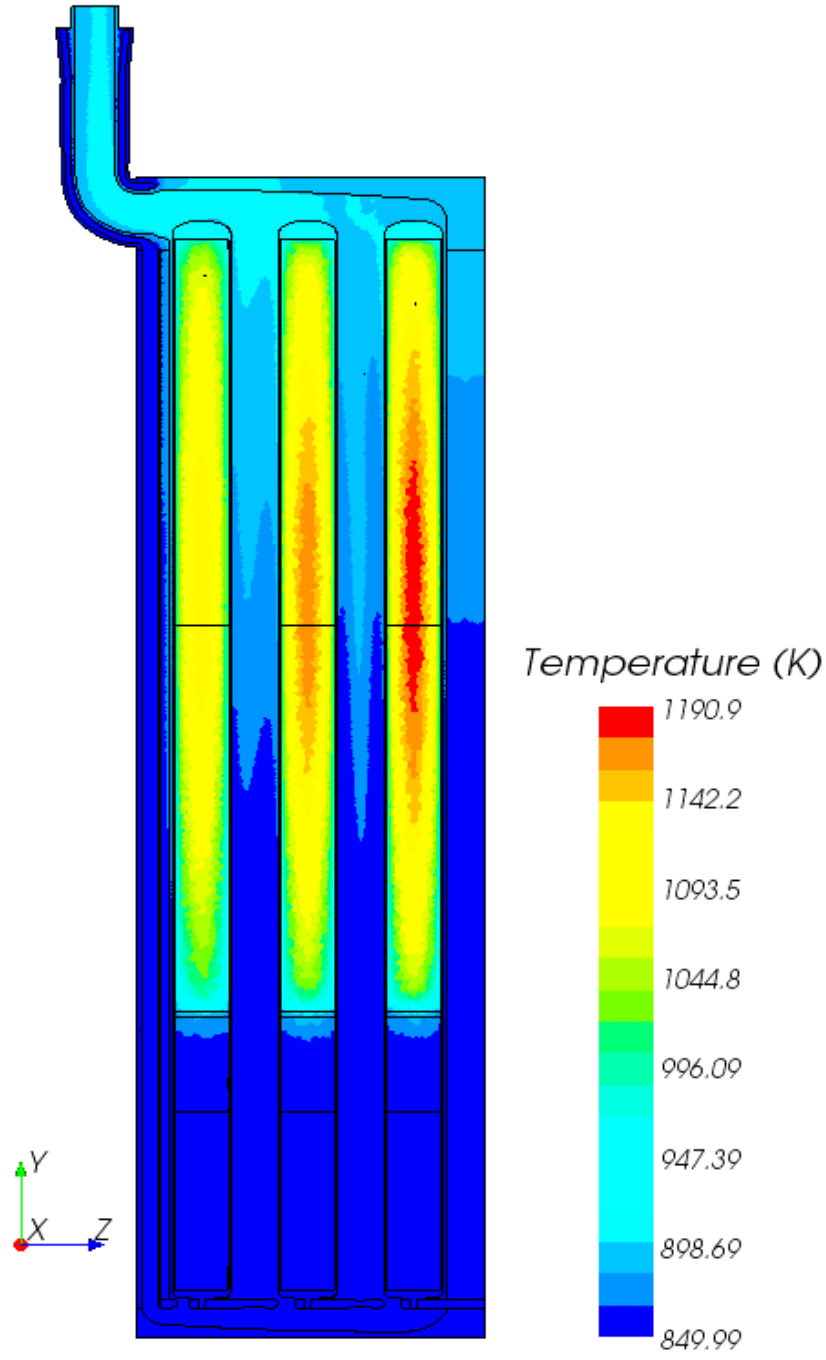

Fig. 3.39. - Calculated temperatures at in a SCoRe-N_5 sector with wire wrapped fuel rods at a nominal power of 1,000 kW_{th} [Schriener and El-Genk 2012b].

In the exit plenum the temperature of liquid NaK varies from 891 K to 904 K (Fig. 3.39). This relatively small difference would not cause thermal stress or effect heat transfer to the PCAs and pump TCAs in the primary loops of the power system (Fig. 3.2). The coolant exits that plenum at an average temperature of 900 K. The total pressure losses in the core sector are 328 kPa. The majority of these losses occur where the coolant enters from the annular inlet duct into the wider coolant annulus and where it leaves the upper plenum into the narrow outlet channel (Fig. 3.9). The pressure losses in the coolant sub-channels in the core sectors are only ~12 kPa (~3.66%).

3.8.3. Thermal Analyses of Core Sector Experiencing a LOC

At a Reactor Power of 166.67 kW_{th} (core sector power of 27.8 kW_{th}) the inlet and exit temperatures of the circulating liquid NaK in the other five, convectively cooled, sectors are 530 K and 560 K, and the temperature of the dividing walls with the sector experiencing a LOC is set at 552 K. This constant wall temperature represents an isothermal heat sink for removing the fission power generated in the core sector experiencing a LOC. Fig. 3.40 shows the calculated temperatures at the core mid-plane in the sector experiencing a LOC near the location of the peak axial power in the core. The fuel rods bordering the 316L scalloped dividing walls radiate and conduct heat directly to the relatively cold sector walls. The rods in the middle of the sector encounter larger resistance of the heat transfer to the cladding of the surrounding fuel rods. Although the rod closest to the core center has the highest power generation, its proximity to the two dividing walls keeps its temperature relatively low. The fuel rods along the dividing walls are hotter than in the corners of the sector, but much cooler than the rods in the middle region of the core sector (Fig. 3.40). This figure shows that the calculated peak fuel and cladding temperatures in the sector experiencing a LOC are 1,983 K and 1,976 K. Though the UN fuel temperature is below the melting point (3,078 K), the cladding temperature for the three hottest fuel rods exceeds the melting point of 316L stainless steel (1,670 K).

Fig. 3.41 shows a tilted view of the calculated temperature field in the core sector experiencing a LOC. The upper wall of the reactor vessel is heated by the thermal radiation from the cladding upper caps of the UN fuel rods. The axial temperature profile

in the fuel rods tracks the axial power profile in the reactor core using the neutronics analyses of the SCoRe-N_5. The high thermal resistance for cooling the middle fuel rods, results in an oval shaped 'hot-spot' in the center of the core sector experiencing a LOC (Fig. 3.41).

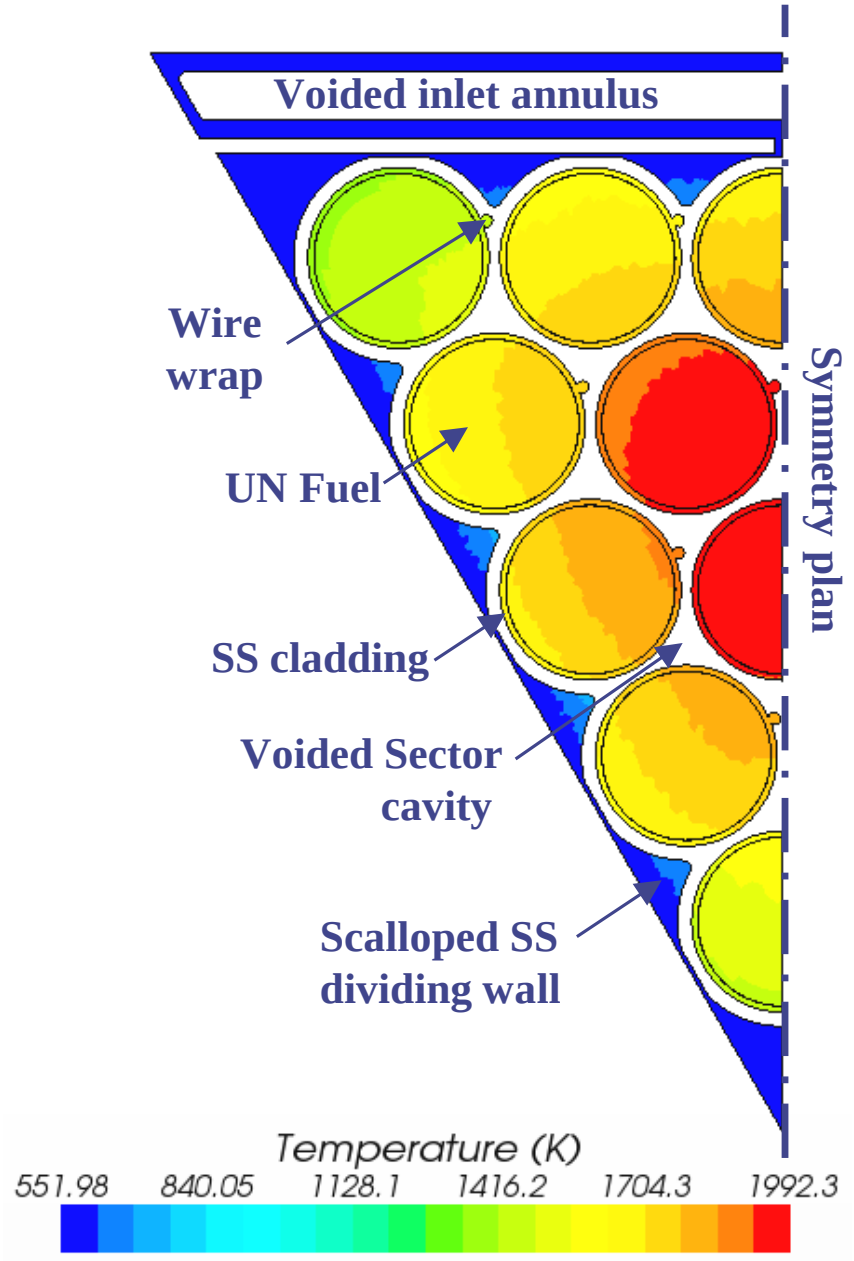

Fig. 3.40. - Calculated temperatures at core mid-plane in the sector experiencing a LOC at a reactor power of 166.67 kW_{th} [Schriener and El-Genk 2012b].

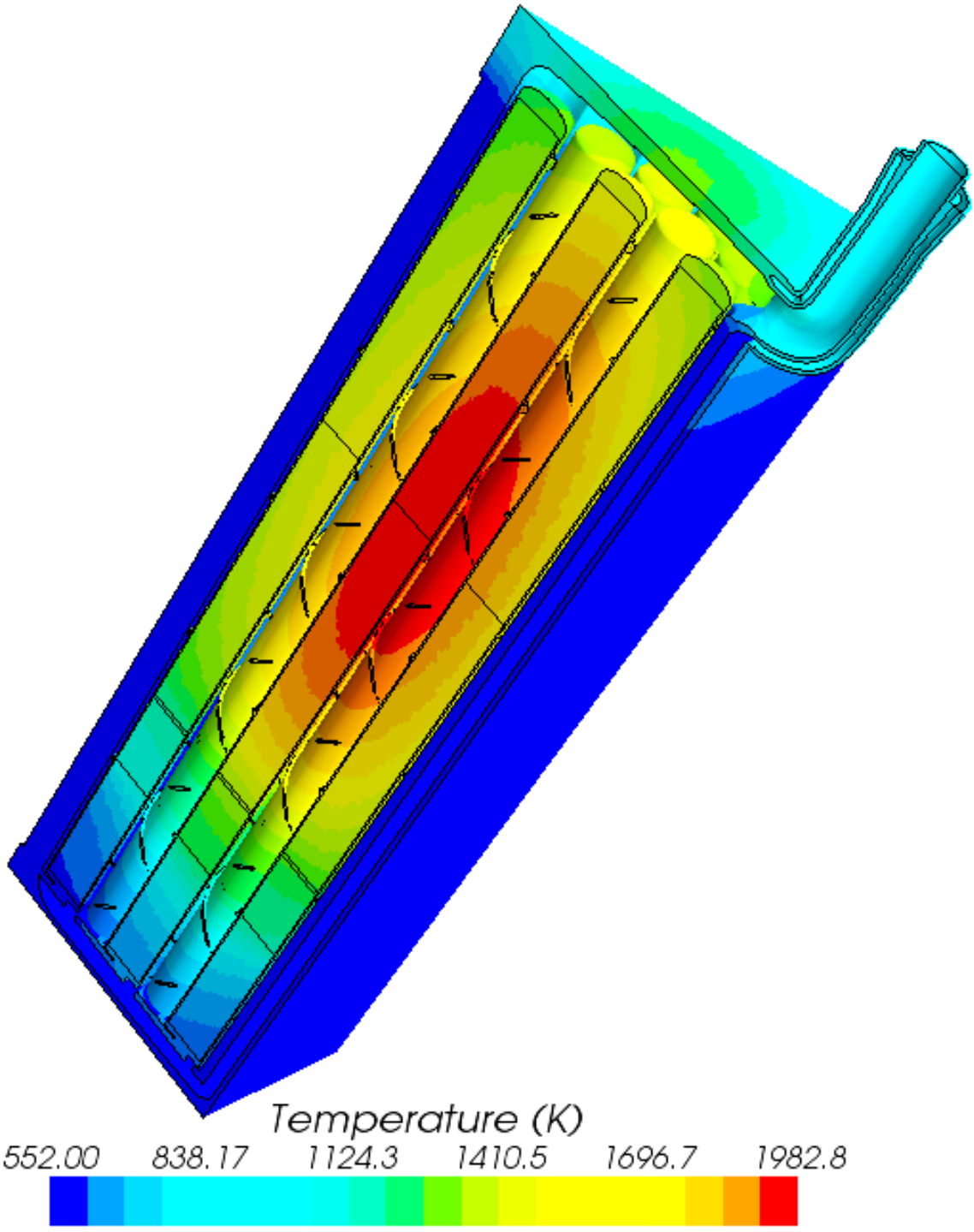

Fig. 3.41. - Perspective view of the core sector experiencing a LOC, with wire wrapped UN fuel rods a reactor power of 166.67 kW_{th} [Schriener and El-Genk 2012b].

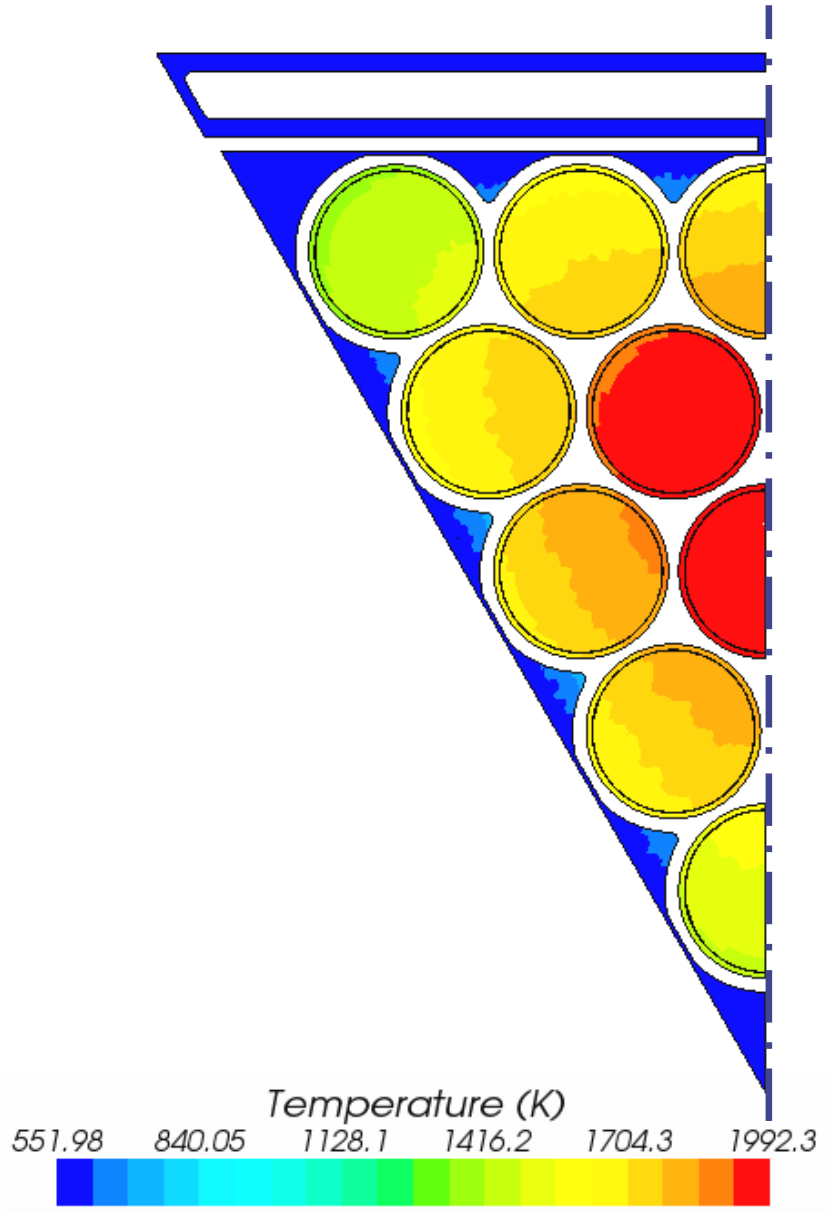

Fig. 3.42. - Calculated temperatures at core mid-plane in the sector experiencing a LOC without wire-wrap at 166.67 kW_{th} [Schriener and El-Genk 2012b].

The wire-wrap on the outside of the cladding for the UN fuel rods in the core sector experiencing a LOC provides a conduction path that partially transfers the generated fission power in the rods to the dividing walls of the core sector. Owing to the very small contact area associated with the wire-wrap, the contribution to heat conduction for cooling the fuel rods is small. Though this conduction lowers the temperatures of the rods in contact with the dividers walls, it is less effective for the rods in the middle of the

sector. To quantify the contribution of the wire-wrap to cooling the fuel rods, thermal analysis is performed of the sector experiencing a LOC without the wire-wrap (Fig. 3.42). The temperatures in the sector without the wire-wrap (Fig. 3.42) are only slightly higher than with the wire-wrap (Fig. 3.40). The peak fuel temperature increases by 9 K (from 1,983 to 1,992 K), while the peak cladding temperature increases by 10 K (from 1,976 K to 1,986 K). While these temperatures are well below the melting temperature of UN fuel they are much higher than the melting temperature of the 316L SS cladding. Although the wire-wrap provides some conduction heat transfer between the fuel rods and the walls, the heat transfer in the sector experiencing a LOC is mostly by thermal radiation. In order to improve cooling of that sector, the interior stainless steel structure is modified to increase heat removal by conduction. Next section presents the introduced design modification.

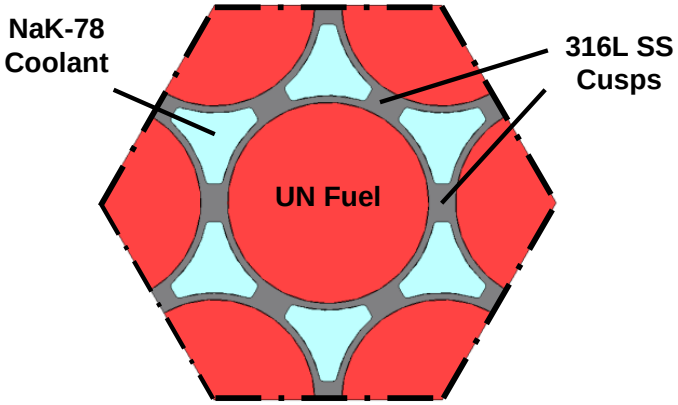

Fig. 3.43. - A fuel rod unit cell with 316L SS 'cusps' [Schriener and El-Genk 2012b].

3.8.4. Modified Core Structure to Enhance Thermal Conductance

To enhance the heat transfer by conduction from the inner fuel rods in the core sector experiencing a LOC to the dividing walls with adjacent sectors, the wire-wrap of the fuel rods is replaced with thick 316L SS cusps (Fig. 3.43). These cusps run the length of the fuel rods, excluding the top and bottom caps. Increasing the width of the contact interface between the cusps and the cladding of the fuel rods increases both the structure strength of the core and the effective thermal conductance in the sector experiencing a LOC. On the other hand, the added stainless steel cusps slightly increase the neutron parasitic

absorption, possibly changing the BOL excess reactivity, and the pressure losses in the core during nominal operation. The increased pressure losses are caused by the decrease in the cross-sectional flow area as well as the increased drag along the interior surfaces of the cusps (Fig. 3.43).

The analyses varied the width of the cusps for the interior fuel rods from 10° to 20° arc length of the outer circumference of the cladding. The width of the cusps along the dividers wall is kept constant at 20° arc length. With these design modifications the thermal analysis of the core sector experiencing a LOC is carried out at a reactor thermal power of 166.67 kW_{th} (or 27.8 kW_{th} per sector). The cusped fuel rods complicate the thermal radiation heat transfer in the core sector experiencing a LOC, taxing the memory and computation requirements. Because of memory limitations of the hardware the 3-D thermal-hydraulic analyses are performed initially with the radiation option disabled. Thus, calculated temperatures are conservative, since enabling thermal radiation would enhance heat transfer and decrease the temperatures in the core sector experiencing a LOC. Without the thermal radiation contribution, increasing the width of the 316L SS cusps in the core from 10° to 15° arc length reduces the peak cladding temperature in the sector experiencing a LOC by 38 K (from 1,494 K to 1,456 K). Increasing the width of the cusps from 15° to 20° arc length decreases the peak cladding temperature by an additional 25 K (from 1,456 K to 1,431 K) (Fig. 3.44).

The calculated temperatures in Fig. 3.44 in the cusped core sector experiencing a LOC, but with the radiation heat transfer disabled, are much lower than those calculated for the same sector with wire-wrapped fuel rods, at the same thermal power and with radiation heat transfer enabled (Fig. 3.40). The temperatures in Fig. 3.45 with 20° arc length SS cusps are 750 K lower for most of the fuel rods next to the dividers walls. The results in Fig. 3.43 with 20° arc length SS cusps show that the cladding temperatures for the majority of the fuel rods next to the dividers walls vary from 750 K to 1300 K. These temperatures are much lower than for the three rods in the interior of the sectors. For these rods, the peak fuel temperature is 1,431 K, and the peak cladding temperature (Fig. 3.44) of 1,431 K is 545 K lower than in Fig. 3.42 (1,976 K), and below the melting point of the stainless steel cladding (~ 1,673 K).

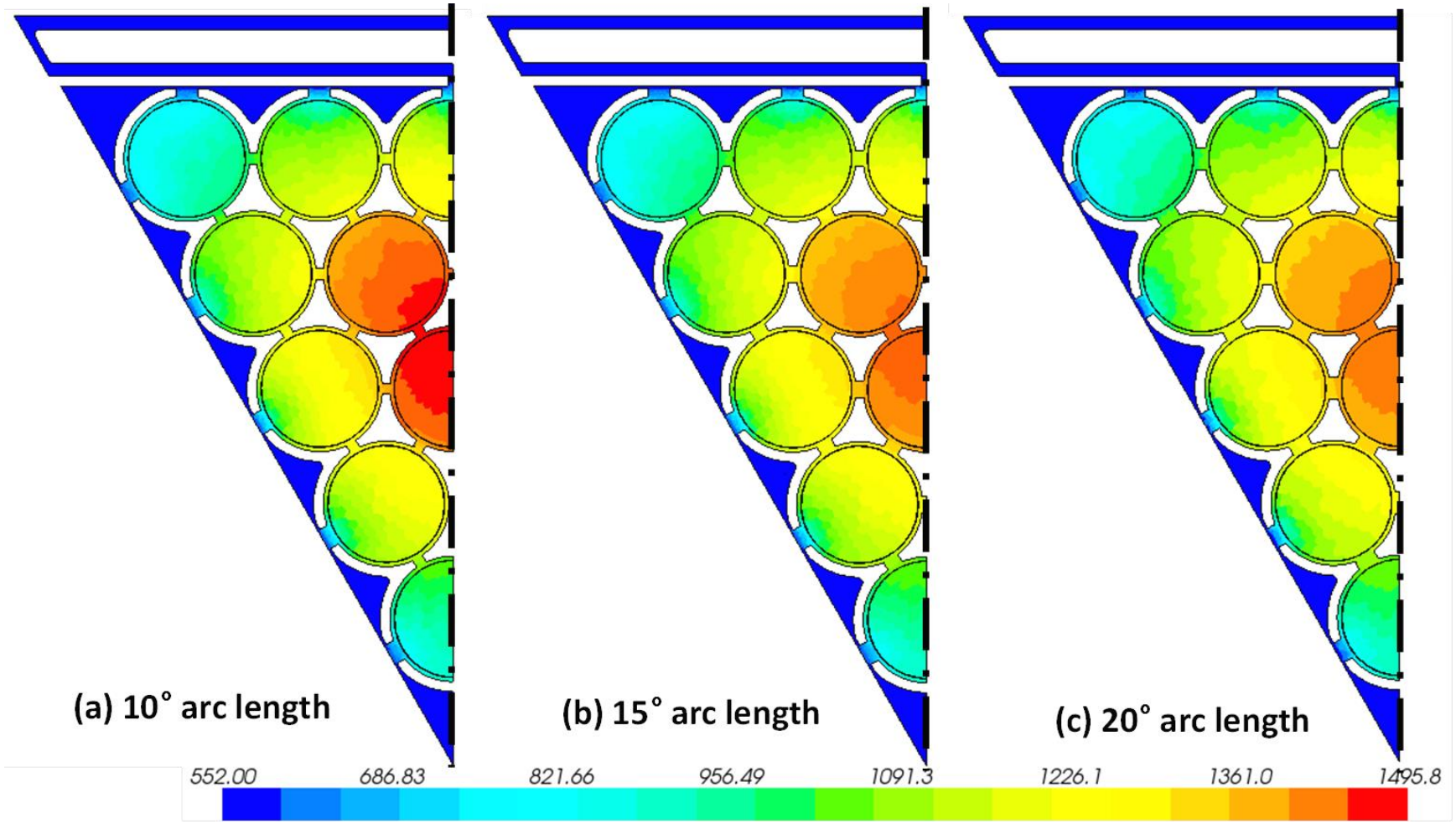

Fig. 3.44. - Calculated temperatures at mid-plane of the core sector experiencing a LOC at 166.67 kW_{th} for: (a) 10° cusped fuel rods, (b) 15° cusped fuel rods, and (c) 20° cusped fuel rods (thermal radiation disabled) [Schriener and El-Genk 2012b].

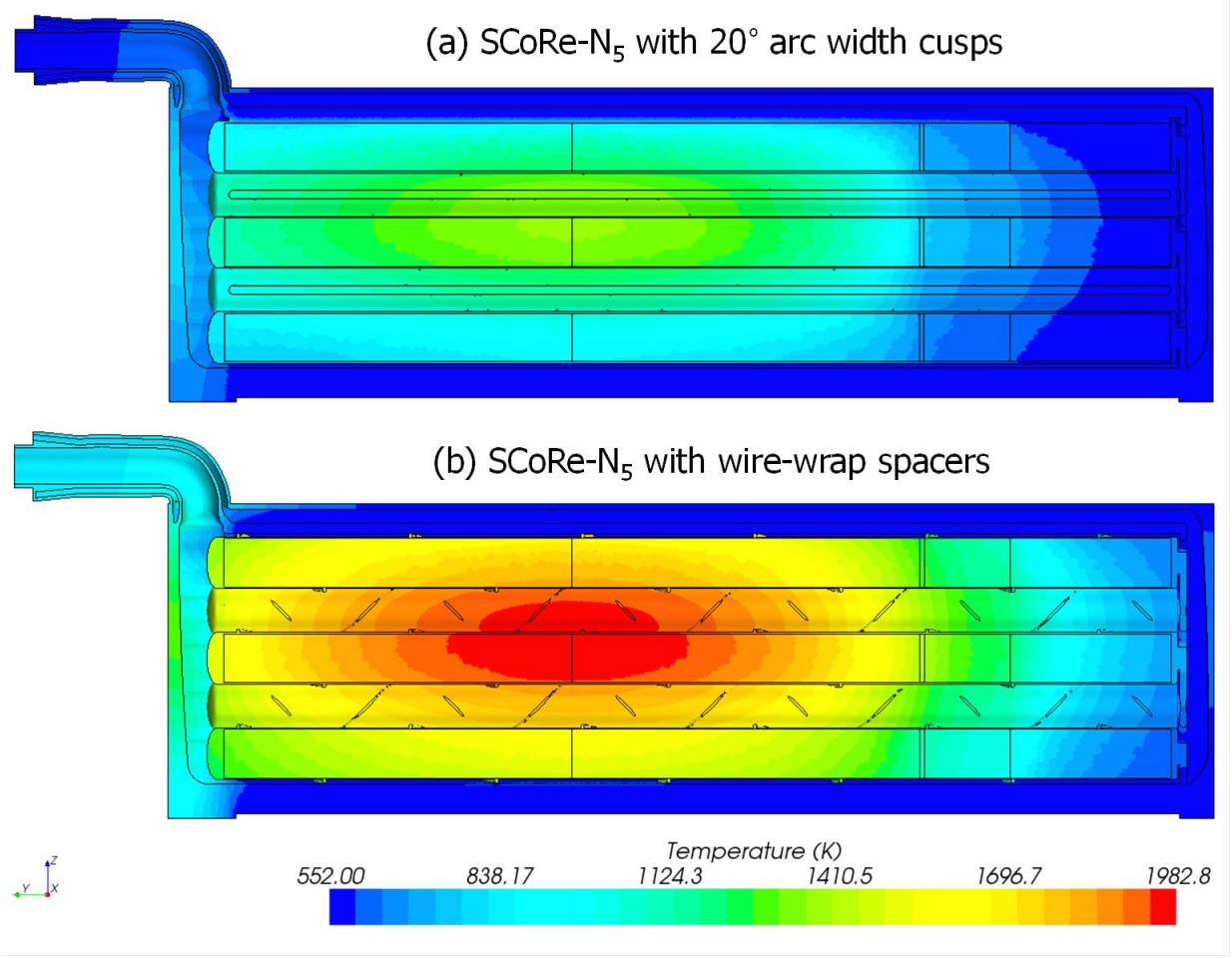

Fig. 3.45. - Calculated temperatures at the core sector experiencing a LOC with 20° cusped fuel rods at 166.6 kW_{th} (with thermal radiation).

Results show that performing the simulations for the sector with 20° arc length SS cusps with the thermal radiation enabled further reduces the peak cladding temperature, from 1,431 down to 1,362 K (Fig. 3.45). The concept of enhancing conduction heat transfer in the core sector experiencing a LOC is expanded further in the design of the Solid Core-Sectored Compact Reactor (SC-SCoRe), for which the performed thermal-hydraulics and safety analyses are presented next.

3.9. Thermal-Hydraulics and Safety Analyses of the SC-SCoRe

The Solid Core-Sectored Compact Reactor (SC-SCoRe) with monolithic solid core structure replaces the design of the SCoRe-N_5 (Fig. 3.11). This structure is intended to enhance conduction heat transfer from the inner fuel pellets in the core sector experiencing a LOC to the potassium heat-pipe dividing walls with the adjacent sectors. The SC-SCoRe is also cooled with liquid NaK-56, instead of the NaK-78 used in the earlier SCoRe designs (SCoRe-N_{18} and SCoRe-N_5) investigated in this work. This section presents results of the performed 3-D CFD thermal hydraulics and safety analyses of the SC-SCoRe during nominal operation, and at a reduced reactor thermal power in the unlikely events of a loss of coolant (LOC) or a loss of cooling (LOCo) in a core sector. The analyses calculate the temperature and flow fields in the coolant channels, the exit ducts and the lower and upper plenums and investigate the effect of using 316L stainless steel and Oxide Dispersion Strengthened Molybdenum (ODS-Mo) core structure on the core structure and UN fuel temperatures during nominal reactor operation at 1,000 kW_{th}. In addition, the analyses investigate flow mixing in the core coolant channels, the upper plenum and the exit ducts of the core sectors. Similar analyses are carried out for both a core sector experiencing a LOC or a LOCo and the adjacent sectors operating at reduced reactor thermal powers of 167.67 kW_{th} and 323 kW_{th}.

The performed analyses used the multi-physics computational fluid dynamics (CFD) code package STAR-CCM+ 7.04 [CD-Adapco 2012]. The steady-state 3-D CFD and thermal-hydraulics analyses of the SC-SCoRe are performed first for the reactor at the nominal power of 1,000 kW_{th} and NaK-56 coolant inlet and exit temperatures of 850 K and 900 K. The analyses calculate the temperature and the flow fields of the NaK-56 in the flow channels, inlet and exit duct, and the upper and lower plenums of the reactor

core. Also calculated are the temperatures of the UN fuel stacks and the solid core structure. Similar calculations are done for the SC-SCoRe at the lower thermal powers (167.67 kW_{th} and 323 kW_{th}), with a LOC and LOCo in one of the core sectors (Fig. 3.7).

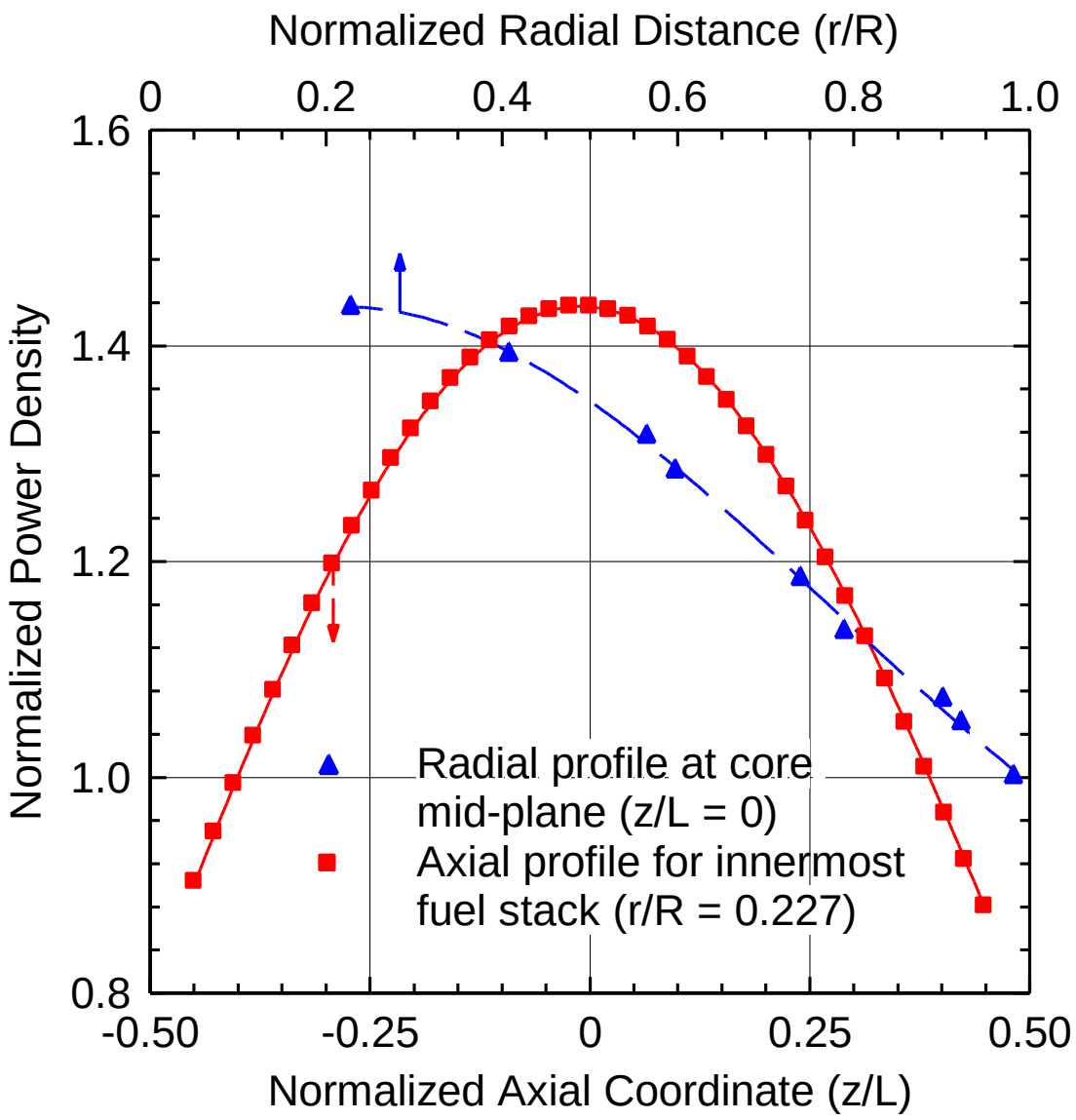

Fig. 3.46. - Calculated axial and radial power profiles for the SC-SCoRe sector during nominal operation using MCNPX [Schriener and El-Genk 2014b].

The performed thermal-hydraulics and safety analyses of the SC-SCoRe employed the SST k-ω turbulence model for the liquid NaK-56 flow in the core sectors. These analyses employed the axial fission power profiles calculated for each of the 15 stacks of

UN fuel pellets in a SC-SCoRe core sector. These profiles are obtained using the Monte Carlo Particles transport code MCNPX 2.7E [Pelowitz et al. 2011] to calculate F6 energy deposition tallies in the fuel stacks. Fig. 3.46 shows the calculated axial power profile for the innermost fuel stack (Fig. 3.11) as well as the radial power profile at the core-mid-plane. The close proximity of the lower internal axial BeO reflector, compared to the upper external BeO reflector, to the reactor core (Fig. 3.7) results in a slightly asymmetrical axial power profile (Fig. 3.46). The heat transport in the potassium heat-pipes dividers between the sectors in the SC-SCoRe core (Figs. 3.10b and 3.6) is modeled using an effective thermal conductance, whose value depends on the heat flow direction in the heat pipes (Section 3.3.2).

In addition to the calculated temperature and flow fields and the pressure losses in the core sectors, the results of the thermal-hydraulics analyses include flow mixing and temperature distribution in the coolant channels, the upper plenum and the exit duct (Fig. 3.11a). The non-uniform radial power profile in the core sectors (Fig. 3.46) increases the exit temperature and velocity of the NaK-56 coolant in the channels closer to the core center and decreases them in the channels close to the inlet coolant duct. The non-uniform exit temperatures and velocities from the tri-lobe shaped coolant channels (Fig. 3.11b) would cause a temperature difference in the upper plenum and the exit ducts. These effects are investigated in detail both during reactor nominal operation and at a lower thermal power, with a core sector experiencing a LOC or a LOCo.

Modeling the entire SC-SCoRe core is a daunting undertaking, in terms of the computation time and the numerical meshing requirements. In order to reduce the computation time, while using a sufficiently refined numerical mesh grid, the thermal-hydraulics analyses of the SC-SCoRe core during nominal operation is for one core sector. The 3-D safety analyses following a LOC or LOCo in one sector use 1.5 sectors (Figs. 3.11b and 3.47), the affected core sector and a half of an adjacent fully functional sector. The numerical grid of the computational mesh elements in the core sectors uses the polyhedral meshing model in the STAR-CCM+ code package and a prism layer meshing near the solid-fluid interfaces [CD-Adapco 2012].

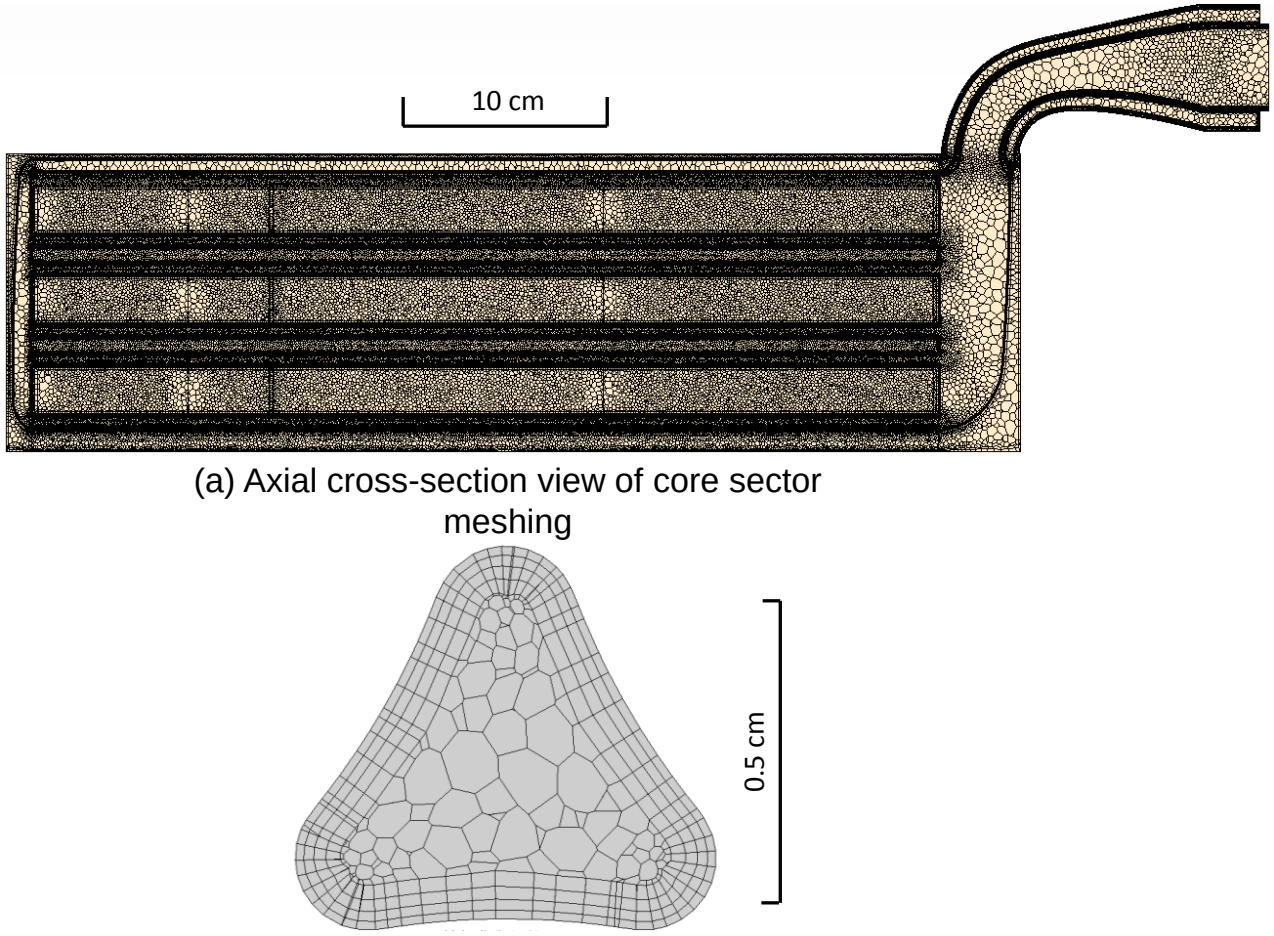

Fig. 3.47. - Thermal-hydraulics analysis of SC-SCoRe meshing grids [Schriener and El-Genk 2014b].

The boundary layer (Fig. 3.47b) at the tri-lobe shaped flow channels wall in the core sectors consists of a number of parallel prismatic layers to help accurately calculate the pressure losses and the convective heat transfer rates. The numerical meshing grid in the flow channels uses polyhedral cells ranging in sizes from 0.25 mm to 0.5 cm. It also incorporates four prism layers in a 1.0 mm-thick boundary layer at the wall. The numerical mesh grid in the surrounding solid core, including the UN fuel stacks, uses polyhedral cell elements with sizes ranging for 0.25 mm to 0.625 cm and a single 1.0 mm-thick prism layer near the solid-liquid interface.

In the 3-D thermal hydraulics analyses of one core sector during nominal reactor operation, the computation domain comprises ~17.0×10^6 numerical mesh cells in the liquid NaK-56 and ~15.5×10^6 cells in the surrounding solid structure, including the UN fuel stacks. In the safety analyses employing 1.5 core sectors, the 3-D computational domain has ~25.4×10^6 numerical mesh cells in the flow channels of the liquid NaK-56 and ~22.6×10^6 cells in the surrounding solid structure, including the UN fuel stacks. Fig. 3.47a shows the implemented computational numerical mesh grid along the center plane of a core sector. Fig. 3.47b is a close up of a single NaK-56 flow channel that shows the implemented numerical mesh grid and the prism layers near the wall. Appendix D provides comparative analyses of the choice of turbulence model and meshing refinement for the CFD thermal-hydraulics analyses of the SC-SCoRe during nominal operation. The next section presents the CFD and thermal-hydraulics analyses results of the SC-SCoRe during nominal operation.

3.9.2. Nominal Operation Results

As indicated earlier, the thermal-hydraulic analyses of the SC-SCoRe during nominal operation investigate the effect of two different materials (316L stainless steel and ODS-Mo) for the solid core on the temperature and flow fields in the core. Results in Fig. 3.48 are of the calculated temperature field during nominal operation in a core sector at the axial location of the peak UN fuel temperature, slightly above the active core mid-plane. The calculated temperatures for a reactor nominal thermal power of 1,000 kW_{th} and liquid NaK-56 inlet and exit temperatures of 850 K and 900 K with the 316L stainless steel solid core are shown in Fig. 3.48a and those with the ODS-Mo core structure are

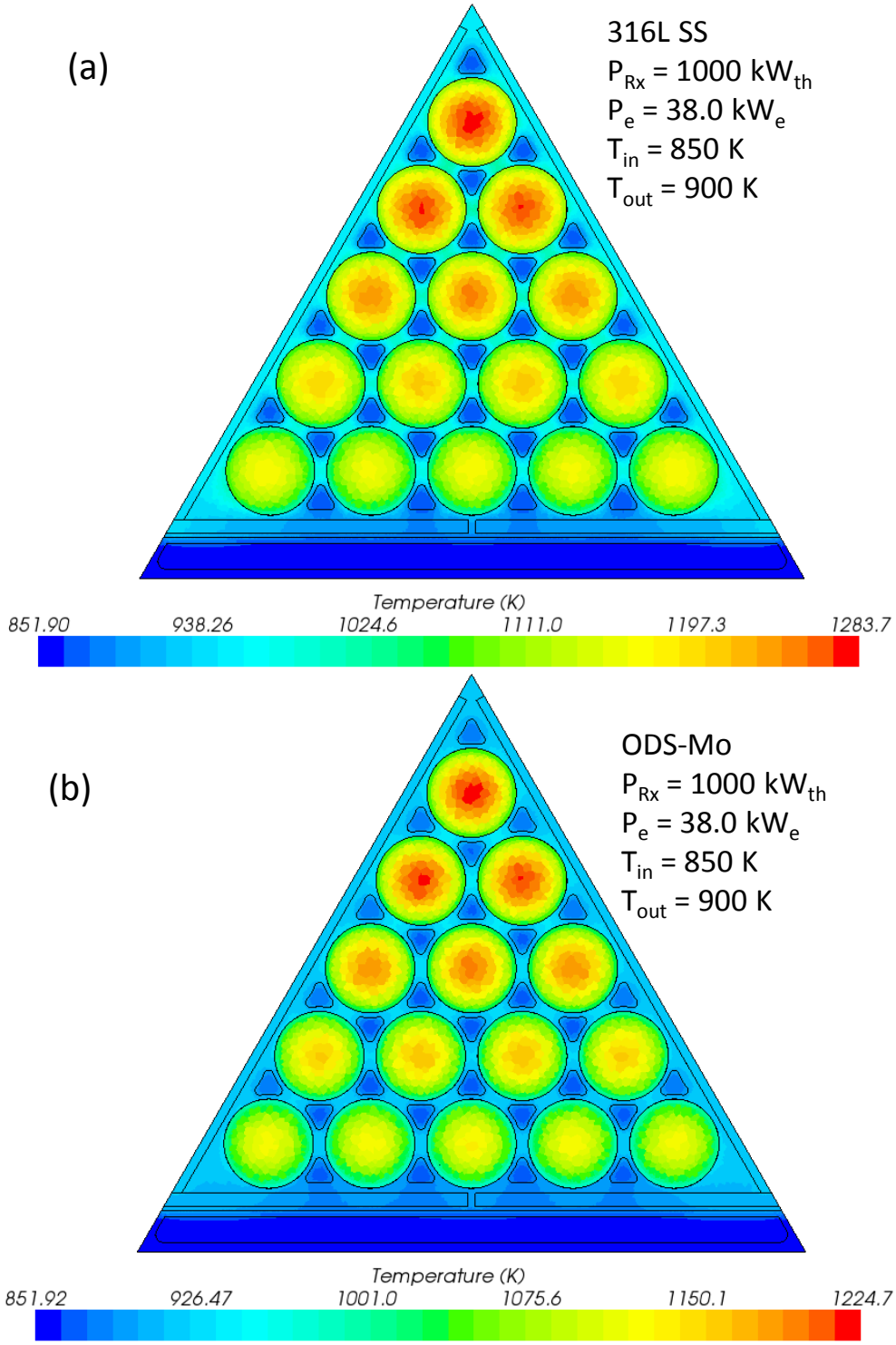

Fig. 3.48. - Calculated temperatures in a SC-SCoRe core sector during nominal operation: (a) 316L solid core and (b) ODS-Mo solid core [Schriener and El-Genk 2014b].

shown in Fig. 3.48b. The calculated peak UN fuel temperature of 1,284 K in the 316L stainless steel core is much higher than that in the ODS-Mo core structure of 1,030 K. The lower UN fuel peak temperature in the solid core is because the thermal conductivity of molybdenum (114.82 W/m-K at 900 K) is significantly higher than that of the 316L stainless steel (23.39 W/m-K at 900 K) [IAEA 2008; Touloukian 1970]. The axial temperature profiles in the UN fuel stacks in the reactor core closely follow the axial fission power profiles at the different radial locations in the core (Fig. 3.45). The 6ighest UN fuel temperatures are in the stacks closest to the core centerline and the lowest are in the stacks close to the coolant inlet annulus and near the potassium heat pipes dividers.

In both the 316L stainless steel and the ODS-Mo solid cores, the high thermal conductivity of UN fuel keeps its temperatures relatively low (> 1,300 K) as well as a small rise across the 2.272 cm diameter UN fuel pellets (< 194 K) [Ross et al. 1988]. Such low temperatures result in minimal fuel swelling and fission gas release, commensurate with the reactor's long operation life of ~21 full power years [Ross et al. 1990]. The peak reactor vessel temperature for the SC-SCoRe with a 316L stainless steel core of 941 K is 16 K higher than with the ODS-Mo solid core (Fig. 3.48a and b). The higher thermal conductivity of the ODS-Mo solid core reduces the temperatures during nominal operation compared to that with a 316L SS solid core. The thermal conductivity of ODS-Mo would also impact the heat transfer from a SC-SCoRe core sector experiencing a LOC or a LOCo analyzed next.

3.9.3. Analyses Results of a SC-SCoRe with a Sector Experiencing a LOC or a LOCo

A pipe break in one of the primary loops of the power system (Fig. 3.2) would cause a loss of coolant (LOC) in one core sector of the SC-SCoRe (Fig. 3.49). A pipe break in a secondary loop or a malfunction of the EM pump in a primary or a secondary loop would cause a loss of cooling (LOCo) in the core sector served by either or both loops (Fig. 3.2). In these unlikely events, the fission heat generated in the affected sector would transport to the two adjacent sectors cooled by circulating liquid NaK-56, aided by the flat potassium heat pipes dividers (Fig. 3.49). The circulating liquid NaK-56 in the adjacent core sectors removes the heat transferred to them from the sector experiencing a LOC or

a LOCo. The heat pipes dividers also help spread the heat removed from the affected sector to the colder zones near the inlet annuli of the adjacent functioning sectors (Fig. 3.49).

In the unlikely event that a core sector experiences a LOC or a LOCo, the reactor thermal power decreases to prevent overheating the UN fuel and the solid structure in that sector. Consequently, the lower inlet and exit temperatures and the circulation rate of the liquid NaK-56 in the remaining five operating core sectors of the SC-SCoRe would decrease the thermal efficiency of the power system and the electrical power supplied to the lunar outpost (Fig. 3.50).

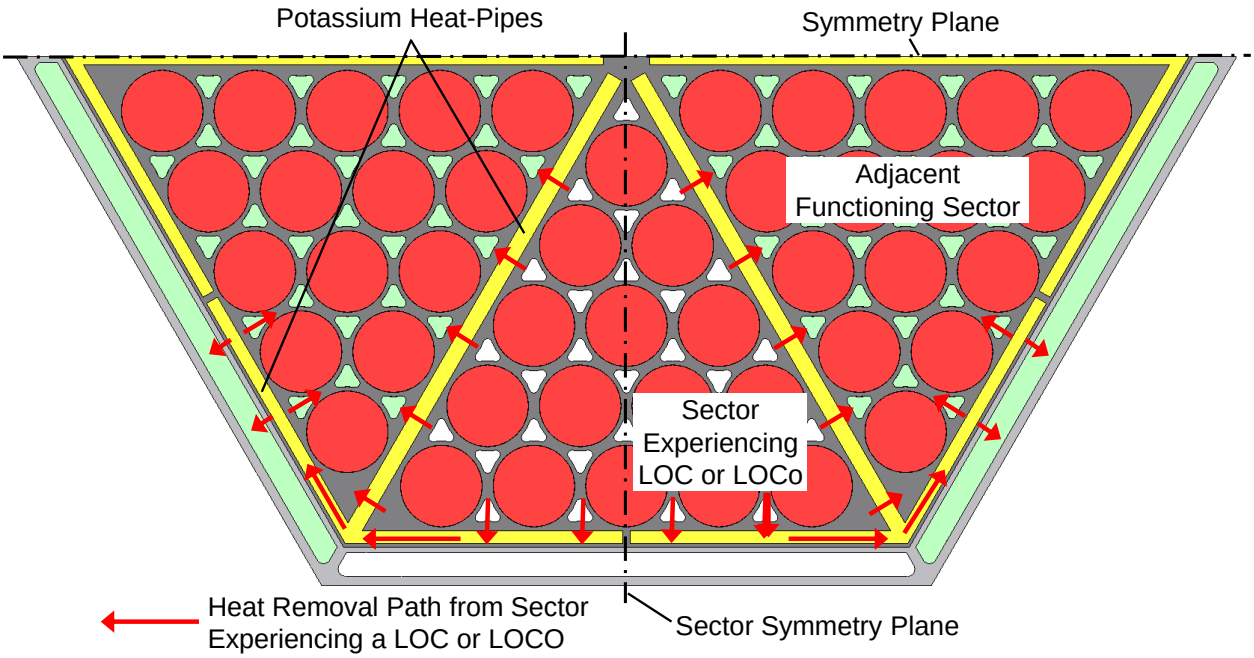

Fig. 3.49. - Heat transfer from a SC-SCoRe sector experiencing a LOC to adjacent sectors [Schriener and El-Genk 2014b].

Reducing the thermal power for the SC-SCoRe integrated power system also decreases the temperatures and the flow rates of the liquid NaK circulating in the primary and secondary loops and the inlet and exit temperature for the core sectors. DynMo-TE [Tournier and El-Genk 2006a] calculates the flow rates and temperatures of the liquid NaK-56 in the core sectors, and determines the operation parameters of the integrated power system at the different power levels. The calculated flow rate and inlet and exit

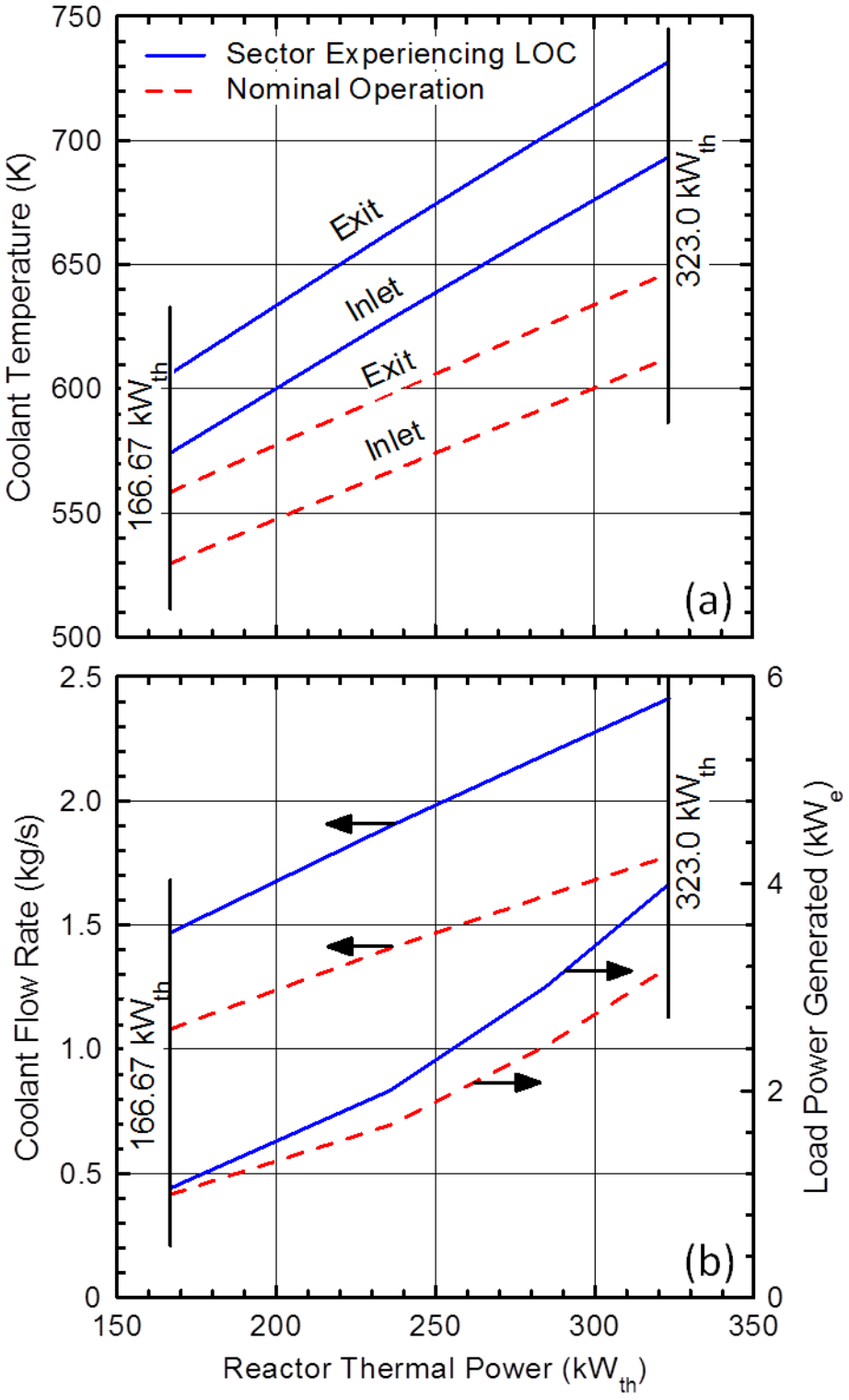

Fig. 3.50. - SC-SCoRe power system operating conditions at reduced power levels during nominal operation and following a sector LOC [Schriener and El-Genk 2014b].

temperatures of NaK-56 for the core sectors, when a core sector experiences a LOC or a LOCo, are incorporated into the present thermal-hydraulics and safety analyses of the SC-SCoRe.

Fig. 3.50 shows the calculated coolant temperature and flow rates at different reactor thermal powers from 167.67 to 323 kW_{th}, representing ~one-sixth and slightly less than one-third of the reactor's nominal thermal power of 1,000 kW_{th}. This figure shows that decreasing the reactor thermal power decreases the coolant flow rates and temperatures in the primary and secondary loops of the SC-SCoRe power system. At the reactor power level of 167.67 kW_{th} and 323 kW_{th} the electrical power generated by the power system and supplied to the outpost are 1.0 kW_e (~2.6% of the nominal 38 kW_e at 1,000 kW_{th}, Fig. 3.9) and 4.0 kW_e (~10.5% of nominal), respectively (Fig. 3.50b). The later electrical power could maintain critical life support to four crewmembers in the lunar habitat of NASA's Altair lunar lander concept [Polsgrove et al. 2009]. At a reactor thermal power of 167.67 kW_{th} (or ~ 28 kW_{th} per core sector), when a core sector experiences a LOC or a LOCo, the calculated inlet and exit temperatures of the liquid NaK-56 circulating in the other 5 operating sectors are 606 K and 574 K (Fig. 3.50a). Increasing the reactor thermal power to 323.0 kW_{th} (or ~ 53.83 kW_{th} per sector) increases the core inlet and exit temperatures of the circulating liquid NaK-56 to 731 K and 693 K [Tournier and El-Genk 2006a]. Next, the results of the safety analyses of the SC-SCoRe with a sector experiencing a LOC or a LOCo are presented and discussed.

The coolant channels in the core sector experiencing a LOC become void of the liquid NaK-56, which continues to circulate through the other five core functioning sectors and their five pairs of primary and secondary loops (Fig. 3.2). On the other hand, the coolant channels in a core sector experiencing a LOCo remains filled with liquid NaK-56, which circulates internally by natural convection. The liquid NaK-56 in the other five functioning core sectors continues to circulate by the EM pumps in their primary loops (Fig. 3.2).

As indicated earlier, the performed safety analyses use a numerical computation domain of 1.5 core sectors, with symmetry boundary conditions (Fig. 3.49). Thus, it is possible to use a sufficiently refined numerical mesh grid and complete the calculations

in a reasonable time. There is a symmetry plane along the middle of the affected core sector and a second plane along the centerline of the reactor core (Fig. 3.49). The implemented computation domain, however, may overestimate the temperatures in the functioning adjacent sector because the symmetry boundaries simulate two sectors experiencing a LOC or a LOCo on both sides of the functioning sector.

Fig. 3.51a and b present the results of the performed safety analyses of the SC-SCoRe at a thermal power of 167.67 kW_{th} with a core sector experiencing a LOC. The contribution of thermal radiation in the voided coolant channels of that sector, inlet annuli, and the bottom and top plenums (Fig. 3.11a) to the temperature estimates for that sector is insignificant, compared to that of conduction in the solid core block. Thus, the present analyses neglect thermal radiation, markedly reducing the computational time and the numerical meshing requirements with little effect on the results. In these analyses, the fission heat generated in the affected core sector transfers by conduction in the solid structure to the heat pipes dividers (Figs. 3.11 and 3.49), to the adjacent sectors cooled by circulating liquid NaK-56.

In the SC-SCoRe with 316L stainless steel core block (Fig. 3.51a), the temperatures of the UN fuel and solid structure in the sector experiencing a LOC are much higher than in the reactor with an ODS-Mo core (Fig. 3.51b). For the 3l6L core, the peak fuel and structure temperatures are 1,208 K and 1,198 K, respectively. The higher thermal conductivity of ODS-Mo (Fig. 3.51b) enhances heat transfer by conduction to the heat pipe dividers and decreases the peak temperatures of the UN fuel and the solid structure in the core sector experiencing a LOC to 936 K and 915 K, respectively. For both core block materials, the highest temperatures in the sector experiencing a LOC are of the three UN fuel stacks in the center region of the sector. These stacks are the furthest away from the potassium heat pipes dividers.

Figures 3.52a and b compare the calculated centerline temperatures for the coolest and hottest UN fuel stacks in the core sector experiencing a LOC (#3 and #4) and in the hottest and coolest stacks in the adjacent functioning sector (#1 and #2) in the SC-SCoRe with 316L stainless steel and ODS-Mo cores. The UN fuel temperatures in the selected fuel stacks in the reactor with a 316L stainless steel core are significantly higher than in

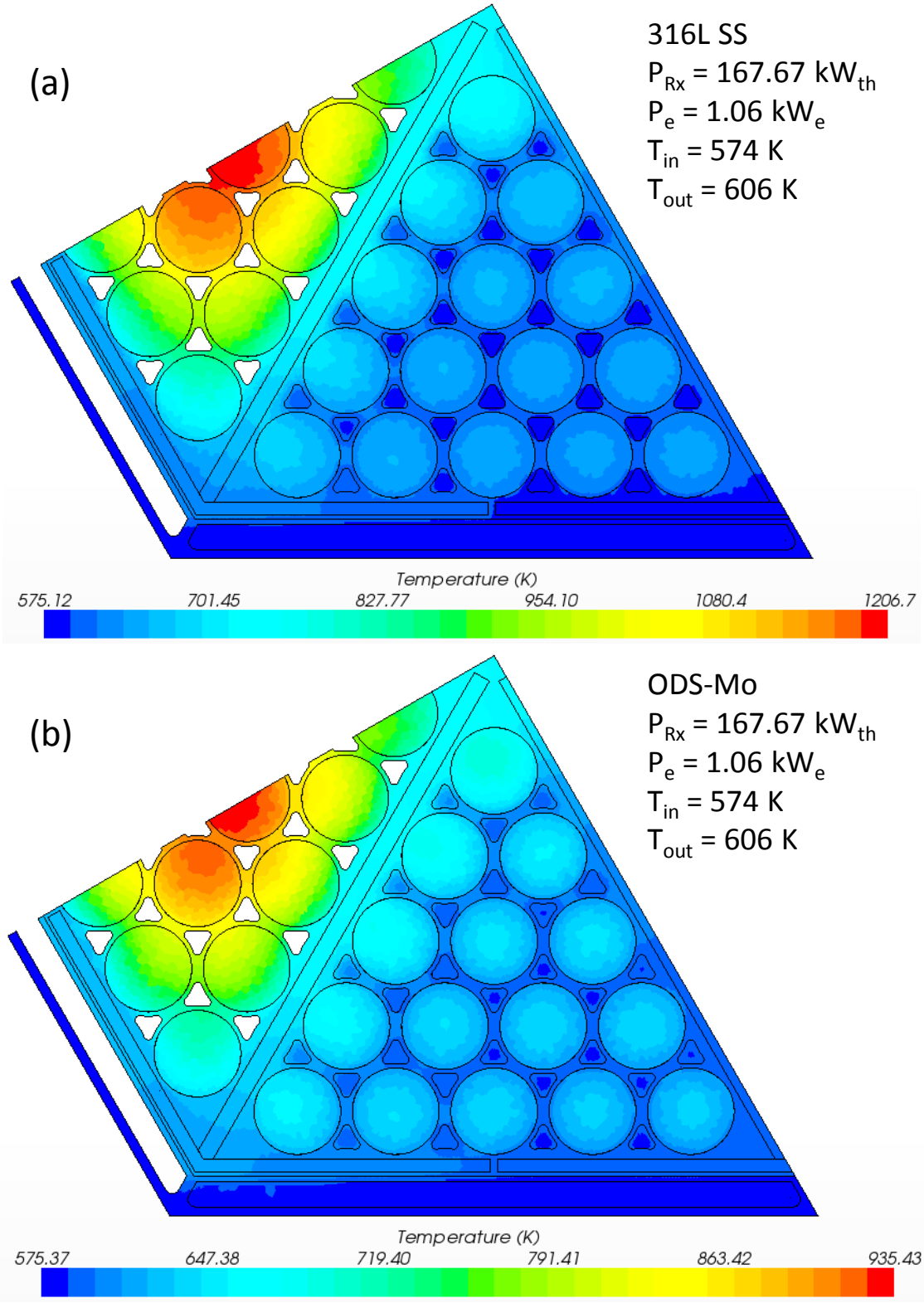

Fig 3.51. - Calculated temperatures in an SC-SCoRe core sector experiencing a LOC: (a) 316L solid core, and (b) ODS-Mo solid core [Schriener and El-Genk 2014b].

the core with ODS-Mo structure. The temperature differences are much larger in the sector experiencing a LOC. The temperatures of the selected fuel stacks in the adjacent sector (#1 and #2) are also lower in the ODS-Mo core than in the 316L stainless-steel core. The highly conductive ODS-Mo core not only decreases the peak temperatures of the selected fuel stacks in the affected and adjacent sectors, but also the radial and axial temperature gradients in these stacks and the surrounding structure.

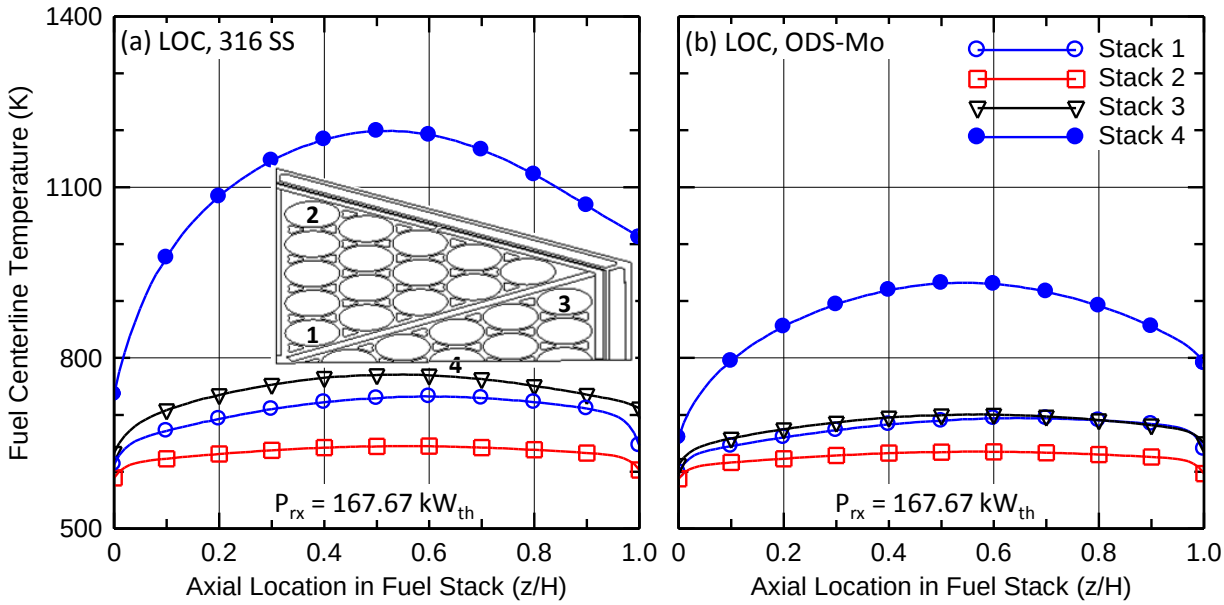

Fig. 3.52. - Centerline temperatures in select UN fuel stacks in an SC-SCoRe core sector experiencing a LOC and adjacent sector when reactor thermal power is 167.67 kW_{th}: (a) 316L solid core, and (b) ODS-Mo solid core [Schriener and El-Genk 2014b].

Although the calculated peak temperatures in the 316L stainless steel core sector experiencing a LOC is several hundred degrees below the melting point of 1673 K, the temperature is beyond the acceptable operational range for 316L SS (< 1000 K) [El-Genk and Tournier 2005; Mueller et al. 2000]. By contrast, the calculated peak temperature in the ODS-Mo core sector experiencing a LOC, at the same reactor thermal power of 167.67 kW_{th}, is well below the melting point and even lower than during nominal reactor operation (Figs. 3.47 and 3.50). Thus, subsequent safety analyses of the SC-SCoRe with a sector experiencing a LOC or a LOCo are performed only for the ODS-Mo core and at a higher reactor thermal power of 323.0 kW_{th} (Figs. 3.53-3.56).

For this reactor the results in Fig. 3.53 show that the peak UN temperature in the three UN fuel stacks closest to the center of the core sector experiencing a LOC is 1,361 K, while that of the surrounding ODS-Mo structure is 1,325 K. The peak temperatures in these UN fuel stacks and in the core structure closest to the heat pipes divider are much lower, ~1,100 and 925 K, respectively. These temperatures at a thermal power of 323.0 kW_{th} are acceptable for a safe operation of the SC-SCoRe with ODS-Mo solid core with a core sector experiencing a LOC (Fig. 3.53). The UN fuel has a high meting temperature (~3100 K) and the ODS-Mo has a high recrystallization temperature (~1900 K) [Bianco and Buckman 1997; Ross et al. 1988], both are well above the calculated peak temperatures in the core sector experiencing a LOC (Fig. 3.53).

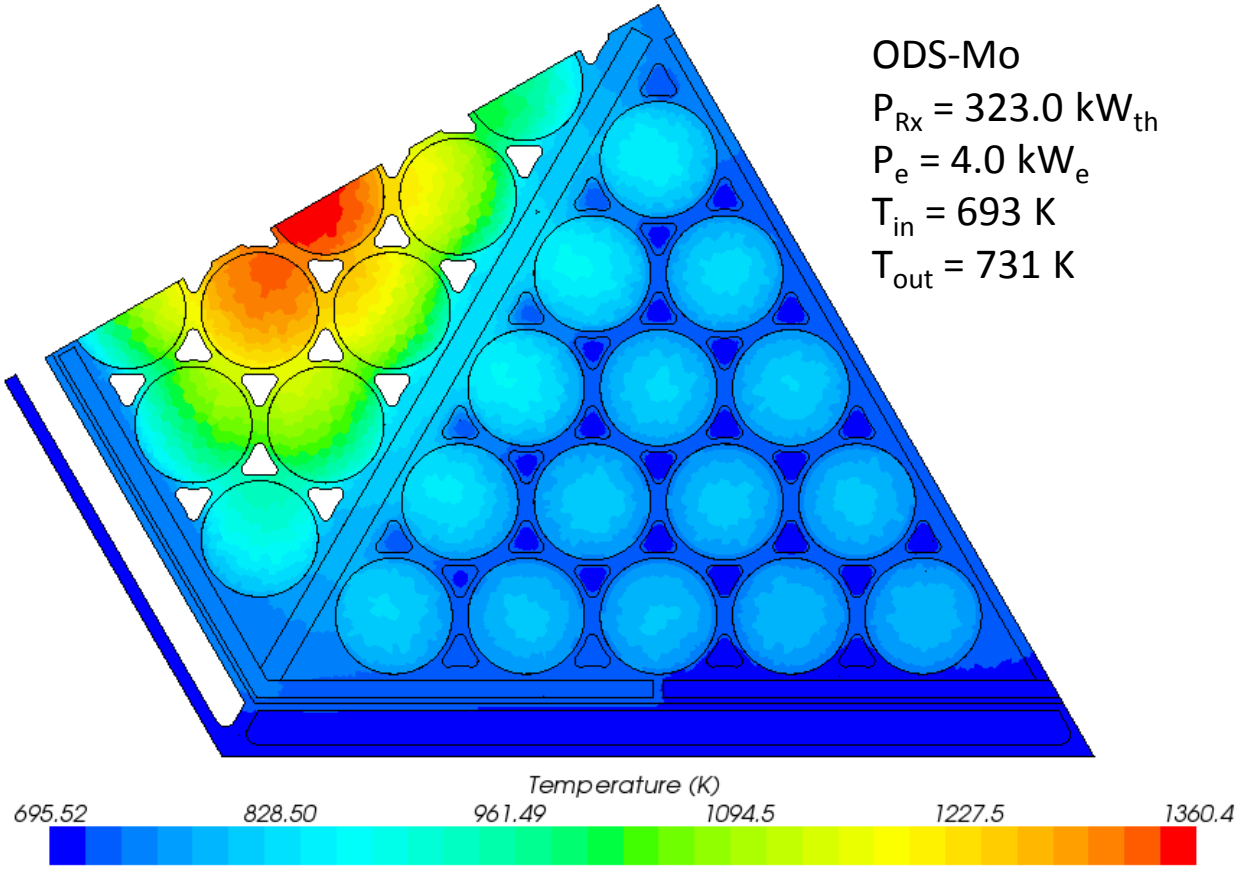

Fig 3.53. - Calculated temperatures in a SC-SCoRe with ODS-Mo solid core at 323.0 kW_{th} and a sector experiencing a LOC [Schriener and El-Genk 2014b].

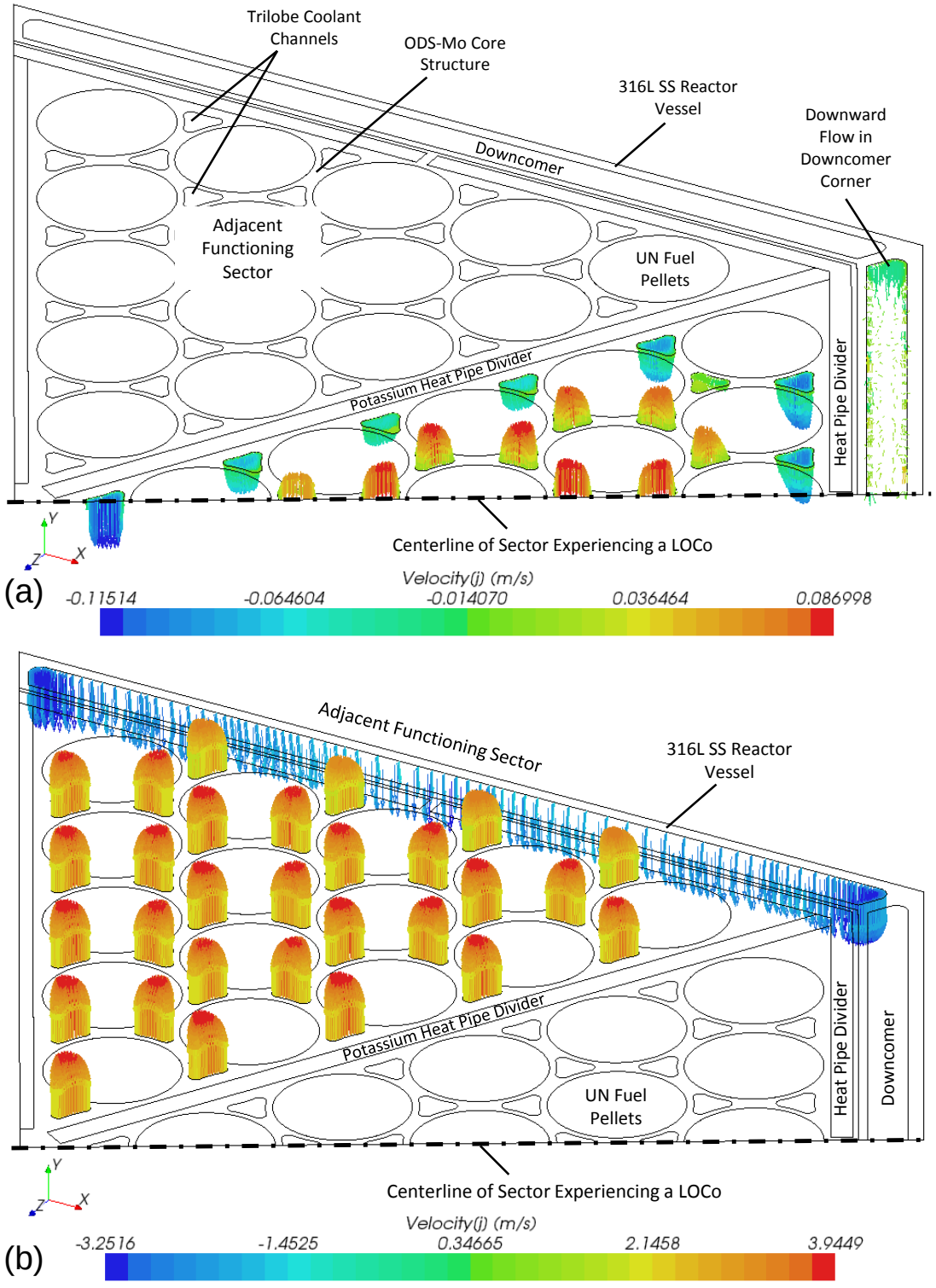

Fig. 3.54. - Flow velocities of liquid NaK-56 in the coolant channels at the core mid-plane of (a) a sector experiencing a LOCo and (b) adjacent functioning sector [Schriener and El-Genk 2014b].

The peak temperature of the innermost UN fuel stack in the adjacent sectors cooled by circulating liquid NaK-56 is only ~869.8 K. This temperature is well below that during nominal reactor operation at 1,000 kW_{th} (~1,224 K, Fig. 3.51b). The conduction heat transfer from the core sector experiencing a LOC to the adjacent sectors increases the temperatures of the UN fuel stacks near the heat pipes dividers in these sectors by only ~20-40 K. In addition, the low temperature gradient in the highly conductive ODS-Mo core structure would reduce thermal stresses.

For a core sector experiencing a LOCo, the liquid NaK-56 in that sector presents an additional heat transfer pathway for the fission power by natural circulation on the lunar surface to the adjacent core sectors. Figs. 3.54-3.55 present the results for the SC-SCoRe with ODS-Mo core and a core sector experiencing a LOCo. The liquid NaK-56 in the coolant channels of that sector circulates, under the effect of the lunar gravity (0.166 g), between the upper and lower plenums (Fig. 3.54a). Figs. 3.54a and b show the velocity vectors illustrating the flow circulation through the coolant channels in the sector experiencing a LOCo and in the adjacent functioning sector, respectively. Figs. 3.55 and 3.58a present the calculated temperatures in the SC-SCoRe core structure and at the centerlines of the UN fuel stacks. The results in Figs. 3.56-3.58 are for the SC-SCoRe operating at a thermal power of 323.0 kW_{th}, at which the calculated inlet and exit temperature and mass flow rate of the NaK-56 coolant for the five functioning core sectors using the DynMo-TE power system model (Figs. 3.50a and b).

The liquid NaK-56 in the sector experiencing a LOCo heats up and rises through the 14 coolant channels in the center region, reverses direction in the upper plenum and then flows down through the 15 channels in the outer region of that sector (Fig. 3.55a). It then cools off as it traverses the tri-lobe coolant channels by heat conduction through the ODS-Mo core structure to the nearest heat pipes dividers. The highest downward flow velocities occur in the flow channel closest to the core center and flanked by two potassium heat pipes dividers and in the flow channels along the heat pipes divider adjacent to the annular downcomer (Fig. 3.56a). Natural circulation also occurs in the annular downcomer of the sector experiencing a LOCo, where the liquid NaK-56 flows

down along the corners as it cools off by transferring heat to the circulating NaK-56 in the inlet ducts of the adjacent functioning core sectors (Figs. 3.54a and b).

As these figures show, the magnitude and the direction of the flow velocity in the coolant channels of the core sector experiencing a LOCo depend on the locations of the tri-lobe channels. The largest upward flow velocity is in the 14 central channels, where the fission heat generated in the surrounding UN fuel stacks is the highest (Fig. 3.46). The total upward flow rate in these channels of 0.0151 kg/s is equal to that of the downward flow in the outer 15 channels (Fig. 3.54a). The velocity and the total flow rate of the circulating liquid NaK-56 in the five functioning core sectors are much higher. The total flow rate of ~2.136 kg/s for each functioning core sector includes 1.052 kg/s in the inner 14 channels and 1.0847 kg/s in the outer 15 channels. The liquid NaK-56 flow velocities in the tri-lobe coolant channels of the sector adjacent to that experiencing a LOCo are almost the same. They are slightly lower in the four channels furthest from the core center and adjacent to the inlet annular duct (Fig. 3.54b).

In the core sector experiencing a LOCo, the peak temperature of the UN fuel is 1,247 K and that of the surrounding ODS-Mo core block is 1,205 K (Fig. 3.55). These temperatures are 114 K and 120 K lower than in a core sector experiencing a LOC (Fig. 3.53). As in the LOC case, the temperatures in the core sector experiencing a LOCo are low enough to continue safe operation of the SC-SCoRe at a thermal power of 323.0 kW_{th}, with the SiGe PCAs in the power system generating ~4 kW of electricity by for the lunar outpost. At this reactor power level, the calculated temperatures in the SC-SCoRe with ODS-Mo structure with a core sector of the experiencing a LOC or a LOCo are compared in Figs. 3.56a and b. These figures present the axial distributions of the centerline temperature of the hottest and coolest UN fuel stacks (#4 and #3) in the core sector experiencing a LOC or a LOCo, and of the hottest and coolest UN fuel stacks (#1 and #2) in the adjacent functioning core sectors.

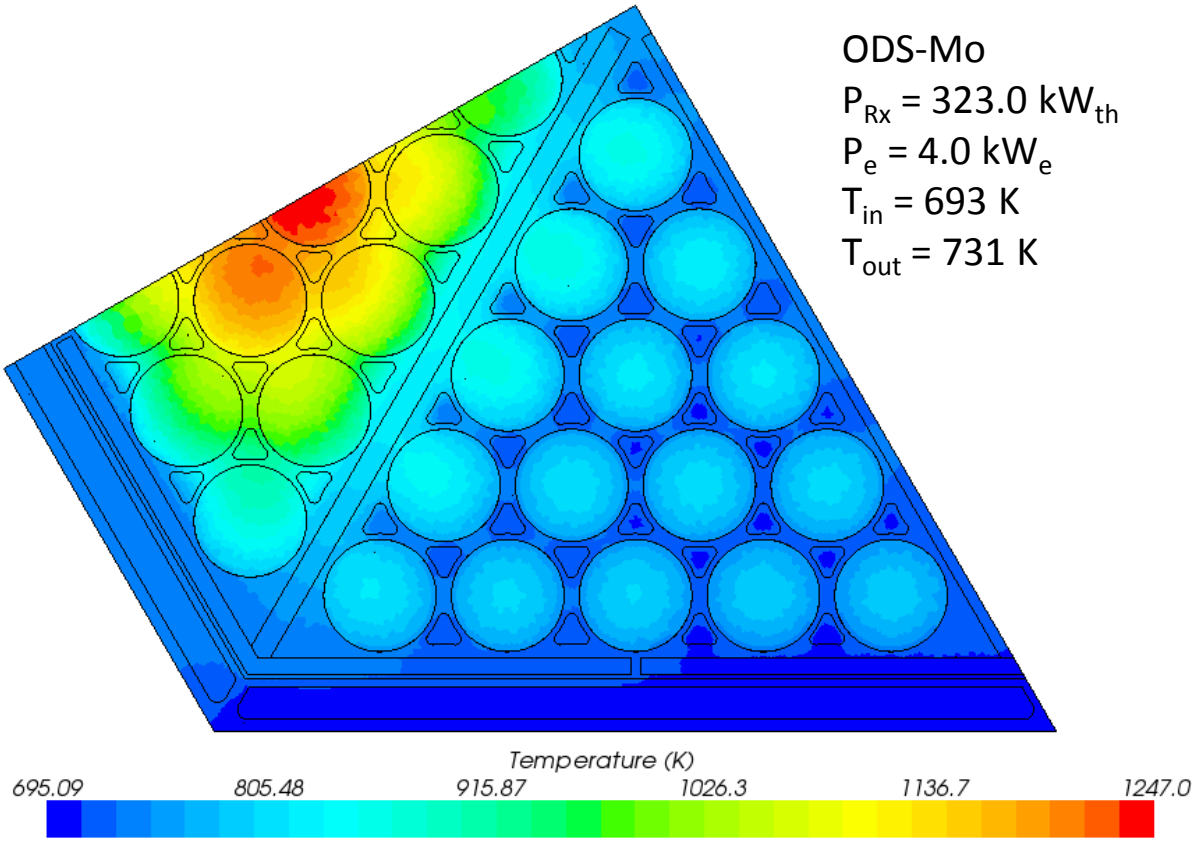

Fig. 3.55. - Calculated temperatures in SC-SCoRe with ODS-Mo solid core at 323.0 kW_{th} and a sector experiencing a LOCo [Schriener and El-Genk 2014b].

The peak centerline temperature of the hottest UN fuel stack #4 in the core sector experiencing LOCo occurs well above the core mid-plane (Fig. 3.56a). This is because the liquid NaK-56 flows upward by natural circulation in the surrounding coolant channels (Fig. 3.56a). When a core sector experiences a LOC, the peak UN fuel in the hottest stack #4 in that sector is much higher and occurs at the core mid-plane (Fig. 3.56a). The axial distributions of the centerline temperatures in the hottest and coolest fuel stacks (#1 and #2) in the adjacent sectors in Fig. 3.56a and b are almost the same.

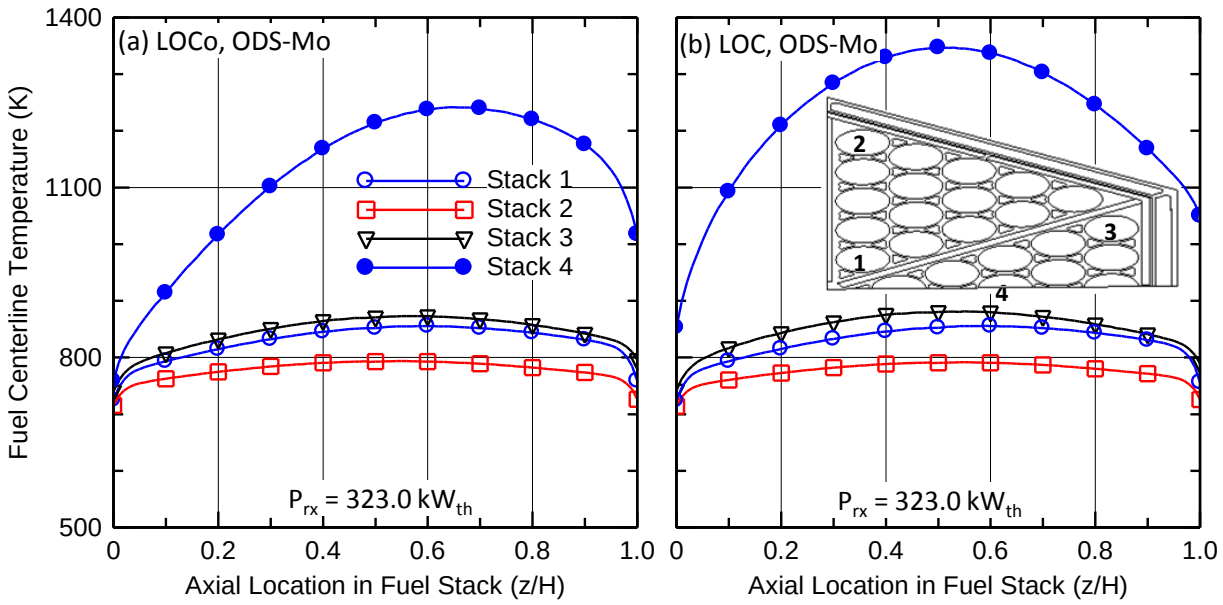

Fig. 3.56. - Calculated centerline temperatures of selected UN fuel stacks in SC-SCoRe operating at 323.0 kW_{th} with a core sector experiencing: (a) a LOCo and (b) a LOC [Schriener and El-Genk 2014b].

3.9.4. Calculated Temperature and Flow Fields in the Upper Plenum and Exit Duct of SC-SCoRe

This section presents the results of the calculated flow mixing in the upper plenums of the core sectors of the SC-SCoRe with ODS-Mo core during nominal operation (Fig. 3.57). This figure shows an axial sectional view of the flow mixing in one of the core sectors. Lateral cross-section views of the flow mixing at the marked locations in Fig. 3.57 are given in Figs. 3.58-60. The image in Fig. 3.57 shows the liquid NaK-56 in the tri-lobe coolant channels in core sector (Section A-A) jets into the upper plenum, generating turbulent mixing eddies in the spaces in-between the flow jets. Nonetheless, the liquid NaK-56 in the upper plenum becomes shows a large temperature difference, but converges when approaching the mouth of the exit duct (Section B-B). The liquid NaK-56 passing through the opening of the exit duct is not fully mixed when it changes direction 90° and enters the part of the exit duct with an oblong cross section (Section C-C). It eventually exits through the circular cross section of the duct (Section D-D) (Fig. 3.57).

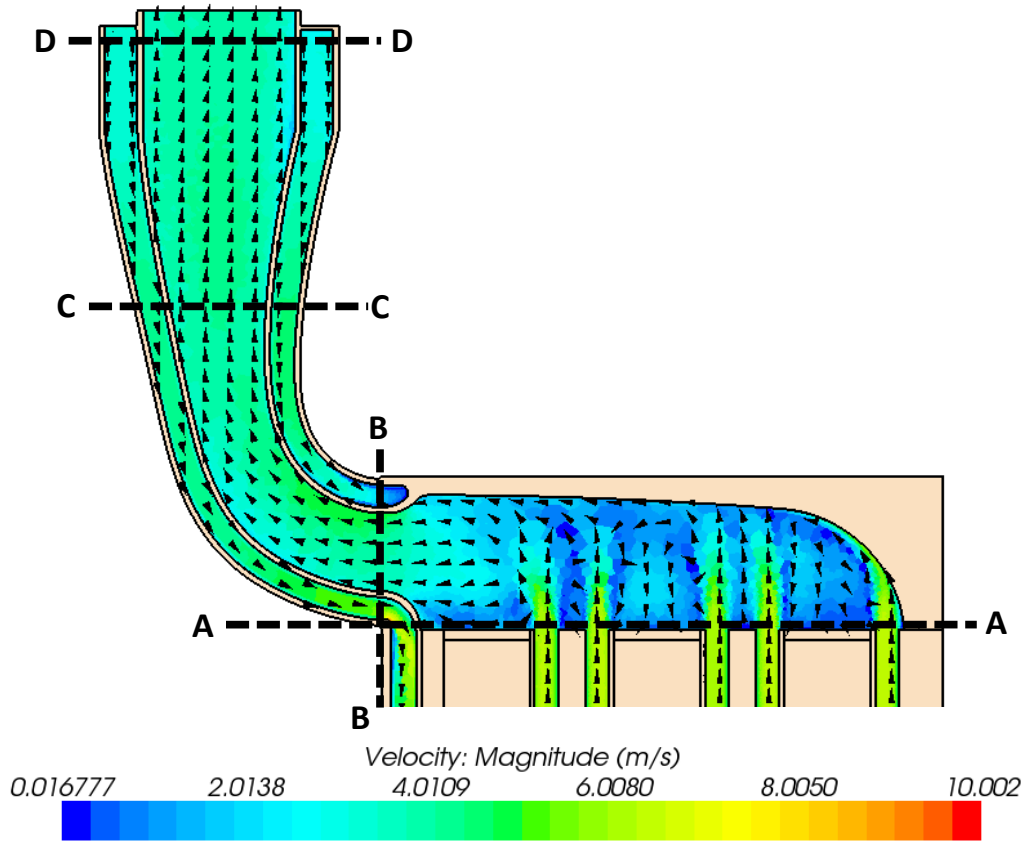

Fig. 3.57. - Calculated velocity field of liquid NaK-56 demonstrating flow mixing in coolant channels, upper plenum and exit duct of SC-SCoRe core operating at nominal conditions [Schriener and El-Genk 2014b].

Figure 3.58a shows differences in the liquid NaK-56 temperatures as it exits the core sector into the upper plenum. Figs. 3.58b-c show the tangential velocity vectors and temperature field of the liquid flowing through the exit duct at different sections. The images of the flow field are in a core sector during nominal reactor operation. The induced mixing reduces the temperature difference within the coolant flow from 40.2 K into the upper plenum (Fig. 3.58a) to 16.7 K at the entrance of the exit duct (Fig. 3.58b). The images of the tangential velocity vectors in Figs. 3.59b-c show the swirling vortices forming at the corners of the entrance section to the exit duct (Fig. 3.58b). These vortices gradually decrease in intensity as the liquid travels up the duct, but do not fully diminish at the duct exit (Fig. 3.58d). The heat transfer across the stainless steel wall of the exit duct, to the colder liquid NaK-56 flowing through the annular inlet channel concentric

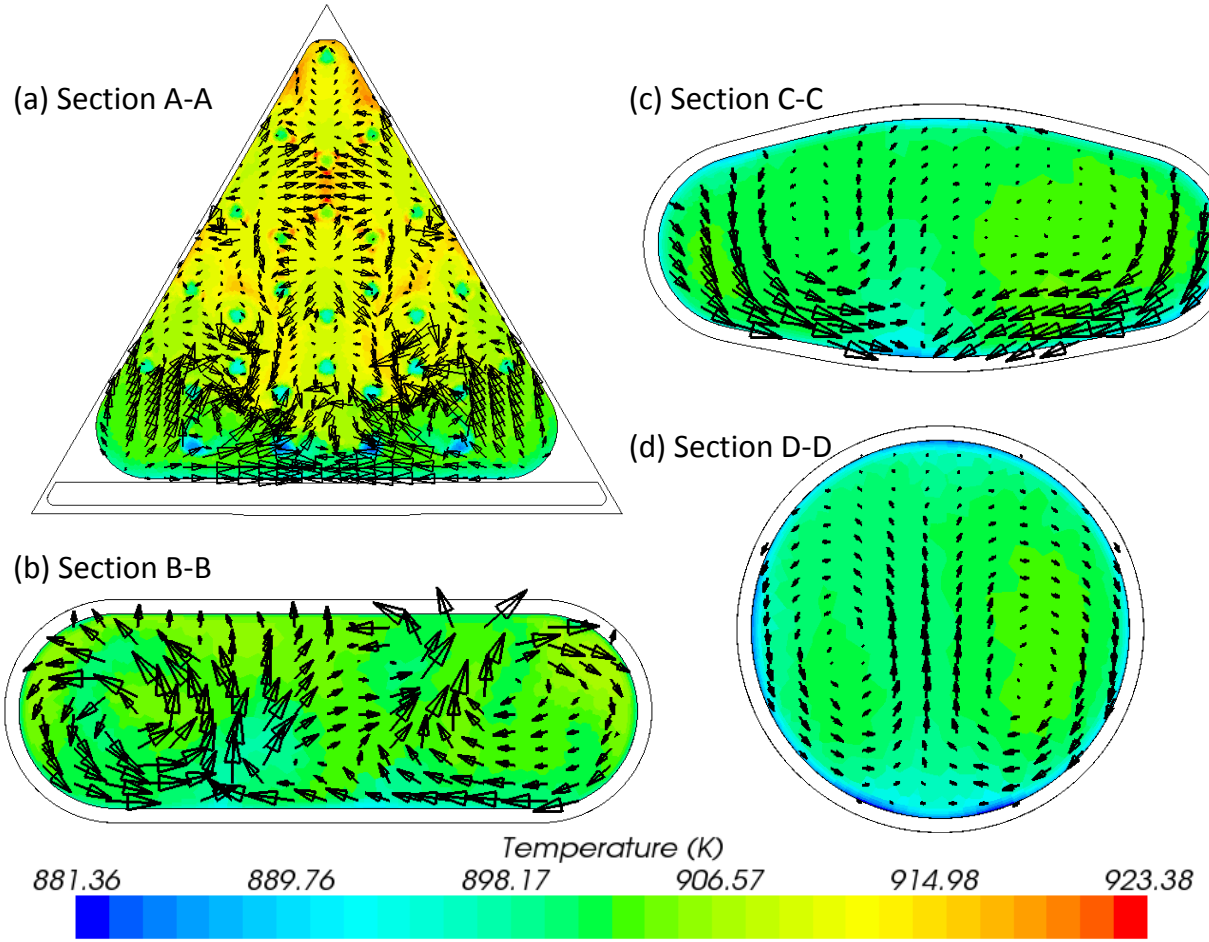

Fig. 3.58. - Calculated temperature fields of liquid NaK-56 in upper plenum 1 mm above the core block (a) and the calculated temperature field and tangential velocity vectors at select location in the exit duct (b, c, and d) at nominal reactor operation [Schriener and El-Genk 2014b].

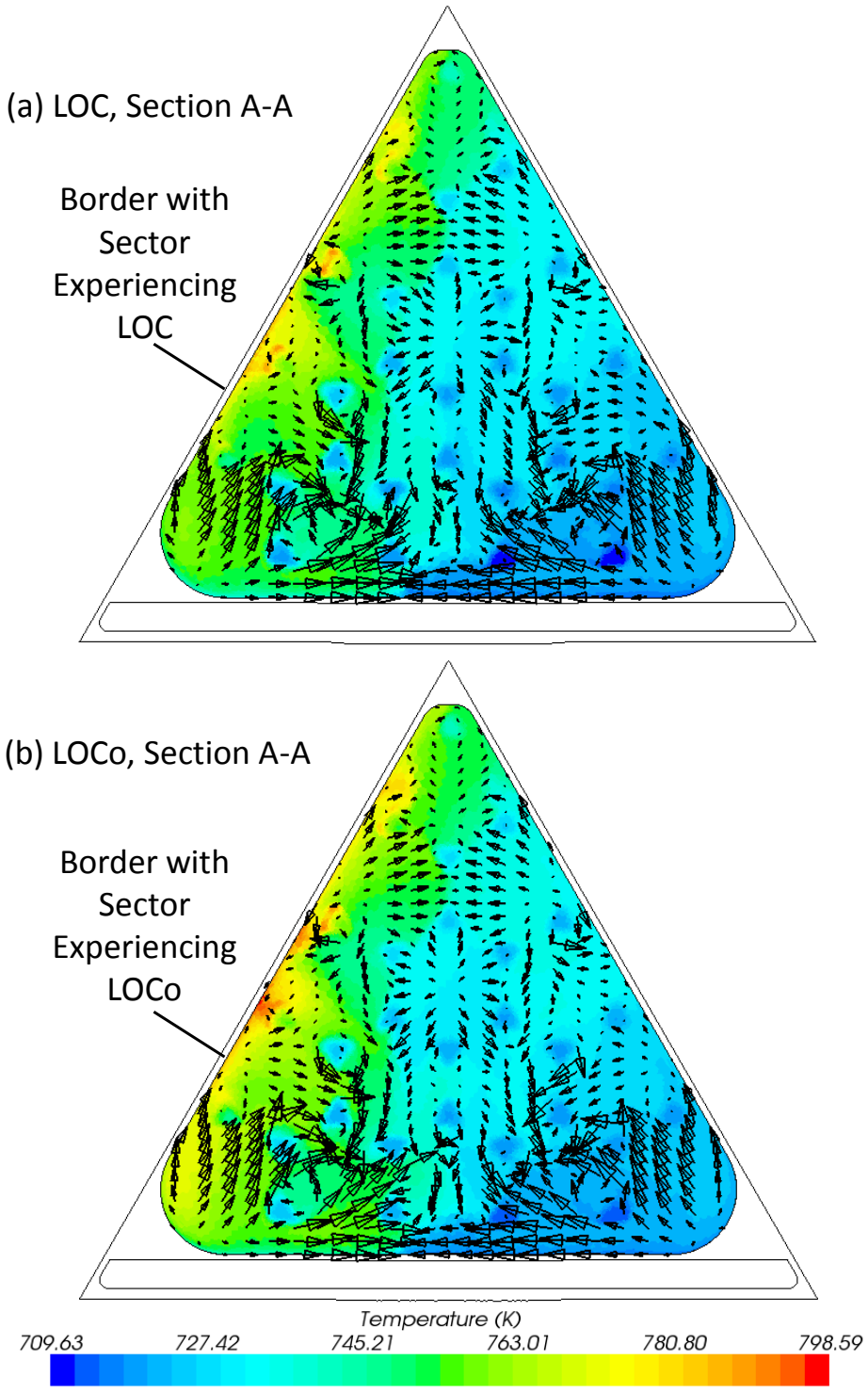

Fig. 3.59. - Calculated coolant temperature distribution in upper plenum, 1.0 mm above core block) of adjacent to that experiencing: (a) a LOC and (b) a LOCo [Schriener and El-Genk 2014b].

with the exit duct, reduces the liquid temperature and contributes to the temperature difference in the exit duct. This difference is 16.7 K at Section B-B, 18.4 K at Section C-C and 21.7 K at Section D-D (Figs. 3.58b-d). The remainder of this section presents and discusses the calculated temperature and velocity fields in the core sector adjacent to that experiencing either a LOC or a LOCo, when operating the SC-SCoRe at a thermal power of 323.0 kW_{th}.

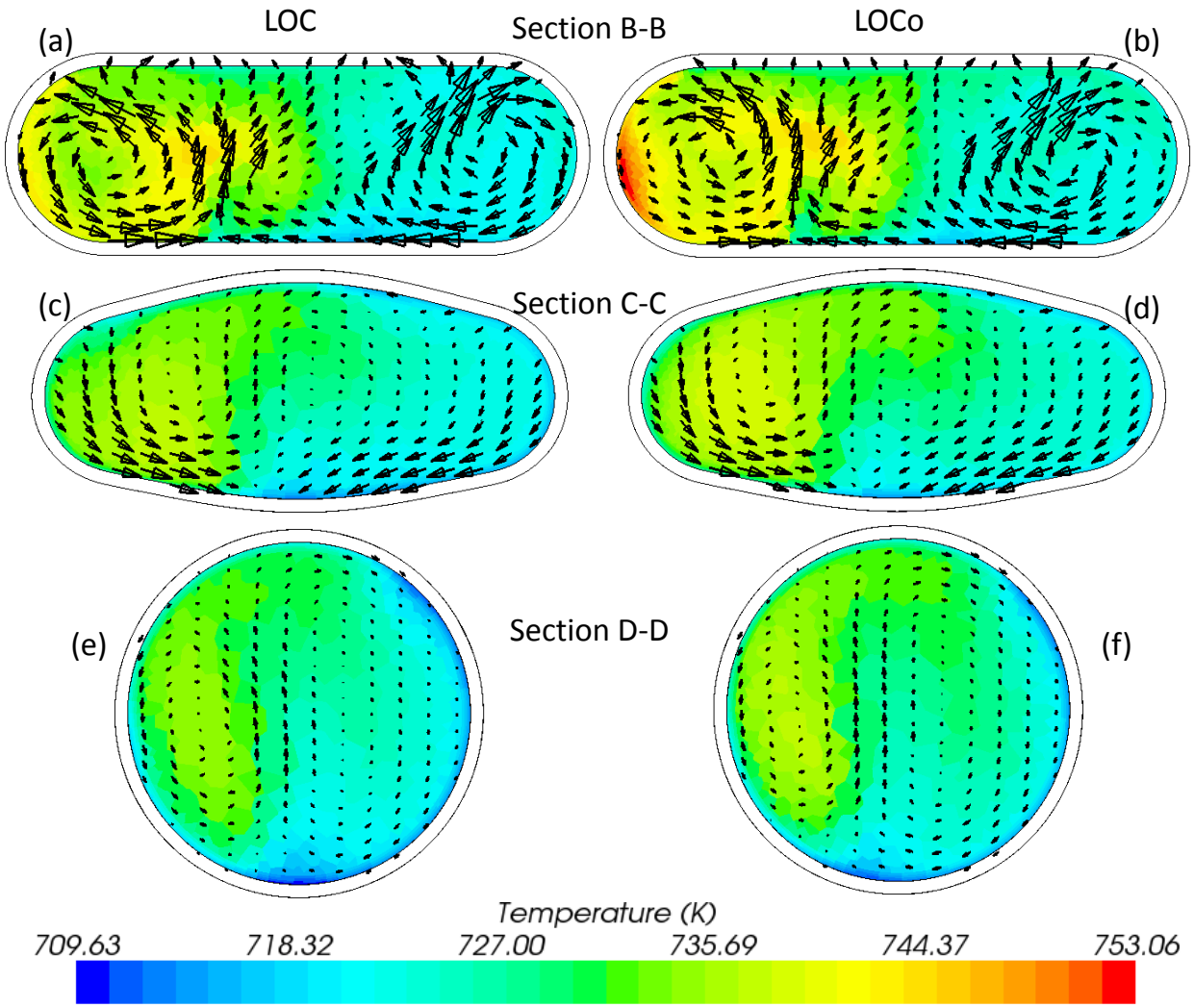

Fig. 3.60. - Calculated coolant temperature distribution and tangential velocity vectors at select locations in the exit ducts of a functioning core sector adjacent to that experiencing a LOC or a LOCo [Schriener and El-Genk 2014b].

When a core sector experiences a LOC or a LOCo, the removed fission heat from that sector to the adjacent functioning sectors results in asymmetric temperature fields in these sectors and increases the temperature difference in their upper plenums. The presented results in Figs. 3.59a and b demonstrates such asymmetry when the SC-SCoRe with ODS-Mo core structure operates at thermal power of 323.0 kW_{th}. The calculated temperature asymmetry and the maximum temperature in the functioning core sectors adjacent to that experiencing a LOCo are higher than when that sector experiences a LOC. This is because of the enhancement in heat removal by natural convection from the sector experiencing a LOCo to the adjacent functioning sectors. The mixing of the liquid NaK-56 exiting the flow channels into the upper plenum of the adjacent functioning sectors helps to decrease the temperature difference. Figs. 3.59a-b show that for a core with a sector experiencing a LOC, the difference in the liquid temperature in the upper plenum of the adjacent operating sector at Section A-A in Fig. 3.59 (1 mm above the core block) is 81.9 K, compared to 83.9 K in the case of a core sector experiencing a LOCo. These temperature differences decrease to 28.8 K and 37.4 K, respectively, (Figs. 3.60a,b) at the entrance of the exit duct, Section B-B in Fig. 3.57.

In Figs. 3.60a and b, the induced vortices in the liquid NaK-56 flow at the entrance of the exit duct for the adjacent functioning sector help mixing and decrease temperature differences within the flow. For the functioning core sectors adjacent to that experiencing a LOC, the variation in the liquid NaK-56 temperatures entering the exit duct (section B-B) is 28.8 K and is 23.6 K at Section C-C (Fig. 3.59). In the case of a core sector experiencing a LOCo, these temperature variations are higher, 37.4 K and 24.9 K, respectively. The mixing vortices in the liquid NaK-56 flowing through the exit duct gradually die out with distance from the duct entrance (section B-B in Fig. 3.59). As the mixing intensity decreases, between Sections C-C and D-D of the exit duct, the temperature difference increases, due to the heat transfer across the exit duct wall, to 25.3 K in the case with a core sector experiencing a LOC and 26.0 K in the case with a sector experiencing a LOCo (Figs. 3.60c-f).

The CFD and thermal-hydraulics analyses for the SC-SCoRe favor the monolithic ODS-Mo solid core. The ODS-Mo solid core results in the lowest fuel and core structure

temperatures during nominal operation at 1,000 kW_{th}, and enables safe operation at 323.0 kW_{th} with a sector experiencing a LOC or LOCo. The neutronics analyses for the SC-SCoRe with ODS-Mo core structure are presented next.

3.10. Neutronics Analyses and Reactor Operation Life Estimate of SC-SCoRe

This section presents the results of the neutronics and fuel depletion analyses of the SC-SCoRe design. Calculated are the cold-clean and hot-clean BOL excess reactivity values for the design which satisfies the water submersion subcriticality and the reactor control shutdown safety requirements. In addition, fuel depletion analyses are performed at nominal operating conditions (thermal power of 1,000 kW_{th} and coolant inlet and exit temperatures of 850 K and 900 K) to determine the reactor operational life in Full Power Years (FPY).

The performed neutronics and fuel depletion analyses use the code MCNPX 2.7E [Pelowitz et al. 2011]. The calculations of the cold-clean and hot-clean reactivity used 20,000 source particles per cycle and 100 skipped and 1,000 active cycles, for a relative error of 0.00014 or ~2¢ of reactivity. The value of β_{eff} = 0.0065 is determined using the KOPT feature in the Monte Carlo code MCNP5 1.6 [X-5 Monte Carlo Team 2010]. The presented hot-clean reactivity values are calculated for the UN fuel and reactor structure temperatures determined from the thermal-hydraulics analyses in Section 3.9 at a thermal power of 1,000 kW_{th} and the BeO reflector temperature of 600 K. The BOL excess reactivity and the reactor shutdown margins are calculated for the reactor core emplaced below grade on the lunar surface and surrounded with backfilled regolith (Fig. 3.13).

The fuel depletion analysis utilizes the internal BURN feature in MCNPX [Pelowitz et al. 2011]. The fuel depletion calculations used 20,000 source particles per cycle and 100 skipped and 1,000 active cycles. The Doppler broadened neutron cross sections are generated for the 42 actinides and 243 fission products and the europium activation products tracked in the simulation to account for the UN fuel burnup in each of the 90 fuel rods in the six core sectors and the depletion of the SSA additive in the fuel pellets. The MCNPX depletion calculations used a time step of 2 years. The default MCNPX

fission Q-values are used in the fuel depletion calculations to convert the reactor thermal power to a neutron flux for determining the neutron reaction rates [Pelowitz et al. 2011].

Table 3.6. - BOL reactivity values of the SC-SCoRe with ODS-Mo solid core.

Cold-Clean at uniform temperature of 300 K	
BOL excess reactivity, ρ_{ex}	\$6.62
Shutdown reactivity with 9 drums rotated with B_4C segments facing the core, ρ_{9sd}	-\$1.20
Shutdown reactivity with 12 drums rotated with B_4C segments facing the core, ρ_{12sd}	-\$3.33
Water submersion reactivity with bare core submerged in wet sand and flooded with seawater, ρ_{wsa}	-\$5.11
Hot-Clean at nominal reactor operation (1,000 kW_{th} with inlet and exit temperatures of 850 K and 900 K	
BOL excess reactivity, ρ_{ex}	\$6.27
Shutdown reactivity with 9 drums rotated with B_4C segments facing the core, ρ_{9sd}	-\$1.42
Shutdown reactivity with 12 drums rotated with B_4C segments facing the core, ρ_{12sd}	-\$3.62

3.10.1. SC-SCoRe Neutronics Results

Table 3.6 presents the reactivity values for the final SC-SCoRe design. The BOL cold-clean reactivity values are for a uniform temperature of 300 K. The high density of the ODS-Mo core structure reduces the neutron leakage from the reactor. To compensate the UN fuel enrichment decreases slightly from 95% to 92.7%, in order for the reactor to meet the required 25% ASM of the rotating B_4C/BeO drums in the 9 cm thick BeO radial

reflector (Fig. 3.11). Despite the slightly lower enrichment, the reduced neutron leakage results in a BOL cold-clean excess reactivity of \$6.62, higher than that of the SCoRe-N_5.The SC-SCoRe, with 15.7 at% ^{151}EuN SSA in the fuel and 0.1 mm thick $^{151}Eu_2O_3$ coating of the 316L SS vessel, is highly subcritical when the bare core is submerged in wet sand and flooded with seawater. Thermal neutron absorption and the low void faction in the ODS-Mo solid core also help reduce the water submersion reactivity in this accident scenario.

The SC-SCoRe has a negative temperature reactivity feedback, due mostly to the thermal expansion of the UN fuel pellets, core structure materials, and NaK-56 coolant. The reactor at a nominal thermal power of 1,000 kW_{th} has a BOL-hot-clean excess reactivity of \$6.27, a decrease of \$0.35 from the cold-clean value (Table 3.6). The temperature reactivity feedback in the SC-SCoRe is smaller than that of the SCoRe-N_5 in Section 3.7 due to the lower thermal expansion of the ODS-Mo core structure compared to that of the 316L fuel rods cladding used in the earlier SCoRe-N_5. This negative temperature reactivity feedback supports passive load following operation of the SC-SCoRe power system with TE energy conversion. An increase in the load demand lowers the temperature in the primary loops, causing the reactors reactivity to increase, and hence its thermal power in response.

3.10.2. Estimate of Reactor Operation Life

The results presented in Fig. 3.61 show that the SC-SCoRe is capable of operating at 1,000 kW_{th} continuously, without refueling, for up to 21 years. Over this time, the reactor generates a total of 7.67 GWd of thermal energy. The excess reactivity in the reactor decreases linearly with operating time at a rate of 8.17×10^{-4} \$/MWd, and depletes fully after 21 full power years (Fig. 3.61). This operation life meets the design requirement of > 20 years. At the EOL the fuel burnup reaches almost 58 MWd/kgU, a level comparable to that achieved in modern commercial light water reactors. At the end of life the 12 rotating B_4C/BeO control drums would be rotated inward with the B_4C segments facing the core to shut down the reactor.

During its operational life, the fission power generated in the reactor core consumes only 8.25% of the ^{235}U inventory in the UN fuel (Fig. 3.61). Future recovery of the post-operation SC-SCoRe, after sufficient storage time of post operation reactor below grade on the lunar surface, could be undertaken to retrieve the remaining large fraction of ^{235}U (91.75%). Analyses of post-operation storage of the SC-SCoRe are discussed in Chapter 6.

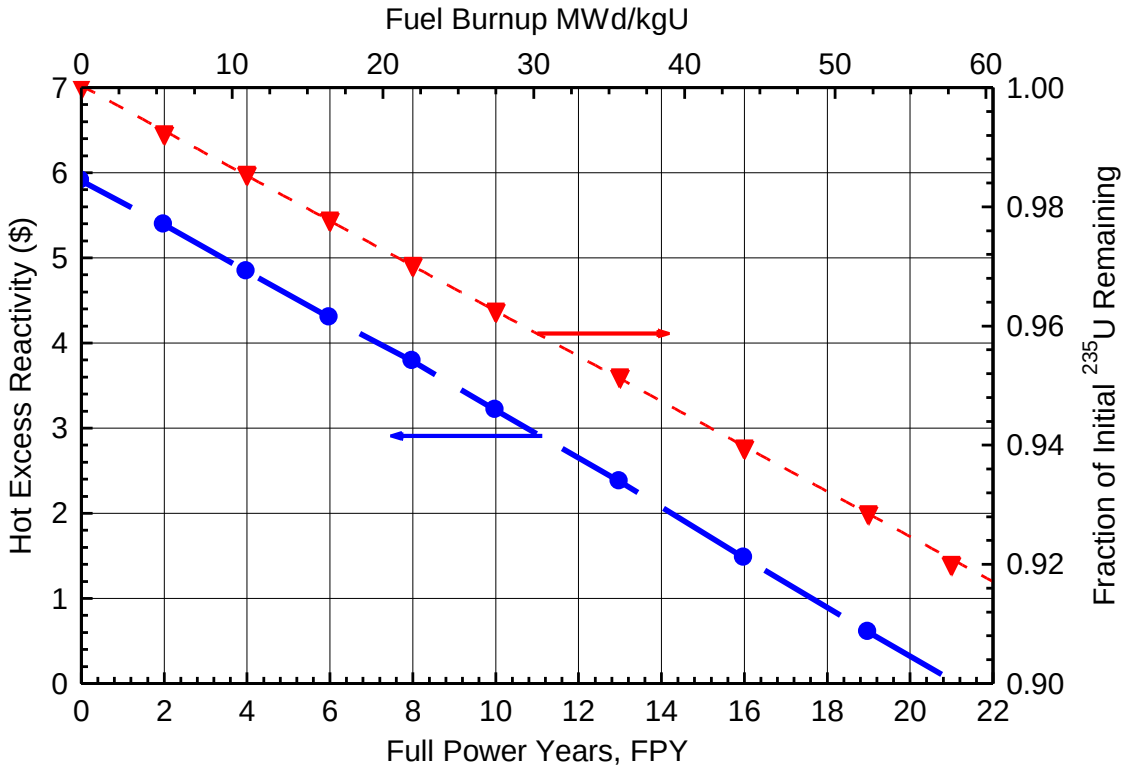

Fig. 3.61. - Reactivity depletion in SC-SCoRe during nominal operation at 1,000 kW_{th}.

3.11. Highlights and Concluding Remarks

This chapter introduced a multi-physics design and analyses methodology for developing lunar surface power reactors and applied it to developing the SCoRe for lunar surface power. The analyses ensured that the reactor design satisfies the launch safety requirements, has redundancy in reactor control, maintains the fuel and core material temperatures within their operating limits, and possess sufficient excess reactivity for a long operation life. The results of this research:

- Developed a multi-physics design and analyses methodology which iteratively couples together the results of MCNPX Monte-Carlo neutronics and STAR-CCM+ CFD and thermal-hydraulics analyses with dynamic modeling of the integrated power system using DynMo-TE [El-Genk and Tournier 2006a]. This methodology is applied to develop the long life SCoRe for lunar surface power.
- Determined that increasing the diameter of the fuel rods in the SCoRe-N_{18} increases the BOL cold-clean excess reactivity and reduces the total reactor mass.
- Showed that scalloping the wall of the core sectors eliminates flow bypass caused by the use of large diameter fuel rods in the SCoRe-N_5, improving the flow distribution and reducing peak fuel and cladding temperatures. The scallops also enhance neutron reflection, increasing the BOL excess reactivity.
- Compared different SSA isotopes for the SCoRe-N_5 and determined that ^{151}Eu resulted in the smallest reactor core, with the highest BOL excess reactivity and the lowest total mass.
- Demonstrated that the high thermal conductivity ODS-Mo solid core enables the SC-SCoRe to continue to operate, at a reduced thermal power of 323.0 kW_{th}, with a sector experiencing a LOC or LOCo. At this power level the system could supply ~4 kW_e to the outpost to maintain life support.
- Showed that the SC-SCoRe achieves a reactor operational life of 21 FPY at a nominal thermal power of 1,000 kW_{th}, while satisfying neutronics and thermal-hydraulics operation and safety requirements.

These analyses showed that the operational lives of lunar power reactors which are fueled at launch can be significantly increased by reconfiguring the reactor to reduce the neutron leakage. The developed SC-SCoRe design successfully meets the operation and safety requirements in these analyses. The next chapter describes the design and analyses performed for the second reactor concept developed in this dissertation, the Pellet Bed Reactor (PeBR) [El-Genk et al. 1990, 1994a,b; Morley and El-Genk 1994; El-Genk and Morley 1993], which is to be launched unfueled and loaded with spherical fuel pellets on the surface of the Moon.

4. DESIGN AND FUEL LOADING ANALYSES OF THE PELLET BED REACTOR (PeBR) FOR LUNAR SURFACE POWER

The Pellet Bed Reactor (PeBR) is investigated in this research for fueling on the lunar surface to achieve a long operational life and simplify launch procedures. The PeBR for surface power is launched unfueled, then loaded with spherical fuel pellets after it is placed below grade and surrounded with regolith on the lunar surface. The fuel pellets are launched to the lunar surface in transport canisters designed to remain sufficiently subcritical during launch and when submerged in wet sand and flooding with seawater in the unlikely event of a launch abort accident.

The fast-neutron spectrum, gas-cooled PeBR concepts have been previously developed for nuclear thermal propulsion (NTP), nuclear electric propulsion (NEP), and bimodal operation [El-Genk et al. 1990, 1994a,b; Morley and El-Genk 1994; El-Genk and Morley 1993]. These concepts were designed for high temperature operation (> 1,000 K) and extensively used refractory metal alloys in their construction. This research develops the PeBR concept for operation at lower temperatures and long life for lunar surface power applications. The developed PeBR uses conventional steel and nickel-based superalloys in its construction, and is emplaced below grade on the lunar surface to utilize the regolith as a supplemental regolith reflector and for radiation shielding.

4.1. Analyses Methodology

The work detailed in this chapter developed the PeBR design for lunar surface power, with a long operation life, and demonstrated the possibility of fueling the reactor on the Moon. The latter task is accomplished by designing safe launch canisters for the fuel pellets and by simulating loading one of the three core sectors in lunar gravity. The components of the performed reactor design and analyses steps are outlined in Fig. 4.1. The design of the PeBR for lunar surface power using multiple Closed Brayton Cycle (CBC) loops (Fig. 4.2) is described in Section 4.2 along with the placement of the reactor on the lunar surface.

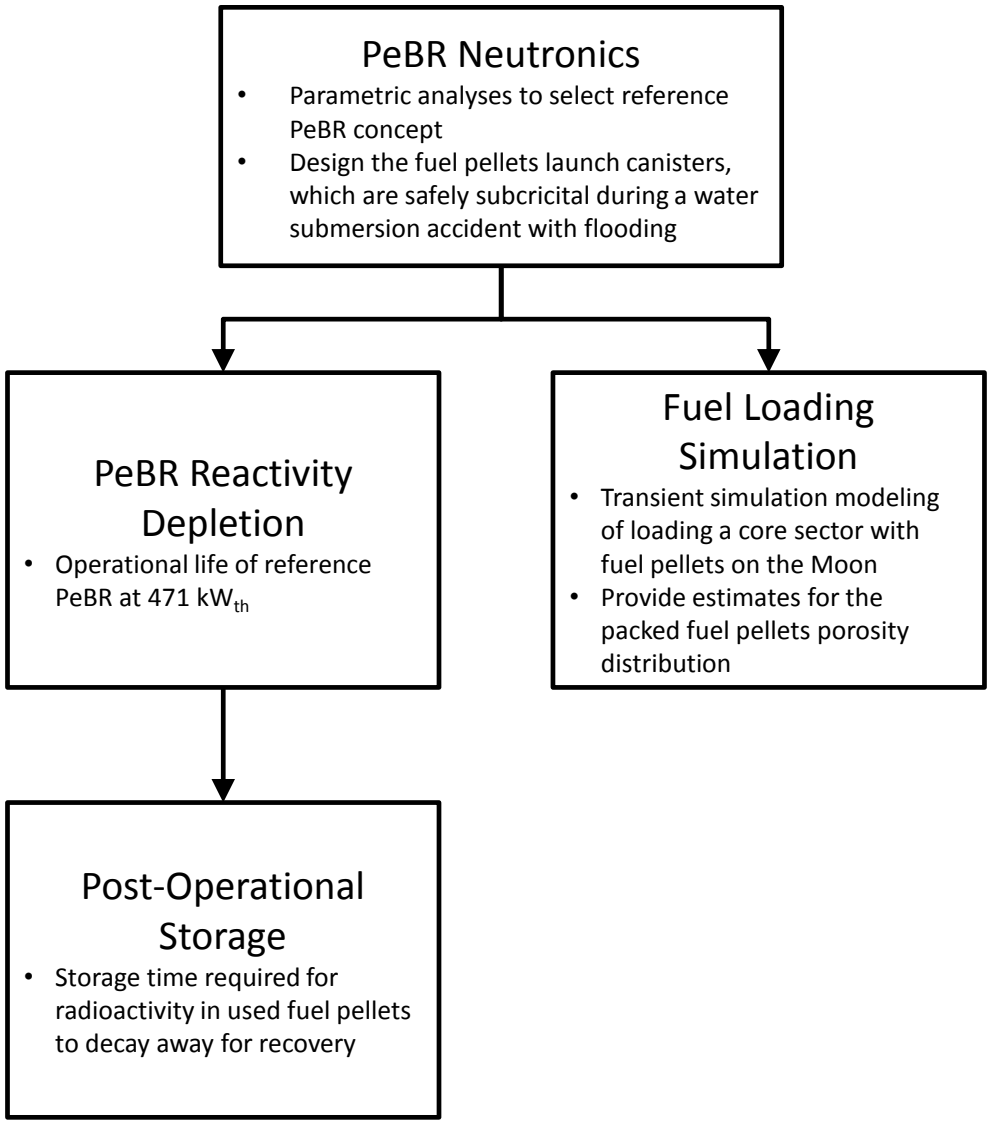

Fig. 4.1. - The design and fuel pellets loading analyses of long operation life PeBR concept for a lunar outpost.

Section 4.3 describes the computational methodology used in performing the neutronics tasks shown in Fig. 4.1. The results of the parametric neutronics analysis are presented in Section 4.4 to develop a reference PeBR concept (Fig. 4.1). The performed analyses investigate the effects of the PeBR core dimensions and the thickness of the BeO radial reflector on the Beginning-of-Life (BOL) excess reactivity and the total reactor mass. These analyses are performed using the Monte-Carlo neutron transport code MCNPX 2.7A [Hendricks et al. 2008] to ascertain that the loaded PeBR with fuel pellets and surrounded with lunar regolith is at least -$1 subcritical at the BOL. These reactors

also have a 25% Additional Shutdown Margin (ASM) in the B_4C/BeO rotating control drums (Fig. 4.3). Based on the parametric design and analyses results, a reference PeBR concept is selected, which has sufficient excess reactivity and a low system mass.

Neutronics analysis is also performed to design the launch canisters of the fresh fuel pellets, each sized to contain pellets for one of the three core sectors in the reference PeBR design. The analysis ensues that the canisters remain at least -$1.0 subcritical when submerged in wet sand (30 vol% seawater and 70 vol% sand) and flooded with seawater, in the unlikely event of a launch abort accident (Fig. 4.1). This requirement applies both to single canisters and a bundled cluster of all three canisters (see Section 4.5).

Loading the developed reference PeBR (Fig. 4.1) with fuel pellets on the lunar surface is investigated in Section 4.6 using a Discrete Element Method (DEM) analysis performed using STAR-CCM+ 6.02 [CD-adapco 2011] (Fig. 4.1). This simulation models loading one of the three core sectors in the PeBR core (Fig. 4.2) with fuel pellets in lunar gravity. The DEM simulation models the interactions between falling fuel pellets and the bottom and walls of the core sector and determines the spatial distribution of the porosity in the randomly packed sector loaded with fuel pellets.

Fuel depletion calculations are carried out using MCNPX for the reference PeBR on the lunar surface to determine the full-power years of operation life at a nominal reactor thermal power of 471 kW_{th} and exit temperature of 910 K (Fig. 4.1). The calculated radionuclide inventory in the fuel pellets in the post-operation reactor is used to evaluate the storage time of the PeBR on the Moon, following shutdown at End-of-Life (EOL). The radioactive source term is calculated from the initial inventory at EOL as a function of post-operation storage time. Determined is the storage time required for the radionuclides to decay to a low level, near background, to allow for a safe recover of the PeBR and fuel elements (see Chapter 6). The next section describes the long operation life PeBR design for lunar surface power and the integrated power system (Figs. 4.2 and 4.3) developed in this chapter.

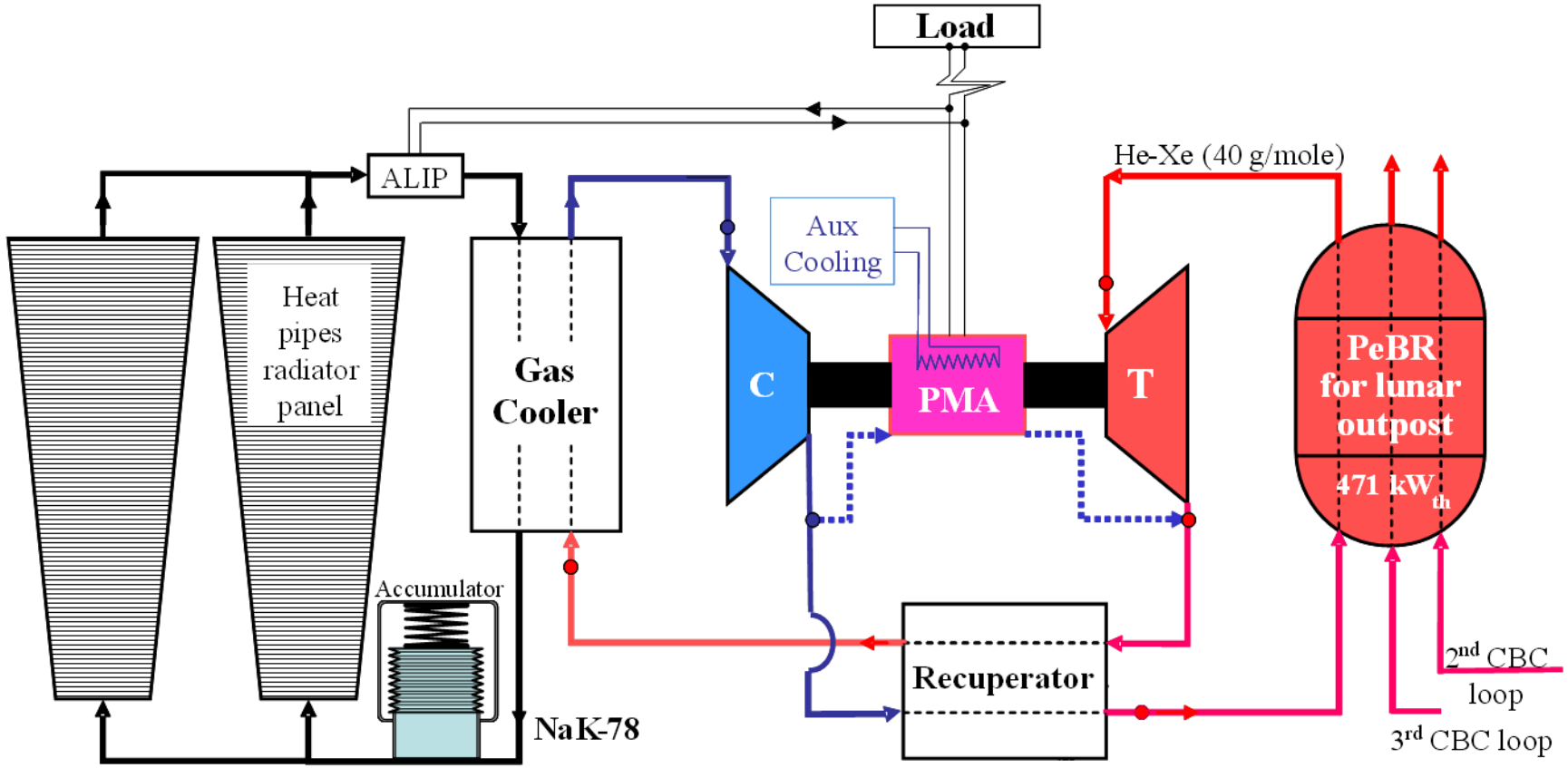

Fig. 4.2. - Schematic of one CBC loop in the PeBR power system for lunar surface power [El-Genk and Schriener 2011].

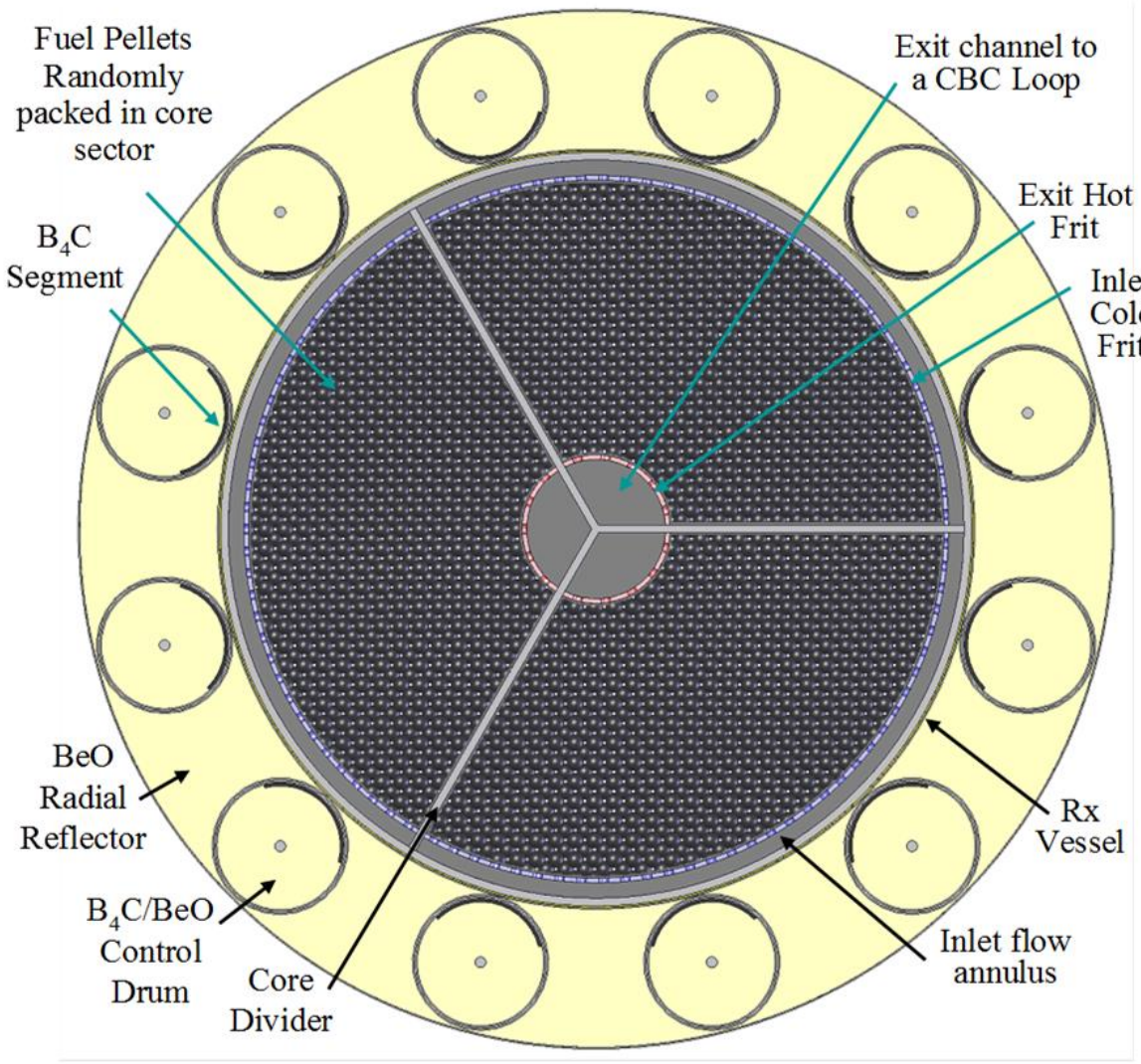

Fig. 4.3. - A radial cross-sectional view of the PeBR with three core sectors loaded with spherical fuel pellets [El-Genk et al. 1990, 1994a; El-Genk and Schriener 2011].

4.2. PeBR Design and Lunar Surface Power System

The three sectors of the fast-spectrum PeBR core (Fig. 4.3) are loaded with spherical fuel pellets and separated by thin metal dividers. During nominal reactor operation all three core sectors are thermally and neutronically coupled, but hydraulically independent. Each sector has separate inlet and exit flow channels and a CBC loop in the PeBR-CBC power system for energy conversion (Fig. 4.2) [El-Genk and Gallo 2010; El-Genk et al. 2010]. The system pressure at the exit of the compressors of the turbo-machine units is

~1.3 MPa (Fig. 4.2). Though the He-Xe reactor coolant and CBC working fluid (40 g/mol) has the same forced convection heat transfer coefficient as pure helium, its higher molecular weight markedly decreases the size of the turbomachine units [Gallo and El-Genk 2009; El-Genk and Gallo 2010; El-Genk and Tournier 2007]. It also increases the pressure losses and slightly decreases the system's thermal efficiency [Gallo and El-Genk 2009; El-Genk and Gallo 2010; El-Genk et al. 2010; El-Genk and Tournier 2007, 2008].

The shorter flow path of the inward radial flow of He-Xe coolant through the PeBR core sectors (Fig. 4.4) decreases pressure losses, compared to using axial flow. Perforated metal sheets or "frits" are placed at the outer and inner radii of the annular core sectors (Figs. 4.3 and 4.4). The He-Xe coolant enters the sectors through the outer or cold frit at ~758 K and 1.3 MPa and exits through the inner or hot frit at ~910 K into three central flow channels (Fig. 4.4). The orifices in the cold frit are sized to axially distribute the inlet flow to ensure an almost uniform exit temperature, thus avoiding developing hot spots in the core sectors during nominal reactor operation. The orifices in the hot frit are of the same diameter to reduce pressure losses. The diameters of the largest orifices in the cold and those of the hot frits are ~0.6–0.8 mm in order to avoid blockages in the frits due to the long term erosion of the fuel pellets.

The PeBR core pressure vessel is surrounded by a 9 cm thick BeO radial reflector and has 4 cm-thick axial BeO reflectors on top and bottom of the reactor vessel. The axial and radial BeO reflectors are clad in thin (0.1 cm) 316L stainless steel (Fig. 4.3) to protect from meteorites impact and prevent sublimation of BeO into space. The radial reflector contains twelve B_4C/BeO rotating control drums for reactor startup, shutdown and operation through the EOL. The BeO control drums are also clad in stainless steel and are faced with thin 120° segments of B_4C that is fully enriched in ^{10}B. Before the reactor startup on the lunar surface, the control drums in the BeO radial reflector would be rotated with the B_4C segments facing the core (Fig. 4.3).

To startup the reactor at BOL and maintain steady thermal power through its operation life, the control drums in the radial BeO reflector are rotated gradually outward. At EOL, the B_4C segments in the control drums would face 180° away from the reactor core. The thickness of the fully enriched B_4C segments in the drums ensures that at BOL

the PeBR, emplaced on the lunar surface and loaded with fuel pellets, would be at least -$1 subcritical with only 9 of the 12 drums are in the shutdown orientation while emplaced below grade on the Lunar surface. The placement of the PeBR on the Moon is the subject of the next subsection.

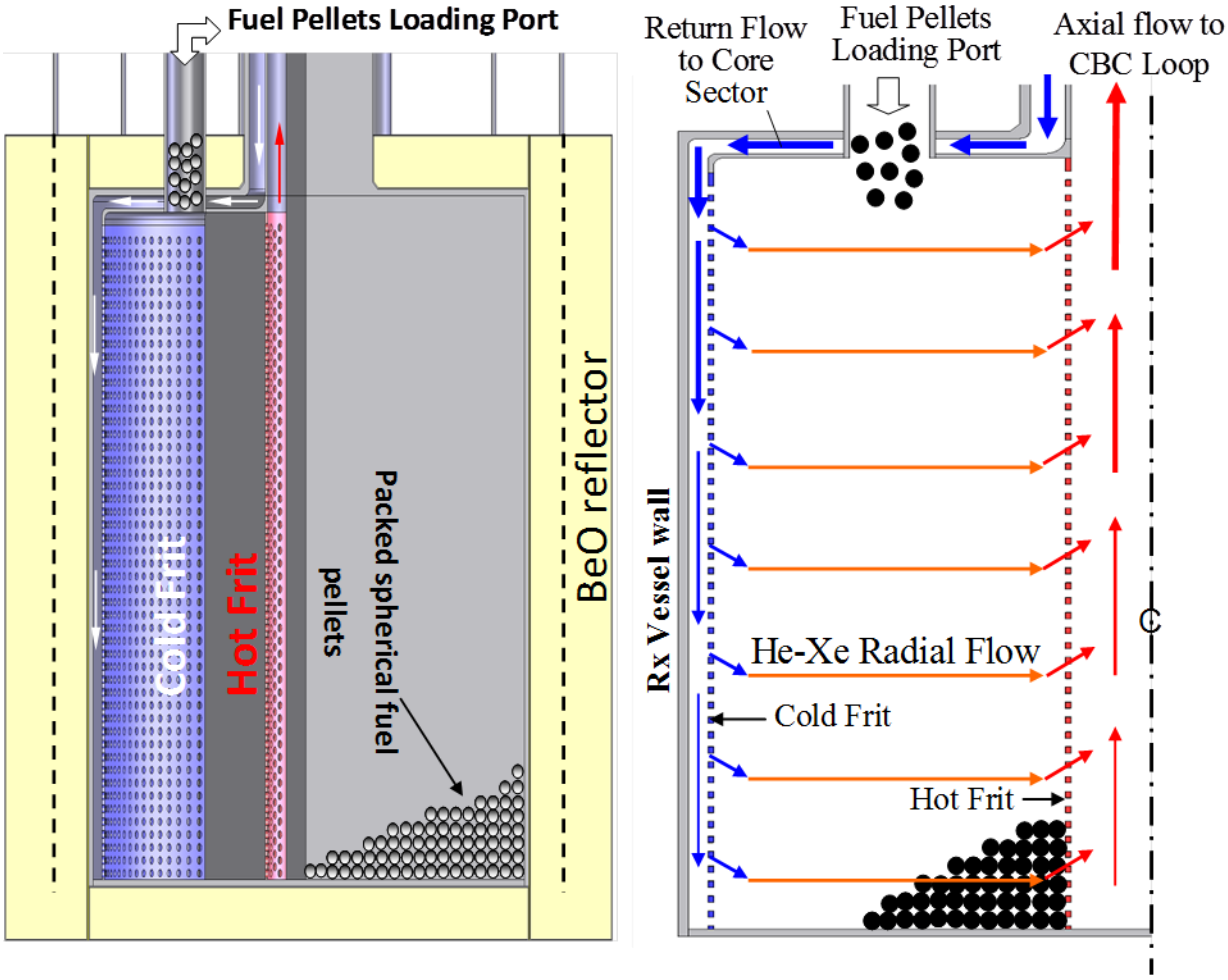

Fig. 4.4. - Schematics of PeBR core showing the cold and hot frits and the He-Xe gas radial flow in a core sector [El-Genk and Schriener 2011]

4.2.1. Placement of PeBR on the Lunar Surface

On the lunar surface, the PeBR would be emplaced ~1–2 m below grade in an excavated hole or trench and then surrounded by backfilled lunar regolith (Fig. 4.5). The regolith serves as supplemental radiation shielding and as neutron reflector [Hatton and El-Genk 2009], increasing the BOL excess reactivity to achieve a long operation life, and

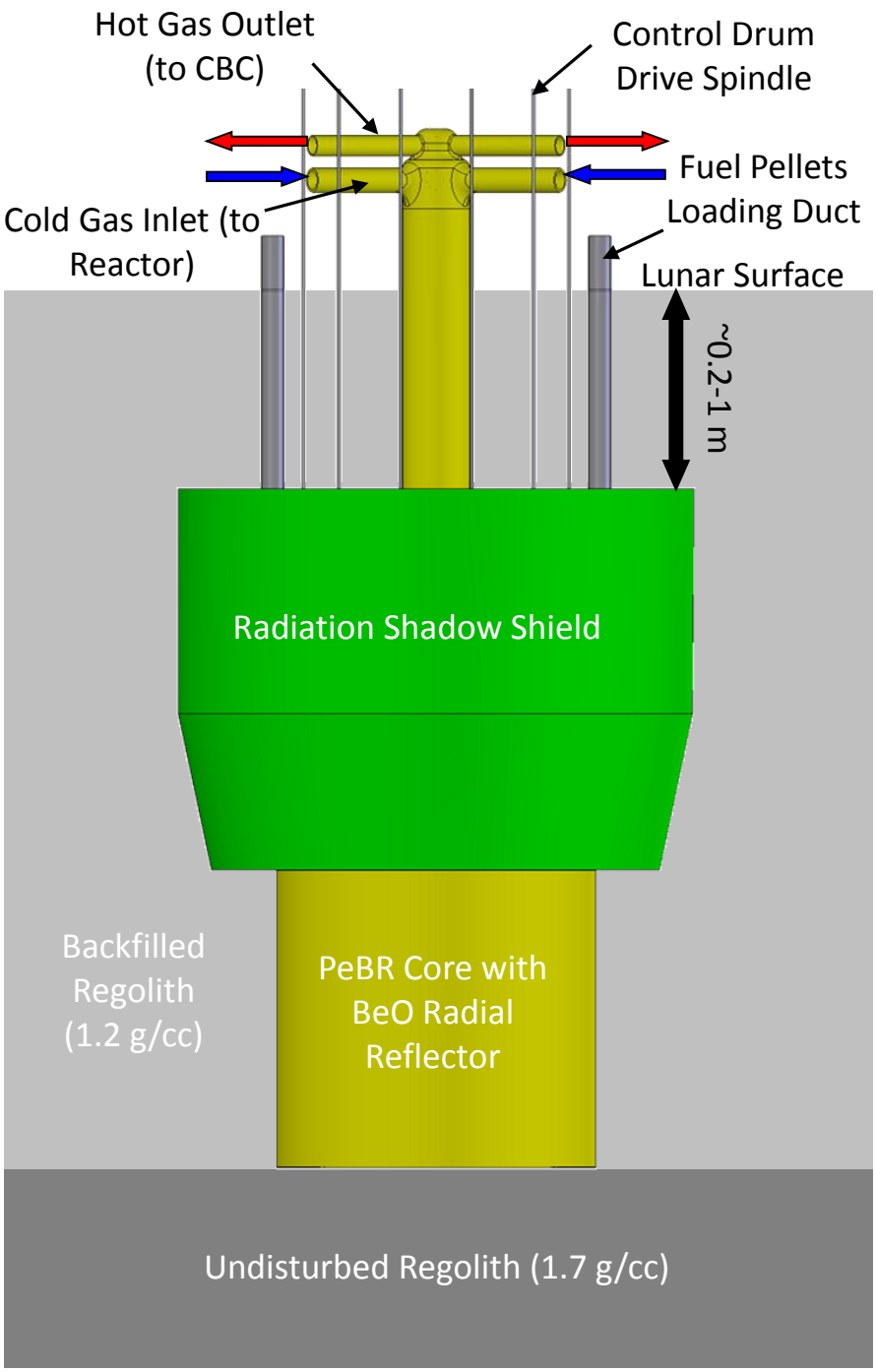

Fig. 4.5. - PeBR emplaced below grade on the lunar surface [El-Genk and Schriener 2011]

reduce the mass of the BeO radial reflector to be launched from Earth. The coolant ducting extends up from the reactor to the surface to carry the He-Xe coolant and working fluid to the CBC loops (Figs. 4.5). Once the reactor is buried beneath the lunar surface the CBC loops and heat-pipes radiator panels (Fig. 4.2) are erected on the surface and connected to the core sector's inlet and outlet coolant ducts.

The reactor fuel loading ports at the top of the three sectors (Fig. 4.4) are connected to circular ducts extending to the lunar surface to allow the spherical fuel pellets to be loaded into core sector using lunar gravity (Fig. 4.6). The fuel pellets loading occurs following emplacement of the reactor below grade on the Moon. The fuel pellets in the PeBR core sectors are randomly packed, thus their loading into the core could be accomplished either remotely using tele-robotics or with a crew assistance. The fresh fuel pellets are launched separately to the Moon in subcritical transport canisters (Fig. 4.6). Each canister contains sufficient fuel pellets to load one of the three core sectors. Once the sectors are filled with the randomly packed pellets, the fuel loading ports would be sealed and the CBC loops charged with the He-Xe coolant and working fluid. The following subsection describes the layout of the PeBR power system with multiple CBC loops.

4.2.2. PeBR Power System for Lunar Surface Power

Fig. 4.2 presents a line diagram of the PeBR power system with one of the 3 CBC loops and nominal operating temperatures and pressures. The turbo-machine unit consists of a turbine, a compressor and a permanent magnet electrical alternator (PMA) mounted on a single shaft (Fig. 4.2) [Gallo and El-Genk 2009; El-Genk and Gallo 2010]. The compressor on the turbo-machine unit circulates the He-Xe working fluid in the CBC loop and the reactor core sector. The gas cooler in the CBC loop removes heat from the He-Xe working fluid, before entering the compressor at 400 K, to a secondary loop of circulating liquid NaK-78 liquid metal for rejection into space.

The waste heat rejection into space is accomplished using water heat-pipes radiator panels, two for each CBC loop. AC Annular Linear Induction Pumps (ALIPs) with a nominal efficiency of ~10% circulate the liquid NaK-78 in the heat rejection loops; each

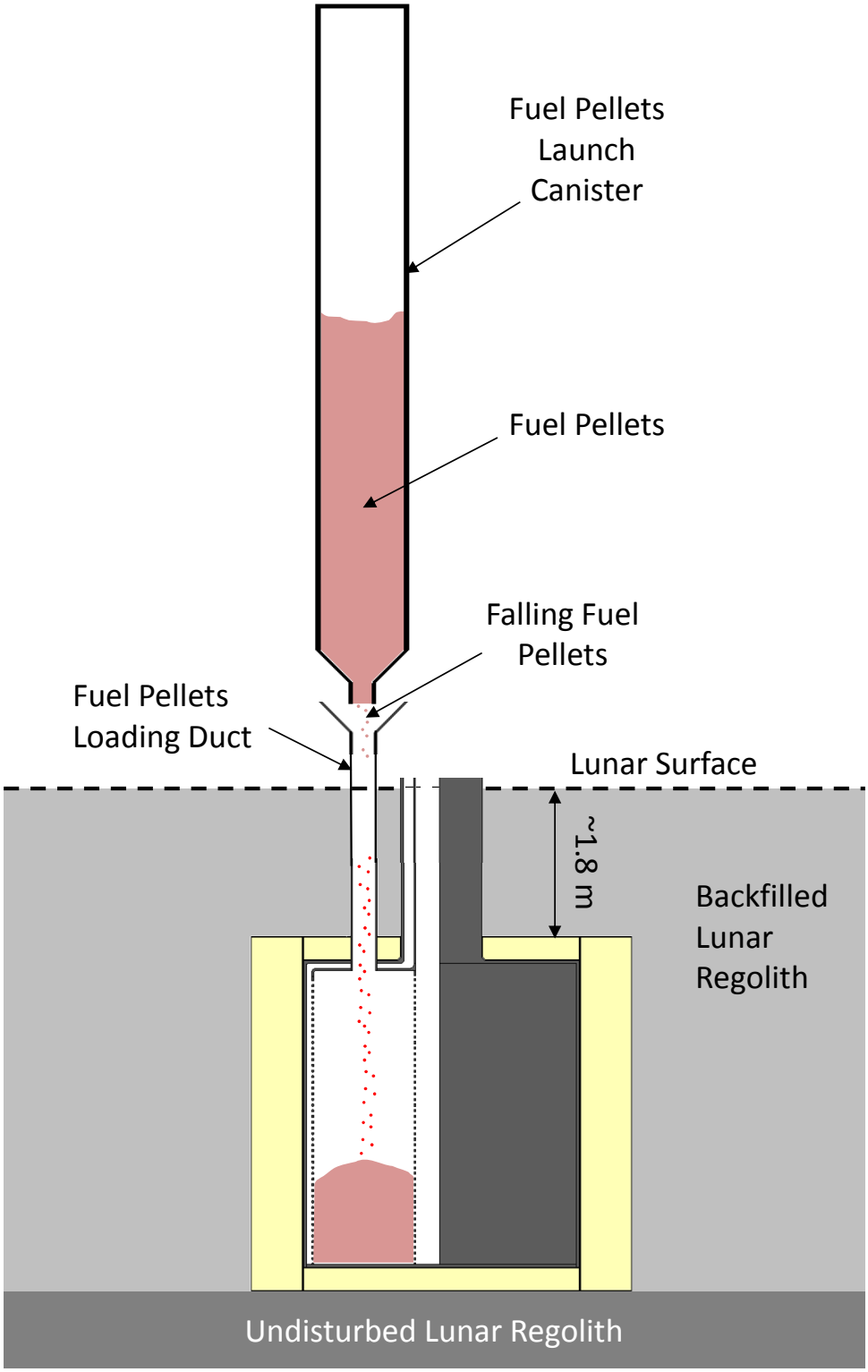

Fig. 4.6. - Loading PeBR sectors with fuel pellets on the lunar surface (not to scale) [El-Genk and Schriener 2011].

ALIP consumes about 1.1 kW_e, for a total of 3.3 kW_e for the power system. The six heat pipes radiator panels, the circulating liquid NaK-78 heat rejection loops, and the control equipment would all be placed on the lunar surface. The radiator panels would be erected vertically to help prevent the accumulation of dust particles that may electro-statically attach onto the surface and decrease its emissivity for heat rejection.

At the PeBR nominal thermal power of ~471 kW_{th} and inlet and exit temperatures of 758 K and 910 K, the thermal efficiency of the power system, η_{sys}, is 21.1%, when the rotation speed of the shafts in the turbo-machine units is 45,000 rpm [Gallo and El-Genk 2009; El- Genk and Gallo 2010; El-Genk et al. 2010]. Each CBC loop (Fig. 4.2) supplies a net electrical power of 31.1 kW_e to the load, for a total of 99.3 kW_e for the integrated PeBR power system.

The sectored core PeBR and the power system with three separate CBC loops enhance operation reliability and potentially avoid single point failures in the reactor cooling and energy conversion. For example, a pipe break in a CBC or NaK-78 heat rejection loop resulting in a Loss of Coolant (LOC) or Loss of Cooling (LOCo) would not terminate the power system operation. Instead, the reactor thermal power would be decreased to a level not to cause an overheating the fuel pellets in the sector experiencing a LOC or LOCo. The fission heat generated in that sector would then be transferred by conduction and radiation to the adjacent sectors and removed by the circulating He-Xe gas in these sectors. The high melting point ceramic materials in the spherical fuel pellets provide a large margin to fuel failure in the affected core sector experiencing a LOC or LOCo. The design of these spherical fuel pellets is presented next.

4.2.3. Fuel Pellet Design

The PeBR fuel pellets are ~1.0 cm in diameter and comprised of ZrC-coated, highly enriched (> 95%) UC fuel particles (~850 μm in dia.) dispersed in ZrC matrix (Fig. 4.7a). The UC coated fuel particles are dispersed with a high packing fraction of ~0.55 in the fuel pellets to increase the ^{235}U loading in the reactor core. The fuel particles (Fig. 4.7b) consist of UC kernels surrounded by a low density (30% TD) ZrC buffer layer and a

dense and strong ZrC coating [Morley and El-Genk 1994; Dobranich and El-Genk 1991; Demkowicz 2006; Meyer et al. 2006]. The low density buffer layer protects the UC kernels from the potentially corrosive gases during the application of the dense outer ZrC coating. It also partially accommodates released fission gases and for the expansion of the UC fuel kernel and protects the outer ZrC coating from radiation damage by recoiling fission fragments [Dobranich and El-Genk 1991; Demkowicz 2006].

The dense outer ZrC coating serves as a pressure barrier for retaining fission gases and products. Its thickness is determined based on considerations of the diameter of the UC fuel kernel, the operation temperature and fuel goal burnup. The ZrC coatings have a small thermal expansion coefficient and good thermal conductivity. Together with the surrounding ZrC matrix in the pellets (Fig. 4.7a), they would provide excellent containment of the fission products during reactor operation and while it is in post-operation long term storage. The ~1 cm diameter fuel pellets are coated with a thin layer of graphite (0.1 mm) that protects the ZrC matrix during handling and launch. The graphite coating also reduces friction between pellets during loading the reactor core sectors with fuel pellets on the lunar surface (Fig. 4.6).

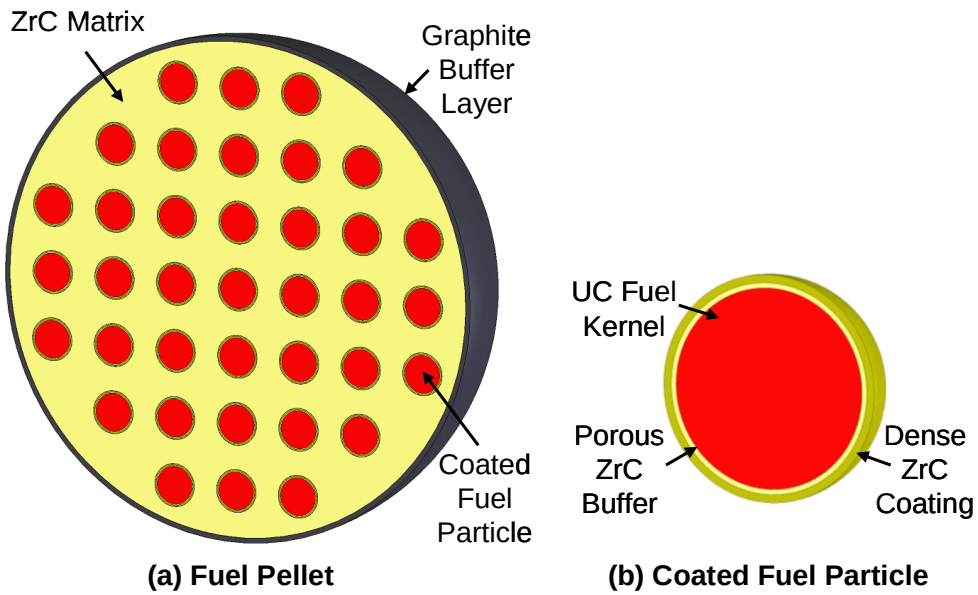

Fig. 4.7. - PeBR fuel pellets and ZrC coated UC particles (not to scale) [El-Genk and Schriener 2011]

The spherical fuel pellets (Fig. 4.7a) provide high heat transfer surface area to the circulating He-Xe gas in the PeBR core sectors during operation (Figs. 4.3-4.4) [El-Genk et al. 1992, 1990, 1994a,b; El-Genk 1995, 2001; Morley and El-Genk 1994; Liscum-Powell and El-Genk, 1994]. The high surface area and the high thermal conductivity of the ZrC decrease the temperature gradient in the pellets, and hence thermal stresses, for long operation life of the PeBR on the lunar surface [Dobranich and El-Genk 1991].

The fresh pellets (Fig. 4.7a) pose practically no radiological concern and are safe for humans to handle. This is because of the very low radioactivity of the highly enriched UC kernels in the coated fuel particles (< 65 mCi/g of uranium, assuming ~1% ^{234}U content) (Fig. 4.7b). Thus, assuming a total of 160 kg of 95% enriched UC fuel, the total radioactivity of the fresh fuel pellets in the subcritical launch canisters will be very low, <10.5 Ci.

The design of the spherical fuel pellets allows for high temperature operation over the reactor's long operation life. The next section briefly reviews potential structural materials for the PeBR pressure vessel, core structure, and power system.

4.2.4. Selection of Structural Materials

The selection of the structure materials for the PeBR core and power system is another important design and operation consideration. Owing to the moderate nominal exit temperature of the PeBR (~910 K), the reactor vessel, the core frits, and the coolant ducts could be made of steel or nickel-based superalloys. The reactor vessel, cold-frit, and inlet ducts will experience temperatures close to the coolant inlet temperature of ~758 K, while the hot-frit and the exit ducts will experience temperatures close to the reactor nominal exit temperature of ~910 K. The top and bottom metal plates of reactor vessel will experience temperatures between these extremes (758-910 K). While different metallic alloys could be used for the hot and cold components, using the same metal alloy for the reactor vessel and core internals simplifies fabrication by avoiding issues of joining dissimilar materials.

Candidate steels for use in the PeBR include AISI 316, mod 9Cr-1Mo, and 12Cr-1Mo-WV (Fig. 4.8a-c) and candidate superalloys include Hastelloy X, Inconel Alloy 617,

and Inconel X750 (Fig. 4.9a-c). The design envelopes of these structural materials are indicated by the grey shaded areas in Figs. 4.8 and 4.9. These envelops are bound by the curves representing 1/4 ultimate tensile strength, 5/8 yield strength at 0.2% offset, 1/3 creep rupture strength after 10,000 h, and the ductile-to-brittle transition temperature in an irradiation environment on the left-hand side. For the PeBR, these design envelopes (dashed area in Figs. 4.8 and 4.9) are further bounded by reactor's inlet and exit temperatures of 758K and 910 K.

The austenitic stainless steel AISI 316, the 12Cr-1Mo-WV martensitic steel (HT-9), and the 9Cr-1Mo-Nb modified ferritic-martensitic steel (T91) (Fig. 4.8a-c) have been tested or used in experimental fast neutron flux reactors in the United States, France, Japan, and Russia for use in fuel rods cladding and structural components [IAEA 2006; Klueh and Harries 2001]. The nickel-based super-alloys of Hastelloy X, Inconel 617, and Inconel X750 (Fig. 4.9a-c) have been used in fittings and components in commercial LWRs and undergone relatively limited testing for use in liquid metal-cooled fast reactors [EPRI 2003; Angeliu et al. 2007]. These superalloys and others are also being investigated for use in the Gen-IV supercritical water and very high temperature reactors due to their high strength at elevated temperatures and high corrosion resistance [Sun et al. 2009; Fuzluddin et al. 2004]. The use of superalloys in LWRs has often been limited by concerns of stress corrosion cracking [Rubel et al. 1989] and irradiation embrittlement caused by helium produced from $^{58}Ni(n,\alpha)$ reactions during reactor operation [Angeliu et al. 2007].

For all steel and superalloys considered herein, the most limiting property is the creep rupture strength (Figs. 4.8 and 4.9). All alloys possess acceptable strength at the reactor inlet temperature of~758 K, but at the outlet temperature of 910 K the strengths of the three steel alloys (Fig. 4.8a-c) are 30-40% lower. The good high temperature performance of the superalloys is due to their superior high temperature creep resistance (Fig. 4.9a-c). The Inconel X750 alloy, which possesses the highest mechanical strength and experiences low swelling due to irradiation [Bates and Powell 1981], is selected as the baseline structural material for the vessel, coolant ducts, and core internals of the PeBR for surface power.

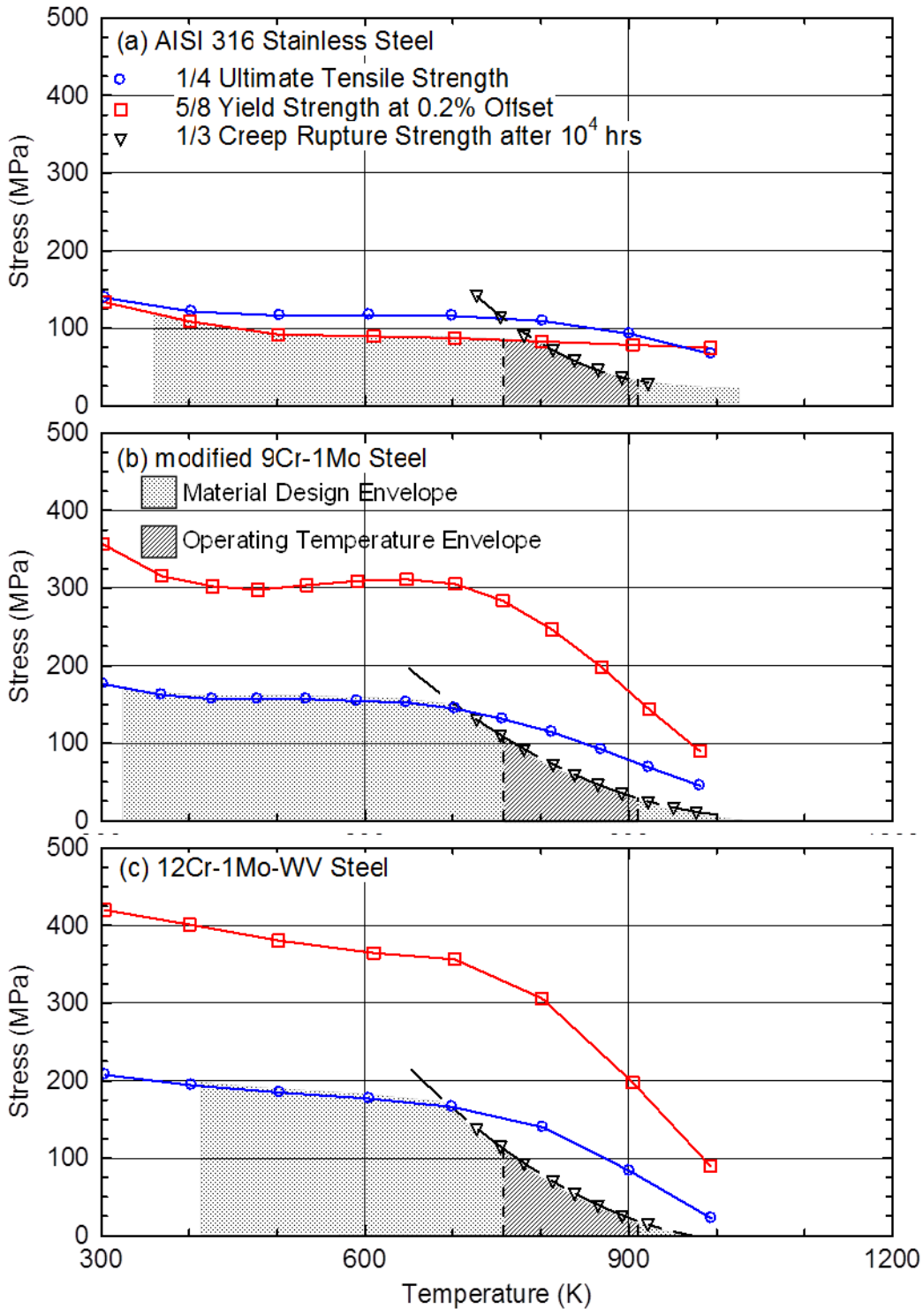

Fig. 4.8. - Design envelopes for the iron-based structural materials: (a) AISI 316 SS [Booker et al. 1981; Akiyama 1991; Margolin et al. 2010], (b) modified 9Cr-1Mo steel [Booker et al. 1981], and (c) 12Cr-1Mo-WV steel [Booker et al. 1981; Akiyama 1991].

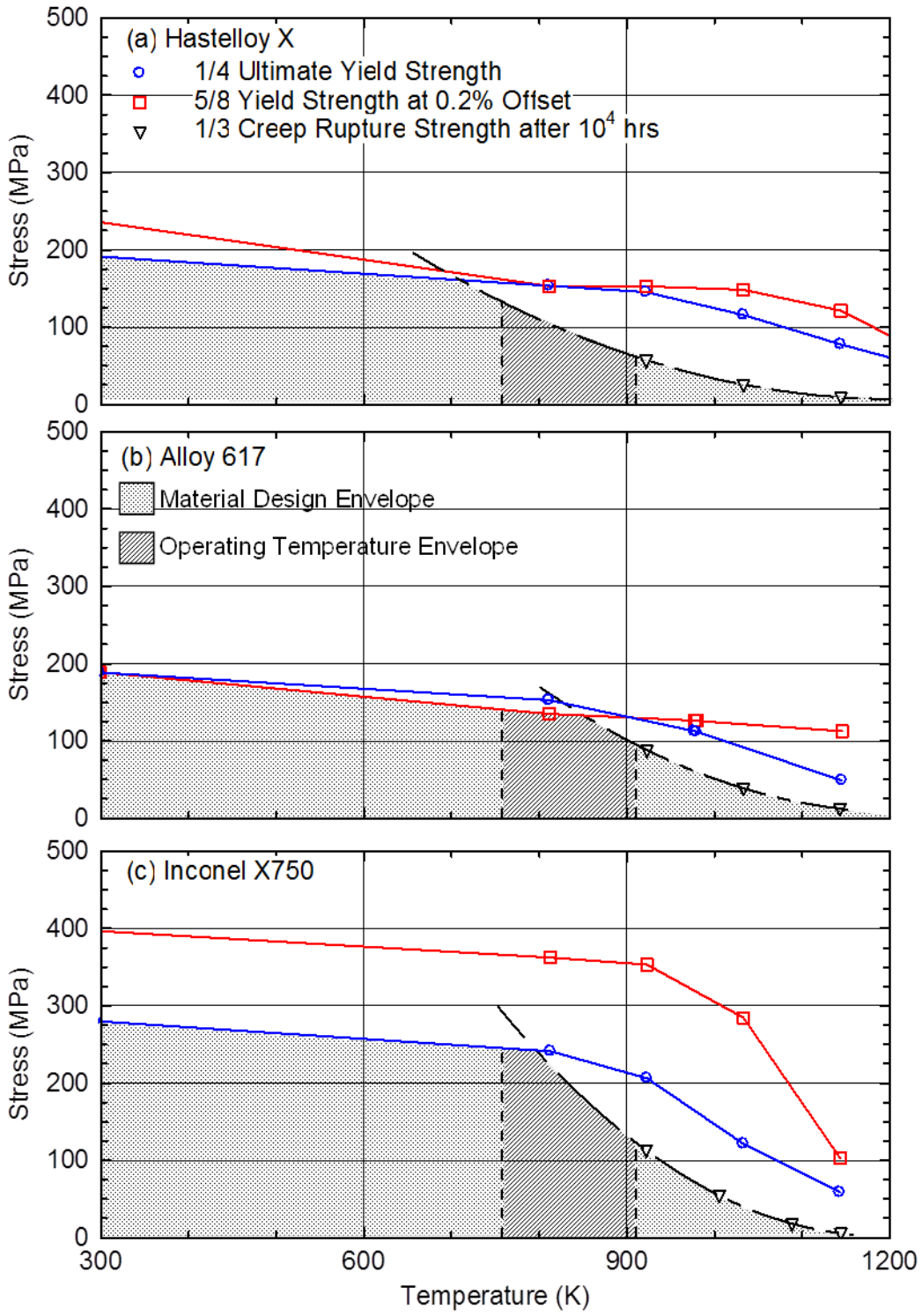

Fig. 4.9. - Design envelopes of the nickel-based structural materials: (a) Hastelloy X [Heynes International 1997], (b) Inconel 617 [McCoy and King 1985; Davis 2000], and (c) Inconel X750 [Special Metals Corporation 2004].

The PeBR reactor and power system for lunar surface power presented in this chapter is designed for long life operation on the Moon. The PeBR design is developed using parametric neutronics analyses of the reactor core emplaced below grade on the lunar surface. The methodology used in performing these analyses is discussed in the next section.

4.3. Neutronics Analysis Methodology for the PeBR

The MCNPX 2.7A Monte Carlo radiation transport code is used to perform the neutronics and the fuel depletion calculations [Hendricks et al. 2008]. The reactivity calculations used 20,000 sources particles per cycle and 100 skipped and 600 active cycles, for a relative error of 0.0002 or 2.9¢ of reactivity. The excess reactivity values in dollars are based on an average delayed neutron fraction, β_{eff} = 0.0068. This fraction is estimated by MCNPX using the k-ratio method [Spriggs et al. 2001]. This method estimates the value of β_{eff} from the calculated values of k_{eff} with and without delayed neutron generation enabled in the simulations.

To reduce the running time for the calculations, the ZrC coating of the UC coated fuel particles in the MCNPX model is homogenized into the ZrC matrix of the fuel pellets. The UC microsphere fuel kernels are still explicitly modeled individually to capture the self-shielding effect within the fuel pellets. This simplification reduced the computational time by almost a half, while underestimating the reactivity by less than 3¢. Additional uncertainties in the reactivity calculations for the PeBR would result from manufacturing and dimension tolerances in vessel, coated fuel particles and pellets, unconformities in enrichment and materials properties and the packing of the loaded fuel pellets into the PeBR sectors.

The calculated hot-clean and cold-clean excess reactivity values are for the PeBR while emplaced on the lunar surface. The hot-clean reactivity values are calculated assuming uniform average temperatures for the reactor core, vessel, and radial reflector. The calculations assume that the reactor is placed atop dense undisturbed regolith (1.7 g/cm^3) and surrounded by 2.5 m of loose packed lunar regolith (1.2 g/cm^3) piled up to a height of 80 cm on top of the reactor (Fig. 4.5). The neutronics simulations used the

composition of JSC-1 lunar simulant for the regolith composition (Table 3.3). The loaded PeBR with fresh fuel pellets and surrounded with lunar regolith is designed to be at least -$1 cold-clean subcritical with only 9, of the 12 control drums in the BeO radial reflector, rotated with the B_4C segments in the drums facing the core. The other 3 drums are assumed stuck 180° outward with the B_4C segments facing away from the reactor core. This stringent design requirement ensures a 25% ASM of the PeBR at BOL. To fulfill this requirement, the thickness of the B_4C segments in the control drums is increased, slightly decreasing the cold-clean excess reactivity.

4.3.1. Fuel Depletion Analysis Methodology

The fuel depletion calculations determine the life of the PeBR, when operating nominally at a thermal power of 471 kW_{th}. In these calculations, the MCNPX code tracks the neutron reactions for 38 actinides and 260 fission products included in the ENDF-VI and the JEFF 3.1 continuous energy cross section libraries [Lemmel et al. 2001; Koning et al. 2006]. The calculations utilized 20,000 particles per cycle for 100 skipped and 600 active cycles and a time step size of two years and used the default MCNPX fission Q-values to convert the reactor thermal power to a neutron flux for determining the neutron reaction rates [Hendricks et al. 2008]. The MCNPX neutronics and fuel depletion calculations accounted for the thermal expansion and the densities of the materials in the fuel pellets, the reactor vessel and the BeO reflector at their respective average temperatures during reactor operation. The utility code Doppler [Mosteller et al. 2003] is used to broaden the MCNPX neutron cross section data files to the average temperatures of the reactor materials during nominal operation.

4.3.2. Design and Analyses of the PeBR for Lunar Surface Power

Neutronics and fuel-depletion analyses are performed to develop a PeBR design for lunar surface power, with a long operation life and design safe launch canisters of the fuel pellets. The neutronics analysis optimizes the PeBR core dimensions and the thickness of the BeO radial reflector for small reactor mass and high BOL excess reactivity. Also determined are the BOL cold-clean and hot clean excess reactivity, and the shutdown margin at BOL. The analysis performed using the Monte Carlo neutron transport code

MCNPX 2.7A [Hendricks et al. 2008] ascertains that the loaded PeBR with fuel pellets and surrounded with lunar regolith is at least -$1 subcritical at the BOL, with only nine of the twelve control drums in the BeO radial reflector rotated inward (e.g., see Fig. 4.2) and 3 drums stuck in the outward-facing position, or a 25% Additional Shutdown Margin (ASM).

Analysis is also performed to design and size the launch canisters of the fresh fuel pellets and ensue that they remain at least -$1.0 subcritical when submerged in wet sand (30 vol% seawater and 70 vol% sand) and flooded with seawater in the unlikely event of a launch abort accident. This requirement applies both to single canisters and all three canisters bundled together. In addition, fuel depletion calculations are carried out of the PeBR on the lunar surface to determine the hot-clean excess reactivity, the temperature reactivity feedback and the full-power years of operation life. The fuel depletion calculations are for a nominal reactor thermal power of 471 kW_{th} and exit temperature of 910 K. The next section presents and discusses the results of the parametric neutronics analyses.

4.4. Analyses Results and Discussion

This section presents the results of the neutronics analysis for the design optimization of the PeBR emplaced on the lunar surface and loaded with fresh fuel pellets. The calculated cold-clean excess reactivities are compared for a number of PeBR core sizes with two different reactor shutdown requirements. The reference requirement is of the reactor being at least -$1 subcritical at BOL with the B_4C segments in all twelve control drums in the radial BeO reflector facing the core. The other requirement of 25% ASM at BOL is of the reactor being at least -$1 subcritical when only 9 of the 12 control drums are in the shutdown position and the remaining 3 control drums rotated 180° away from the core. The thickness of the B_4C absorber segments is adjusted so that the reactor meets the -$1 shutdown requirement. For the selected PeBR design for lunar surface power, estimates of the hot-clean excess reactivity along the reactor's operational life are calculated.

Investigated are the effects of increasing the thicknesses of the radial BeO reflector and the loading of the fuel pellets in the reactor core on the BOL excess reactivity. The analysis used the same nominal core configuration and fresh fuel pellets dimensions (Figs. 4.2, 4.4 and 4.6), but increased the core diameter to increase the fuel loading, while keeping the core height-to-diameter ratio constant at 1.15 (Figs. 4.10 and 4.11). Thus, the active core height and diameter and the height of the radial BeO reflector increased as the loading of the fresh fuel pellets in the PeBR increased. The obtained design surfaces for the PeBR are shown in Figs. 4.10 and 4.11. They consist of grids made of lines of the thicknesses of the radial BeO reflector (8, 9, 10, and 12 cm) and intersecting lines of the cold-clean excess reactivity values ($2, $3, $4, $5, $6, $7 and $8). Figs. 4.10 and 4.11 plot the total mass of the reactor, including the radial and axial BeO reflectors, versus the mass of the fuel pellets loaded in the core. The fuel pellets mass is directly proportional to the volume of the reactor core. Thus, the points on the design surfaces in Figs. 4.10 and 4.11 with the same fuel pellets mass are also for the same core dimensions.

The cold-clean excess reactivity estimates in Figs. 4.10 and 4.11 are for the PeBR surrounded with lunar regolith and the core loaded with randomly packed fresh fuel pellets, the reactor core and the BeO reflector at an isothermal temperature of 300 K and the surrounding lunar regolith at ~268 K. In both Figs. 4.10 and 4.11, the thickness of the B_4C segments ensures that the shutdown reactor at BOL is at least -$1.0 subcritical with only 9 drums rotated inward. For the same BOL excess reactivity and radial BeO reflector thickness, the total reactor mass and that of the fuel pellets are lower in Fig. 4.10 than in Fig. 4.11. The 25% ASM requirement in Fig. 4.10, increases the thickness of B_4C absorber segments in the control drums, which reduces the gain in excess reactivity due to the supplemental regolith reflector.

The cold-clean excess reactivity of the PeBR increases by increasing either the loading of the fresh fuel pellets in the core or the thickness of the BeO radial reflector (Figs. 4.10 and 4.11). The values of the fuel pellets loading and the radial BeO reflector thickness that correspond to the minimum total reactor mass depend on the values of the cold-clean excess reactivity. The minimum total mass of the PeBR with the smallest cold-

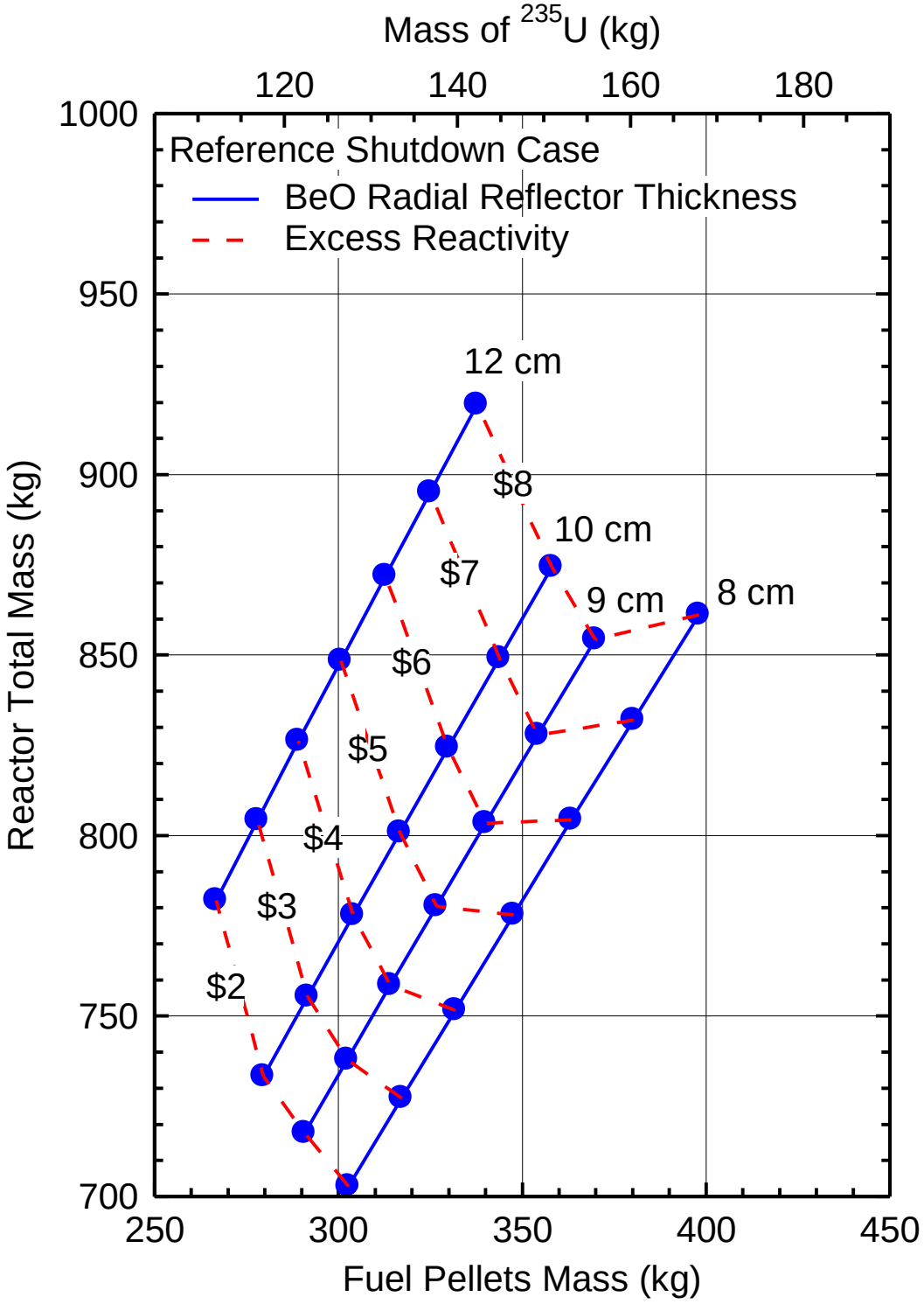

Fig. 4.10. - A design surface for the long life PeBR for lunar outposts, -$1 shutdown at BOL using 12 control drums [El-Genk and Schriener 2011].

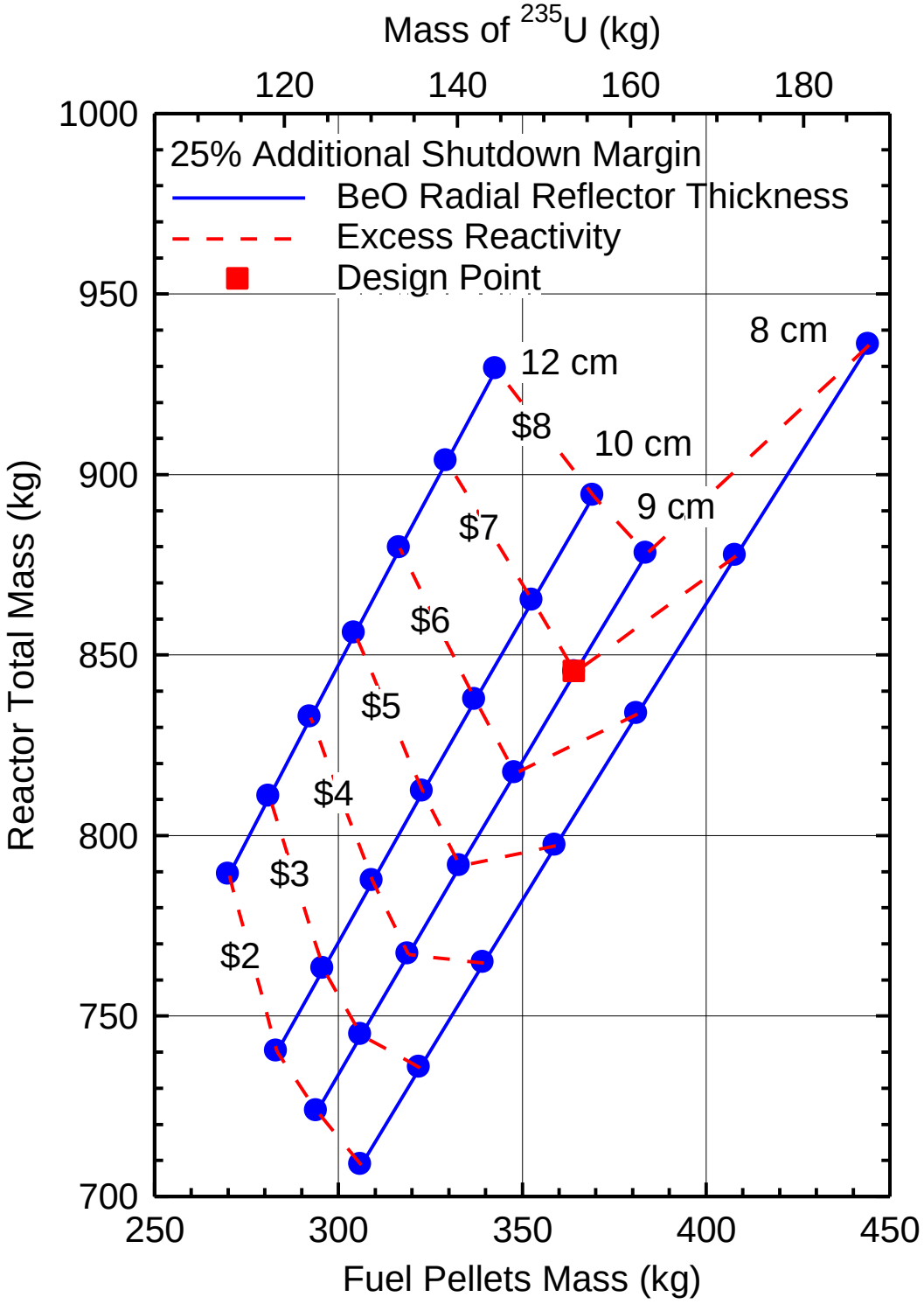

Fig. 4.11. - A design surface for the long life PeBR with 25% ASM at BOL [El-Genk and Schriener 2011].

clean excess reactivity (< \$4 for the reference shutdown case, and < \$5 for the case of 25% ASM) corresponds to the radial BeO reflector of 8 cm (Figs. 4.10 and 4.11). Thus, for these constant excess reactivity levels, increasing the thickness of the BeO radial reflector decreases the fuel pellets loading in the core, but increases the total reactor mass.

Increasing the design cold-clean excess reactivity (> \$4 for the reference shutdown case, and > \$5 for the case of 25% ASM), shifts the minimum reactor total mass to a 9 cm thick radial BeO reflector. As the dimensions of the core loaded with fresh fuel pellets increase, it becomes increasingly difficult to shut down the PeBR with 8 cm thick radial BeO reflector. It would require a large increase in the thickness of the B_4C absorber segments in the control drums, which reduces the reactivity worth of the supplemental regolith and thus require higher fuel pellets loading in the PeBR in order to compensate for the decrease in the excess reactivity BOL.

The calculated reactivity worth of the supplemental regolith reflector for different thicknesses of the BeO radial reflector is displayed in Fig. 4.12. This figure shows the cold-clean excess reactivity for the PeBR with an active core diameter of 44.94 cm, which corresponds to the fuel pellets loading indicated by the square symbol in Fig. 4.11. The difference between the solid and dashed curves in Fig. 4.12 is the regolith's contribution to the cold-clean excess reactivity of the PeBR. For the 44.94 cm diameter reactor core and with 8 cm thick radial BeO reflector, the reactor is -\$0.95 subcritical without regolith, but has a cold-clean excess reactivity of \$5.75 when surrounded by regolith. This is a regolith reactivity worth of \$6.70. The reactivity worth of the supplemental regolith reflector decreases as the thickness of the BeO radial reflector increases; decreases to only \$3.34 for the 44.94 cm diameter core with a 13 cm thick BeO radial reflector.

The PeBR design selected for further investigation is indicated in Fig. 4.11 by the sold square symbol. It has the lowest total mass, a cold clean excess reactivity of \$7.0, a 9 cm-thick radial BeO reflector and 25% ASM at BOL. This PeBR has a total mass of 845.8 kg, including 376.3 kg for the axial and radial BeO reflectors and of 364.4 kg for the fuel pellets in the core. The active core is 44.94 in diameter and 51.68 cm high and

contains ~90,000 fuel pellets in the three sectors. At the reactor nominal thermal power of 471 kW_{th}, the average fission power density in the core is relatively low, ~18.4 kW_{th}/l. This helps limit the temperature rise in the fuel pellets during operation. Neutronics analysis of this PeBR design (Fig. 4.11) is performed to calculate the spatial neutron flux and fission power profiles in the reactor core. The results are presented and discussed next.

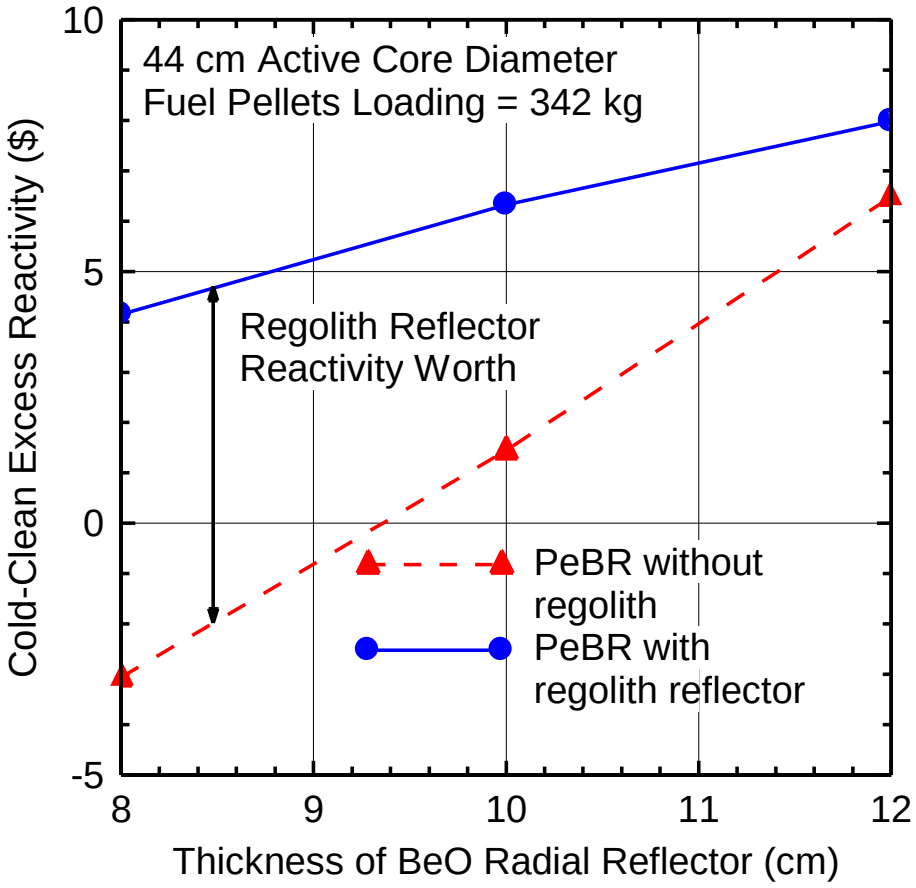

Fig. 4.12 - Reactivity worth estimates of the lunar regolith as a PeBR supplemental reflector [El-Genk and Schriener 2011].

4.4.1. Neutron Energy Spectra and Power Profiles in the Selected PeBR Core

Despite the carbon atoms in the UC kernels, the ZrC coating of the fuel particles and the ZrC matrix of the fuel pellets (Fig. 4.6), the PeBR has hard fast neutron energy spectrum (Fig. 4.13). It varies with radial distance from the cold frit. Near the cold frit (r

= 21.57 cm) and mid-way in the core sectors (r = 14.61 cm), the fast neutrons energy spectra are slightly softer and the peak neutron fluxes are lower than near the hot frit (r = 5.62). This is where the temperatures of the fuel pellets and the He-Xe gas coolant in the core are the highest (Fig. 4.13). The softening of the neutron energy spectrum with radial distance from the hot frit is caused by the moderating effect of the BeO radial reflector. Fission neutrons from the core, as well as those generated by the (n,2n) and (γ,n) reactions in ^{9}Be, lose energy by scattering off the beryllium and oxygen atoms, slightly softening the energy spectrum of the neutrons entering the core from the reflector.

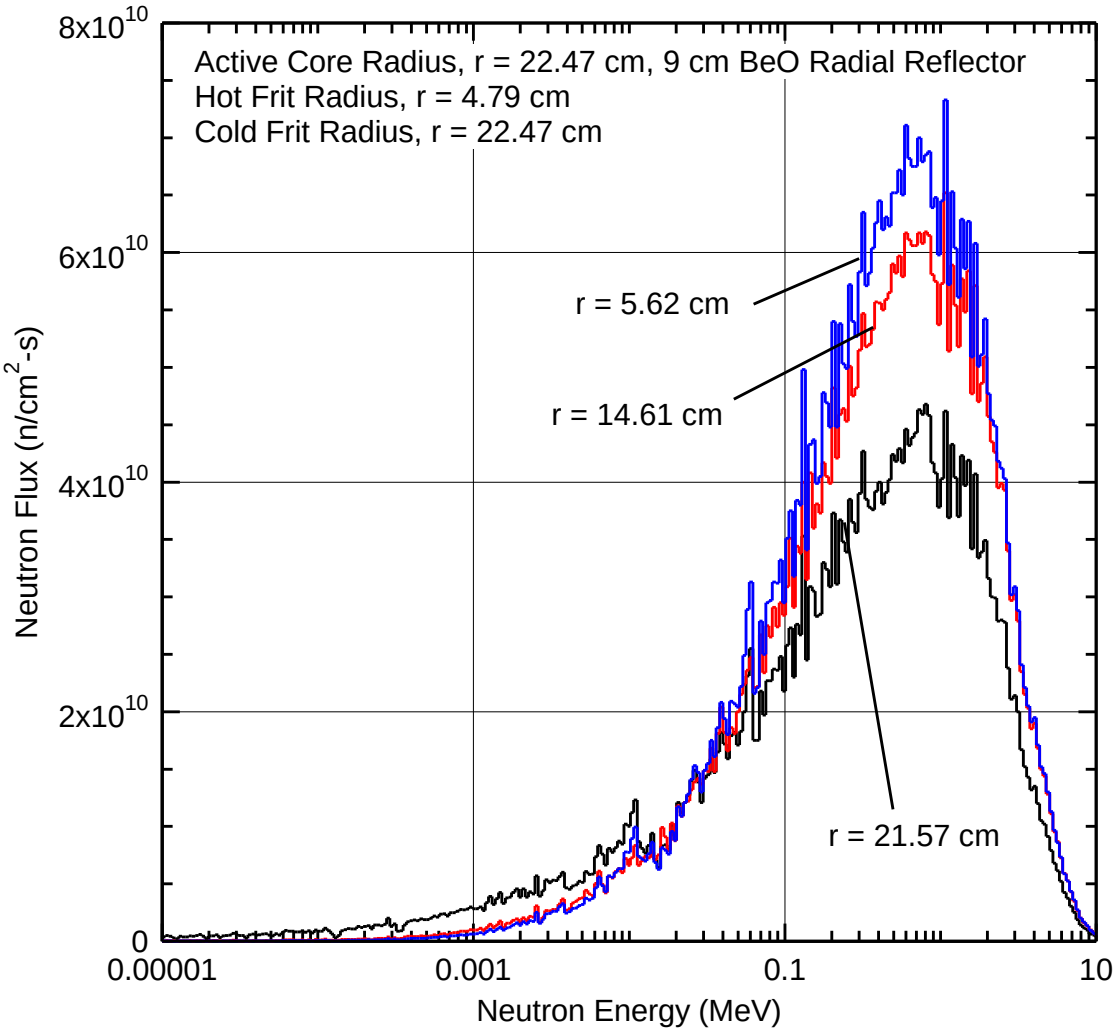

Fig. 4.13 - Neutron energy spectra at different radial locations within the reference long life PeBR core at BOL [El-Genk and Schriener 2011].

These lower energy neutrons increase the fission power generation closer to the cold frit (Fig. 4.14). Fig. 4.14 displays the calculated and normalized radial profiles of the neutron flux and the fission power density in the selected PeBR design. These profiles are calculated using MCNPX F4 (neutron flux) and F6 (neutron energy deposition) tallies within discretized axial and radial sections of the core model geometry. Fig. 4.15 presents the normalized axial profiles of the neutron flux and fission power density. The BOL profiles in Figs. 4.14 and 4.15 are normalized to the average values in the PeBR operating at its nominal thermal power of 471 kW_{th}. The depression in the neutron flux near the center of the core that is void of fuel pellets shifts the peak flux into the reactor core, ~2.6 cm from the hot frit (Fig. 4.14). The radial neutron flux in the core decreases with radial distance following a Bessel, J_o(r), like distribution; and is lowest near to the cold frit.

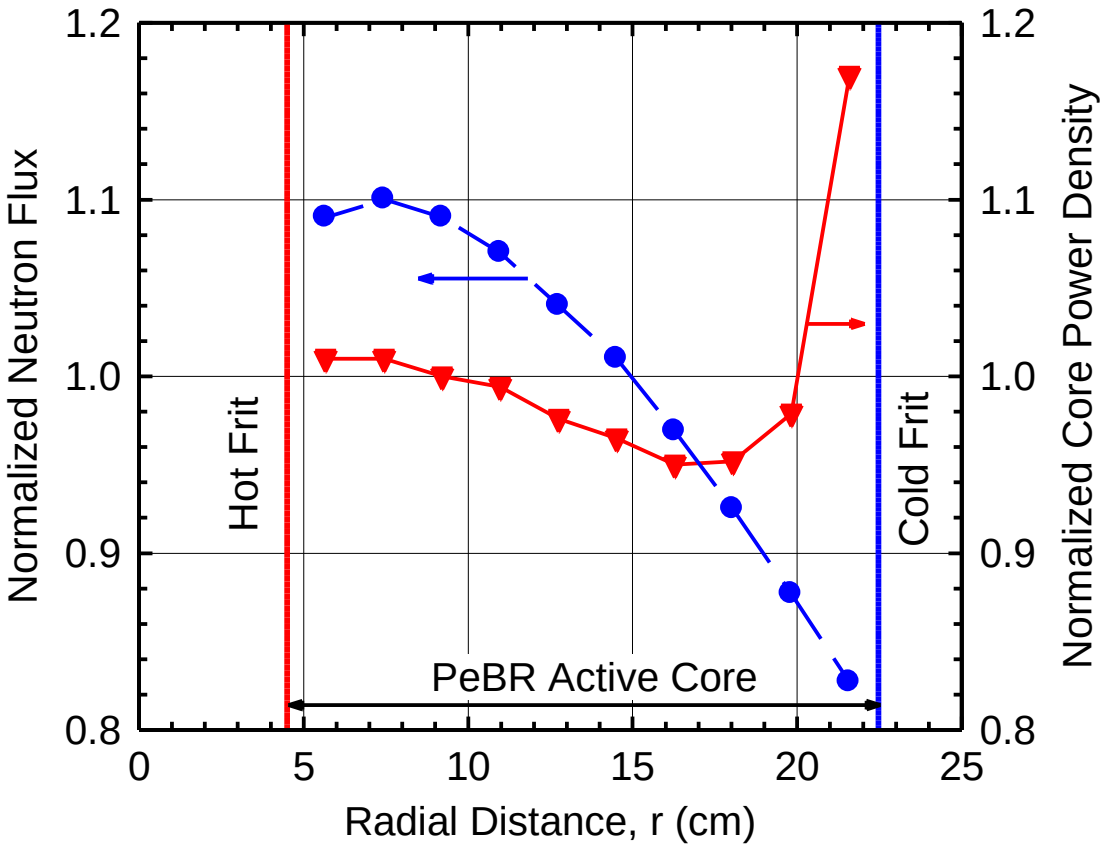

Fig. 4.14. - Normalized radial neutron flux and fission power density profiles for the long life PeBR at BOL [El-Genk and Schriener 2011].

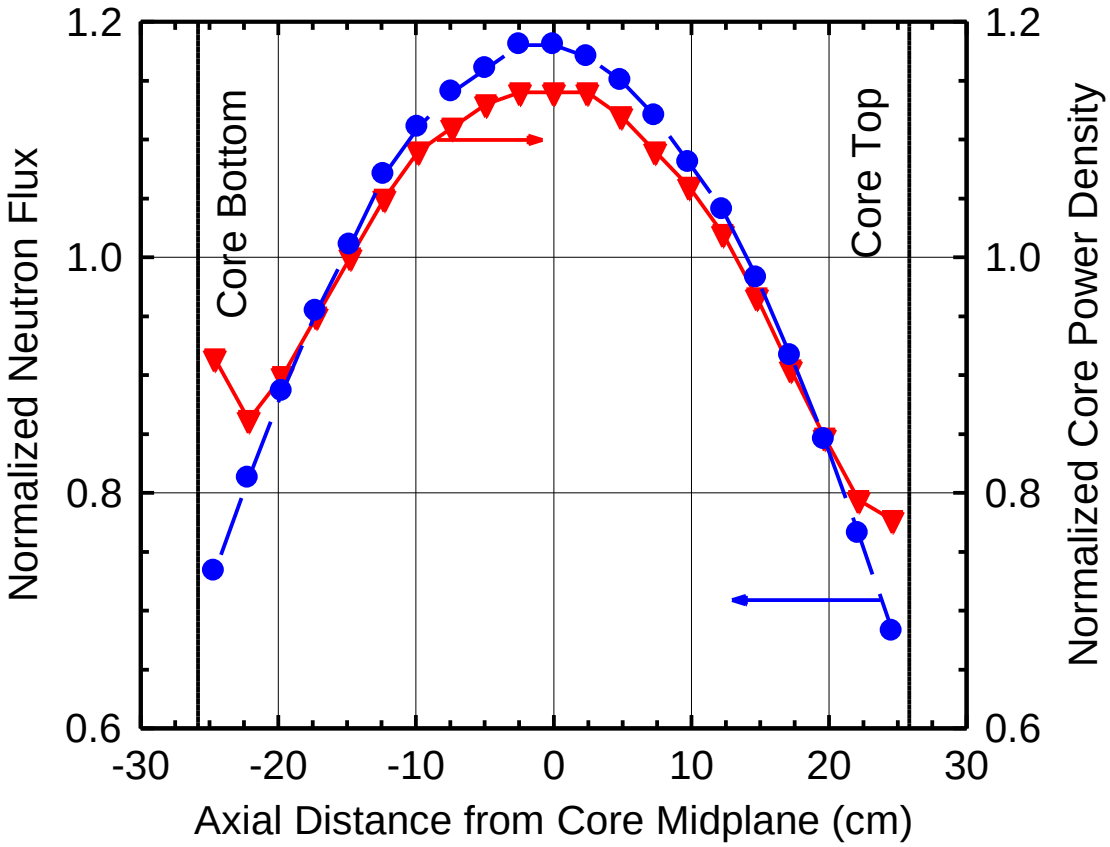

Fig. 4.15. - Normalized axial neutron flux and fission power density profiles for the long life PeBR at BOL [El-Genk and Schriener 2011].

The calculated radial profile of the fission power density is much flatter than that of the neutron flux throughout much of the PeBR core (5.8 cm ≤ r ≤ 20 cm). The fission power density reaches a minimum at r ≈ 17 cm, then increases rapidly with increased radial distance to its highest value near the cold frit (r = 22.47 cm) (Fig. 4.14). The rise in the fission power density near the cold frit is caused by the influx of the moderated neutrons returning from the radial BeO reflector and of the added neutrons produced by the (n,2n) and (γ,n) reactions. The peaking in the fission power density in the PeBR core near the cold frit is expected to decrease over time due the increase in fuel burnup. The axial profiles of the neutron flux and power density are cosine-like distributions (Fig. 4.15). The axial BeO reflectors slightly increases the fission power density near the top and bottom of the PeBR core, but insignificantly affects the neutron axial flux profile. The slightly higher neutron flux and fission power density near the core bottom plate is

due to its closer proximity to the lower axial BeO reflector (Fig. 4.4). The upper axial reflector is placed further away from the active core by the coolant duct connected to the inlet annulus, outside the cold frit. The results of the fuel depletion calculations and the full power operation life of the selected PeBR, indicated by the solid red square symbol in Fig. 4.11, and presented next.

4.4.2. PeBR Operational Life Estimate

The operation life of the selected PeBR design is determined for a nominal thermal power of 471 kW_{th} and time steps of 2 years (Fig. 4.16). The depletion calculations account for the Doppler broadening of the neutron cross sections [Mosteller et al. 2003] at the respective average temperatures of the fuel, reactor vessel and BeO reflector. Results indicated that the PeBR has a small negative temperature reactivity feedback. The calculated estimate of the hot-clean excess reactivity is \$6.86, which is only \$0.14 lower than the cold-clean value of \$7. Such small negative temperature reactivity feedback in the calculations is due to the low thermal expansions of the fuel pellets and the Inconel X750 reactor vessel and structure.

Fig. 4.16 indicates that the selected PeBR design has an operation life of 66 FPY, which corresponds to an average fuel burnup of 70.1 MWd/kg. The PeBR generates 11,354 MWd of energy over this operational life. The ^{235}U inventory in the fuel pellets decreases by < 10% over the reactor's operation life of 66 FPY, and almost linearly with operation time (Fig. 4.16). This is because the average neutron flux in the core changes very little over time. Operating the PeBR for 66 FPY, however, may require intermittent replacements and maintenance of the power system components, such as the turbo-machine units and the water heat pipes radiators, and irradiation testing of the reactor structure materials.

Over the estimated operation life of 66 FPY for the PeBR, the Inconel X750 reactor vessel would be exposed to a fast neutron fluence of $\sim 1.82 \times 10^{22}$ n/cm^2 (E > 0.1 MeV) or ~10.1 dpa, estimated using a flux-to-dose relationship for Inconel X750 irradiated in EBR-II [Allen et al. 1999]. The EBR-II irradiation experiments showed that Inconel X750 exhibits classic radiation hardening at ~10.1 dpa, but little radiation induced

swelling [Allen et al. 1999]. At such irradiation exposure, the increase in the yield strength and the ultimate tensile strength are ~60% and ~10%, respectively. Despite the decrease in ductility of the Inconel X750, thermal annealing at the high temperatures in the PeBR should reduce the loss in ductility [Allen et al. 1999]. Since the irradiation experiments in the EBR-II [Allen et al. 1999] were performed at lower temperatures (650-680 K) than in the PeBR (750-800 K), additional irradiation testing might be required in a future hardware development program.

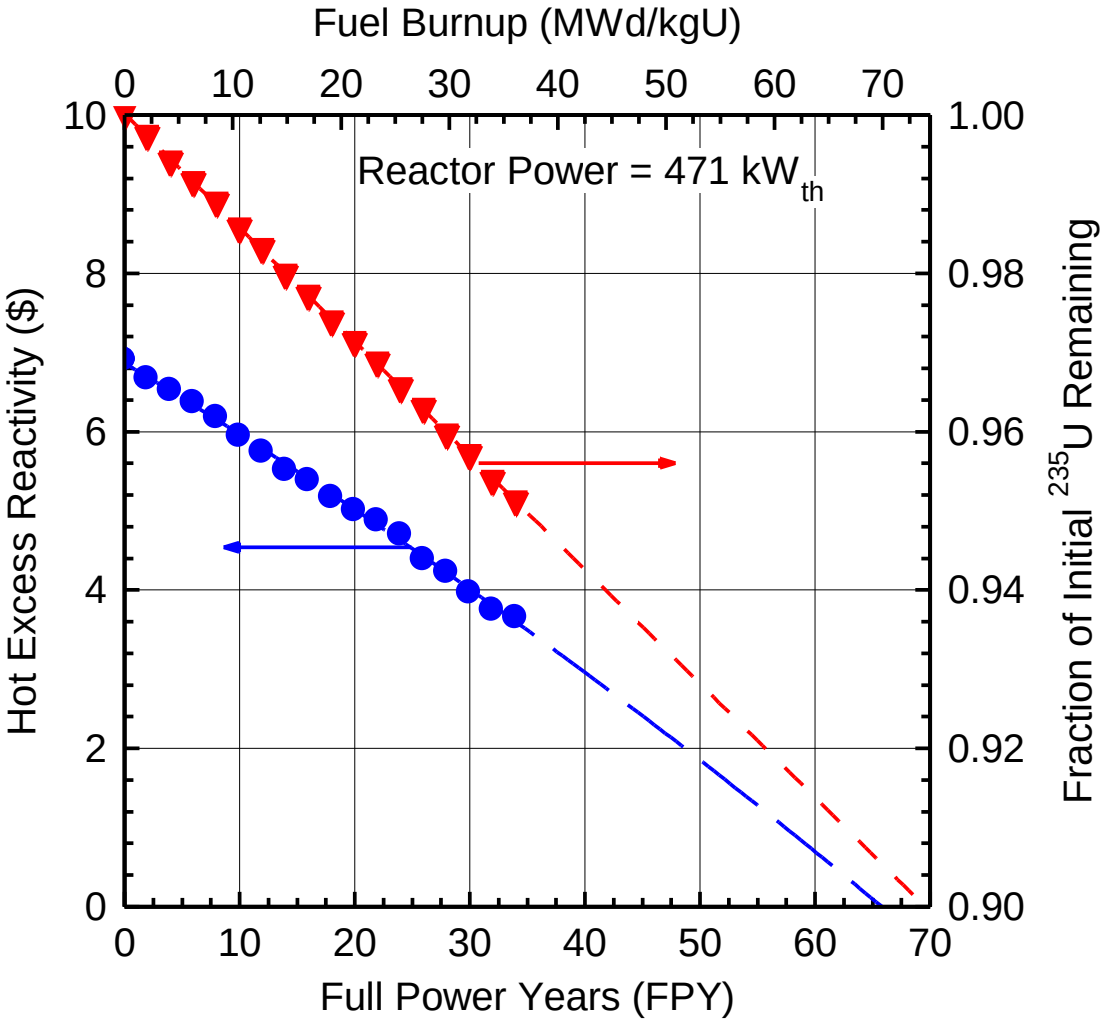

Fig. 4.16. - Estimates of the full-power operation life of and the ^{235}U inventory in the reference PeBR for lunar surface power [El-Genk and Schriener 2011].

After operating continuously for 66 FPY, the used fuel in the post-operation PeBR contains 138.5 kg of ^{235}U or ~90% of the initial ^{235}U in the fresh fuel pellets. Due to the simultaneous depletion of the ^{234}U and ^{238}U isotopes, the ^{235}U enrichment in the used fuel (~92%) is only slightly lower than in the fresh fuel (95%) (Fig. 4.16). Such high fissile inventory in the used fuel is attractive for eventual recovery and reuse. The long operation life of the PeBR is made possible by fueling the reactor on the lunar surface. The next section performs design and analyses of the fuel pellets launch canisters used transport to transport the fresh pellets to the Moon.

4.4.3. Analysis of Fuel Pellets Launch Canisters

This section presents the results of the neutronics analysis performed to size and optimize the launch canisters design of the PeBR spherical fuel pellets to the lunar surface. This analysis ensures that the loaded canisters with fresh fuel pellets are sufficiently subcritical during launch and when submerged in wet sand and flooded with seawater, in the unlikely event of a launch abort accident. As indicated earlier, the PeBR would be launched unfueled and then loaded with fresh fuel pellets after it is placed below grade on the lunar surface and surrounded by regolith. Each launch canister is large enough to contain sufficient fuel pellets to fill one of the three core sectors in the reference PeBR design develop in Section 4.2. The fuel pellets launch canisters are sized to remain at least -$1.0 subcritical during launch and when submerged in wet sand and flooded with seawater, in the unlikely event of a launch abort accident. These requirements are applied to the individual canisters and to the bundle of the three canisters, assuming the canisters are surrounded by wet sand comprised of 30 vol% seawater and 70 vol% sand. This wet sand produces higher reactivity than dry sand or sand/water mixtures with a higher water fraction than 30 vol%. The neutronics analysis of the canisters is performed for two packing conditions of the fresh fuel pellets: random (61 vol%) and face-center cubic packing (74 vol%).

The cylindrical stainless steel launch canisters (Fig. 4.17) have a thin neutron absorber liner. The liner is comprised of dispersed particles of B_4C, fully enriched in ^{10}B in aluminum with a volume fraction of 45%, in aluminum [Ceradyne 2010]. This and other boron–aluminum composites are widely used for criticality control in the nuclear

industry. Though the neutron absorber liner provides some structural support, the stainless steel wall of the canisters principally provides the needed structural strength. The canisters loaded with randomly packed fresh fuel pellets have a height-to-diameter ratio of 7.6:1. This elongated shape increases the neutron leakage, reducing the reactivity. The tapered upper section readily discharges the fresh pellets into the PeBR core sectors on the lunar surface.

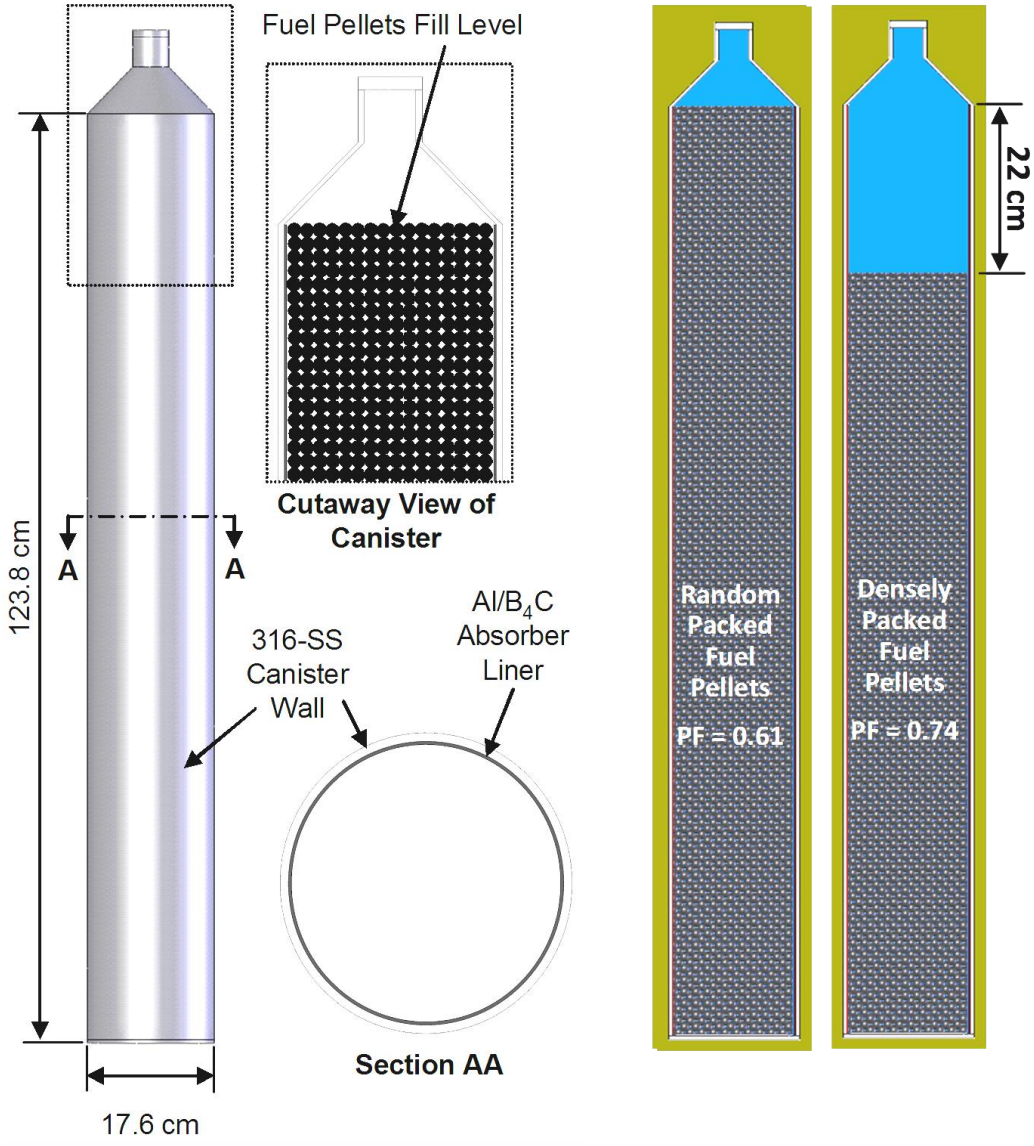

Fig. 4.17. - A schematic of launch canisters of fresh fuel pellets to the lunar surface [El-Genk and Schriener 2011].

The mouth of the canister neck is four pellet diameters wide to avoid jamming during loading the core sectors with pellets. The fueling channels connect the openings of the launch canisters to the loading ports in the top metal plates of the PeBR core sectors. The fresh fuel pellets pour out of the canisters into the reactor sectors, either by gravity or assisted by a gas back pressure. After the PeBR sectors are loaded with randomly packed fresh fuel pellets, gas-tight valves close the fueling channels. Subsequently, the PeBR core and CBC loops of the power system are charged with the He-Xe gas mixture to an initial pressure of 1.3 MPa.

The neutronics analysis for determining the subcriticality of the launch canisters in the unlikely event of a launch abort accident investigated the effects of changing the thickness of the Al-B_4C liner and the packing fraction of the fresh fuel pellets on the criticality of the canisters. The analysis assumes that the canisters are flooded with seawater and reflected on all sides with wet sand (70 vol% quartz sand and 30 vol% seawater). Fig. 4.18 presents the calculated values of the cold-clean reactivity of the canisters for two packing factions (PFs) of the fresh fuel pellets: random (PF = 0.61) and tight face-centered cubic packing (PF = 0.74) (Fig. 4.17). The latter is the most compact packing of the fresh fuel pellets in the launch canisters. Increasing the packing fraction of the fuel pellets in the launch canisters from 0.61 to 0.74 (Fig. 4.18) decreases the effective height the packed pellets and hence their height-to-diameter ratio inside the canisters from 7.6 to 6.3. This decreases the neutrons leakage and increases reactivity. The corresponding decrease in the average volume porosity from 0.39 to 0.26, however, reduces the effective water-to-fuel ratio in the flooded the canisters. The net effect is a decrease in the reactivity as the packing fraction of the fresh fuel pellets in the launch canisters increases (Fig. 4.18).

Fig. 4.18 shows that even without an Al/B_4C liner, the submerged and flooded fuel pellets individual canisters are at least -\$1.0 subcritical; however a tight cluster of three canisters would be highly critical. With a thin Al/B_4C liner (~0.8 mm thick), the cluster of three canisters, when submerged in wet sand and flooded with seawater, would be -\$1.0 subcritical, and the individual canisters would be ~-\$47 subcritical. Increasing the thickness of the Al-B_4C liner only slightly to 1 mm, makes the individual canisters ~-\$49

subcritical and the cluster of three canisters with randomly and high packed fresh fuel pellets would be ~-$3.5 and -$6.5 subcritical, respectively (Figs. 4.17 and 4.18). On the lunar surface the canister s are used to fill the PeBR core sectors. The next section presents the results of a fuel pellets loading simulation for one of the three core sectors on the Moon.

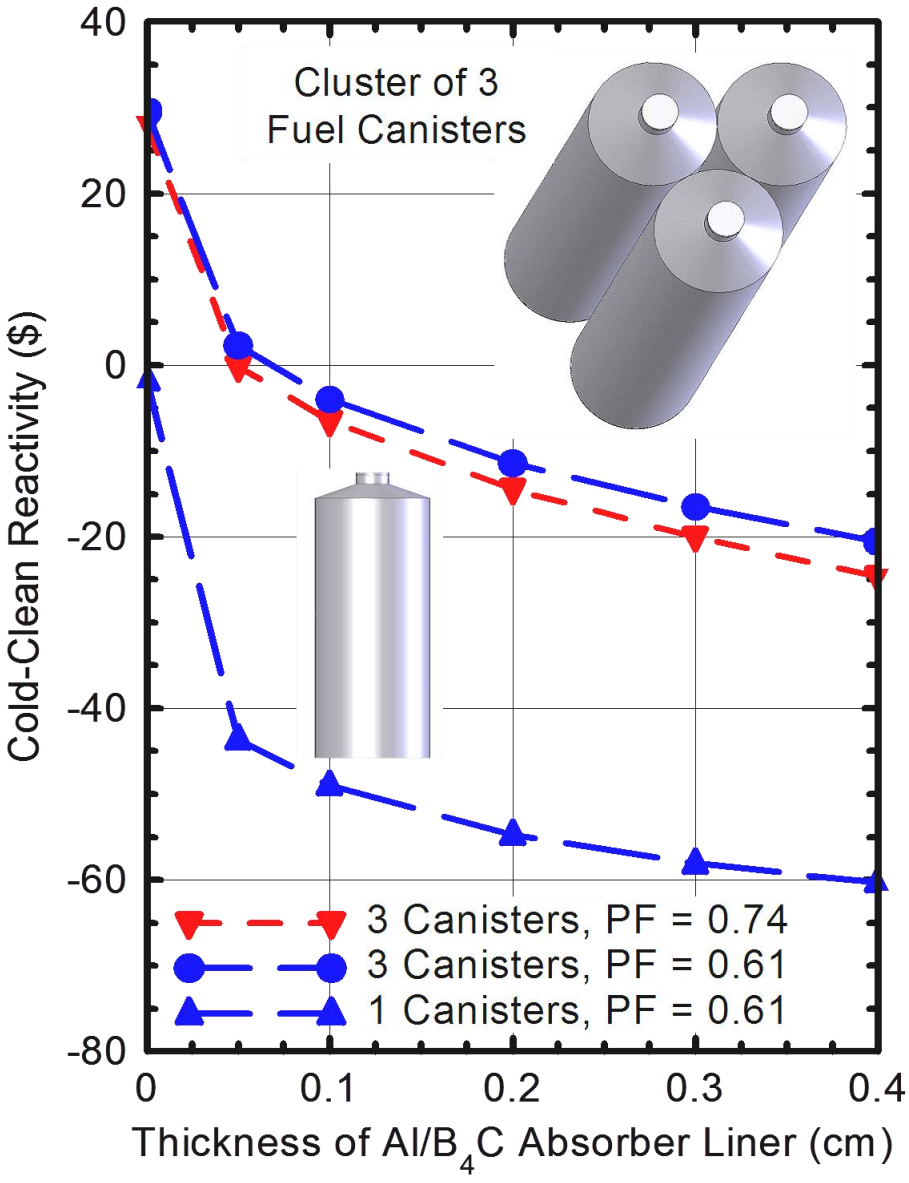

Fig. 4.18 - Criticality estimates of the canisters loaded fresh fuel pellets in the unlikely event of a launch abort accident [El-Genk and Schriener 2011].

4.5. Fuel Loading on the Lunar Surface

Launching the reactor unfueled and loading it with fuel pellets on the lunar surface enables the PeBR to achieve a very long operational life. This design feature, however, is based on the PeBR being able to be filled with pellets on the Moon by pouring the spherical fuel pellets into the core sectors under lunar gravity. The objective of this section is to numerically simulate the loading process of a PeBR core sector on the Moon with fuel pellets (Figs. 4.4-4.6). The 3-D simulation uses the Discrete Element Method (DEM) capabilities in the commercial software package STAR-CCM+ version 6.02 [CD-adapco 2011]. The transient solver models the interactions of the spherical fuel pellets with the each other and the walls of the core sector. The results are used to provide estimates of the spatial porosity distribution throughout the sector to assist in improving future neutronics and thermal-hydraulics analysis of the PeBR.

4.5.1. Simulation Methodology

The present 3-D numerical analysis simulates the loading process of a core sector with pellets on the lunar surface. The transient loading analysis employs the commercial software package STAR-CCM+ version 6.02 [CD-adapco 2011]. The DEM option is an extension of the Lagrangian multiphase transport model in this code simulates the pellets' interactions during loading. The STAR-CCM+ simulation uses classical particle mechanics to simulate the flow of the pellets through the loading ducts and their interactions in the core sector. Each discrete element in the granular flow simulation represents a single fuel pellet. The two phase pairs (pellet-pellet and pellet-wall) defined in the DEM analysis account for the elastic and friction properties in the interactions. The Hertz-Mindlin no-slip contact model in the code simulates the physical interactions of the two-phase pairs. This model treats the fuel pellets as elastic spheres using two spring-dashpot oscillators for the normal and tangential forces. It also accounts for the repulsive forces and viscous dampening for the two-phase-pairs.

In the 3-D transient fuel loading simulation, the pellets emerge from a square-pitch injector grid inside the 4 cm diameter upper loading ports (Fig. 4.4). Two evenly spaced loading ports at the top of the core are used to achieve a more even distribution for the

fuel pellets, and minimize the piling of pellets directly under the openings. From the opening, the pellets are assumed to drop freely into the core sector at a rate of 100 pellets per second. This rate might be different from the actual rate, and further analysis would be needed investigate the effect of changing the loading rate of the pellets on the results. At a loading rate of 100 pellets/s, the present transient simulation of loading a core sector with pellets on the Moon uses a time step of 10 ms. Initial injection velocity of the pellets through the loading ports into the core sector is that of a pellet after free falling a distance of 1.18 m in the Moon gravity. This is the drop distance of the pellets from the lunar surface to the loading ports in the top plate of the reactor vessel (Fig. 4.6).

Table 4.1. – Discrete Elements Method (DEM) simulation phase parameters.

Phase	Pellet	Wall
Density, kg/m^3	7,687.8	8,000
Poisson Coefficient	0.3	0.3
Young's Modulus, MPa	4,800	193,000

The numerical simulation tracks the pellets as they emerge through the loading ports and fall into the core sector. The simulation captures the movements, the internal shifts and the compaction of the pellets to form a randomly packed bed in the core sector. The axial and radial distributions of the average volume porosity of the packed pellets depend on their final position in the sector. These distributions are determined in the analysis by tracking the centers of loaded pellets and dividing the pellets' packed bed into small axial and radial elements.

The loading simulation is performed on a desktop computer. The primary objective was not to precisely determine the local volume porosity, but rather provide a preliminary understanding and assessment of the loading process. Due to the stochastic nature of the simulation, multiple runs would be needed to accurately calculate the volume porosity

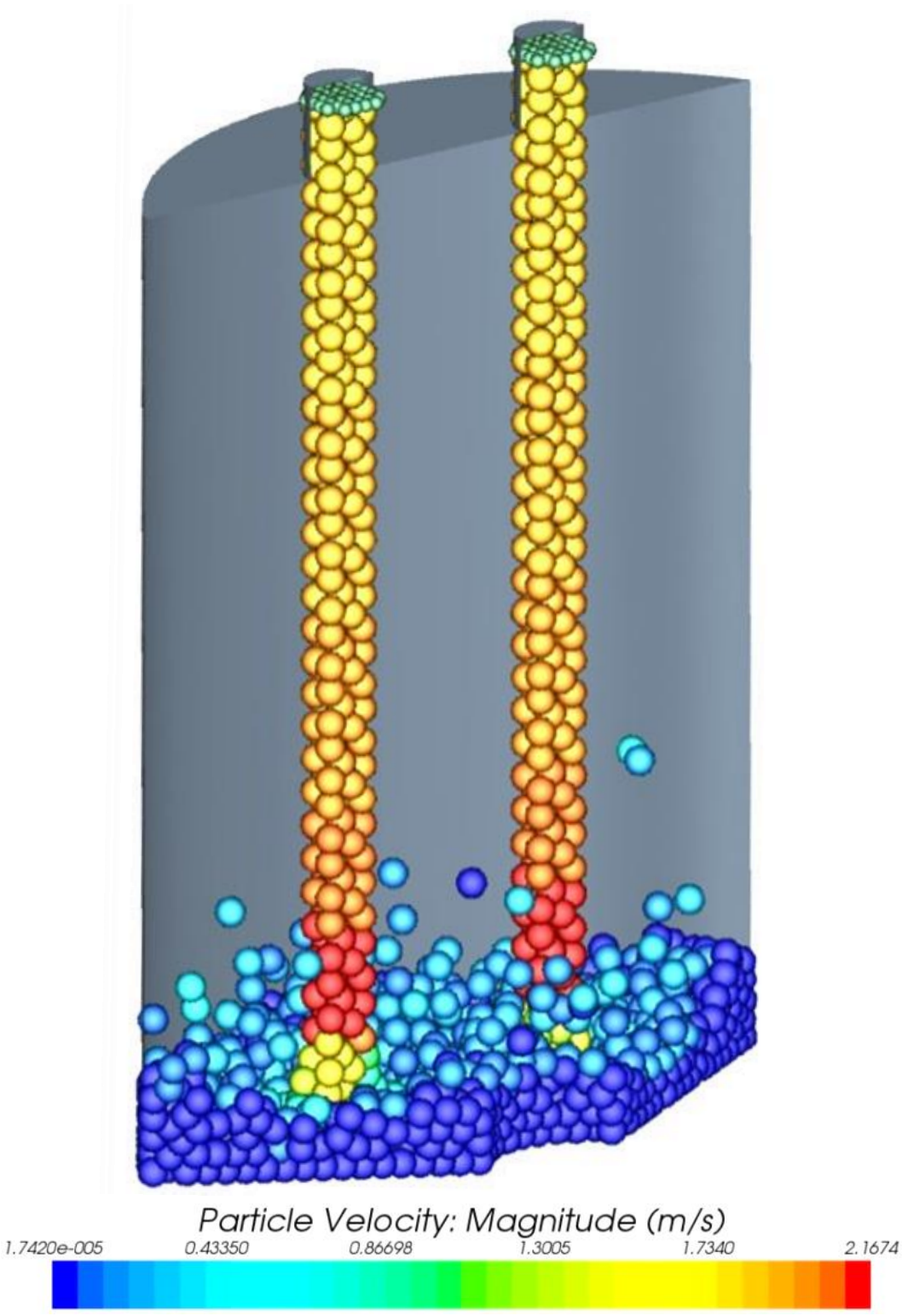

Fig. 4.19. - A PeBR core sector while being loaded with fuel, containing ~2,000 fuel pellets [Schriener and El-Genk 2012c].

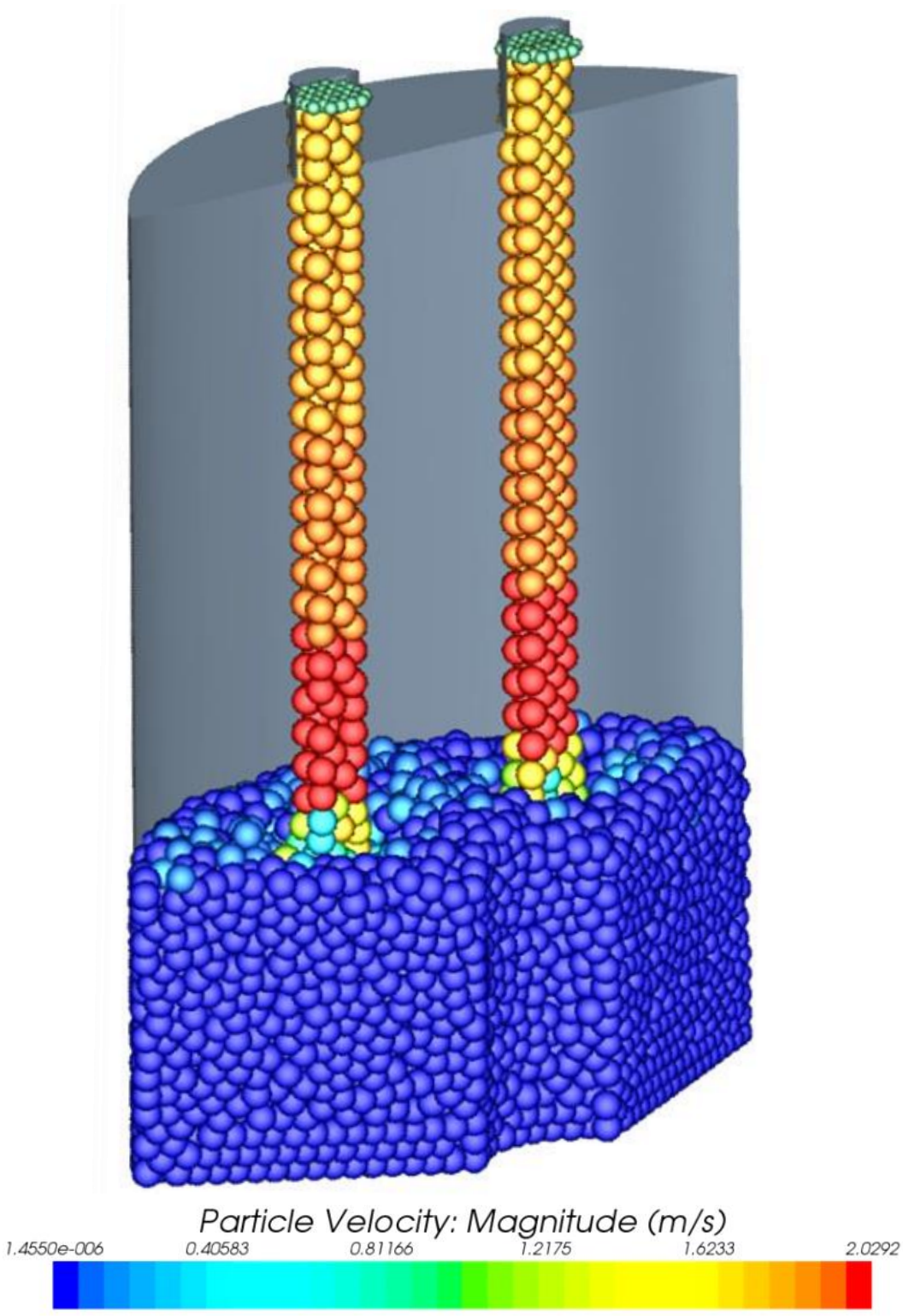

Fig. 4.20. - A PeBR core sector while being loaded with fuel, containing ~10,000 Fuel Pellets [Schriener and El-Genk 2012c].

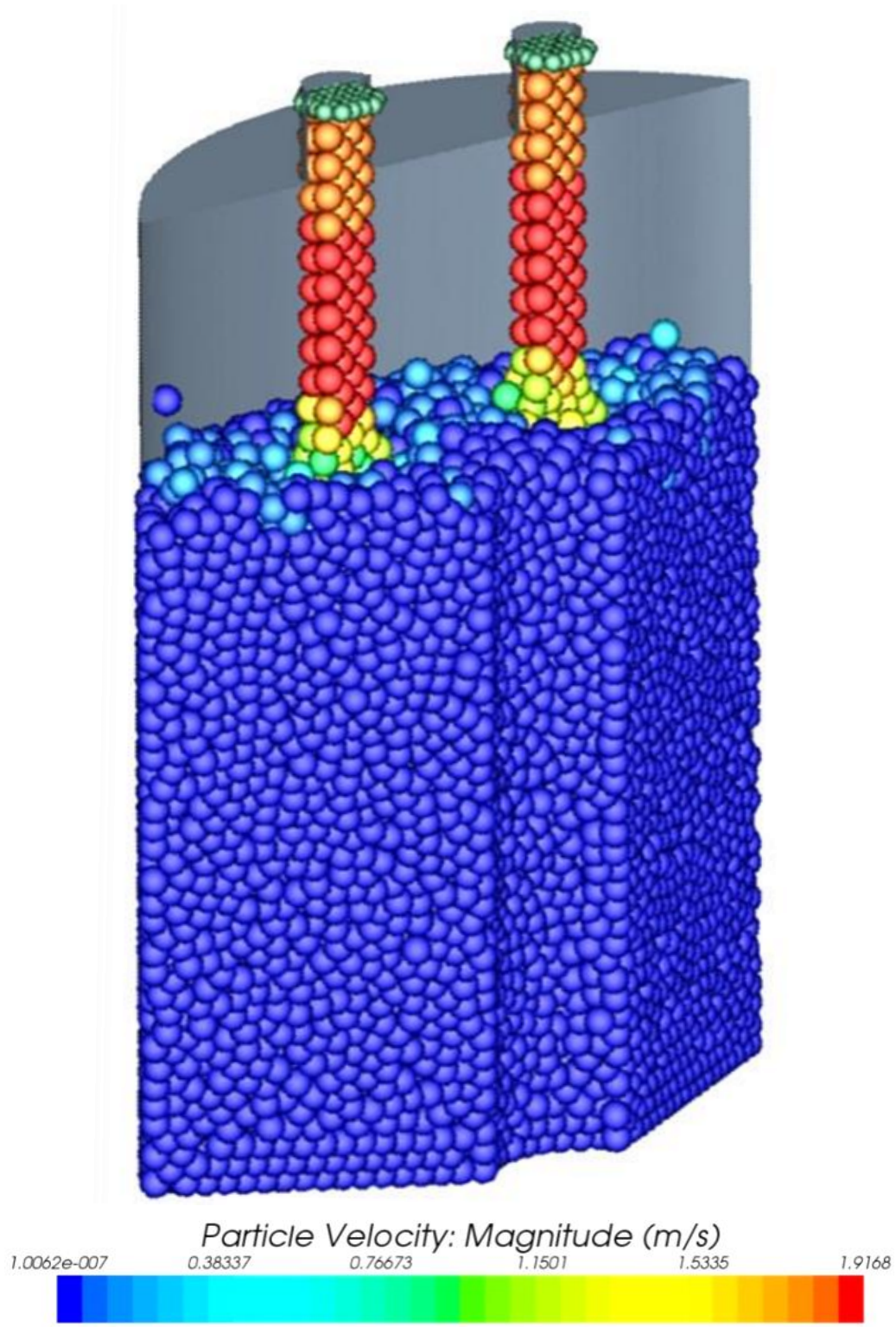

Fig. 4.21. - A PeBR core sector while being loaded with fuel, containing ~22,000 Fuel Pellets [Schriener and El-Genk 2012c].

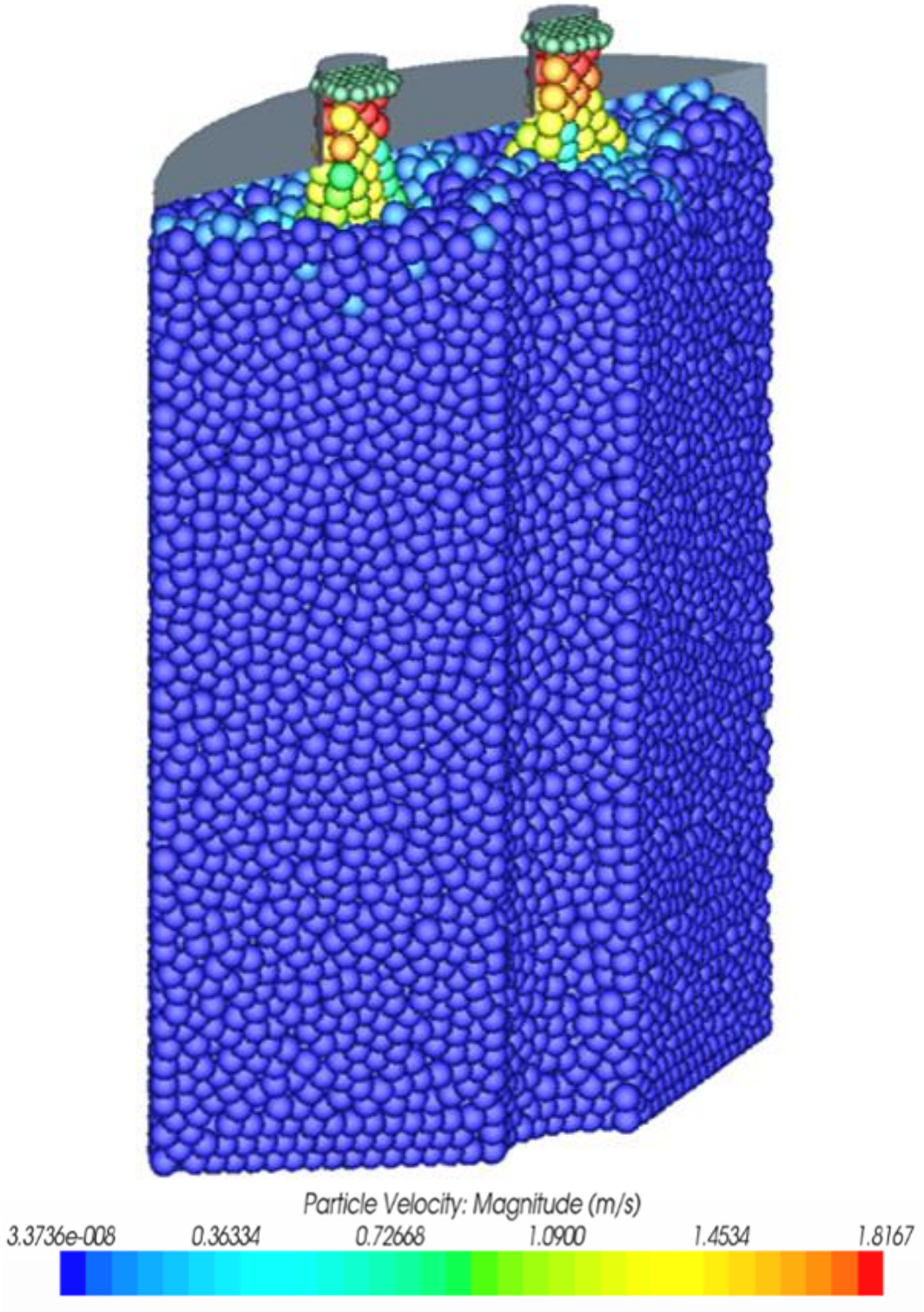

Fig. 4.22. - A PeBR core sector while being loaded with fuel, containing ~28,000 Fuel Pellets [Schriener and El-Genk 2012c].

distributions in the core sector. The next section discusses the results of the performed loading simulation of a core sector with fuel pellets on the lunar surface.

4.5.2. Results and Discussion

This section discusses the results of the present numerical analysis of loading a PeBR core sector with fuel pellets on the lunar surface. At the start of the simulation discrete spherical fuel pellets are injected through two evenly spaced loading ports into an empty core sector. Figs. 4.19–4.22 present snapshots of the various stages of the loading the core sector with pellets. The first batch of falling pellets strike the Inconel X-750 bottom wall of the reactor vessel. These pellets scatter and bounce considerably around the nearly empty sector (Fig. 4.19). This chaotic bouncing and scattering, however, only occurs early in the loading process. After a few thousand pellets have been loaded into the sector, the violent scattering of the falling pellets (Fig. 4.19) largely ceases. Subsequently, a randomly packed bed of the loaded pellets builds up, pushing against the hot and cold frits and the dividing walls with adjacent core sectors (Figs. 4.20-2.21). This stage continues for the remainder of the loading process, with the forming packed bed compacting slightly with time under the weight of the loaded pellets (Fig. 4.22).

Figures 4.24a and b show images of the upper portion of sector at the final stage of loading it with pellets. At this stage, the 28,126 pellets loaded into the sector represent 94.2% of the total in a launch canister (29,854 pellets). In Figs. 4.23a and b, the lateral distribution of pellets across the top of the mostly loaded sector is relatively flat, with a few high and low points. A flat distribution is desirable for an orderly loaded sector. The pellets at the top slope down by one pellet diameter from the center to the hot frit and by as much as 6 pellet diameters to the cold frit (Fig. 4.23). The shallow depressions appearing near the injection ports are due to the scattering of the loaded pellets away from their points of impact in the core sector. Recoiling pellets form ridges that are up to 2-pellet diameter high. The formed depressions and ridges at the top of the core sector that is partially loaded with pellets are also visible in Figs. 4.20-4.22. The next section analyzes the distribution of the randomly packed pellets to calculate the spatial porosity distribution.

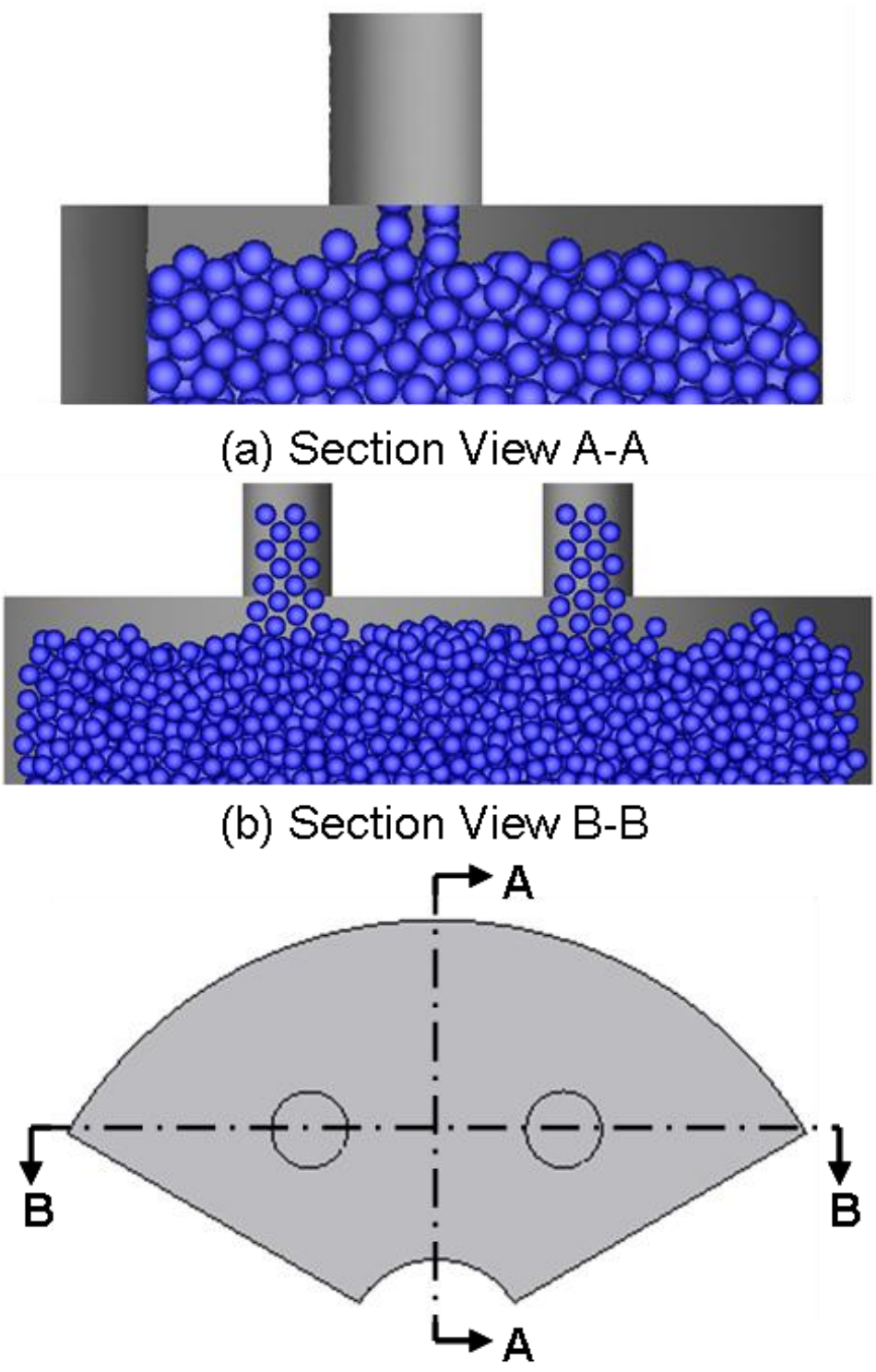

Fig. 4.23. - Section views of the top of partially loaded sector with fuel pellets (pellets to scale) [Schriener and El-Genk 2012c].

4.5.3. Spatial Porosity Distributions

One of the objectives of the present numerical simulation is to determine the effective volume porosity and the number of fuel pellets needed for a fully loaded sector (Figs. 4.24 and 4.25). The calculated axial and radial profiles of the average volume porosity in a core sector that is almost fully loaded with pellets (Fig. 4.23) are presented in Figs. 4.24 and 4.25. For the axial porosity profile, the sector is divided into 26, 2 cm thick axial segments. The average volume porosity in each segment is then determined from the calculated volume fraction of the pellets in that segment. Similarly, for the determination of the radial porosity profile each axial segment in the sector is divided into 100 radial sections of equal width. The average volume porosity in each section is then determined from the calculated fraction of each pellet's volume within the radial section.

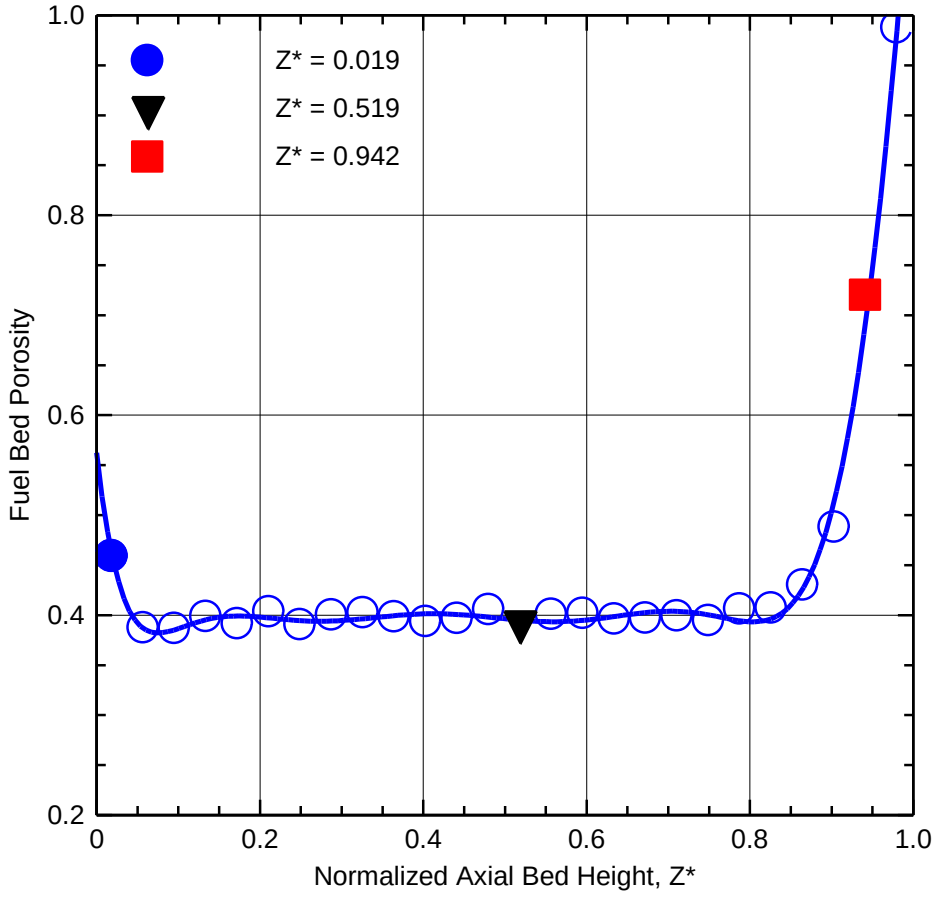

Fig. 4.24. - Calculated axial distribution of the volume porosity of loaded pellets in a PeBR core sector [Schriener and El-Genk 2012c].

Figure 4.24 presents the calculated axial distribution of the average volume porosity in the core sector that is almost fully loaded with pellets (Fig. 4.23). Figure 4.25 compares the radial distributions of the volume porosity at different axial locations in the sector. The axial porosity distribution in Fig. 4.24 is flat over much of the sector, averaging 0.39 - 0.41, except near the top and bottom walls where the volume porosity is much higher. A median porosity of 0.40 is that of randomly packed spheres.

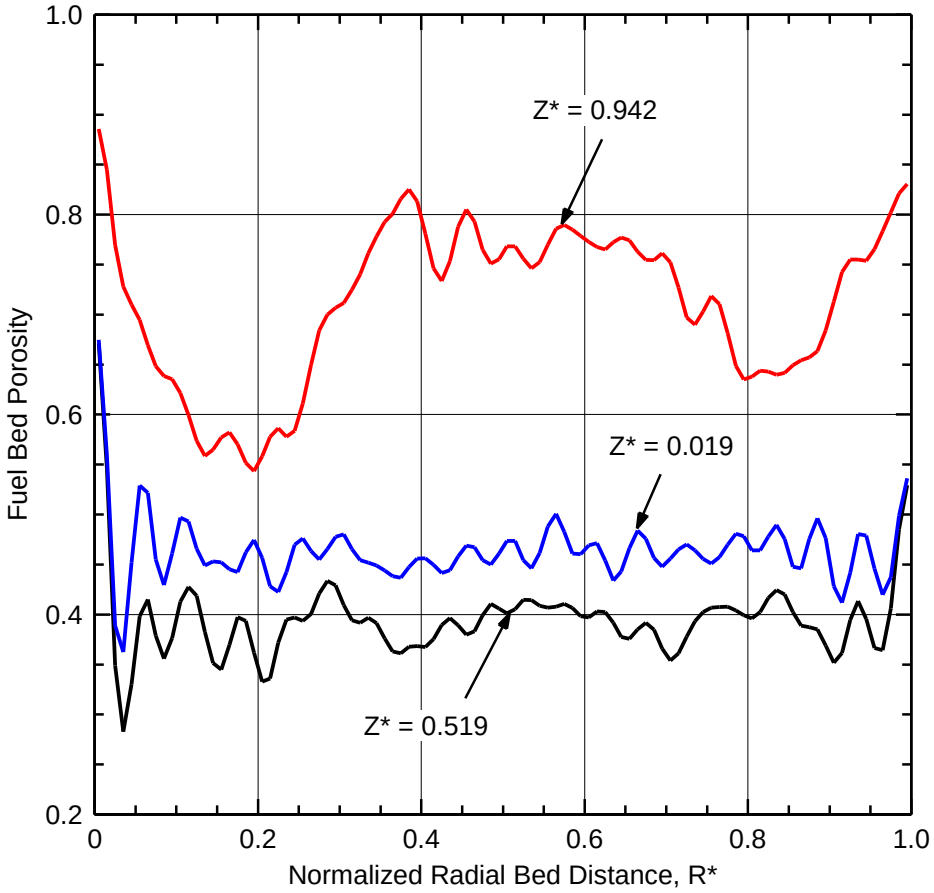

Fig. 4.25. - Radial distributions of the volume porosity of loaded pellets at different axial locations [Schriener and El-Genk 2012c].

The local volume porosity at the flat bottom of the sector is 0.55, but drops to 0.39-0.41 within 2 cm from the bottom (Fig. 4.24). The random arrangement and loose packing of the pellets near the top of the sector (Fig. 4.23) result in a much higher local bed porosity (Fig. 4.24). The calculated radial distributions of the volume porosity in the

sector that is not quite fully loaded with pellets (Fig. 4.23) are presented in Fig. 4.25 at different axial locations.

The radial porosity is highest next to the hot frit (R* = 0). It oscillates for about 3 pellet diameters (R* = 0.15) before approaching the mean values of the randomly packed pellets at the specified axial locations. The mean porosity increases from 0.40 near the sector mid-plane (Z* = 0.519) to more than 0.70 near the top of the sector (Z* = 0.942). Near the bottom plate (Z* = 0.019), the mean volume porosity is about 0.45. These porosities are higher than that assumed initially for PeBR core sector of 0.39, suggesting that less than 29,854 pellets are needed to fully load the sector.

Figure 4.25 shows that the increase in the volume porosity in the core sector near the cold frit (R* = 1) is smaller than that near the hot frit. The larger radius of the cold frit allows for a closer packing of the spherical pellets. Near the top of the core sector that is not fully loaded with pellets (Z* = 0.942), the radial porosity distribution is uneven, peaking at the hot and cold frits as well as in the middle of the sector. This distribution and the high porosities are indicative of the scattering of the loaded pellets away from the loading ports.

Fig. 4.26 shows three plane views of the loaded pellets at the three axial locations indicated in Fig. 4.25. The dots in Figs. 4.26a - c represent the centers of the loaded pellets, shown at a reduced scale for clarity. The images in these figures show loosely packed pellets near the cold and hot frits and the dividing walls with the adjacent sectors in the PeBR core. The high volume porosity of the loaded pellets near the top of the sector (Figs. 4.24 – 4.25) is clearly visible in Fig. 4.26a. It shows loose packing of the pellets directly below the loading ports (Figs. 4.22 and 4.23). Near the bottom of the sector (Fig. 4.26c) the pellets are orderly arranged, which is not the case near the middle and at the top of the sector (Figs. 4.27a and b). However, the pellets near the middle of the sector (Fig. 4.26b) are more packed than near the bottom and top (Figs. 4.26a and c).

The research in this chapter developed the PeBR for lunar surface power with a long operation life. The highlights of this research are summarized next.

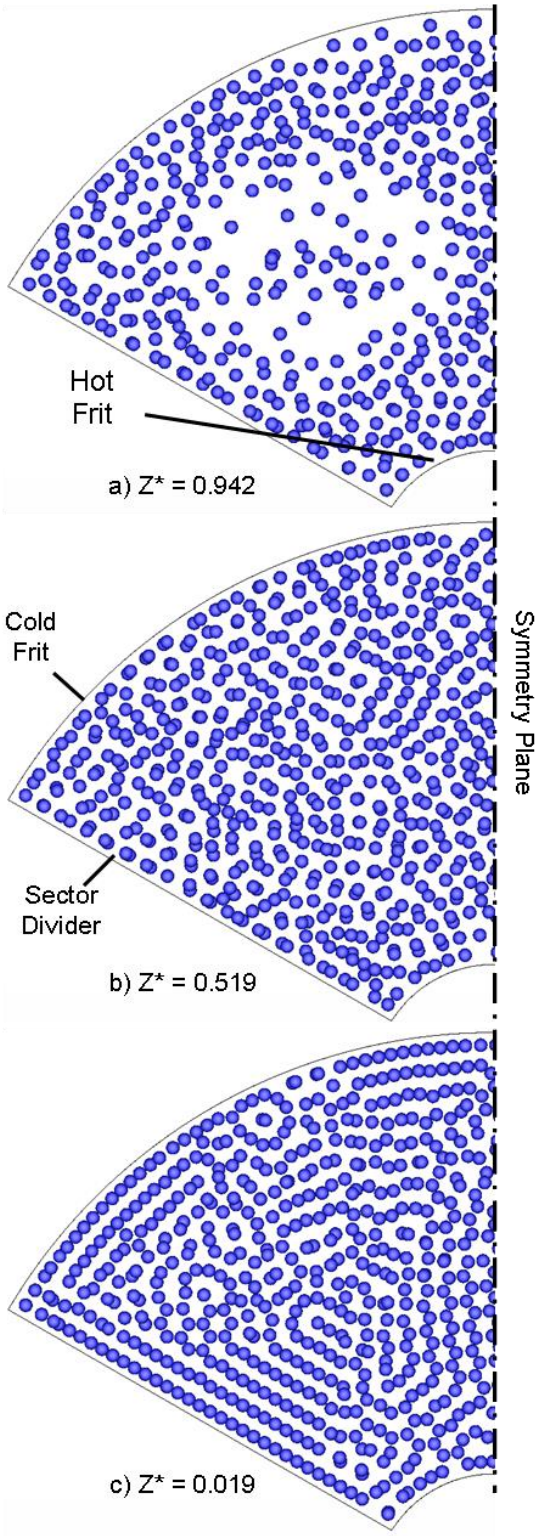

Fig. 4.26. - Plane-view images of the loaded fuel pellets at selected axial locations in the PeBR core sector (see Fig. 4.24) (pellets not to scale) [Schriener and El-Genk 2012c].

4.6. Highlights and Concluding Remarks

This chapter describes the results of neutronics and fuel loading analyses of the PeBR for lunar surface power. This research investigated the possibility of the PeBR concept to achieve a very long operational life, by launching the reactor to the moon unfueled and subsequently loading it with spherical pellets only after it is emplaced below grade and surround by lunar regolith. Analyses was performed to develop a reference PeBR design and estimate its operational life, design safe fuel pellets launch canisters, and investigate loading the core sectors with fuel pellets on the Moon. The results of these analyses show that:

- A BeO reflector thickness of 9 cm results in the lowest total reactor mass for long life PeBRs. The selected reference PeBR design has \$7 of cold-clean excess reactivity and a 9 cm BeO reflector with 25% ASM.
- The PeBR with \$7 cold-clean excess reactivity and \$6.86 hot-clean excess reactivity can operate for up to 66 years at a nominal power of 471 kW_{th}.
- Safety analysis of the fuel pellets transport canisters, using a combination of favorable geometry and neutron absorbers, demonstrated the design to be highly subcritical in the postulated water submersion accident conditions.
- The spherical fuel pellets can be loaded into the PeBR core sector in lunar gravity

By fueling the reactor on the Moon, the PeBR can achieve an operational life well beyond that of the SC-SCoRe. The research in this chapter shows that lunar power reactors designed to be fueled on the Moon can result in simplified launch procedures and very long operational lives. The SC-SCoRe and PeBR lunar surface reactors developed in this dissertation are both capable of long operational lives. After the end of lives, however, the reactors must be safely stored to allow the radioactive fission products and actinides accumulated in the fuel during operation to decay down to a safe level. The next chapter investigates the post-operation storage of these reactors on the Moon.

5. POST-OPERATION STORAGE OF REACTORS FOR LUNAR SURFACE POWER

This chapter presents post-operation analyses of the SCoRe and PeBR concepts while in long term storage below grade on the lunar surface. The performed analyses investigate the decay of the accumulated radionuclides within the used fuel in the post-operation reactors. Estimates of the radioactivity source terms are determined at the End-of-Life (EOL) using the output of the MCNPX fuel depletion calculations for the two reactor concepts (Sections 3.10.2 and 4.4.2). These post-operation analyses calculated changes in the fuel compositions and the total radioactivity with time after shutdown. The radioactivity source terms of the SC-SCoRe are used to perform radiation dose calculations for the excavated reactor core to determine the exposure to nearby crew during the recovery operation. This chapter also investigates the decay heat removal from the SCoRe and PeBR lunar power systems after shutdown of the reactors. The next section describes the placement of the SC-SCoRe and PeBR on the lunar surface and discusses their post-operation storage on the Moon.

5.1 Placement and Post-Operation Storage of Nuclear Reactors on the Moon

The SC-SCoRe and PeBR are designed to be emplaced below grade on the lunar surface in part to utilize the surrounding regolith as supplemental radiation shielding. Fig. 5.1 shows views of the reactors, after being placed in an excavated hole or trench and then surrounded with loose backfilled regolith. The surrounding lunar regolith helps shield the crew on the surface from the reactor's intense neutron and gamma photon radiation emitted both during nominal operation and following reactor shutdown at EOL. The reactor would also be located a short distance (200-500 m) from the lunar outpost to further reduce the crew radiation dose.

The higher radiation dose rates closer to the reactor could require that a radiation exclusion zone be established around the emplaced reactor [Elliott et al. 2005]. The crew would be restricted from entering the exclusion zone to limit their radiation dose while

working on the lunar surface. Strict guidelines for the allowed reactor radiation dose to astronauts on the Moon have not yet been established. During the NASA Constellation program, however, the dose limit to the crew from the reactor's radiation was < 5 rem/yr at the lunar outpost, and < 50 rem/yr at the boundary of the postulated radiation exclusion zone [Elliot et al. 2005].

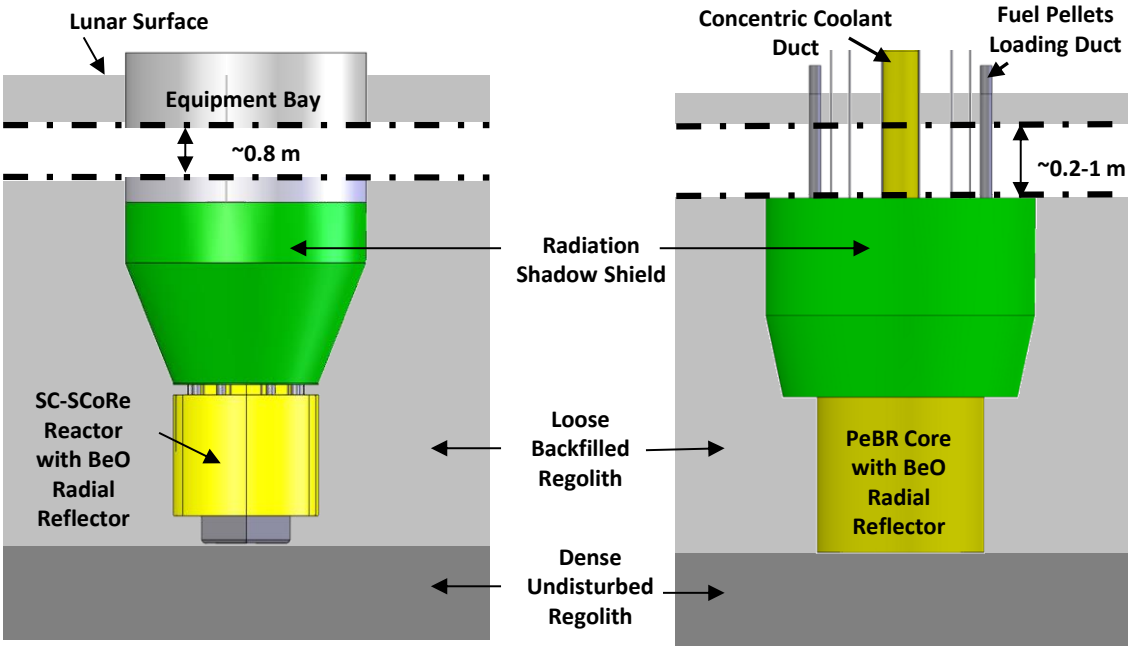

Fig. 5.1. - Placement of SC-SCoRe and PeBR during post-operation storage below the lunar surface.

Operational and safety requirements of a lunar reactor power system do not end at the conclusion of its operational life [El-Genk 2010a,b]. Following a reactor shutdown, the radioactive decay of the accumulated fission products in the fuel continues to generate heat within the reactor core. This decay heat generation needs to be safely removed from the reactor, preferably using passive means. The neutron and gamma radiation field emitted from the post-operation reactor core would decrease rapidly with the decay of the short-lived fission products in the fuel. As the intensity of the radiation field declines, the required size of the exclusion zone would shrink in area. The reactor's thick regolith shielding should result in a very small radiation exclusion zone after shutdown, minimizing the impact of the post-operation reactor on surface activities around the lunar

outpost [Elliot et al. 2005]. Emplacing the reactors below grade thus allows for their post-operation storage in place, below the surface, to allow the radioactivity in the core to decay down to a low level [El-Genk 2010a].

Article IX of the *UN Treaty on Principles Governing the Activities of States in the Exploration and Use of Outer Space, including the Moon and Other Celestial Bodies*, also known as the *Outer Space Treaty*, requires signatories to avoid unduly contaminating the lunar environment [United Nations 2002]. This could include the eventual recovery of a nuclear reactor from its emplaced location below the surface for a final disposition, and/or retrieval for reprocessing of the valuable highly enriched uranium in the used fuel. The recovery of the post-operation reactors would require that the radioactivity decay down to a low enough level, near background, to allow for excavation and handling by the outpost's crew.

The following sections describe the performed post-operation analyses of the SC-SCoRe and PeBR designs to determine the storage time required for safe recovery of the reactors from the lunar surface. First, the radionuclide composition of the used fuel is determined from the isotope concentrations calculated by the fuel depletion analysis of the two reactors (Sections 3.10.2 and 4.4.2). This composition is the decayed to determine the radionuclide source terms during the post-operation storage period. The radiation emission rates are calculated from the source term for use in radiation transport simulations to estimate the dose field around the reactor core. The next section presents the analysis to determine the accumulated radioactivity source term in the post-operation SC-SCoRe.

5.2. Radioactivity Source Term in the SC-SCoRe

Radioactive fission products and minor actinides accumulate in the reactor's UN fuel during its 21 year operation life. The MCNPX fuel depletion calculations described in Section 3.10.2 track the concentrations of 42 actinides and 243 fission products in the reactor's UN fuel pellets [Pelowitz et al. 2011]. It was found that the MCNPX fuel depletion capability does not track the concentrations of some of the very short-half-life nuclides, therefore these isotopes are not included in the radioactivity source terms

reported in this chapter. However, as these very short half-life isotopes decay away within the first few days after reactor shutdown, this omission insignificantly affects the radioactivity source term for long term storage of the reactor. The concentrations of the tracked actinides and fission products are used to provide estimates of the radioactivity source term in the reactor core with operating time.

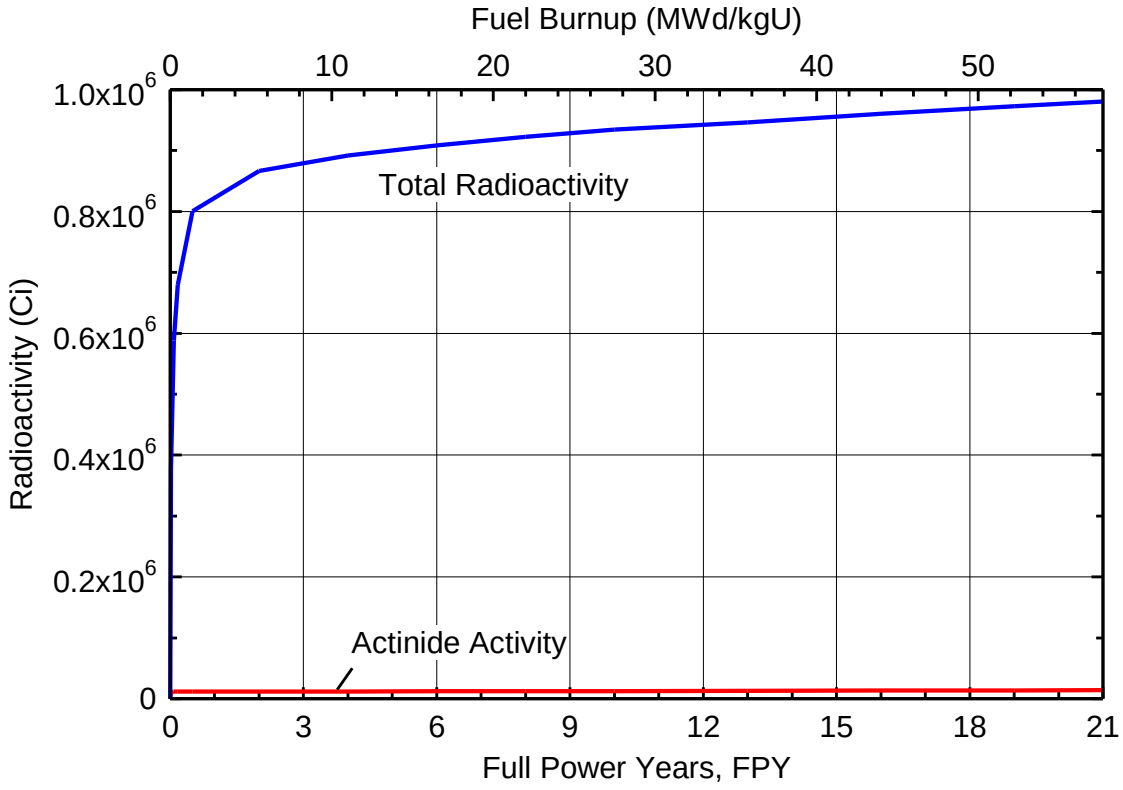

Fig. 5.2. - Radioactivity source term in SC-SCoRe during full power operation [Schriener and El-Genk 2013].

Figure 5.2 displays the change in the radioactivity source term tracked using MCNPX in the SC-SCoRe during nominal operation at 1,000 kW_{th}. During the first few weeks of operation, the total radioactivity in the reactor core increases rapidly, mostly due to the buildup of the shorter-lived fission products (Fig. 5.2). The inventories of these fission products reach equilibrium within a few days, as their rates of production by fission equals the sum of those for their depletion by neutron capture and natural radioactive decay. Thereafter, the buildup of the radioactivity in the core increases slowly, but steady, with operation time of the reactor as the longer-lived fission products accumulate

in the fuel. The total radioactivity in the reactor core during nominal operation approaches 9.84×10^5 Ci at the EOL (Fig. 5.2). The activity due to the actinides is only 1.41×10^4 Ci, representing only a tiny fraction of the total radioactivity (Fig. 5.2). The EOL radioactivity source term calculated by the MCNPX fuel depletion calculations is used as the input for the decay analysis to investigate the post-operation storage of the SC-SCoRe, which is discussed next.

5.3. SC-SCoRe Post-Operation Storage

The fuel depletion capability in MCNPX 2.7E [Pelowitz, et al 2011] was used to decay the radionuclide source term determined by the fuel depletion analysis at EOL. The radioactivity decay simulations calculates changes in the source term in the post-operation SC-SCoRe during storage below grade on the lunar surface for up to 1,000 years. Fig. 5.3 presents the calculated total radioactivity source term during post-operation storage, as well as the individual source terms of the significant radioisotopes in the used fuel. Within two weeks after reactor shutdown, the total radioactivity in the reactor drops from the EOL value of 9.84×10^5 Ci down to 5.12×10^5 Ci (Fig, 5.3). The radioactivity source term decays to 7.90×10^4 Ci after 10 years, 2.18×10^4 Ci after 50 years, and down to 666 Ci after 200 years of post-operation storage below grade on the Moon (Fig, 5.3).

Fig. 5.3 shows that during the first 100 years of post-operation storage, the radionuclides contributing the most to the total radioactivity source term in the reactor fuel are ^{152}Eu ($T_{1/2}$ = 13.54 years), ^{137}Cs ($T_{1/2}$ = 30.07 years), ^{90}Sr ($T_{1/2}$ = 28.78 years) and its daughter ^{90}Y. The ^{90}Y isotope ($T_{1/2}$ = 2.67 days) exists in equilibrium with its longer-lived parent, ^{90}Sr. The ^{152}Eu is produced primarily by neutron activation of ^{151}Eu, which is added to UN fuel pellets in the form of ^{151}EuN as a Spectral Shift Absorber (SSA). The actinides make up only a small fraction of the total radioactivity source term, as the small amount of ^{238}U in the highly enriched UN fuel restricts the production of minor actinides during operation (Fig. 5.2).

Immediately after reactor shutdown, the activity of ^{152}Eu is twice as much as either ^{137}Cs or ^{90}Sr, but because of its shorter half-life, the radioactivity of ^{152}Eu drops below

that of ^{137}Cs after 30 years of post-operation storage (Fig, 5.3). At such time, ^{90}Sr+^{90}Y and ^{137}Cs are the largest contributors to the total radioactivity source term in the reactor core. After 250 years of post-operation storage, the radioactivity of these nuclides in the reactor core drops below that of ^{151}Sm ($T_{1/2}$ = 90 years) (Fig, 5.3). After 300 years of storage, the total radioactivity source term in the reactor core reaches 164 Ci and decreases thereafter very slowly with storage time. As such time, the primary contributors to the total reactivity source term in the reactor are ^{151}Sm and ^{14}C ($T_{1/2}$ = 5715 years) (Fig, 5.3). The ^{14}C is generated in the fuel during reactor operation through (n,p) interactions with the ^{14}N atoms in the nitride fuel.

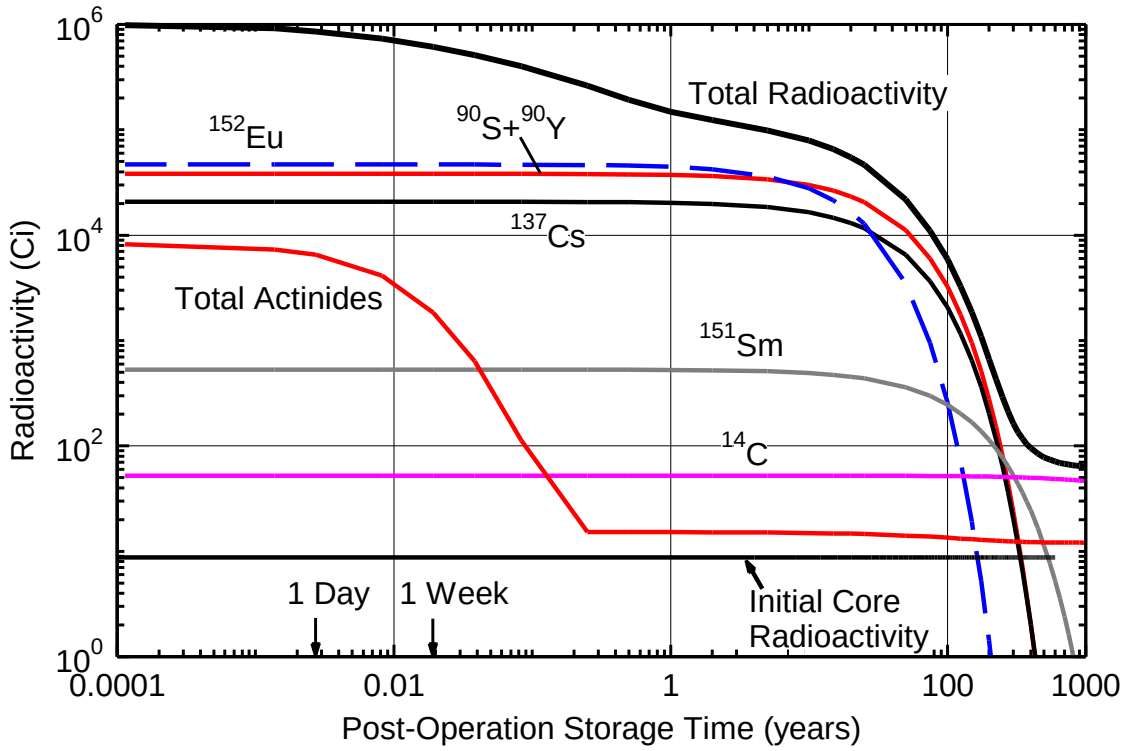

Fig. 5.3. - Radioactivity source term in post-operation SC-SCoRe in storage for up to 1,000 years [Schriener and El-Genk 2013].

Radioactive decay of the fission products and actinides in the fuel emits ionizing radiation. The radioactivity source terms calculated for the post-operation storage period using MCNPX are used to calculate estimates of the neutron and gamma photon radiation field around the reactor core. The next section presents analyses estimating the dose rates

to the crew from the reactor's emitted radiation during excavation and recovery after post-operation storage beneath the lunar surface.

5.2.2. Radiation Field around the Post-Operational SC-SCoRe

The lunar regolith surrounding the buried reactor core during post-operation storage shields astronauts on the surface from the neutron and gamma photon radiation emitted by radioactive decay. During recovery of the reactor, the core would be excavated, removing the supplemental regolith shielding and exposing the outpost crew to the reactor's radiation field. Recovery of the post-operation reactor requires that the dose rate to the crew decreases to a safe level. Radiation transport calculations are performed to determine the radiation field around the excavated post-operation SC-SCoRe and estimate the radiation dose rates.

The code ORIGEN-S [Gauld, Hermann, and Westfall 2006] is used to calculate 44-energy group neutron and gamma photon fluxes from the radionuclide source terms determined using MCNPX with time following shutdown (Fig. 5.3). The neutron emission rate in the fuel is due to a combination of the decay of actinides by spontaneous fission and from (α,n) interactions with the light elements in the fuel by α particle radiation emitted by decaying actinides. The total neutron emission rate of the post-operation SC-SCoRe is much lower than that of the gamma photons, insignificantly contributing to the total dose (Fig. 5.4a). The gamma photon emission rate of the post-operation reactor (Fig. 5.4b) totals 7.69×10^{16} photons/s for the source term at EOL. This decreases to 1.72×10^{14} photons/s after 100 years of storage, and 1.15×10^{12} photons/s after 300 years.

MCNPX 2.7E [Pelowitz et al. 2011] simulates the transport of the neutron and gamma photon sources calculated above and determines the radiation dose field around the excavated post-operational SC-SCoRe. The particle source in the MCNPX model is simulated as an isotropic, uniform volumetric source within the UN fuel stacks. The radiation dose field is calculated using MCNPX mesh tallies using 20 million source photons and 10 million source neutrons. The dose equivalent rates in rem/hr are calculated using the NCRP 38 flux-to-dose conversion factors in the MCNPX code.

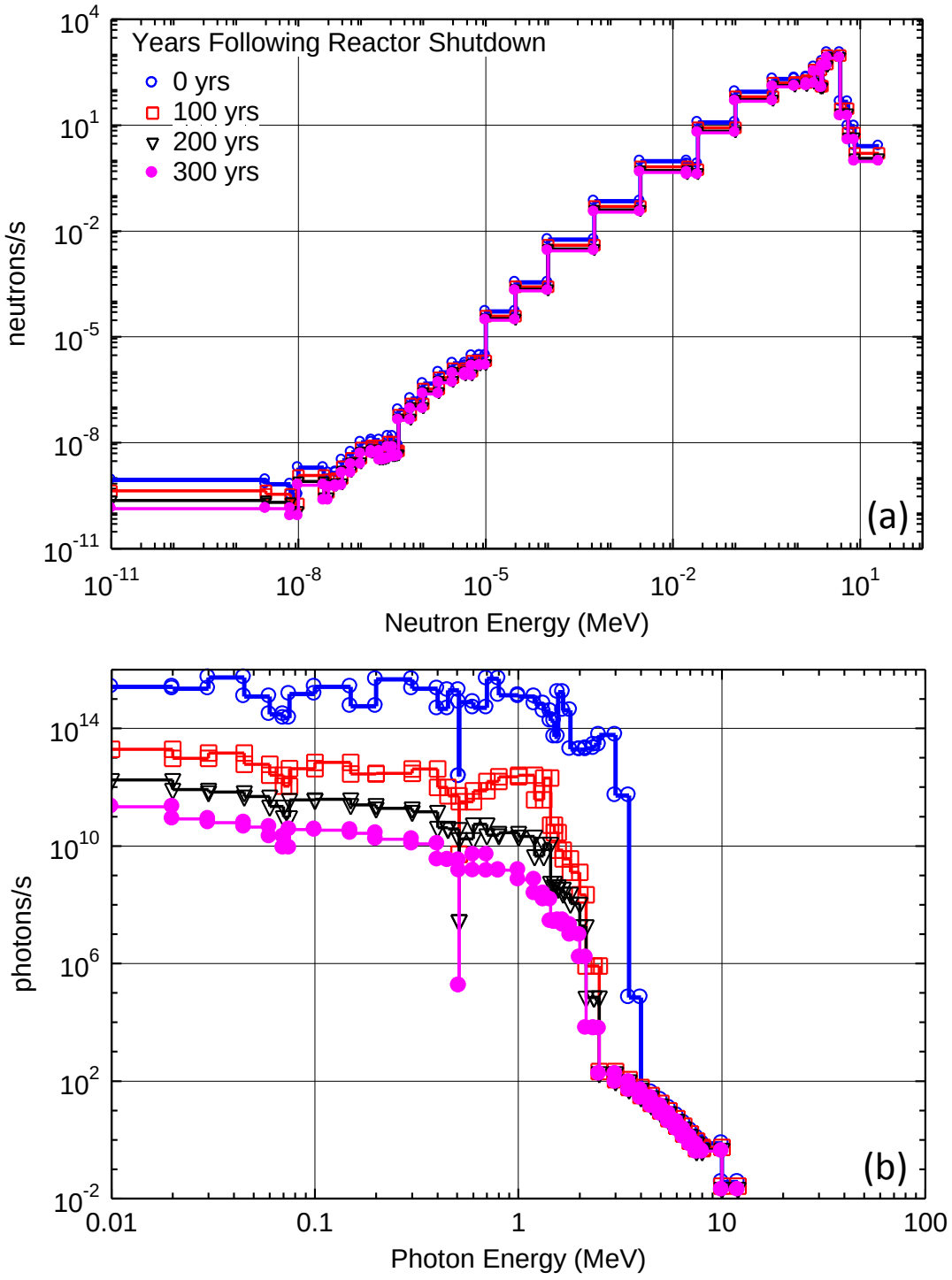

Fig. 5.4. - Emitted neutron and gamma photon spectra of the post-operation SC-SCoRe with time after reactor shutdown.

Although specific dose limits have not yet been established for astronauts on the Moon, US federal radiation protection regulations classify the area around a radiation source as a radiation area if the dose rate is ≥ 5 mrem/hr at 30 cm from any surface of the emitting radiation source [10CFR20.1003]. The area around the reactor would be classified as a high radiation area if the dose rate at 30 cm reaches ≥ 100 mrem/hr [10CFR20.1003]. The results of the MCNPX calculations show that dose field around the reactor at EOL is very high, reaching ~6.7×10^5 mrem/hr at a distance 30 cm from the BeO radial reflector (Figs. 3.10 and 5.1). This dose rate reaches as high as 3.34×10^6 mrem/hr at the surface of the radial reflector. Following 200 years of post-operation storage the radiation field at a distance of 30 cm from the reactor decreases to 99 mrem/hr, allowing the area around the excavated reactor to be classified as a high radiation area.

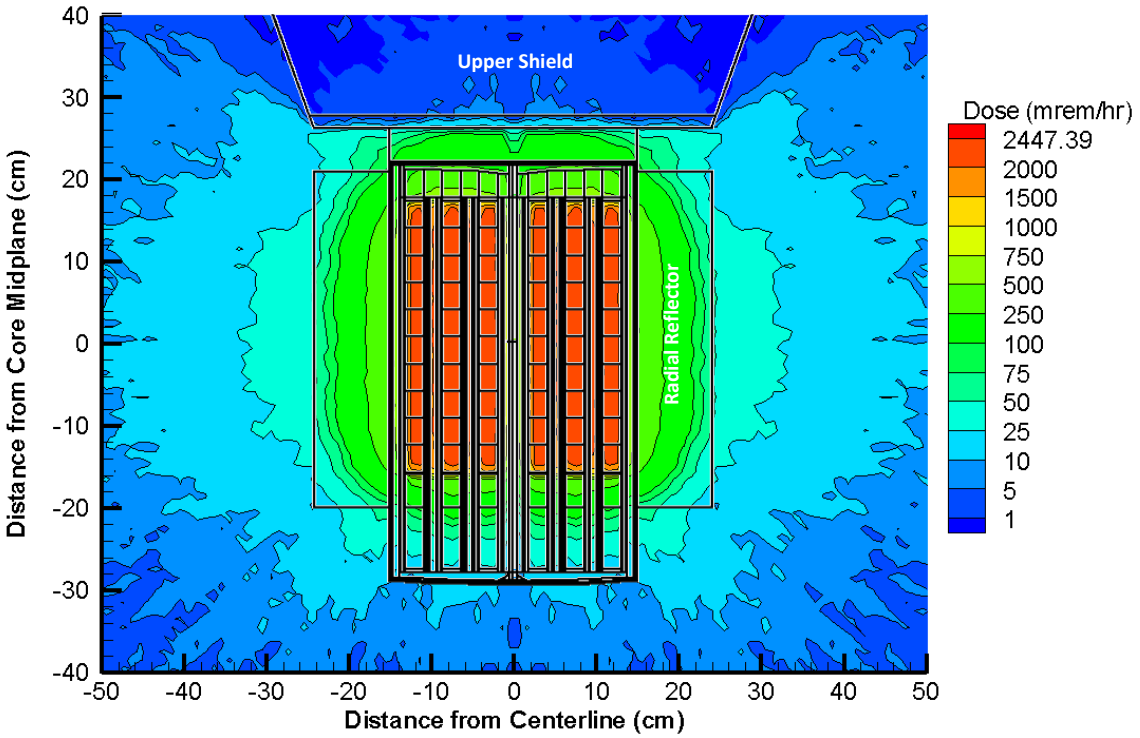

Fig. 5.5. - Radiation dose around excavated post-operation SC-SCoRe, with regolith shielding removed, following 300 years of storage [Schriener and El-Genk 2013].

The total radioactivity source term in the reactor decreases to a sufficiently low level for safe removal and handling of the reactor after 300 years of post-operation storage.

Fig. 5.5 shows the contours of the estimated biological radiation dose determined using MCNPX around the post-operation SC-SCoRe reactor after excavation from the lunar regolith following 300 years of post-operation storage. At this time, the ODS-Mo core structure and BeO neutron reflectors provide sufficient shielding to protect humans from the emitted radiation (Fig. 5.4). The estimated dose rate at the surface of the BeO radial reflector is still as high as 50 mrem/hr, but it decreases to ~10 mrem/hr at a distance of 30 cm from the surface of the reflector (Fig. 5.5). At a distance of 1.0 m from the surface of excavated reactor, the radiation dose is only ~1 mrem/hr, which is below the level required to allow the reactor core to be transported according the US radiation protection regulations [10CFR20.1301].

These dose rates compare favorably with the lunar background due to space radiation. Crew exposure from the natural lunar radiation environment is due to both Galactic Cosmic Rays (GCR) and Solar Energetic Particles (SEP), as well as any secondary radiation particles produced from the interaction of the GCR and SEP with the lunar regolith. The annual dose from SEPs is typically concentrated in a few brief Solar Particle Events (SPE) lasting from several hours to several days [Hayatsu et al. 2008], during which time the crew would withdraw to a shielded 'storm shelter' for the duration [Adamczyk et al. 2011; Pham and El-Genk 2009]. Dose from GCR, in contrast, forms a more steady radiation background that varies with the magnetic strength of the Sun during its solar activity cycle [Adams et al. 2007; Hayatsu et al. 2008].

Table 5.1 includes estimates of the background dose rate on the lunar surface due to both GCR and secondary neutrons generated by the interaction of GCR particles with the lunar regolith. The background dose rate estimates range from 1.2 to 9.5 mrem/hr, depending on the solar cycle, with an average of ~5 mrem/hr [Adamczyk et al. 2011; Adams et al. 2007; Campbell 1992; Hayatsu et al. 2008]. This dose rate of 5 mrem/hr is comparable to the SC-SCoRe dose rate estimated at a distance of ~50 cm from the surface of the radial BeO reflector during excavation and recovery after 300 years (Fig. 5.5). At greater distances from the excavated reactor, the estimated dose rate drops well below the lunar background (Fig. 5.5). Thus, no special radiation protection measures

would be necessary for the crewmembers working around the reactor during the excavation and recovery process.

Table 5.1. - Radiation dose rate estimates for the lunar surface [Schriener and El-Genk 2013].

Author	GCR (mrem/hr)	Neutrons (mrem/hr)	Total (mrem/hr)	
Adamczyk et al. (2011)	3.522	0.513	4.035	
Hayatsu et al. (2008)	8.653	0.832	9.522	Solar Min.
	5.930	0.592	6.550	Solar Ave.
	3.032	0.290	3.340	Solar Max.
Adams et al. (2007)	2.783	0.537	3.321	Solar Min.
	1.021	0.226	1.247	Solar Max.
Campbell (1992)	-	-	6.219	

These analyses show that the post-operation SC-SCoRe can be safely recovered after 300 years of storage below grade on the Moon. The next section describes the results of the post-operation storage analyses of the PeBR concept.

5.4. Post-Operational Storage of PeBR Fuel Pellets

The radioactivity source term of the PeBR at EOL is determined from the composition calculated by the fuel depletion analysis performed using MCNPX 2.7A [Hendricks et al. 2008] (Section 4.4.2). In this calculation, the MCNPX code tracked the isotope concentrations of 38 actinides and 260 fission products. At EOL, following 66 years of operation at 471 kW_{th}, the radioactivity source term in the post-operation PeBR reaches $4.93x10^5$ Ci. This is approximately half that of the SC-SCoRe following 21 years of operation at 1,000 kW_{th} ($9.84x105^6$ Ci). The radionuclide inventory at EOL is mostly due to short-lived fission products, the concentrations of which are closely tied to the fission rate in the reactor, and hence the thermal power level. Thus, the difference in operating power between the two reactors results in the post-operation PeBR containing a

smaller EOL radioactivity source term than the shorter operation life SC-SCoRe. Neutron activation of the ZrC in the fuel pellets during reactor operation and, hence the contribution to the total radioactivity, is fairly minor due to the small neutron absorption cross sections for carbon and zirconium isotopes.

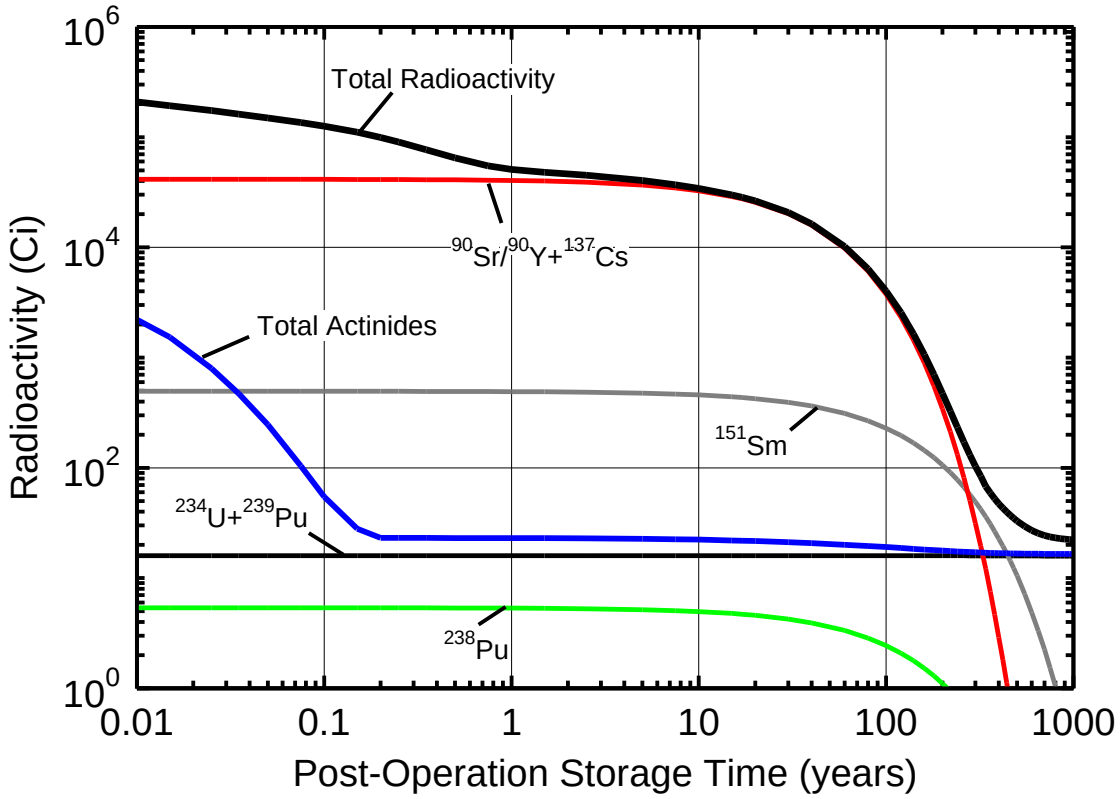

Fig. 5.6. - Estimates of radioactivity source term in post-operation PeBR while in long term storage on the lunar surface [El-Genk and Schriener 2011].

MCNPX is then used to decay the radioactivity source term in the fuel pellets of the post-operation PeBR to investigate changes in the source term with storage times up to 1,000 years after reactor shutdown (Fig. 5.6). The radioactivity source term in the post-operation PeBR decreases abruptly after shutdown and continues to decrease exponentially with storage time (Fig. 5.6). The total radioactivity decreases from ~4.93×10^5 Ci at EOL to 3.43×10^4 Ci after 10 years of storage. At that time, ~95% of the total radioactivity is contributed by the isotopes ^{137}Cs ($T_{1/2}$ = 30.07 years) and the pair ^{90}Sr ($T_{1/2}$ = 28.78 years) and its daughter ^{90}Y ($T_{1/2}$ = 2.67 days). The combined contributions of the trio ^{137}Cs, ^{90}Sr, and ^{90}Y dominate the total radioactivity during the

first 300 years of storage. Beyond that time and up to ~500 years of storage, the major contributor to the total radioactivity in the post-operation PeBR core is ^{151}Sm ($T_{1/2}$ = 90 years).

After 300 years of post-operation storage, the total radioactivity in the PeBR used fuel pellets decreases to only 103.3 Ci, with the major contributors being ^{151}Sm (49.1 Ci), the trio ^{137}Cs, ^{90}Sr, and ^{90}Y (31.5 Ci), and the longer-lived actinides (17.1 Ci) (Fig. 5.6). Following 1000 years of storage, the total radioactivity in the post operation PeBR decreases to only 22.3 Ci, with the major contributors being ^{99}Tc ($T_{1/2}$ = 211,100 years) (5.17 Ci), ^{234}U ($T_{1/2}$ = 245,500 years) (9.65 Ci), and ^{239}Pu ($T_{1/2}$ = 24,110 years) (6.14 Ci) (Fig. 5.6). This total radioactivity is a little more than twice that of the fresh fuel pellets (10.4 Ci) when loaded in the PeBR core at BOL. These results affirm that a storage time of the post-operation PeBR of 300 years would be sufficient for the total radioactivity of the spent fuel pellets to decay a low level. This would allow the core to be safely excavated to recover the reactor and possible retrieve the considerable quantity of ^{235}U in the fuel pellets (Fig. 4.16).

The decay of the isotopes making up the radioactivity source terms in the post-operation SC-SCoRe and PeBR reactors generates heat within the core, which needs to be safely removed after shutdown. The removal of this decay heat generation is the subject of the next section.

5.5. Decay Heat Removal Following Shutdown at End-of-Life

The safe removal of the decay heat generation following shutdown is an important concern for nuclear reactors. Failure to remove the generated thermal energy could result in the temperatures within the reactor rising to levels high enough to possibly damage the core materials. Fortunately, as the decay heat generation is mostly due to the very-short lived fission products, the heat generation rate drops down to a low level within a few days following shutdown of the reactor.

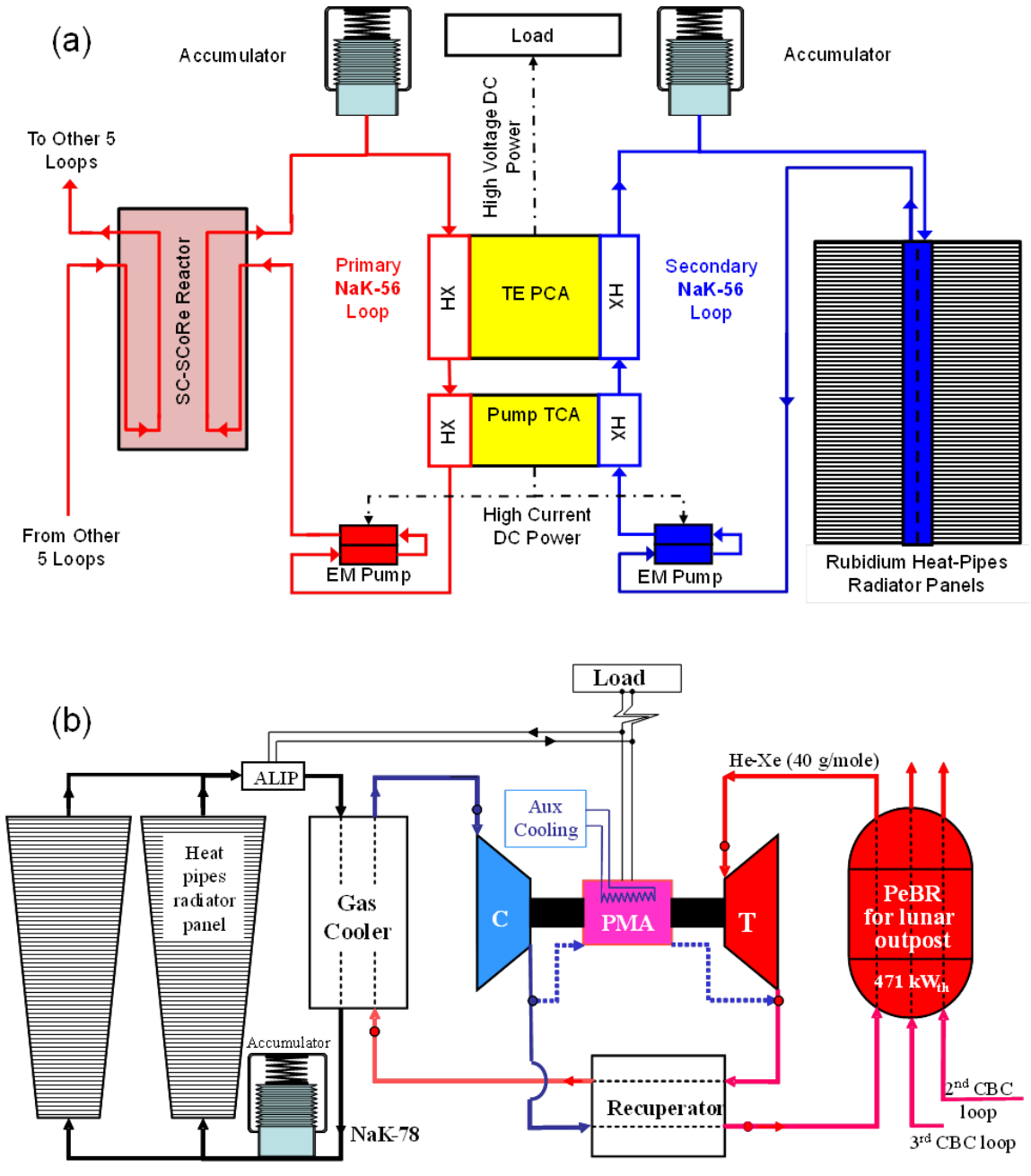

Fig. 5.7. - Integrations of power system for lunar surface power: (a) SC-SCoRe and (b) PeBR [Schriener and El-Genk 2013; El-Genk and Schriener 2011].

The process of removing the decay heat from the post-operation SC-SCoRe and PeBR reactor cores differs due to the system integrations used in the two reactor power systems. Layouts of the integrated power systems of the SC-SCoRe and PeBR are shown in Fig. 5.7. The SC-SCoRe power system (Fig. 5.7a) uses all static components with no moving parts. The NaK-56 coolant in the six pairs of primary and secondary loops is circulated using the DC Electromagnetic (EM) pumps, one in each loop, powered by dedicated the Thermoelectric Conversion Assemblies (TCAs) thermally coupled between each pair of loops (Fig. 5.7a). This power system integration ensures that, as long as a temperature difference exists between the primary and secondary loops, the TCAs and EM pumps will passively circulate the liquid NaK-56 coolant through the loops. The passive heat-pipes radiator panels would then reject the generated decay heat to space.

Figure 5.8 shows the results of a transient system analysis performed using DynMo-TE [El-Genk and Tournier 2006a] modeling decay heat removal following shutdown for a previous version of the SCoRe power system with the same system integration layout as the SC-SCoRe [El-Genk and Schriener 2010]. This simulation is described in detail in Appendix C. DynMo-TE is a dynamic space reactor power system simulation tool developed at the University of New Mexico's Institute for Space and Nuclear Power Studies which includes detailed models of the individual components in the reactor power system [El-Genk and Tournier 2006a,b].

At Location (1) on Figs. 5.8a and b the control drums are slowly rotated inward over a 24 hour period to shut down the reactor. The thermal power generated in the core drops down rapidly within the first hour, to ~7% of that during nominal operation (Fig. 5.7a). The circulation rate of the coolant in the primary and secondary loops decreases commensurate with the heat generation in the core (Fig. 5.8b). The decreasing heat generation rate results in the reactor inlet and exit temperatures decreasing as the stored energy in the liquid NaK coolant and reactor core structure are removed and rejected by the heat-pipes radiator panels (Fig. 5.8a). By the end of the 24 hour shutdown period, the heat generation and core temperatures stabilize and then decrease slowly thereafter with time. This shows that the similar system integration used in the SC-SCoRe power system,

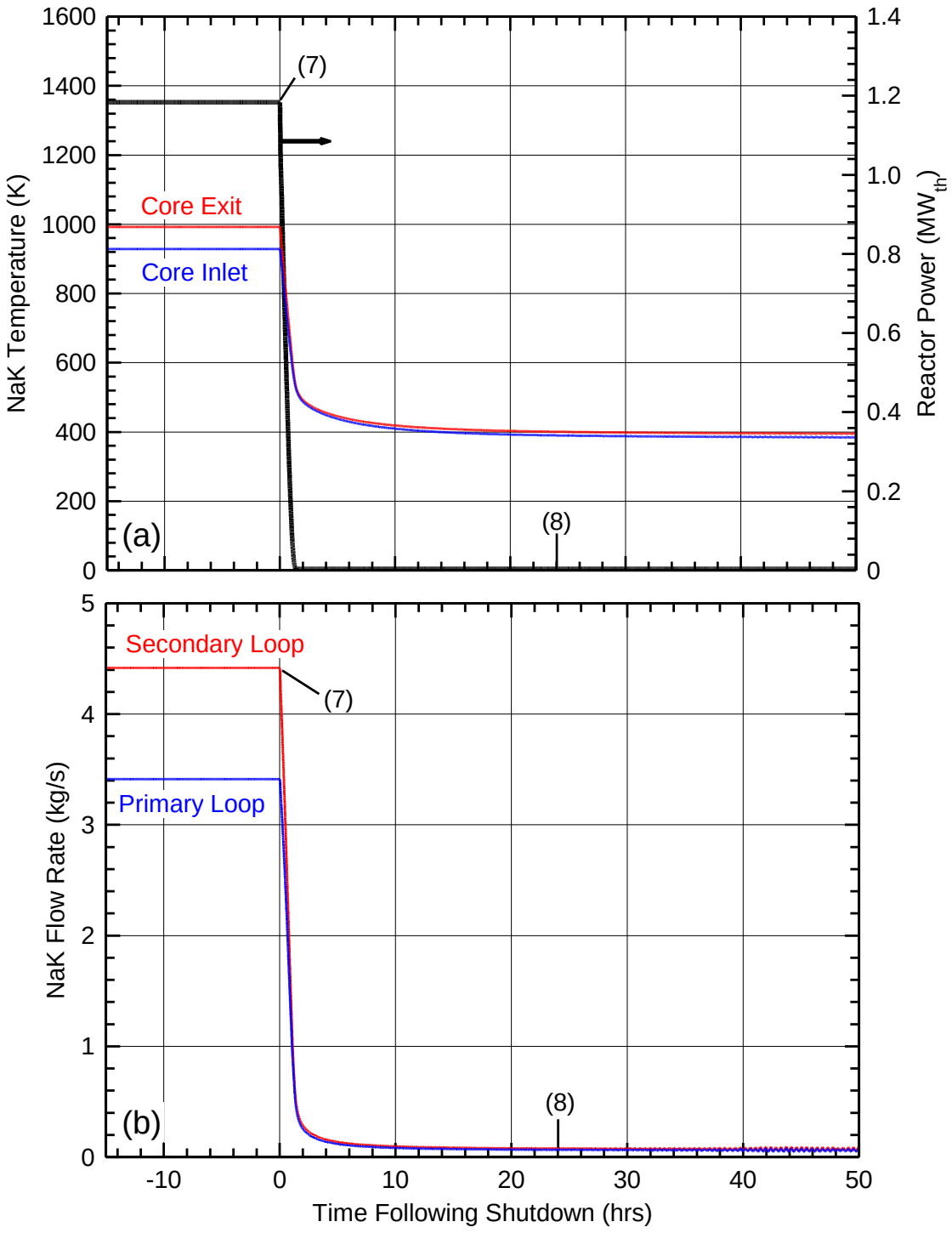

Fig. 5.8. - DynMo-TE simulation of earlier version of SCoRe power system showing passive decay heat removal following shutdown (see Appendix C) [El-Genk and Schriener 2010].

with TE powered EM pumps and heat-pipes radiator panels, allows for the safe and passive removal of the decay heat generation following reactor shutdown.

The PeBR power system (Fig. 5.7b) uses dynamic Closed Brayton Cycle (CBC) energy conversion in the three pairs of coolant loops. The He-Xe primary coolant and working fluid is circulated during nominal operation by the centrifugal compressors of the single-shaft CBC turbo-generator units, using a portion of the shaft power generated by the centrifugal turbine [El-Genk, Tournier, and Gallo 2010]. Each primary CBC loop has a liquid NaK-78 secondary loop connected to two water heat-pipes radiator panels. The liquid NaK-78 in the secondary loops is circulated using AC Annular Linear Induction Pumps (ALIPS) powered by electricity supplied by the CBC turbo-generator units. Following shutdown of the reactor at EOL, the rapid drop in the heat generation in the core will eventually result in the turbines of the CBC units no longer supplying sufficient shaft power to the compressors for circulating the He-Xe coolant and working fluid. The CBC turbo-generator units include starter motors to spin the shafts up to the required rotation rate during startup of the reactor power system [El-Genk, Tournier, and Gallo 2010]. After shutdown, an external power source, such as a solar array, could supply electricity to the starter motors to rotate the compressors and circulate the coolant until such time that the decay heat generation decreases to a sufficiently low level, within a few days. After this time, the low decay heat generation could be removed by conduction to the surrounding lunar regolith.

In addition to providing for safe post-operation storage, the designs of the SC-SCoRe and PeBR reactors and power systems allow for the removal of decay heat generation from the cores after shutdown. The highlights of this chapter investigating the post-operation storage of these reactors on the Moon are discussed next.

5.6. Highlights and Concluding Remarks

This chapter investigated the post-operational storage of nuclear reactors on the Moon. Analyses are performed of the long term storage of the post-operation SC-SCoRe and PeBR designs developed in this dissertation. These analyses determined the storage

time required for the radioactivity in the post-operation reactors to decay down to a low level to allow for safe recovery. The results of this research showed that:

- Emplacement of the SC-SCoRe and PeBR reactors below grade on the lunar surface allows for safe, long-term post-operation storage, to allow the radioactive fission products and actinides to decay down to a low level. This would allow for the eventual recovery of the post-operation reactor and potentially the retrieval of the considerable amounts of ^{235}U remaining in the cores.
- The total radioactivity source term in the post-operation SC-SCoRe decrease to only 164 Ci after 300 years of storage beneath the lunar surface. At this time the radiation field around the excavated post-operation SC-SCoRe is below the lunar radiation background at a distance of 0.5 m from the reactor. This low radiation level allows astronauts to safely work around the reactor during recovery.
- The radioactivity source term in the post-operation PeBR decays to only 103 Ci after 300 years of storage, allowing for the safe recovery of the reactor core.
- The decay heat generation in the post-operation SC-SCoRe would be removed passively, following shutdown of the reactor, by the NaK-56 coolant circulated by the static TE powered EM pumps in the power system's primary and secondary loops. For the PeBR an external power source is required to circulate the He-Xe gas coolant for a short period following shutdown.

The safe post-operation storage of surface power reactors for lunar outposts is an important subject that had often been overlooked in previous research. The next chapter presents a summary and conclusions of the research in this dissertation, along with suggestions for future work.

6. SUMMARY AND CONCLUSIONS

The research in this dissertation performed multi-physics design and analyses of long operational life reactors for lunar outposts. It investigated examples of both a reactor that is fueled at launch, the Sectored Compact Reactor (SCoRe), as well as an advanced concept which is fueled on the Moon, the Pellet Bed Reactor (PeBR). The SCoRe and PeBR concepts are designed to operate at temperatures ≤ 900 K and use conventional stainless steels and superalloys for the structure in the reactor core and power system. These reactors are emplaced below grade on the Moon to take advantage of the regolith as a supplemental neutron reflector and shielding of the lunar outpost from the reactors' neutron and gamma radiation.

The core of the liquid NaK cooled SCoRe is divided into six sectors which are thermally and neutronically coupled but hydraulically decoupled. Each sector is served by a separate pair of primary and secondary NaK coolant loops, with separate SiGe thermoelectric (TE) energy conversion modules, TE powered electromagnetic pumps, and rubidium heat-pipes radiator panels. This combination of a sectored core and passive power system integration with multiple loops avoids single point failures in reactor cooling, energy conversion, and heat rejection. A small amount of spectral shift absorber (SSA) thermal neutron poison is mixed into the UN fuel pellets and added as a coating onto the reactor vessel to ensure that the bare core is at least -$1 subcritical when submerged in wet sand and flooded with seawater, in the unlikely event of a launch abort.

The He-Xe gas-cooled PeBR concept is launched unfueled and loaded with spherical fuel pellets only after being emplaced below grade on the lunar surface. The PeBR has an unstructured core of randomly packed spherical fuel pellets, allowing the reactor to be fueled on the Moon. The fuel pellets are launched separately in special subcritical launch canisters. The PeBR and power system are also designed for the avoidance of single point failures. The annular core is divided into three sectors, each of which is served with a separate Closed Brayton Cycle (CBC) conversion loop, with a separate NaK-78 secondary heat rejection loop and water heat-pipes radiator panels.

This research develops a multi-physics design and analyses methodology for lunar power reactors which couples MCNPX neutronics analyses and CFD and thermal-hydraulics analysis performed using the commercial code STAR-CCM+. In addition, these analyses incorporate dynamic simulation of the integrated power system using DynMo-TE [El-Genk and Tournier 2006a] to determine the reactor operating temperatures and flow rates at different power levels. This multi-physics methodology ensures that the reactor design satisfies the launch safety requirements, has redundancy in reactor control, is adequately cooled during nominal operation, and possesses sufficient excess reactivity for a long operation life > 20 years.

Results of the multi-physics design and performance analyses of the SCoRe show that reconfiguring the core geometry can significantly increase the operational life, for the same mass of uranium in the core. The design of the SCoRe changed as the result of these analyses from the initial SCoRe-N_{18}, to the SCoRe-N_5, and finally to the Solid Core-Sectored Compact Reactor (SC-SCoRe). Parametric analyses of the SCoRe-N_{18} showed that increasing the diameter of the UN fuel rods, for two geometrical scaling arrangements, increase the excess reactivity of the reactor and simultaneously decrease its total mass. Increasing the fuel rods' diameter decreased the height of the active core, reducing the neutron leakage and increasing the Beginning of Life (BOL) cold-clean excess reactivity. The BOL cold-clean excess reactivity of \$2.69 for the SCoRe-N_{18} with 0.630 cm diameter UN fuel pellets, increases to \$4.35 for the SCoRe-N_5-U, with 2.272 cm diameter UN fuel pellets and \$5.45 for the SCoRe-N_5-S with 2.396 cm diameter fuel pellets.

CFD and thermal-hydraulics analyses for the developed SCoRe-N_5 design, with 2.272 cm diameter UN fuel pellets, determined that the larger diameter fuel rods increase the NaK-78 flow bypass close to the walls of the core sectors. This bypass flow is eliminated by scalloping the 316L stainless steel sector walls. The scalloped sector walls resulted in reduced peak fuel and cladding temperatures and improved the temperature distribution in the exiting NaK-78 flow. Neutronics analysis of the SCoRe-N_5 showed that the stainless steel scalloped walls also reduce neutron leakage from the reactor core sectors, increasing the BOL cold-clean reactivity from to \$5.43 to \$5.83.

The neutronics analyses for the SCoRe-N_5 also compared several different SSA isotopes, determining their effects on the BOL excess reactivity and the total reactor mass. ^{151}Eu was found to be the most effective SSA isotope for the SCoRe-N_{15}, resulting in both the highest excess reactivity and lowest total reactor mass. This isotope has the largest absorption cross section in the neutron energy spectrum inside the bare and flooded SCoRe-N_5 core during a water submersion accident. This resulted in the lowest needed SSA concentration in the UN fuel, reducing the active height of the core and hence the neutron leakage. The SCoRe-N_5 with ^{151}Eu SSA has \$6.72 of BOL cold-clean excess reactivity, an increase of \$0.89 compared to that of the core using ^{157}Gd. The shorter active core height also reduces the total mass of the reactor and BeO radial reflector from 474 kg to 415 kg.

Results of the thermal-hydraulics analyses of the SCoRe-N_5 design performed at nominal thermal power levels of 200, 500, and 1,000 kW_{th} confirmed adequate cooling of the UN fuel rods and coolant mixing in the upper plenum and the exit duct. The calculated peak fuel and cladding temperatures in the SCoRe-N_5 core operating at 200 kW_{th} are 952 K and 919 K, at 500 kW_{th} they are 1,041 K and 935 K, and are 1,190 K and 964 K at the nominal thermal power level of 1,000 kW_{th}. Thermal expansion of materials in the reactor core causes a negative temperature reactivity feedback. This decreases the cold-clean BOL excess reactivity of \$6.72 by \$1.05 for hot-clean conditions at 200 kW_{th}, by \$1.08 at 500 kW_{th}, and by \$1.12 at 1,000 kW_{th}. Thermal-hydraulic safety analyses of the SCoRe-N_5 are performed for the reactor operating at a reduced reactor thermal power of 166.67 kW_{th} with a core sector experiencing a Loss of Coolant (LOC). The results showed that the peak cladding temperature of the wire wrapped UN fuel rods in the coolant voided sector exceeds the melting point of the 316L stainless steel cladding.

The multi-physics analyses of the SCoRe for lunar surface power resulted in the design of the SC-SCoRe with a monolithic solid core. The SC-SCoRe is cooled using liquid NaK-56 instead of the NaK-78 alloy used in the SCoRe-N_{18} and SCoRe-N_5. Despite its slightly higher melting temperature (279.4 K vs 260.7 K), for turbulent convection and the same temperature rise in the SC-SCoRe core, the pumping power required using NaK-56 is ~30% lower than that of liquid NaK-78. Performed CFD and

thermal-hydraulics analyses compared 316L SS and Oxygen Dispersion Strengthened Molybdenum (ODS-Mo) solid cores. Results favor the SC-SCoRe reactor with the ODS-Mo solid core, as its much higher thermal conductivity reduces the core temperatures. The peak UN fuel and core structure temperatures inside the SC-SCoRe with ODS-Mo core structure operating at thermal power of 1,000 kW_{th} are 1,225 K and 949 K, respectively.

Analyses showed that the SC-SCoRe with ODS-Mo solid core can safely continue operating with a core sector experiencing a LOC, at a reduced power of 323.0 kW_{th}. The calculated peak temperatures of the UN fuel and the core's ODS-Mo structure in the affected sector are 1,361 K and 1,325 K, respectively. These temperatures are well below the melting points of UN (~3,100 K) and the recrystallization temperature of ODS-Mo (~1,900 K). In the event that a core sector experiences a Loss of Cooling (LOCo), natural circulation of the NaK-56 coolant on the lunar surface helps transfer heat to the adjacent sectors. This decreases the peak core temperatures, compared to those of the reactor with a core sector experiencing a LOC. The SC-SCoRe power system, operating at a reduced thermal power of 323.0 kW_{th}, with a sector experiencing a LOC or a LOCo could continue to supply ~4 kW_e to the lunar outpost to maintain crew life support. In addition to its favorable thermal-hydraulic performance, the SC-SCoRe has a long operational life of 21 years, at a nominal thermal power of 1,000 kW_{th}, generating a total of 7.67 GWd.

Neutronics analyses for the PeBR concept confirmed that launching the reactor unfueled, and fueling the core sectors on the lunar surface, could simplify launch procedures and allow the reactor to achieve a long operational life well in excess of 20 years. Performed parametric neutronics analyses of the PeBR concept on the lunar surface determined that a 9 cm thick BeO radial reflector results in the lowest total mass for reactors with > \$5 excess reactivity. The selected reference PeBR design has \$7 of cold-clean excess reactivity and a 9 cm BeO reflector. This reference PeBR design could operate for up to 66 years at a nominal power of 471 $kW_{th,}$ generating 11.35 GWd. This operational life is much longer than that of the SC-SCoRe. In addition, this research developed designs of the launch canisters for the fuel pellets, which are highly subcritical in a water submersion accident, either separately or with all three canisters, bundled

together. The design achieves this using a combination of favorable geometry and neutron absorbers.

The transient Discrete Elements Method (DEM) fuel loading simulation of the PeBR on the lunar surface confirmed that the fuel pellets can be loaded into the core sectors on the Moon using only lunar gravity. The calculated average volume porosity in the middle of the randomly packed bed of pellets is 0.39-0.41, with higher porosity near the cold and hot frits, the bottom plate, and the sector dividing walls. As a result, the effective volume porosity of a loaded PeBR core sector on the Moon would be close to 0.42, which is only slightly higher than that of ideal random packing of spheres (0.39).

The post-operation SC-SCoRe and PeBR could be safely stored below grade on the lunar surface following the end of their operational lives. Analyses showed that the total radioactivity in the post-operation SC-SCoRe and PeBR decreases within 300 years of storage to a safe level, near background, allowing for the reactors' recovery. Analyses for the SC-SCoRe shows the radiation field around the excavated reactor core, after 300 years of post-operation storage, would result in a dose rate of only ~1 mrem/hr at a distance 1 m, which is below the lunar background. This suggests that no special radiation protection measures would be necessary for the crewmembers working around the reactor during excavation and recovery operations. This could allow for the retrieval of the still considerable amount of ^{235}U remaining in the used fuel (~92% of the initial inventory).

6.1. Recommendations for Further Research

Space nuclear reactors have traditionally used Highly Enriched Uranium (HEU) fuels (> 90 wt% ^{235}U) as their high fissile density minimizes the size and mass of the reactor core. This can result in considerable savings in the launch costs for a space nuclear power system. Over the last 30 years, however, there has been an international movement away from the civilian use of HEU, such as the Reduced Enrichment for Research and Test Reactor (RERTR) program aimed at converting research reactors around the world to using low enriched uranium (< 20 wt% ^{235}U). There are significant nuclear safeguards concerns relating to the production of effectively weapons grade HEU by non-nuclear weapons states for any purpose, include space exploration. With growing international interest in human space exploration, the expanded future use of nuclear fission reactors for space exploration may require the use of reduced enrichment fuels with lower nuclear safeguards requirements. Therefore further research for surface power reactors is warranted to investigate design options for minimizing the mass penalty of utilizing fuels with reduced safeguards requirements. This could help open up access to space nuclear power technology for all spacefaring nations, and not just the space programs of the nuclear weapons states.

APPENDIX A: Methods for Determining Operation Life for Space Reactors with Fast Energy Spectra

Developing long life lunar power reactors requires methods for estimating of the operation life of the reactor core. This appendix examines a number of widely used code packages for performing criticality and burnup analysis, namely: Monteburns 2.0 [Poston and Trellue 1999], MCNPX 2.6C [Hendricks et al. 2006] and SCALE 5.1's TRITON module [DeHart 2005]. These general-purpose code packages are advertised as capable of modeling reactors with either fast or thermal neutron energy spectra. Space reactor designs differ from commercial power reactors by being very small in size, utilizing very high fuel enrichment (>80 wt%), and having a tight arrangement of the fuel rods, requiring code packages with flexible geometry modeling capabilities. The predictions of these code packages are compared with reported depletion data for a commercial PWR fuel pin. These code packages are then used to calculate the operation lives of the Sectored Compact Reactor (SCoRe-S_{11}) [El-Genk et al. 2005; Hatton and El-Genk 2009] and the Submersion Subcritical Safe Space (S^4) [King and El-Genk 2006a,b, 2007] space reactors. Both of these reactors are loaded with highly enriched UN fuel (95 wt%) and are designed with a cold clean excess reactivity of $2.0–3.0.

The calculated operation life estimates for the two space reactors are compared to those calculated using a simplified method developed at the University of New Mexico's Institute for Space and Nuclear Power Studies (UNM-ISNPS). This method combines MCNP5 [X-5 Monte Carlo Team 2003] to a burnup analysis model using Simulink® [The MathWorks 2005], and only considers the 10 most probable low-Z and high-Z elements of the fission yield peaks plus ^{149}Sm [King and El-Genk 2006a]. Although the simplified method accounts for the accumulation of fission productions, it neglects their depletion by capture and radioactive decay. Determining the accuracy of this method for estimating the operation lives of space reactors with fast neutron energy spectra is a major focus of this appendix.

A.1. Methods and Validation

Monte Carlo depletion code packages consist of a neutronics solver and fuel burnup code coupled together in an iterative manner. The packages evaluated here use the same basic methodology for the neutronics codes to communicate with the fuel burnup codes. They use either a probabilistic or a deterministic neutron transport code to perform the neutronic calculations to calculate neutron reaction rates and export the results to the burnup code to estimate the changes in the fuel composition for a specific period of reactor operation. The new fuel compositions calculated using the burnup code are then sent to the neutron transport code to redo the neutronics calculations for the reactor. The process continues to the end of the burnup (operation) period.

The code MCNPX 2.6C uses the CINDER90-based BURN module to conduct the fuel burnup calculations. Monteburns 2.0 links the Monte Carlo solver MCNP5 1.4 to Origen 2.2, which performs the fuel burnup calculations. SCALE 5.1's TRITON depletion module uses the 2-D discrete ordinates code NEWT to model the neutronics and Origen-S to perform the fuel depletion in the reactor core. The predictions of the three criticality and fuel burnup code packages investigated in this chapter are compared to actual PWR fuel depletion data to assess their accuracy in determining the nuclide concentrations.

A.2. Simplified Method for Burnup Analysis

A simplified code package for estimating the operation lives of space reactors with fast neutron energy spectra has recently been developed at the UNM-ISNPS [King and El-Genk 2006a], but its predictions have never been benchmarked. This method uses MCNP5 to perform the neutrons transport calculations and a burnup analysis model, built in Simulink [The MathWorks 2005], that solves a series of radioactive decay, production and depletion equations for a limited number of nuclides. It only considers the 10 most probable low-Z and high-Z elements of the fission yield peaks plus ^{149}Sm [King and El-Genk 2006], and neglects the depletion of the accumulated fission products by either capture or radioactive decay. This method calculates the fission and capture rates from MCNP neutron capture tallies of the selected nuclides. Fission products are modeled

using the number of fission events for each actinide. The concentrations for fission products of interest are generated using the fission product yield [England and Rider 1994]. Currently, the communication process between the MCNP5 and the burnup analysis model in the UNM-ISNPS simplified method is done manually, not automated as in the other code packages investigated in this appendix.

Studies have been performed to investigate the effect of changing the number of fission product species in the Simulink® burnup model on the operation life estimates of the S^4 space reactor using the UNM-ISNPS method [King and El-Genk 2006a]. Results showed that including the 20 nuclides in the low-Z fission yield peak and the 20 nuclides in the high-Z fission yield peak covers 95% of the low-Z and 96% of the high-Z total fission yield. On the other hand, the 10 nuclides in each of the fission yield peaks account for 61% of the low-Z and 64% of the high-Z total fission yield. It was found that including ^{149}Sm in addition to the 10 nuclides in each of the fission yield peaks produced almost the same reactivity depletion rate in the S^4 space reactor as including the 20 nuclides in the fission yield peaks [King and El-Genk 2006]. It was therefore decided to use the scheme with the 10 most probable low-Z and high-Z elements of the fission yield peaks plus ^{149}Sm for the current reactivity depletion calculations. Because the UNM-ISNPS simplified method accounts for the accumulation, but not the depletion, of fission products, it eliminates the reaction tallies for these nuclides. Thus, even with the same fission product array, the UNM-ISNPS methodology requires less computational time than the other Monte Carlo code packages investigated in this work.

The rates for neutron reactions are determined using the calculated nuclide specific ‘‘Fission Factors’’ (FF) and ‘‘Capture Factors’’ (CF) using MCNP5 [King and El-Genk 2006a]. These represent the product of the atom density for a given nuclide and the result of an MCNP ENDF/B reaction tally. The results are expressed in terms of events per cm^3 per MCNP source particle. For fissionable actinides both FFs and CFs are determined, while only CFs are calculated for non-fissionable actinides and spectral poisons. They are given as:

$$FF_i = N_i \times \text{MCNP MT-18 Tally Result} \quad \text{(A.1)}$$

$$CF_i = N_i \times \text{MCNP MT-101 Tally Result} \quad \text{(A.2)}$$

The MT 101 tally includes the total capture cross sections for all neutron reactions, excluding fission. The FF values are used to determine the source strength in the reactor in terms of the MCNP source particles per second according to the relationship:

$$\dot{S} = \frac{Q_{th}}{\sum_i V_{fuel,i} \times Q_i \times FF_i \times 1.60205 \times 10^{-16}} \quad \text{(A.3)}$$

With the calculated values of the FFs and CFs and at the source strength, the atom densities for the transmuted nuclides are calculated by:

$$N_{EOT} = N_{BOT} + \int_0^T \left(D_{in} - D_{out} + \dot{S} \times (CF_{in} - CF_{out} - FF) \right) dt \quad \text{(A.4)}$$

In this equation, the long-lived nuclides losses due to radioactive decay are neglected and the FF term only applies for fissionable actinides. For the fission products, the atom densities are calculated by:

$$N_{EOT} = N_{BOT} + \sum_i \int_0^T \dot{S} \times FF_i dt \times y_i \quad \text{(A.5)}$$

The values of the CFs are not calculated for the fission products in this method; therefore MCNP tallies are not needed for these nuclides, reducing the computational bookkeeping in the MCNP simulations.

A.3. Comparison of Code Packages

The predictions of the three code packages investigated in this work are compared against actual fuel depletion data for a commercial PWR; similar data for space reactors are non-existent. The PWR data are from an experiment conducted at the Calvert Cliffs Nuclear Power Plant (CCNPP) for a Combustion Engineering 14x14 PWR fuel assembly [Hermann et al. 1995]. Fuel pellets from three different assemblies were assayed following storage for 1870 days in the spent fuel cooling pool (Table A.1). The data of the concentrations of a selected number of nuclides in the spent fuel were used by Oak Ridge National Laboratory (ORNL) to validate the SCALE package [Hermann et al. 1995]. The information on the data used in this work was taken from the validation document of SCALE using the PWR spent fuel isotopic composition analyses.

Table A.1 - Operation history of assembly D047 [Hermann et al. 1995].

	Operation period (days)	Average power (MW_{th}/MTU)	Shutdown period (days)
Cycle 1	306	31.12	70
Cycle 2	381.7	32.51	81.3
Cycle 3	466	26.2	85
Cycle 4	461.1	22.12	
Cooling period	1,870		

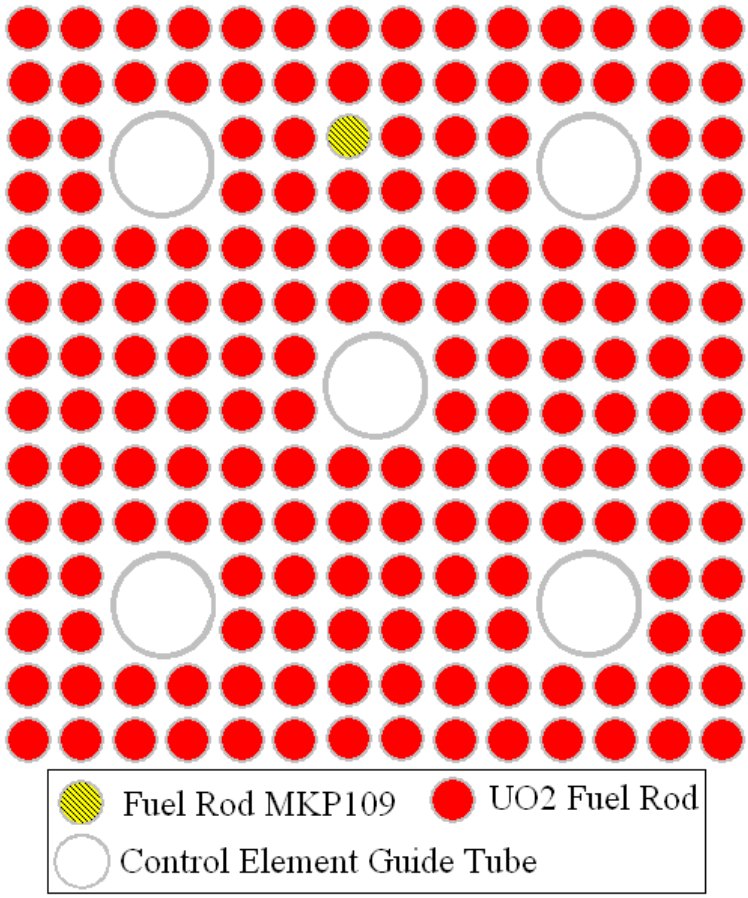

Fig. A.1. - Layout of Calvert Cliffs assembly D047 [Schriener and El-Genk 2009a].

The fuel concentration assay from the pellet in the assembly D047 rod MKP109 at the axial location 165.22 cm is used in the present comparison with the predictions of the

three code packages. The position of the rod MKP109 can be seen in Fig. A.1. The fuel assembly was placed in the reactor for four consecutive operating periods, separated by refueling outages, and its location and mean power level is changed for each period under power as profiled in Table A.1. To simplify the modeling effort, the temperatures and chemical shim concentration were assumed to be the average for the time the assembly was in the reactor. This case is modeled using MCNPX, Monteburns, and TRITON code packages with temperature dependent material densities and ENDF VI temperature dependent neutron cross sections. To speed the calculations the fuel assembly is modeled as a thin reflected slice at the axial position of the assayed fuel pellet. The predictions of the three code packages are compared to the reported data for the discharged fuel, along with the calculated results using Origen-ARP, a widely used LWR burnup code in SCALE 5.1 [Gauld 2005].

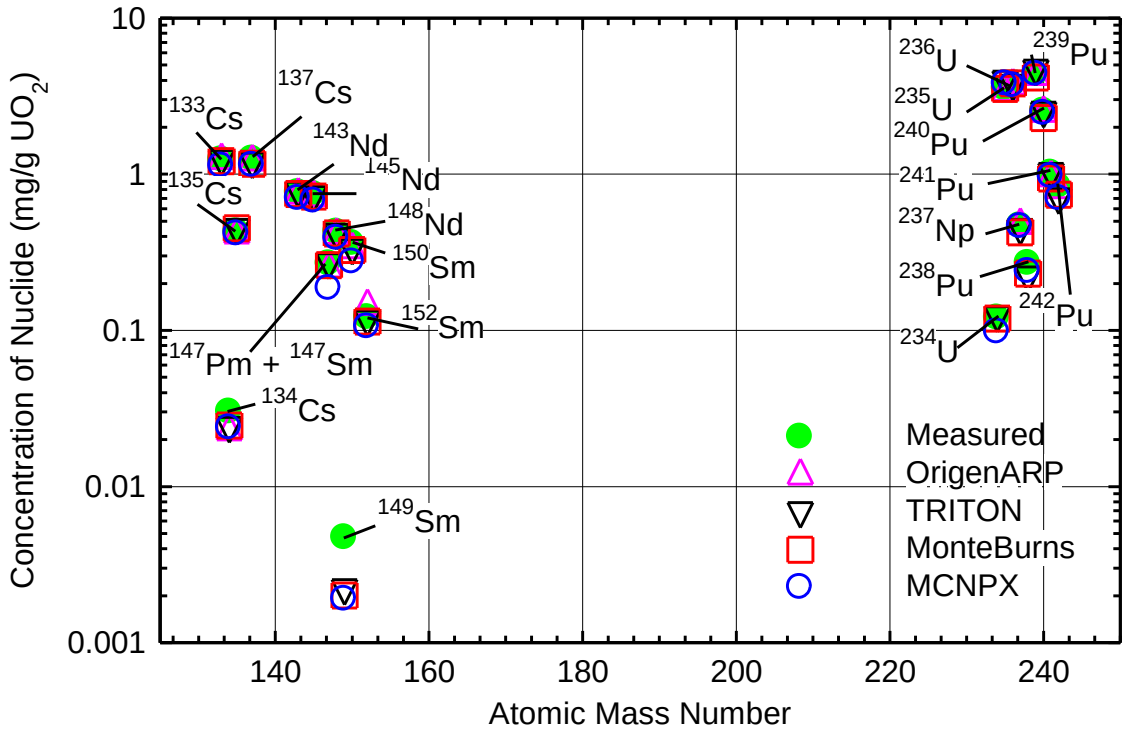

Fig. A.2. - Measured and calculated nuclide mass concentrations in fuel pellet of rod MKP109 [Schriener and El-Genk 2009a].

Figure A.2 compares the measured mass concentrations of the assayed nuclides in the fuel composition with the predictions of Monteburns, MCNPX, TRITON, and Origen-ARP. The predictions of the four codes generally match the reported data. The errors in predicting specific nuclides vary, and are affected by the accuracy of the neutron cross sections used in the transport codes and the kinetics models used in the burnup codes. As delineated in Fig. A.2, for a number of nuclides there were large discrepancies in the predictions of these codes.

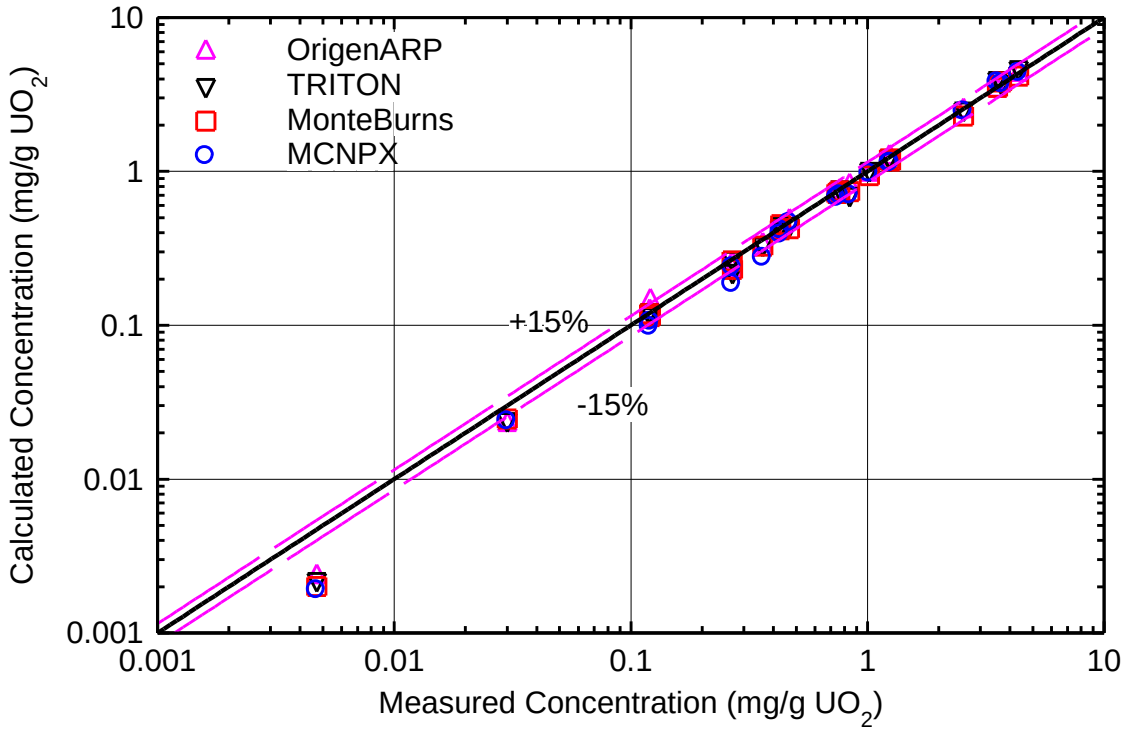

Fig. A.3. - Comparison of calculated to measured mass concentrations of nuclides [Schriener and El-Genk 2009a].

Figure A.3 compares the measured and the calculated results, revealing that the largest discrepancies tend to be for the nuclides with the lowest concentrations. The low concentrations of these nuclides make it more difficult for the transport simulations to produce good reaction rate data. Errors in the neutron cross sections and/or in the tabulated fission yield data may have also contributed to these discrepancies. The calculated mass concentrations of the various nuclides using the four code packages are

compared to the measured concentrations in Fig. A.4. In general, the predictions of the four codes are mostly are within ± 10% of the measured values. Some of the fission product concentrations predicted by MCNPX are lower, while the major actinide concentrations predicted by TRITON are higher than the reported data. Monteburns performed the best, while the overall performance of the other two codes is satisfactory, based on the shown differences between the measurements and calculations of most nuclides (Figs. A.2–A.4).

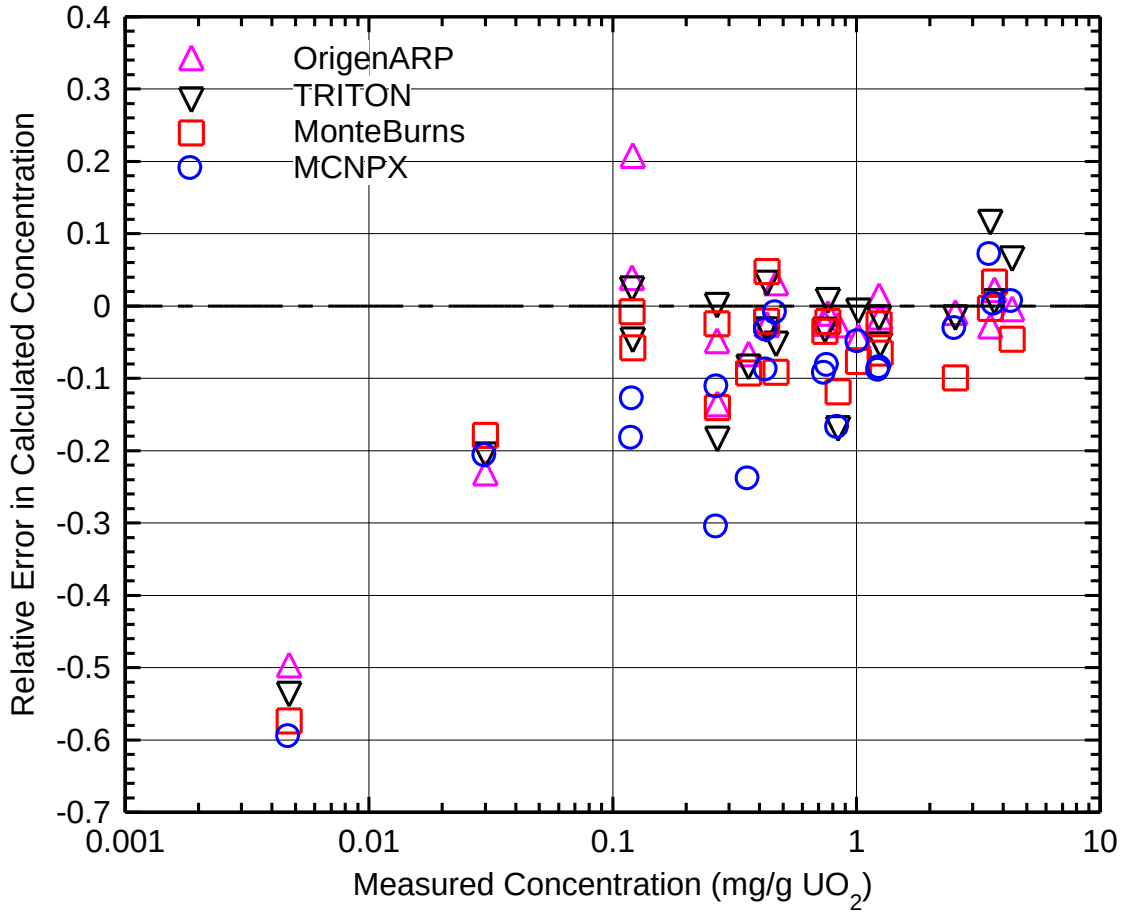

Fig. A.4. - Relative error in calculated mass concentrations of nuclides [Schriener and El-Genk 2009a].

Using the Calvert Cliffs model, a study is performed using Monteburns to quantify the effect of timestep size on the calculated values of k_{eff}. The initial benchmark used fairly wide timesteps. Fig. A.5 shows the trend of the calculated values of k_{eff} using three

different timestep sizes. The same trend is obtained with all three timestep sizes, suggesting that the sensitivity of the results to the size of the timestep is small. It is worth noting that the initial k_{eff} values calculated using the MCNP-based packages are different. For the initial ‘‘clean’’ fuel, the calculated values of k_{eff} using MCNPX and Monteburns are lower than that calculated using MCNP5 alone. When investigated further, the difference is found to be caused in part by the renormalization of the material fractions.

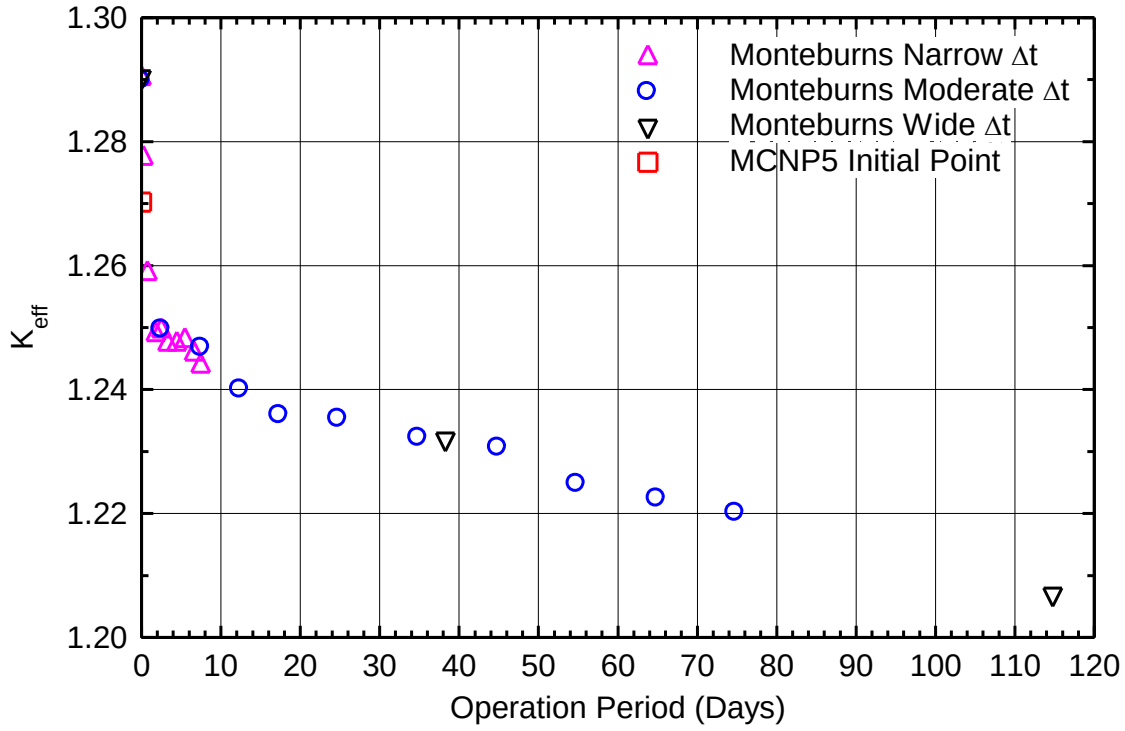

Fig. A.5. - Effect of timestep size on k_{eff} of the system [Schriener and El-Genk 2009a].

A.4. Application to Space Reactors

The code packages investigated are used to model two space reactor designs with hard, fast neutron energy spectra: the SCoRe-S_{11} [El-Genk et al. 2005; Hatton and El-Genk 2009] and S^4 [King and El-Genk 2006a,b, 2007]. The detailed geometry of these reactors could not be modeled using TRITON at the time, due to the sectoring scheme in the SCoRe-S_{11} and the tight grouping of the coolant channels in the S^4. The predictions of Monteburns and MCNPX for these reactors are compared with the results of the

UNM-ISNPS simplified method [King and El-Genk 2006a, 2007]. The next section provides a brief description of the two space reactors investigated.

A.4.1. Operational Life Estimates

The operation life estimates obtained using Monteburns and MCNPX for the two space reactors, SCoRe-S_{11} and S^4, are compared in Figs. A.6 and A.7 with those determined using the simplified method developed at UNM–ISNPS. In the present calculations the average delayed neutron fraction used for these reactors is 0.0066 corresponding to $1.00 of reactivity. The SCoRe-S_{11} has $3.03 hot-clean excess reactivity, and is subcritical by $1.11 when the bare core is submerged in wet sand and flooded with seawater, following a launch abort accident [King and El-Genk 2006]. The S^4 has $1.48 hot-clean excess reactivity, and is subcritical by $1.17 when the bare core is submerged in wet sand and flooded with seawater. Table A-3 lists the salient design dimensions and operating temperatures of these space reactors [Hatton and El-Genk 2007].

The operation lives of both space reactors are determined in this section for continuous operation (see Table A.2). In these calculations, MCNPX and Monteburns use the 60 most probable fission products from the fission yield curve. The UNM-ISNPS developed method uses the 10 most probable low-Z and high-Z elements of the fission yield peaks plus ^{149}Sm. The obtained operation life estimates for the SCoRe-S_{11} are compared in Fig. A.6 and those for the S^4 space reactor are compared in Fig. A.7. The Monteburns estimates in Fig. A.6, performed at the same operating temperatures listed in Table A-2, are close differing by only 2.7% from the estimates obtained using the simplified method of UNM-ISNPS. The method's estimates differ from those using MCNPX by 12.5%.

Monteburns results show that the SCoRe-S_{11} can produce a total of 3,638 MWd of fission energy over its operation life, compared to 3,323 MWd determined by MCNPX, and 3,737 MWd calculated using the UNM-ISNPS method. For a nominal fission power of 2.565 MW_{th} for SCoRe-S_{11}, these fission energy figures translate into 3.88 years, 3.55 years, and 3.99 years of operation life. As indicated in Fig. A.6, the operation life of the

SCoRe-S_{11} reactor is solely dependent on the cumulative fission power generated and not on the operation power level. Therefore, the reactor's operational lifetime is inversely proportional to its operating power, as the reactivity decreases linearly with operation time, or the cumulative fission energy generated increases.

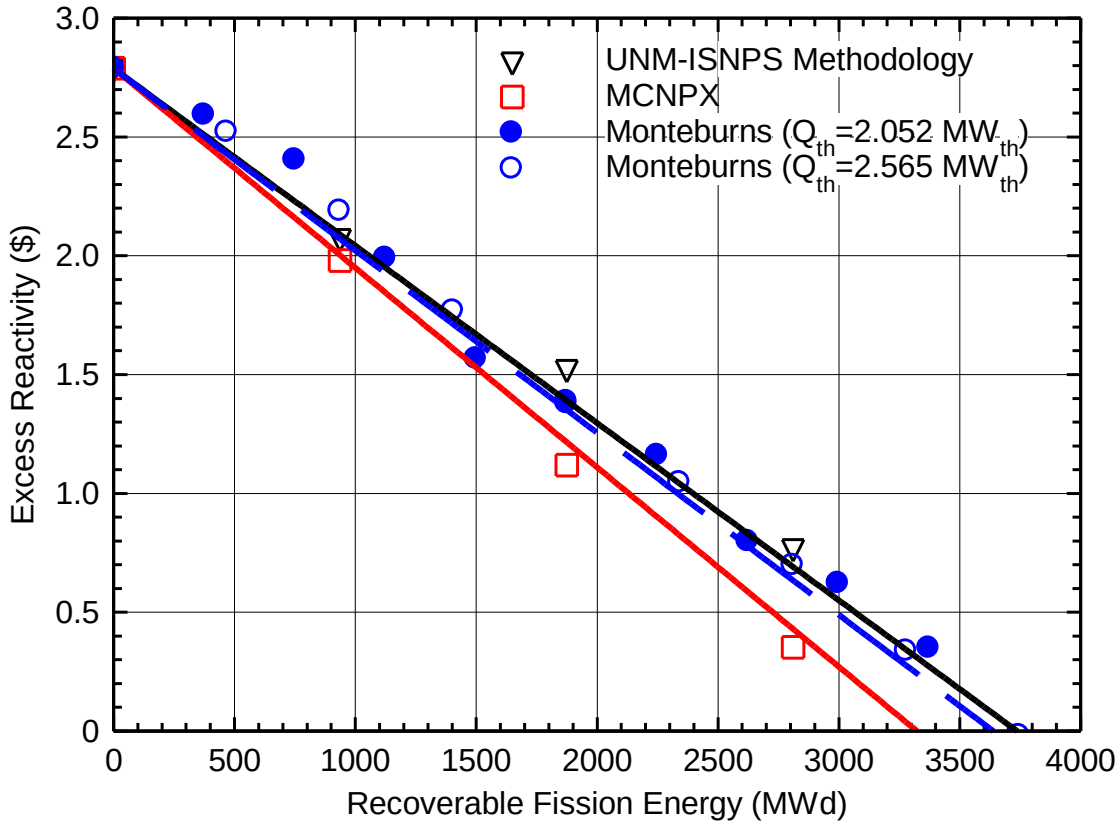

Fig. A.6. - Operational lifetime estimates of SCoRe-S_{11} [Schriener and El-Genk 2009a].

For the nominal operation power and temperatures listed in Table A.2, Fig. A.7 compares the operation life estimates for the S^4 reactor. Results show that this reactor is capable of producing 2,136 MWd of fission energy determined by Monteburns, 2,283 MWd determined by MCNPX, and 2,289 MWd determined by the UNM-ISNPS method [King and El-Genk 2006]. When operating the S^4 space reactor at its nominal design power level of 471 kW_{th} these fission energies correspond to an operation life of 12.41 years, 13.27 years, and 13.31 years, respectively [King and El-Genk 2007]. The predicted operation life of the S^4 reactor using UNM-ISNPS method differs from those determined using Monteburns and MCNPX, by 7.2% and 0.29%, respectively.

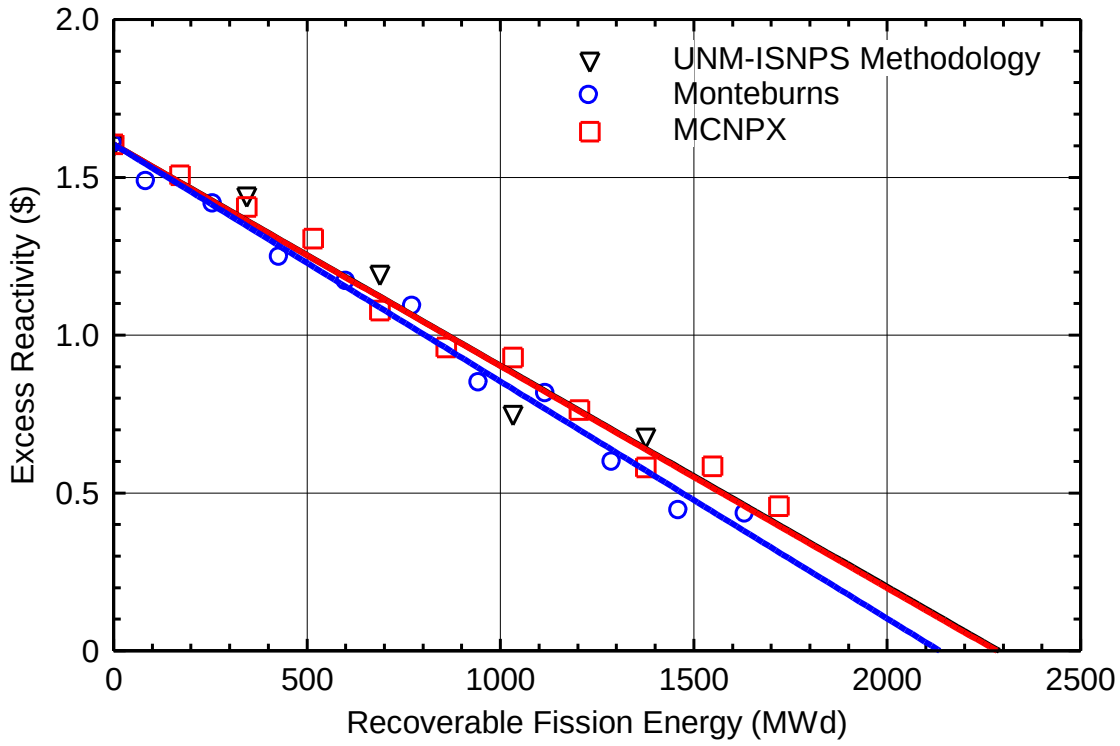

Fig. A.7. - Operational lifetime estimates of S^4 reactor [Schriener and El-Genk 2009a].

The present calculations are carried out using 2.2 GHz AMD Athlon 64x2 PC with 2GB of RAM that runs Windows XP operating system. For the SCoRe-S_{11}, using a total of 1,050 cycles and 5,000 histories/cycle/1-year timestep for a total of 5 years, the UNM-ISNPS method requires 21.94 h of computer time, while Monteburns requires 75.36 h, and MCNPX requires 144.63 h. For the S^4, using the same number of histories, but 10, 1-year time-steps, the UNM-ISNPS method requires 12.61 h of computer time, Monteburns requires 99.93 h, and MCNPX requires 118.5 h.

Despite the simplicity of the UNM-ISNPS method, the obtained operation life predictions of the fast neutron energy spectrum space reactors match well with those calculated using the comprehensive code packages of Monteburns and MCNPX. The simplifying assumptions in this method do not appear to have a major impact on the calculated reactivity depletion rate in these reactors. As seen in Table A.3, for the S^4 space reactor there are large discrepancies between the predicted fission product concentrations by the UNM-ISNPS method and Monteburns. Despite these differences,

the operation life estimates using the two codes differ only by 7.2%, suggesting that for these small space reactors with hard, high neutron energy spectra, detailed modeling of the fission products is not required to achieve accurate values of the reactivity depletion and the operation life estimates.

Table A.2. - Temperatures used in neutronics analysis for SCoRe-S_{11} and S^4 space reactors [Schriener and El-Genk 2009a].

Parameter	**SCoRe-S_{11}**	**S^4**
Region	Temperature (K)	
Core block matrix	–	1,105
Fuel stack	1,150	1,134
Fission gas plenum	1,130	1,160
Clad	1,130	1,160 upper/1,134 lower
Coolant before entering core block	–	904
Coolant within core	1,130	1,062
Coolant after leaving core block	–	1,149
Reflector	600	900
Oxide coating	1,130	–

The computational time for Monteburns using the reduced fission products array used by the UNM-ISNPS method reduced by 40% compared to that of the case that used the 60 most probable fission products. The reduced fission product array results in a difference in the estimated operation life of only 2.01%. With the reduced fission product array, the computer time used by Monteburns is still much longer than that used the UNM-ISNPS methodology to complete the same calculations. This is because the UNM-ISNPS method does not calculate MCNP reaction tallies for fission products. The next section examines the validity of the UNM-ISNPS method to calculate the reactivity depletion in thermal neutron spectrum reactors, such as a PWR.

A.5. Application of the Simplified Method to PWRs

When the predictions of the simplified UNM–ISNPS method are compared with the Calvert Cliffs benchmark data [Hermann et al. 1995], the results are very unsatisfactory. The simplifications in the UNM-ISNPS method of accounting for the accumulation, but not the depletion, of fission products proved inappropriate for thermal neutron spectrum reactors. The UNM–ISNPS method over predicts the reactivity depletion in the Calvert Cliffs Nuclear Power Plant (CCNPP) benchmark. It predicts that plant will become subcritical in the first of the four operating cycles (Table A.1). As seen in Table A.4, the differences in the predicted concentrations of fission products between the UNM-ISNPS method and the Monteburns are quite large in many cases, especially for the poison ^{149}Sm. Since the UNM–ISNPS method only follows stable fission products, neglecting the contributions of the radioactive fission products contributes to the error.

The difference in the energy spectra between the CCNPP and the two space reactor designs investigated in this paper is evident in Fig. A.8a and b. Both the SCoRe-S_{11} and the S^4 have fairly hard neutron energy spectra, in contrast to the thermal energy spectrum of the CCNPP. Thus, the fission product poisons such as ^{149}Sm have a much smaller impact on the reactivity of the space reactors, because of the lower neutron cross sections in the fast energy range. Their impact on the reactivity depletion in a PWR is significantly greater. In the case of ^{149}Sm, the impact of neglecting its depletion produced only a 31% difference in its concentration in the S^4 (Table A.3), but almost a 3700% difference for the CCNPP benchmark case (Table A.4) [Hermann et al. 1995].

Although the predicted concentrations for the fission products by the UNM-ISNPS method and both Monteburns and MCNPX differ greatly, the small difference in the predicted operation life suggests that the simplifications of the UNM-ISNPS are justified when applied to space reactors with high fuel enrichment and fast neutron energy spectra. However, this is not the case when applied to LWRs with significantly lower fuel enrichment and a thermal neutron energy spectrum. For these reactors, the UNM-ISNPS simplified method should not be used because neglecting the depletion and decay of the fission products result in significantly over predicting the depletion rates of reactivity, compared to the more comprehensive code packages of Monteburns and MCNPX. The

more comprehensive models, however, are required for analysis where the composition of the radionuclide source term in the spent fuel is important.

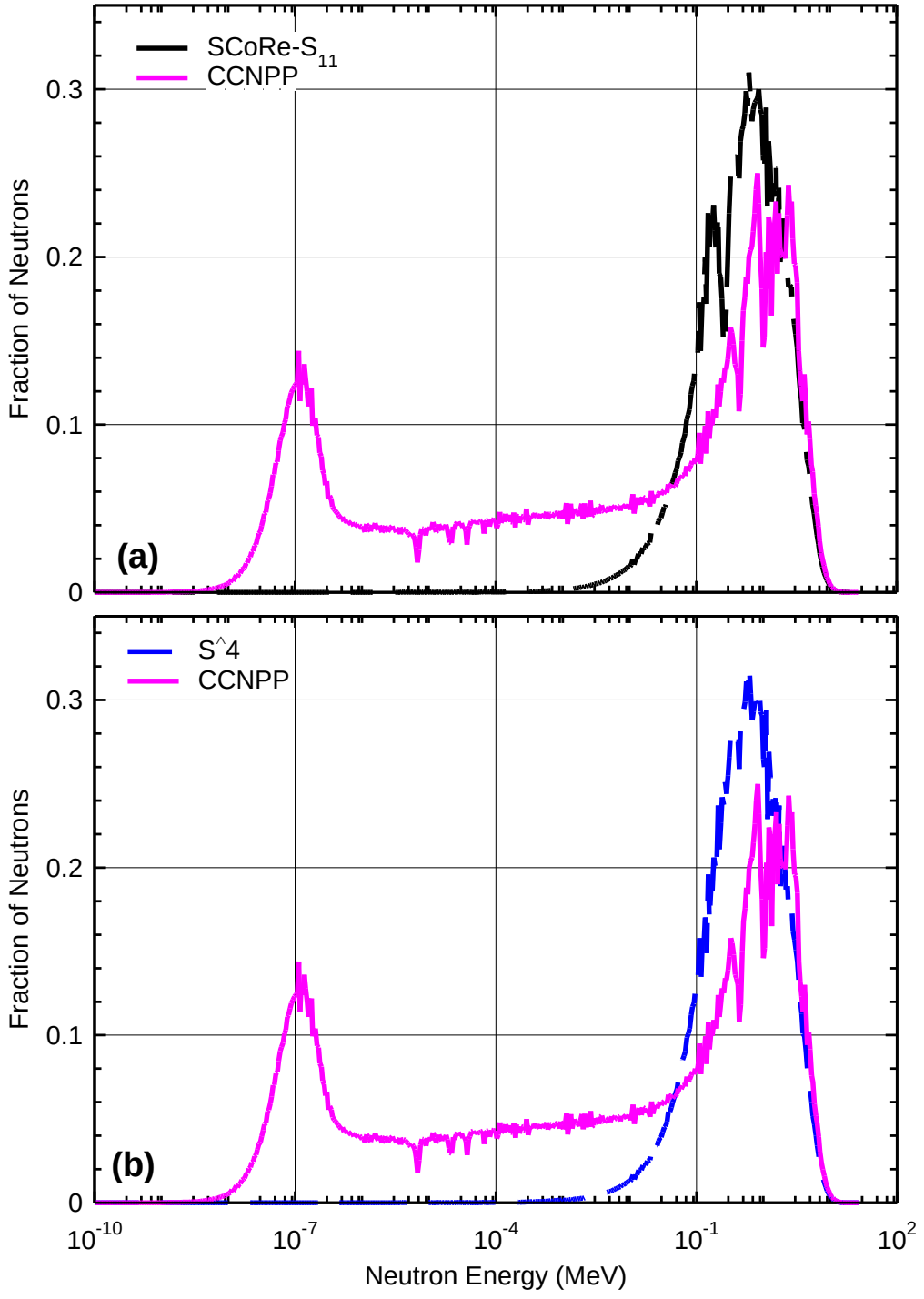

Fig. A.8. - Calculated neutron energy spectra of the analyzed space reactors [Schriener and El-Genk 2009a].

Table A.3. - Fuel composition for S^4 at 1,376 MWd [Schriener and El-Genk 2009a].

Nuclide	Concentration in fuel [mg/g(U, Gd)N]		Relative difference (%)
	UNM-ISNPS	Monteburns	
235-U	9.631E+02	9.701E+02	-0.72
236-U	3.174E+00	1.800E+00	76.37
238-U	5.168E+01	5.174E+01	-0.11
239-Pu	1.339E-01	6.327E-02	111.67
14-N	6.332E+01	6.327E+01	0.09
15-N	2.590E-01	2.587E-01	0.11
91-Zr	3.689E-01	2.179E-01	69.29
92-Zr	3.786E-01	2.299E-01	64.68
93-Zr	3.940E-01	2.524E-01	56.10
94-Zr	4.209E-01	2.432E-01	73.06
96-Zr	4.067E-01	2.545E-01	59.81
99-Tc	4.193E-01	2.418E-01	73.40
133-Cs	5.957E-01	3.705E-01	60.80
134-Xe	6.894E-01	4.401E-01	56.66
135-Cs	5.720E-01	3.670E-01	55.88
136-Xe	4.260E-01	3.719E-01	14.56
137-Cs	5.722E-01	3.234E-01	76.96
138-Ba	6.181E-01	3.859E-01	60.16
141-Pr	4.225E-01	3.557E-01	18.77
143-Nd	4.090E-01	3.445E-01	18.73
149-Sm	4.735E-02	6.896E-02	-31.34
152-Sm	5.751E-02	5.420E-02	6.11
151-Eu	2.014E+01	2.032E+01	_0.87
152-Eu	3.198E-01	9.982E-02	220.35

Table A.4. - Fuel composition for Calvert Cliffs benchmark at the end of Cycle 1 [Schriener and El-Genk 2009a].

Nuclide	Concentration in fuel [mg/gUO2]		Relative difference (%)
	UNM-ISNPS	Monteburns	
234-U	2.065E-01	2.070E-01	-0.24
235-U	1.850E+01	1.890E+01	-2.10
236-U	1.607E+00	1.216E+00	32.12
237-U	2.634E-03	3.591E-03	-26.65
238-U	8.483E+02	8.505E+02	-0.26
237-Np	3.843E-02	6.552E-02	-41.35
238-Pu	3.389E-03	5.639E-03	-39.89
239-Pu	3.102E+00	2.678E+00	15.86
240-Pu	4.832E-01	4.001E-01	20.79
241-Pu	2.123E-01	1.755E-01	21.01
16-O	1.183E+02	1.184E+02	-0.13
91-Zr	2.468E-01	1.244E-01	98.35
92-Zr	2.544E-01	2.309E-01	10.19
93-Zr	2.752E-01	1.922E-01	43.20
94-Zr	2.801E-01	1.903E-01	47.22
96-Zr	3.503E-01	2.010E-01	74.29
99-Tc	3.619E-01	1.972E-01	83.55
103-Rh	9.570E-02	9.828E-02	-2.63
132-Xe	9.182E-02	2.158E-01	-57.45
133-Cs	5.194E-01	2.911E-01	78.46
134-Xe	5.897E-01	3.528E-01	67.14
135-Cs	5.280E-01	9.923E-02	432.06
136-Xe	5.034E-01	5.450E-01	-7.63
137-Cs	4.958E-01	2.879E-01	72.21
138-Ba	5.201E-01	3.141E-01	65.60
141-Pr	4.703E-01	2.369E-01	98.54
143-Nd	3.648E-01	2.391E-01	52.57
149-Sm	6.174E-02	1.638E-03	3669.23

APPENDIX B: Effect of Reactivity Control Options on Space Nuclear Reactors

Over the past fifty years, several in-core and ex-core control options of space fission reactors have been proposed. These can be in-core with the control element located inside the reactor core, or ex-core with the control elements located in the external radial neutron reflector. Most space reactors use ex-core control elements as the small size of the reactor cores results in high neutron leakage, increasing the reactivity worth of the external reflector. These ex-core elements also avoid the need for penetrations in the reactor vessel, which complicate the design and present potential failure points for the primary reactor coolant boundary.

To systematically compare the impact of two ex-core control options, analysis is performed for the same space reactor design, the compact fast-neutron spectrum, gas-cooled Submersion Subcritical Safe Space (S^4) reactor [King and El-Genk 2006a,b, 2007]. For the S^4 reactor, this appendix investigates two ex-core reactivity control options and compares the effects on the Beginning of Life (BOL) excess reactivity, operational life, and the neutron spatial flux and fission power distributions in the core. These control options are (a) rotating drums with thin 120° segments of enriched B_4C in the radial BeO reflector and, (b) sliding segments in the BeO radial reflector. With both reactivity control options, the reactor core maintains the same volume, external dimensions, and approximately the same mass. This appendix also investigates the effect of reducing the thickness of the enriched B_4C segments in the control drums on the BOL excess reactivity, in case one or two of the six drums stuck in the shutdown position.

B.1. S^4 Reactor Core Design

The S^4 high-temperature, fast neutron energy spectrum reactor is cooled with He-30%Xe binary gas mixture (40 g/mol) and nominally generates 471 kW of thermal power when operating at inlet and exit temperatures of 904 K and 1,149 K, and inlet pressure of 1.985 MPa [King and El-Genk 2006a,b, 2007]. The reactor core is divided into three neutronically and thermally coupled, but hydraulically independent sectors (Fig. B.1). The 217 fuel cavities in the solid Mo-14%Re core block of the S^4 reactor are filled with

43.5 cm high and 1.25 cm diameter fuel stacks comprised of pellets of highly enriched (95 wt%) UN mixed with 1.95 wt% ^{151}EuN (Fig. B.1). The ^{151}EuN ensures that the bare reactor core remains subcritical when flooded with seawater and submerged in wet sand, following a launch abort accident. Each UN fuel stack has a gas plenum with a Mo-14%Re spring and is caped flush with the upper and lower surfaces of the Mo-14%Re core block [King and El-Genk 2006a,b, 2007].

The cavities filled with the fuel stacks are arranged in 9 hexagonal rings in a triangular lattice with a pitch of 1.78 cm (Fig. B.1). The coolant channels, 0.3 cm in diameter, are pierced through the core block, nine per fuel stack, for removing the fission power generated in the reactor core. The core block is surrounded by a hexagonal annulus through which the gas coolant returning from the CBC power conversion loops enters the reactor core sectors. The coolant mixes in the plenum at the opposite end before reversing direction and flowing through the small diameter coolant channels in the core (Fig. B.1).

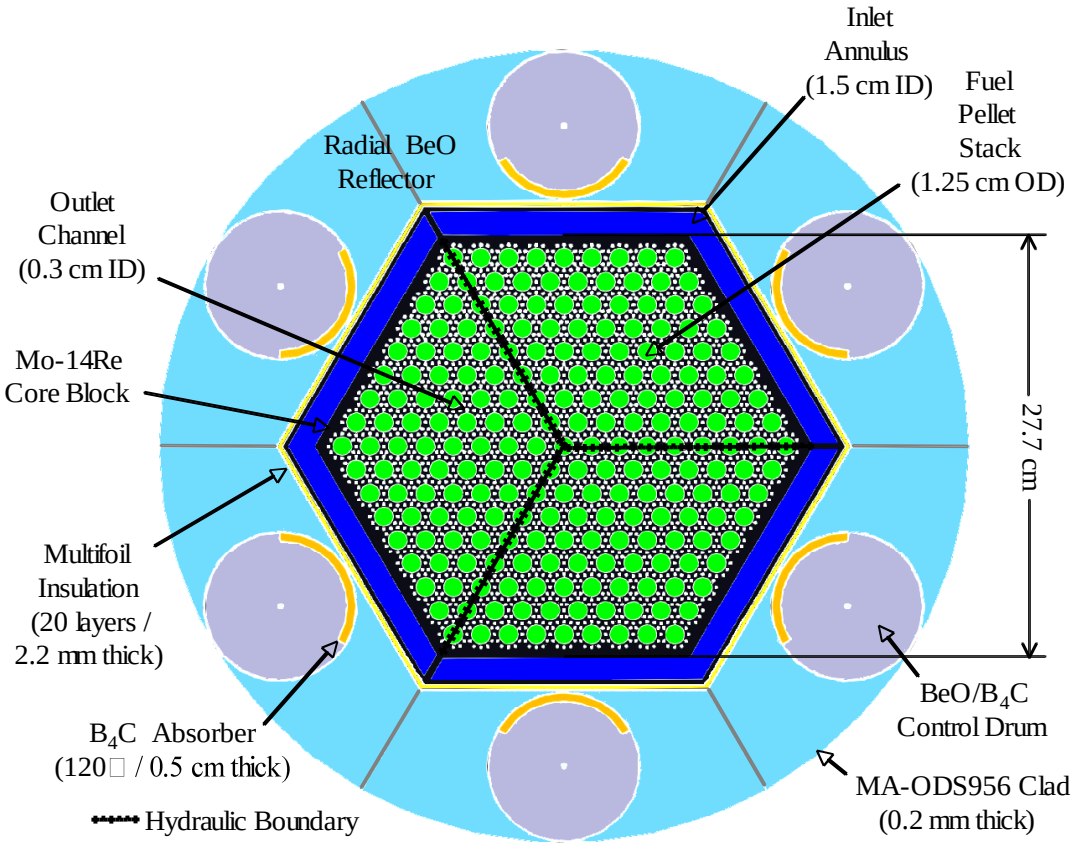

Fig. B.1. - Radial section view of S^4 reactor [King and El-Genk 2007].

B.2. Control Options for the S^4 Reactor

The radial reflector of the S^4 reactor core consists of six BeO panels encased in a thin MA-ODS S954 steel for structural support and protection from the impact by orbital debris. The upper and lower axial BeO reflectors consist of 5 cm thick disks with penetrations in the upper reflector for the upper concentric coolant ducts. The cylindrical BeO reflector surrounding the hexagonal reactor vessel consists of six 62.63 cm long panels having a maximum thickness of 10.46 cm. The BeO radial reflector panels, along with the axial BeO reflector disks, are designed to fully disassemble upon impact on a solid or water surface, following a launch abort accident [King and El-Genk 2006b].

In the original design [King and El-Genk 2006b], the S^4 reactor is controlled using 6 rotating BeO drums with 0.5 cm thick, 120° segments of enriched B_4C (Fig. B.1). In the shutdown configuration, the B_4C segments face the reactor core and in the end-of-life configuration they face away from the core. Each BeO radial reflector panel has a 10.398 cm diameter cylindrical cavity for a 10.198 cm diameter rotating drum. The BeO drums clad in MA-ODS S954 run the full length of the radial reflector and rotate by means of central drive shafts that extend to an electrical motor behind the radiation shadow shield.

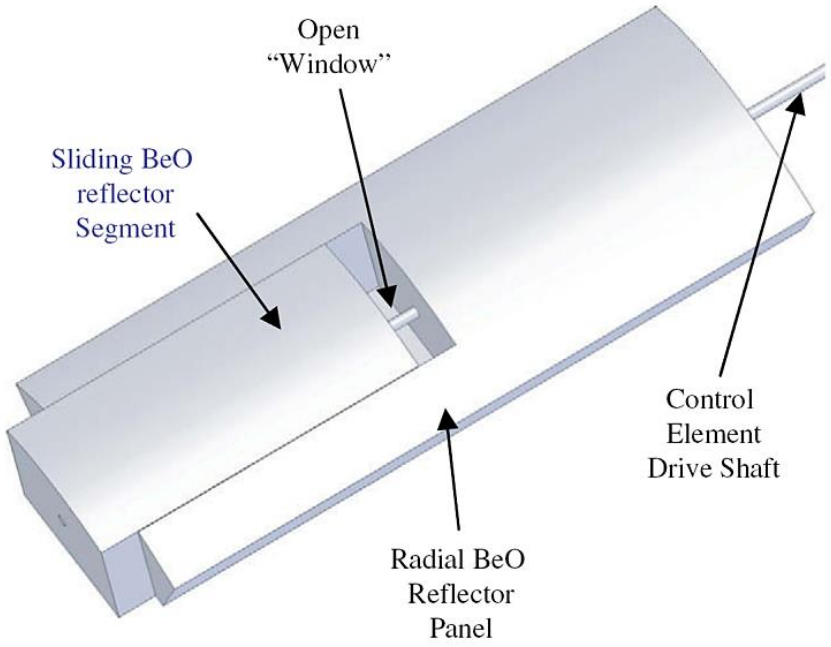

Fig. B.2. - Radial reflector panel with sliding segment [Schriener and El-Genk 2009b].

For the S^4 reactor with sliding segments in the BeO radial reflector panels for the reactivity control (Fig. B.2), the segments are 15.398 cm wide, 31.11 cm long, and clad in MA-ODS S954. The sliding reflector segments travel linearly inside slots in the BeO reflector panels. The open ‘‘windows’’ in the radial reflector panels allow neutrons to leak out of the reactor core. In the shutdown position, the sliding reflector segments are withdrawn to their maximum displacement position. During operation the displacement or the height of the open ‘‘windows’’ in the radial reflector panels gradually decreases, reducing the neutron leakage from the core.

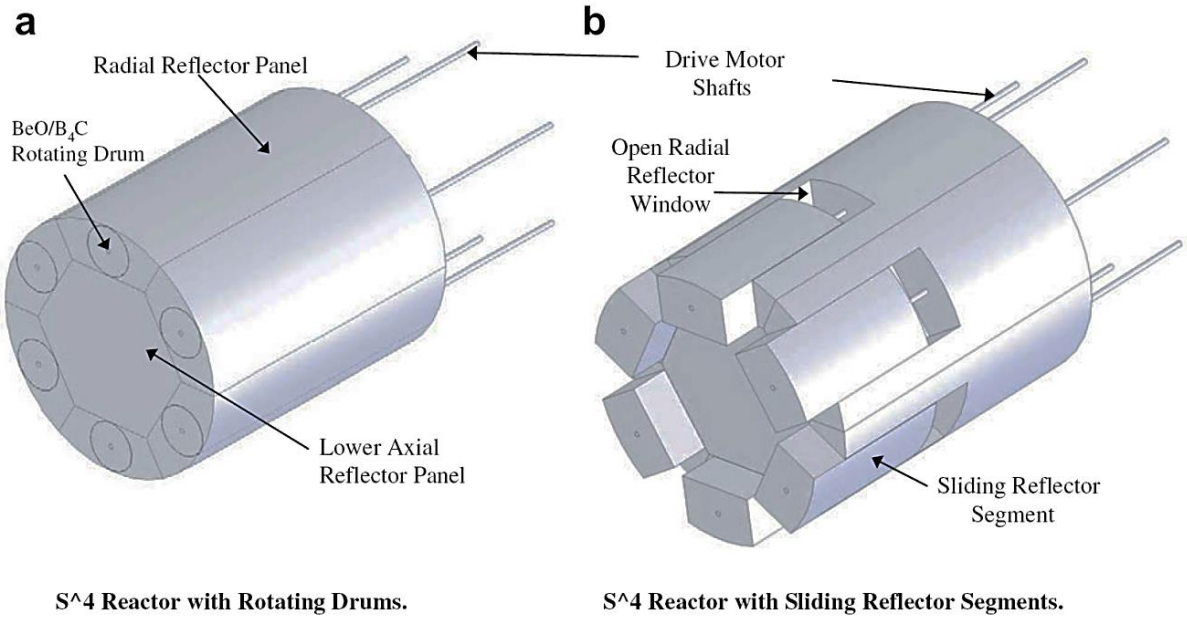

Fig. B.3. - Isometric views of S^4 reactor with different control configurations [Schriener and El-Genk 2009b].

The open ‘‘windows’’ in the radial reflector panels are centered across the core mid-plane to minimize the displacement for the sliding reflector segments between the BOL and End of Life (EOL) positions. This is to limit the reflectors; impact on the axial power distribution in the core, where the neutron leakage could shift the distribution towards one half of the core [Wollman and Zika 2006]. When in the fully inserted position, the bottom of the sliding reflector segments is flush with the lower axial BeO reflector disk and the external dimensions of the S^4 are same as the reactor with the rotating drums control (Figs. B.3a and b).

B.3. Reactivity Requirements

The S^4 reactor with six rotating drums in the BeO radial reflector was designed to operate for at least 1,400 MWd at the full nominal power of 471 kW_{th} [King and El-Genk 2007]. In the original design [King and El-Genk 2006b], each control drum had a 0.5 cm thick segment of enriched B_4C. The reactor was designed with at least +$4.0 of BOL cold-clean excess reactivity. This excess reactivity compensates for the decrease in reactivity due to the negative temperature reactivity feedback, and the fissile depletion and the accumulation of fission product poisons during reactor operation. The dimensions and operation temperatures of the S^4 reactor with rotating control drums and sliding reflector segments control schemes are compared in Table B.1.

Table B.1. - S^4 reactor dimensions and operation temperatures [Schriener and El-Genk 2009b].

Parameter	Value
(a) Control drums	
Number of rotating drums	6
Drum diameter (cm)	10.198
B_4C segment thickness (mm)	5
B_4C segment height (cm)	43.5
B_4C segment angle (°)	120
Total radial reflector mass (kg)	227.8
(b) Sliding reflector segments	
Number of sliding segments	6
Segment width (cm)	15.398
Widow height (cm)	31.11
Total radial reflector mass (kg)	226.4

Table B.2 compares the calculated excess and shutdown reactivity for the S^4 with rotating drums and sliding reflector segments control. The S^4 reactor is designed to be > -$2.25 subcritical in the cold-clean shutdown condition. Cold-clean refers to BOL

operation at 300 K with fresh fuel in the core, while hot-clean refers to BOL operation at nominal operating temperatures in the reactor core with fresh fuel (Table B.2). Following a launch abort accident, the bare S^4 reactor core is designed to be > -$1.0 subcritical when surrounded by wet sand and flooded with seawater.

B.4. Methods and Analysis

The present analyses used the Monte Carlo neutron transport code MCNP5 1.40 [X-5 Monte Carlo Team 2004] to perform the neutronic calculations for the S^4 reactor with the two ex-core control options. The criticality calculations, without material reaction rate tallies, used 20,000 particles/history, and 50 skipped and 1,000 active cycles. The calculations with reaction rate tallies used 20,000 particles/history, and 50 skipped and 5,000 active cycles. The calculations are performed on a computer running Windows XP with a 2.4 GHz Intel Core 2 Duo processor and 2 GB RAM. Except where noted, these calculations are performed at hot-clean condition, using the temperatures listed in Table B.2 in the various regions of the reactor core and the BeO reflector.

To avoid distorting the neutron flux profile in the core and to remove the tallies dependence on k_{eff}, the calculations of the neutron reaction rate and flux tallies are performed with the S^4 critical in the hot-clean condition ($k_{eff} = 1$). The value of k_{eff} is calculated for each 20° rotation of the control drums and each 1 cm displacement of the sliding reflector segments. The results are then used to determine the rotation angle of the control drums in the radial BeO reflector and the displacement of the sliding reflector segments corresponding to a $k_{eff} = 1$.

To determine the spatial neutron flux distributions in the S^4 core during operation, the MCNP mesh tallies are calculated at the BOL hot-clean condition, at the rotation angle of the control drums or the axial displacement of the sliding reflector segments for $k_{eff} = 1$. The tally mesh utilizes a cubic XYZ grid (64 cm x 64 cm x 64 cm) comprised of 0.125 cm^3 cubic mesh elements. A total of 20,000 particles/cycle and 50 skipped and 5,000 active histories are used in the MCNP runs for calculating the mesh tallies.

Table B.2. - Excess and shutdown reactivity for S^4 with rotating drums and sliding reflector segments control [Schriener and El-Genk 2009b].

	Rotating control drums with 0.5 cm B_4C segments	**Rotating control drums with 0.283 cm B_4C segments**	**Sliding reflector segments**
Cold-clean excess reactivity	+$4.09	+$4.19	+$4.19
Hot-clean excess reactivity	+$1.59	+$1.76	+$1.78
Cold-clean shutdown reactivity	-$2.76	-$1.02	-$1.01
Hot-clean shutdown reactivity	-$5.13	-$3.33	-$3.47
Cold-clean excess reactivity with one stuck control element	+$2.88	+$3.31	+$3.30
Hot-clean excess reactivity with one stuck control element	+$0.47	+$0.89	+$0.89
Cold-clean excess reactivity with two stuck control elements	+$1.71	+$2.38	+$2.37
Hot-clean excess reactivity with two stuck control elements	-$0.74	+$0.03	-$0.05

To capture the spatial effects of the neutron flux distributions on fuel depletion, each of the 217, 43.5 cm long fuel stacks in the S^4 reactor core are divided into 14 axial segments of equal length, for a total of 3,038 computational segments. The fuel composition and power production in each computational segment are tracked independently using a combination of MCNP5 and a simplified UNM-ISNPS reactivity

depletion or burnup code (Chapter 3). This burnup analysis code solves a series of radioactive decay, production, and depletion equations for a limited number of nuclides, 13 actinides and 30 non-actinide fission products and ^{151}Eu activation products, encompassing the 10 most probable low-Z and high-Z elements of each fission yield peak plus ^{149}Sm.

B.5. Rotating Drums Control

The original design of the S^4 reactor with 0.5 cm thick 120° enriched B_4C segments in the control drums has +$1.59 hot-clean BOL excess reactivity (Table B.2). The excess reactivity is reduced if one or more of the control drums fail with the B_4C segment in the drum(s) facing the core. With one rotating drum stuck in the shutdown position, the hot-clean BOL excess reactivity deceases from +$1.59 to as little as +$0.47. With two rotating drums stuck in the shutdown position, the hot-clean BOL reactivity decreases to -$0.74, thus the reactor is subcritical and could not start up with the remaining four drums operational and fully rotated outward. To improve the redundancy in the control of the S^4 reactor with rotating drums, the hot-clean BOL excess reactivity in the core with one or more drums stuck in the shutdown position needs to be increased. This is accomplished by decreasing the reactivity worth of each rotating drum via reducing the thickness of the B_4C absorber segments in the drums. Reducing the individual drum worth lessens the reactivity penalty of a control drum failing to rotate outward at startup.

B.5.1. Effect of B_4C Segments Thickness on Reactivity

The effect of reducing the thickness of the B_4C segments in the rotating drums in the BeO radial reflector from 0.5 cm to 0.238 cm on the reactivity of the S^4 reactor is presented in Fig. B.4 and listed in Table B.2. Such a decrease in the thickness of the B_4C segments results in a +$0.17 increase in BOL hot-clean excess reactivity from +$1.59 to +$1.76. With one rotating drum stuck in the shutdown position, the BOL hot-clean excess reactivity increases by +$0.42 from +$0.47 to +$0.89, an almost ~90% increase. With the smaller thickness of the B_4C segments in the control drums, the reactor is still at least ~$1.0 subcritical in the cold-clean shutdown condition (Table B.2). Table B.2 shows that the hot and cold-clean reactivities of the S^4 reactor when the rotating drums have

0.283 cm thick B_4C segments are almost identical to those of the reactor with sliding reflector segments control.

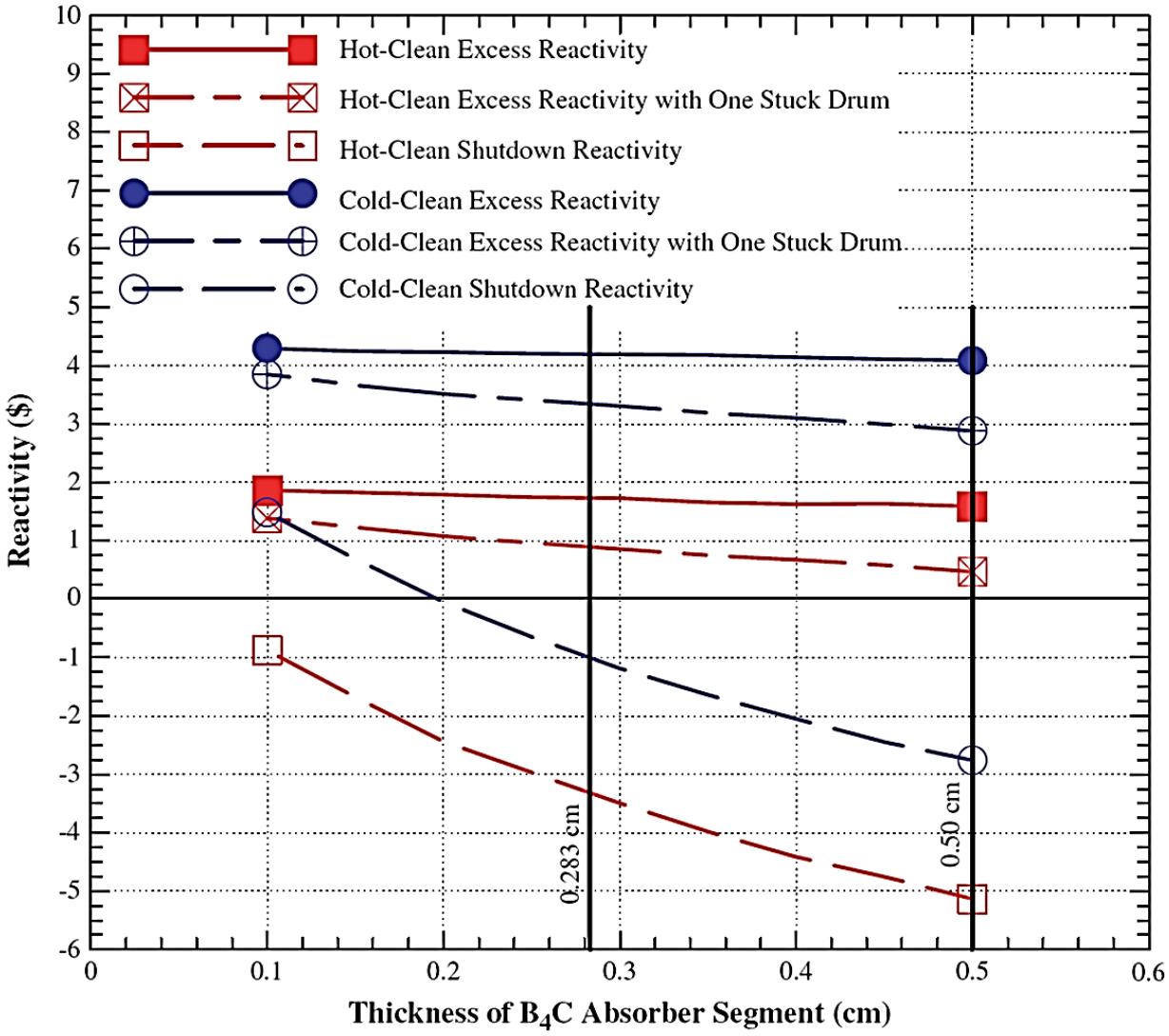

Fig. B.4. - Effect of B_4C absorber thickness on S^4 reactivities [Schriener and El-Genk 2009b].

B.5.2. Effect of B_4C Segments Thickness on Operational Life

This section investigates the effect of decreasing the thickness of the B_4C segments in the rotating control drums from 0.5 cm to 0.283 cm of the operational life of the S^4 reactor. In the first scenario considered, the reactor operates at a nominal thermal power of 471 kW_{th} with all six rotating drums operational through EOL. With 0.5 cm thick B_4C

segments in the drums, the reactor is capable of generating 2,133 MWd over an operational life of 12.4 years (Fig. B.5). With the thickness of the B_4C segments reduced to 0.283 cm, the S^4 is capable of generating as much as 2,255 MWd over longer operational life of 13.1 years. These results translate into an extra 259 days of full power operation or a 5.7% longer operational life.

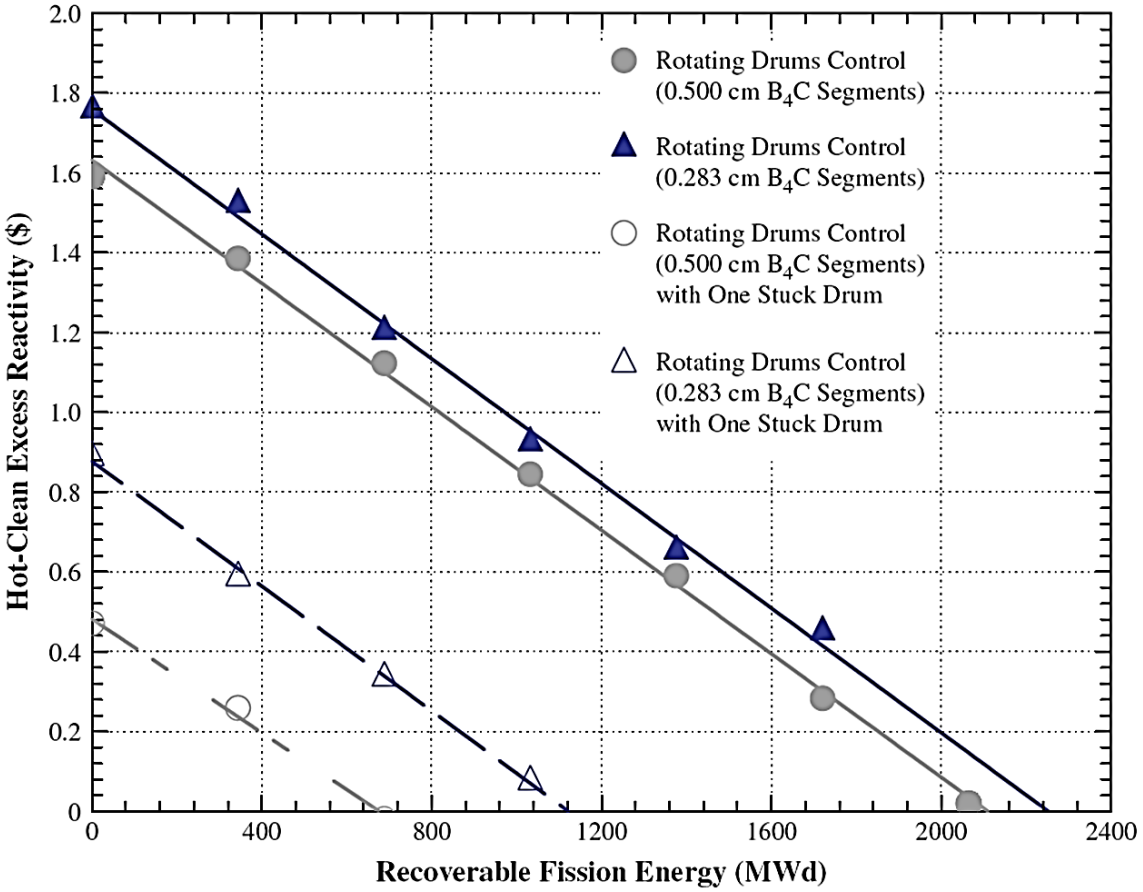

Fig. B.5. - Operational life estimates for S^4 reactor with rotating drums control [Schriener and El-Genk 2009b].

In the second scenario investigated, the S^4 operates at 471 kW_{th} with one drum stuck in the shutdown position at BOL. The remaining five rotating drums provide for the reactivity control through EOL. When a drum with 0.5 cm thick B_4C segment is stuck in the shutdown position, the reactor is capable of generating 678 MWd over an operational life of 3.9 years. The S^4 with the control drums having 0.283 cm thick B_4C segments and one drum stuck in the shutdown position is capable of generating 1,115 MWd over

6.5 years, an increase of over 927 days of operation at full power, or ~64% increase in operational life. Therefore, reducing the thickness of the B_4C segments in the rotating drum not only increases the BOL excess reactivity, but also reduces the impact on the operational life of the reactor with a drum stuck the shutdown position. In the following analysis the operation characteristics of the S^4 reactor with control drums having 0.283 thick B_4C segments is compared to those of the reactor with sliding reflector segments control.

B.6. Performance Comparisons of Rotating Drums and Sliding Reflector Segments Control

This section compares the results of the S^4 reactor with rotating drums control and sliding reflector segments control. The drums have 0.283 cm thick, 120° B_4C segments. In both control options, the BOL hot-clean reactivity of the reactor is identical (Table B.2), however, they regulate the neutrons in the reactor during startup and operation differently. With the rotating drums, the B_4C neutrons absorber segments, which extend the entire length of the active core, regulate the amount of neutrons reflected back into the core. On the other hand, with the sliding reflector segments, the narrow ‘‘windows’’ in the radial reflector panels, just above the core mid-plane, regulate the neutrons’ leakage through the reflector. The difference in regulating the reactivity in the reactor by the two control options may affect the spatial distributions of the neutron flux, fission power and the fuel depletion.

B.6.1. Reactor Reactivity Control

The BOL hot-clean excess reactivity in the S^4 reactor with rotating drums control is calculated for each 20° of angular rotation, from 180° (B_4C segments in the drums facing the core) to 0° (B_4C segments facing away from the core). For the S^4 reactor with the sliding reflector segments control, the BOL hot-clean excess reactivity is calculated for each centimeter of axial displacement of the segments, from 5.64 cm (fully withdrawn) to 0 cm (fully inserted). The results delineated in Fig. B.6 indicate that the BOL hot-clean reactivity and the excess reactivity values are almost identical for both control methods,

but the change in the reactivity with the control drum rotation outward and with the reflector segments displacement are different.

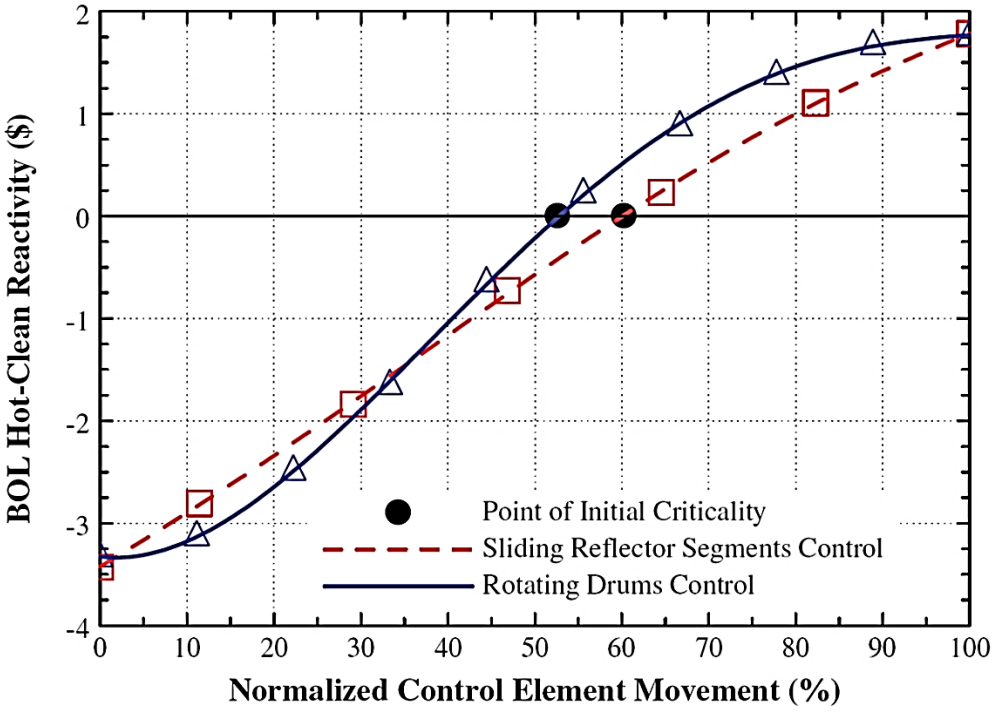

Fig. B.6. - Reactivity change over the full range of control element movement [Schriener and El-Genk 2009b].

With the rotating drums control, the reactivity insertion per a percentage of the total rotation angle varies with the value of the rotation angle outward. This is because the reactivity worth of the drums changes non-linear with the rotation angle outward. On the other hand, the reactivity insertion per a percentage of the total displacement of the sliding reflector segments is almost constant because the neutron leakage from the reactor core is directly proportional to the height of the open windows in the radial reflector. These results suggest that the sliding reflector segments control may be simpler to implement into an automated controller scheme than the rotating drums control. In Fig. B.6, the solid circle symbol indicates the point of reaching hot-clean criticality at BOL for the S^4 reactor with the rotating drums and the sliding reflector segments control options. This point is reached when the ‘‘windows’’ in the radial reflector panels are open 2.24 cm, and when the control drums are rotated 94.79° outward.

B.6.2. Neutron Flux Distributions

The calculated neutron flux distributions in Figs. B.7-9 using MCNP5 mesh tallies in the S^4 reactor with the two ex-core control options are normalized to the peak flux in the core. Fig. B.7 shows the normalized flux distributions along the YZ plane of the core, and the flux distributions along the XY plane are shown in Figs. B.8 and B.9. Alongside the flux plots, there are scale plots of the MCNP model geometry generated by the MCNP Visual Editor program [Carter and Schwarz 2005]. Fig. B.7b and d shows that the overall flux distributions in the S^4 reactor core with the two control options are very similar. The peak neutron flux is slightly (~2%) higher in the reactor with the rotating drums control, although the total core neutron fluence is higher in the reactor with the sliding reflector segments control, to make up for the neutrons leakage. The most notable difference between the two control options is the high neutron leakage through the open ‘‘windows’’ in the radial reflector panels with the sliding segments (Fig. B.7d). However, the small size of the open ‘‘windows’’ limits the distortion of the neutron flux profile on the inside radial reflector and in the outer few rings of the fuel stacks in the S^4 reactor core. There is also a slight flux depression in the peak neutron flux compared to that in the reactor core with the rotating drums control (Fig. B.8c and B.9c).

The B_4C absorber segments in the rotating drums induce local depressions in the neutron flux in their vicinity within the reactor core. This effect cannot be seen in Fig. B.7b as the section view does not bisect any of the B_4C segments. It is, however, clearly visible in the plots shown in Fig. B.8b–d, with the crescent-shaped flux depressions corresponding to the positions of the B_4C absorber segments in the rotating drums. These depressions are largely limited to the radial reflector and the coolant annulus between the core block and the reactor vessel, causing only a slight deformation in the neutrons isoflux lines in the outer rings of fuel stacks. The difference between the neutron axial flux profiles at z = 10.75 cm (z/h = + 0.25) (Fig. B.8b) and z = -10.75 cm (z/h = -0.25) (Fig. B.8d) is slight, with the flux weighted slightly towards the lower half of the core. This is due to the closer proximity of the lower axial BeO reflector to the active core and the large penetrations in the upper axial BeO reflector by the coolant ducts (Fig. B.7a).

The results for the S^4 reactor with the sliding reflector segments control are shown in Fig. B.9b–d. The increase in the neutron leakage through the open ‘‘windows’’ in the radial reflector panels appears prominently in Fig. B.9c, an XY section at z = 2 cm (z/h = +0.045). This figure corresponds to the middle of the open ‘‘windows’’ in the radial reflector. The neutrons isoflux lines on the inside of the radial reflector and within the open ‘‘windows’’ are still nearly circular. The neutron flux in the active core is only slightly distorted by the neutrons leakage through the ‘‘windows’’ in the radial reflector. The small height of the open ‘‘windows’’ in the radial reflector, only 2.24 cm at BOL hot-clean criticality, and their location near the peak axial neutron flux in the S^4 core minimizes these distortions. In the S^4 reactor with the sliding reflector segments, there is greater axial variation in the neutron flux distribution in the core, with the distribution weighted more heavily towards the lower half of the active core. This asymmetry in the neutron axial flux profile is because the open ‘‘windows’’ in the radial reflector panels are located 2 cm above the core mid-plane.

B.6.3. Fission Power Profiles

Low fission power peaking in the reactor core is desirable from the thermal-hydraulic, fuel utilization, and operation safety perspective. It lowers the thermal stress in-core, decreases the fuel swelling and fission gas release, and results in a more uniform fissile burnup and coolant outlet temperature from the reactor core. The thermal power generated in each fuel segment in the S^4 reactor core is calculated using the depletion code after 60 s of BOL operation at the nominal thermal power of 471 kW_{th}. The results in Fig. B.10a and b show the variations in the normalized axial fission power profiles from the bottom (z/h = -0.5) to the top (z/h = +0.5) of the active core and radially across the hexagonal rings of fuel stacks in the core, from the center fuel stack (Ring 1) to the outermost ring of fuel stacks (Ring 9) (Fig. B.1).

With both control options, the S^4 has high power peaking at the center of the core. A comparison of the fission profiles in the S^4 core with rotating drums control (Fig. B.10a) and with the sliding reflector segments control (Fig. B.10b) shows that the power peaking in the latter is ~4% lower than the former. The fission power generated in the upper and lower portions of the S^4 core with the sliding reflector segments control is

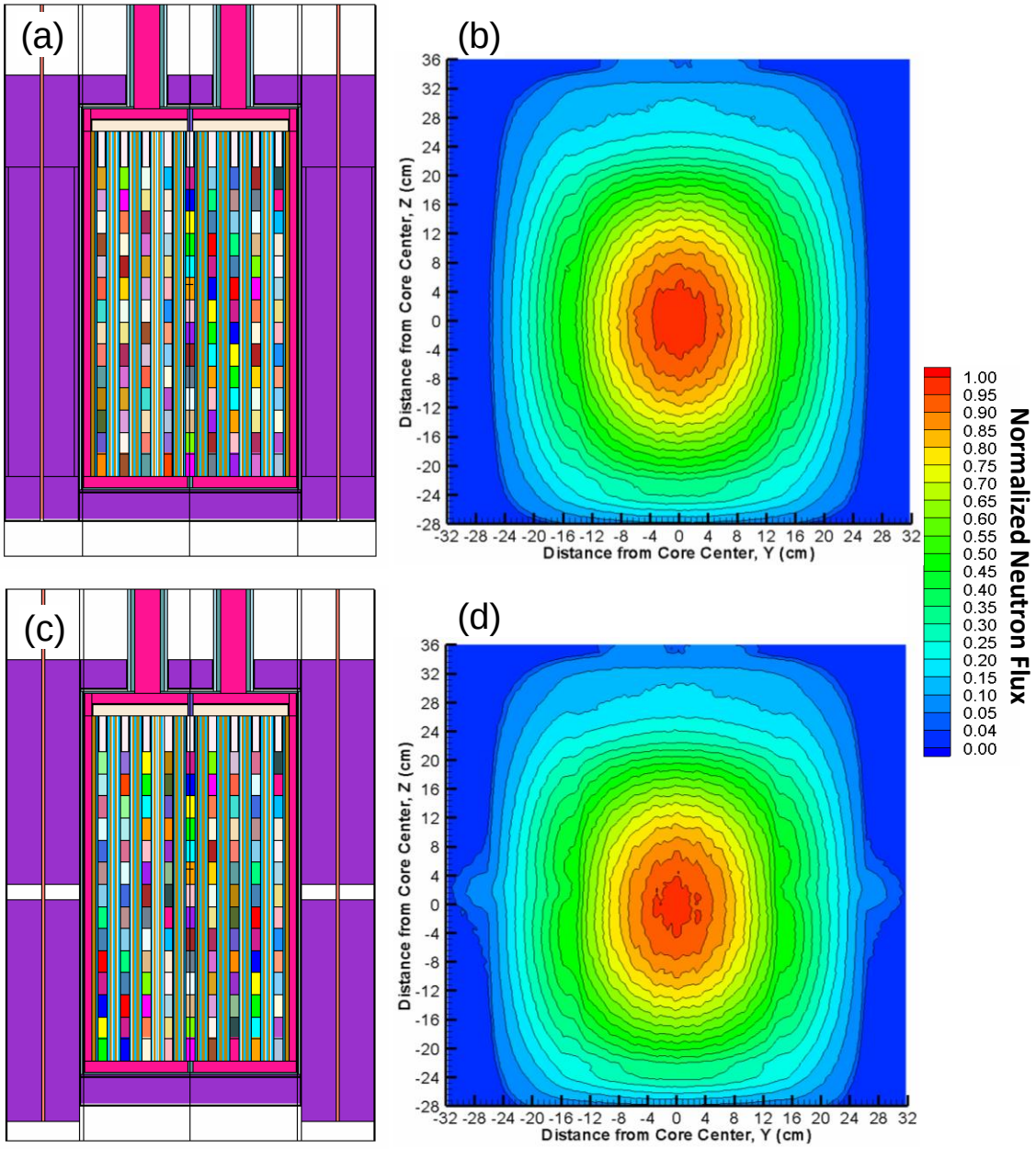

Fig. B.7. – Axial cross sectional view and normalized neutron flux contours in S^4 reactor with rotating drums and sliding reflector segments control: (a) MCNP model of S^4 with rotating control drums, (b) neutron flux plot of S^4 with rotating control drums, (c) MCNP model of S^4 with sliding reflector segments, (d) neutron flux plot of S^4 with sliding reflector segments [Schriener and El-Genk 2009b].

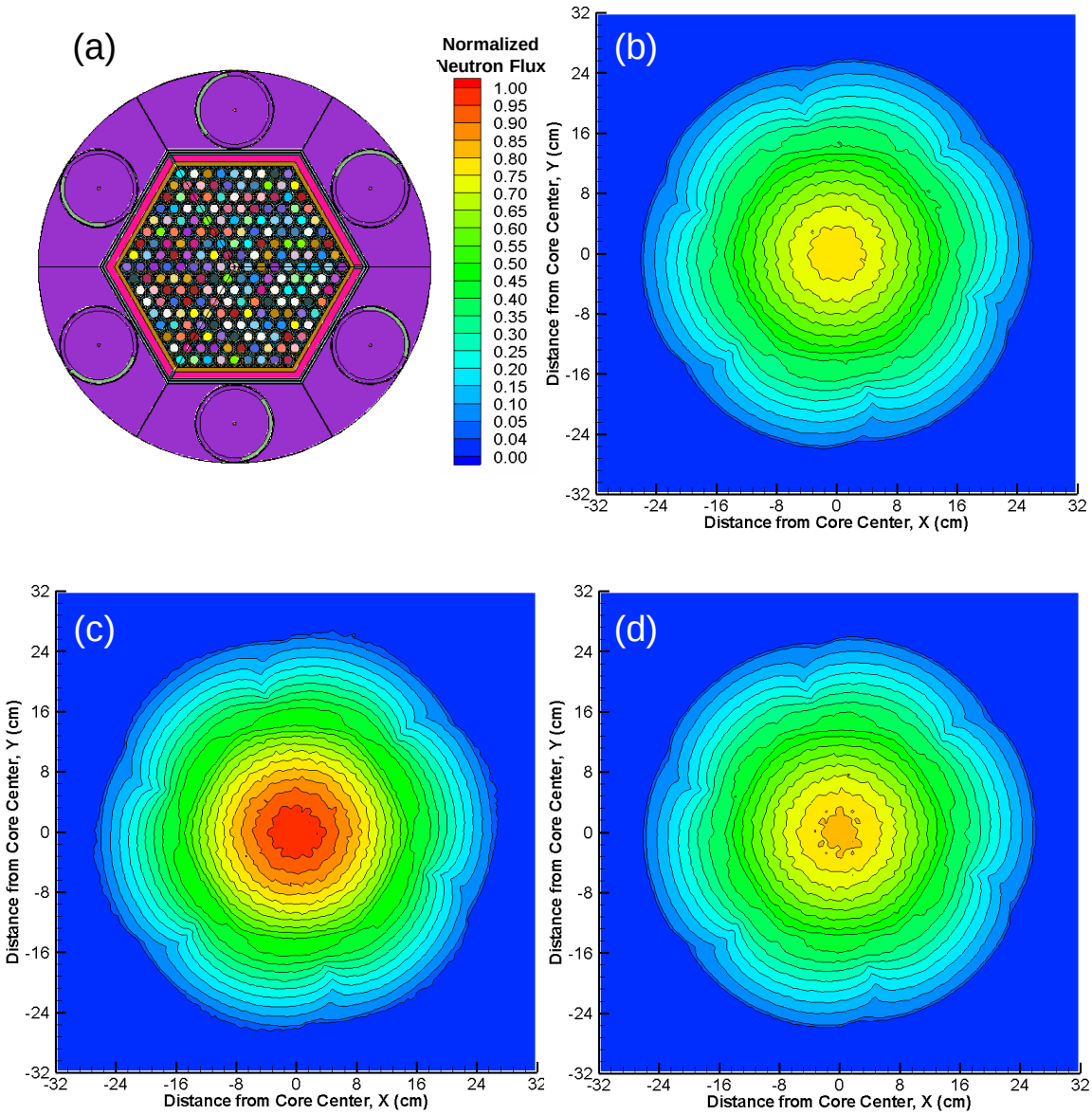

Fig. B.8. - Radial cross sectional view and normalized neutron flux contours in S^4 reactor with rotating drums control: (a) MCNP model of S^4 with rotating control drums at Z = 2 cm from core mid-plane, (b) neutron flux plot at Z = 10.75 cm from mid-plane, (c) neutron flux plot at Z = 2 cm from mid-plane, (d) neutron flux plot at Z = -10.75 cm from mid-plane [Schriener and El-Genk 2009b].

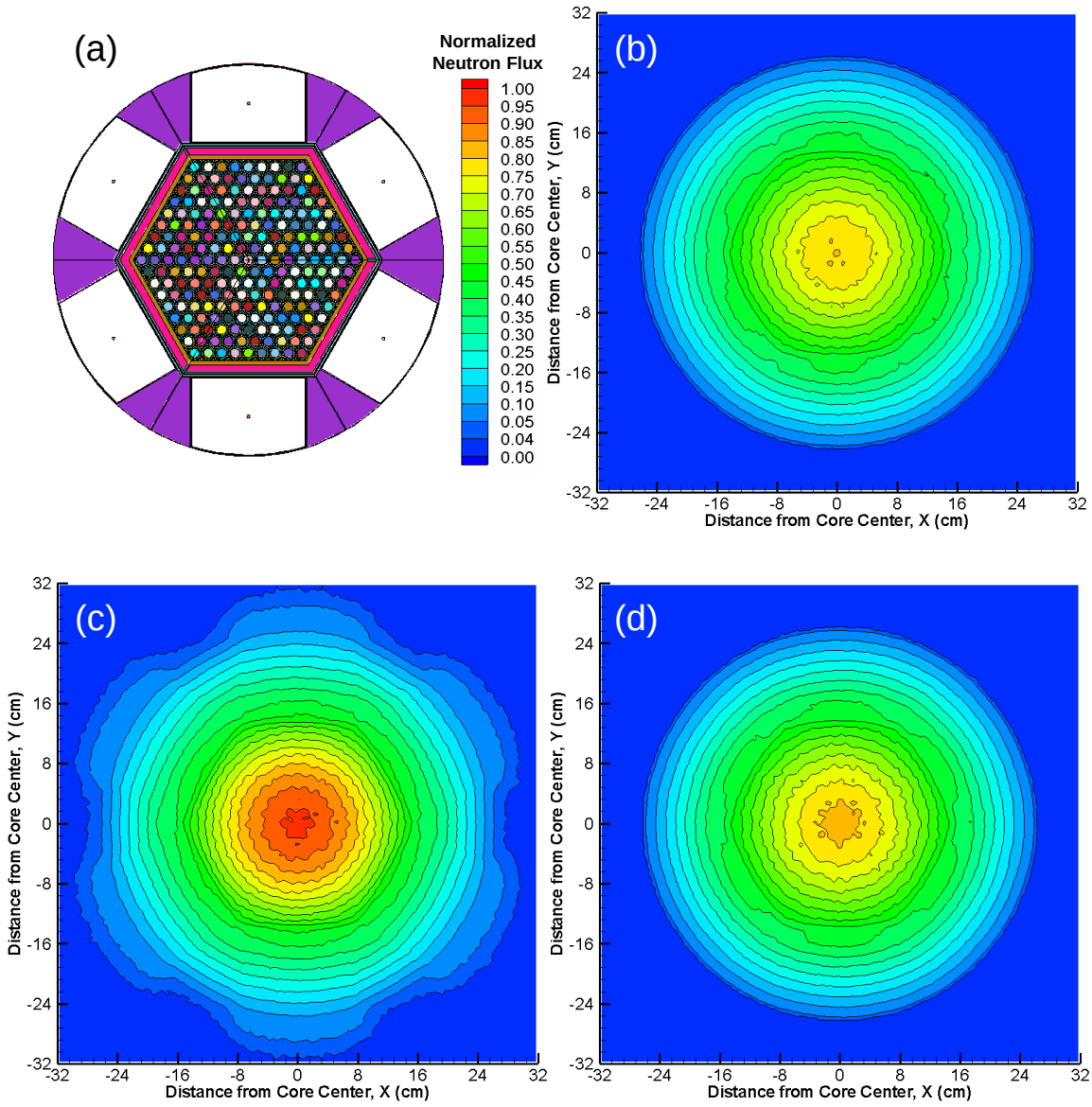

Fig. B.9. – Radial cross sectional view and normalized neutron flux contours in S^4 reactor with sliding reflector segments control: (a) MCNP model of S^4 with sliding reflector segments at Z = 2 cm from core mid-plane, (b) neutron flux plot at Z = 10.75 cm from mid-plane, (c) neutron flux plot at Z = 2 cm from mid-plane, (d) neutron flux plot at Z = -10.75 cm from mid-plane [Schriener and El-Genk 2009b].

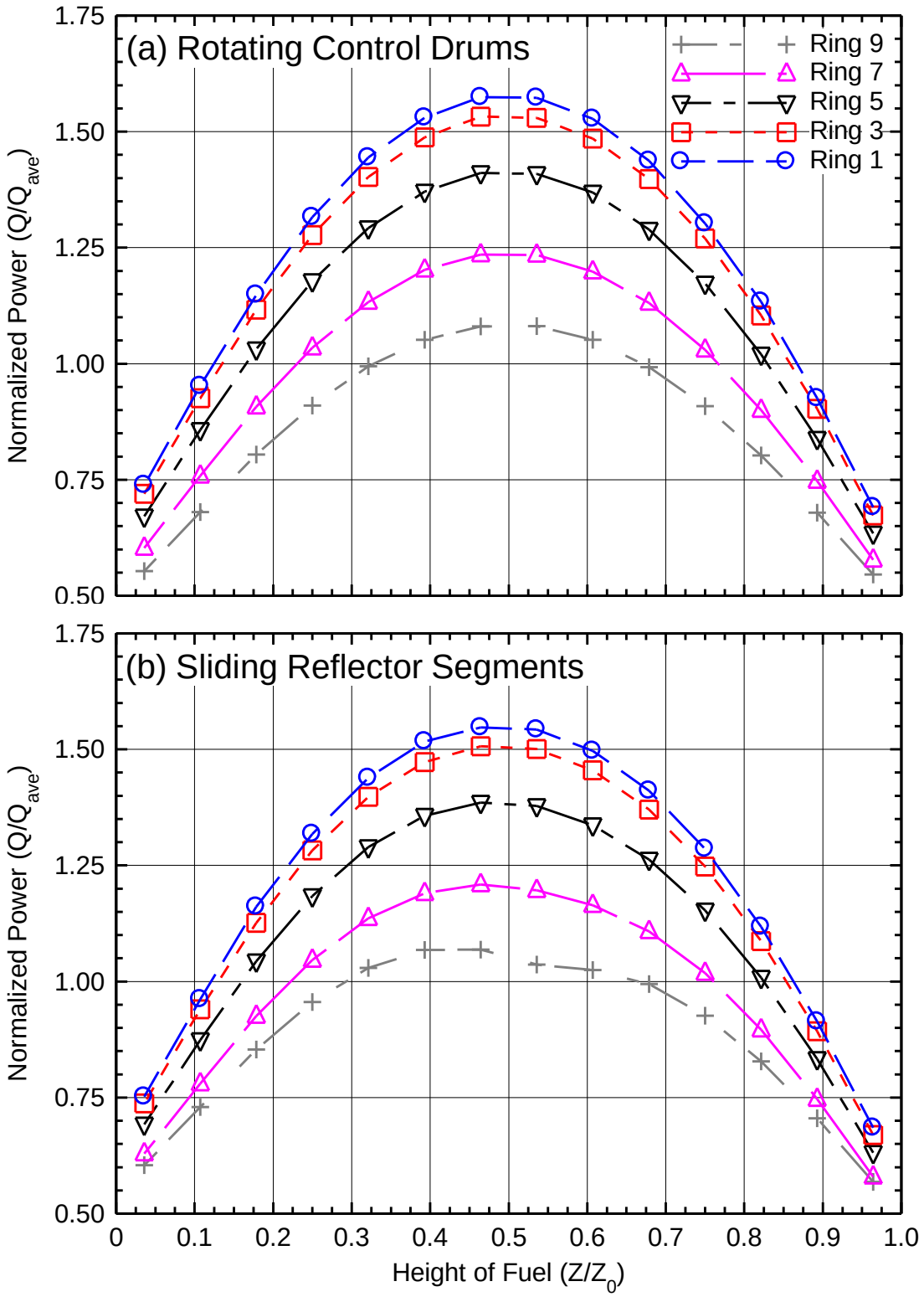

Fig. B.10. - Normalized core power distributions in S^4 reactor: (a) S^4 with rotating control drums, (b) S^4 with sliding reflector segments [Schriener and El-Genk 2009b].

higher, in order to make up for the reduced power generation along the core mid-plane (Fig. B.10b). The power generation in the outer ring of the fuel stacks (Ring 9) along the open ‘‘windows’’ in the radial reflector, decreases in the outer four rings, but is indistinguishable from that in the Ring 5 inward. The S^4 reactor with the sliding reflector segments control generates relatively less of its fission power in the center region of the core and more at the upper and lower extremities, resulting in a slightly more even axial fission power profile than the reactor with the rotating drums control.

B.6.4. Reactor Operational Life

The operational life of the S^4 reactor is limited by the amount of BOL hot-clean excess reactivity and the rate of reactivity depletion during operation. The reactivity depletion is the sum of those due to the fissile consumption and the accumulation of fission products. Fuel burnup is modeled using the UNM-ISNPS fuel depletion code at a constant reactor thermal power of 471 kW_{th}. The reactivity depletion calculations are performed for the S^4 with both the rotating drums control and the sliding reflector segments control. Fig. B.11 displays the results of the depletion calculations for the S^4 reactor with the two control options, and considering two scenarios: (a) all six control elements are functional through EOL, and (b) one control element stuck in the shutdown position at BOL and the remaining five control elements are used to control the reactivity of the reactor through EOL.

As shown earlier, during nominal operation at a full thermal power of 471 kW_{th}, the S^4 with all the six rotating drums operational would generate a total of 2,255 MWd over an operational life of 13.1 years. The S^4 with all six sliding reflector segments operational would generate 2,277 MWd over an operational life of 13.2 years, < 1% increase over the S^4 with the rotating drums. In the scenario for one of the six reactivity control elements failed to operate at BOL, the estimated operational life of the S^4 reactor is greatly reduced. Operating at a full thermal power of 471 kW_{th}, the reactor with five rotating drums operational would generate 1,115 MWd over an operational life of 6.5 years. In comparison, the S^4 with only five sliding reflector segments operational would generate 1,131 MWd over the course of an operational life of 6.6 years.

In both operating scenarios, the difference in the operational life of the S^4 reactor with either control options is very small. In the operation scenario (a), the S^4 with six operational sliding reflector segments generates < 1% more energy over its operational life. When one control element fails in the shutdown position, the difference in the amount of energy generated by the S^4 reactor with the two control options is < 1.5%.

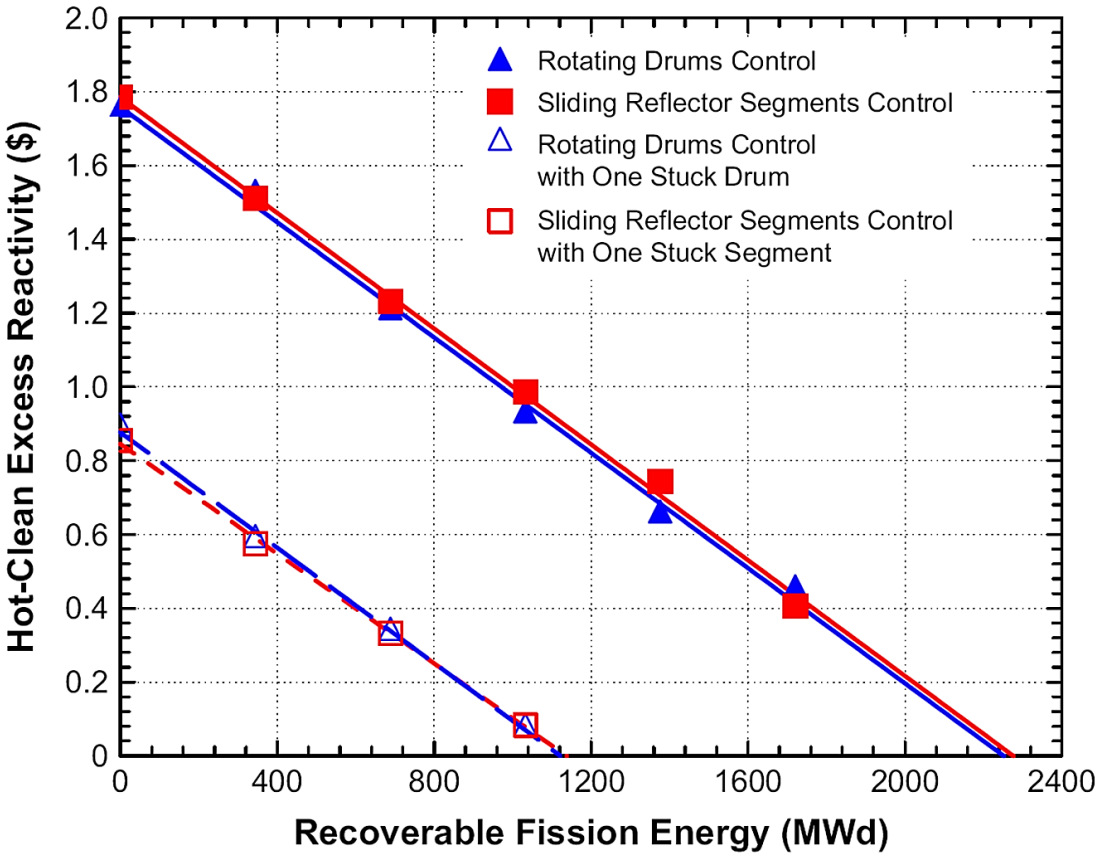

Fig. B.11 - Operational life estimates for S^4 reactor with rotating drums and sliding reflector segments control [Schriener and El-Genk 2009b].

In both scenarios the S^4 with the sliding reflector segments control has a slightly longer operational life than the S^4 with the rotating drums control. The difference in the operational life using the two control methods, however, is small. These results suggest that for the fast neutrons spectrum S^4 reactor the choice of an ex-core reactivity control option is not driven by the operational life of the reactor. Other parameters, such as the reactor and system integration, launch mass and the type of the drive mechanisms for the reactor control, will likely be stronger deciding factors.

APPENDIX C: Transient DynMo-TE Simulation of the SCoRe Power System

This appendix presents results of performance and safety analyses of an earlier version of the SCoRe power system, called the SCoRe-NaK-TE integrated power system. It employs a Sectored Compact fission Reactor (SCoRe-S_{11}) heat source cooled by circulating liquid NaK-78 (22 wt% Na and 78 wt% K) using TE powered DC Electromagnetic Pumps (EMPs) (Fig. 2.6). This power system also uses static SiGe Thermoelectric (TE) elements for energy conversion. The SCoRe-NaK-TE power system presented in this analysis is designed to nominally generate 37.1 kW_e for > 6 FPY. The use of passive and static components throughout the SCoRe-TE power system enhances operation safety and enables the passive removal of decay heat following shutdown.

Operation analyses of the SCoRe-NaK-TE space power system during the startup and shutdown transients and steady-state nominal operation for up to 6 years are performed using the Dynamic simulation Model with Thermoelectric conversion (DynMo-TE) [El-Genk and Tournier 2006a]. The effects of the period of inserting external reactivity by rotating the control drums outward on the operation parameters of the SCoRe heat source and the power system are investigated. The reactivity depletion and radioactivity buildup in the reactor core during nominal operation up to 6 year and decay after shutdown are calculated using the fuel depletion capability of MCNPX 2.6F [Hendricks et al. 2008]. The decay heat generation in the reactor core and other system parameters, particularly those of the TEM pumps and the circulating NaK-78 coolant throughout the system, are calculated as functions of time after reactor shutdown, following 6 years of continuous operation at a nominal thermal power of 1,183.6 kW_{th}. The next section describes the SCoRe-NaK-TE power system.

C.1. Description of the SCoRe-NaK-TE Power System

This power system employs a fission reactor (SCoRe-S_{11}) heat source with a core divided into 6 sectors that are neutronically and thermally coupled, but hydraulically independent (Fig. 2.5) [El-Genk et al. 2005]. Each sector in the SCoRe-S_{11} core has separate inlet and exit plenums and pipes (Fig. C.1), separate primary loop with a SiGe .

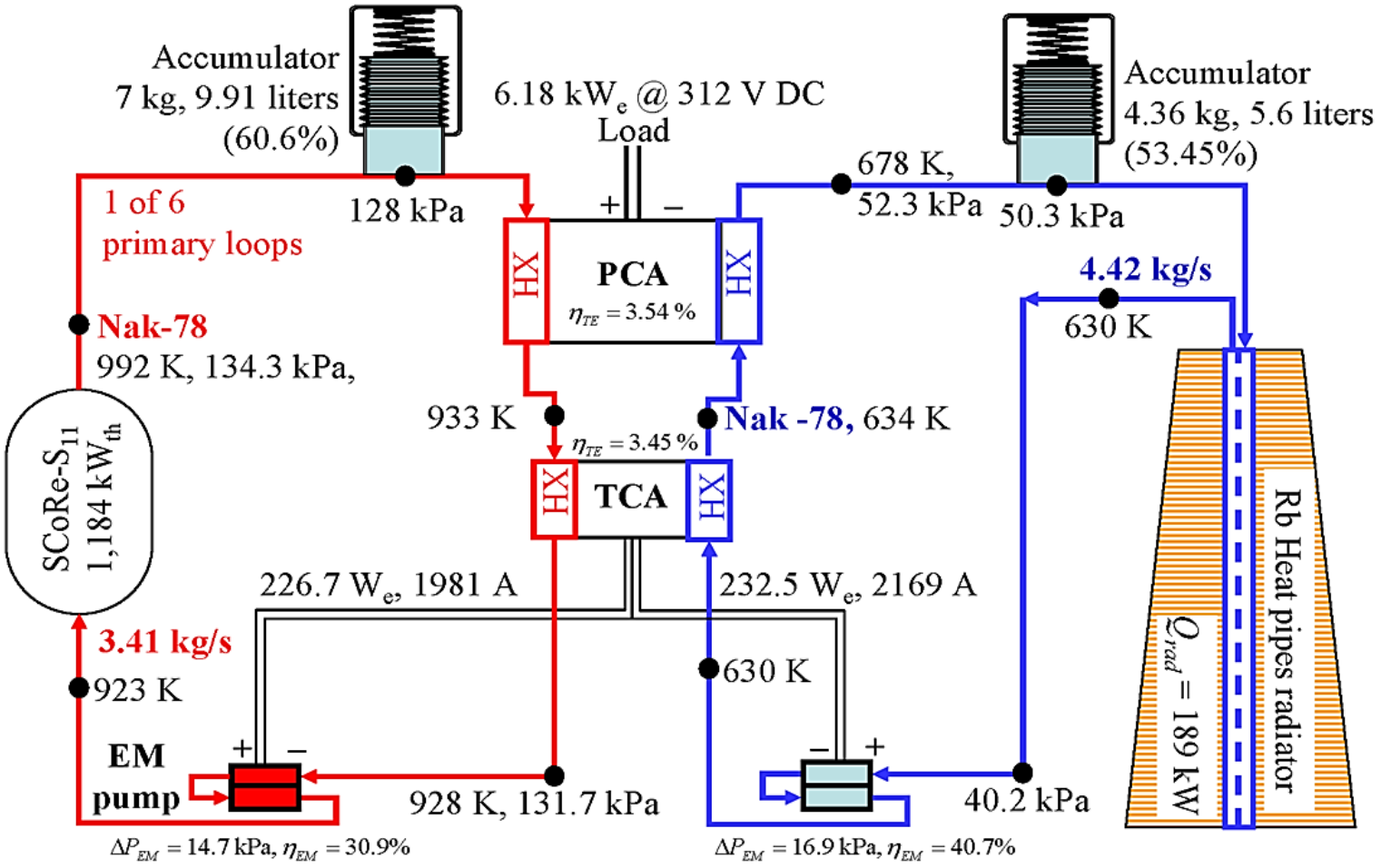

Fig. C.1. - A line diagram of a pair of primary and secondary loops in the SCoRe-NaK-TE space power system with nominal operation parameters [El-Genk and Tournier 2006a; El-Genk and Schriener 2010].

TE Power Conversion Assembly (PCA) and a secondary loop with three rubidium heat pipes radiator panels. Each primary and secondary loop has a separate DC Electromagnetic (EM) pump for circulating the liquid Nak-78 and a bellows-type accumulator for accommodating the changes in its volume during operation, startup and shutdown of the power system. The electrical power to operate the TEM pumps in the 6 secondary and primary loops is supplied by six separate SiGe Thermoelectric Conversion Assembles (TCAs). The SiGe TE converters in the PCAs and TCAs are static with no moving parts and have had extensive space flight experience in Radioisotope Thermoelectric Generators (RTGs). Thermoelectric conversion elements had also been used in the US SNAP-10A and the Russian's "BUK" space reactor power systems [Furlong and Wahlquist 1999; Buden 1995; Bennett 1989; El-Genk and Tournier 2006a; El-Genk 2009; El-Genk and Schriener 2010].

Each pair of primary and secondary loops are served by three rubidium heat pipe radiator panels [El-Genk et al. 2005]. The returning liquid NaK from the primary loop flows upward in the annulus on the inside of the reactor vessel. The flow then reverses direction at the opposite end, removing the fission heat generated in the UN fuel rods in the core sectors before exiting to the primary loops (Fig. C.1). The reactor nominally generates 1,183.6 kW_{th} at an exit temperature of 992 K and has a negative temperature reactivity feedback.

The radiator panels are hydraulically connected in parallel in order to reduce the pressure losses in the secondary loops and reduce the size and mass of the radiator [El-Genk and Tournier 2006b; Tournier and El-Genk 2006a]. The PCAs provide DC power to the electrical load at > 300 VDC, while the TCAs provide high current, low voltage power to the EM pumps. The pumps continue to operate so long as there is a sufficient temperature difference between the circulating liquid NaK in the primary and the secondary loops (Fig. C.1). Thus, the operation of the SCoRe-NaK-TE power system during both nominal full power and after shutdown is passive, except for rotating the control drums.

C.2. DynMo-TE Simulation Model

The DynMo-TE simulation model [El-Genk and Tournier 2006a] is used to calculate the operation parameters of the SCoRe–NaK-TE power system during the startup and shutdown transients and nominal steady-state operation up to 6 years. This dynamic system model is comprised of a multitude of integrated physical models of the various system components and fission reactor (Fig. C.1). These include: (a) a coupled reactor thermal-hydraulics and six-point kinetics model; (b) thermal-hydraulics models of the primary and secondary loops; (c) models of EM pumps in the primary and the secondary loops; (d) models of the bellows-type accumulators in the primary and secondary loops; (e) models of the PCAs and the pumps' TCAs; and (f) a comprehensive model of the radiator that couples a thermal-hydraulics model of the radiator panels to a transient model of the rubidium heat pipes.

The radiator's rubidium heat pipes have C–C armor to protect against the impact of space debris and C–C fins for enhancing heat rejection into space [El-Genk and Tournier 2006b; Tournier and El-Genk 2006a]. The radiator model in DynMo-TE calculates the vapor flow and temperature drops in the rubidium heat pipes and both the surface temperature and the heat rejection rate along the radiator panels. The PCA and TCA models in the primary and secondary loops (Fig. C.2) simulate the transient operation of the SiGe elements in these assemblies. The SiGe elements in the PCAs are connected in series, in a number of parallel strings for redundancy and to provide a load voltage > 300 VDC during nominal steady state full-power operation. In order to provide high current for operating the EM pumps in the primary and secondary loops, the SiGe elements in the TCAs are connected in parallel. The accumulator model in DynMo-TE accounts for the changes in the thermal inertia and in the volume of liquid NaK-78 in the primary and secondary loops and calculates the pressure and temperature at the accumulators' inlet [Tournier and El-Genk 2006b]. The calculated operation parameters of the SCoRe-NaK-TE space power system during the startup transient to nominal steady state are presented and discussed next.

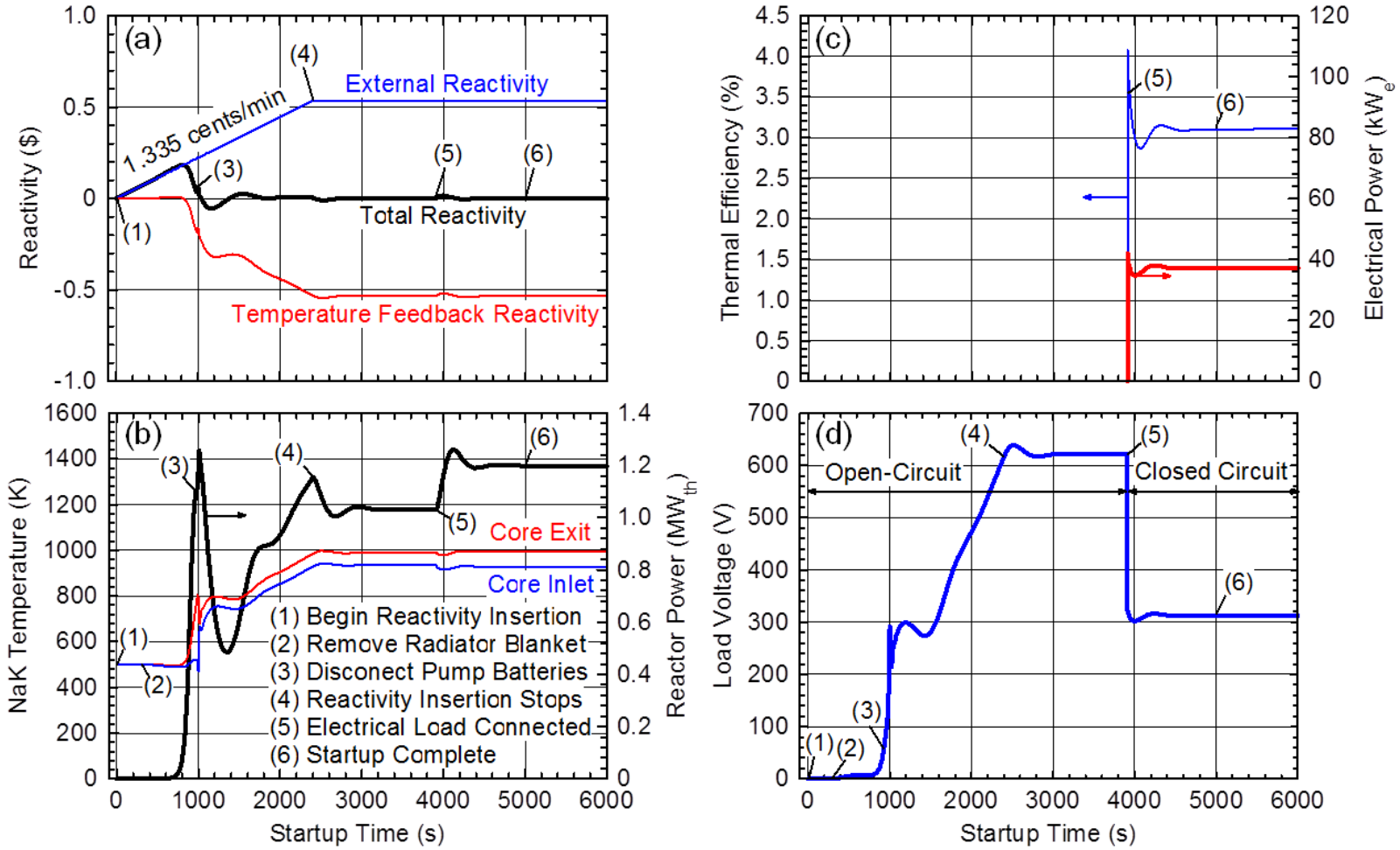

Fig. C.2. - Startup procedures and operation parameters of the SCoRe-NaK-TE power system [El-Genk and Tournier 2006a; El-Genk and Schriener 2010].

C.3. Transient Simulation Results and Analyses

In this section, DynMo-TE is used to simulate the startup of the SCoRe-NaK-TE power system in orbit to the nominal steady-state operating condition. Also investigated is the effect of the period of inserting external reactivity by rotating the control drum outward on the operation parameters of the SCoRe-NaK-TE power system. In addition, the results of the reactor shutdown transient following up to 6 years of nominal full-power operation are presented and discussed.

C.3.1. Power System Startup

The startup of the SCoRe-NaK-TE power system begins after it is safely at its destination and the radiator panels are fully deployed. With the electrical load connected, the reactor nominally generates 1,183.6 kW_{th} and the SCoRe-NaK-TE power system power system provides 37.1 kW_e to the load at > 300 VDC.

While on the launch pad, the temperature of liquid NaK in the primary and secondary loops of the SCoRe-NaK-TE system is raised to 600-800 K using plug-in electrical heaters, while the radiator panels are covered with a thermal blanket. The blanket minimizes thermal losses from the power system during launch, while in route, and after it is deployed. Depending on the amount of time between launch and startup electric heaters may be needed to prevent the NaK-78 in the coolant loops from freezing. During launch and before starting up the SCoRe-S_{11} reactor the six control drums in the BeO radial reflector (Fig. 2.13a) are rotated inward with the enriched B_4C segments facing the reactor core.

To startup the power system, first the control drums are rotated slowly outward to bring the reactor to a critical state ($k_{eff} \approx 1$) at a low-thermal power of ~10 W_{th}, while the radiator panels are still covered by the thermal blanket. The temperature of the liquid NaK temperature in the power system is assumed initially to be ~500 K, much higher than its freezing temperature of 261 K (or -12 C). At 500 K, the liquid NaK in the secondary and the primary loops is subcooled at pressures of 34 kPa and 51 kPa, respectively. The accumulators maintain the liquid NaK in these loops subcooled not only at startup, but also during nominal full power operation and after shutdown [El-

Genk and Tournier 2006a; Tournier and El-Genk 2006b]. The startup procedures from the low-power critical condition to full-power nominal operation last for ~5,000 s and include a number of successive actions indicated in Fig. C.2.

With the radiator panels are still covered with the thermal blanket, the TE EM pumps in the secondary and primary loops are started up with the aid of an auxiliary battery. During the first 978 s of the startup procedures, the battery supplies 600 A (50 A to each EM pump in the six primary and six secondary loops of the power system). The capacity of the auxiliary battery is > 180 A-hr.

The cold-clean excess reactivity (+\$2.8) in the SCoRe-S_{11} core decreases to +\$2.05 at the end of the startup procedures, when the reactor's exit and inlet temperatures are 992 K and 923 K (Figs. C.1 and C.2). This is because of the negative temperature reactivity feedbacks in the reactor core and the BeO reflector [Hatton and El-Genk 2008]. The reactor's startup from a low-thermal power of 10 W_{th} critical condition at 500 K are initiated (point 1 in Fig. C.2) by rotating the control drums in the radial BeO reflector outward to insert reactivity in the reactor core at a constant rate of 1.335 ¢/min during the first 40 min (2300 s) of the startup procedures, for a total reactivity insertion of \$0.534. Point (4) in Fig. C.2 indicates the end of the reactivity insertion stage of the startup procedures of the power system.

After 300 s into the startup procedures, the radiator thermal blanket is jettisoned, allowing the temperature of the circulating liquid NaK in the secondary loops and the radiator panels to decrease. Subsequently, temperature differentials develop across and the EM pumps' TCAs (Fig. C.3a). During the initial phase of the startup procedures, the electric load to the PCAs is disconnected. Thus, the load open-circuit voltage increases as the reactor thermal power and the temperatures of the circulating liquid NaK in the primary and secondary loops increase. When the open-circuit voltage of the pumps' TCAs becomes high enough to provide more than 50 A to each TEM pump in the secondary and primary loops, the TCAs are connected to the pumps, while simultaneously disconnecting the auxiliary battery. This action, taken 978 s into the startup procedures, is indicated by point (3) in Figs. C.2a, C.2c, C.3a and C.3b.

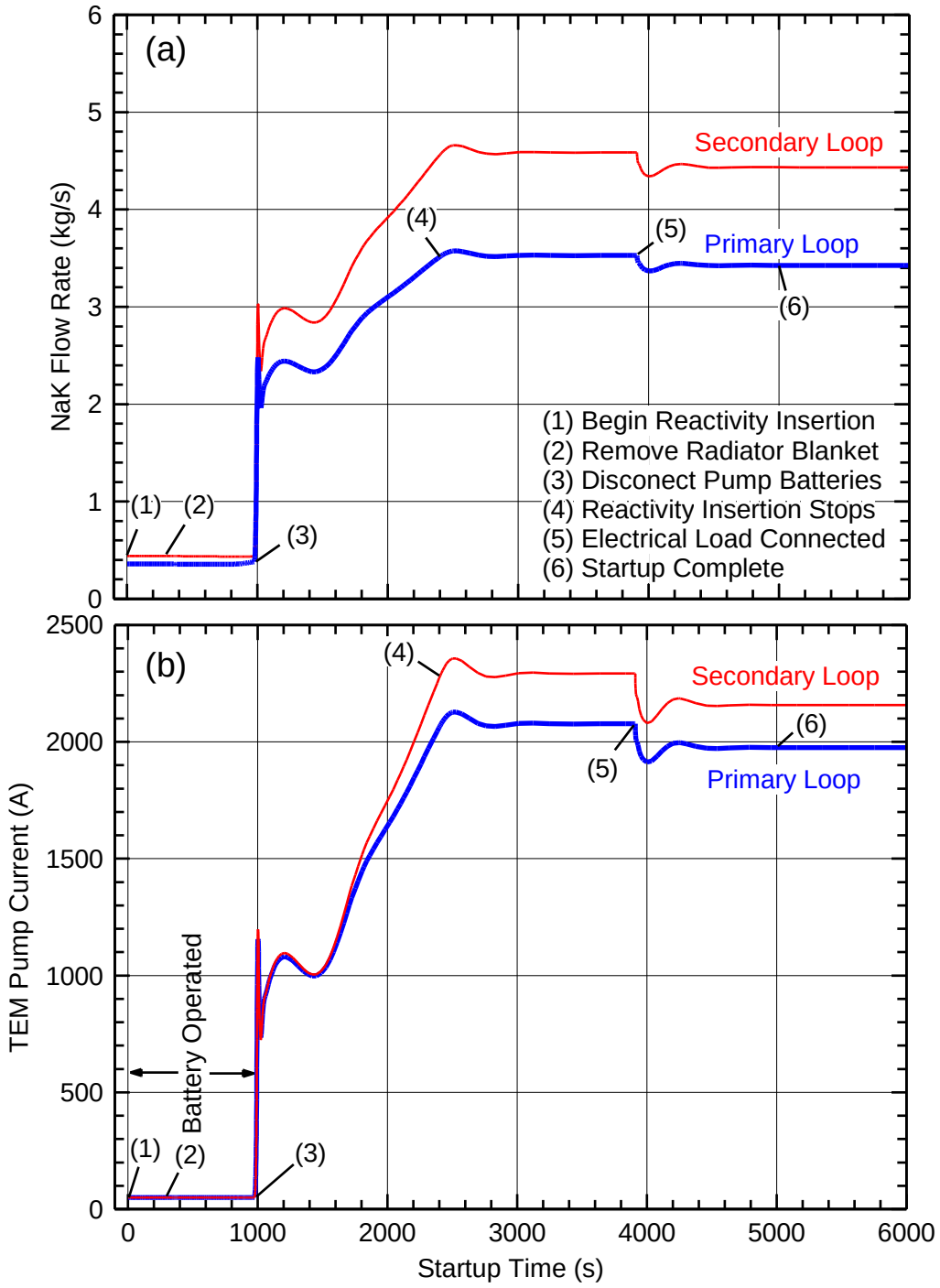

Fig. C.3. - Coolant flow rates and EM pump current during system startup: (a) NaK-78 coolant flow rates in primary and secondary loops, (b) TEM pump curent [El-Genk and Schriener 2010].

After 3,900 s into the startup procedures, and before connecting the electrical load, the reactor thermal power reaches a steady state value of 1,030 kW_{th} and the PCAs' open-circuit voltage reaches 620 VDC (point (5) in Figs. C.2a–C.2d). The six PCAs in the SCoRe-NaK-TE power system are connected electrically in parallel. When the electrical load is connected to the PCAs, the load voltage drops to 312 VDC and the reactor thermal power increases to a nominal steady-state value of 1,183.6 kW_{th}. This occurs at ~5,000 s into the startup procedures (Figs. C.2b and C.2c). At such time, which marks the end of the startup procedures, the nominal electrical power provided to the load by the SCoRe-NaK-TE power system is 37.1 kW_e at a thermal efficiency of 3.137%.

The flow rate of the circulating liquid NaK-78 in the primary loops at the reactor's nominal steady-state thermal power of 1,183.6 kW_{th} is lower than that in the secondary loops (Figs. C.1 and C.3a). This is because the current supplied by the TCAs to the EM pumps in the secondary loops is higher, by design, than that supplied to the EM pumps in the primary loops (Fig. C.3b). During the startup procedures and until the TCAs are connected to the EM pumps (point 3 in Fig. C.3a), the difference between the flow rates of the circulating liquid NaK in the primary and secondary loops is very small. As the reactor thermal power increases during the startup procedures, the values of and the difference in the flow rates of the circulating liquid NaK-78 in the primary and secondary loops increase (Fig. C.3a). Similarly, the electric current supplied to the EM pumps by the TCAs increases as the reactor thermal power increases during the startup procedures. When the electric load is connected to the PCAs (point 5 in Figs. C.3a and C.3b), the electrical current supplied to the EM pumps by the TCAs drops momentarily. It then approaches steady-state values of 2,169 A and 1,981 A, respectively, to each TEM pump in the primary and secondary loops (point 6 in Figs. C.2 and C.3b).

C.3.2. Reactor Nominal Operation

During the 6 years of steady-state nominal operation of the SCoRe-NaK-TE power system, the hot-clean excess reactivity of the SCoRe-S_{11} (+\$2.05) is used up gradually to compensate for the partial depletion of the ^{235}U in the fuel and the accumulation of fission products in the UN fuel pins. Thus, the nominal operation thermal power and temperatures of the reactor are maintained by periodically inserting reactivity by rotating

the control drums in the BeO radial reflector incrementally outward. The period and the amount of reactivity inserted depend on the allowed drop in the reactor temperature and the load voltage between subsequent reactivity insertions.

C.3.2.1. Reactivity Depletion during Nominal Operation

The calculations of the reactivity depletion rate in the SCoRe-S_{11} core during nominal, full-power, steady state operation are performed using the internal CINDER fuel depletion capability in MCNPX 2.6F [Hendricks et al. 2008]. MCNPX estimates the changes in the composition of the UN fuel that is mixed with ^{157}GdN spectral shift absorber and of the $^{157}Gd_2O_3$ thin coating on outer surface of the reactor vessel. It tracks the neutron reactions for 42 actinides and 243 fission products included in the ENDF-VI and the JEFF 3.1 continuous energy cross section libraries [Lemmel et al. 2001; Koning et al. 2006].

The MCNPX depletion calculations for the SCoRe-S_{11} core during nominal steady-state operation are performed with the control drums in the radial reflector rotated partially outward to make the reactor critical ($k_{eff} \approx 1$). This approach produces the correct neutron flux distribution in the core and minimizes the effect of the k_{eff} bias on the calculated depletion tallies. The fuel depletion calculations utilized 10,000 particles per cycle for 50 skipped and 500 active cycles using the continuous energy cross section data from the ENDF-VI and JEFF 3.1 libraries. The calculations are performed using two year time-steps at the average nominal reactor thermal power and temperature over each time-step, and the default MCNPX fission Q-values.

The MCNPX calculations during nominal full-power operation of the SCoRe-S_{11} are performed at the average nominal operation temperatures in the reactor core. The reactor model used is comprised of three isothermal regions. The first region is the fuel pellets in the UN fuel rods, the second region includes all other materials in the core inside the reactor vessel, and the third region consists of the materials located outside the reactor vessel, such as the BeO radial and axial reflector. To account for the temperature induced reactivity effects, the neutron transport cross-sections used were Doppler broadened for the core materials to the mean temperatures for each depletion time-step.

The MCNPX fuel depletion calculates determine that the SCoRe-S_{11} with NaK-78 coolant can operate for up to 6 years at the nominal thermal power of 1,183.6 kW_{th}. This equates to an operational life of 2,630 MWd. The reactivity depletion in a fast-neutron spectrum space reactor with highly enriched fuel is linear with the fission energy generated (Appendix A). The determined linear reactivity depletion rate of 0.078 ¢/MWd is incorporated into the DynMo-TE [El-Genk and Tournier 2006a] transient simulation to account for reactivity loss due to fuel burnup during operation.

C.3.2.2. Effect of the Interval of External Reactivity Insertion

To maintain the reactor thermal power and temperatures constant during nominal full-power operation, the control drums would need to be adjusted continuously over the operational life of the reactor of 6 years, placing great strain on the electrical drive motors that rotate the drums. Instead, the reactor for the SCoRe-NaK-TE power system utilizes a periodic reactivity adjustment scheme, by incrementally rotating the control drums at a selected interval. The value of the interval depends on the allowed drop in the load voltage and/or the reactor exit temperature between successive reactivity insertions. In the interval between successive reactivity insertions, the reactor thermal power and exit temperature, and hence the load voltage, decrease gradually. The resulting increase in the reactor reactivity due to the decrease in its temperature between successive externals reactivity insertions compensates for the decrease in reactivity due to fuel burnup and the accumulation of fission products in the fuel. Following each incremental reactivity insertion, the reactor's thermal power and exit temperature as well as the load voltage increase to their nominal values.

Fig. C.4 shows the nominal operation of the SCoRe-NaK-TE power system using a controller that allows the load voltage from the PCAs to change between 312 and 300 VDC. As the reactor power decreases due to the burnup reactivity feedback, the load voltage drops gradually from 312 to 300 VDC over the course of 28.6 days of operation. When the load voltage drops to 300 VDC, the controller signals the control drums to incrementally rotate outward, inserting reactivity at a rate of 10 ¢/hr, until the load voltage has risen back to 312 VDC (Fig. C.4a).

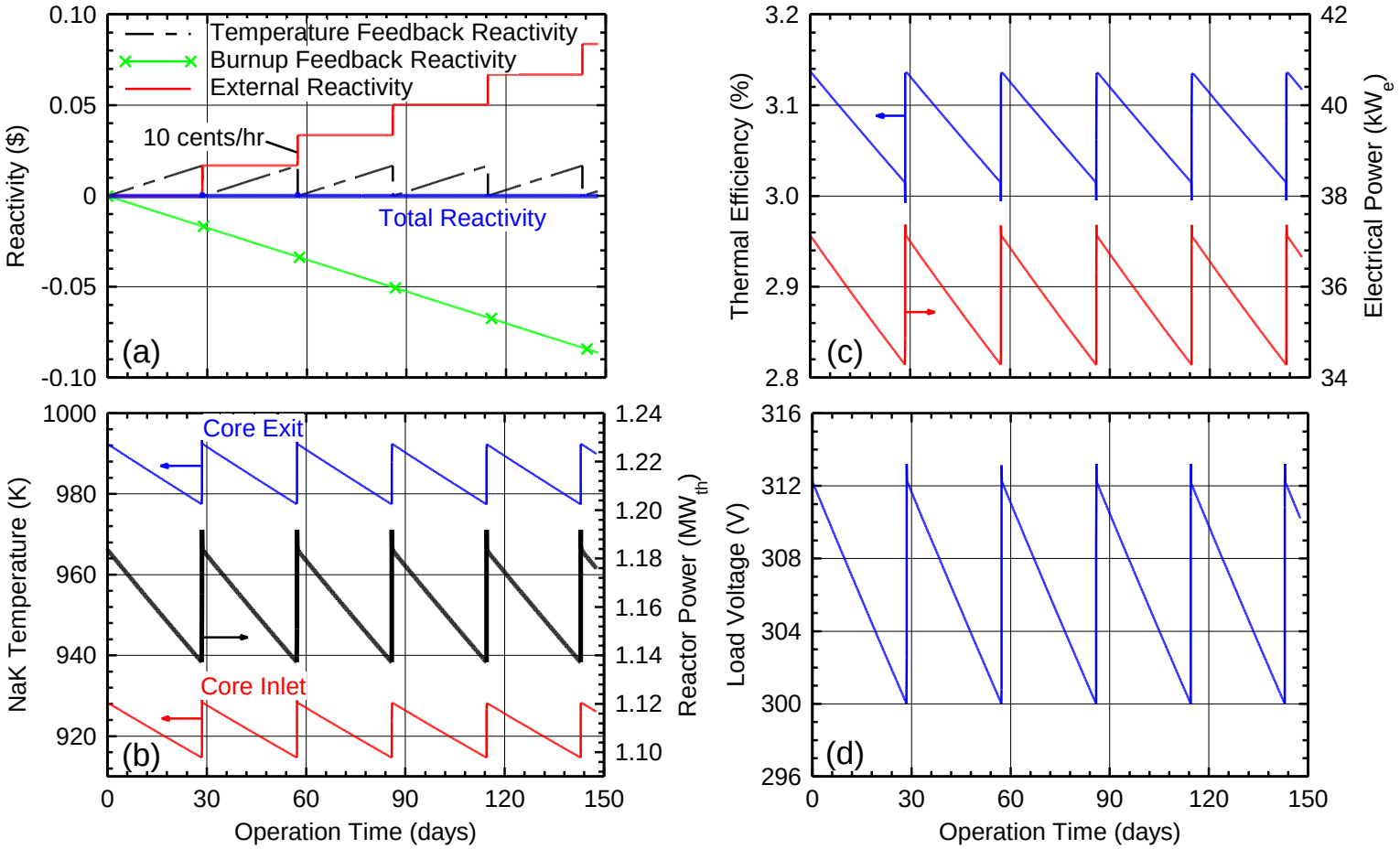

Fig. C.4. - The SCoRe-NaK-TE system parameters for periodic adjustment of reactivity: (a) core reactivity, (b) NaK-78 coolant temperatures and reactor thermal power, (c) system thermal efficiency and electrical power generation, (d) PCA load voltage [El-Genk and Schriener 2010].

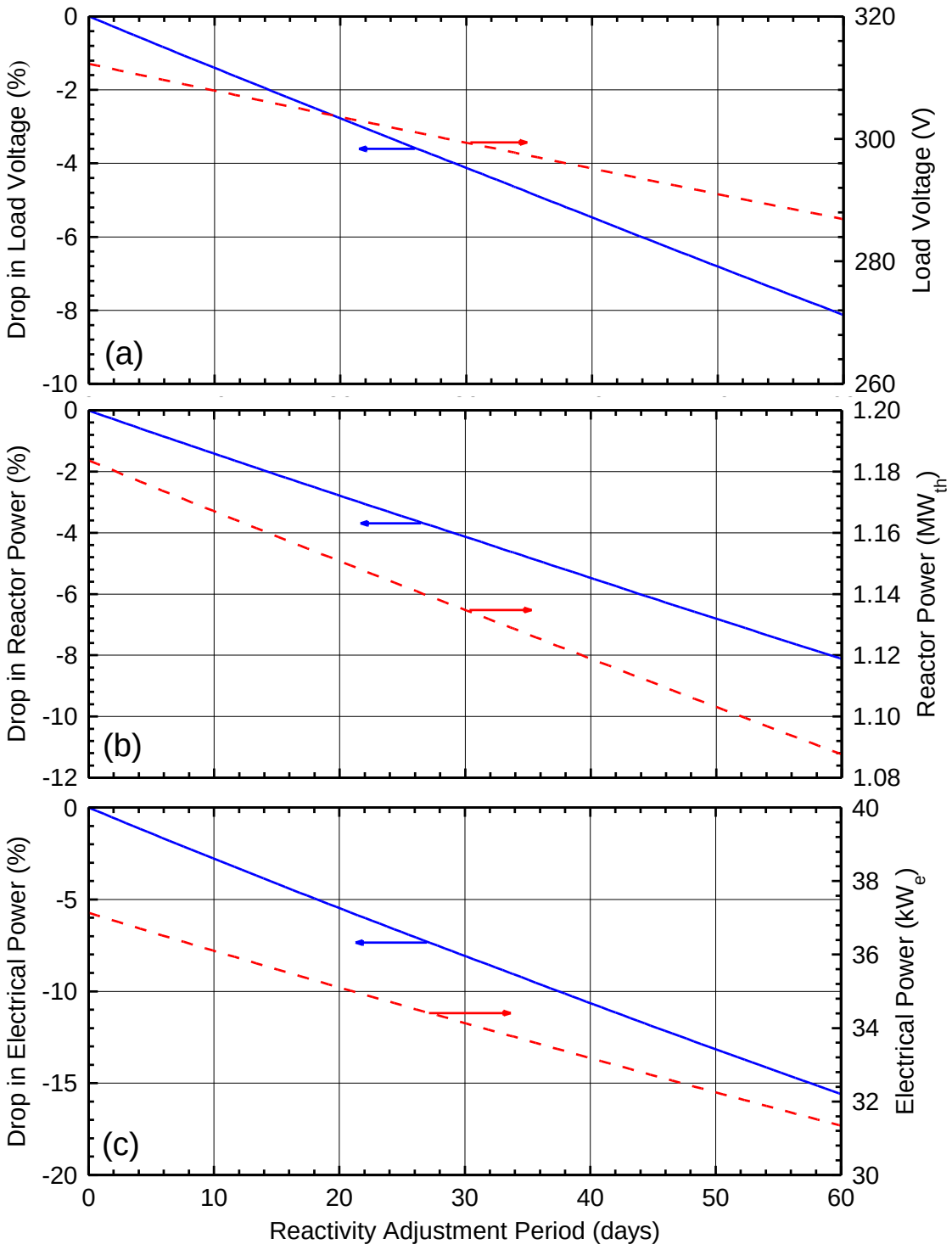

Fig. C.5. - Effect of the reactivity adjustment period on the operation margins for the power system: (a) load voltage, (b) reactor thermal power, (c) electrical power generation [El-Genk and Schriener 2010].

As indicated in Figs. C.4 and C.5, during the interval of 28.6 days between successive external reactivity insertions, the load voltage is maintained within 3.92% of its nominal value of 312 VDC (Fig. C.5a), the reactor thermal power is maintained within 3.93% of its nominal value of 1,183.6 kW_{th} (Figs. C.4b and C.5b), the load electrical power is maintained within 7.40% of its nominal value of 37.1 kW_e (Figs. C.4c and C.5c), the thermal efficiency is maintained to within 4.54% of its nominal value of 3.137% (Fig. C.4c) and the liquid NaK-78 temperature at the exit of the reactor is maintained to within 1.50% of it nominal value of 996 K (Fig. C.4b). The value of the interval between successive external reactivity insertions depends on the allowed decrease in one or more of the operation parameters of the power system from their nominal values (Figs. C.5a-7.5c). The larger the allowed drops in the system parameters from their nominal values, the longer the interval between successive external reactivity insertions by incrementally rotating the control drums outward.

C.3.3. Power System Shutdown at End-of-Life

The total hot-clean excess reactivity in the SCoRe-S_{11} core is used up when the control drums in the radial reflector are rotated fully outward, marking of the end of the nominal operation life of the reactor and the power system. The control drums are then rotated inward until the B_4C segments in the drums face the reactor core, marking the end of the reactor shutdown process. Figs. C.6a–C.6c present the operation parameters of the SCoRe-NaK-TE power system during and after shutdown, following 6 years of full power operation.

The reactor shutdown is initiated by rotating the control drums inward over a 24 h period (Fig. C.6). During the shutdown process, negative reactivity is inserted into the reactor core at a constant rate of 0.585 ¢/min (Fig. C.6a). The reactor that is critical at the start of the shutdown procedures (point 7 in Figs. C.6a–C.6c) becomes $9.3 subcritical at the end of the shutdown procedures (point 8 in Figs. C.6a–C.6c). The reactor thermal power and temperatures drop precipitously following shutdown (Fig. C.6b). At the end of the shutdown process of 24 h, the reactor exit and inlet temperatures decrease to 389.9 K and 400 K, and the reactor thermal power drops to only 4.75 kW_{th}. This power is mostly due to the radioactive decay of the fission products in the reactor core (Fig. C.6b).

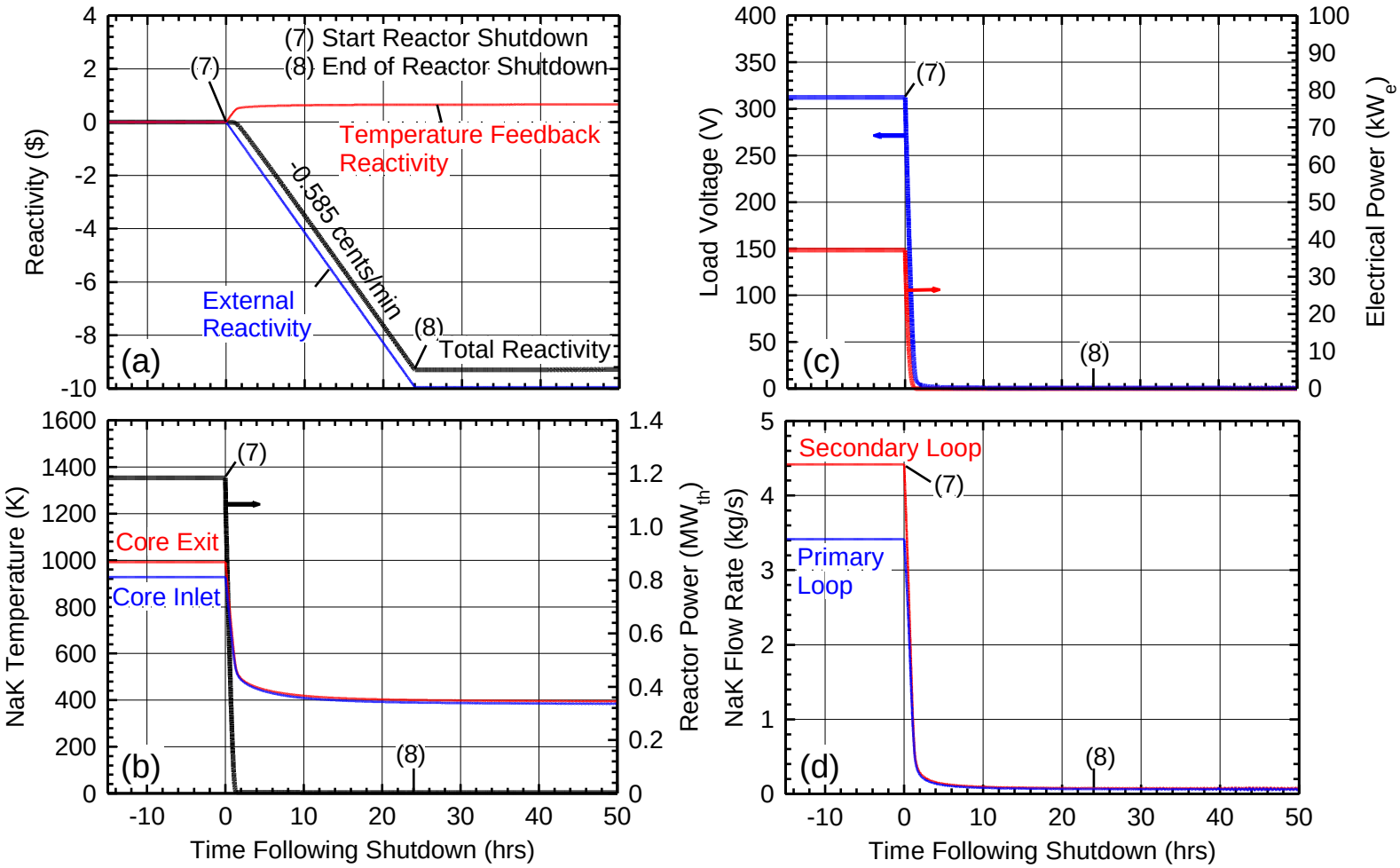

Fig. C.6. - Operation parameters of the power system after reactor shutdown: (a) core reactivity, (b) NaK-78 coolant temperatures and reactor thermal power, (c) PCA load voltage and electrical power generation, (d) NaK-78 flow rates [El-Genk and Schriener 2010].

The flow rates of the circulating liquid NaK in the primary and secondary loops also drop rapidly from 3.41 kg/s and 4.42 kg/s before shutdown to only ~77 g/s and 66 g/s at the end of the shutdown process (point 8 in Fig. C.6d). At such time, the electric currents supplied to the EM pumps by the TCAs in the primary and secondary loops drop to 5.6 and 7.6 A, respectively, and the electrical power supplied by the PCAs to the load becomes negligible, ~146 mW_e (Figs. C.6c and C.6d).

During the shutdown process, the reactor thermal power rapidly drops to that of the decay heat due to the radioactive decay of the fission products in the UN fuel pins. The MCNPX fuel depletion simulation determines the concentrations of radioactive fission products and actinides in the reactor core following 6 years of operation at the nominal power of 1,183.6 kW_{th}. The total decay power in the SCoRe-S_{11} core after shutdown is calculated using specific power (W/Ci) conversion factors for each radionuclide in the fuel pins. These factors, taken from the ORIGEN-S depletion and decay code [Gauld et al. 2006], are multiplied by the activities determined in the MCNPX depletion calculations to estimate the decay power in the reactor core after shutdown.

Immediately at shutdown of the SCoRe-NaK-TE space power system, the decay power generated in the reactor core is 9.905 kW_{th}, mostly due to the radioactive decay of the short-lived fission products (Fig. C.7a). One hour following reactor shutdown, the decay power generated in the core decreases to 8.153 kW_{th}. It decreases to 4.602 kW_{th}, 2.616 kW_{th} and 1.362 kW_{th} at the end of one day, one week and 4 weeks after reactor shutdown. At the end of the first year after reactor shutdown, the short and moderate lived nuclides decay away, reducing the decay power in the SCoRe-S_{11} core to 109 W_{th}.

Without an effective and continuous removal of the decay power generated in the SCoRe-S_{11} core, the cumulative decay thermal energy in the reactor core within the first 13 h after reactor shutdown would be ~$3x10^{-1}$ GJ (Fig. C.7b). Without heat losses from the reactor, this decay heat is sufficient to boil away the liquid NaK in the primary and secondary loops of the SCoRe-NaK-TE power system. This enforces the need for passive means to remove the decay heat from space nuclear reactors after shutdown.

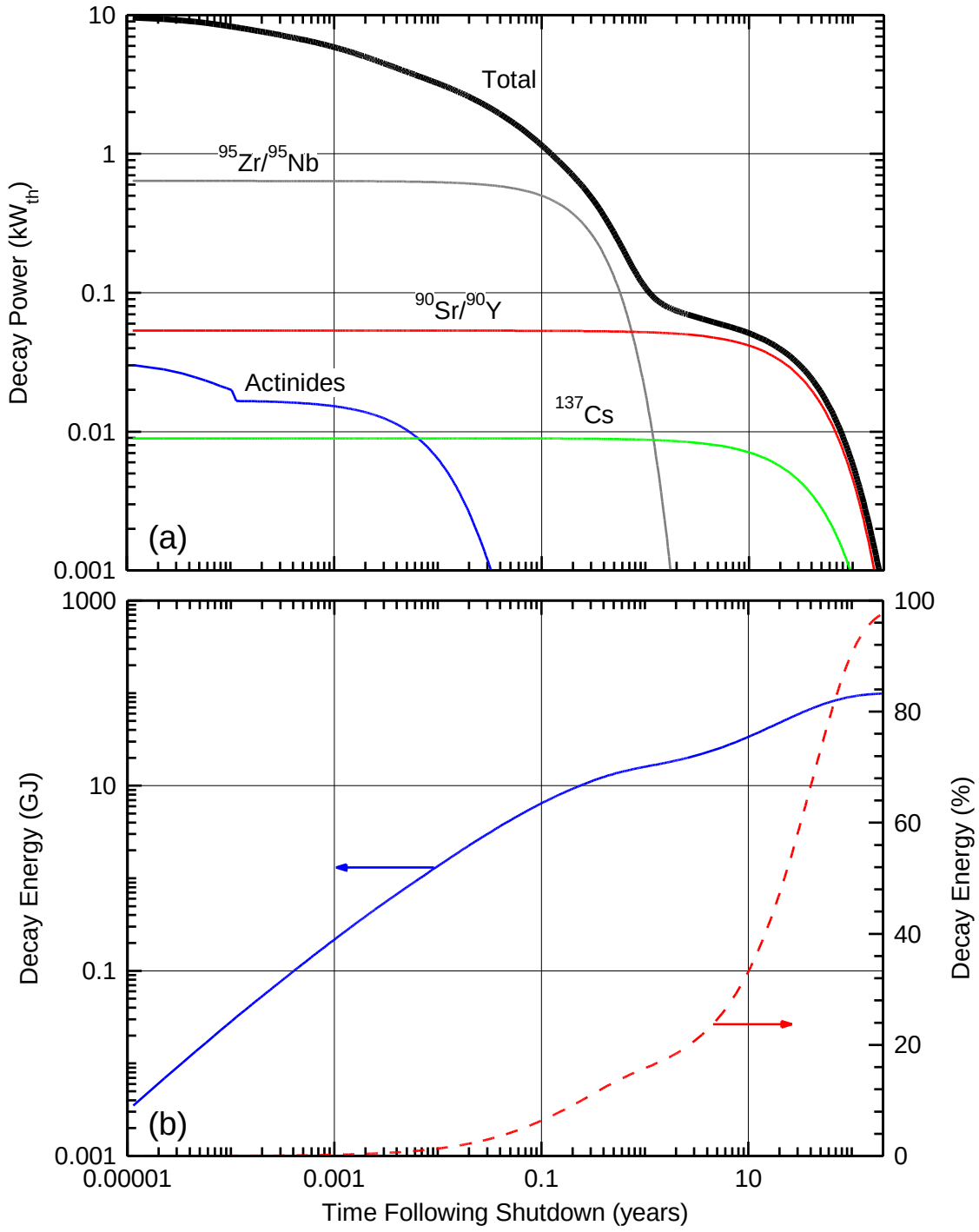

Fig. C.7. - Decay heat generation in the reactor core after shutdown: (a) decay heat power generation, (b) cumulative decay energy generation [El-Genk and Schriener 2010].

APPENDIX D: Comparative Analyses of CFD and Thermal-Hydraulics Methodology for the SC-SCoRe

This Appendix investigates the effects of the turbulence model and mesh refinement of the results of the CFD and thermal-hydraulics analyses of the NaK-56 liquid metal cooled Solid Core Sectored Compact Reactor (SC-SCoRe) (Chapter 3.7). The analyses compare results using the commercial STAR-CCM+ code package [CD-adapco 2012] for the two-layer k-ε and the Shear Stress Transport (SST) k-ω linear turbulence models with different numerical mesh refinements. Investigated are the effects on the computation time and the calculated reactor performance parameters. These are the temperatures of the ODS-Mo solid core structure and the UN fuel stacks, the velocity and temperature profiles in the core flow channels, the turbulent eddies and the flow mixing in the lower and upper plenums and exit duct, as well as the total pressure and the pressure losses along the flow path in the reactor core.

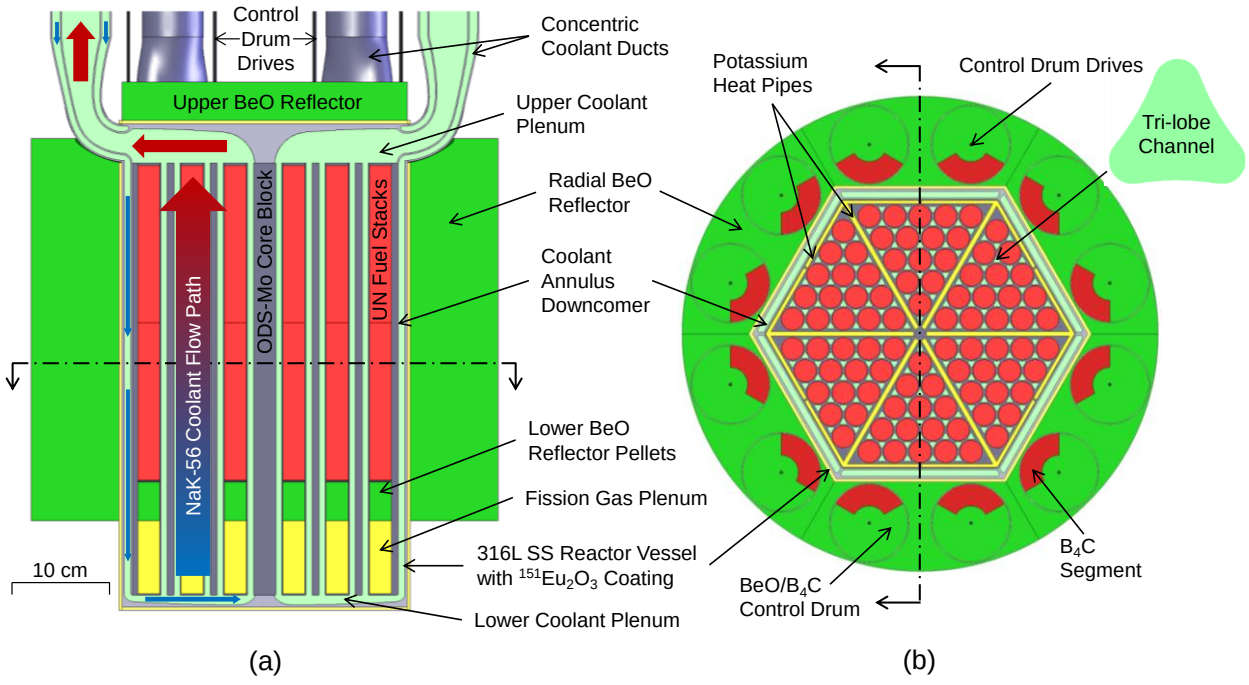

Fig. D.1. - Cross-section views of SC-SCoRe: (a) elevation view and (b) plane view [Schriener and El-Genk 2014a].

For alkali metal coolants with very small Prandtl number, Pr, ranging from 0.004 – 0.007, the turbulent heat transfer in the coolant channels is neither conduction nor convection dominated. Thus, using LES or hybrid turbulent models may be beneficial, but at the expense of increasing computation cost, subject to validation with experiment results, which unfortunately do not exist [Grötzbach 2013]. To examine this issue, the calculated results for the liquid metal NaK-56 flow and heat transfer in a single tri-lobe flow channel (Fig. D.1) using the linear k-ε and k-ω linear turbulent models are compared to those using a higher fidelity simulation model. This is the Detached Eddy Simulation, a hybrid LES and RANS model. The next section describes the methodology used in these comparative analyses.

D.1. Methodology

The performed CFD and thermal-hydraulics analyses of the SC-SCoRe examine the realizable two-layer k-ε and the SST k-ω turbulence models for simulating the highly turbulent liquid NaK-56 flow in the core sectors. The analyses also examine different numerical mesh refinements (Table D.1). Investigated are the effects on the computation time and calculated performance parameters. These are the temperatures of the ODS-Mo solid core structure and the UN fuel stacks, the velocity and temperature profiles in the core flow channels, the turbulent eddies and the flow mixing in the lower and upper plenums and exit duct, as well as the total pressure and the pressure losses along the flow path in the reactor core.

The performed 3-D CFD and thermal-hydraulics analyses are for a single sector, or a 1/6 full core of the SC-SCoRe, in the lunar gravity (~1/6 g). These analyses use the STAR-CCM+, version 7.04 commercial code package [CD-adapco 2012] running on a dual quad-core CPU 2.27 GHz Xeon E5507 workstation with 144 GB of DDR3 RAM. In addition the axial and radial fission power profiles in the reactor core (Fig. D.2) in these analyses are those obtained using the Monte-Carlo radiation transport code MCNPX 2.7E [Hendricks et al. 2011; Schriener and El-Genk 2012a]. The radial fission power profile changes with axial location in the core and the axial power profile depends on the radial location of the UN fuel stack in the core.

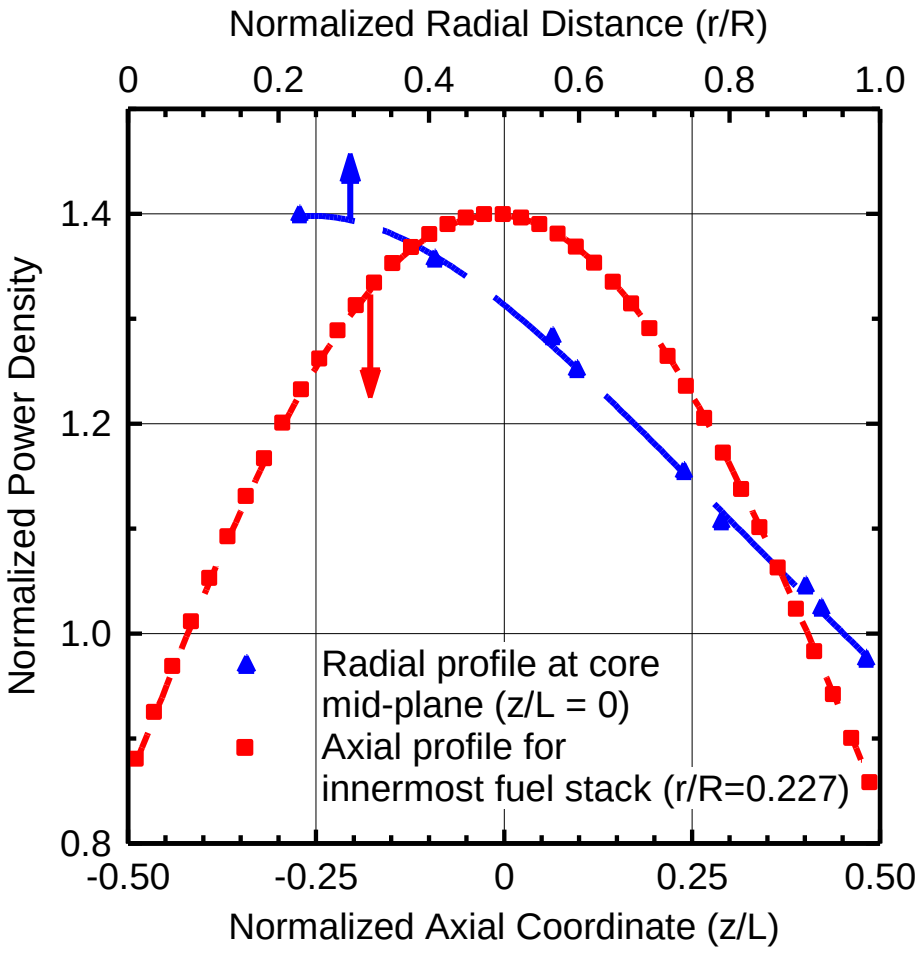

Fig. D.2. - Normalized radial fission power profile at active core mid-plane (z/L = 0) and axial power profile for innermost fuel stack in the core sectors (r./R = 0.227), Fig, D.1b [Schriener and El-Genk 2014a].

The analyses incorporate the heat transport in the flat potassium heat-pipes dividers (Fig. D.1b) in the SCoRe core using an effective thermal conductance, whose value depends on the heat transport path/direction (Fig. D.1b). The analyses assume the top and bottom and the side surfaces of the reactor core vessel (Fig. D.1b) are thermally insulated and the calculation domain of a single sector (or 1/6 of the core) has symmetry boundary conditions along the axis of the potassium heat pipe dividers (Fig. D.1b). The domain includes the portion of the concentric coolant duct whose cross section changes from oblong to circular (Fig. D.1a). The analyses are performed for a liquid NaK-56 flow rate for the core sector of 3.395 kg/s at a uniform inlet temperature of 850 K at a fixed outlet

pressure of 1.0 MPa. The analyses are for incompressible flow with non-slip at the liquid-solid interfaces and account for the change in the properties of the liquid NaK-56, UN fuel and solid core structure material with temperature. The next subsection briefly introduces the linear turbulence models examined in the present analyses.

D.1.1 Turbulence Models

The performed, 3-D comparative CFD and thermal-hydraulic analyses investigated two linear RANS turbulent models for simulating the liquid NaK-56 circulating through the SC-SCoRe during nominal operation at inlet temperature of 850 K and exit temperate and pressure of 900 K and 1.0 MPa. RANS turbulence models assume that the flow Navier-Stokes equations can be decomposed into an averaged component, whose form is similar to the baseline equations, and a fluctuating component known as the Reynolds stress tensor. Additional transport closure equations solve for the components of this tensor. The forms of these equations differentiate between the many proposed RANS models and their variants. The unique properties of alkali liquid metal coolants with Pr ranging from 0.004 to 0.007 present additional challenges in the simulations, depending of the flow Reynolds number [Cheng and Tak 2006; Grötzbach 2013]. The linear RANS turbulent models of k-ε and k-ω used in the present analyses assume that the eddy viscosity and eddy heat diffusivity are related using a turbulent Prandtl number, Pr_t. In the STAR CCM+ Code, the default value for Pr_t is a constant 0.9, which is not suitable for modeling low Pr fluids like alkali metals [Cheng and Tak 2006; Grötzbach 2013; Reynolds 1975]. To account for the high thermal diffusivity of the liquid NaK-56 the Pr_t equation developed by Reynolds [Reynolds 1975] is used instead, producing values of Pr_t close to ~2.0 for the modeled conditions.

The k-ε turbulence model solves the transport equations for the turbulence kinetic energy, k, and its dissipation rate, ε [Rodi 1991]. The default model in STAR-CCM+ is the realizable two-layer k-ε model based on the formulation of Wolfstein's [Wolfstein 1969]. It divides the computational domain for the fluid flow into two distinct regions; one next to the wall, where the values of the turbulent viscosity, μ_t, and ε are determined as functions of distance from the wall, and one region further from the wall where the solution smoothly blends together. The selected options for the realizable two-layer k-ε

model are the second order upwind convection scheme, the Durbin Scale limiter realizability scheme that constrains the time variable and the All y+ wall treatment model

The SST k-ω turbulence model is a default model in STAR-CCM+ code package. This model supposedly improves fluid simulation in the boundary layer with an adverse pressure gradient [Wilcox 1998]. Rather than solving for ε, the second closure equation in k-ω model solves for the specific dissipation rate, ω, or the dissipation rate per unit of the turbulence kinetic energy. The SST k-ω turbulent model uses a formulation developed by Menter [Menter 1994] to reduce the sensitivity of the results to the initial conditions. This formulation effectively blends a k-ε like model far from the wall with the k-ω model near the wall. The performed analyses with the SST k-ω model use the options of the second order convection and the Durbin Scale limiter realizability as well as the All y+ wall treatment model.

These two RANS turbulence models have limitations in modeling thermal-hydraulics of low Pr liquid metal coolants. They assume isotropic eddy diffusivity, and thus could not simulate anisotropy effects due to in the Reynolds stress tensor, such as the secondary flows generated in noncircular geometries [Baglietto and Ninokata 2005; Grötzbach 2013]. These secondary flows, if important, could result in inaccurate predictions of the velocity and temperature fields along the flow path. In addition, the RANS linear k-ε and k-ω turbulence models are not suited for modeling liquid metal flows where buoyancy forces play a significant role [Cheng and Tak 2006; Grötzbach 2013]. This is not an issue for the present analyses involving highly turbulent forced convection with Reynolds number ranging from $1.3x10^5 – 6.8x10^5$ in lunar gravity of 1/6 G.

The primary focus of this work is examining the linear k-ε and k-ω turbulent models for simulating the thermal hydraulics of the NaK-56 cooled SCoRe. However, the results of these models for liquid NaK-56 flow and heat transfer is a single tri-lobe flow channel in the reactor core are compared to those calculated using the high fidelity Detached Eddy Simulation (DES) model. This model is a hybrid approach that combines a LES modeling in the detached flow regions with a RANS based closure model in the boundary layers [Spalart et al. 1997]. The Detached Eddy Model in STAR-CCM+ is examined using the converged RANS solution as the initial condition for the unsteady DES

simulation. The results of this comparison at the end of the results section, quantify any potential differences in the predictions of the linear k-ε and k-ω models for liquid NaK-56 with those of the DES turbulent model. Note that, unlike the k-ε and k-ω linear models, the DES turbulence model is transient and requires a fine numerical mesh grid, thus takes much longer time for the results to converge. Next subsection describes the implemented numerical meshing schemes in the present analyses.

D.1.2 Numerical Meshing

The numerical mesh grid used for performing the 3-D thermal-hydraulics and CFD analyses of the SC-SCoRe using the linear RANS k-ε and k-ω turbulence models is generated using STAR-CCM+'s tools for polyhedral volume and prism layer meshing. The polyhedral volume mesher generates unstructured polyhedral cells in the UN fuel and the solid core structure. The prism mesher generates parallel prismatic layers to better model the boundary layer in the flow regions. To quantify the effects on the computation time and the solution convergence, the analyses with the k-ε and k-ω turbulence models examine seven levels of numerical mesh refinement (Table D.1), the finest mesh grid is 'a' and the coarsest mesh grid is 'g'. The different mesh refinements are implemented by proportionally reducing the base and minimum sizes of the mesh cells in the flow and solid regions of the core sector.

The numerical mesh cells in the solid core structure and UN fuel stacks are relatively larger, which allow using refined mesh cells in the flow regions without excessively taxing the computation hardware. For simulating the liquid NaK-56 in the flow regions of the reactor core sector, the analyses use four prism layers next to solid surfaces. The total thickness of these layers is 20% of the base mesh size (Table D.1). This prism layer thickness is large enough to accommodate both the thermal and hydraulic boundary layers at the walls. Table D.1 shows how the average wall y^+ in the tri-lobe coolant channels of the core sector are comparable for the two linear RANS turbulence models. The wall y^+ decreases rapidly from 153-157 to 82-83 with increasing the mesh refinement up to ~$9x10^6$ fluid cells (mesh grid 'e'). It then decreases relatively slower to 79 with further increasing the refinement of the numerical mesh grid from 'e' to 'b' with ~ $25.1x10^6$ fluid cells. For the finest mesh grid 'a' with ~$43.3x10^6$ fluid cells, the wall y^+

Table D.1. - Numerical mesh cells for various levels of mesh refinement [Schriener and El-Genk 2014a].

Mesh Refinement	Liquid Base/Min mesh cell size (mm)	Solid Base/Min mesh cell size (mm)	Liquid Cells	Solid Cells	Total Cells	Average Wall y+ in the Tri-Lobe Core Channels	
						k-ω Model	k-ε Model
a	3/0.15	3.75/0.15	$43.3x10^6$	$28.8x10^6$	$72.1x10^6$	63	62
b	4/0.2	5/0.2	$25.1x10^6$	$20.2x10^6$	$45.3x10^6$	79	79
c	5/0.25	6.25/0.25	$17.0x10^6$	$15.6x10^6$	$32.6x10^6$	80	80
d	6/0.3	7.5/0.3	$11.7x10^6$	$12.8x10^6$	$24.5x10^6$	81	81
e	7/0.35	8.75/0.35	$8.7x10^6$	$11.2x10^6$	$20.0x10^6$	82	83
f	9/0.45	11.25/0.45	$6.0x10^6$	$10.0x10^6$	$16.0x10^6$	96	97
g	15/0.75	18.75/0.75	$2.2x10^6$	$5.8x10^6$	$8.0x10^6$	153	157

is 62-63. The difference in values of the wall y+ between the two linear RANS turbulence models is very small (Table D.1).

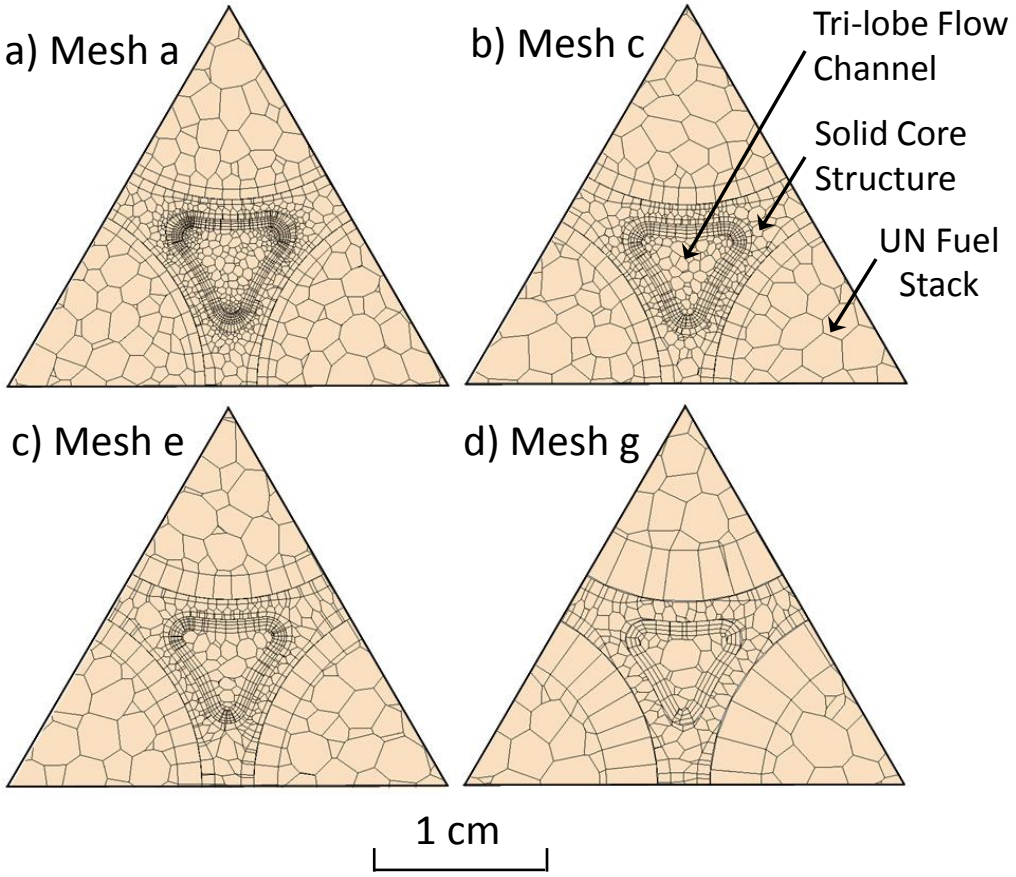

Fig. D.3. - Cross-sectional views of triangular element using different numerical mesh refinements (Table D.1) [Schriener and El-Genk 2014a].

Figures D.3a-d present cross-sectional views of a triangular element of the SCoRe core with a single tri-lobe flow channel surrounded by solid core structure and three 60^o segments of UN fuel stacks. These cross-sections show the implemented computational grids in the triangular element for different levels of mesh grid refinement. The majority of the numerical mesh cells are in the coolant flow channel, compared to those in the surrounding ODS-Mo solid core structure and UN fuel stacks. The numerical mesh cells in the fuel stacks are close to the upper size, only slightly increasing the total number of the numerical mesh cells. Table D.1 lists the numbers of cells in the different meshing schemes investigated. There are 43.3×10^6 liquid cells and 28.8×10^6 solid cells in finest

grid ‘a’, and only 2.2x10^6 liquid cells and 5.8 x10^6 solid cells in the coarsest grid ‘g’. In the different mesh refinements listed in Table D.1, the total number of the numerical mesh cells varies by a factor of ~9, the number of the solid cells varies by a factor of ~5, and the number of the liquid cells varies by a factor of ~19.

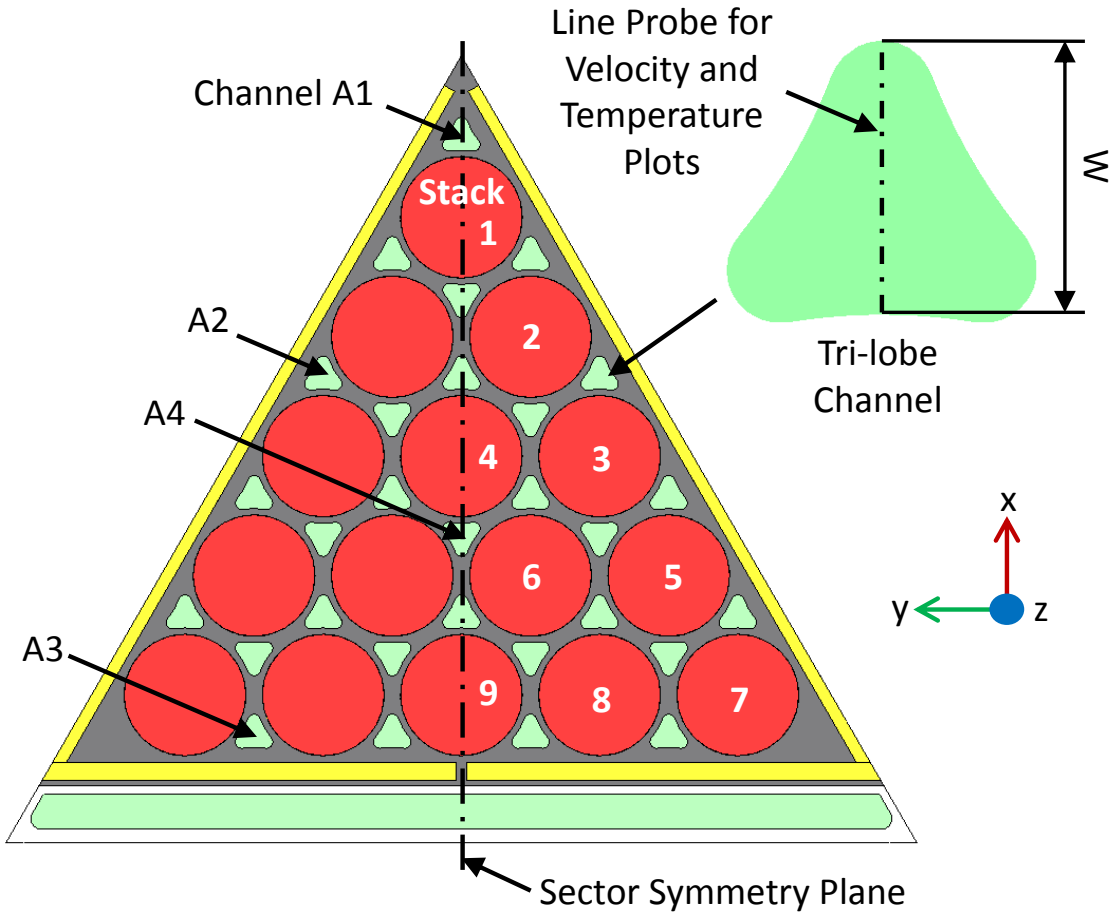

Fig. D.4. - Arrangements of fuel stacks and tri-lobe channels in a single core sector (yellow areas are the flat potassium heat pipes dividers) [Schriener and El-Genk 2014a].

Figure D.4 shows the arrangement of the UN fuel stacks and the liquid NaK-56 flow channels in a single core sector. Nine fuel stacks and four tri-lobe channels are labeled for later reference in the results section. The flow channels are A1, closest to the center of the core sector, A2 representing those along the wall of the heat-pipe divider, A3, the coldest channel close to the heat-pipes divider of in the core sector from the flow downcomer, and A4 in the middle of the core sector. In addition, the selected nine fuel stacks in the

core sector are #1 to #9 (Fig. D.4). Next section presents the calculated velocity and temperature profiles in the various flow channels and estimates of the peak temperatures in the UN fuel stacks in a core sector (Fig. D.4) at nominal operation conditions of the SC-SCoRe.

D.2. Results and Discussion

This section presents the results the performed thermal-hydraulics and CFD analyses of a SC-SCoRe core. Results quantify the effects of using the realizable two-layer k-ε and the Shear Stress Transport (SST) k-ω turbulence models with different levels of numerical mesh refinements to simulate the liquid metal flow in a core sector on the computation time and performance parameters. These are the UN fuel solid core structure temperatures, the radial temperatures and velocity profiles for the liquid metal flow at different axial locations in the tri-lobe channels, the turbulence eddies and the flow mixing in the lower and upper plenums and the exit duct, and the pressure losses along the liquid NaK-56 flow path in the core sector. As indicated earlier, the present analyses are at the nominal operating conditions of 1000 kW_{th} reactor thermal power (or 166.7 kW_{th} per core sector) and liquid NaK-56 inlet and exit temperatures of 850 and 900 K, respectively. Next subsection presents the results of the effect of the numerical mesh refinement on the calculated fuel and solid core temperatures.

D.2.1 Fuel Stacks and Solid Core Temperatures

The results presented in Figs. D.5a and D.5b are for the k-ω turbulence model of the liquid NaK-56 flow in the tri-lobe channels with different refinements of the numerical mesh grid in the core sector (Table D.1). Knowledge of the peak UN fuel and solid core structure temperatures in the core sector is important for ensuring safe reactor operation. The results presented in Fig. D.5a show the effect of refining the numerical mesh grid in the liquid NaK-56 flow channels on the axial location and the magnitude of the peak UN fuel temperature in the core sector (Fig. D.4). Fig. D.5b compares the calculated peak temperatures in the UN fuel stacks identified in Fig. D.4 using seven different numerical mesh refinements (‘a’ to ‘g’ in Table D.1). As indicated earlier, refining the numerical

mesh grid in the flow channels is associated with the refinements, but at lower magnitudes, of the meshing grid in the UN stacks and the solid core structure.

The peak UN fuel temperature occurs in the hottest stack #1 (Fig. D.4), which operates at the highest thermal power in the core sector. This temperature increases by a few degrees with refining the numerical mesh grid from 'g' to 'c' (Table D.1), then changes very little with further refinement of the grid (Fig. D.5a). The numerical grid 'c' includes ~$1.7x10^7$ liquid cells and ~$1.6x10^7$ cells in UN fuel stacks and the solid structure of the core sector with average wall $y^+ = 80$ (Table D.1). Fig. D.5a shows that the axial location of the peak fuel temperature in the sector shifts closer to the active core mid-plane with increasing the refinement of the numerical mesh grid from 'g' to 'd', then remains almost unchanged with further refinement of the grid. The numerical grid refinement 'd' includes ~$1.2x10^7$ liquid cells and ~$1.3x10^7$ solid cells with average wall $y^+ = 81$ (Table D.1). Results in Figs. D.5a and D.5b demonstrate that with numerical mesh grids having more than 20 million liquid cells in the flow regions of the core sector, the calculated results are practically independent of the mesh refinement.

The results in Fig. D.5b illustrate the effect of increasing the numerical mesh refinement on the calculated peak temperatures in the nine UN fuel stacks named in Fig. D.4, stack #1 through 9. The values of these temperatures also changes commensurate with the radial distribution of the fission power in the fuel stacks in the core sector. The radial power decreases, and so does the UN fuel temperature, with distance from the centerline of the core sector (Figs. D.4 and D.5b). The peak temperatures in the fuel stacks along the walls of heat-pipes dividers are the lowest because of the additional cooling by the dividers. They partially transfer the heat generated in the UN fuel stacks near the center of the core sector to the cooler regions along the wall of the liquid NaK-56 flow downcomer. The dependence of the peak temperatures in the UN fuel stacks #2-9 on the refinements of the numerical mesh grid is the same as that in the hottest fuel stack #1.

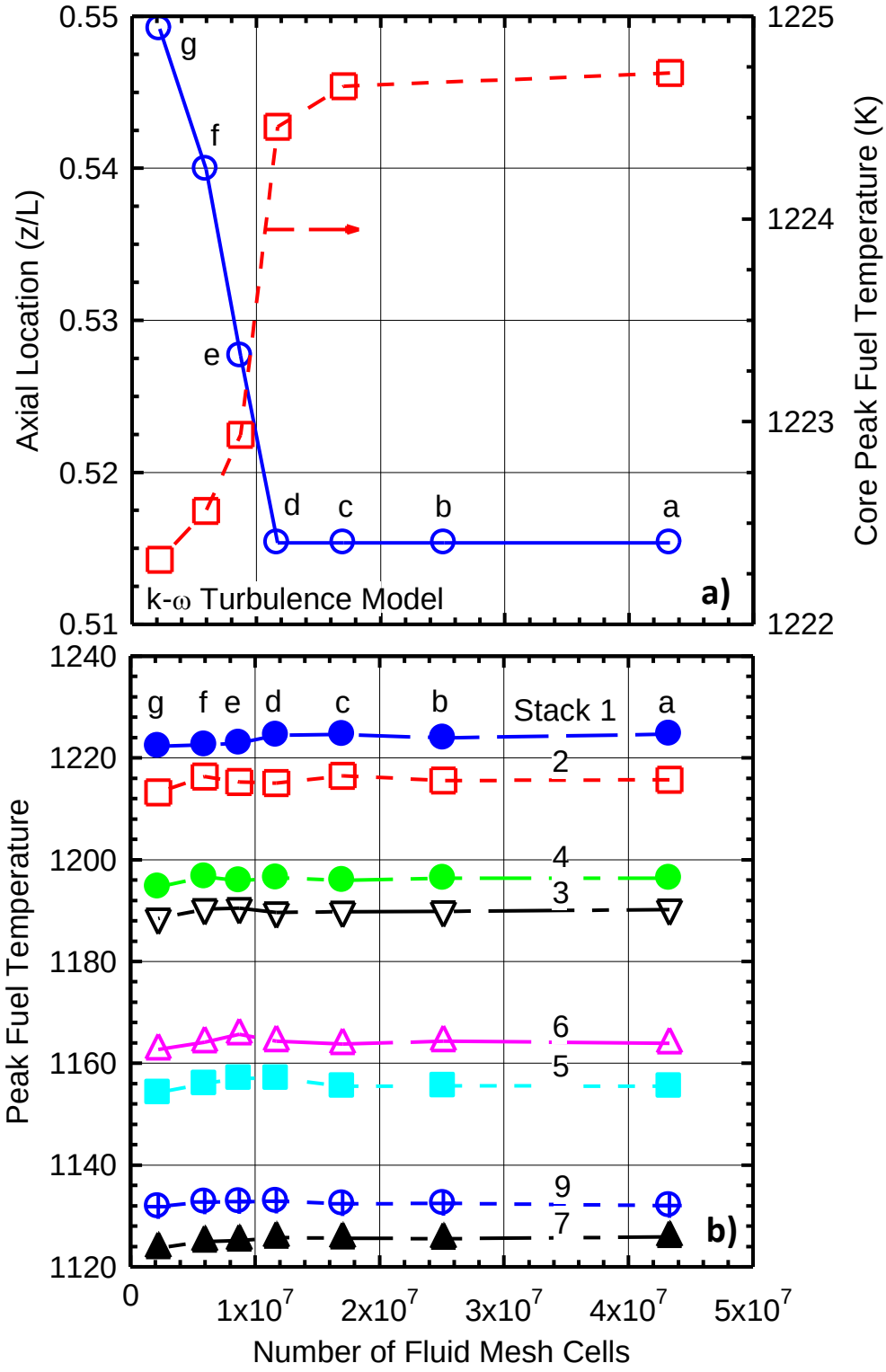

Fig. D.5. - Effect of mesh refinement on peak temperatures: (a) UN fuel and solid structure in core sector, and (b) select UN fuel stacks [Schriener and El-Genk 2014a].

The choice of the turbulence model negligibly affects the calculated peak UN fuel temperatures. The difference in the calculated peak temperatures in UN fuel stacks #1-9 when using the k-ε and k-ω turbulence models is ≤ 1.7 K, representing < 3.5% of the total rise of the liquid NaK-56 temperature in the reactor core during nominal operation (50 K). With the realizable two-layer k-ε turbulence model, the calculated peak UN fuel temperatures are consistently higher than with the k-ω turbulence model. The core solid structure temperatures show similar dependence on the choice of the turbulence model. The difference in the calculated peak temperatures of the ODS-Mo core structure when using the two RANS linear turbulence models is ~2.9 K representing ~5.9% of the total rise of the liquid NaK-56 temperature in the reactor core (50 K).

The mesh refinement needed for the calculated temperatures to converge includes a base cell size of ~4.6 mm, and at least ~2.0×10^7 liquid cells, ~1.2×10^7 cells in the core sector solid structure, and 5.4×10^6 cells in the UN fuel stacks and internals. Next subsection presents the results of the effects of the numerical mesh grid refinement and the choice of the turbulence model on the calculated radial distribution of the flow velocities and temperatures at different axial locations in the flow channels of the core sector (Figs. D.6-D.7).

D.2.2 Temperature and Velocity Profiles in Flow Channels

Liquid NaK-56 enters the SC-SCoRe at a uniform temperature of 850 K and exits at 900 K. It heats up slightly in the downcomer and mostly while flowing through the tri-lobe coolant channels, 29 per core sector (Fig. D.4). Figs. D.6 and D.7 compare the calculated radial temperature and velocity profiles of the NaK-56 liquid at different axial locations in channels A1 and A4 (Fig. D.4) within the active core height. Note that the orientation of the tri-lobe flow channel A4 is opposite to that of channel A1. The temperature of the liquid NaK-56 entering the active core region from the lower plenum is ~5-10 K above its inlet temperature (850 K). This temperature increase is due to the heat removal from the core structure by the liquid NaK-56 flowing in the annular downcomer. The liquid exits into the lower plenum before entering the NaK-56 tri-lobe flow channels in the SC-SCoRe core sector (Fig. D.1).

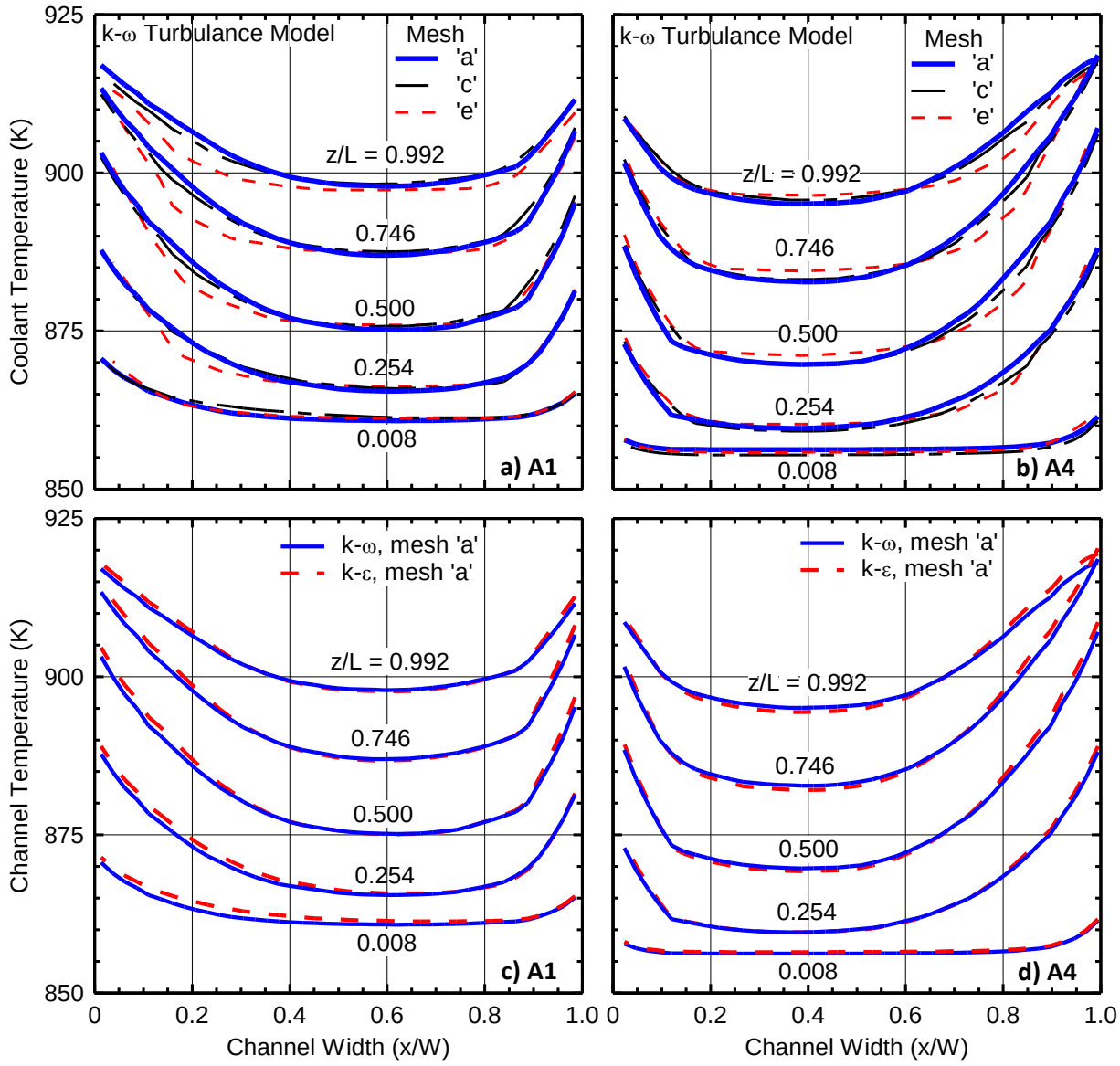

Fig. D.6. - Effect of numerical mesh refinement and the choice of turbulence model on the calculated temperature profiles in coolant channels: (a,c) channel A1, and (b,d) channel A4 (Fig. D.4) [Schriener and El-Genk 2014a].

Figures D.6a-d compares the calculated radial temperature profiles of the flowing NaK-56 in channels A1 and A4. Figs. D.6a and D.6b compare the calculated profiles at different axial location in the channels using the k-ω turbulence model with three different numerical mesh grids. The results in Figs. D.6c and D.6d compare the calculated temperature profiles in the flow channels using the k-ω and k-ε turbulence

models and the most refined mesh grid ‘a’. The liquid NaK-56 enters channel A1 of the core sector (Fig. D.4) from the lower plenum at a slightly higher temperature than channel A4. Close to the entrance (z/L = 0.008), the temperature profiles are relatively flat in the middle of the channels and higher close to the channel walls (Figs. D.6a – D.6d). Asymmetric parabolic-like temperature profiles develop with increasing axial distance up the flow channels as the liquid NaK-56 heats up. The liquid NaK flows in channels A2 and A3 (Fig. D.4) show similar temperature profiles as in channel A1, but the actual temperatures are slightly different because of the differences in the power generation rate in the UN fuel stacks closest to the channels and the liquid flow rate in the channels.

The results in Figs. D.6a and D.6b show the effect of the numerical mesh refinement on the calculated temperature profiles across the liquid metal flow channels, particularly at large axial distances (z/L = 0.254, 0.500, and 0.746). With the coarse mesh grids, the calculated temperature profiles are flatter in the center of the flow channels and have steeper gradients closer to the wall, in part because of the larger size of the numerical cell elements (Fig. D.6a). Near the exit of the flow channels (z/L = 0.992), the gradient near the wall decreases and the temperature profiles become more flat because of flow mixing and the lower wall heat flux, owing to the sinusoidal-like axial power profile in the core. The restricted flow in the corners of the tri-lobe flow channels (x/W = 0 in Fig. D.6a and x/W = 1 in Fig. D.6b) increases the liquid temperature at these locations (Fig. D.4).

Figures D.6c-d of the calculated temperature profiles with the finest numerical mesh grid ‘a’ (Fig. D.3) show that the choice of the turbulence model for the liquid flow in the coolant channels only slightly affects the results. The calculated temperature profiles using the two turbulence models are very close, < 1.5 K in channel A1 and 1.7 K in channel A4 (Fig. D.4). The temperature profiles based on using the k-ε turbulence model have slightly steeper gradients in the boundary layer near the flow channel walls. In addition, the temperatures in the center of the channels are slightly lower than those calculated using the k-ω turbulence model. The results presented in Figs. D.6c-d also show that the calculated temperature profiles of the flowing liquid NaK-56 in the coolant channels using the finest numerical mesh grid ‘a’ are practically independent of the

choice of the turbulence model. Both the SST k-ω and the realizable two-layer k-ε turbulence models use similar All y^+ wall treatment models. The convergence of the calculated temperature profiles using both turbulence models requires approximately the same mesh refinement (> $2x10^7$ liquid mesh cells, Table D.1 and Fig. D.5). Next, the presented results are of the effect of the turbulence model choice for liquid flow on the calculated velocity profiles in the coolant channels of the SC-SCoRe core (Figs. D.7a–d).

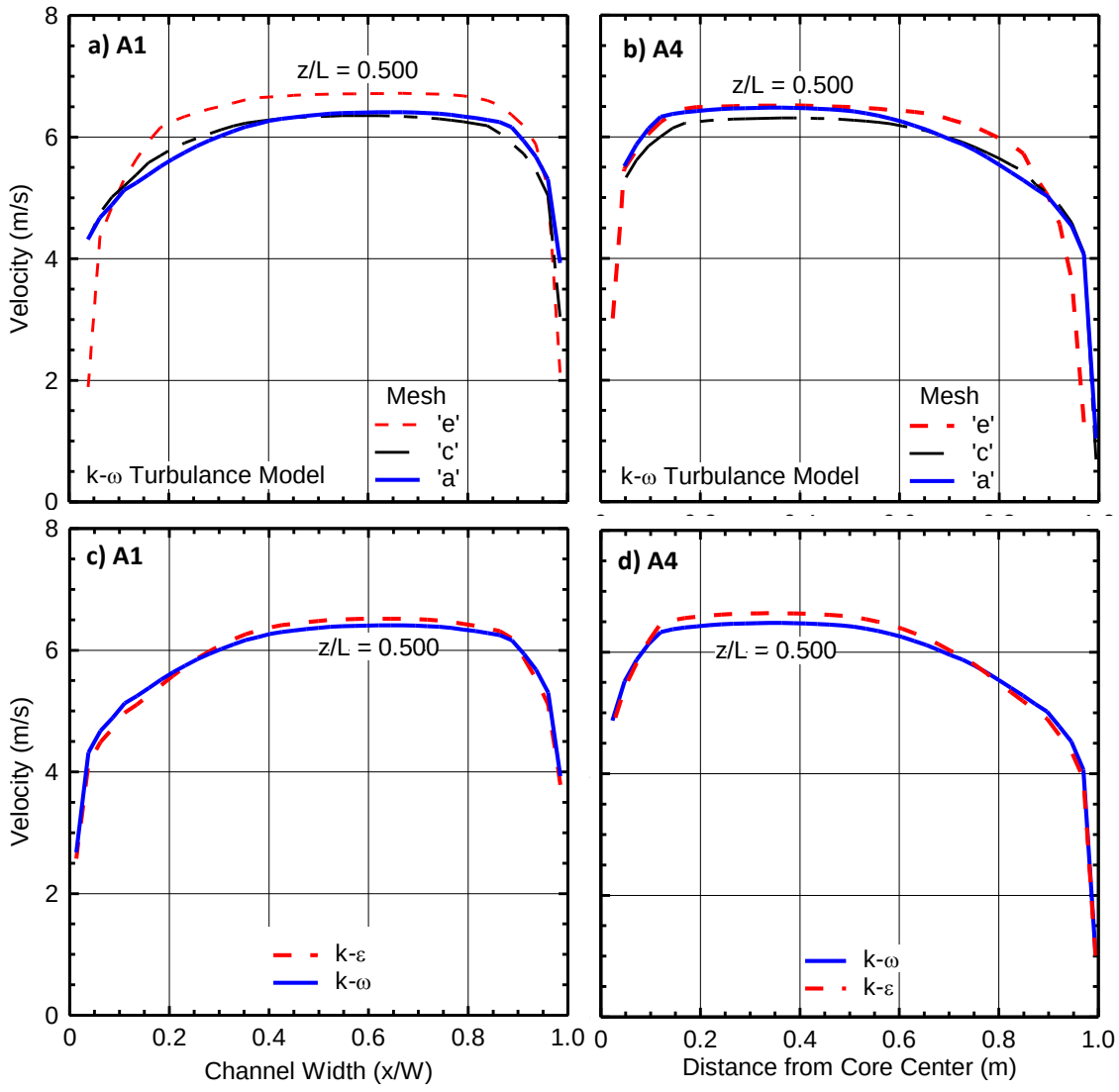

Fig. D.7. - Effect of numerical mesh grid refinement and the choice of turbulence model on the velocity profiles: (a,c) coolant channel A1, and (b,d) channel A4 [Schriener and El-Genk 2014a].

D.2.3 Velocity Profiles in Coolant Channels

Results in Figs. D.7a and D.7b show the effect of the numerical mesh refinement on the calculated velocity profiles for the liquid NaK-56 flow using the k-ω turbulence model in channels A1 and A4 at the core mid-plane (z/L = 0.5). At that location, the velocity profiles are hydro-dynamically fully developed. Those calculated with the coarsest mesh 'e' are more uniform across the channels and change with axial location. As the numerical mesh grid is refined, the velocity profiles converge but become more asymmetric due to the reduced flow near the corners of the tri-lobe channels (x/W= 0 in Fig. D.7a and x/W = 1 in Fig. D.7b). For the converged solution using the refined mesh 'a' in Table D.1, the velocity profile in channel A1 is close to that in channel A4, although the peak velocity is higher (Figs. D.7a and D.7b).

The results delineated in Figs. D.7c and D.7d show that the calculated velocity profiles in the tri-lobe flow channels using the two turbulence models appear to be quite similar. However, the values obtained with the k-ε model are lower than calculated using the k-ω turbulence model near the walls and higher in the middle of channels A1 and A4. The largest difference in the calculated velocity profiles in channel A1 using the two turbulence models is ~4.64% and ~3.68% in channel A4.

Figure D.8 presents the calculated temperature (Fig. D.8a) and flow velocity fields (Fig. D.8b) in the liquid NaK-56 flow channels A1-A4 using the k-ε and k-ω turbulence models with the finest mesh 'a'. Fig. D.8a shows asymmetrical temperature profiles of in these four coolant channels. The wall temperature is highest around the perimeter of the lobed corners of the channels where the liquid flow is most restricted (Fig. D.8b). The non-uniform spatial power profile in the reactor core and the non-uniform heat flow to the coolant channels from the adjacent fuel stacks contribute to the asymmetry of the calculated temperature fields in the channels. The liquid flow in channel A1 experiences higher temperatures along the bottom side, adjacent to UN fuel stack # 1 (Fig. D.4), than along the left and right faces adjacent to the heat pipe dividers. Similarly, along the left side of channel A2 and the bottom side of channel A3, the liquid temperatures near the walls of the heat pipes dividers are lower than in the rest of the channels. The temperature field in channel A4 in the center of the reactor core sector is more symmetric than in

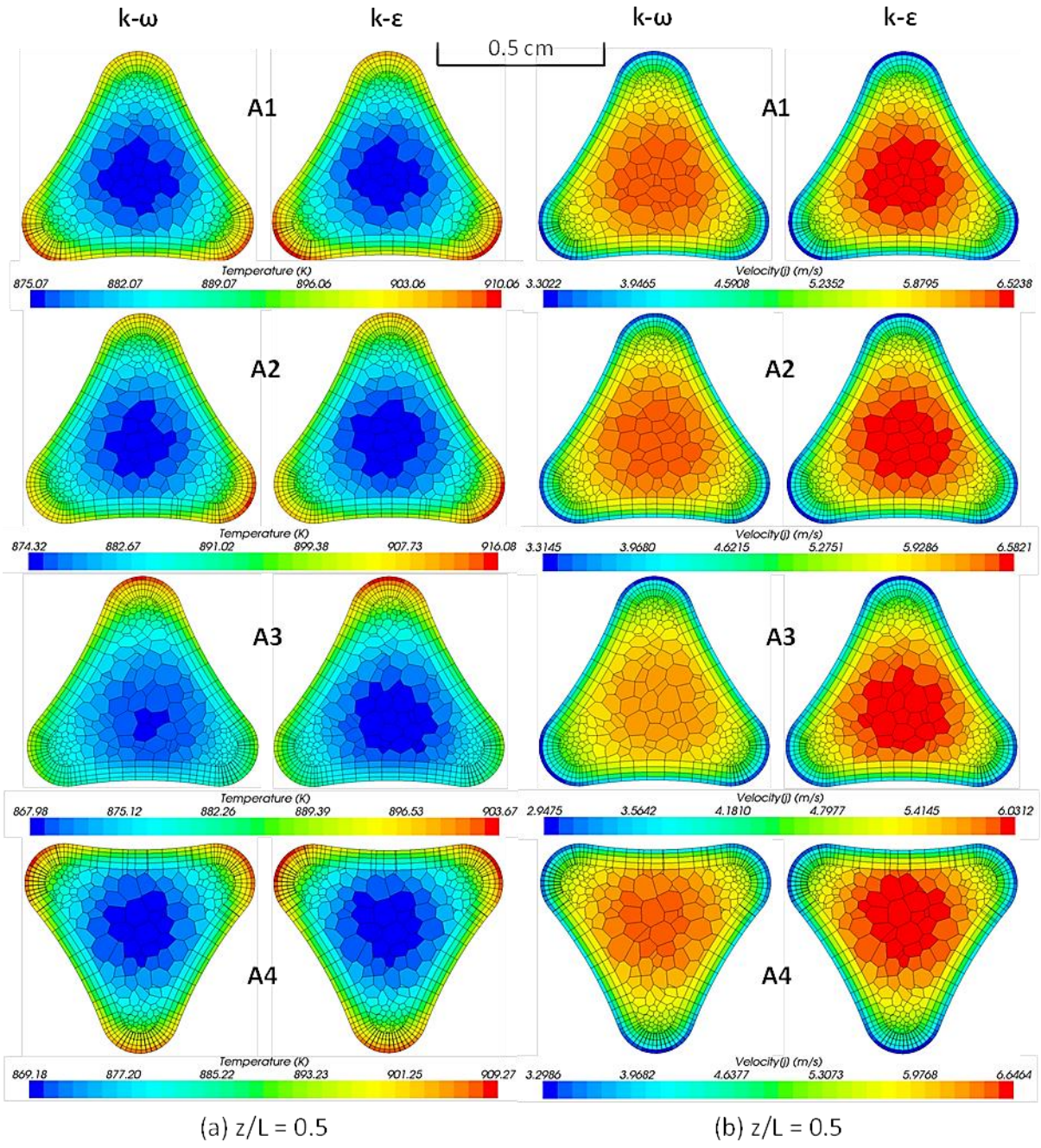

Fig. D.8. - Comparisons of the calculated temperature and velocity fields in selected liquid NaK-56 flow channels at core mid-plane using the k-ε and k-ω turbulence models with the finest numerical mesh 'a' (Table D.1) [Schriener and El-Genk 2014a].

channels A2 and A3. The decreasing radial power profile away from the core center causes the liquid temperatures in corners of the tri-lobe channel A4 adjacent to UN fuel stack # 4 to be higher than in the bottom corner adjacent to fuel stack #6.

Figure D.8b presents images of the calculated liquid flow fields in the four channels A1-A4. The velocity profiles are consistent with the asymmetric temperature profiles in the channels with the highest velocities remaining close to the center of the channels. In channel A3 the peak velocity shifts toward the cooler bottom face and toward the top of channel A4. The calculated axial flow velocities at the center of the flow channels in the core sector using the k-ω turbulence model are lower than those calculated using the k-ε model. However, those calculated along the wall in the corners of the tri-lobe flow channels using the k-ε model are lower (Fig. D.8b). The limited flow mixing and the turbulence vortices developing of in the lower plenum (Fig. D.1b) affect the flow distribution among the tri-lobe flow channels in the core sector.

Figure D.9 shows the variances in the mass flow rate in the 29 tri-lobe coolant channels of the core sector, when operating the reactor at the nominal thermal power of 1000 kW_{th} and liquid NaK-56 inlet and exit temperatures of 850 K and 900 K. Except for the channels adjacent to the inlet flow annulus (Channels 6-9), the flow rates in the remaining 25 channels in the sector are within $\pm$ 4-5% of the mean value. The flow rates in channels 6-9 are 6-10% lower than the mean rate, owning to the sharp 90° turn in the flow direction from the inlet annulus to the lower plenum (Fig. D.1b). The flow rates calculated using the k-ε and k-ω turbulence models in any given coolant channel in the core sector differ by less than 4.5%, with an average difference of 1.13% (Fig. D.9). The non-uniform distribution of the liquid NaK-56 flow in the coolant channels as well as the limited mixing the formation turbulence eddies in the lower plenum also affect pressure losses in the SC-SCoRe core sector. Next subsection compares the calculated total pressure and the pressure losses using the k-ω and k-ε turbulence models along the liquid NaK-56 flow path in the core sector.

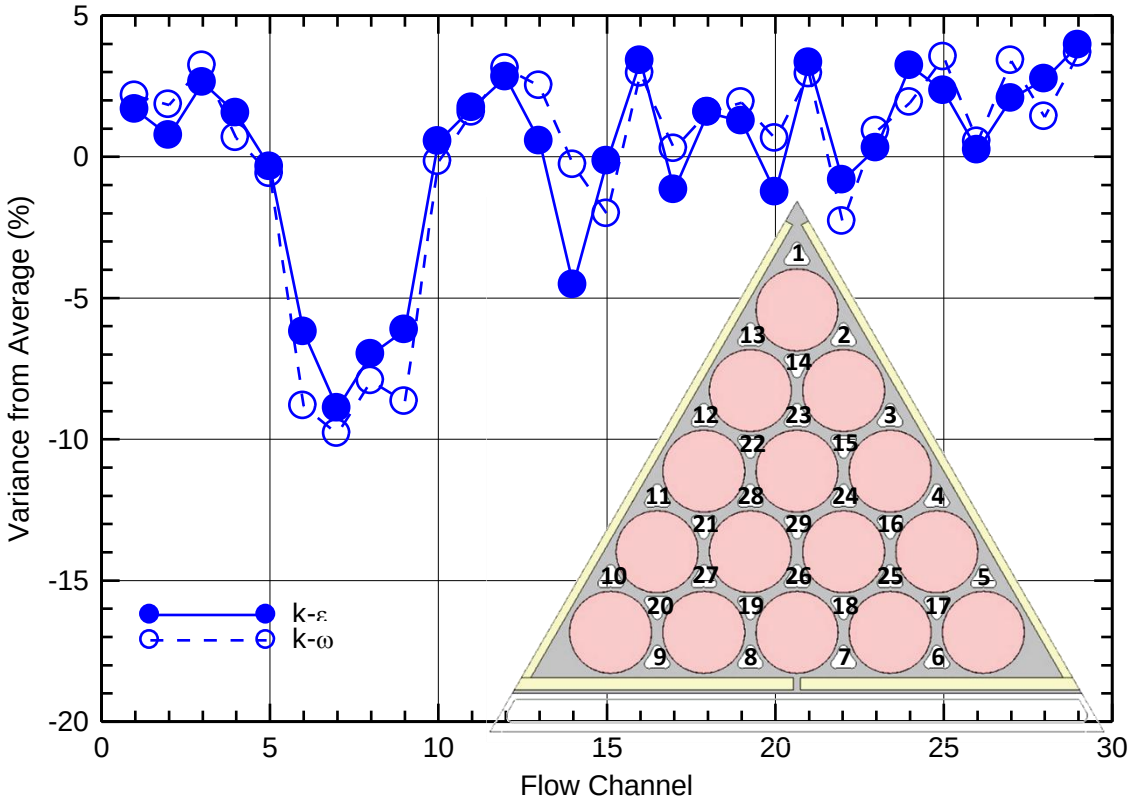

Fig. D.9. - Comparison of liquid NaK-56 mass flow rates in tri-lobe coolant channels using the k-ε and k-ω turbulence models with the finest numerical mesh 'a' [Schriener and El-Genk 2014a].

D.2.4. Pressure Losses

The total pressure and the pressure losses are calculated along the flow path in the reactor core sector (Fig. D.10) at a fixed exit pressure of 1.0 MPa using the k-ε and k-ω turbulent models in the STAR-CCM+ Code. At 1.0 MPa, the boiling point of the liquid NaK-56 is as much as 1,419 K, which is much higher the nominal exit temperature (900 K) in the SCoRe core during nominal operation (Foust 1972). This design margin of 519 K decreases but remains in excess of 200 K in the unlikely event that a core sector experiences a LOC or a LOCo while the reactor continues to operate at a power level of 321 kW_{th} (Schriener and El-Genk 2013).

The path of the liquid NaK-56 in a core sector traverses a number of sections of different geometry and flow conditions. Fig. D.10 compares the relative pressure losses

calculated at the nine locations along the liquid flow path. Results in Fig. D.11 show the effects of the numerical mesh grid refinement and the choice of turbulence model on the calculated pressure losses in the core sector. The axial cutaway view in Fig. D.10 presents a visual display of the liquid local pressure in the core sector, calculated using the finest mesh grid 'a' with the k-ω turbulence model. In this figure, station 1 is at the entrance of the inlet duct to the core sector, station 2 is at the entrance to the downcomer, station 3 marks the start of the fully developed pressure loss section in the downcomer annulus, and station 4 is at the exit of the downcomer to the lower plenum. Station 5 marks the entrance of the liquid from the lower plenum into the tri-lobe flow channels of the core sector. Station 6 marks the start of the fully developed pressure loss region in the channels, station 7 is where the liquid metal exits the channels into the upper plenum and station 8 is at the entrance of the exit duct section that ends at station 9.

Fig. D.11a compares the calculated relative pressure losses and Fig. D.11b compare the total pressure values along the flow path in the reactor core sector using the k-ε and k-ω turbulence models with both the finest mesh grid 'a' and the coarsest mesh grid 'g' (Table D.1) at the marked stations in Fig. D.10. Results show that the largest contributor to the pressure losses in the reactor core sector are the tri-lobe flow channels between stations 5 and 7 (37.8%). They are followed by the pressure losses in the inlet duct between stations 1 and 2 (22.8%), in the lower plenum between stations 4 and 5 (13.8%), and the finally in the exit duct between stations 8 and 9 (13.2%). There is a strong dependence of the total pressure losses as well as of their magnitudes in the various sections along the flow path of the liquid coolant on the numerical mesh refinement (Table D.1). The largest differences in the calculated pressure losses using either turbulence model with different numerical mesh grid refinement are in the sections from the entrance duct to the down-comer between stations 1 and 2, and in the lower plenum between stations 4 and 5. The sharp 90° turns in the flow direction at these locations create eddy vortices that contribute to increasing the pressure losses. The fine numerical mesh grid 'a' helps capture details of these vortices and flow mixing and hence, their effects on the pressure losses. As delineated in Fig. D.11a, the coarser mesh grid 'g' consistently overestimates the pressure losses along the flow path of the liquid NaK-56 in

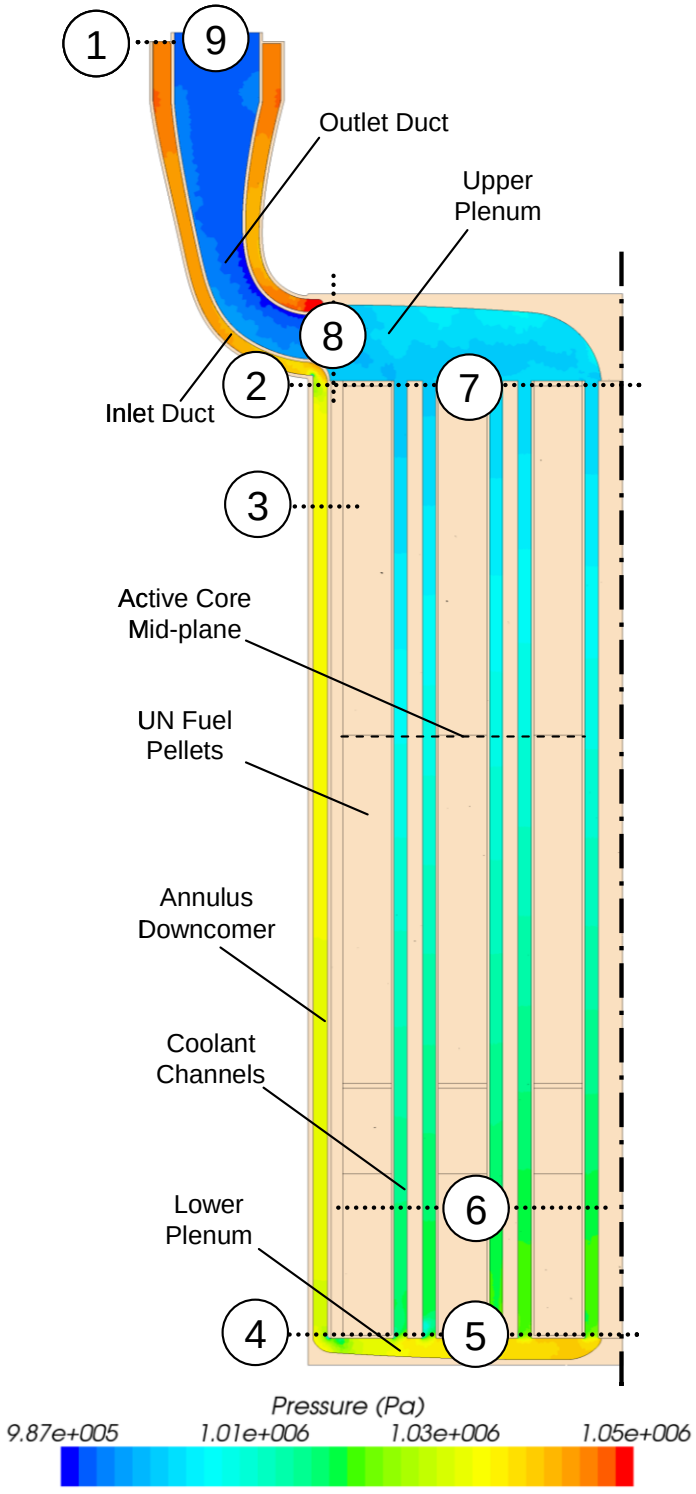

Fig. D.10. - Locations along the flow path in a core sector for reporting calculated pressure losses in the core sector using the k-ω turbulence model with the finest numerical mesh grid 'a' (Table D.1) [Schriener and El-Genk 2014a].

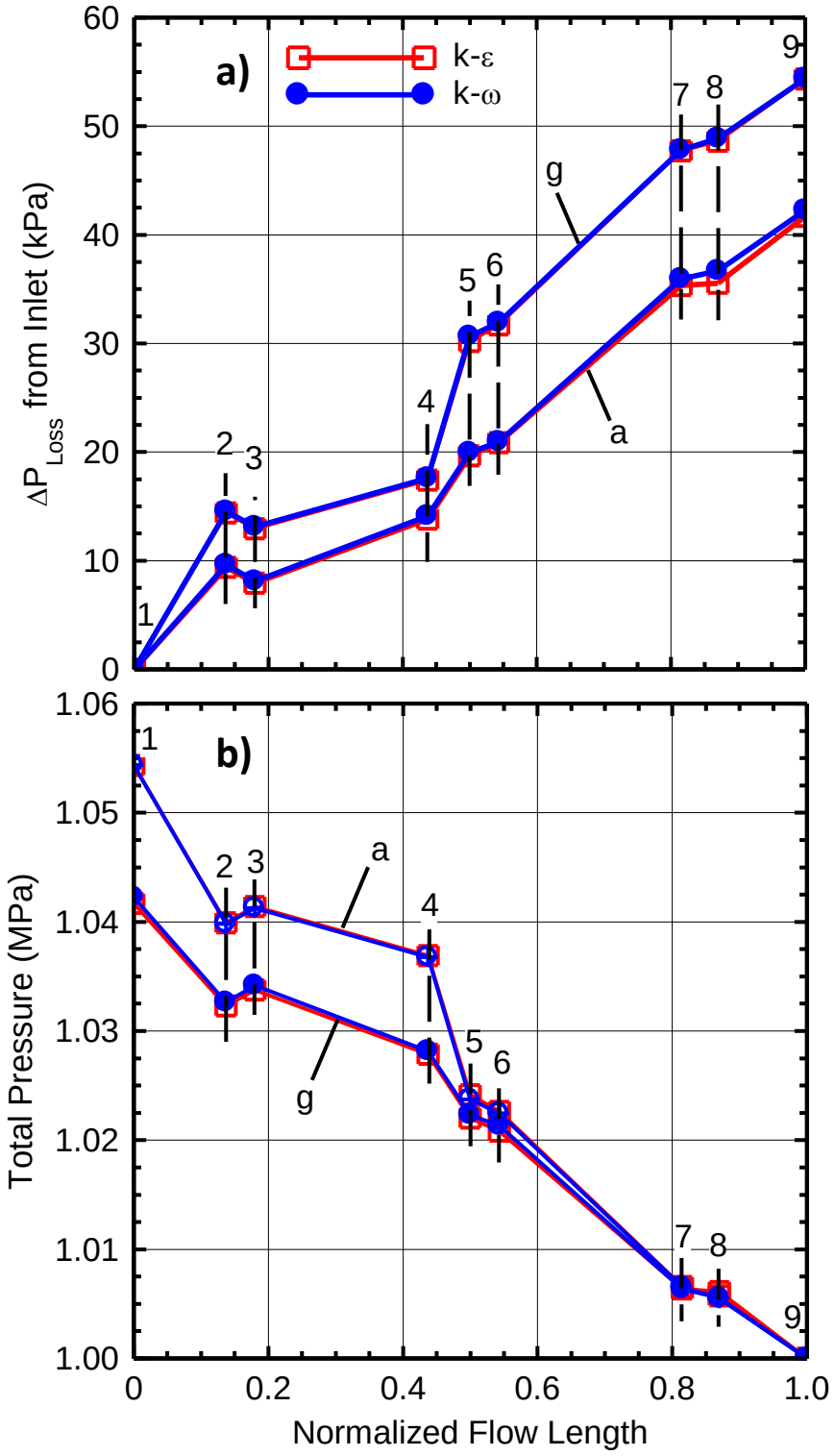

Fig. D.11. - Effects of mesh refinement and choice of turbulence model on calculated: (a) pressure losses and (b) total pressure in core sector [Schriener and El-Genk 2014a].

the core sector and underestimate the total pressure (Fig. D.11b) along the flow path to the upper plenum (between stations 1and 7 in Figs. D.10).

The choice of the turbulence model insignificantly affects the calculated pressure losses and the total pressure. The calculated pressure losses with the k-ω model are slightly higher than with the k-ε turbulence model. With the coarsest numerical mesh 'g', the calculated total pressure losses using the two turbulence models differ by less than 0.07%, and by 1.4% when using the finest mesh grid 'a'. The largest relative difference in the calculated pressure losses using the two turbulence models occurs in the upper plenum between stations 7 and 8 in Fig. D.10, where the pressure losses are small. The k-ω model calculates pressure losses of 0.77 kPa, which are ~226% higher than those calculated using the k-ε model (0.24 kPa). The next largest relative difference occurs in the exit duct, where the k-ω model calculates pressure losses of 6.08 kPa, which are 9.11% lower than those with the k-ε model. Similarly, the calculated pressure losses in the flow channels of the core sector using the k-ω turbulence model of 14.98 kPa, are 3.61% higher than those calculated using the k-ε model. This may be partially attributed to the difference in simulating the liquid flow mixing and formation of the eddy vortices in the upper plenum by the two models.

While the calculated peak temperatures of the UN fuel and the core solid structure and the liquid NaK-56 temperatures and velocity profiles in the flow channels converge using numerical mesh grids with at least ~$2x10^7$ liquid cells, the core pressure losses requires a much a finer mesh grid for convergence (Table D.1). At least ~$4x10^7$ liquid cells are needed for the pressure losses estimates to converge, particularly in the sections where the liquid flow experiences sharp turns, such as between stations 1-2 and 4-5 (Figs. D.10 and D.11). The largest differences in the calculated pressure losses using the two turbulence models are in the upper plenum and the exit duct (stations 7-9), where intense flow mixing and formation of eddy vortices occur. The following subsection investigates the effects of the numerical mesh grid refinement and the choice of the turbulence model on the liquid flow mixing and formation of eddy vortices as well as the temperature differences in the upper plenum and exit duct (Fig. D.12).

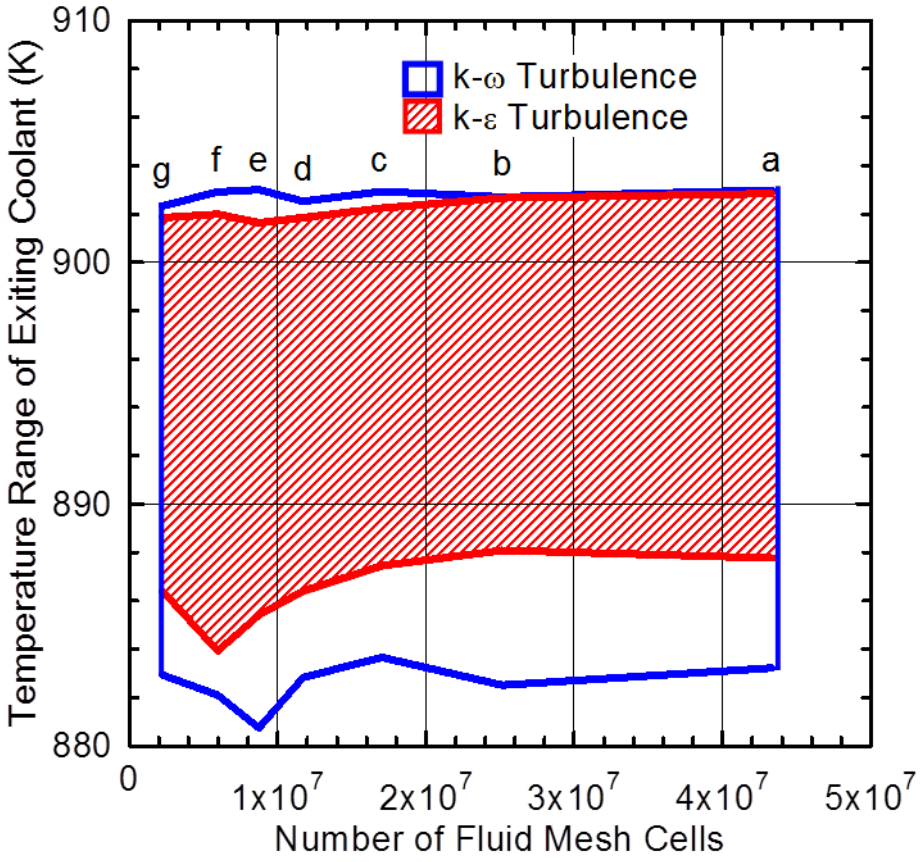

Fig. D.12. - Effects of mesh refinement and choice of turbulence model on the temperature differences in upper plenum and exit duct [Schriener and El-Genk 2014a].

D.2.5. Mixing in Upper Plenum and Exit Duct

The hot liquid NaK-56 exiting the tri-lobe channels of the core sector jets into the upper plenum where it partially mixes before entering the exit duct (Figs. D.10 and D.13). Despite the intense liquid mixing in the upper plenum there is a difference in the temperature of the liquid exiting the upper plenum into the exit duct. Fig. D.12 compares the ranges of calculated liquid temperatures at the entrance to the exit duct (Location 8 in Fig. D.10). These calculations are of the k-ε and the k-ω turbulence models in the liquid regions of the core sector with different numerical mesh grid refinements (Table D.1). The open and shaded areas in Fig. D.12 indicate the magnitude of the difference in the liquid temperature predicted in the present CFD and thermal-hydraulics analyses of the SC-SCoRe core sector using the k-ω and k-ε models, respectively.

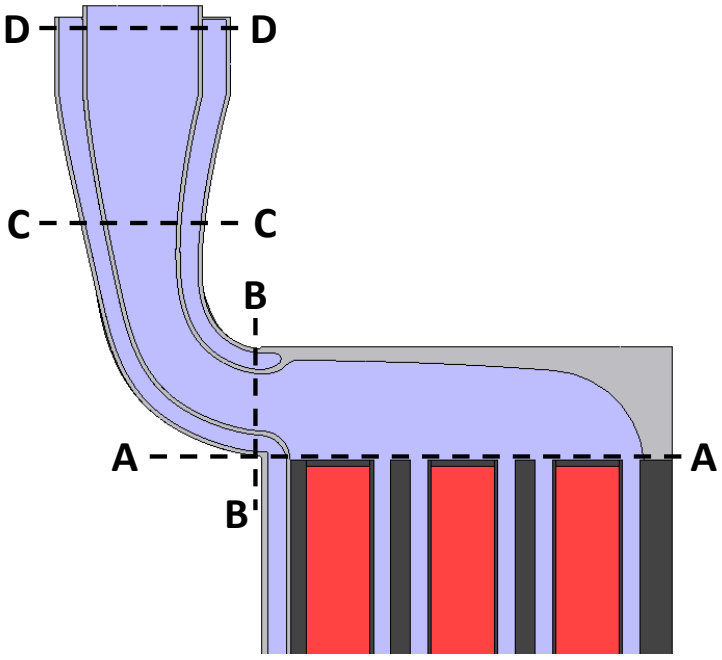

Fig. D.13. - Location of flow field images of the liquid NaK-56 flow in the upper plenum and exit duct [Schriener and El-Genk 2014a].

The highest temperatures in Fig. D.12 are only slightly (< 3 K) higher than that of the average liquid exit temperature from the reactor sector (900 K), while the lowest temperatures are 12-20 K lower than the average exit temperature. The temperature difference in the liquid flow into the exit duct is due to the insufficient mixing in the upper plenum. The temperatures of the liquid NaK-56 exiting the tri-lobe flow channel in the core sector next to the exit duct are lower than that exiting the channels near the center and in the middle region of the core sector. The calculated temperatures in Fig. D.12 generally converge with almost the same numerical mesh grid refinement of at least ~$2x10^7$ liquid cells.

The highest temperatures calculated by the turbulence models converge to almost the same values (Fig. D.12). Conversely, the lower temperatures in Fig. D.12 calculated using the k-ε model converge before those calculated using the k-ω model and are more than 2 K higher. With same numerical mesh refinement in the liquid region, the calculated differences in the liquid temperature at the entrance of the exit duct using the k-ε turbulence model in the liquid flow regions are consistently smaller than calculated

by the k-ω model by ~ 5 K (Fig. D.12). The following discussion investigates liquid mixing, which affects the liquid temperatures in the upper plenum and at the different locations in the exit duct. To illustrate this effect, Fig. D.14 presents the obtained flow field images at the labeled cross-sections in Fig. D.13.

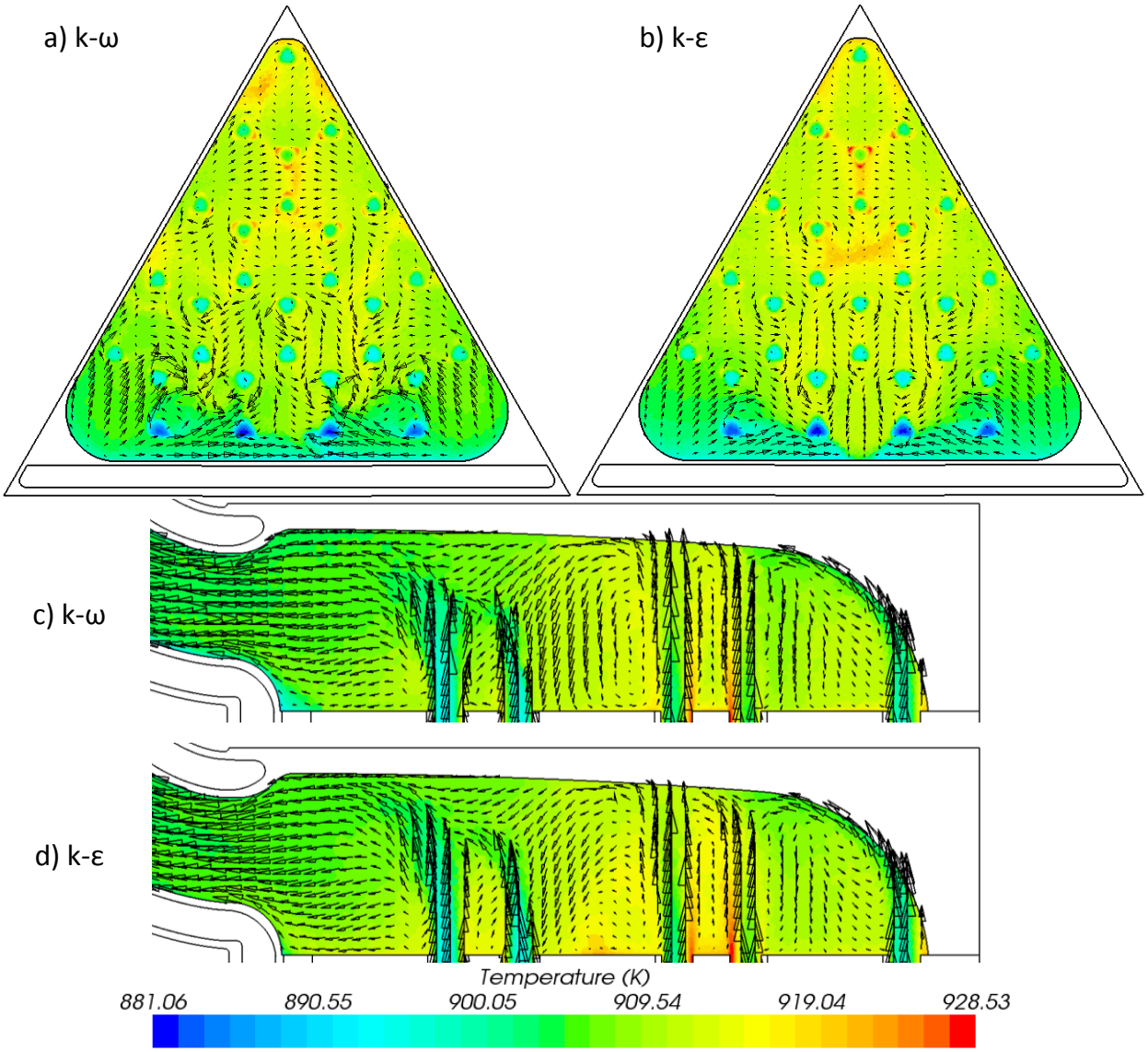

Fig. D.14. - Calculated temperature fields, tangential velocity vectors and liquid turbulence eddies in the upper plenum using the k-ω and k-ε turbulence models with the finest mesh gird 'a' in Table D.1: (a-b) at section A-A in Fig. D.13, and (c-d) at the sector symmetry plane (Fig. D.4) [Schriener and El-Genk 2014a].

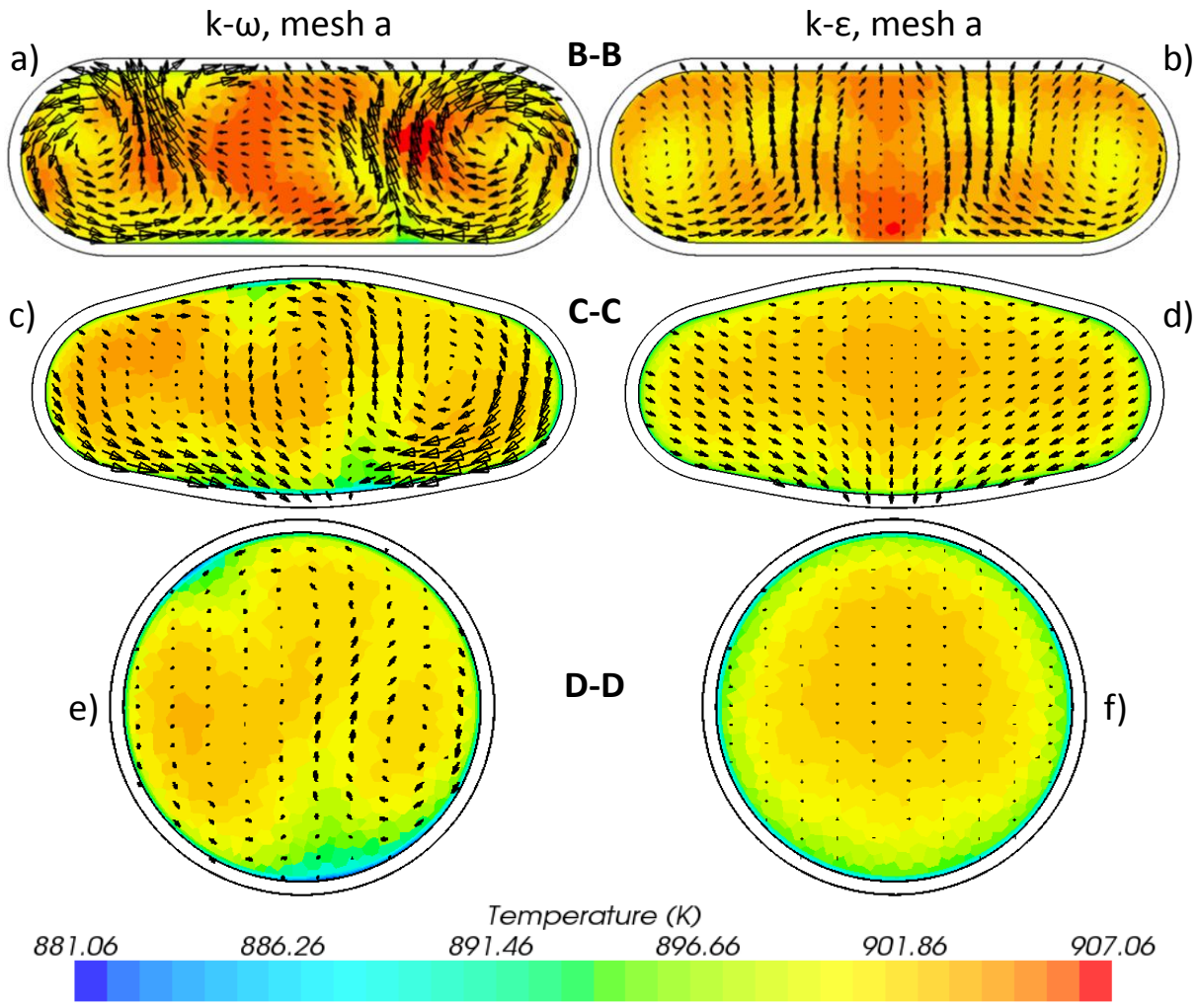

Fig. D.15. - Calculated temperature fields, tangential velocity vectors, and mixing eddies in the exit duct using the k-ω and k-ε turbulence models with the finest numerical mesh gird 'a' in Table D.1: (a-b) at Section B-B, (c-d) at section C-C, and (d-e) at section D-D in Fig. D.13 [Schriener and El-Genk 2014a].

These images of the mixing profiles in the upper plenum and the exit duct of the core sector (Fig. D.14a–d) include those at the sector symmetry plane (Fig. D.4). In this figure, the plane A-A is 1.0 mm above the top surface of the solid ODS-Mo core block. The shape and the cross section of the exit duct changes from oval at section B-B to oblong as the duct changes direction 90° at section C-C, and to circular at section D-D (Fig. D.13). Figs. D.14-D.15 compare the calculated velocity vectors at these locations superimposed over the calculated liquid temperature fields using the k-ω and k-ε turbulence models

with finest numerical mesh refinement ‘a’ in Table D.1. Figs. D.14a and D.14b compare the calculated velocity vectors and temperature fields at Section A-A in Fig. D.13 and Figs. D.15c and D.15d compare those calculated along the symmetry plane of the core sector. Fig. D.15 compares the calculated velocity vectors and temperature profiles at sections B-B, C-C and D-D of the exit duct (Fig. D.13). The temperature field in Fig. D.14c shows a larger variance than in Fig. D.14d, consistent with the results displayed Fig. D.12.

The results in Figs. D.14 and D.15 show details of the liquid flow fields, including the forming vortices and turbulence eddies. The hot liquid exits the tri-lobe channels closer to the center of the core sector, jets into the upper plenum. It then turns and mixes with the cooler liquid exiting the channels closer to the entrance to the exit duct. The proximity of the colder channels to the exit duct limits the liquid NaK-56 mixing in the upper plenum, before entering the exit duct. Such limited mixing contributes to the temperature difference within the liquid flow into the exit duct (Figs. D.14c-d and D.15). In these figures, the results of the k-ω and k-ε turbulence models differ in the intensity of the flow mixing and the size, shape and details of the forming eddy vortices. The analyses results using the k-ε model indicate more symmetrical mixing (Fig. D.14b) than those using the k-ω turbulence model. In the upper plenum, the turbulence mixing eddies using the k-ε model converge at a lower level of numerical mesh refinement than those calculated with the k-ω model. Along the sector symmetry plane, flow eddies form in between the liquid jets exiting into the upper plenum. The calculated eddies using the k-ω model (Fig. D.14c) are more fine with smaller turning radii than those predicted with the k-ε model (Fig. D.14d).

The tangential flow vortices calculated by the k-ω model at the mouth of the exit duct (Fig. D.15a) are more intense and less symmetric than those calculated using the k-ε model (Fig. D.15b). The intensity of these vortices decreases along the length of the exit duct. The predicted tangential eddies using the k-ω model at section D-D in the exit duct are relatively weak (Fig. D.15e). At that section, there no visible turbulence eddies calculated using the k-ε model (Fig. D.15f). The low liquid flow temperature along the exit duct wall is due to the heat transfer across the duct wall to the colder NaK-56

entering through the annular portion of the concentric duct to the core sector (Fig. D.1). The predicted liquid flow fields in the upper plenum by the k-ω and k-ε turbulence models using the finest numerical mesh grid 'a' in Table D.1 show different mixing patterns (Figs. D.14-D.17). The differences in these patterns are consistent with the predicted flow fields, pressure losses (Fig. D.11) and the differences in the calculated liquid exit temperatures (Fig. D.12) using these models. The next section presents the results of the effects of refining the numerical mesh grid and the choice of the turbulence model for simulating the liquid flow regions in the SC-SCoRe sector on the computation time to complete the analyses.

D.3. Computational Requirements

This section investigates the effects of the numerical mesh refinement and using the k-ε and k-ω turbulence models for simulating the flow regions of the liquid NaK-56 in a SC-SCoRe core sector on the total computation time (Fig. D.16). For all numerical mesh grid refinements, the k-ω model consistently requires significantly more CPU time than the k-ε model to complete the calculations on the same computer hardware. As indicated in Fig. D.16, the analyses using the k-ω turbulence model require 40% to 120% more CPU time than with the k-ε model, depending on the refinement of the numerical mesh grid. The CPU time for the calculations monotonically increases, and so does the difference in the CPU time for completing the calculations with the k-ε and k-ω turbulence models, with increasing the refinement of the numerical mesh grid.

The memory required also increase with increasing mesh refinement. It increases from as little as 20.2 GB of RAM for the k-ε turbulence model with the course mesh grid 'g' in Table D.1 to as much as 134 GB of RAM for the k-ω turbulence model with the finest numerical mesh grid 'a' (Table D.1). Given the relatively small differences in the calculated values of the peak UN fuel and solid core structure temperatures, the temperature and flow velocity fields in the flow channels of the core sector and pressure losses (Figs. D.6-D.9, D.11), the k-ε model appears to be an economic choice. However, the supposed improved predictions of the flow swirling and turbulence eddies using of the k-ω model (Wilcox 1998) suggest that it would be a better choice for capturing more details of the eddy vortices and liquid mixing. To examine the suitability of using the k-ε

and k-ω linear RANS model for the present thermal-hydraulics analyses of the liquid NaK-56 cooled SCoRe, the calculated results for a single tri-lobe flow channel (Fig. D.1) are compared to those calculated using the Detached Eddy Simulation, a hybrid LES and RANS model. The next subsection presents and discusses the obtained results.

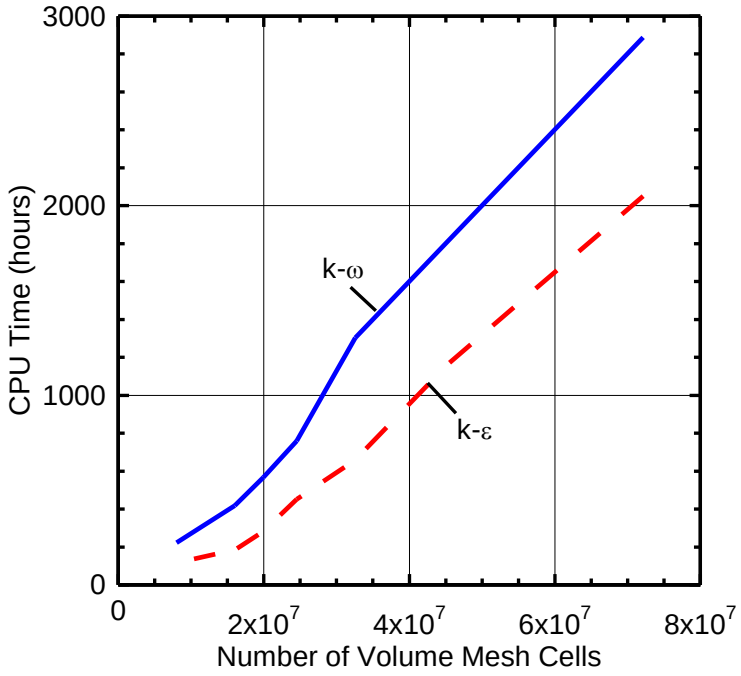

Fig. D.16. - Effects of the numerical mesh refinement and the choice of turbulence model on the CPU time to complete the analyses [Schriener and El-Genk 2014a].

D.4. Comparison with the Detached Eddy Simulation Model

The thermal hydraulics results for a representative tri-lobe flow channel in the SCoRe obtained using the k-ε and k-ω linear turbulent models are compared with those using the a DES model. The use of a single flow channel instead of a full sector of the reactor core is because the latter with the DES model demand relatively large computation requirements and take long time to complete on the same computer hardware. For example, the analysis of single reactor core sector the computation domain with the DES model requires >232 GB of memory (73% more than the SST k-ω model), exceeding the current physical memory of the computer. Thus, the performed comparative analysis in this subsection employs a single triangular element, with a tri-lobe flow channel

surrounded by the ODS-Mo core structure and three 60^o segments of UN fuel stacks (Figs. D.3, and insert in D.17). The sides of the triangular element have symmetry boundary conditions. The computation domain includes a 2 cm tall lower plenum and a 10 cm tall upper plenum. The mass flow rate of the liquid NaK-56 coolant in the coolant channel and the total fission power generated in the three, 60° UN fuel stacks are those of an average triangular element of the reactor core sector during nominal operation. This is at a total reactor thermal power of 1000 kW_{th} and liquid NaK-56 inlet and exit temperatures of 850 and 900 K. The numerical grid implemented in the single channel triangular element uses the same settings as the finest mesh 'a' in Table D.1 (Figs. D.3 and D.17). The used implicit unsteady solver is first order in time with a time step of $1x10^{-5}$ s and 15 inner iterations per time step. The SST k-ω portion of the DES simulation uses the same options as the linear RANS SST k-ω calculations. The DES transient simulation uses the converged k-ω steady-state solution for the initial condition.

Figure D.17 compares the results of the performed comparative thermal-hydraulic analyses for the single-channel triangular elements using the k-ε and k-ω linear turbulence models and the DES turbulence model in the flow channel. The DES model only slightly affects the values of the calculated performance parameters, namely: the wall temperature and the local pressure losses (ΔP_{Losses}) and Nusselt (Nu) in the coolant channel and the peak temperature in the UN fuel stacks (insert in Fig. D.17). The difference in the calculated pressure losses in the tri-lobe coolant channel using k-ε model ranges from +3.9 % to -4.3% relative to those calculated using the DES model, compared to +4.1% and -0.16% using the k-ω model.

The local Nu along the tri-lobe flow channel varies by a factor of ~3. It is lowest in the narrow corner tri- lobes of the channel and highest in the portions of the channel perimeter nearest the UN fuel stake, separated by a thin ODS-Mo structure (Fig. D.17). The difference in the calculated local Nu values using k-ε model, compared to those calculated using DES model varies from +6% to -13.5%, compared to +7.5% to -6% using the k-ω turbulent model. These differences in the Nu values cause the calculated temperatures of the liquid NaK-56 and surrounding ODS-Mo structure using the DES results and those of the two linear RANS models to vary by less than 2 K. The results in

Fig. D.17 also show that the calculated liquid NaK-56 temperature along the channel wall varied by less 1.8 K between the k-ε and DES models, compared to less than 0.6 K between the k-ω and DES models. The calculated peak temperature along the centerline of the UN fuel stacks in the triangular elements varies by less than 1.5 K between the k-ε and DES models and less than 0.3 K between the k-ω and DES models (Fig. D.17).

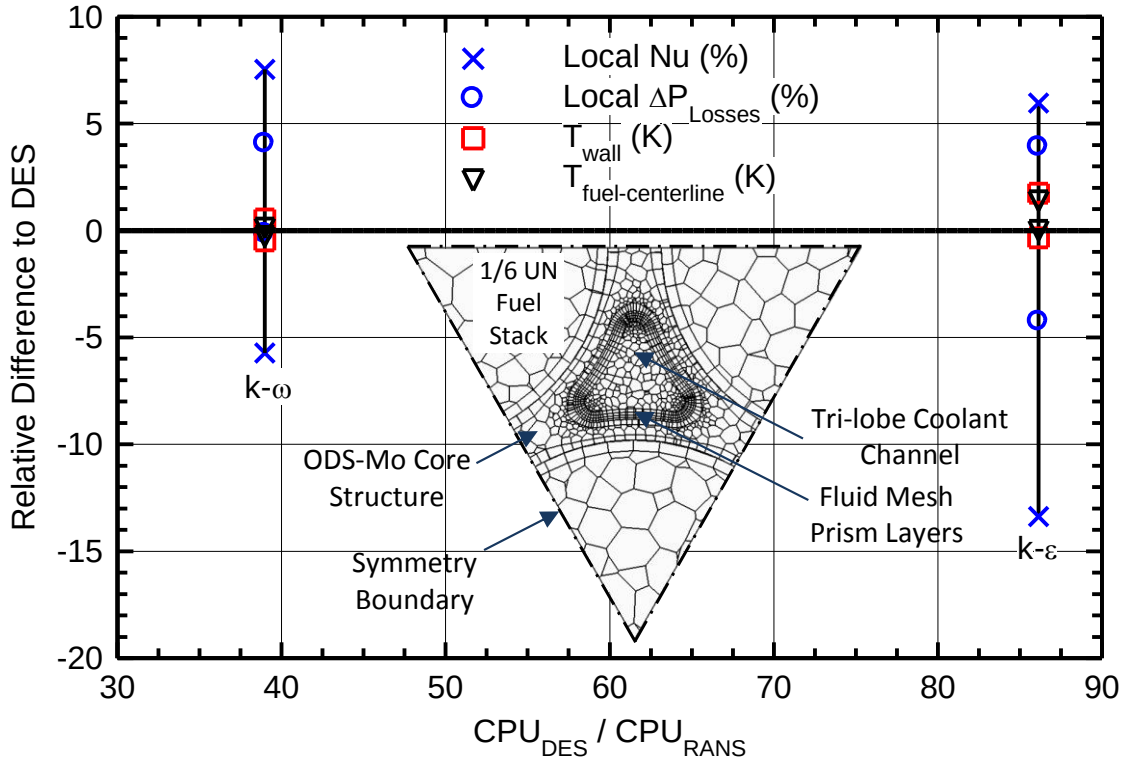

Fig. D.17. - Comparison of the calculated performance parameters for a triangular element with a single, tri-lobe flow channel using the DES turbulence model and both k-ω and k-ε linear turbulence models versus the relative CPU running time [Schriener and El-Genk 2014a].

Despite these relatively small differences in the calculated performance parameters using the DES turbulence model and the linear k-ε and k-ω turbulence models, the DES model requires significantly more computational resources (Fig. D.17). The memory requirement for the thermal-hydraulics analyses of the single triangular element using the k-ε and k-ω models is comparable, 4.76 and 4.87 GB, respectively, compared to 5.72 GB using the DES model (~ 20% more than k-ε). The difference in CPU time to complete the

calculations is far larger, with the DES model requiring 38 times that with the k-ω model and 86 times that with the k-ε model (Fig. D.17). This raises an important question of whether the results using the DES model are more accurate that those obtained using the k-e and k-w linear turbulence models. Owing to the absence of experimental liquid metal heat transfer data for tri-lobe shaped channels, to address this question, the calculated Nu values using the three models for a single circular tube with a uniformly heated wall with the reported correlations by various investigators [Lyon 1949, Subbotin 1961, Skupinski 1965, Baker and Sesonske 1962] based on experimental measurements for liquid NaK-56, NaK-78 and Na (Fig. D.18).

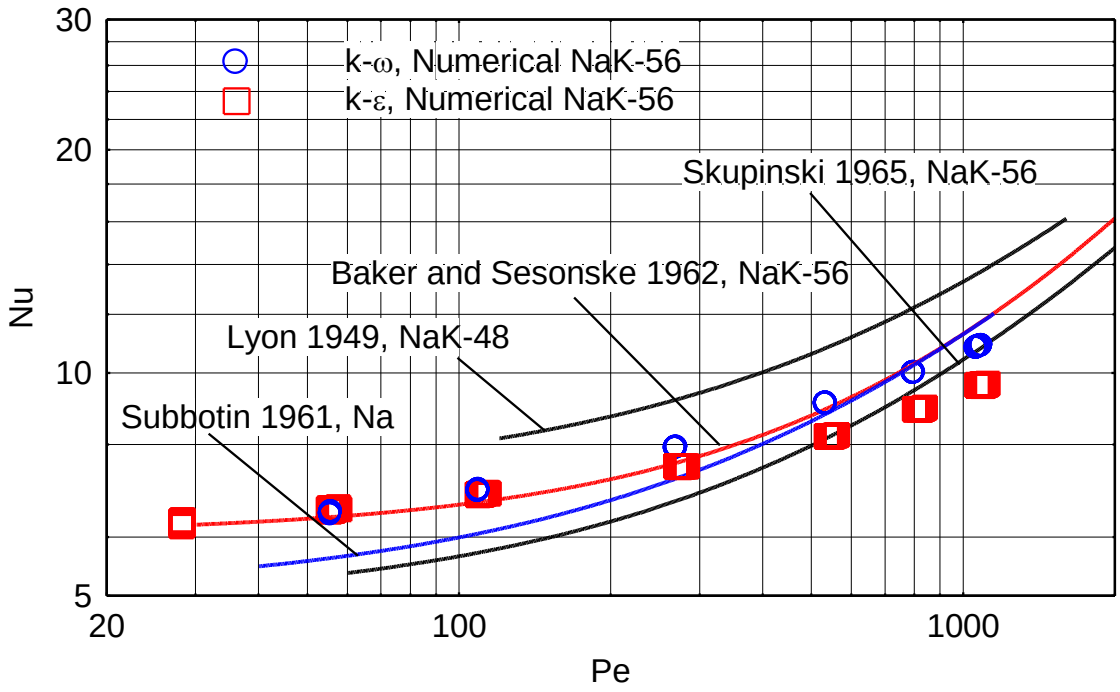

Fig. D.18. - Comparison of the calculated fully developed Nu values in a circular, uniformly heat tube with reported correlations [Schriener and El-Genk 2014a].

For the comparison in Fig. D.18, the numerical grid for the thermal-hydraulics calculation using the different turbulent models circular channel is generated with the hexahedral trimmer mesher with cell sizes ranging from 2.5 to 0.25 mm. The implemented numerical grid also comprises 12 prism layers with a total thickness of one mm near the heated wall, resulting in wall y+ values of 5.3 - 6.0. The numerically

calculated values of the fully developed Nu versus the liquid metal Peclet number, Pe, are compared with reported empirical correlations by different investigator for alkali metal liquids, based on experimental measurements [Lyon 1949, Subbotin 1961, Skupinski 1965, Baker and Sesonske 1962]. The Nu values calculated using the k-ω turbulence model at low Pe values < 200 are very close to those calculated using the k-ε model. At higher Pe, however, the Nu values using the k-ω model are higher with the difference progressively increases with increasing Pe, but remains less than 15%. Lyon correlation consistently over predicts Nu, by more than 100%, compared to the other three correlations and the present numerical Nu values calculated using the k-ε and k-ω turbulent models. The calculated Nu values using the k-ω turbulence model are closest to the correlation of Baker and Sesonske (1962), to within 3.5% for Pe $\leq$ 800 and lower at higher Pe, but within 8.5% at Pe = 1,100 (Fig. D.18). For Pe values > 600, the Nu values calculated using the k-ε model are much lower the Baker and Sesonske correlation and closest to correlation of Skupinski (1965), to within less than 9 % for Pe up to 1,100 (Fig. D.18).

The comparisons in Fig. D.18 show that the numerically calculated Nu values using either the k-ε or the k-ω linear turbulence models are consistent with the reported correlations for the liquid NaK- 56 [Skupinski 1965, Baker and Sesonske 1962]. The differences are much smaller that the reported scattering in the experimental data (in excess of $\pm$30%) used in developing the empirical Nu correlations in Fig. D.18. In addition, based on the comparison in Fig. D.17, the calculated Nu values using the DES turbulence model are expected to be close to those calculated in Fig. D.18 using the k-ω model. Thus the additional computation cost of using higher fidelity turbulence models like DES may not be, in some cases, justified for determining the performance parameters for alkali metal liquid metal systems, given that the numerical mesh grid is adequately refined. In the thermal-hydraulics analyses of the SC-SCoRe, the results presented earlier in this paper show that the k-ε or k-ω linear turbulence model are adequate for design optimization and assessing of the thermal performance of the reactor

REFERENCES

Adamczyk, A. et al., 2011. Full Mission Astronaut Radiation Exposure Assessments for Long Duration Lunar Surface Missions, in Aerospace Conference, 2011 IEEE, IEEE proceedings, 1-15.

Adams, J.H. et al., 2007.The Ionizing Radiation Environment on the Moon, Advances in Space Research, 40, 338-341.

Akiyama, M., 1991. Design Technology of Fusion Reactors. World Scientific Publishing Co. Pye. Ltd., Singapore.

Allen, T.R., Trybus, C.L., Cole, J.I., 1999. The effects of low dose rate irradiation and thermal aging on reactor structural alloys. J. Nuclear Materials 270, 290–300.

Amiri, B.W., Poston, D.I., 2005. Effect of neutron absorbers mixed in or coating the fuel of a 1-MWt lithium-cooled space reactor. In: El-Genk, M.S. (Ed.), Space Technology and Applications International Forum (STAIF-2005), AIP Conference Proceedings 746. American Institute of Physics, Melville, NY, 868-872.

Amiri, B.W., Sims, B.T., Poston, D.I., Kapemick, R.J., 2006. A Stainless-Steel, Uranium-Dioxide, Potassium-Heatpipe-Cooled Surface Reactor. In: El-Genk, M.S. (Ed.), Space Technology and Applications International Forum (STAIF-2006), AIP Conference Proceeding 813. American Institute of Physics, Melville, NY, pp. 289-297.

Angelo, J., Buden, D., 1985. Space Nuclear Power. Orbit Book Co., Malabar, FL.

Baglietto, E., Ninokata, H., 2005. A turbulence model study for simulating flow inside tight lattice rod bundles. J. Nuclear Engineering Design 235, 773–784.

Baker, R.A., Sesonske, A., 1962. Heat transfer in sodium–potassium alloy. Nuclear Science and Engineering 13, 283–288.

Bates, J.F., Powell, R.W., 1981. Irradiation-induced swelling in commercial alloys. J. Nuclear Materials 102, 200–213.

Bennett, G.L., 1989. A look at the soviet space nuclear program. In: Proc. 24th IECEC, Institute of Electronics and Electrical Engineering, Paper No. 899009.

Bennett, G.L., 2008a. Radar Men on the Moon: A Brief Survey of Fission Surface Power Studies. In: El-Genk, M.S. (Ed.), Space Technology and Applications International Forum (STAIF-2008), AIP Conference Proceedings 969. American Institute of Physics, Melville, NY, 372-379.

Bennett, G.L., 2008b. Mission interplanetary: Using radioisotope power to explore the solar system. J. Energy Conversion and Management 49, 382–392.

Bess, J.D., 2008. A Basic LEGO Reactor Design for the Provision of Lunar Surface Power. In: Proceedings of ICAPP 2008, Anaheim, CA USA, June 8-12, 2008, Paper No. 8344.

Bianco, R., Buckman, R.W., 1997. Mechanical Properties of Oxide Dispersion Strengthened (ODS) Molybdenum Alloys. Bettis Atomic Power Laboratory Report No.WAPD-T-3175, West Mifflin, Pennsylvania.

Booker, M.K., Sikka, V.K., Booker, B.L.P., 1981. Comparison of the Mechanical Strength Properties of Several High-Chromium Ferritic Steels. Oak Ridge National Laboratory, Oak Ridge, TN, USA, CONF-811069-1.

Campbell, P.D., 1992. Crew Habitable Element Space Radiation Shielding for Exploration Missions, Lockheed Engineering and Sciences Company, NASA Technical Report LESC-30455

Carter, L.L., Schwarz, R.A., 2005. MCNP Visual Editor Computer Code Manual. Visual Editor Consultants.

Cataldo, R.L., and Bozek, J.M., 1993. Power Requirements for the First Lunar Outpost. NASA Technical Memorandum 105925, Lewis Research Center, Cleveland, OH.

CD-Adapco,2011. STAR-CCM+ Release 6.02. www.cd-adpco.com.

CD-Adapco, 2012. STAR-CCM+ - 7.04. http://www.cd-adapco.com/products/starccm%C2%AE.

Ceradyne, Inc., 2010. Neutron Absorber Materials, http://www.ceradyneboron.com/uploads/Neutron%20Absorber%202-08.pdf.

Chandra, L., Roelofs, F., Houkema, M., Jonker, C., 2009. A stepwise development and validation of a RANS based CFD modeling approach for the hydraulic and thermal-hydraulic analysis of liquid metal flow in a fuel assembly. J. Nuclear Engineering and Design 239, 1988–2003.

Cheng, X., Tak, N.I., 2006. Investigation on turbulent heat transfer to lead-bismuth eutectic flows in circular tubes of nuclear applications. J. Nuclear Engineering and Design 236, 385-393.

Chi, S.W., 1976. Heat Pipe Theory and Practice. Hemisphere Publishing Company, Washington, DC

Cockeram, B.V., Smith, R.W., Snead, L.L., 2005. Tensile properties and fracture mode of wrought ODS molybdenum sheet following fast neutron irradiation at temperatures ranging from 300°C to 1000°C. J. Nuclear Materials 346, 165-184.

Colaprete, A.C., 2010. Detection of Water in LCROSS Ejecta Plume. Science, 330, no 6003, 463-468

Dallas T., Diaguila A.J., Saltsman J.F., 1971. Design Studies on the Effects of Orientation, Lunation, and Location on the Performance of Lunar Radiators, Lewis Research Center, Cleveland, OH. NASA TM X-1846

Davis, J.R., 2000. ASM Specialty Handbook: Nickel, Cobalt, and their Alloys. ASM International, Materials Park, OH, USA.

DeHart, M.D., 2005. TRITON: A Two-Dimensional Depletion Sequence for Characterization of Spent Nuclear Fuel, vol. I. Oak Ridge National Laboratory, Oak Ridge, TN. ORNL/TM-2005/39 Version 5. (Book 3, Section T1).

Demkowicz, P.A., 2006. Evaluation of Alternative Materials for Coated Particle Fuels for the Gas-Cooled Fast Reactor. Idaho National Laboratory, Idaho Fall, ID, USA, Final Report INL/Ext-06-11749.

Devan, J.H. et al., 1966. Lithium and potassium corrosion studies with refractory metals. In: IAEA Symposium on Alkali Metal Coolants, Vienna Austria, 675-694.

Dieckamp, H.M., September 1967. Nuclear space power systems. Atomics International.

DiStefano, J.R., Hoffman, E.E., 1963. Corrosion Mechanisms in Refractory Metal-alkali Metal Systems. Oak Ridge National Laboratory, Oak Ridge, TN. ORNL-3224.

Dobranich, D., El-Genk, M.S., 1991. Thermal stress analysis of the multilayered fuel particles of a particle-bed reactor. J. Nuclear Technology 94, 372–382.

Duke, M.B., Eendell, W.W., Roberts, B.B., 1985. Strategies for a Permanent Lunar Base, In: Mendell, W.W. (Ed.), Lunar Bases and Space Activities of the 21st Century, , Lunar and Planetary Institute, Houston, TX, 35-46.

El-Genk, M. S., 1995. Apparatus and Method for Nuclear Power and Propulsion, U. S. Patent No. 5,428,653.

El-Genk, M. S., 2008a. Space Nuclear Reactor Power System Concepts with Static and Dynamic Energy Conversion, J. Energy Conversion and Management 49(3), 402-411.

El-Genk, M.S., 2008b. Space Reactor Power Systems with No Single Point Failures, Nuclear Engineering and Design 238, pp. 2245 - 2255.

El-Genk, M.S., 2009. Deployment history and design considerations for space reactor power systems. Acta Astronautica 64 (10), 833-849.

El-Genk, M.S., 2010a. Post-operation storage options for space fission reactors. J. British Interplanetary Society 63, 61-73.

El-Genk, M.S. 2010b. Safety Guidelines for Space Nuclear Reactor Power and Propulsion Systems, In Space Safety Regulations and Standards (J. Pelton and R. Jakhu, Eds.), Elsevier Publishing Company, Chapter 26, 320–370.

El-Genk, M.S., Buden, D. and Mims, J., 1992, Nuclear Reactor Refuelable in Space, U. S. Patent No. 5,106,574.

El-Genk. M.S. and Gallo, B.M., 2010. High-Power Brayton Rotating Unit for Space Reactor and Solar Power Systems, J. Propulsion and Power, 26(1), 167-176.

El-Genk, M.S., Hatton, S., Fox, C., Tournier, J.-M., 2005. SCoRe – Concepts of Liquid Metal Cooled Space Reactors for Avoidance of Single-Point Failure. In: El-Genk, M.S. (Ed.), Space Technology and Applications International Forum (STAIF-05). AIP Conference Proceedings No. 746, American Institute of Physics, Melville, NY, 473–484.

El-Genk, M.S., Liscum-Powell, J., Pelaccio, D.G., 1994a. Bimodal, low power pellet bed reactor system design concept. In: El-Genk, M.S. (Ed.), Eleventh Symposium on Space Nuclear Power and Propulsion, AIP Conference Proceedings No. 301, American Institute of Physics, Melville, NY, 1535–1548.

El-Genk, M.S., Morley, N.J., Pelaccio D.G., and Juhasz, A.M., 1994b. Pellet Bed Reactor Concept for Nuclear Propulsion Applications, J. Propulsion and Power, 10(6), 817–827.

El-Genk, M.S., Parlos, A.G., McGhee, J.M., Lapin, S., Buden, D., Mims, J., 1990. Integrated system design optimization for multimegawatt space nuclear power applications. J. Propulsion and Power 6 (2), 194–202.

El-Genk, M.S., Saber, H.H., Caillat, T., 2002. A Performance Comparison of SiGe and Skutterudite Based Segmented Thermoelectric Devices. In: El-Genk, M.S. (Ed.), Space Technology and Applications International Forum (STAIF-2002), AIP Conference Proceedings No. 608, American Institute of Physics, Melville, NY, 1007-1015.

El-Genk, M.S. and Schriener, T.M., 2010. Performance and radiological analyses of a space reactor power system deployed into a 1000–3000 km earth orbit. Progress in Nuclear Energy 52, 236-248.

El-Genk M.S, Schriener T.M., 2011. Long operation life reactor for lunar surface power," J. Nuclear Engineering and Design 241, 6, 2339-2352.

El-Genk, M.S., Tournier, J.-M., 2005. Review of refractory metal alloys and mechanically alloyed-oxide dispersion strengthened steels for space nuclear power systems. J. Nuclear Materials 340, 93-112.

El-Genk, M.S., Tournier, J.-M., 2006a. DynMo–TE: Dynamic simulation Model for space reactor power systems with ThermoElectric converters. J. Nuclear Engineering and Design 236 (23), 2501–2529.

El-Genk, M.S., Tournier, J.-M., 2006b. High Temperature Water Heat Pipes Radiator for a Brayton Space Reactor Power System. In: El-Genk, M.S. (Ed.), Space Technology and Applications International Forum (STAIF-06). AIP Conference Proceedings No. 813. American Institute of Physics, Melville, NY, 716–729.

El-Genk, M.S. and Tournier, J-M., 2008. On the Use of Noble Gasses and Binary Mixtures as Reactor Coolants and CBC Working Fluids, J. Energy Conversion and Management, 49(7),1882–1891.

El-Genk, M.S., Tournier, J-M., and Gallo, B.M., 2010. Dynamic Simulation of a Space Reactor System with Closed Brayton Cycle Loops, J. Propulsion and Power, 26(3), 394 -406.

Elliott, J. et al., 2005. Prometheus – Project Lunar Fission Surface Power System Study Report. NASA Jet Propulsion Laboratory, JPL-982-R66153.

England, T.R., Rider, B.F., 1994. Evaluation and Compilation of Fission Product Yields 1993. Los Alamos National Laboratory, Los Alamos, NM. LA-UR-94-3106.

EPRI, 2003. Materials Reliability Program: A Review of Thermal Aging Embrittlement in Pressurized Water Reactors (MRP-80). EPRI, Palo Alto, CA, USA.

Foust, O.J., 1972. Sodium-NaK Engineering Handbook Volume I: Sodium Chemistry and Physical Properties. Gordon and Breach and Publishers, Breach, Science Publishers, Inc., New York, NY.

Freeh, J.E., 2008. Analysis of Stationary, Photovoltaic-Based Surface Power System Designs at the Lunar South Pole. Glenn Research Center, Cleveland, Ohio, USA, NASA/TM-2009-215506.

Fuzluddin, S., Smit, K., Slabber, J., 2004. The use of advanced materials in VHTR's. In: Proceedings of the 2nd International Topical Meeting on High Temperature Reactor Technology, Beijing, China, 22–24 September, Paper No. E06.

Gallo. B.M, and El-Genk, M.S., 2009. Brayton Rotating Units for Space Reactor Power Systems, J. Energy Conversion and Management, 50(9), 2210 - 2232.

Gauld, I.C., 2005. Origen-ARP: Automatic Rapid Processing for Spent Fuel Depletion, Decay, and Source Term Analysis, vol. I. Oak Ridge National Laboratory, Oak Ridge, TN. ORNL/TM-2005/39 Version 5. (Book 2, Section D1).

Grötzbach, G., 2013. Challenges in low-Prandtl number heat transfer simulation and modeling. J. Nuclear Engineering and Design 264, 41–55.

Gu, H., Shouzhi, Z., Zhiyong, S., Chengzhi, Y., 2013. A heat pipe cooled modular reactor concept for manned lunar base application, In: Proceedings of 2013 21st International Conference on Nuclear Engineering (ICONE21), Chengdu, China, July 29, 2013. Paper No. ICONE21-16006.

Gylfe et al., 1967. Reactor Power Plants for Lunar Base Application. Atomics International, NASA-CR-104189.

Hawley, J.P., September 1967. Water immersion safety for SNAP reactors. Atomics International, NAA-SR-11361.

Hatton, S.A., El-Genk, M.S., 2009. Sectored Compact Space Reactor (SCoRe) Concepts with a Supplementary Lunar Regolith Reflector. Progress in Nuclear Energy 51, 93-108

Hayatsu, K. et al., 2008. Radiation Doses for Human Exposed to Galactic Cosmic Rays and Their Secondary Products on the Lunar Surface, Biological Sciences in Space, 22, 2, 59-66

Heiken, G.H., Vaniman, D.T., French, B.M., 1991. Lunar Sourcebook: A User's Guide to the Moon. Cambridge University Press.

Hendricks, J.S. et al., 2006. MCNPX, Version 2.6.B. Los Alamos National Laboratory, Los Alamos, NM, LA-UR-06-3248.

Hendricks, J.S. et al., 2008.MCNPX2.7.A Extensions. Los Alamos National Laboratory, Los Alamos, NM, LA-UR-08-07182.

Hermann, O.E. et al., 1995. Validation of the SCALE System for PWR Spent Fuel Isotopic Composition Analyses. Oak Ridge National Laboratory, Oak Ridge, TN. ORNL/TM-12667.

Heynes International, 1997. Hastelloy X Alloy. Kokomo, IN, USA.

IAEA, 2006. Fast Reactor Database 2006 Update. IAEA Nuclear Power Technology Development Section, IAEA-TECDOC-1531.

Kaden R A., 1991. Methodology for Forming and Placing Lunar Concrete, Lunar Concrete, American Concrete Institute (ACI), SP-125, 71-96

Kang, S., Lipinski, R., McAlpine, W., 2006. Lunar surface reactor shielding study. In: El-Genk, M.S. (Ed.), Space Technology and Applications International Forum (STAIF-2006). AIP Conference Proceeding 813. American Institute of Physics, Melville, NY, 707–715.

Kerslake, T.W., 2005. Electrical Power System Technology Options for Lunar Surface Missions. NASA/TM-2005-213629, Glenn Research Center, Cleveland, OH.

King, J.C., El-Genk, M.S., 2006a. Submersion criticality safety of fast spectrum space reactors: Potential Spectral Shift Absorbers. Nuclear Engineering and Design 236 (3), 238–254.

King, J.C., El-Genk, M.S., 2006b. Submersion subcritical safe space (S^4) reactor. Nuclear Engineering and Design 236, 1759–1777.

King, J.C., El-Genk, M.S., 2007. Thermal Hydraulic Analyses of the Submersion-Subcritical Safe Space (S^4) Reactor. In: El-Genk, M.S. (Ed.), Proceedings of Space Technology and Applications International Forum (STAIF-2007). AIP Conference Proceedings, Melville, NY. 261-270.

Koning, A., Forrest, R., Kellet, M., Mills, R., Henriksson, H., Rugama, Y., 2006. The JEFF-3.1 Nuclear Data Library. OECD/NEA, Paris, France, JEFF Report 21.

Lemmel, H.D., McLaughlin, P.K., Pronyaev, V.G., 2001. ENDF/B-VI Release 8 (Last Release of ENDF/B-VI). International Atomic Energy Agency, Vienna, Austria, IAEA Report No. IAEA-NDS-100 Rev 11.

Lenard. R.X, and Binder, A.B., 1999. Power system requirements and concepts for a commercially viable lunar base architecture. In: El-Genk, M.S. (Ed.), Space Technology and Applications International Forum (STAIF-1999). AIP Conference Proceeding 458. American Institute of Physics, Melville, NY, 1647-1652.

Liscum-Powell and El-Genk, 1994. Options for Enhanced Performance of Pellet Bed Reactor Bimodal System. In: 30th Joint Propulsion Conference and Exhibit, Indianapolis, IN, USA. Paper No. AIAA 94-3167

Littman, F.D., 1992. Power System Commonality Study (Task Order No. 10, Subtask 1). NASA Contractor Report CR–190765.

Lowman, P.D, 1985. Lunar Bases: A Post-Apollo Evaluation, In: Mendell, W.W. (Ed.), Lunar Bases and Space Activities of the 21st Century, Lunar and Planetary Institute, Houston TX. 35-46

Lundberg, L.B., 1981. A Critical Evaluation of Molybdenum and Its Alloys for Use in Space Reactor Core Heat Pipes. Los Alamos Scientific Laboratory, Los Alamos, NM. LA-8685-MS,

Lyon, R.N., 1949. Forced Convection Heat Transfer Theory and Experiments with Liquid Metals. Oak Ridge National Laboratory, Oak Ridge, ORNL-361.

MacFarlane, R.E, Talou, P., 2005. DOPPLER: A Utility Code for Preparing Customized Temperature-Dependent Data Libraries for the MCNP Monte Carlo Transport Code.

Margolin, B.Z., Fomenko, V.N., Sorokin, A.A., 2010. Embrittlement and fracture toughness of highly irradiated austenitic steels for vessel internals of WWER type reactors. Strength and Materials 42 (3), 258–271.

Mason, L., 2006. A Comparison of Fission Power System Options for Lunar and Mars Surface Applications. NASA Glenn Research Center, NASA/TM-2006-214120.

Mason, L., Poston, D., Qualls, L., 2008. System Concepts for Affordable Fission Surface Power. NASA Glenn Research Center, NASA/TM-2008-215166.

Matsumoto, S., Namba, H., Kai, Y., & Yoshida, T., 1992. Concrete structure construction on the Moon, In NASA. Johnson Space Center, The Second Conference on Lunar Bases and Space Activities of the 21st Century, Volume 2 (SEE N93-13972 03-91), 493-496

McCoy, H.E., King, J.F., 1985. Mechanical Properties of Inconel 617 and 618. Oak Ridge National Laboratory, Oak Ridge, TN, USA, ORNL/TM-9337.

McKay, D.S. et al., 1994. JSC-1: a new lunar soil simulant. In: Galloway, R.G., Lokaj, S. (Eds.), Engineering, Construction, and Operations in Space IV, vol. 2. American Society of Civil Engineers, New York, New York, 857–866.

Menter, F.R., 1994. Two-equation eddy-viscosity turbulence modeling for engineering applications. AIAA J. 32 (8), 1598–1605.

Meyer, M.K., Fielding, R., Gan, J., 2006. Fuel Development for Gas-Cooled Fast Reactors. Idaho National Laboratory, Idaho Falls, ID, USA, INL/CON-06-11085.

Morley, N. J., and El-Genk, M. S., 1994. Thermal-Hydraulic Analysis of the Pellet Bed Reactor for Nuclear Thermal Propulsion, Nuclear Engineering and Design, 149, 387-400.

Mosteller, R.D., MacFarlane, R.E., Little, R.C., White, M.C., 2003. Analysis of hot and cold kritz criticals with MCNP5 and temperature-specific nuclear data libraries. In: Proceedings of the Advances in Nuclear Fuel Management III (ANFM). American Nuclear Society, USA, ID:700296/ISBN:0-89448-670-5.

Nikitin, V.P., Ogloblin, B.G., Sokolov, E.N., Klimov, A.V., Barabanshchikov, A.A., Ponomarev-Stepnio, N.N., Kukharkin, N.F., Usov, V.A., NikolaevYu, V., 2000. ‘‘Yenisei’’ space nuclear power system. Atomic Energy 88 (2), 98–110.

Papike, J.J., Simon, S.B., Laul, J.C., 1982. The lunar regolith: chemistry, mineralogy and petrology. Reviews of Geophysics and Space Physics 20, 761–826.

Pelowitz, D.B. et al., 2010. MCNPX 2.7.C Extensions. Los Alamos National Laboratory, Los Alamos, NM. LA-UR- 10-00481.

Pelowitz, D.B. et al., 2011. MCNPX 2.7.E Extensions. Los Alamos National Laboratory, Los Alamos, NM. LA-UR- 11-01502.

Pham, T.T., and El-Genk, M.S., 2009. “Dose estimates in a Lunar Shelter with Regolith Shielding,” Acta Astronautica 64, 697-713.

Pham, T.T., and El-Genk, M.S., 2010. “Shielding Electronic Devices from Monoenergetic 100 MeV protons,” J. Nuclear Science and Engineering 166, 58-72.

Polsgrove, T., Button, R., Linne, D., 2009. In: Altair Lunar Lander Consumables Management. AIAA SPACE 2009 Conference & Exposition, AIAA, Washington, DC. Paper No. AIAA 2009-6589

Poston, D.I., Kapernick, R.J., Guffee, R.M., 2002. Design and analyses of the SAFE-400 space fission reactor. In: El-Genk, M.S. (Ed.), Space Technology and Applications International Forum (STAIF-2002). Conference Proceeding 608. American Institute of Physics, Melville, NY, 578–588.

Poston, D.I., and Marcille, T.F., 2006. Design Options to Reduce Development Cost of First Generation Surface Reactors. In: El-Genk, M.S. (Ed.), Space Technology and Applications International Forum (STAIF-2006), Conference Proceeding 813. American Institute of Physics, Melville, New York, 281-288.

Poston, D.I., Trellue, H.R., 1999. User's Manual, Version 2.0, for Monteburns, Version 1.0. Los Alamos National Laboratory, Los Alamos, NM. LA-UR-99-4999.

Reynolds, A.J., 1975. The prediction of turbulent Prandtl and Schmidt numbers. International J. Heat and Mass Transfer 18, 1055–1069.

Rodi, W., 1991. Experience with two-layer models combining the k–ε model with a one-equation model near the wall. In: 29th Aerospace Sciences Meeting, Reno, NV, January 7–10. Paper No. AIAA 91-0216.

Rogozkin, B.D., Stepennova N.M. and Proshkin, A.A., 2003. Mononitride fuel for Fast Reactors, Atomic Energy, 95, 3, 624-636.

Ross, S.B., El-Genk, M.S., Matthews, R.B., 1988. Thermal conductivity correlation for uranium nitride fuel between 10 K and 1923 K. J. Nuclear Materials 151, 313-317.

Ross, S.B., El-Genk, M.S., Matthews, R.B., 1990. Uranium nitride fuel swelling correlation. J. Nuclear Materials 170 (2), 169-177.

Rubel, H., Marschke, D., Tautz, J., Micheel, G., 1989. Inconel X-750 as material for core internals and core components – status of in-service experience and replacements at Siemens KWU Group. J. Nuclear Engineering and Design 112, 329–336.

Schriener T.M., El-Genk M.S., 2009a. Methods for determining operation life and reactivity depletion for space reactors with fast energy spectra, Progress in Nuclear Energy 51 (2), 366-373.

Schriener T.M., El-Genk M.S., 2009b. Reactivity control options of space nuclear reactors, Progress in Nuclear Energy 51 (3), 526-542.

Schriener T.M., El-Genk M.S., 2011. A neutronics analysis of long-life, sectored compact reactor concepts for lunar surface power, Progress in Nuclear Energy 53 (1), 106-118.

Schriener T.M., El-Genk M.S., 2012a. Neutronics and thermal–hydraulics analysis of a liquid metal fast reactor for expandable lunar surface power, Annals of Nuclear Energy 41, 48-60.

Schriener T.M., El-Genk M.S., 2012b. Thermal-hydraulics and safety analysis of sectored compact reactor for lunar surface power, In: Proceedings of ICAPP ’12, Chicago, USA, June 24-28, 2012.

Schriener T.M., El-Genk M.S., 2012c. Fuel loading of PeBR for a long operation life on the lunar surface, In: Proceedings of ICAPP’12, Chicago, USA, June 24-28, 2012. Paper No. 12044.

Schriener T.M., El-Genk M.S., 2013. Inherently safe and long-life fission power system for lunar outposts, J. British Interplanetary Society 66, 388-394.

Schriener T.M., El-Genk M.S., 2014a. Comparative CFD analyses of liquid metal cooled reactor for lunar surface power, J. Nuclear Engineering and Design 280, 105-121.

Schriener T.M., El-Genk M.S., 2014b. Thermal-hydraulics and safety analyses of the Solid Core-Sectored Compact Reactor (SC-SCoRe) and power system, Progress in Nuclear Energy 76, 216-231

Skupinski, E., Tortel, J., Vautrey, L., 1965. Determination des coefficients de convection d'un alliage sodium-potassium dans un tube circulaire. International J. Heat and Mass Transfer 8, 937–951.

SolidWorks, 2006. COSMOS FloWorks Fundamentals. SolidWorks Corporation.

Spalart, P.R., Jou, W.H., Strelets, M., Allmaras, S.R., 1997. Comments on the feasibility of LES for wings, and on a hybrid RANS/LES approach. In: Liu, C., Liu, Z. (Eds.), 1st AFOSR Int. Conf. on DNS/LES, Advances in DNS/LES. Greyden Press, Columbus, OH. August, 4–8 1997.

Special Metals Corporation, 2004. Inconel Alloy X-750. Special Metals Corporation, Huntington, WV, USA.

Spriggs, G.D., Busch, R.D., Campbell, J.M., 2001. Calculation of the delayed neutron effectiveness factor using ratios of k-eigenvalues. Annuls of Nuclear Energy 128, 477–478.

Stacey, W.M., 2001. Nuclear Reactor Physics. Wiley and Sons, New York, NY. 140.

"Standards for Protection Against Radiation", 10 C.F.R. part 20, section 1003, 2002

"Standards for Protection Against Radiation", 10 C.F.R. part 20, section 1301, 2002

Staub, D. W., 1967. SNAP 10A Summary Report, Atomic International Report NAA-SR-12073

Subbotin, V.I. et al., 1962. A study of heat transfer to sodium in tubes. Atomic Energy 13(4), 991–994.

Sun, C., Hui, R., Qu, W., Yick, S., 2009. Progress in corrosion resistant materials for supercritical water reactors. Journal of Corrosion Science 51, 2508–2523.

The MathWorks, Inc., 2005. Simulink– Simulation and Model Based Design, 11.

Touloukian, Y.S. (Ed.), 1970. The Thermophysical Properties of Matter - the TPRC Data Series - Volume 1: Thermal Conductivity Metallic Elements and Alloys. Plenum Press, New York, NY, 222-227.

Tournier, J.-M., El-Genk, M.S., 2006. Liquid metal loop and heat pipes radiator for space reactor power systems. J. Propulsion and Power 22 (5),1117–1134.

United Nations, 2002. United Nations Treaties And Principles On Outer Space, United Nations Publication ST/Space/11, New York.

Weeks, J.R., Klamut, C.J., Gurinsky, D.H., 1966. Corrosion by the Alkali Metals. In: Proceedings of IAEA Symposium on Alkali Metal Coolants, Vienna, Austria, 3-21.

Wilcox, D.C., 1998. Turbulence Modeling for CFD, 2nd ed. DCW Industries, Inc.

Winsche,W.E., 1965. Annual Report Nuclear Engineering Department, December 31, 1964. Brookhaven National Laboratory, Upton, NY, BNL 900 (S-67), 139-140.

Wolfstein, M., 1969. The velocity and temperature distribution in one-dimensional flow with turbulence augmentation and pressure gradient. International J. Heat Mass and Transfer 12, 301–318.

Wollman, M.J., Zika, M.J., 2006. Prometheus Project Reactor Module Final Report. Knolls Atomic Power Laboratory and Bettis Atomic Power Laboratory. SPP-67110–0008.

X-5 Monte Carlo Team, 2003. MCNP – A General Monte Carlo N-Particle Transport Code, Version 5 – Volume II: Users Guide. Los Alamos National Laboratory, Los Alamos, NM. LA-CP-03-0245.